Normandie Université

THÈSE

Pour obtenir le diplôme de doctorat

Spécialité Energétique

Préparée à l'INSA de Rouen Normandie

Investigations of yawed offshore wind turbine interactions through aero-servo-elastic Large Eddy Simulations

présentée et soutenue par

Félix HOUTIN–MONGROLLE

Thèse soutenue publiquement le 20 juin 2022 devant le jury composé de		
J. N. Sørensen	Professeur à l'Université technique du Danemark, DTU	Rapporteur
P. Chatelain	Professeur à l'Université catholique de Louvain-la-Neuve, iMMC, TFL	Rapporteur
G. Pinon	Professeur à l'Université du Havre, LOMC	Examinateur
N. Mazellier	Professeur à l'Université d'Orléans, PRISME	Examinateur
L. Bricteux	Professeur à l'Université de Mons, UMONS	Examinateur
P. Benard	Maitre de Conférence à l'INSA de Rouen Normandie, CORIA	Encadrant de thèse
V. Moureau	Chargé de recherche CNRS, CORIA	Encadrant de thèse
J. Reveillon	Professeur à l'Université de Rouen Normandie, CORIA	Directeur de thèse

Thèse dirigée par Pierre Bénard, Vincent Moureau et Julien Reveillon, laboratoire CORIA (UMR 6614 CNRS)

INSA INSTITUT NATIONAL DES SCIENCES APPLIQUÉES ROUEN NORMANDIE

ED PSIME

CORIA UMR 6614

Abstract: Investigations of yawed offshore wind turbine interactions through aero-servo-elastic Large Eddy Simulations

In the context of maximizing the electrical power production of offshore wind farms, new active control strategies become more and more common. The use of yaw misalignment on upstream turbines to reduce wake interactions and the associated power losses seems a promising technique. Yet, it highlights the necessity of a proper understanding of the aerodynamics of yawed wind turbine wakes. Given the constant growth of computational resources, the emulation of such flows through numerical simulations tends to be a suitable solution. Nevertheless, the investigation of offshore wind turbines with rotor diameters reaching up to 200 meters lacks reliable flow diagnostics as it brings new challenges. The interactions between the flow and the wind turbine structure generate large deformations on the blades. Moreover, even if an active yaw control strategy is applied, each wind turbine possesses a controller that regulates the operating conditions based on the incoming wind. Simulating large rotors, therefore, requires the use of a multiphysical approach. To this end, this doctoral thesis is at the crossroads of three engineering and physics fields: aerodynamics, control, and structural mechanics. This work presents the coupling of these three components, resulting in an aero-servo-elastic simulation tool. It thus contributes to understanding the behavior of the wake of yaw misaligned turbines in close to real scenarios.

For aerodynamics, the wind turbine wake is investigated thanks to Large-Eddy Simulations (LES). Numerical simulations give access to a set of important parameters to measure the relevance of yaw misalignment. However, the aerodynamics surrounding a wind turbine is complex as it can generate large flow structures downstream of the rotor. The interaction between the blades and the fluid impacts the generated wake, which is transported over large distances. This underlines the multi-scale nature of the wake. Even if the computational resources grow, the simulation of the small turbulent scales generated within the blade boundary layer remains too expensive to investigate the wind turbine wake behavior. The LES is thus coupled with the Actuator Line Method (ALM) to reduce this cost. The ALM allows the modeling of the forces generated by each airfoil section of the blades, reducing the range of resolved scales. Nevertheless, the simulation of the wake and its interaction with downstream turbines necessitates using a large number of processors in parallel. The Computational Fluid Dynamics library YALES2, developed at CORIA laboratory, features massively parallel high-order numerical methods for solving the low-Mach number Navier-Stokes equations on unstructured grids. Such an environment requires the proper implementation and optimization of the ALM to achieve efficient computational performances.

Structural deformations and control are investigated using the nonlinear servo-elastic software BHawC, developed at Siemens Gamesa Renewable Energy. It is based on a finite beam element model to simulate the dynamic response and calculate the loads on three-bladed wind turbines. The control is provided through the coupling to an actual industrial turbine controller. This software is mainly used for the design and certification of wind turbines, and it is continuously being validated against measured data.

By coupling these codes, this doctoral thesis aims at investigating the wake of yawed offshore wind turbine interactions through aero-servo-elastic Large Eddy Simulations. The thesis is divided into three parts:

(i) The first part is the refactoring, optimization, and validation of the ALM in the massively parallel CFD library. The framework is validated over a wind tunnel scenario. This is done from the generation of background turbulence towards the wake interaction of a two

wind turbine array with the first operating with yaw misalignment. The results are then compared to experimental measurements.

(ii) Then, the development of quantitative post-processing over the wake envelope is presented. The methodology is based on Accurate Conservative Level Set functions to track the wake and generate streamtubes surrounding the wind turbines. Budgets of mean kinetic energy and mean momentum are applied to these envelopes to understand how the wake recovers. This methodology allows the proper comparison of integrated quantities and wakes envelope topology for various operating conditions, i.e., yaw misalignment and background turbulence intensity.

(iii) The last part presents the coupling between the ALM-LES framework with the servo-elastic code. This methodology is applied to actual industrial offshore wind turbines in a wake interactions scenario. Several cases are investigated to quantify the impact of yaw misalignment on structural deformations and wake quantities.

Keywords: Wake Interaction, Yaw Misalignment, Actuator Line Method, Incompressible flow, Large-Eddy Simulation, Finite Volume, Servo-Elasticity, Finite Element, Streamtubes, Budgets

Résumé : Simulation aux grandes échelles des intéractions de sillages d'éoliennes en dérapage avec couplage aéro-servo-élastique

Dans le contexte de la maximisation de la production d'électricité des parcs éoliens offshore, de nouvelles stratégies de contrôle actif deviennent de plus en plus courantes. La mise en dérapage d'éoliennes situées en amont pour réduire les interactions de sillage et les pertes de puissance associées semble une technique prometteuse. Pour y parvenir il est nécessaire de bien comprendre l'aérodynamique des sillages d'éoliennes en dérapage. Compte tenu de la croissance constante des ressources informatiques, l'émulation de tels écoulements par des simulations numériques tend à être une solution appropriée. Néanmoins, l'étude de l'écoulement autour des éoliennes offshore, avec des diamètres de rotor atteignant 200 mètres, manque encore a l'appel car elle comporte de nouveaux défis. Premièrement, les interactions entre l'écoulement et la structure de l'éolienne génèrent de grandes déformations sur les pales. De plus, même si une stratégie active de contrôle de l'angle de dérapage est appliquée, chaque éolienne possède un contrôleur qui régule ses conditions d'exploitation en fonction du vent. La simulation de grand rotors nécessite donc une approche multiphysique. À cette fin, cette thèse de doctorat est à la croisée de trois domaines d'ingénierie et de physique : l'aérodynamique, le contrôle et la mécanique structurelle. Ce travail présente le couplage de ces trois composants, résultant en un outil de simulation aéro-servo-élastique. Celui-ci contribue ainsi à comprendre le comportement du sillage d'éoliennes en dérapage dans des scénarios proches de ceux réels.

Concernant l'aérodynamique, le sillage des éoliennes est étudié grâce aux simulations aux grandes échelles (SGE). Les simulations numériques donnent accès à un ensemble de paramètres importants pour mesurer la pertinence de l'angle de dérapage. Cependant, l'aérodynamique entourant une éolienne est complexe car elle peut générer de grandes structures d'écoulement en aval du rotor. L'interaction entre les pales et le fluide a un impact sur le sillage généré, qui est transporté sur de grandes distances. Cela souligne la nature multi-échelle du sillage. Même si les ressources informatiques augmentent, la simulation des petites échelles turbulentes générées dans la couche limite des pales reste trop coûteuse pour étudier le comportement du sillage d'éoliennes. Les rotors sont donc modélisé à l'aide de lignes actuatrices (ALM) pour réduire ce coût. Cette méthode permet de modéliser les forces générées par chaque section de profil des pales, réduisant ainsi la gamme des échelles résolues. Néanmoins, la simulation du sillage et son interaction avec les turbines en aval nécessitent l'utilisation d'un grand nombre de processeurs en parallèle. L'outil de résolution d'écoulement YALES2, développée au laboratoire CORIA, propose des méthodes numériques massivement parallèles pour résoudre les équations Navier-Stokes à faible nombre de Mach sur des maillages non structurées. Un tel environnement nécessite la mise en œuvre et l'optimisation appropriées de l'ALM pour obtenir des performances de calcul efficaces.

Les déformations structurelles et le contrôle sont étudiés à l'aide du logiciel non linéaire servo-élastique BHawC, développé chez Siemens Gamesa Renewable Energy. Il est basé sur un modèle à éléments finis pour simuler la réponse dynamique de la structure et calculer les charges sur les éoliennes à trois pales. Le contrôle est assuré par le couplage au contrôleur utilisé sur des éoliennes industrielle existantes. Ce logiciel est principalement utilisé pour la conception et la certification des éoliennes, et il est continuellement validé par rapport aux données mesurées.

En couplant ces codes, cette thèse de doctorat vise à étudier les interactions de sillage d'éoliennes offshore en dérapage au moyen de simulations aux grandes échelles aéro-servo-élastiques. Cette thèse est donc divisée en trois parties :

(i) La première partie est le refactoring, l'optimisation et la validation de l'ALM dans la

bibliothèque massivement parallèle YALES2. L'implémentation est validé sur un scénario en soufflerie. Cette application vise a étudier la génération de turbulence de soufflerie puis l'interaction de sillage d'un réseau de deux éoliennes avec la première en dérapage. Les résultats sont ensuite comparés à des mesures expérimentales.

(ii) Ensuite, le développement de post-traitement quantitatif sur l'enveloppe sillage est présenté. La méthodologie est basée sur les fonctions Accurate Conservative Level Set pour suivre le sillage et générer des tubes de courant autour des éoliennes. Des bilans d'énergie cinétique moyenne et de quantité de mouvement sont appliqués à ces enveloppes pour comprendre comment le sillage se rétablit de son déficit de vitesse. Cette méthode permet de comparer correctement les quantités intégrées et la topologie de l'enveloppe de sillage pour diverses conditions d'exploitation, c.-à-d., l'impact de l'angle de dérapage et intensité turbulente de l'environnement extérieur.

(iii) La dernière partie présente le couplage entre le code ALM-SGE et le code servo-élastique. Cette méthodologie est appliquée aux éoliennes industrielles offshore dans un scénario d'interactions de sillage. Plusieurs cas sont étudiés pour quantifier l'impact de l'angle de dérapage sur les déformations structurelles ainsi que sur le sillage.

Mots-clés : Interactions de Sillages, Eoliennes en Dérapage, Méthode de la Ligne Actuatrice, Fluide Incompressible, Simulation aux Grandes Echelles, Volumes Finis, Interactions Fluides Structures, Servo-Elasticité, Tubes de Courant, Bilans

Remerciements

Dans un premier temps je tiens à remercier les éminents membres de mon jury pour avoir lu et questionné mes travaux de thèse réalisés durant ces dernières trois années et demie. Un grand merci à Jens Nørkær Sørensen et Philippe Chatelain pour avoir été les rapporteurs de cette thèse. Vos retours sur le manuscrit ont été très constructif ainsi que les questions, discussions qui en ont suivis. C'était pour moi un honneur d'avoir vos avis sur mon travail et je vous en remercie énormément. Un grand merci à Gregory Pinon pour avoir été le président de ce jury de thèse. Tu as eu la lourde tâche de réguler le temps lors de cette séance de questions bien longue, je te remercie fortement pour cette charge supplémentaire. Enfin merci aux deux examinateurs restant de ce jury, Nicolas Mazellier et Laurent Bricteux pour leurs questions et la discussion qui en a suivi.

Enfin, je rentre dans le gros du sujet, j'en viens à mes encadrants légendaires ! Un grand merci à Julien Réveillon pour avoir accepté d'être mon directeur de thèse ainsi que pour la confiance que tu as su me faire pendant ces trois années. Ensuite, merci à toi Vincent Moureau pour ton encadrement, ta rigueur et les plus ou moins longues discussions sur les tubes de courants et autres bilans. J'espère ne pas t'avoir fait trop de frayeurs capillaires tout de même. Ça été un plaisir de travailler avec toi au cours de ces dernières années, merci pour tout. Ghislain Lartigue, ou Guylaing pour les intimes, tu es l'un des piliers qui fait que les thèses numériques dans l'équipe se passent si bien ! Les bugs et autres n'ont plus de secret pour toi et quand on veut faire un couplage c'est bien pratique. Je garderai sous silence tous les merveilleux souvenirs de soirée ainsi que le nom de ce superbe poisson d'anniversaire qui t'a été offert. Merci pour tout, sauf peut-être certains shots. Enfin, je fini par toi Pierre Bénard ! Jeune maitre de conférences que tu étais quand je suis arrivé, tu as su montrer une belle progression tout au long de ces trois années. Blague à part, merci beaucoup pour tout l'investissement que tu as mis dans ma thèse, ainsi que le soutient et les super projets. La liste de bons souvenirs est longue, et je ne voudrais pas rédiger un autre manuscrit pour les citer mais en gros c'était bien chouette ! Merci pour tout.

J'en viens maintenant à la communauté YALES2, qui dépasse les régions et frontières et qui est constitué de gens des plus intéressants et intelligents, non ce n'est pas de la lèche. Surtout lors de ces fameux Extrême CFD workshops qui nous ont emmenés dans des superbes lieux pour passer une semaine derrière un écran et surtout un accès privilégié au bar. Merci à toutes et tous ainsi que pour les discussions à la pause-café de 2h du matin. Un remerciement particulier à Renaud Mercier et Julien Leparoux mes encadrants de stage chez Safran, sans qui je n'aurai sans doute pas fait cette thèse au Coria et ne serais pas resté dans cette communauté.

J'ai aussi eu la chance de pouvoir travailler avec d'autres équipes de recherches donc : Merci aux Montois avec qui j'ai pu travailler, Laurent, Stephanie, Ulysse, Patrick. Laurent Bricteux je reviens sur toi car tu étais là aux prémices de ces 3 années de thèse, c'était très intéressant de travailler avec toi, au début comme à la fin avec le projet PRACE. Je me souviendrais beaucoup

de cette après-midi studieuse où tu faisais du playback sur Aya Na'.

Merci à toute l'équipe de Siemens (GRE) avec qui nous avons pu construire des projets et initier/développer ce fameux couplage. Plus particulièrement merci à toi Bastien Duboc pour les longues heures passées à faire des "battues" aux bugs. Enfin, merci aussi de m'avoir proposé de continuer à travailler avec vous, qui a été sans doute ma lumière au bout du tunnel qu'est la rédaction de ce manuscrit.

J'en vient maintenant aux membres du CORIA qui ont rendu cette thèse bien agréable. A partir de là je ne sais pas trop comment classer entre doctorant/post-doctorants/maitre de conférence (oui Kevin c'est toi) mais je vais essayer un truc pas trop chaotique. Je commence par les wind turbine guys, Simone et Etienne avec qui on s'est bien cassé la tête sur ce fameux couplage, c'était toujours sympa de venir discuter, encore et encore, de bras de levier, mollification et j'en passe ! Enfin j'en viens au gros de la troupe : Gab, Louise, Yann, Clément, Léa, Julien, Yacine, Patricia, Francesco, Kevin, Romain, Adrien, Pierre, Iason, Serge, Antoine, Ulysse... Je pense avoir une petite anecdote sympathique sur chacun de vous mais ça ferait trop long encore une fois. Juste, Léa, as-tu retrouvé le dernier nain ?

Je reviens quand même sur trois/quatre/cinq affreux rassemblé sous cette bannière de la KLYG, la communauté des trois pintes à jeun, les représentants du wakeboard, les habitués des sorties du Dimanche, Lundi, Mardi, Mercredi,... (vous avez l'idée). Je ne pouvais pas ne pas parler de cette fameuse sortie en bateau ou l'un de nous a fini dans le troisième "bout", mais aussi de ces concours de blanquettes et tartiflettes. C'était vraiment chouette de pouvoir s'épauler comme on l'a fait. La pellicule de mon appareil photo restera à jamais une mine d'or de souvenirs, un vrai plaisir que d'avoir passé ces trois années avec vous !

Un remerciement particulier à toi aussi Marion, tu fais partie des plus belles rencontres de cette thèse et sans qui elle n'aurait pas été la même, surtout à la fin. Un chaleureux et bienveillant Merci.

Et enfin un grand merci à ma mère, mon père, mon adelphe et Romulus. Surtout pour les années qui ont précédé cette thèse et pour tout ce soutien et ces moment chaleureux passés ensemble, pas sans hausser la voix de temps en temps quand même, on est humains !

Merci à tous ceux que j'aurai oublié par mégarde, et courage a ceux qui lieront ce manuscrit...

Contents

1 Context and objectives **1**

1.1 The global energy challenge . . . 2

1.1.1 Energy consumption and neutral carbon emission . . . 2

1.1.2 Wind Energy . . . 3

1.2 Yaw misalignment, a relevant active control strategy? . . . 7

1.2.1 Relevance of yaw misalignment configurations . . . 7

1.2.2 Aerodynamic loading of a yawed turbine . . . 8

1.2.3 Yaw impact on the wind turbine wake . . . 10

1.2.4 Active yaw control . . . 12

1.3 Aim of this thesis and manuscript content . . . 12

1.4 Publications . . . 14

1.4.1 Peer-reviewed journals and conference papers . . . 14

1.4.2 Conferences . . . 15

2 Governing equations and modeling of HAWT in incompressible flows **17**

2.1 Numerical modeling for turbulent flows . . . 18

2.1.1 Equations of conservation . . . 18

2.1.2 Turbulent flows . . . 19

2.1.3 Turbulent flow modeling approaches: RANS, LES and DNS . . . 24

2.1.4 LES filtered equations . . . 26

2.1.5 Sub-grid scale modeling for turbulence . . . 27

2.2 YALES2 CFD platform . . . 30

2.2.1 Global overview and challenges . . . 30

2.2.2 Main tools and strategies . . . 31

2.2.3 Incompressible constant density solver (ICS) . . . 32

2.3 Horizontal Axis Wind Turbine modeling . . . 35

2.3.1 Overview of the existing methods . . . 35

2.3.2 Actuator Line Method . . . 37

2.3.3 Implementation in YALES2 . . . 40

2.3.4 Optimizations and primary validations of the ALM in YALES2 . . . 42

2.4 Conclusions . . . 49

3 Application to small wind tunnel turbines **51**

3.1 Introduction . . . 52

3.1.1 Objectives . . . 52

3.1.2 Case description . . . 52

3.1.3 Numerical parameters . . . 55

3.2 Turbulence grid modeling: A dynamic actuator line method . . . 57
3.2.1 A new actuator line method-based turbulence generation approach . . . 57
3.2.2 Validation on NTNU turbulence generation passive heterogeneous grid . . 65
3.2.3 Results with heterogeneous and homogeneous passive grid . . . 72
3.3 Single Turbine configuration: wake deflection . . . 73
3.3.1 Turbine performance and loads . . . 73
3.3.2 Wake flow topology . . . 78
3.3.3 Wake destabilisation and generated turbulence . . . 86
3.4 Two Turbines configuration: wake interaction . . . 88
3.4.1 T1 wake impact on T2 loads . . . 90
3.4.2 Flow topology . . . 91
3.5 Conclusion . . . 94

4 Recovery and turbulent mixing within the yawed wind turbine wake 97
4.1 Introduction . . . 98
4.2 A level set framework for the wind turbine wake analysis . . . 98
4.2.1 Wake envelope definition . . . 98
4.2.2 Accurate conservative level set functions: a numerical tool to define the wake . . . 101
4.2.3 Parallel with the 1D momentum theory . . . 104
4.3 Application to the DTU10MW: cases overview . . . 106
4.4 Evolution of the wake topology . . . 109
4.4.1 Streamtube . . . 109
4.4.2 Turbulent mixing layer expansion for yawed wind turbines . . . 112
4.5 Budgets applied on streamtubes . . . 119
4.5.1 The wake recovery explained from Mean Kinetic Energy budget . . . 120
4.5.2 The wake deflection explained from Mean Momentum budget . . . 126
4.5.3 Comparison to the 1D momentum theory . . . 128
4.6 Conclusions . . . 130

5 Aero-servo-elastic simulations of yawed wake interactions 133
5.1 Introduction . . . 134
5.2 Coupling to a structural solver . . . 135
5.2.1 A Aero-servo-elastic solver: BHawC . . . 135
5.2.2 Coupling between YALES2 and BHawC . . . 136
5.3 Case and Numerical parameters . . . 143
5.3.1 Industrial wind turbine: SWT-6.0-154 . . . 143
5.3.2 Two turbine configuration . . . 143
5.3.3 Numerical setup . . . 144
5.4 Two aligned wind turbines: Reference case . . . 150
5.4.1 Singular events occurring in the flow and wind turbines performances . . . 150
5.4.2 Flow topology . . . 155
5.4.3 Structural deformations . . . 157
5.4.4 Discussion . . . 162
5.5 Influence of yaw misalignement . . . 162
5.5.1 Flow topology . . . 163
5.5.2 Streamtubes . . . 164

5.5.3 Mean kinetic energy budgets . . . 169
5.5.4 Turbines response and performances . . . 172
5.5.5 Loads repercussions on structural deformations and fatigue . . . 173
5.6 Conclusions . . . 180

6 Conclusions and perspectives **183**
6.1 Conclusions . . . 183
6.1.1 Implementation, optimizations, and validations of the Actuator Line Method in YALES2 . . . 184
6.1.2 Quantify the yawed wind turbine wake recovery and the turbulent mixing layer expansion . . . 185
6.1.3 Multiphysical approach by coupling ALM-LES to a servo-elastic solver . . . 186
6.2 Perspectives . . . 188
6.2.1 Optimizations and improvements of the framework . . . 188
6.2.2 Wake investigations and models . . . 188
6.2.3 Extend the solved physics and further investigation of strategies relying on yaw misalignement . . . 189

Appendices **191**
A. Wind turbine reference frames and transformations . . . 191
A.1 Rotor reference frame . . . 191
A.2 Blade basis . . . 192
A.3 Element basis . . . 194
B. High fidelity mesh generation . . . 195
B.1 What is important on a mesh for wind turbines applications ? . . . 195
B.2 Methodology and applications . . . 195
C. Summary of research on HAWT rotors in yaw . . . 198

Figures index **201**

Table index **202**

References **205**

Chapter 1

Context and objectives

This chapter introduces the context and scope of this thesis. The global energy challenge that societies are facing is rapidly discussed. After a quick introduction on the relevance of offshore wind energy, the notion of wake interaction and active yaw control strategies is presented. Then, the fundamental physics of Horizontal Axis Wind Turbines aerodynamics under yaw misalignement is reviewed concerning some of the latest scientific research covering both measurements and numerical modeling. To follow up, the aim of this thesis and the manuscript content is shown. A list of the publications and attended conferences during this thesis is also given.

Contents

1.1 The global energy challenge 2
1.1.1 Energy consumption and neutral carbon emission 2
1.1.2 Wind Energy 3
1.2 Yaw misalignment, a relevant active control strategy? 7
1.2.1 Relevance of yaw misalignment configurations 7
1.2.2 Aerodynamic loading of a yawed turbine 8
1.2.3 Yaw impact on the wind turbine wake 10
1.2.4 Active yaw control 12
1.3 Aim of this thesis and manuscript content 12
1.4 Publications 14
1.4.1 Peer-reviewed journals and conference papers 14
1.4.2 Conferences 15

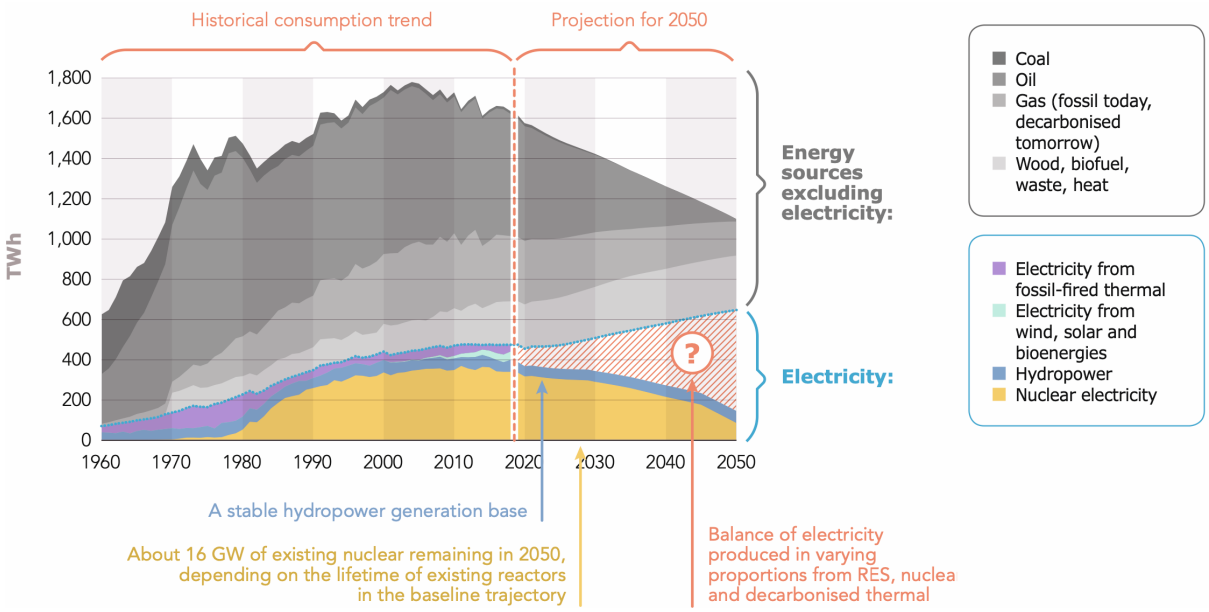

Figure 1.1: Trend in total electricity consumption and final energy consumption for other energies in France, taken from RTE's report [4].

1.1 The global energy challenge

Energy production and consumption have always been critical aspects for societies. It is fundamental to economic and social development. At the dawn of the 21st century, communities face one of the toughest challenges ever: the stability of the energy supply. The world energy mix relies in the majority on fossil fuels, reaching more than 80% of the total consumption in 2020 (oil, coal, and gas) [1]. In France, the challenge to achieve energy independence started in the 70's following the market oil shocks and relying on its nuclear electricity program. The notion of energy independence becomes more and more critical as the successive energy crises add fluctuations in energy product prices and impact the geopolitical stage, e.g. Nord Stream pipelines for gas importation between Russia and European countries.

Furthermore, the energy challenge is bonded with the notion of global warming or, more recently, "climate change". The major problem with the actual consumption of fossil fuels relies upon greenhouse gas and carbon emissions. The worldwide scientific community is clear on this point: to limit the potentially catastrophic effects of climate change, it is mandatory to reduce these emissions. In this matter, 196 nations gathered and agreed to reach carbon neutrality by 2050 through the Paris agreement in December 2015 [2]. These agreements targeted to limit the increase of global temperature to 2°C by 2100. Recently, the Intergovernmental Panel on Climate Change (IPCC) [3] reminded, once again, of the urge to take action.

1.1.1 Energy consumption and neutral carbon emission

The notion of energy consumption does not only rely on electric production. More than 70% of the energy consumption in France is not related to electricity; even more, 60% of this global energy consumption is related to fossil fuels. This consumption is due to transport, heat, and industry. The 30% leftover is the electricity production based at 70% on nuclear energy, see **Fig. 1.1**. In the report: "Energy Pathways to 2050" [4], France transmission system operator (Réseau de Transport d'Électricité - RTE) recall that to uphold its climate commitments, France must move away from the fossil fuel energy on which its current economy and lifestyles are built.

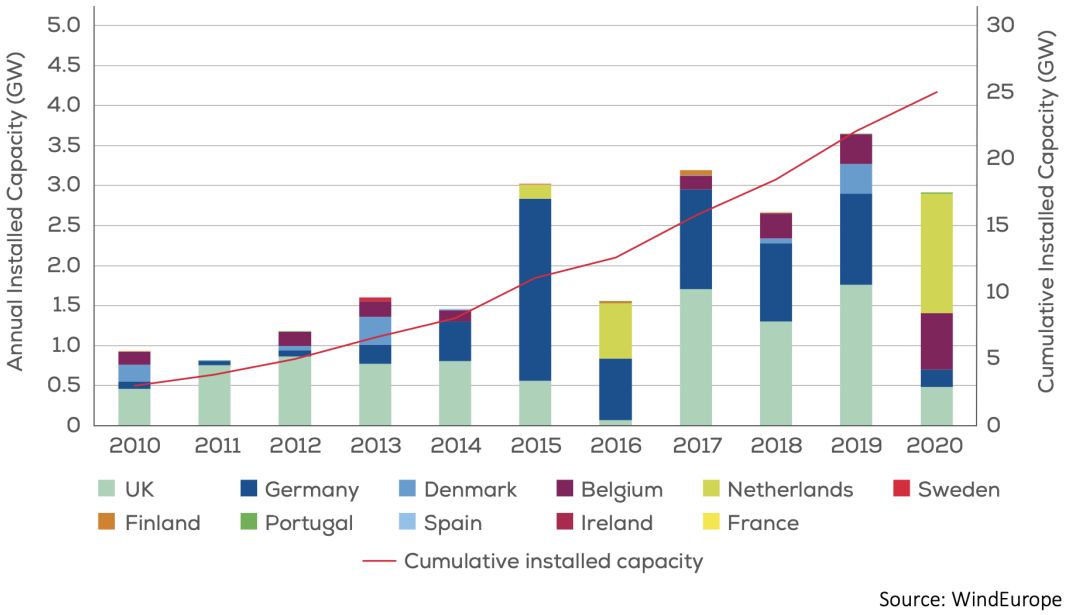

Figure 1.2: Annual offshore wind installations by country (left axis) and cumulative capacity (right axis) (GW) [5].

The key to reaching this neutral carbon emissions target relies on reducing energy consumption through energy efficiency and sufficiency. The central aspect would be the electrification of certain end-use such as electric vehicles, heat-pump which have energy efficiency higher than internal combustion engines, and fossil fuel-fired boilers. The consequence would be a lower energy consumption but an increase in electricity demand. The RTE reports present different scenarios matching the future electricity demands, considering many parameters, from economic to technological improvements. These scenarios are either a mix of renewable energy (solar and wind) and nuclear (historical and new) or only renewable energy. In these various scenarios, the installed wind energy capacity ranges from 25% to more than 50% of the expected electrical production, between 65 GW and 136 GW. These percentages are for onshore and offshore wind energy, yet, at the moment the actual installed capacity is purely onshore and is slightly above 18 GW. In comparison to the neighboring countries, this number is relatively small. Indeed, significant investments have been made in Europe for wind energy in the past ten years. This can be observed from the growth from 25 GW [5] capacity of installed offshore wind energy business in Europe. **Fig. 1.2** depicts the evolution of installed offshore wind installations per country in Europe, and France is taking a rough start. Yet, there are four offshore wind projects in France at the moment: three in the channel, Dunkirk (600 MW), Fécamp (500 MW), Courseulles (450 MW), and one on the Atlantic coast at Saint-Nazaire (480 MW). These wind farms will start to produce between 2022 and 2024. Since more and more projects of this size will arise in the next decade, it is fundamental to investigate and tackle the dilemmas occurring in these wind farms.

1.1.2 Wind Energy

In the past 30 years, the size of wind turbine rotors increased rapidly from about 15 m in diameter having a capacity of 50 kW to about 200 m for a capacity of 15 MW. These augmentations are the consequences of three design objectives: maximize the energy yields, reduce the costs and maximize the lifetime. But before digging more into the subject, let us recall the wind turbine

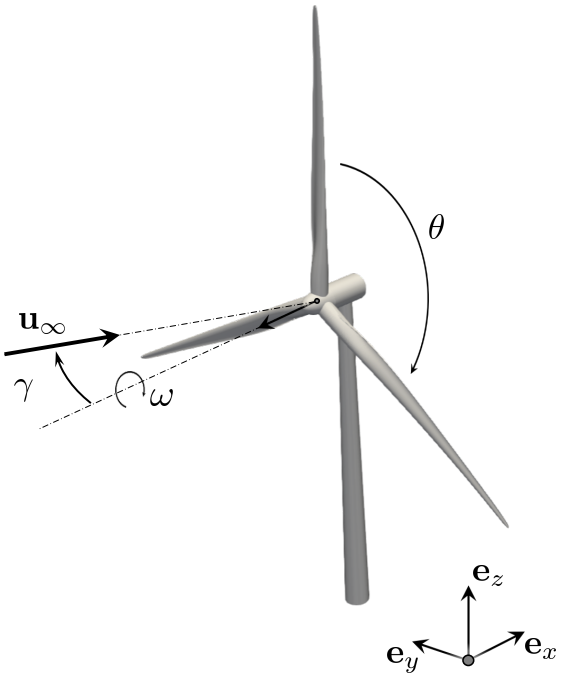

Figure 1.3: Scheme of a horizontal axis wind turbine operating with a yaw angle γ under inflow $\mathbf{u}_\infty$ at a constant rotation speed ω.

principles.

1.1.2.1 Wind turbines principles

A wind turbine converts the kinetic energy from the wind to electrical energy. The power which can be extracted is proportional to the cube of the wind speed. However, there is a theoretical limit to the power that the turbine can extract. This is known as the Betz limit. This limit was derived by Betz [6] to correspond to 59% of the maximum available power which the turbine can extract. The efficiency of a wind turbine is called the power coefficient and is defined by the following:

$$C_P = \frac{P}{\frac{1}{2}\rho U_\infty^3 A}\,, \tag{1.1}$$

where P is the turbine power, ρ is the fluid density, U_∞ is the wind velocity, and A is the rotor area. Due to various practical reasons, only a fraction of the Betz limit can be exploited. Some reasons for this reduction in the overall efficiency of the turbines are mostly associated with the wind resource itself and include wind shear [7, 8], wind turbulence [9, 10], and yaw misalignment [11]. The following gathers various definitions around wind turbines

HAWT: Acronym for Horizontal Axis Wind Turbine. Other types exist, such as Vertical Axis Wind Turbine (VAWT), but only HAWTs are investigated in this thesis.

Yaw misalignment: Yaw occurs when the wind direction on the horizontal plane is not perpendicular to the rotor plane of the wind turbine. When the HAWT operates with non-zero yaw angle, the average power extracted by the turbine reduces compared to when the wind is perpendicular to the rotor plane. This yawed flow situation is depicted in **Fig. 1.3** where γ is the yaw angle. The blade will experience a varying relative velocity and angle of attack with the azimuthal blade position, leading to an unsteady aerodynamics problem.

Tilt misalignement: In a similar way to yaw, tilt occurs when the wind direction on the vertical plane is not perpendicular to the rotor plane of the wind turbine. This parameter cannot be tuned on actual wind turbines, and this angle is often set at $\sim 5^\circ$ to prevent the blades from colliding with the tower.

Wake: Wind turbines extract energy from the wind, and the wake results from this energy absorption. It can be represented by an area downstream of the wind turbine where wind speed is reduced and turbulence is increased. The wake spreads and recovers towards free stream conditions as the flow proceeds downstream. The wake effect is the aggregated influence on the energy production of the wind farm, which results from the changes in wind speed caused by the impact of the turbines on each other. It is crucial to consider the wake effects of neighboring turbines to optimize power production.

Active and passive control: A wind turbine needs to adapt to wind conditions, and this is why the notion of control is essential [12]. The two primary goals are to maximize power production and minimize load-induced fatigue. Turbine control can be divided into passive control and active control. A considerable amount of research has been performed in these two areas. Passive techniques improve turbine performance and/or reduce loads without external energy expenditure. This includes the yaw movement of a free-to-yaw downwind rotor and aeroelastic blade twist. Active control requires external energy or auxiliary power. Therefore, more in-depth studies must be conducted to ensure that the increase in energy output can offset the external energy required for load control and increase turbine capital and O&M costs. Some traditional wind turbine active control methods are blade pitch, variable-speed rotors, and yaw alignment with the wind.

Wind farm: Wind farms represent a local gathering of wind turbines where wind resources are sufficient. They are often located in remote areas, far from cities and habitations where electricity is needed. Transmission lines must be built to bring the electricity from the wind farm to the town.

As mentioned before, two large wind energy categories are present in the world, the onshore and offshore, more details are presented below.

1.1.2.2 Onshore wind energy

Onshore wind energy refers to wind farms or single wind turbines located on land. In 2004, the available worldwide wind energy on land is estimated to be $96\,\mathrm{PWh.year^{-1}}$ [13]. Based on the technological evolutions and spatio-temporal database, a recent study from 2017 reevaluated this estimation to $580\,\mathrm{PWh.year^{-1}}$ [14]. In 2020, the global energy consumption from all sources was evaluated at $171.3\,\mathrm{PWh.year^{-1}}$ in the world by the IEA. The wind energy could respond to the actual demand, yet the repartition of the suitable location is heterogeneous. For instance, the European generation potential based on the season is evaluated between $17\,\mathrm{PWh.year^{-1}}$ [14] and $45\,\mathrm{PWh.year^{-1}}$ [15] while the consumption is $58.3\,\mathrm{PWh.year^{-1}}$. Given the current technological advances, onshore wind energy would not be sufficient in Europe. Furthermore, several constraints are present for onshore wind turbines. First of all, wind resource development might not be the most profitable use of the land. Land suitable for wind-turbine installation must compete with alternative uses for the land, which might be more highly valued than electricity generation. Although wind power plants have relatively little impact on the environment compared to conventional power plants, concern exists over the noise produced [16] by the turbine

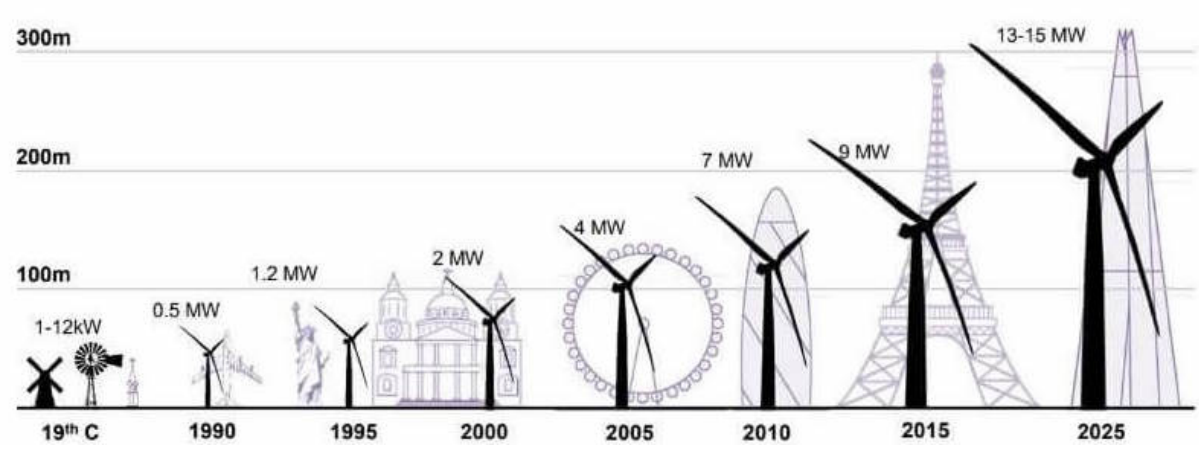

Figure 1.4: Chronological evolution of the largest wind turbine compared to various worlwide structures [19].

blades and the visual impact on the landscape. In a second time, wind farms can impact the local wildlife. Birds have been killed by flying into spinning turbine blades [17]. Most of these problems have been resolved or significantly reduced through technological development or adequately siting wind plants. Turbine blades have also killed bats, and research is ongoing to develop and improve solutions to minimize the impact of wind turbines on these species [18]. Like all energy sources, wind projects can alter the habitat on which they are built, which may change the suitability of that habitat for certain species. Furthermore, the wind generally fluctuates more on land than on the sea. Various ground-induced effects such as building positioning, tree, and landscape can induce fluctuations and impact the wind farm/wind turbine production and lifetime.

1.1.2.3 Offshore wind energy

Offshore wind energy refers to wind farms located on the sea, and different anchoring technologies are available depending on the water depth. In 2018, the total generation potential worldwide was estimated at 329PWh.year^{-1} based on the viable offshore area of each country and the depth [20]. In Europe, the generation potential is evaluated between 30PWh.year^{-1} [15] and 39PWh.year^{-1} [20] and this for a depth below 50 m and a distance from the coast above one kilometer. When depths are larger than $\sim$ 100 meters, it is not profitable to use the existing technologies of tripods, jackets, or monopile foundations. This paved the way for the development of floating wind turbines. Nonetheless, floating wind turbines still have a long road ahead since no actual farms exist in the world and only prototypes are in test. Apart from this depth dilemma, this gives an idea of why offshore wind energy has seen that much investments in European countries as seen previously in **Fig. 1.2**. There are several differences between offshore and onshore wind energy because of the marine environment.

On the downside, the cost of foundation for fixed offshore wind farms is much higher than onshore [21]. The installation and maintenance require the use of costly vessels and depend on meteorological conditions. Since wind farms are installed in areas with sufficient wind energy available, low wind conditions represent a short window of opportunity for the installation. The saline environment leads to corrosion and specific design are mandatory.

As for onshore wind energy, offshore wind energy has an impact on the local wildlife. It is either positive or negative, depending on how you look at it. As an example, the notion of reef

effect is majorly positive as the submerged parts of wind turbines act as artificial reefs, providing new habitats and likely affecting fisheries resources [22]. Nevertheless, those offshore wind farms should remain far from the path of migration birds [23, 24]. This is often the reason for activism from different organizations [25].

On the plus side, offshore winds are generally stronger than on land, and capacity factors are higher on average, reaching 49% for new projects [21] against 42% for onshore wind turbines [26]. The capacity factor of offshore floating wind turbines could be reaching 80% [27], close to the capacity factor of a nuclear power plant, but significant technological improvements are necessary.

The cost of installation and maintenance led to increasing the size of rotors. The populations being absent compared to onshore sites, there is mostly no size constraint for these wind turbines. This is why the size of offshore wind turbines is tremendous compared to onshore turbines. The evolution of the wind turbine power and rotor size is illustrated in **Fig. 1.4**. For example, the turbines constructed in the Channel have a nominal power of 8 MW for a 154 meters diameter, where the top onshore turbines usually reach 5 MW. The last generation of offshore wind turbines is even more significant, with nominal power above 10 MW and diameters reaching 200 meters. This introduces several scale problems, the majority being the blade deformations becoming larger, up to ten meters at the tip in the wind direction. It is mandatory to prevent singular effects increasing these deformations and reducing the lifetime of the wind turbines.

Exempted from the large meteorological variations no other external effect can disturb the production of an offshore windfarm. The wakes interaction with the downstream turbines is the primary disturbance within offshore wind farms. In the last decade, new control strategies are appearing in the literature. These strategies aim at controlling the wind farm globally and not letting each turbine focus on its performance alone. This global control aims at maximizing the power output while minimizing structural fatigue. This is where active control using yaw misalignment might be relevant.

1.2 Yaw misalignment, a relevant active control strategy?

1.2.1 Relevance of yaw misalignment configurations

Although modern wind turbines allow for various yaw mechanisms to align the turbine to the incoming wind, the response to variations in wind direction is prolonged. Consequently, the turbine will be in yaw during most of its operational time. Eggleston and Starcher [28] and Madsen et al. [29] showed the time evolution of wind direction obtained by sensors installed on two different experimental turbines in the field. A time series for the wind yaw angle measured from the experimental turbines is shown in **Fig. 1.5**. For the Tellus turbine (right figure), the yaw angle increases and varies dramatically during a particular instant in time. The yaw angle can reach up to around 60°, depending on the wind flow characteristic on site. While the yawed flow scenario presents an important and challenging problem, the basis of understanding the wind turbine aerodynamics is the axial flow case. The major challenges in the understanding of wind turbine flows are associated with the root and tip flows [30, 31, 32].

Unsteady aerodynamics inevitably results in irregular loads that negatively affect wind turbines power quality and fatigue lifetime. The work of J. Leishman [33] provides a detailed overview of the various challenges in modeling wind turbines under unsteady conditions. This paper presents a yawed rotor showing the lack of understanding of many aerodynamic phenomena associated with the wake structure developed behind the turbine and the dynamics of

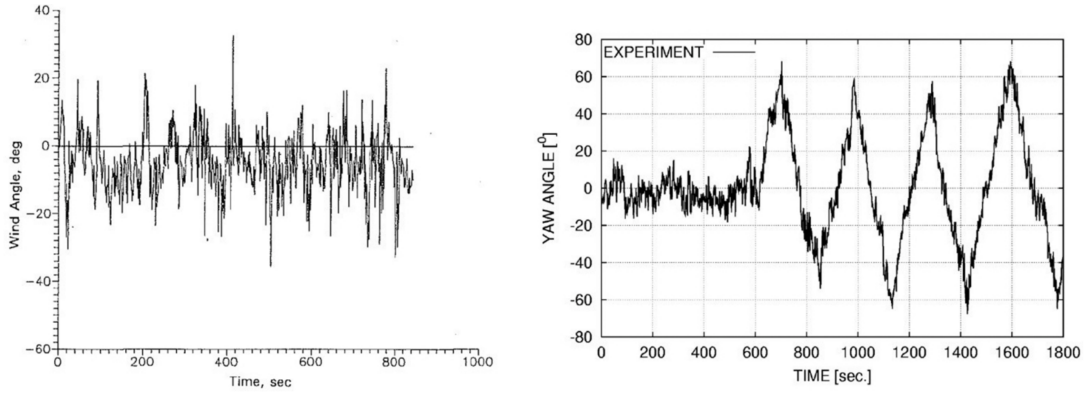

Figure 1.5: Time series of yaw angle during testing of (left) the Carter 25 turbine (wind direction sensor behind nacelle) [28] and (right) the Tellus turbine [29].

unsteady flows over the blade sections. Wind turbines operating in wind farms are well known to suffer from significant aerodynamic interference losses, primarily due to the axial velocity deficit incurred by the wind flowing through the upstream turbines. The power output from full-scale turbines operating in large wind farms may be as low as 40% of a standalone turbine, depending on the turbine spacing as well as environmental flow conditions, including the mean wind speed, turbulence intensity, and atmospheric stability [34]. Yaw aerodynamics may eventually become more critical for large offshore wind farm design, given the possibility of mitigating such wake losses by skewing the upstream turbine wake using active rotor yaw control. A non-exhaustive list of various experiments on yaw misaligned HAWT rotors under both experiments and open field conditions is given in **Appendix C.**

1.2.2 Aerodynamic loading of a yawed turbine

The immediate impact of the yaw misalignment on a HAWT lies in the power production losses and the unsteadiness of the loads. This is mainly due to azimuthal discrepancies of the local angle of attack, as firstly depicted by Butterfield et al. [35]. This first study showed variation up to 30° of the Angle of Attack, highlighting dynamic stall occurring in the blade root region for HAWT operating at $\gamma = 30°$ (see **Fig. 1.6**). Similar phenomena have been observed by S. Scott [36], where he presented the impact of yaw angle on a 2-bladed ten meters diameter turbine. **Fig. 1.6** illustrates the variation of normal force coefficient according to the blade azimuth, pointing out dynamic stall from 280° to 80°.

The latest technology development trends of wind turbines design involve larger but more flexible blades. Therefore, the azimuthal variation in the Angle of Attack and load observed in the literature will play a significant role in the structure fatigue and blades deformation. It will request a proper estimation in further studies.

Lately, the loads on a yawed wind turbine have been established directly through stereo particle image (SPIV) measurements (see [37]) and reported in [38, 39]. Still, these are limited to only one blade position, thus not establishing the time variation of the blade loads in yaw. The impact on the global power generation of yaw misaligned turbines was investigated by Grant et al. [40] showing that the power coefficient of a turbine reduces with increasing yaw. **Fig. 1.7** presents the normalized power coefficient against yaw angle for different experimental cases and a low order model. The difference in results is primarily due to the rotor geometries. The results, however, agree qualitatively, showing the power production dependency to yaw misalignment.

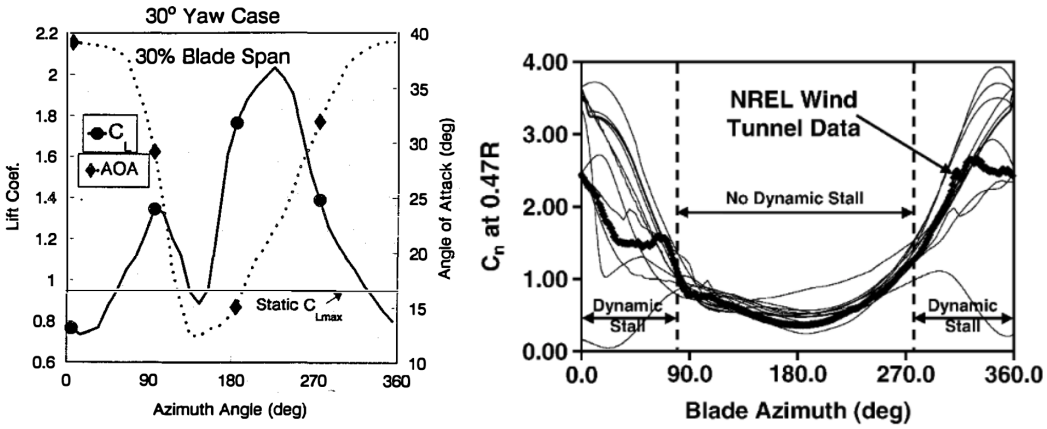

Figure 1.6: (left) Azimuth averaged Angle of Attack and lift coefficient at 30% span for 30^o yaw case [35]. (right) Predicted and measured normal force coefficient (C_n) at $0.47R$ for a test section speed of $15m.s^{-1}$ and a yaw angle of 60^o [36].

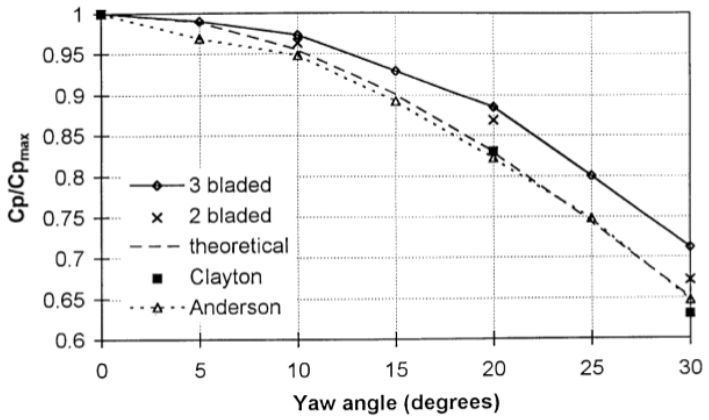

Figure 1.7: Power coefficient normalised by the maximum power coefficient (zero yaw) against yaw angle. Experimental data of Grant et al. (2 bladed and 3 bladed rotor) [40] are compared to experimental data of Clayton and Filby (3-bladed rotor) [41] and Anderson BEM analysis (2-bladed rotor) [42].

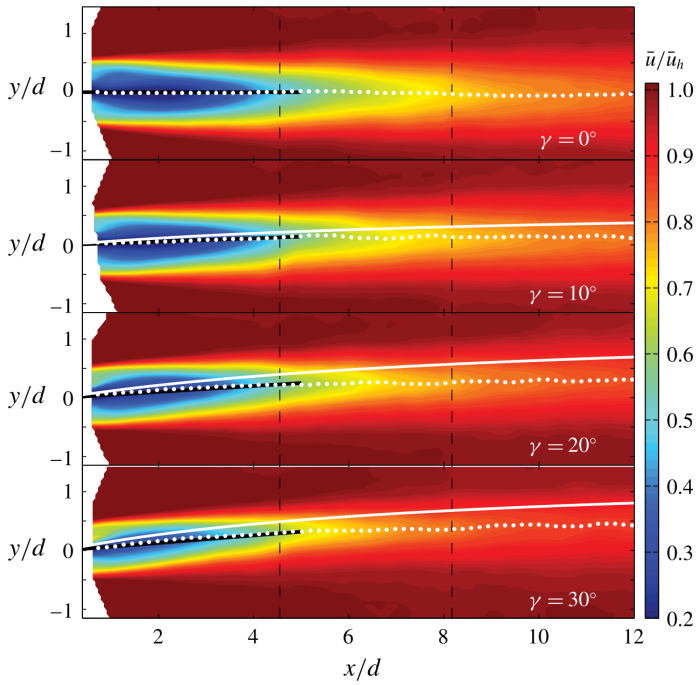

Figure 1.8: Contours of the normalised mean streamwise velocity u/u_h in the horizontal plane at hub height downwind of a turbine for different yaw angles ($\gamma = 0°, 10°, 20°$ and $30°$) at the optimal tip speed ratio of the turbine. White dots and represent the wake-centre trajectory in the horizontal plane obtained from the wind tunnel measurements [43]. Black and white lines show models results [45].

1.2.3 Yaw impact on the wind turbine wake

The second impact of yaw on a HAWT lies in the generated wake behind the turbine. Experimental and numerical analysis have shown similar results on the difference of wake topology between a yawed turbine and an aligned turbine. The work presented by Bastankhah M. and Porté-Agel F. [43] showed, on a small scale wind turbine (15 cm diameter) in a wind tunnel, the curled shape of the wake as well as its deviation. This study is then followed by the derivation of a low order model to predict the wake center position and its width under yawed conditions. **Fig. 1.8** shows how the wake velocity deficit deviates and can reach a lateral deviation eleven diameters downstream the rotor up to half a diameter for a 30° yaw angle. The wake curled shape can be observed in **Fig. 1.9** for different yaw angles and downstream transverse slices. Bastankhah M. and Porté-Agel F. [43] related the curled shape to a Counter-rotating Vortex Pair (CVP) deforming the wake. This phenomenon is furtherly discussed in Chapter 3.

The experimental results provided in Bartl J. et al. [44] present the influence of inflow turbulence and shear on yawed turbines wake deviation. The model derived by Bastankhah M. and Porté-Agel F. [43] is in good accordance with these results even if the rotor diameter is increased (0.9 m diameter). Moreover, the study recommends considering the inflow turbulence level as an essential parameter for deflection models implemented in wind farm controllers, as it affects the yaw-angle-dependent symmetry in shape and deflection.

In the same wind tunnel, Bartl J. et al. [46] demonstrated that upstream turbine yaw misalignment could increase the combined power production of a pair of turbines for both partial and complete wake overlap setups. Indeed, the experimental case presents the wake interaction between two turbines, either yawed or misaligned with each other according to the wind

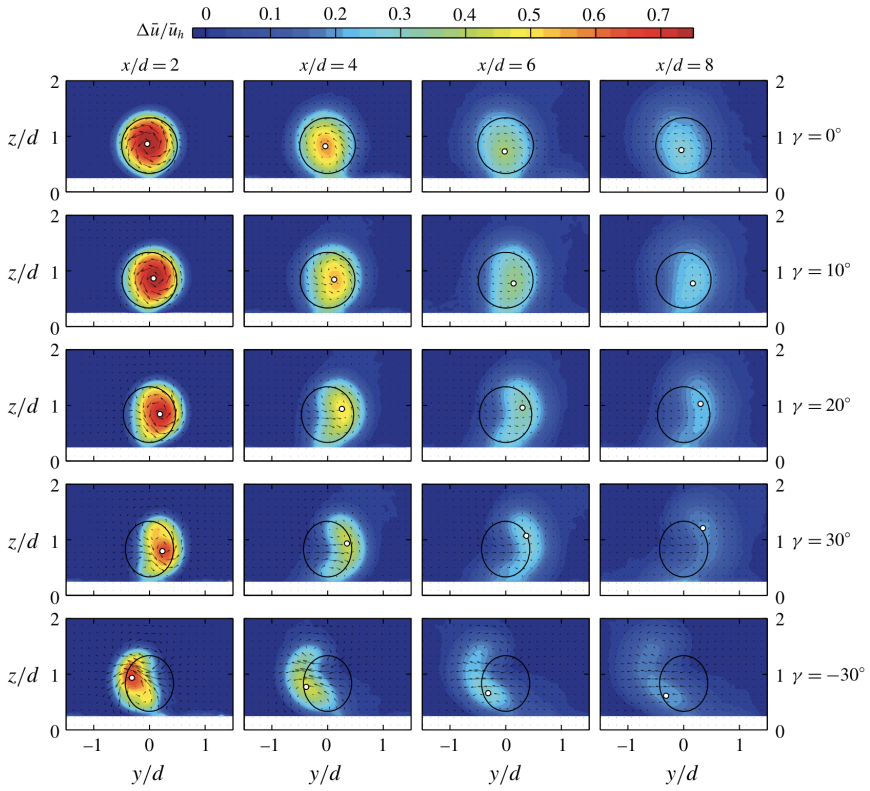

Figure 1.9: Contours of the normalized streamwise velocity deficit in the transverse planes at different downwind locations and different yaw angles for a turbine operating at the optimal tip speed ratio. Black circles indicate the frontal area of the wind turbine and white dots represent the wake-center position at each downwind location. The vector field represents the in-plane velocity components. [43]

axis. This setup provides an exciting study quantitatively showing the advantages of upstream turbine yaw control for load reduction and power increases on an offset downstream turbine. For situations where the downstream turbine is intruded by a partial wake, upstream turbine yaw control can redirect the wake either on or away from the downstream rotor. If the wake is directed onto the downstream turbine rotor-swept area, its yaw moment and power production are reduced. Open fields study on full-scale wind turbines (77 m diameter) are showing similar results on the wake deviation [47]. Still, the reliability of such measurements remains low due to the vast scales and the LIDAR measurement precision. Open fields experimental studies remain harder to process due to fluctuating inflow conditions while requiring the latest sophisticated measurement techniques.

These experimental studies are significant for the scientific community. They allow to more accurately understand the various phenomena involved in the wake of yawed turbines. But experimental data on actual wind farms scales are not affordable for the moment. Therefore, given the constant growth of computational resources, researchers are using these numerous data sets to validate simulations and models [48]. A vast amount of articles aimed at assessing the reliability of wind turbine simulation compared to experimental data. This simulation and validation framework allows to retrieve far more information from simple cases [49] and will enable the study of more significant domains representative of actual windfarms [50]. Various methods are used nowadays, either to emulate the mechanical loads of a turbine or its wake and will not be enumerated in this introduction.

1.2.4 Active yaw control

Wake interactions in wind farms result in decreased power extraction in downstream rows. The promise of increasing total power extraction through coordinated wind-farm control has incited a multitude of studies into different active control methods of wind turbines [12, 51, 52]. The most common mechanisms considered include axial induction control, yaw control, and even tilt control in the case of floating offshore wind turbines [53]. The interesting aspect of yaw control is the induced wake deflection presented in the previous subsection. As it can be exploited to steer the wakes away from downstream turbines.

Even if yaw misaligned turbines experience a decrease in power production, various literature studies have shown that steering the wake away from other downstream turbines results in a net gain on the wind farm production. This tendency has been observed in wind tunnel experiments [54, 46], simulations [55, 56, 57], and even field tests [58, 59]. To increase the wind farm production for a given wind condition it is necessary to optimize each wind turbine yaw angle based on the trade-off between the reduction of the wind turbine performance and the induced wake deviation. This optimization is not straightforward as the wake and wind conditions within the wind farm are unsteady and involve complex flow structures and fluctuations. Several methodologies are presented in the literature to adjust the yaw angles, either by a continuous variation between the first and last turbine [60, 61, 62], or by a fine discretization of the yaw angles [63, 64]. These methodologies aim at determining the best combinations of yaw angles for a given wind condition. From this, the yaw angles of each turbine are converged to their optimal values by using gradient-based or gradient-free algorithms. Yet, even if they are mainly based on wake models to evaluate the wind farm performances, these algorithms can be computationally expensive. Recent work from Stanley et al. [65] presented a Boolean optimization approach lowering the complexity of the algorithm for a similar fidelity with a 50 to 150 computational speed-up when compared to continuous optimization.

Such methodologies open many perspectives on the use of fast yaw optimization for coupled turbine design, wind farm layout, and real-time yaw optimization of wind plants. Yet, it is essential to mention that these methodologies depend on wake models to predict the velocity deficit deflection and recovery. The use of advanced simulation tools to improve the fidelity of wake models remains a central topic to achieve yaw optimization with accuracy. Furthermore, the additional fatigue loading induced by the interaction with deflected wakes must be adequately investigated. The resulting deformations occurring on the rotor could highlight favorable/unfavorable scenarios of wake interaction but would require an aero-elastic turbine model.

1.3 Aim of this thesis and manuscript content

From the previous context, this thesis investigates the wake interactions of yawed wind turbines in close-to-real scenarios. For this matter, and since experimental studies of the wakes on large-scale offshore wind turbines are not achievable at the moment, this thesis aims at replicating the flow surrounding wind turbines under yaw misalignment numerically. Three main objectives can be highlighted:

- Reach the state-of-the-art in terms of wake simulation in an extensive high-performance computing and Computational Fluid Dynamic (CFD) framework. This gathers the implementation and optimization of the methodologies towards validation against experimental results.

- Develop quantitative post-processing based on streamtubes and Level-set functions, allowing to understand how the yawed wind turbine wake recovers and behaves.
- Achieve a multiphysical approach by coupling the framework developed earlier to a servo-elastic code. This aims at combining the fidelity of CFD and the structural deformations occurring on real wind turbines to quantify the relevance of yaw misalignment strategies.

To this extent, the manuscript is organized as follows:

Chapter 2: Governing equations and modelling of HAWT in turbulent incompressible flows
The methodology and theoretical background of fluid dynamics and wind turbines are presented in this chapter. The first section deals with the numerical modeling of turbulent flows. The balance equations for mass and momentum are presented, followed by an introduction to the fundamental mechanisms of turbulence. Standard numerical methods for simulating turbulent flows are presented, focusing on the LES filtered equations and the closure models. The second section introduces the YALES2 CFD library used during this thesis. Finally, the third and last section presents the horizontal axis wind turbine modeling. After a quick overview of the available numerical approach, the actuator line method (ALM) used in this thesis is presented. The last subsections describe the implementation of this method in the YALES2 library and the different optimizations used.

Chapter 3: Application to small wind tunnel turbines
This chapter applies the numerical framework combining ALM and LES to wind turbines in a complex wind tunnel configuration. The wind tunnel combines different inflows with a turbulence grid, and an original strategy is presented for the turbulence grid modeling using a dynamic version of the ALM. By changing the yaw misalignment, various wind turbine wake interactions are investigated. The wake deflection of a single wind turbine is investigated under three inflows and three yaw angles. Then, the wake interaction with a second downstream wind turbine is presented.

Chapter 4: Recovery and turbulent mixing within the yawed wind turbine wake
The methodology validated in the previous chapter is applied in this chapter to real-scale offshore wind turbines. This chapter aims to quantitatively discuss the wake recovery and the turbulent mixing within a yawed wind turbine wake. For this matter, a methodology based on the transport of level-set functions by the instantaneous and mean flow is conducted. The time-averaged flow transporting the second function has the property of a streamtube surrounding the turbine. At first, mean kinetic energy and mean momentum budgets are integrated over the streamtubes depicting four wake regions with similar flow dynamics and correlated to local flow structures. Secondly, the wake turbulent mixing layer width is evaluated using the level-set functions transported by the instantaneous velocity field.

Chapter 5: Aero-servo-elastic simulations of yawed wake interactions
This chapter investigates the yaw misalignment impact in a close-to-real scenario. For this matter, the previously used framework of Large Eddy Simulation and Actuator Line Method is coupled to an aero-servo-elastic solver named BHawC. Industrial wind turbines are modelized for this case, with their actual geometry, deformation, and control. At first BHawC solver and the coupling with YALES2 are presented. A scenario of a two turbines row is then investigated.

The first scenario of two aligned wind turbines is discussed and compared to representative low order models (Blade Element Momentum Theory). To follow up, yaw misalignment is introduced on the first turbine. The wake, loads, and deformations of the turbines are analyzed. The globality of the results is discussed, showing the positive yaw strategy to be relevant for this particular configuration.

Chapter 6: Conclusion
The final chapter summarizes the general conclusions of this thesis and the perspectives of this work.

1.4 Publications

1.4.1 Peer-reviewed journals and conference papers

First author:

- F. Houtin-Mongrolle, P. Benard, G. Lartigue & V. Moureau *Recovery and turbulent mixing within the yawed wind turbine wake*, Journal of Fluid Mechanics (2022). *Under review.*
- F. Houtin-Mongrolle, P. Benard, G. Lartigue & V. Moureau *A level-set framework for the wind turbine wake analysis: from high-fidelity unsteady simulations to 1D momentum theory*, Journal of Physics: Conference Series 1618, (2021).
- F. Houtin-Mongrolle, P. Benard, G. Lartigue, V. Moureau, L. Bricteux & J. Reveillon *Actuator grid method for turbulence generation applied to yawed wind turbines*, Journal of Physics: Conference Series 1618, (2020).
- F. Houtin-Mongrolle, L. Bricteux, P. Benard, G. Lartigue, V. Moureau & J. Reveillon *Actuator Line Method Applied To Grid Turbulence Generation for Large-Eddy Simulations*, Journal of Turbulence 21, pp.407-433 (2020).

Co-author:

- S. Gremmo, E. Muller, F. Houtin-Mongrolle, B. Duboc & P. Benard *Field data based validation of an aero-servo-elastic solver for high-fidelity LES simulations of industrial wind turbines*, Computers & Fluids (2022). *Under review.*
- S. Gremmo, E. Muller, F. Houtin-Mongrolle, B. Duboc & P. Benard *Rotor-Wake Interactions in a Wind Turbine Row: a Multi-Physics Investigation with Large Eddy Simulation*, Journal of Physics: Conference Series (2022).
- U. Vigny, P. Benard, F. Houtin-Mongrolle, P. Tene Hedje, S. Zeoli & L. Bricteux *Adaptive mesh refinement to capture wind turbine wakes during LES simulations*, Journal of Physics: Conference Series (2022).
- P. Tene Hedje, S. Zeoli, U. Vigny, F. Houtin-Mongrolle, P. Benard & L. Bricteux *Large Eddy Simulation of HAWT and VAWT performances in the vicinity of a building.*, Journal of Physics: Conference Series (2022).

- S. Zeoli, G. Balarac, P. Bénard, G. Georis, F. Houtin-Mongrolle & L. Bricteux *Large eddy simulation of wind turbine wakes using adaptative mesh refinement*, Journal of Physics: Conference Series 1618, (2020).

1.4.2 Conferences

- F. Houtin-Mongrolle, P. Benard, G. Lartigue & V. Moureau *A level-set framework for the wind turbine wake analysis: from high-fidelity unsteady simulations to 1D momentum theory*, Wake Conference, Visby, Sweden, 2021.

- F. Houtin-Mongrolle, P. Benard, G. Lartigue, V. Moureau, L. Bricteux & J. Reveillon *Actuator grid method for turbulence generation applied to yawed wind turbines*, TORQUE conference, Delft, Netherlands 2020.

- F. Houtin-Mongrolle, P. Benard, G. Lartigue, V. Moureau, L. Bricteux & J. Reveillon *Wake deviation of a yawed wind turbine by Large-Eddy Simulation*, 15th EAWE Ph.D. Seminar on Wind Energy, Nantes, France 2019.

- F. Houtin-Mongrolle, P. Benard, G. Lartigue, V. Moureau, L. Bricteux & J. Reveillon *Wake interaction of yawed wind turbine by Large-Eddy Simulation*, EMRSIM2019 , Roscoff, France 2019.

- F. Houtin-Mongrolle, P. Benard, G. Lartigue , V. Moureau, L. Bricteux & J. Reveillon *Wake interaction of yawed wind turbine by Large-Eddy Simulation*, WESC conference, Cork, Ireland 2019.

- F. Houtin-Mongrolle, L. Bricteux, P. Benard, G. Lartigue, V. Moureau & J. Reveillon *Actuator Line Method Applied To Grid Turbulence Generation for Large-Eddy Simulations*, DLES12, Madrid, Spain 2019.

Chapter 2

Governing equations and modeling of HAWT in incompressible flows

The methodology and theoretical background of fluid dynamics and wind turbines are presented in this chapter. The first section deals with the numerical modeling of turbulent flows. The balance equations for mass and momentum are presented, followed by an introduction to the fundamental mechanisms of turbulence. Standard numerical methods for simulating turbulent flows are presented, focusing on the LES filtered equations and the closure models. The second section introduces the YALES2 CFD library used during this thesis. Finally, the last section presents the horizontal axis wind turbine modeling. After a quick overview of the available numerical approaches, the actuator line method used in this thesis is presented. The last subsections describe the implementation of this method in the YALES2 library and the different optimizations used.

Contents

2.1 Numerical modeling for turbulent flows 18
2.1.1 Equations of conservation 18
2.1.2 Turbulent flows 19
2.1.3 Turbulent flow modeling approaches: RANS, LES and DNS 24
2.1.4 LES filtered equations 26
2.1.5 Sub-grid scale modeling for turbulence 27
2.2 YALES2 CFD platform 30
2.2.1 Global overview and challenges 30
2.2.2 Main tools and strategies 31
2.2.3 Incompressible constant density solver (ICS) 32
2.3 Horizontal Axis Wind Turbine modeling 35
2.3.1 Overview of the existing methods 35
2.3.2 Actuator Line Method 37
2.3.3 Implementation in YALES2 40
2.3.4 Optimizations and primary validations of the ALM in YALES2 42
2.4 Conclusions 49

2.1 Numerical modeling for turbulent flows

The equations of fluid motion are based on treating fluids as continuous media. S. B. Pope [66] and others did the exercise to review the "continuum hypothesis", regrouping the discrete molecular nature of fluids with the continuum view. It is even more straightforward when dealing with large-scale motion dynamics surrounding wind turbines. Flows surrounding wind turbines involve a broad spectrum of scales and the simulation of wind turbine wake is a multi-scale challenge. The largest scales can reach hundreds of meters in a wind farm layout, while the smallest reach up to 0.1×10^{-3} m near the airfoils boundary layers. The tip speed ratio (TSR) being the common limiting factor, relative velocity to the blade section can reach up to $100\,\mathrm{m.s^{-1}}$ at the tip, giving a flow timescale larger than 10^{-6} s. Taking the air under atmospheric conditions, the average spacing between molecules is 3×10^{-9}m, the mean free path is 6×10^{-8} m, and the mean time between successive collisions is close to 10^{-10} s. From this, the Knudsen number, the ratio between the mean free path and the macroscopic reference length: $\mathrm{Kn} = \frac{6\times10^{-8}}{0.1\times10^{-3}} = \mathcal{O}(10^{-3})$, is below 0.01. From this and with the flow scales exceeding the molecular scales by three orders of magnitude, the continuum hypothesis is valid.

2.1.1 Equations of conservation

For a continuous medium and Newtonian fluid, the dynamic is governed by the Navier-Stokes equations. This set of equations can rigorously be derived from statistical mechanics over control volumes and from fundamental principles such as the mass and momentum conservation equations. The derivation is not straightforward and can be found in the litterature [66, 67, 68]. These equations are expressed hereafter using the conservative form and Einstein's notation.

- **The continuity or mass-conservation equation** is

$$\frac{\partial \rho}{\partial t} + \frac{\partial \rho u_i}{\partial x_i} = 0\,, \tag{2.1}$$

  with ρ the fluid density and u_i the fluid velocity. In this thesis the fluid is set to a constant density and therewith **Eq. 2.1** gives the velocity field to be divergence-free:

$$\frac{\partial u_i}{\partial x_i} = 0\,. \tag{2.2}$$

- **The momentum-conservation equation** is expressed as

$$\frac{\partial \rho u_j}{\partial t} + \frac{\partial \rho u_i u_j}{\partial x_i} = \frac{\partial \sigma_{ij}}{\partial x_i} + \rho f_j\,, \tag{2.3}$$

  where f_j denotes volumic forces and σ_{ij} refers to the stress tensor that may be expressed for constant property Newtonian fluids as

$$\sigma_{ij} = -P\delta_{ij} + \tau_{ij}\,, \tag{2.4}$$

  with P the pressure, δ_{ij} the Kronecker symbol and τ_{ij} the viscous stress tensor which is expressed as

$$\tau_{ij} = \rho\nu\left(\frac{\partial u_i}{\partial x_j} + \frac{\partial u_j}{\partial x_i}\right) \text{ the divergence free gives: } \frac{\partial \tau_{ij}}{\partial x_i} = \rho\nu\frac{\partial^2 u_j}{\partial x_i \partial x_i}, \tag{2.5}$$

where ν is the kinematic viscosity. The viscous stress tensor can be rewritten according to the strain rate tensor S_{ij}:

$$\tau_{ij} = 2\rho\nu S_{ij}, \quad \text{with:} \quad S_{ij} = \frac{1}{2}\left(\frac{\partial u_i}{\partial x_j} + \frac{\partial u_j}{\partial x_i}\right). \tag{2.6}$$

The velocity field being divergence free from **Eq. 2.2**, the strain rate tensor is purely deviatoric meaning that the stress tensor is expressed as the sum of isotropic, $-P\delta_{ij}$, and deviatoric contributions, τ_{ij}. The substitution of the stress tensor into the momentum-conservation equation finally gives the Navier-Stokes equations

$$\frac{\partial u_j}{\partial t} + \frac{\partial u_i u_j}{\partial x_i} = \nu\frac{\partial^2 u_j}{\partial x_i \partial x_i} - \frac{1}{\rho}\frac{\partial P}{\partial x_j} + f_j\,. \tag{2.7}$$

2.1.2 Turbulent flows

The notion of turbulent flows arose in 1883 when O. Reynolds [69] identified two different states of fluid motion: laminar and turbulent. The laminar flow, often represented by low velocities, sees its perturbations damped due to the molecular viscosity while the flow remains "organized". In opposition, when the velocity increases, the fluid viscosity can no longer dissipate these perturbations amplified by several instability mechanisms. Then, the flow evolves to a turbulent state where its behavior becomes chaotic and intermittent, related to the apparition of a large range of temporal scales and spatial structures in the flow. Yet, turbulent and laminar flows are governed by the same conservation equations, **Eq. 2.1** and **Eq. 2.7**. The Navier-Stokes equations can describe both regimes as well as the transition due to their non-linearity behavior. The transition from one regime to another can be quantified by looking at the balance between inertial forces that increase instabilities and viscous forces that absorb and dissipate structures. The dimensionless number introduced by Reynolds represents this balance and is expressed hereafter

$$Re = \frac{\mathcal{U}\mathcal{L}}{\nu}. \tag{2.8}$$

where $\mathcal{U}$ refers to the characteristic velocity scale of the flow, $\mathcal{L}$ to a characteristic length of the configuration, and ν represents the kinematic viscosity of the fluid. Hence, small Reynolds numbers are associated with laminar flows while large ones correspond to turbulent flows. When speaking of turbulent flows, the notion of scales is essential. The different levels of spatial scales or turbulent structures are associated with different energetic levels. The largest scales, where the most significant structures develop, have a greater energetic level. When large scales transfer the energy of motion to small scales, it is called the energy cascade. This notion of energy cascade was firstly introduced by Richardson [70] and Kolomogorov [71]. The various energy scales involved in the energy cascade are depicted in **Fig. 2.1**. They can be divided into three ranges:

- **Energetic range:** or integral range gathers the most energetic scales and corresponds to the largest structures of the flow. It is associated with the integral length scale ℓ_0. In general, the large eddies are anisotropic. The limitation of the energetic range is the length ℓ_{EI}, which defines the limitation between large anisotropic eddies and the biggest isotropic eddies. This characteristic length arises from Kolmogorov's hypothesis of local isotropy.

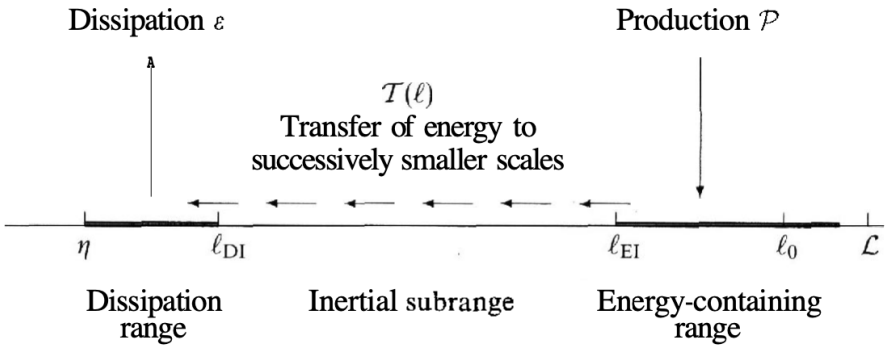

Figure 2.1: A schematic diagram of the energy cascade at very high Reynolds number. From Pope [66].

- **Inertial subrange:** The energy starts to cascade when the large anisotropic eddies are breaking into smaller ones, which is translated by an energy transfer from the large scales towards the small scales. The inertial forces are still sufficient to prevent the viscosity from dissipating the energy of the flow. The energy cascade remains uninterrupted as the isotropic eddies continue to transfer energy to smaller eddies according to a $-5/3$ power law. The most miniature scale at which the eddies are not dissipating energy from the flow is defined by ℓ_{DI}.

- **Dissipation range:** The dissipation zone is characterised by the highest frequencies of the flow. In this zone, the small turbulent structures are dissipated due to dominant viscous effect, and therewith energy is dissipated. The smallest turbulent structures are characterised by the Kolmogorov scale whose length and velocity are defined as

$$\eta = \left(\frac{\nu^3}{\varepsilon}\right)^{1/4} \quad \text{and} \quad u_\eta = (\nu\varepsilon)^{1/4}\,, \tag{2.9}$$

  with ε the dissipation rate of turbulent kinetic energy, that converts this same energy into heat due to the molecular viscosity of the fluid. The Reynolds number based on the Kolmogorov scale is unity and thus $Re_\eta = \eta u_\eta/\nu = 1$.

It is interesting to notice the dependence of the scales range to the Reynolds number. The ratio of the smallest to the largest scale evolves with the following similarity to the Reynolds number:

$$\frac{\eta}{\ell_0} \sim Re^{-3/4}\,. \tag{2.10}$$

This implies that when the Reynolds number increases, the number of scales that transfer or dissipate energy also grows. And therefore, more information is required to represent high Reynolds number flows.

The following presents some of the post-processing for the quantification of the turbulent flow behavior:

- **Statistics and turbulence:** Due to the random behavior of the flow variables that have to be computed, represented here by φ, it is not possible to build a mathematical model allowing to predict them. Therefore, a numerical model has to provide a statistical description of ψ through the prediction of its Probability Density Function (PDF) [66]

noted $\mathcal{P}$. The probability of the random variable φ being lower or equal to φ_1, noted $\mathbb{P}(\varphi \leq \varphi_1)$, is defined as follows:

$$\mathbb{P}(\varphi \leq \varphi_1) = \int_{-\infty}^{\varphi_1} \mathcal{P}(x)\mathrm{d}x\,. \tag{2.11}$$

Moreover, $\mathcal{P}$ of a variable φ can be determined only if all statistic moments are known. The statistic moment of order q can be defined as

$$\mathcal{M}_q(\varphi) = \langle \varphi^q \rangle = \int_{-\infty}^{+\infty} x^q \mathcal{P}(x)\mathrm{d}x\,. \tag{2.12}$$

From this, the first-order moment corresponds to the average value of the random variable:

$$\langle \varphi \rangle = \int_{-\infty}^{+\infty} x\mathcal{P}(x)\mathrm{d}x\,. \tag{2.13}$$

For a sufficiently long time, it is common to apply the ergodicity hypothesis to relate this first-order moment to the time-averaged value of the random variable. The fluctuations around this average value are defined as

$$\varphi' = \varphi - \langle \varphi \rangle \quad \text{with} \quad \langle \varphi' \rangle = 0\,. \tag{2.14}$$

This deviation from the average refers to the turbulent motions. Hence, it is interesting to know the statistical moments of the fluctuation φ'. These moments are called the centered statistical moments. The zeroth-order is equal to unity while the first order is equal to zero as expressed in **Eq. 2.13**. The second-order moment is known as the variance of φ and is expressed as

$$\mathrm{var}(\varphi) = \langle \varphi'^2 \rangle = \int_{-\infty}^{+\infty} (x - \langle \varphi \rangle)^2 \mathcal{P}(x)\mathrm{d}x \tag{2.15}$$

The variance is often depreciated compared to the Root Mean Square (RMS), defined as $\sqrt{\mathrm{var}(\varphi)} = \sqrt{\langle \varphi'^2 \rangle}$.

- **Energy spectra and Taylor frozen hypothesis:** The energy cascade from the large scales to the smaller one can be observed from the energy spectrum. It shows the distribution of turbulent kinetic energy among the different sizes of eddies. Some mathematical tools can be used to estimate this distribution. Indeed, the turbulent kinetic energy contained in the eddy of characteristic length r can be achieved through the introduction of the two-point velocity correlation tensor that indicates how much the velocity fluctuations are correlated for points separated by a distance $\mathbf{r}$:

$$R_{ij}(\mathbf{r}, t) = \left\langle u_i'(\mathbf{x}, t) u_j'(\mathbf{x} + \mathbf{r}, t) \right\rangle\,. \tag{2.16}$$

Under homogeneous and isotropic assumptions and considering the wavenumber $\boldsymbol{\kappa}$ that refers to the length scale l defined as $|\boldsymbol{\kappa}| = 2\pi/l$, the Fourier transform of $R_{ij}(\mathbf{r}, t)$ can be expressed as

$$\Phi_{ij}(\boldsymbol{\kappa}, t) = \frac{1}{(2\pi)^3} \int_{\mathbb{R}^3} e^{-i\boldsymbol{\kappa}\cdot\mathbf{r}} R_{ij}(\mathbf{r}, t)\mathrm{d}\mathbf{r}\,, \tag{2.17}$$

where $\Phi_{ij}(\boldsymbol{\kappa}, t)$ is the velocity-sprectrum tensor which corresponds to the contribution of the wavenumber $\boldsymbol{\kappa}$ to the turbulent kinetic energy. In order to avoid directional considerations over velocities but also on the wavenumber $\boldsymbol{\kappa}$, the turbulent kinetic energy spectrum

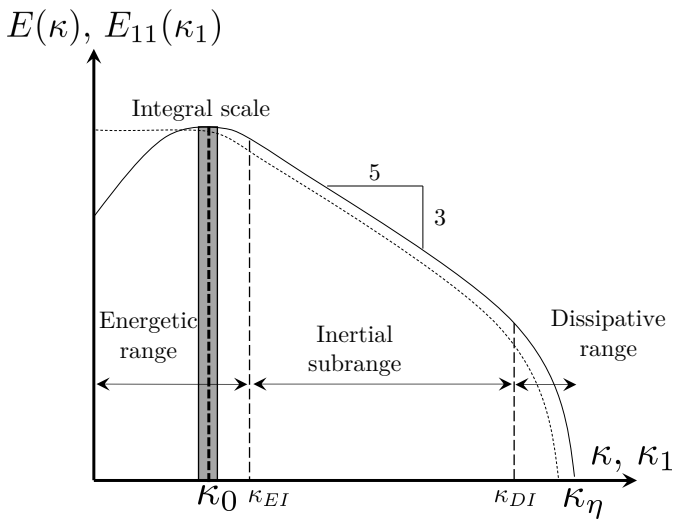

Figure 2.2: Arbitrary representation of $E(\kappa)$ (——) and the one-dimensional energy spectrum, $E_{11}(\kappa_1)$ (- - -) in isotropic turbulence. The maximal production of turbulent kinetic energy, $E(\kappa_0)\mathrm{d}\kappa$ is represented by (▬). Inspired from [66].

is defined by integrating half the trace of the $\Phi_{ij}(\boldsymbol{\kappa}, t)$ tensor on the $\kappa = |\boldsymbol{\kappa}|$ radius sphere in the Fourier space as:

$$E(\kappa, t) = \int_{\mathbb{R}^3} \frac{1}{2}\Phi_{ii}(\boldsymbol{\kappa}, t)\delta(|\boldsymbol{\kappa}| - k)\mathrm{d}\boldsymbol{\kappa}\,, \tag{2.18}$$

where δ is the dirac function. The integration of $E(\kappa, t)$ over all spheres of radius κ allows to retrieve the actual turbulent kinetic energy. Evidently, $E(\kappa, t)\mathrm{d}\kappa$ represents the energetic contribution of the scales within the infinitesimal shell $\kappa \leq |\boldsymbol{\kappa}| < \kappa + \mathrm{d}\kappa$ in wavenumber space. The production of the turbulent kinetic energy is maximal at $\kappa_0 = 2\pi/\ell_0$. An example of energy spectra in isotropic turbulence is given in **Fig. 2.2**. Within the inertial subrange, the energy spectrum of homogeneous isotropic turbulence is represented as follows:

$$E(\kappa, t) = C\varepsilon^{2/3}\kappa^{-5/3}\,, \tag{2.19}$$

with ε the dissipation rate of turbulent kinetic energy and C a universal Kolmogorov constant.

Yet, the computation of such a spectrum from experiments or simulations can be difficult or impossible due to the number of data necessary to sample the two-point velocity correlation. However, with a single probe, it is possible to approximate the value of $R_{ij}(\mathbf{r})$. A common technique is to use Taylor's hypothesis or the frozen-turbulence approximation, which evaluates spatial correlations using temporal correlations. Nevertheless, this is valid only if the velocity fluctuations, u', are small compared to the mean streamwise velocity $\langle u \rangle$. If the turbulence is statistically homogeneous in the $\mathbf{e}_1$ direction, the temporal autocovariance can be expressed as:

$$R_{ij}(\mathbf{e_1}r_1) = \left\langle u_i'(\mathbf{x}, t)u_j'(\mathbf{x}, t + s)\right\rangle\,, \tag{2.20}$$

where r_1 is the spatial representation of the temporal evolution based on the streamwise velocity $\langle u_1 \rangle$ and the offset time s as $r_1 = \langle u_1 \rangle s$. From this, the one-dimensional energy

spectra in the longitudinal or transverse direction can be determined as twice the one-dimensional Fourier transform of $R_{ij}(\mathbf{e_1}r_1)$:

$$E_{ij}(\kappa_1) \equiv \frac{1}{\pi}\int_{-\infty}^{\infty} R_{ij}(\mathbf{e_1}r_1)\, e^{-i\kappa_1 r_1} \mathrm{d}r_1 \,. \tag{2.21}$$

An example of one-dimensional energy spectra in the longitudinal direction, $E_{11}(\kappa_1)$, for isotropic turbulence is given in **Fig. 2.2**. The major difference with the energy spectra is in the large scales - low wavenumber - where $E(\kappa)$ tends to reach zero while the one-dimensional spectra reach is maximum for a zero wavenumber. Yet, it barely impacts the evaluation of the integral length scale, ℓ_0. In this thesis, the longitudinal, $E_{11}(\kappa_1)$ and transverse, $E_{22}(\kappa_1)$ energy spectra are discussed.

- **Turbulence anisotropy:** The quantification of the turbulence anisotropy might be handy in the wind turbine wake analysis, as shown by Ali et al. [72]. The anisotropy invariants [73] are computed using the eigenvalues of the Reynolds stress anisotropy tensor:

$$a_{ij} = \frac{\langle u_i' u_j' \rangle}{2k} - \frac{\delta_{ij}}{3}, \text{ where } k = \frac{\langle u_i' u_i' \rangle}{2} \,. \tag{2.22}$$

This different states of turbulence according to a_{ij} are discussed by Lumley [73] using two invariants $\eta^2 = \frac{1}{3}\left(\lambda_1^2 + \lambda_1\lambda_2 + \lambda_2^2\right)$ and $\xi^3 = -\frac{1}{2}\lambda_1\lambda_2(\lambda_1 + \lambda_2)$. Where λ_1, λ_2 and λ_3 are the eigenvalues of the anisotropy tensor a_{ij}. The vizualisation of such states is presented in **Fig. 2.3.a)**, where the vertices of this map correspond to three limiting states of turbulence:

  - $\mathbf{x}_{1c}$: one-component or "cigar-shaped" turbulence
  - $\mathbf{x}_{2c}$: two-component or "pancake-like" turbulence
  - $\mathbf{x}_{3c}$: isotropic or spherical turbulence.

Another representation of this anisotropy tensor is proposed by Banerjee et al. [75]: the barycentric map. From this, any anisotropy tensor can be associated with a point inside an equilateral triangle, whose vertices correspond to the same three limiting states of turbulence. This tensor is represented inside the above-described triangle by the point $\mathbf{x}_B$ such that:

$$\mathbf{x}_B = C_{ic}\mathbf{x}_{ic} \,, \tag{2.23}$$

where the weights are computed as

$$C_{1c} = \lambda_1 - \lambda_2 \,, \tag{2.24a}$$

$$C_{2c} = 2(\lambda_2 - \lambda_3) \,, \tag{2.24b}$$

$$C_{3c} = 3\lambda_3 + 1 \,. \tag{2.24c}$$

By definition, these weights sum to one. To help the interpretation of the barycentric map, Emory and Iaccarino [74] proposed a clearer way to vizualise such maps by redefining $\mathbf{x}_B$ such that

$$\mathbf{x}_B = (C_{ic} + C_{off})^{C_{exp}}\mathbf{x}_{ic} \,, \tag{2.25}$$

with C_{off} and C_{exp} two constant used when plotting $\mathbf{x}_B$ as a Red-Green-Blue (RGB) triplet. An exemple is given in **Fig. 2.3.b)**. This type of postprocessing gives an insight into how the turbulence evolves in complex 3D domains, especially when it tends to an isotropic state and the turbulence starts decaying. This is mainly used in the wake of turbulence grids in Chapter 3.

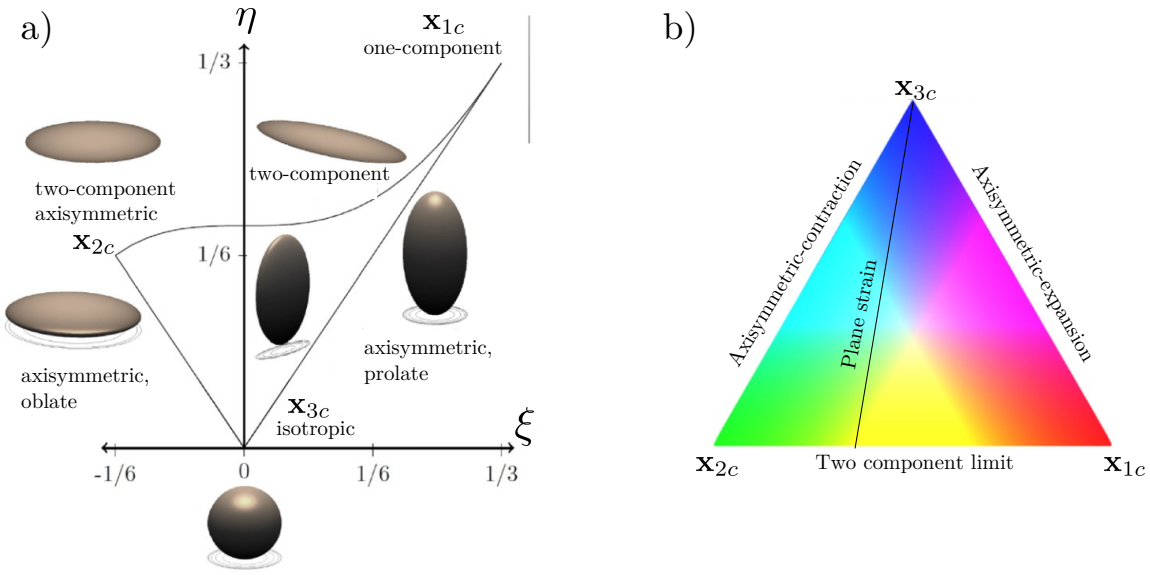

Figure 2.3: a) Lumley map representing the limits of invariant η and ξ with a spheroid visualization of the different turbulent states [73]. b) Barycentric map of the anisotropy tensor using $C_{off} = 0.65$ and $C_{exp} = 5$ [74].

- **Vortex identification in turbulent flows:** Several criteria are defined in the literature to identify vortex within turbulent flows. They mostly rely on iso-surface of high vorticity [76], pressure iso-surface since the pressure tends to decrease because of the centrifugal force [77], or the eigenvalues of the tensor resulting from a combination of the antisymmetric and symmetric parts of the gradient of $\mathbf{u}$ named as λ_2 [78]. The criterion used in this thesis is based on the velocity gradient tensor proposed by Hunt et al. [79]: the Q-criterion, named after the second invariant of this tensor :

$$Q_{\text{criterion}} = \frac{1}{2}\left(\Omega_{ij}\Omega_{ij} - S_{ij}S_{ij}\right) \tag{2.26}$$

where Ω_{ij} and S_{ij} are respectively the antisymmetric part and symmetric part of the divergence of the velocity field :

$$\Omega_{ij} = \frac{1}{2}\left(\frac{\partial u_i}{\partial x_j} - \frac{\partial u_j}{\partial x_i}\right) \text{ and } S_{ij} = \frac{1}{2}\left(\frac{\partial u_i}{\partial x_j} + \frac{\partial u_j}{\partial x_i}\right) \tag{2.27}$$

This criterion compares, locally, the rotation rate to the shear rate. The presence of a vortex implies large positive values of the $Q_{\text{criterion}}$. Therefore, vortices are defined as regions of positive $Q_{\text{criterion}}$, i.e., where the vorticity magnitude is higher than the strain rate, with the additional low-pressure condition. Most of the time, this second condition is assumed to be satisfied if $Q_{\text{criterion}} > 0$ [78].

2.1.3 Turbulent flow modeling approaches: RANS, LES and DNS

As previously mentioned, the Navier-Stokes equations enable the representation of both laminar and turbulent flows dynamics. The solving of these equations can be achieved thanks to various numerical methods. DNS, RANS, and LES are three main numerical approaches to perform turbulent flow simulations. They are briefly summarized hereafter; a representative overview is given in **Fig. 2.4**.

- **Direct Numerical Simulation (DNS):** the DNS approach consists in solving the discretized form of the Navier-Stokes equations under the assumption that all turbulent structures are well resolved, guarantying that the discretized terms are as close as possible to the continuous terms. In that case, there are only discretization errors and no modeling errors. However, this approach is extremely costly for highly turbulent flows, even for non-reacting ones. Therefore it is generally only possible to perform such simulations for academic studies without limited computational resources. As DNS cannot systematically be applied, other formalisms have to be chosen by adding physical models that avoid resolving all the spatial scales of the turbulence and thus decreasing the computational cost of the simulation.
- **Reynolds-Averaged Navier-Stokes (RANS):** this approach deals with the solving of the Navier-Stokes equations through the application of the Reynolds decomposition. Hence, this formalism enables access to the static fields only as it computes the mean flow field while completely modeling the fluctuating contribution of the flow. Therefore, none of the scales of the turbulent spectrum are resolved. Moreover, because of the non-linearity of the Navier-Stokes equations, unresolved terms appear in the statistical equations, and thus their closures necessitate turbulence models. The RANS approach is prevalent and attractive for industries as it does not require refined meshes and presents short restitution times.
- **Large-Eddy Simulation (LES):** the LES formalism can be considered as a trade-off between the high computational cost of the DNS approach and the entire modeling of turbulent scales in the RANS approach. Indeed, it consists in applying a spatial filtering operator to the Navier-Stokes equations to resolve only the largest scales of the flow. Some criteria aim at estimating the needed resolution of the LES approach [66, 80, 81]. Contrary to the RANS approach, it does not rely on the computation of a mean flow field but instead on a filtered instantaneous field, where the smallest scales have been removed. In that case, unclosed filtered terms, which represent the effects of the smallest scales on the largest ones, have to be modeled. Moreover, as these small structures are assumed to be isotropic, universal, and dissipative, they are well suited to this modeling. Finally, LES decreases the computational cost of turbulent flow simulations compared to DNS and can be applied to various complex configurations.

All simulations performed in this thesis will use the LES formalism, which is presented in detail hereafter.

2.1.4 LES filtered equations

The LES formalism relies on modeling the dissipative scales of the flow. Therefore it implies the scale separation between the resolved and modeled structures through a spatial filtering operation applied to the Navier-Stokes equations. By considering a scalar $\phi(t, \mathbf{x})$, the low-pass spatial filtering process is defined by a spatial convolution product presented hereafter.

$$\bar{\phi}(\mathbf{x}, t) = \int_{\mathbb{R}^3} \phi(\mathbf{y}, t) G_\Delta(\mathbf{y} - \mathbf{x}) \mathrm{d}\mathbf{y} \,, \tag{2.28}$$

where $\bar{\phi}$ is the filtered scalar and G_Δ the filtering kernel associated to the filter size Δ. The filter operator has to be normalized such that:

$$\int_{\mathbb{R}^3} G_\Delta(\mathbf{x}) \mathrm{d}\mathbf{x} = 1 \,. \tag{2.29}$$

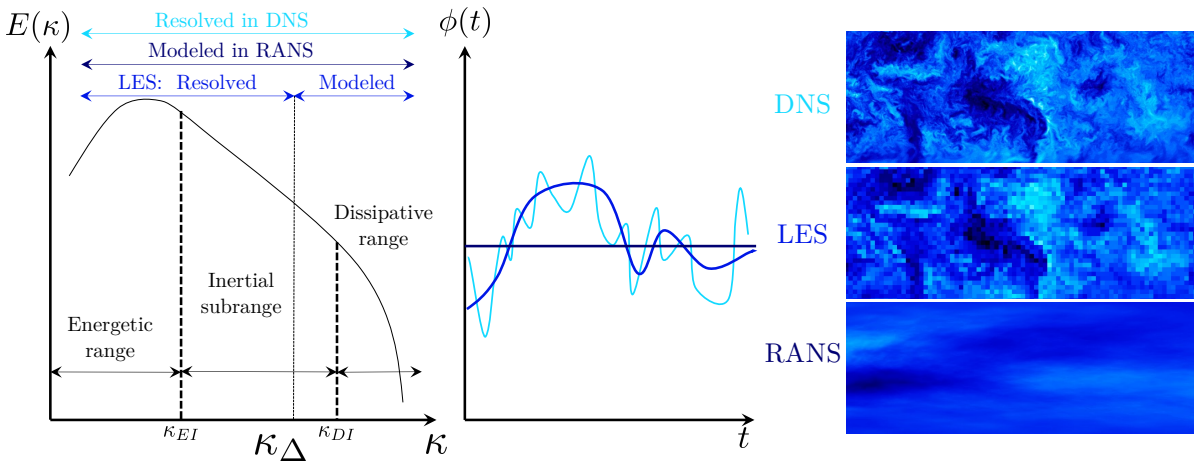

Figure 2.4: Representative overview of the different CFD approaches: Spectra representing the Energy evolution as function of the wavenumber (proportional to the inverse of the length scales) (left), temporal evolution of a local variable (middle) and slice of the velocity field representing the turbulent structures in an atmospheric flow (right).

Moreover, the hypothesis on the commutativity property for spatial and temporal derivation operators is made:

$$\frac{\partial \bar{\phi}}{\partial t} = \overline{\frac{\partial \phi}{\partial t}} \quad \text{and} \quad \frac{\partial \bar{\phi}}{\partial x_i} = \overline{\frac{\partial \phi}{\partial x_i}}\,. \tag{2.30}$$

However, this hypothesis is correct only if the filter is constant in time and space. The spatial commutativity error has been well studied [82, 83] and non-spatially uniform filters with exact commutativity of their spatial derivative have been stated [84, 85]. The case of temporally deformable meshes is addressed in the literature [86], yet in this thesis, mesh discretization is constant over time. From this filter operator, the ϕ variable may be decomposed into two parts: a first part that involves scales larger than Δ, noted $\bar{\phi}$ and a second that refers to the sub-grid fluctuating part, involving scales smaller than Δ noted ϕ'':

$$\phi(t, \mathbf{x}) = \bar{\phi}(t, \mathbf{x}) + \phi''(t, \mathbf{x}) \tag{2.31}$$

The filtering process can thus be applied to **Eq. 2.2** and **Eq. 2.7** leading to the instantaneous filtered balance equations defined as follows:

- **Filtered continuity equation**

$$\frac{\partial \bar{u}_i}{\partial x_i} = 0\,, \tag{2.32}$$

- **Filtered momentum-conservation equation**

$$\frac{\partial \bar{u}_j}{\partial t} + \frac{\partial \bar{u}_i \bar{u}_j}{\partial x_i} = \nu \frac{\partial^2 \bar{u}_j}{\partial x_i \partial x_i} + \frac{1}{\rho}\frac{\partial}{\partial x_i}\underbrace{\tau_{ij}^R}_{(1)} - \frac{1}{\rho}\frac{\partial \bar{P}}{\partial x_j} + \bar{f}_j \tag{2.33}$$

The complete derivation of these equations can be found in [66]. The filtered momentum-conservation equation possesses an unresolved term, (1) which needs to be closed. This term is

hereafter named the residual stress tensor and can be expressed as:

$$\begin{aligned}\tau_{ij}^{R} &= -\rho\left(\overline{u_i u_j} - \bar{u}_i\bar{u}_j\right) ,\\ \tau_{ij}^{R} &= -\rho\left(\underbrace{\overline{\bar{u}_i\bar{u}_j} - \bar{\bar{u}}_i\bar{\bar{u}}_j}_{\mathcal{L}_{ij}^{\circ}} + \underbrace{\overline{\bar{u}_i u_j'} + \overline{u_i'\bar{u}_j} - \bar{\bar{u}}_i\bar{u_j'} - \bar{u_i'}\bar{\bar{u}}_j}_{\mathcal{C}_{ij}^{\circ}} + \underbrace{\overline{u_i' u_j'} - \bar{u_i'}\bar{u_j'}}_{\mathcal{R}_{ij}^{\circ}}\right) .\end{aligned} \tag{2.34}$$

The second line of **Eq. 2.34** presents the decomposition of the residual stress in three different tensors as proposed by Germano [87] which is Galilean-invariant, in opposition to the one from Leonard [88]. $\mathcal{L}_{ij}^{\circ}$ is the Leonard stress which can be computed from the filtered values and derives from the none idempotence property of the filter. The tensor $\mathcal{C}_{ij}^{\circ}$ defines the cross stresses and represents the energy transfer between large and small structures. The scale separation hypothesis from Kolmogorov induces that if the filter cutoff frequency is within the inertial scales, this term is negligible. The last tensor, $\mathcal{R}_{ij}^{\circ}$ is the sub-grid scale (SGS) Reynolds stress which represents the energy dissipation of the small scales. This tensor necessitates the introduction of a turbulent model to close the momentum conservation equation.

2.1.5 Sub-grid scale modeling for turbulence

Based on the fluctuations of the velocity moments, which refer to the accuracy of the statistical flow representation, several turbulent SGS models exist in the literature. The number of moments taken into account may thus be the first criterion to classify them. Hence, they can be segregated into two categories [80]: the first-order moment models based on the averaged values and referred to as *functional modeling* or turbulent viscosity modeling. And the second-order moment models named *structural modeling* based on the reconstruction of τ_{ij}^{R} by using an evaluation of $\bar{u}_i$. These two categories do not request the same modeling knowledge: structural modeling needs enough knowledge of the structure of the small scales in the solution. The functional modeling requires to know the nature of the interactions [89] and the effect of small scales on the large must be equivalent in the computational domain. The strength of functional modeling relies on applying a local turbulent viscosity and, therefore, is numerically more stable than structural modeling, especially near complex geometries: wind turbine tower and nacelle for example. In this thesis, only the functional models [90, 91, 92] have been used and are based on the Boussinesq hypothesis presented hereafter.

2.1.5.1 Boussinesq hypothesis

The majority of the functional closure models for the momentum balance equation are built upon a turbulent viscosity based on the Boussinesq eddy viscosity assumption [93]. The idea is to supplement the fluid molecular viscosity by a local turbulent viscosity represented with a similar relation to the one of Newton for the viscous stress tensor, $\bar{\tau}_{ij}$. Therewith, the residual stress tensor from **Eq. 2.33** can be written as

$$\tau_{ij}^{R} = \rho\nu_t\left(\frac{\partial\bar{u}_i}{\partial x_j} + \frac{\partial\bar{u}_j}{\partial x_i}\right), \quad \text{so:} \quad \tau_{ij}^{R} = 2\rho\nu_t\bar{S}_{ij} , \tag{2.35}$$

where the sub-grid scale turbulent viscosity is written as ν_t. From this hypothesis **Eq. 2.33** can be finally written as

$$\frac{\partial\bar{u}_j}{\partial t} + \frac{\partial\bar{u}_i\bar{u}_j}{\partial x_i} = \frac{\partial}{\partial x_i}\left[2(\nu+\nu_t)\bar{S}_{ij}\right] - \frac{1}{\rho}\frac{\partial\bar{P}}{\partial x_j} + \bar{f}_j . \tag{2.36}$$

It can be highlighted that thanks to the Boussinesq assumption, the SGS models have only to model the turbulent kinematic viscosity ν_t. Various sub-grid scale models have been developed in the literature from different assumptions. The dynamic Smagorinsky and the $\sigma-$model are used in this thesis and presented in the following subsections.

2.1.5.2 Dynamic Smagorinsky model

The classical Smagorinsky SGS model [94] postulates that an equilibrium exists between the production and dissipation rate of the kinetic energy at the LES filter size Δ. Hence, turbulence can thus be considered at this scale as a purely dissipative phenomenon. The eddy viscosity is expressed as

$$\nu_t = (C_s\Delta)^2\,\bar{\mathcal{S}}, \quad \text{with:} \quad \bar{\mathcal{S}} = \sqrt{2\bar{S}_{ij}\bar{S}_{ij}}\,, \tag{2.37}$$

where C_s is the Smagorinsky constant, Δ is the LES filter size proportional to the grid size Δ_x. However this model is related to the resolved velocity strain rate and one of the shortcomings being the model activation in near-wall regions or in the case of laminar flow.

A major improvement of the classical Smagorinsky model is proposed by Germano [91] and Lilly [92] by using a dynamic procedure to overcome the aforementioned limitation. In this approach, the Smagorinsky constant C_s is locally determined and not based on the global flow configuration. For this dynamic version, the main idea is based on the fact that the sub-grid scales characteristics can be deduced from the smallest resolved scales. In order to achieve this, another filtering operator noted here $\widehat{\circ}$ is introduced and the resolved instantaneous velocity field is filtered with a width Δ' larger than Δ. The residual stress term $\tau_{ij}^{R} = -\rho\left(\overline{u_iu_j} - \bar{u}_i\bar{u}_j\right)$ and the residual stress term based on the double-filtered velocity $\tau_{ij}^{R'} = -\rho\left(\widehat{\overline{u_iu_j}} - \widehat{\bar{u}}_i\widehat{\bar{u}}_j\right)$ may be written according to the Smagorinsky model as

$$\begin{aligned} \tau_{ij}^{R} &= 2\rho\; C_s^2\Delta^2\bar{\mathcal{S}}\cdot\bar{S}_{ij}\,, \\ \tau_{ij}^{R'} &= 2\rho C_s^2\Delta'^2\widehat{\bar{\mathcal{S}}}\cdot\widehat{\bar{S}}_{ij}\,. \end{aligned} \tag{2.38}$$

Here, by considering a sharp cut-off spatial filter, the double-filter size is equivalent to the test filter width, Δ'. The resolved stress, $\mathcal{L}_{ij}$ between the two filtering sizes Δ' and Δ is called the Germano identity. And can be expressed by taking the difference between the two previous residual stress tensors as

$$\mathcal{L}_{ij} = \tau_{ij}^{R'} - \widehat{\tau_{ij}^{R}} = -\rho\left(\widehat{\bar{u}_i\bar{u}_j} - \widehat{\bar{u}}_i\widehat{\bar{u}}_j\right)\,. \tag{2.39}$$

It is important to notice that $\mathcal{L}_{ij}$ is known in terms of $\bar{u}_i$ which is not the case for τ_{ij}^{R} and $\tau_{ij}^{R'}$ depending on filtered and double filtered cross-correlations of the velocity. Moreover, if the two filters (Δ and Δ') have the same size, then $\mathcal{L}_{ij}$ is equivalent to the Leonard stress tensor $\mathcal{L}_{ij}^{\circ}$, presented in **Eq. 2.34**.

By injecting τ_{ij}^{R} and $\tau_{ij}^{R'}$ in the previous equation and contracting with the filtered strain rate tensor $\bar{S}_{ij}$, the Smagorinsky constant can be computed from the two filtered velocity fields as follow

$$\left(\widehat{\bar{u}_i\bar{u}_j} - \widehat{\bar{u}}_i\widehat{\bar{u}}_j\right)\bar{S}_{ij} = 2C_s^2\left(\Delta^2\widehat{\bar{\mathcal{S}}\bar{S}_{ij}}\bar{S}_{ij} - \Delta'^2\widehat{\bar{\mathcal{S}}}\cdot\widehat{\bar{S}}_{ij}\bar{S}_{ij}\right)\,. \tag{2.40}$$

Implicitly, this model implies similarity between the SGS stresses at the two different scales Δ and Δ'. Therefore, the sub-grid scales characteristics, through the turbulent viscosity, are based on the same characteristics as those on the range $[\Delta, \Delta']$. The quantity in the right-hand side parentheses can result in zero values, thus leading to indeterminate or ill-conditioned values for the C_s constant. Moreover, the computation of the local constant values may locally

lead to negative values, which implies a negative turbulent viscosity that corresponds to energy transfers from the small structures to the largest ones, also called backscatter [95]. A specific treatment has to be applied to avoid this phenomenon as it may produce numerical problems. The dynamic Smagorinsky model is relevant for many applications but is costly and complex to use. It requires explicit filtering operators in opposition to the classical formulation.

2.1.5.3 $\sigma-$model

The $\sigma-$model, developed in the work of Nicoud et al. [90], proposed an interesting approach which relates the SGS to the singular values of the resolved velocity gradient tensor. Here the turbulent viscosity is computed from the following relation

$$\nu_t = (C_\sigma \Delta)^2 \mathcal{D}_\sigma \quad \text{with :} \quad \mathcal{D}_\sigma = \frac{\sigma_3 (\sigma_1 - \sigma_2)(\sigma_2 - \sigma_3)}{\sigma_1^2}, \tag{2.41}$$

where σ_1, σ_2 and σ_3 are the three singular values from a combinaison of the local velocity gradient tensor, $\mathbf{g}^t\mathbf{g}$ with $\mathbf{g} = \partial \bar{u}_i / \partial x_j$. C_σ is the model constant set at 1.35 as advised from the initial model development. The previously mentioned singular values respect the following equality $\sigma_1 \geq \sigma_2 \geq \sigma_3 \geq 0$, thus making the model positive by construction. This model aims to meet the following properties:

- The SGS term should drain the proper overall amount of kinetic energy from the resolved velocity scales and, in addition to that, remain positive and evaluated locally.
- The eddy-viscosity should decay as the distance to the solid boundary to the third power, similarly to WALE [96] or Vreman [97] models.
- No eddy-viscosity should be added when the flow is two-dimensional or two-components, like the classical Smagorinsky model when the flow is in solid rotation, and like the WALE and Vreman models for pure shear.
- When the resolved scales are in pure axisymmetric or isotropic expansion/contraction, the model should not add eddy-viscosity.

It is important to note that the $\sigma-$model may be used in a dynamic form, similar to the classical Smagorinsky model. Yet, Nicoud suggested the use of a dynamic global procedure more than a local one. This dynamic global procedure amounts to integrate over the all computational domain **Eq. 2.40**, thus giving the model constant to be uniform over space. In this thesis only the static $\sigma-$model with $C_\sigma = 1.35$ is used.

2.1.5.4 SGS model selection

As aforementioned, two functional models are used in this thesis, and the selection between one or the other depends on the configuration. Two factors are considered: the SGS model impacts on the wind turbine wake and the simulation environment. Concerning the wind turbine wake, a study from Sarlak et al. [98] compared the role of different SGS models on the predicted flow structures in the vicinity of a turbine modeled with actuator lines (see **Section 2.3** for the actuator lines description). The outcome of this study showed that with a sufficient resolution, enabling the capture of the blade tip vortices, the choice of the SGS model is not a determining factor in the simulation accuracy. The highlighted limiting resolution is at least 30 points per rotor blade, i.e., 64 mesh cells at the rotor positionx and in the wake. In the presented studies,

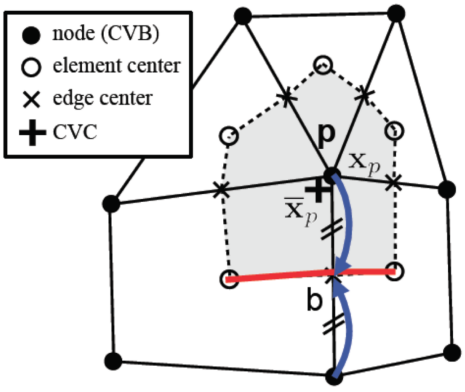

Figure 2.5: Control volume based on a mesh node in YALES2: $\mathbf{x}_p$ representing the mesh node and $\overline{\mathbf{x}}_p$ the barycenter of the control volume. The control volume is in grey ( ) and one of the interface between the control volume and a neighbour is represented (—). From [100]

this limiting resolution is respected. As for the environment, complex geometries impact the SGS model behavior and, consequently, the resolved flow characteristics. In 2014, the study of Reith et al. [99] compared the two models for a channel flow and past a turbulence grid. The conclusions show the $\sigma-$model comparable to the dynamic Smagorinsky, near complex geometry (channel flow walls and in grid generated turbulence) at significantly lower computational costs. Therefore, in the wind tunnel study presented in Chapter 3 the $\sigma-$model is used due to the presence of wind tunnel walls, turbulence grid, tower, and nacelle geometries. While for the open fields scenarios in Chapter 4 and Chapter 5 the Dynamic Smagorinsky model is used.

2.2 YALES2 CFD platform

This section attempts to present the CFD library called YALES2. It gives a global overview of all the numerical tools and strategies that have been implemented to circumvent the challenges when solving the Navier-Stokes equations on massive meshes.

2.2.1 Global overview and challenges

The numerical simulations presented in this thesis are performed using the finite-volume CFD library YALES2 [100], a low-Mach number Large-Eddy Simulation (LES) and Direct Numerical Simulation (DNS) solver based on unstructured meshes. This library allows having a multi-physics approach to solve the incompressible or low-Mach number Navier-Stokes equations in two and three dimensions. This multi-physical approach arises from the various solvers available in this library going from non-reactive turbulent flows [101, 102] to two-phase flows [103] and reactive variable density flows [104, 105]. YALES2 enables the management of all types of elements through dual control volumes for the integration of the transport equations; the control volume is provided in **Fig. 2.5**. Moreover, YALES2 is specifically tailored to solve the incompressible and low-Mach number equations on massively parallel machines with billion-cell meshes [106].

One of the significant difficulties when computing large-scale turbulent flows, such as the wake generated by offshore wind turbines, is the resolution of very heterogeneous spatial and temporal structures. Indeed, in the wake of a wind turbine, the convection and diffusion terms

from the Navier-Stokes are associated with the characteristic time and length scales which are not necessarily at the same magnitude order at a different distance from the rotor. The previously introduced Reynolds number represents the ratio between the convective and diffusive characteristic timescales. As the range of scales of the turbulent spectrum increases in turbulent flows, these two timescales become very different. This increases the cost of the Navier-Stokes equations solving as the time integration is based on the related smaller time step to guarantee the accuracy and stability of the numerical schemes. Moreover, the numerical simulations have to ensure some of the following aspects:

- The computational domain has to be able to resolve the largest scales of the flow. This strongly depends on the considered physics; the largest scales can reach kilometers for offshore wind turbines if one wants to consider atmospheric or site effect.
- The mesh has to be fine enough to resolve the smallest turbulent flow scales for the DNS formalism or until the cutoff frequency for the LES methodology.
- In the case of open field simulations, proper care has to be given to prevent any interaction between the blocage effect generated by the turbine and the boundary conditions. This can significantly increase the computational domain size.

2.2.2 Main tools and strategies

In LES, fidelity increases with the mesh resolution, the simulated physical time, or by adding complexity to the physics of the flow. Therefore, the steady increase of computational resources supports the development of the CFD field. Here is a list of some of the main tools and strategies developed in the CFD library YALES2 to perform high-performance computing.

- Low-Mach number approach, for constant and variable-density cases
- Interface tracking for two-phase flows
- Parallel dynamic mesh adaptation and dynamic load balancing
- High-order filtering (HOF)

The majority of these strategies are not used in this thesis, yet the YALES2 library allows to easily couple different methodologies. For example, in Chapter 4, a methodology based on Level set functions is developed to compute budgets on wind turbine wakes. Level set functions are initially used in the case of two-phase flows yet are pertinent for wake tracking. In the same way, the coupling of YALES2 with the remeshing library MMG3D allows to obtain meshes based on the local flow characteristics, see **Appendix B.** The following subsections give an insight into the double-domain decomposition and parallelism in YALES2 and the numerical schemes used in this thesis.

2.2.2.1 Double-domain decomposition and parallelism

To solve the incompressible Navier-Stokes equations on unstructured mesh in a massively parallel framework, YALES2 splits its computational domain. Each processor has a part of the domain assigned. The dependency between each sub-domain is taken into account thanks to communications between processors. These processors exchange information at the interface of each cell group using MPI (Message Passing Interface) instructions. The mesh decomposition

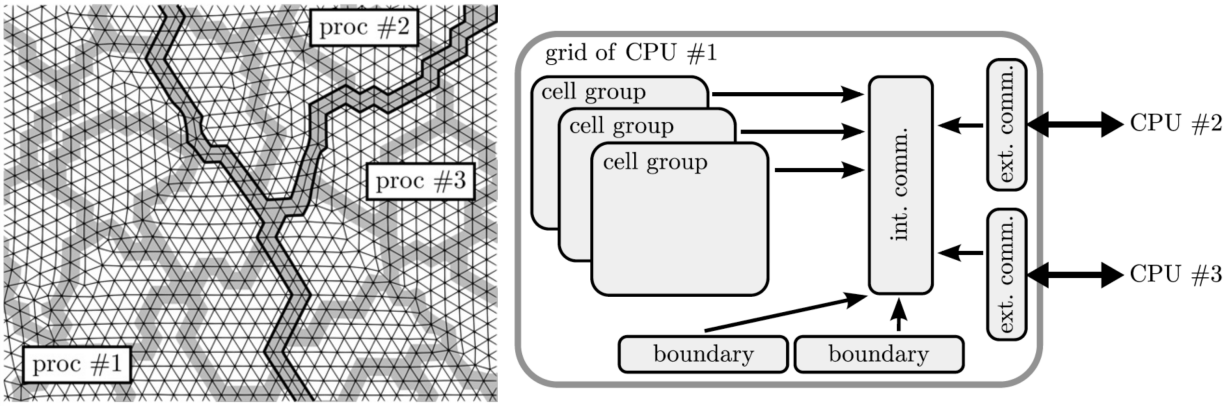

Figure 2.6: Representation of the Double-Domain Decomposition (DDD) (left). The highlighted elements are participating in the communications inside and outside each processor and those in the black subdomain are participating in the communications between processors. Scheme of the communications and structures used during the simulations (right). From [100]

must assure an optimal workload repartition between processors. In a purely Eulerian context, the most obvious way is to cut the mesh into sub-domains containing the same number of control volumes. While this decomposition might be trivial for structured meshes, it is not for unstructured meshes. In YALES2, this operation is done thanks to the external libraries METIS [107] and SCOTH [108].

In addition to that, YALES2 uses a Double-Domain decomposition (DDD) to optimize the computing performances in simulations with large meshes on thousands of processors. The DDD is organized as follows: as mentioned earlier, a first coarse grain level where the mesh elements are divided between processors. And a finer grain level is then introduced. Within the processor, cell groups are gathered as ELement GRouPs (ELGRPs), see **Fig. 2.6**(left). In 3D, ELGRPs gathers $\mathcal{O}(10^3)$ elements. This DDD is used to optimize the Poisson solver performances. The Poisson equation is presented in **Section 2.2.3.3**. The cell groups provide a coarse mesh, which is used by the two-level linear solvers such as PCG [109] with deflation [110]. This DDD allows better memory management than Single-level Domain Decomposition in cache-aware type algorithms. The communication scheme between groups of elements, communicators, and boundaries is represented in **Fig. 2.6**(right). More information on the structures can be found in [100], especially on the communications ELGRP-ELGRP, ELGRP-processor, and processor-processor.

2.2.2.2 Numerical schemes

The CFD library YALES2 features several numerical schemes for the explicit time advancement of the temporal integration, such as the classical third and fourth-order Runge-Kutta schemes. In this thesis, only the TFV4A scheme is used. This scheme has been proposed by Kraushaar [111] and combines both Runge-Kutta and Lax-Wendroff methods. Concerning spatial integration, second and fourth-order schemes have been implemented. This notion will not be further developed, but more details can be found in Vantieghem's thesis [112]. In this thesis, only the fourth-order spatial schemes are used. Moreover, even if many solvers dedicated to different physical phenomena are implemented into YALES2, only the Incompressible solver (ICS) at constant density has been used during this thesis and is presented hereafter.

2.2.3 Incompressible constant density solver (ICS)

2.2.3.1 Incompressible Navier-Stokes equations

The previously introduced Navier-Stokes equations for incompressible flows (**Eq. 2.2** and **Eq. 2.33**) can be rewritten in vectorial form as

$$\begin{aligned} &\nabla \cdot \mathbf{u} = 0\,, \\ &\frac{\partial \mathbf{u}}{\partial t} + \nabla \cdot (\mathbf{u} \otimes \mathbf{u}) = -\frac{1}{\rho}\nabla P + \frac{1}{\rho}\nabla \cdot \boldsymbol{\tau} + \mathbf{f}\,. \end{aligned} \tag{2.42}$$

This set of equations, where the velocity is unknown, is solved by the incompressible solver of YALES2. This solver is mainly used for impacting 3D jet, non-reactive flow in closed geometries, and open-field wind turbine applications where buoyancy and other atmospheric effects are neglected.

2.2.3.2 Prediction correction method

The solving of the Navier-Stokes equations for incompressible flows is based on the projection method proposed by Chorin [113] modified by Kim and Moin [114]. It is noticeable that this formalism resolves the instantaneous velocity field at each time step (associated to integer indices such as n, $n+1$, etc...) when the density, the pressure, and other scalar fields are resolved on staggered time step (associated to non-integer indices such as $n+1/2$, $n+3/2$, etc...). The main stages of this methodology are presented hereafter.

The classical projection method, often used for the simulation of incompressible flows, relies on the Helmholtz-Hodge decomposition under relatively smooth assumption. At each time step, the velocity field can be decomposed into an irrotational part and a solenoidal part as

$$\mathbf{u} = \Pi_i(\mathbf{u}) + \Pi_s(\mathbf{u})\,, \tag{2.43}$$

where $\Pi_i(\mathbf{u})$ refers to irrotational component and $\Pi_s(\mathbf{u})$ to the solenoidal component of instantaneous velocity field with respectively the following properties $\nabla \times \Pi_i(\mathbf{u}) = 0$ and $\nabla \cdot \Pi_s(\mathbf{u}) = 0$. These projection operators are defined as

$$\begin{aligned} \Pi_i &= \nabla \Delta^{-1} \nabla \cdot\,, \\ \Pi_s &= -\nabla \times \Delta^{-1} \nabla \times\,, \end{aligned}$$

Δ^{-1} as no mathematical interpretations, yet this form is written for symplifications purposes. Some important relationships can be highlighted:

$$\begin{aligned} \Pi_i\Pi_i &= \Pi_i & \Pi_s\Pi_i &= 0 & \nabla \cdot \Pi_i &= \nabla \cdot\,, \\ \Pi_s\Pi_s &= \Pi_s & \Pi_i\Pi_s &= 0 & \nabla \times \Pi_s &= \nabla \times\,. \end{aligned}$$

The irrotational component derives from a potential scalar and can thus be written as $\Pi_i(\mathbf{u}) = \nabla\phi$. The application of the divergence operator enables to express the previous relation as follows:

$$\nabla \cdot \mathbf{u} = \nabla \cdot [\Pi_i(\mathbf{u}) + \Pi_s(\mathbf{u})] = \nabla \cdot \Pi_i(\mathbf{u}) = \Delta\phi\,. \tag{2.44}$$

Thanks to this decomposition, the velocity balance equation can therefore be solved in two steps:

- **Prediction step:** A first estimation of the velocity field for the time $n+1$, noted $\mathbf{u}^\star$, is obtained by advancing the velocity equation without the contribution of the pressure

gradient as it does not contribute to the solenoidal part but to the irrotational part of the velocity field.

$$\frac{\mathbf{u}^\star - \mathbf{u}^n}{\Delta t} = -\nabla \cdot (\mathbf{u}^\star \otimes \mathbf{u}^n) + \frac{1}{\rho}\nabla \cdot \boldsymbol{\tau}^n + \mathbf{f}^n \tag{2.45}$$

- **Correction step:** Once the prediction has been done, leading to $\mathbf{u}^\star$, the velocity field is corrected by taking into account the pressure gradient:

$$\frac{\mathbf{u^{n+1}} - \mathbf{u}^\star}{\Delta t} = -\frac{1}{\rho}\nabla P^{n+1/2} \tag{2.46}$$

The computation of the corrected velocity, noted here $\mathbf{u^{n+1}}$, necessitates the knowledge of $P^{n+1/2}$ which can be determined by solving the Poisson equation. This equation can be obtained by taking the divergence operator of the previous equation and integrating the zero divergence constraint for $\mathbf{u^{n+1}}$.

$$\nabla \cdot \mathbf{u}^\star = \nabla \cdot \Pi_i (\mathbf{u}^\star) = \frac{\Delta t}{\rho}\Delta P^{n+1/2} \tag{2.47}$$

However, the advancement of the velocity equation that is implemented in the incompressible solver of YALES2 slightly differs [115] from Chorin's approach:

- **Prediction step:** In that case, the prediction step is done by considering the contribution of the pressure gradient at the time $n - 1/2$ that is generally a relatively good approximation of $P^{n+1/2}$. This approach leads to a better estimation of the predicted velocity $\mathbf{u}^\star$ that therefore enables to reduce the numerical errors due to the splitting of the temporal advancement.

$$\frac{\mathbf{u}^\star - \mathbf{u}^n}{\Delta t} = -\nabla \cdot (\mathbf{u}^\star \otimes \mathbf{u}^n) - \frac{1}{\rho}\nabla P^{n-1/2} + \frac{1}{\rho}\nabla \cdot \boldsymbol{\tau}^n + \mathbf{f}^n \,. \tag{2.48}$$

- **Correction step:** Then, the correction step can therefore be written as

$$\frac{\mathbf{u}^{n+1} - \mathbf{u}^\star}{\Delta t} = -\frac{1}{\rho}\nabla \left(P^{n+1/2} - P^{n-1/2} \right) , \tag{2.49}$$

which leads to a Poisson equation of the following form:

$$\Delta \left(P^{n+1/2} - P^{n-1/2} \right) = \frac{\rho}{\Delta t}\nabla \cdot \mathbf{u}^\star \,. \tag{2.50}$$

Finally, the solving of the Poisson equation is the critical point of the methodology as it necessitates efficient linear solvers to guarantee good performances for massively parallel computations. This point will be further discussed in the next section.

2.2.3.3 Poisson equation solving

The Poisson equation for the pressure presented in the previous section are equations that can be expressed in the form:

$$\Delta \varphi = RHS \tag{2.51}$$

in this case $\varphi = P^{n+1/2} - P^{n-1/2}$ and the value of the RHS, the right-hand side is set from the previous prediction-correction method. This equation deals with the solving of a linear system in which the discretized values of the pressure field at each computational node in the domain are unknown variables. Therefore, solving this system requires efficient linear solvers as

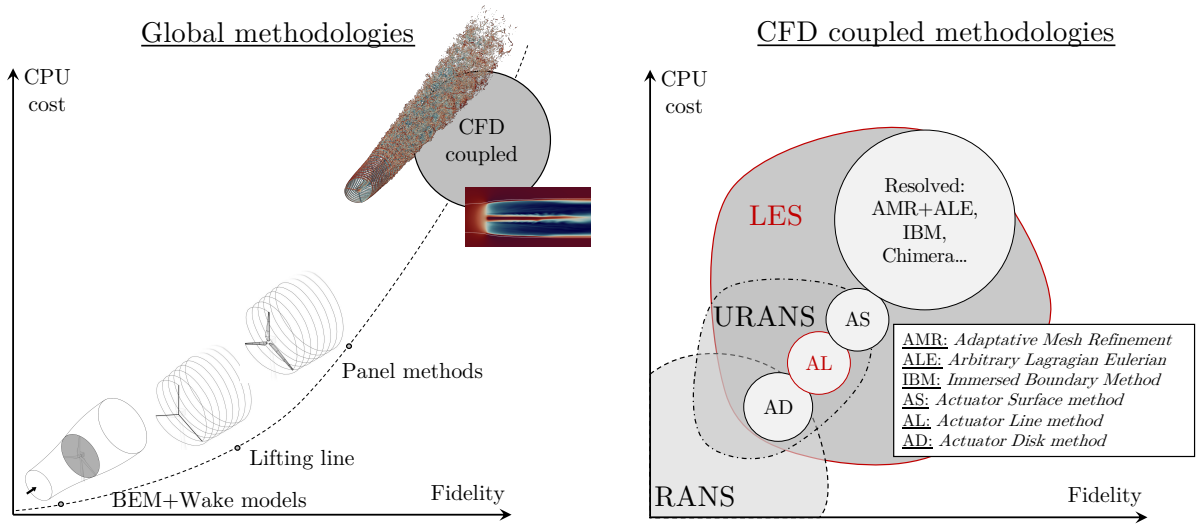

Figure 2.7: Schematic diagram of the evolution of the computational costs and fidelity of the different wind turbines modeling methods. a) Global methodologies b) CFD coupled methodologies.

it has to be done for each time step and may represent a predominant part of the CPU cost of the simulation. Indeed, these solvers are based on iterative numerical methods, and a high number of iteration to reach a sufficiently accurate estimation of the solution might be necessary. The number of iterations depends on the algorithms but also the characteristics of the discrete Laplacian operator. Moreover, each iteration of the linear solver requires some communications between the processors that can represent a non-negligible part of the total simulation time. This proportion can reach 80% if no special considerations are taken into account for the method implementation [116]. Therefore, the optimization of the Poisson equation resolution is one of the significant challenges for the simulation of incompressible flows; more detailed information can be found in Malandain's thesis [117]. Finally, several algorithms are available in the CFD code YALES2: The Preconditioned Conjugate Gradient (PCG) [109], the Deflated PCG [110] but also the BICGSTAB scheme [118].

2.3 Horizontal Axis Wind Turbine modeling

This section presents how horizontal axis wind turbines are modeled in this work. At first, an overview of the various way to represent a horizontal axis wind turbine in the LES framework is given. Then, a complete presentation of the Actuator Line Method (ALM) is provided. To finish, the implementation in the YALES2 library and the different optimizations are described.

2.3.1 Overview of the existing methods

Different methodologies exist for the emulation of a wind turbine in a CFD framework. They are related to different fidelity and computational cost levels. **Fig. 2.7** presents a non-exhaustive representation of the different methodologies for wind turbine numerical analysis [48]. The three main methodologies: ADM, ALM, and Resolved are briefly summarised hereafter and in **Fig. 2.8**:

- **Actuator Disk Method (ADM):** In this method, the geometry of the blades is not fully represented, and the effect of the rotor is accounted for through a disk of equivalent

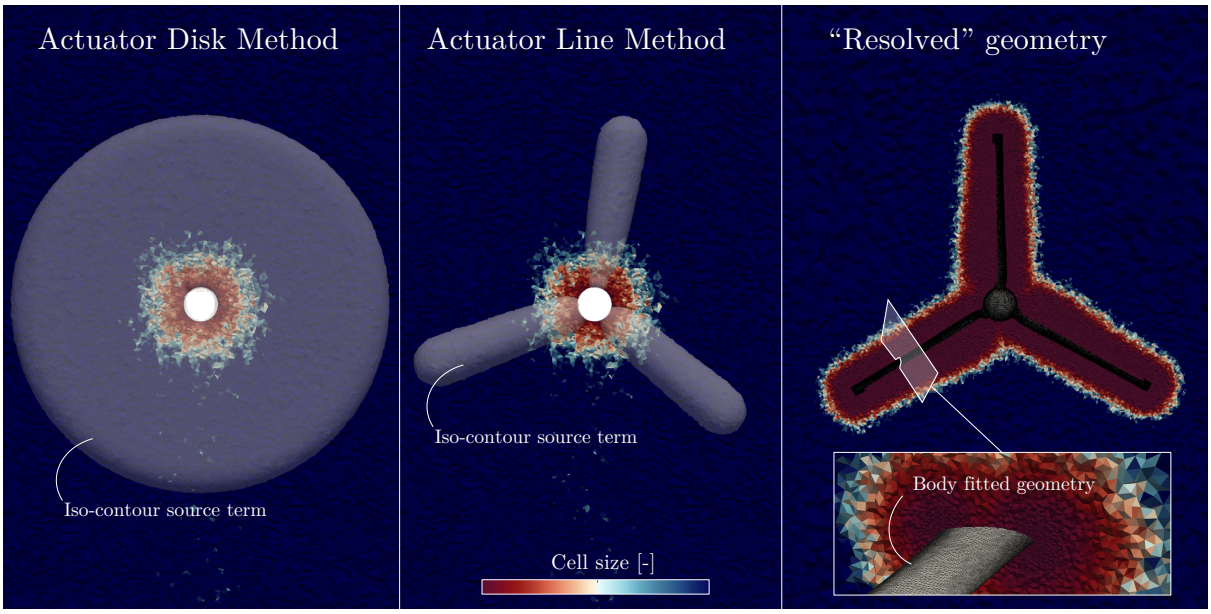

Figure 2.8: Exemple of the cell size requested arround the rotor according to the Actuator Disk Method, Actuator Line Method or a "Resolved" geometry. For the Disk and Line methodlogies an iso-contour of the source term emulating the turbines forces in the momentum equation is represented. For the resolved geometry, a closer look on a profile section is shown.

forces. The concept of an ADM [119, 120] consists in considering an average effect of the blades over their surface swept through one rotation. By fetching the local velocity of the flow field and knowing the turbine operating point, an averaged set of forces is computed and applied through a projection process on the Eulerian mesh used to solve the Navier-Stokes equations as a source term. This model slightly differs from one study to another, and additional features can be supplemented [121, 122]. Similar to the Blade-Element-Momentum [123], corrections of the forces can be applied either for tip loss correction or dynamic stall effects [124, 125].

- **Actuator Line Method (ALM):** The ALM [126] goes a step further in the blade geometry representation. Lines, one for each blade, represent the rotor. These lines are then discretized by airfoil sections, and from the tabulated aerodynamic coefficient, a local force is computed. Similar to the AD, the forces are mollified on the Eulerian mesh and used as volumic forces during the solving of the Navier-Stokes equations. This model proposes a higher level of fidelity than the AD by considering the blade motion and the generation of tip vortices. Yet this method does not resolve the flow around each airfoil section; the potential 3D effects occurring in the airfoil boundary layers are not taken into account without corrections [125, 127, 128].

- **Resolved geometry:** Considered as the "brute" force, the resolution of the geometry is the method reaching the highest level of fidelity. In this case, the blades geometries are taken into account either by body-conforming mesh to the blade [129, 130] or by immersed boundary methods [131]. The solving of the Navier-Stokes equations considers - depending on the local cell size - the airfoils boundary layers and, consequently 3D effects occurring near the airfoils. Many problems arise from this point. First, for offshore wind turbines, the Reynolds number at the blade tip is high ($Re = \mathcal{O}(10^7)$) and requests to resolve the vast range of generated eddies near the blade. Thus resulting in small

cell sizes and small-time discretization to keep the numerical scheme stable. Second, the resolution or not of the airfoil boundary layer, which can be bypassed by using wall models yet depends on the local effects [132, 133, 134]. The last problem lies in how the blades are "resolved". The use of mesh fitted to the blade demands peculiar care to take into account the blade movement. In this way, different techniques exist: the use of a rotating reference frame [135, 136] - more significant 3D effects such as the tower cannot be taken into account. The use of overlapping rotating meshes, the Chimera or Arbitrary Mesh Interface (AMI) approach [137, 138, 139] which strongly depends on the interpolation between meshes. The use of Arbitrary Lagrangian-Eulerian method (ALE) and Adaptative Mesh Refinement (AMR) [140] to impose the displacement of the near blades boundary cells while conserving mesh quality is really accurate yet counterbalanced by a high computational cost [141]. At the opposite, the immersed boundary methods are exonerated from the mesh evolution over time by imposing weight on the flow at the blade position. The accuracy of this technique depends on the local mesh resolution and the numerical methods used to reconstruct the blade boundaries [131].

A parallel to these three methods can be drawn with the numerical approach used to solve the Navier-Stokes equations. The standard Actuator Disk would be represented by the RANS where the averaged behavior of the turbine loads is modeled. The Actuator Line method would correspond to the LES formalism where the largest scales are resolved (the blade motion resulting in tip vortices). Yet, the local loads are modeled according to the local flow characteristics. And the resolved geometry to the DNS where every scale of the flow is resolved, thus increasing the computed load accuracy but at a tremendous computational cost. Other existing methodologies are used for the emulation of the wind turbine loads and wake global properties [142, 48]. They are often at a much lower computational cost since they are not coupled with the solving of the Navier-Stokes equations but based on models calibrated with experimental data or RANS/LES simulations. This thesis aims at studying the wake characteristics in realistic configurations, and therefore, the method requires considering the unstable effect impacting the wake flow behavior. Under this assumption, the ALM is used: an appropriate level of fidelity at an achievable computational cost.

2.3.2 Actuator Line Method

The Actuator line method was introduced in 2002 in the work of Sørensen and Shen [126]. This method has become a state-of-the-art strategy and relies on emulating the forces surrounding the turbine blades without resolving the flow around them. It has been widely used with Large-Eddy Simulations (LES) [143, 144] since the constraint is exonerated from the small limiting scales of the flow around the blade geometry while generating a representative helicoidal flow in the wake. Yet significant uncertainties remain on the proper load evaluation and various works investigated on how to improve the accuracy of this method, either on velocity evaluation, force corrections, or the mollification kernels. The complete methodology is presented hereafter, and the different steps are represented in **Fig. 2.9**.

0 (Blade discretisation): The blade is represented by a line and then discretised in N elements as displayed on **Fig. 2.9** a). Each element represents an airfoil of a given width w and chord c. This airfoil is based on the actual blade geometry at the element position, $\mathbf{x}_i$. The orientation of the airfoil is represented by the chord axis $\mathbf{e}_c$, the thickness axis $\mathbf{e}_t$ and the blade spanwise axis $\mathbf{e}_{blade}$. The chord and thickness axes are rotated to consider

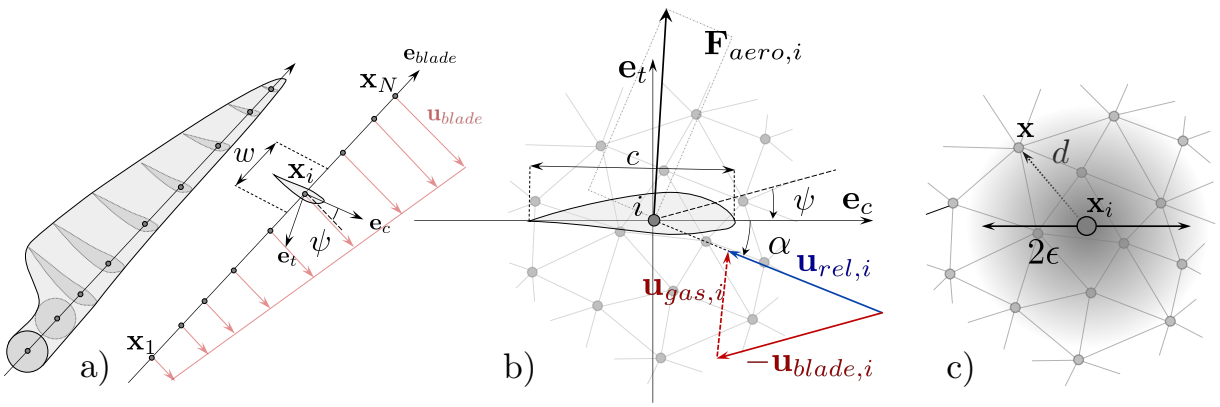

Figure 2.9: Scheme representing the different steps of the Actuator Line Method. a) Blade geometry discretisation as a line of N elements. b) Evaluation of the aerodynamic forces, $\mathbf{F}_{aero,i}$ for each element i. c) Mollification of the previously computed forces $\mathbf{F}_{aero,i}$ on the eulerian grid with a gaussian kernel of standard deviation $\epsilon/\sqrt{2}$.

the local blade twist, ψ. In the case of a deformable blade, the airfoil width axis is not always colinear to the blade axis.

1 **Local velocity evaluations:** After the initial discretization of the blade and during the temporal advancement, the first step is the evaluation of the velocity relative to each of the blade elements. Two velocities are required as depicted in **Fig. 2.9** b), the airfoil velocity $\mathbf{u}_{blade,i}$ and the gas velocity $\mathbf{u}_{gas,i}$ near the airfoil location. The first is given from the blade displacement based on the wind turbine various degrees of freedom (DOF). This depends on the operating conditions and the structural properties, if the wind turbine is submitted to constant rotations or if a controller regulates the DOF, or if the blade structure is subjected to deformations. For instance, the turbine rotation velocity and the blades dynamic pitching impact the local element displacement. The local gas velocity can be evaluated in various ways; commonly, it is assessed at the element location, yet this suffers from interpolation noise. To improve that, Churchfield et al. [145] derived the local gas freestream velocity by integrating the near velocity field with a weight function, representative of the mollification function of step four. Xie S. [146] addressed the use of a Lagrangian averaging method to recover an undisturbed upstream velocity, yet at a higher computational cost. In the original formulation, blade and gas velocities are projected in the airfoil plane to remove the spanwise contribution, and the relative velocity to the airfoil is obtained as follows:

$$\mathbf{u}_{rel,i} = \mathbf{u}_{gas,i} - \mathbf{u}_{blade,i}, \text{ commonly: } \mathbf{u}_{rel,i} = (u_{\theta,i} - \omega r_i, u_{z,i}, 0)\,, \tag{2.52}$$

with ω the rotor rotation speed, r_i the distance between the rotor center and the element i. The two other velocities, $u_{\theta,i}$ and $u_{z,i}$ denote the azimuthal and axial gas velocity in the rotor cylindrical reference frame. It is important to note that the spanwise gas velocity contribution is removed with this formulation.

2 **Force computations:** From the previous step, the relative velocity to the airfoil $\mathbf{u}_{rel,i}$ is used to compute the angle of attack α from which the forces are predicted according to the 2D aerodynamics of the local airfoil.

$$\mathbf{F}_{2D,i} = \frac{1}{2}\rho\|\mathbf{u}_{rel,i}\|^2 c\,(C_L(\alpha_i)\mathbf{e}_L + C_D(\alpha_i)\mathbf{e}_D)\ . \tag{2.53}$$

The lift C_L and drag C_D coefficient are dependent to a given α and the local chord based Reynolds number $Re_c = \|\mathbf{u}_{rel}\| c/\nu$. The unit vectors $\mathbf{e}_L$ and $\mathbf{e}_D$ can be expressed according to the chord and thickness axis of the airfoil as follows:

$$\begin{aligned} \mathbf{e}_L &= \sin(\alpha)\mathbf{e}_c + \cos(\alpha)\mathbf{e}_t \,, \\ \mathbf{e}_D &= -\cos(\alpha)\mathbf{e}_c + \cos(\alpha)\mathbf{e}_t \,. \end{aligned} \tag{2.54}$$

The lift and drag coefficients are either determined from measurement or the computation of two-dimensional airfoil data corrected for three-dimensional effects. These so-called 3D corrections aim at emulating rotational effects that limit the growth of the airfoil boundary layer at the separation point. Several 3D corrections formulas are present in the literature [147, 148, 149, 150]. The second correction is based on the aspect ratio of the blade and the element proximity to the root and tip. These corrections are called the tip loss corrections [151, 152, 125, 153] and aim at taking into account the flow rate generated at the blade extremities induced by the pressure gradient between the pressure and suction faces of the airfoil. Other corrections consider the dynamic stall effect that may occur on the element, increasing the drag and reducing the lift. These dynamic stall models/corrections [154, 155] are based on the temporal evolution of the angle of attack and the airfoil properties. The local force is then integrated over the element section and is expressed by:

$$\mathbf{F}_i = \int_w \mathbf{F}_{2D,i} \mathrm{d}w \,. \tag{2.55}$$

3 Force mollification: The third step is the application of the forces as source terms in the filtered Navier-Stokes equations (**Eq. 2.36**). To prevent any singular momentum source values at the element position, this step introduces the regularisation of the forces on the Eulerian grid. This is done by taking the convolution of the local force, $\mathbf{F}_i$ and a regularisation kernel, η_ϵ. The force resulting from this convolution is given as

$$\mathbf{F}_{\epsilon,i} = \mathbf{F}_i * \eta_\epsilon \,. \tag{2.56}$$

The regularisation kernel can be expressed as

$$\eta_\epsilon(d) = \frac{1}{\epsilon^3 \pi^{3/2}} \exp\left[-(d/\epsilon)^2\right] \,, \tag{2.57}$$

d being the distance between a grid node and the element position and ϵ the mollifier width parameter. To ensure a conservative treatment of the forces on a numerical grid with a given cell size h, ϵ/h has to be set such that:

$$\int_{\mathbb{R}^3} \eta_\epsilon(\mathbf{x}) \, \mathrm{d}\mathbf{x} = 1 \,. \tag{2.58}$$

A lower bound limit has been identified in previous studies [156, 126] as $\epsilon/h \geq 2$ from a numerical point of view. This technique provides a smooth force $\mathbf{f}$ distributed on the grid obtained from the forces concentrated on a given element depicted in **Fig. 2.9** c). Finally, the body force source term $\mathbf{f}$ at a position $\mathbf{x}$ in the momentum balance equation reads:

$$\mathbf{f}(\mathbf{x}) = -\frac{1}{\rho} \sum_{i=1}^{N} \mathbf{F}_i \, \eta_\epsilon \left(\|\mathbf{x} - \mathbf{x}_i\|\right) , \tag{2.59}$$

where N is the number of actuator points along the span of the geometry to respect the mollifier width, this operation is repeated for all the turbine blades. A comprehensive

discussion on the mollification kernel appears in the literature. In 2014, Martínez-Tossas et al. [157] rediscussed the impact of the mollification kernel width on the wind turbine loads by comparing various grid resolution and ϵ values. Then, the first introduction to a variable ϵ based on an elliptic planform of the chord along the blade span is introduced by Jha et al. [158]. From this, other works [159, 160] presented an "optimal smoothing length" for epsilon based on geometrical properties and introduced an anisotropic 2D [160], and then 3D [159, 145] gaussian kernel for the ALM. The "optimal smoothing length" is estimated to be close to 0.25 airfoil chord from a 2D comparison with inviscid flows and aims to prevent the use of tip loss corrections. Yet, this optimal kernel remains relatively small, as one-quarter of the chord is often considered too expensive for practical applications. To tackle this problem, four recent studies [161, 162, 163, 164] revisited the classical lifting line theory [165] to obtain a proper load evaluation without reaching the optimal smoothing length.

4 Flow resolution: The remaining step is to solve the Navier-Stokes equations with the generated source term representing the wind turbine effect on the flow.

2.3.3 Implementation in YALES2

The last subsection relates the various way of using the actuator line method in an LES framework. To clarify the methodology used in this thesis, this subsection presents how the different steps of the ALM are implemented in the YALES2 library.

0 Blade discretization: The blade discretization in N elements can be either user-defined or computed from the unstructured mesh local cell size. During the initialization, the code fetches the minimum and maximum local grid cell size in the rotor area, $h_{\min}$ and $h_{\max}$. The minimum number of elements per blade, according to the mesh is then computed from the following formula

$$N \geq L_{\text{blade}}/h_{\max}\,, \tag{2.60}$$

with L_{blade} the length of the blade from root to tip. This allows to achieve a sufficiently fine blade discretization, giving an element width roughly equal to the maximum cell size in the rotor area, $w \sim h_{\max}$. If N is smaller, the blade discretization is insufficient and discontinuities can appear in the mollified source terms. In the majority of the computations, the cell size is set at constant in the rotor area. Yet, when the tower and nacelle are body-fitted, this requests small cells near the hub to capture the structures generated at the solid boundary. In addition to that, the blade discretization requires to take the coarsest cells to prevent any numerical discontinuities in the mollification process. Recent work [166] targets an adaptative mesh refinement (AMR) strategy to properly capture the wake structures at a lower computational cost where usually the cell size is set to constant in the rotor region. In this case, after each mesh adaptation, this equality is tested to prevent any poorly discretized blade. Then each blade element is located at the corresponding blade radius assumed to be at the quarter-chord line of the blade

1 Local velocity evaluations: During this step, the velocities are evaluated at the initial position of the elements. At first, the element velocity is computed from the structural displacement, according to the different DOF and the angular velocities imposed by the user or a controller. The definitions of the reference frame, DOF, and angular velocities are presented in **Appendix A.** With the different angular velocities, the future position

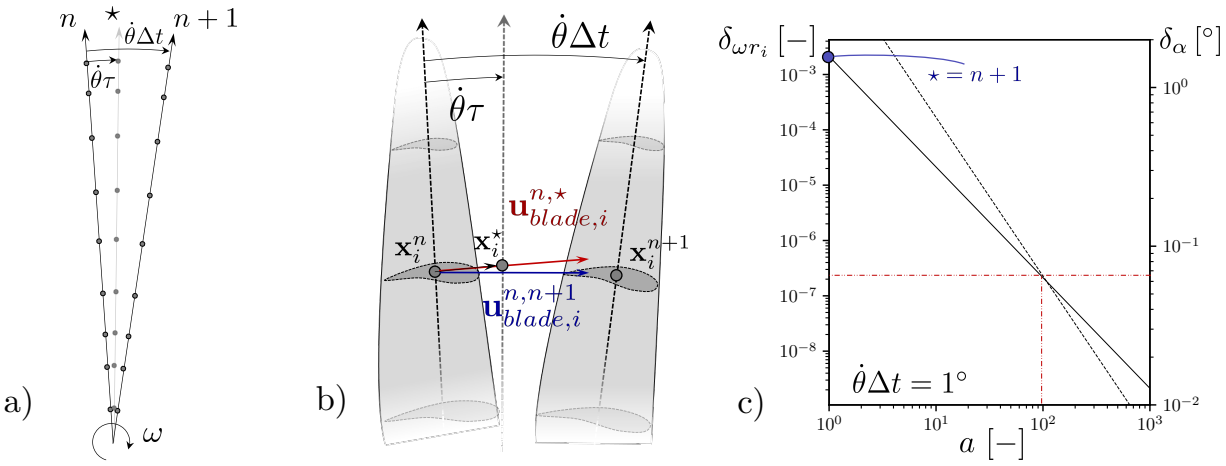

Figure 2.10: Representation of the element velocity evaluation for a given time-step, Δt. a) The actuator line is advanced from time n to $n+1$, an intermediate time $\star$ is introduced with $\tau = \Delta t/a$. b) The element velocity is computed from the positions at n and $\star$, if $a = 1$ the intermediate time is equivalent to $n+1$. c) Impact of a on $\mathbf{u}^{n,\star}_{blade,i}$ for one DOF, $\omega r_i \mathbf{e}_\theta$ is the exact velocity: (left axis) error on amplitude, $\delta_{\omega r_i} = \frac{\omega r_i - \|\mathbf{u}^{n,\star}_{blade,i}\|}{\omega r_i}$ (——) and (right axis) misalignment with the tangential unit vector, $\delta_\alpha = \cos^{-1}\left(\frac{\mathbf{e}_\theta \cdot \mathbf{u}^{n,\star}_{blade,i}}{\|\mathbf{u}^{n,\star}_{blade,i}\|}\right)$ in degree (- - -).

of the elements are evaluated, see **Fig. 2.10** a) with one DOF. From this position, the element velocity can be computed as follows:

$$\mathbf{u}_{blade,i} = \frac{d\mathbf{x}_i}{dt} \simeq \frac{\mathbf{x}^\star_i - \mathbf{x}^n_i}{\tau} = \mathbf{u}^{n,\star}_{blade,i}\,, \tag{2.61}$$

where τ is an infinitesimal portion of the actual fluid timestep, i.e. $\tau = \Delta t/a$ where $a \geq 1$. The initial position of the element is $\mathbf{x}^n_i$ and $\mathbf{x}^\star_i$ is the position of the element after a time equal to τ, see **Fig. 2.10**b). This evaluation of the local velocity is necessary when more than one DOF impacts the wind turbine, i.e. when pitch control is activated, for a deformed blade or when a dynamic yaw is investigated. This hypothesis on the velocity is easily verified with a constant rotation speed by comparing the direction and intensity of the resulting velocity for different values of a, see **Fig. 2.10** c). For this example the angular velocity is set to obtain $\dot{\theta}\Delta t = 1°$. When $a = 1$, i.e. without an intermediate time, the misalignment angle between the exact velocity and the approximated velocity reaches $\sim 6.5°$. From this, a is set to 100, reaching an error on the amplitude of 2.10^{-7} and a misalignment of 0.06°. In the following, the approximation $\mathbf{u}_{blade,i} = \mathbf{u}^{n,\star}_{blade,i}$ is considered exact with $a = 100$.

Secondly, the local fluid velocity, $\mathbf{u}_{gas,i}$ is evaluated from the Eulerian grid. A linear interpolation from the surrounding mesh nodes towards the actuator element is made.

Finally with these two velocities, the relative velocity to the airfoil projected in the airfoil plane at the time n is written

$$\mathbf{u}_{rel,i} = (\mathbf{u}_{gas,i} \cdot \mathbf{e}_c - \mathbf{u}_{blade,i} \cdot \mathbf{e}_c)\mathbf{e}_c + (\mathbf{u}_{gas,i} \cdot \mathbf{e}_t - \mathbf{u}_{blade,i} \cdot \mathbf{e}_t)\mathbf{e}_t\,. \tag{2.62}$$

2 Force computations: From the previous step, the relative velocity to the airfoil $\mathbf{u}_{rel,i}$ is used to compute the angle of attack α_i as

$$\alpha_i = \text{atan2}\left(\mathbf{u}_{rel,i} \cdot \mathbf{e}_t, -\mathbf{u}_{rel,i} \cdot \mathbf{e}_c\right)\,. \tag{2.63}$$

The forces are then evaluated from the $C_L(\alpha_i)$ and $C_D(\alpha_i)$ tabulated polars according to **Eq. 2.53**. The induced moment $\mathbf{M}_{\mathbf{x}_i}$ on each actuator elements is evaluated by using the moment coefficient, $C_M(\alpha_i)$:

$$\mathbf{M}_{\mathbf{x}_i} = \frac{1}{2}\rho\|\mathbf{u}_{rel,i}\|^2 wc^2 C_M(\alpha_i)\mathbf{e}_s\,. \tag{2.64}$$

$C_M(\alpha_i)$ is evaluated and tabulated at a given position on the airfoil, along the chord and the thickness axis. This position is commonly taken to be at the quarter of chord, coinciding with the actual actuator element positions. Moreover, various corrections have been implemented in YALES2 and can be applied to the forces. They are listed below:

- 3D stall delay: [147, 148, 149, 150]
- tip/hub losses: [151, 152, 125, 153]
- Dynamic stall: [154]
- Filtered lifting line: [162]

Then, the eventually corrected forces and moments are saved in the element reference frame before the blade displacement and the mollification of the forces.

3 **Blade displacement:** After the force evaluation at the initial blade position, the blade is displaced to its final place where the forces will be mollified. It is important to note that the loads are computed in the element reference frame. After the blade displacement, i.e., the rotation(s) of the element reference frame, the previously calculated forces in the local reference frame are projected into the global reference frame of the computational domain according to the new element orientation.

4 **Force mollification:** After the blade advancement, the forces are mollified on the Eulerian grid at the new actuator position using the regularisation kernel η_ϵ. From here, two different mollification kernels can be selected, the original isotropic gaussian [126] or the anisotropic gaussian [159, 145] kernel. Yet, the second solution requests a much more resolved Eulerian grid in the proximity of the blade. In this thesis, only the original isotropic Gaussian is used; see **Eq. 2.57**. During the mollification, proper care is given to select the grid cells close to the actuator line element to reduce the computational time. This is discussed in **Section 2.3.4**. Since YALES2 uses unstructured meshes with potentially different node volumes, the forces can be normalized on the grid, adding a supplementary MPI communication. Moreover, the limiting constraint of the blade displacement during the time-step is reduced through a substeping advancement of the actuator line. This method is presented and validated in **Section 2.3.4**.

5 **Solving of the Navier Stokes equations:** The convoluted force, $\mathbf{f}$ is used in the prediction step of the incompressible solver (see **Eq. 2.45**).

2.3.4 Optimizations and primary validations of the ALM in YALES2

Implementing the ALM in a massively parallel framework requires considering its impact on the computational cost. Two strategies are developed to reduce the computational cost with a low impact on the flow physics. The first is in the mollification process where the cells close to the blade position need to be selected to apply the mollified force. The second is the notion of substepping to reduce the number of fluid iterations, which can be seen as a temporal

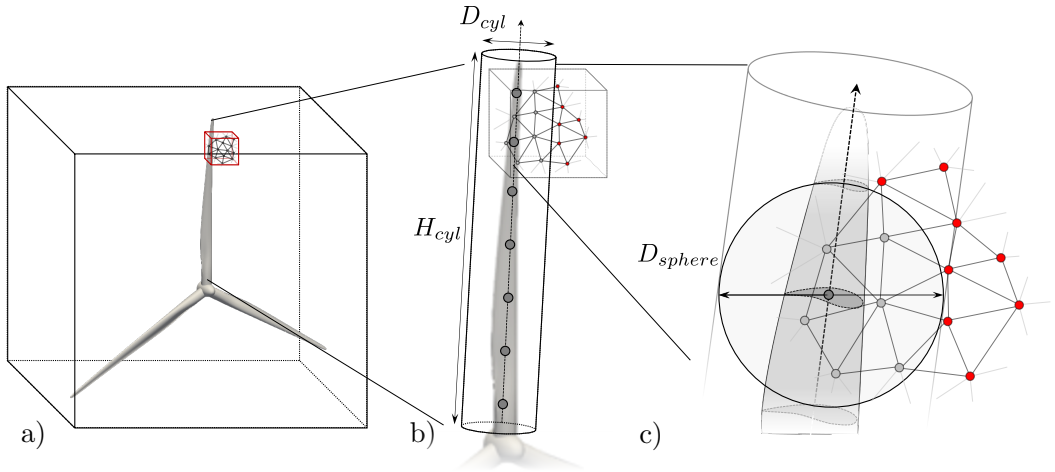

Figure 2.11: Principle of the three level algorithm allowing to select the nodes close to the actuator element. a) Coarse level: Bounding box comparison rotor-ELGRP. b) Medium level: Nodes proximity to the blade (Cylinder). c) Fine level: Nodes proximity to the blade element (Sphere).

mollification of the forces. These optimizations of the ALM are introduced and discussed in the following sections.

2.3.4.1 Mollification process

The properties of the YALES2 library in the partitioning of unstructured meshes are essential to understand how to optimize the mollification process; they are presented in **Section 2.2**. When applying a local volume source term, dealing with a sizeable unstructured grid can lead to high CPU costs. This occurs at each time iteration when the actuator line forces are mollified on the Eulerian grid. The mollification aims at dividing a localized quantity on a surrounding cloud of cells based on a mollification function. The notion of ELGRPs and the processor-processor communications are important for the mollification process. To mollify the forces, it is sufficient to locate the grid nodes surrounding the actuator line element. For this purpose, a three-level algorithm is used to select the close-nodes, as depicted in **Fig. 2.11**.

- **Coarse level:** The coarse selection level will compare a square bounding box surrounding the rotor and the ELGRPs square bounding box. The bounding box surrounding the rotor is a squared box of side $H_{box} = D + 1.4\xi$, where D is the turbine rotor diameter and ξ the extension based on ϵ. This first selection allows to retrieve the groups of elements in the vicinity of the turbine rotor, see **Fig. 2.11** a).

- **Medium level:** Then, by looping on the nodes within the selected ELGRPs, a finer selection level checks if the elements are within a cylinder surrounding each of the rotor blades, see **Fig. 2.11** b). The cylinder is defined according to the actuator elements position and mollification kernel width, ϵ. The length of the cylinder is defined as $H_{cyl} = L + 2 \times \xi$, where L is the blade length. The diameter of the cylinder is $D_{cyl} = 2 \times \xi$.

- **Fine level:** In the fine level of selection, see **Fig. 2.11** c), the proximity of the remaining nodes to each actuator element is evaluated, i.e., the nodes must be within a sphere centered on the actuator element. The sphere diameter is the same as the cylinder diameter, $D_{sphere} = D_{cyl} = 2 \times \xi$.

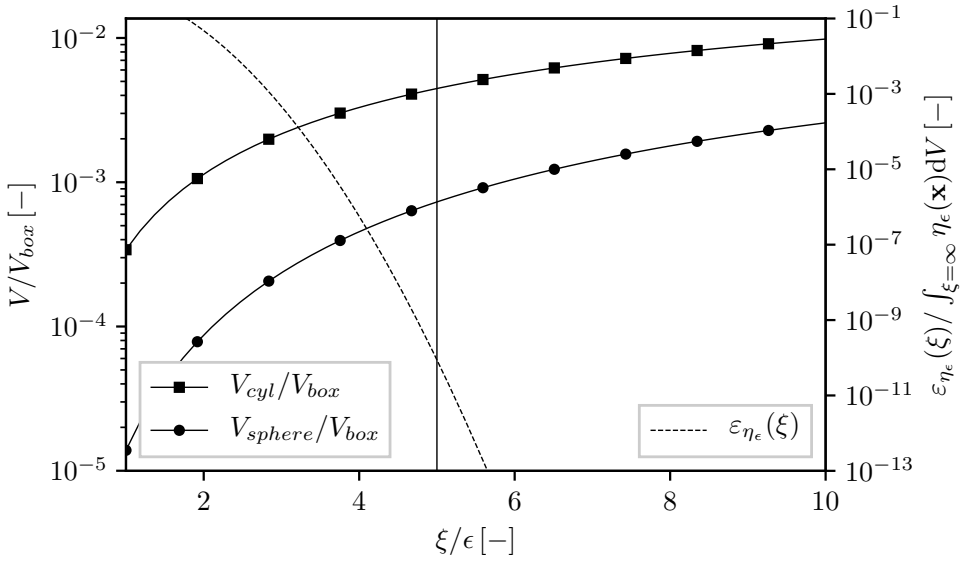

Figure 2.12: Evolution of the volume fraction for the medium and fine levels according to the cylinder and sphere bounding length, ξ (left axis). Evolution of the volume integral of the mollification kernel $\eta_\epsilon(\mathbf{x})$ according to the considered ξ values (right axis).

These different levels of selection allow the reduction of the number of mesh nodes on which to apply the forces multiplied by the mollification factor. This is shown in **Fig. 2.12** by comparing the considered volume of the coarse level and the one from the medium and fine levels. The selection of ξ, the cylinder and sphere bounding length, is set to apply most of the force on the grid. The integral of the gaussian kernel for different values of ξ is presented on the secondary axis of **Fig. 2.12**. For $\xi = 5\epsilon$ the volume integral of the mollification function, $\eta(\mathbf{x})$ gives :

$$\varepsilon_{\eta_\epsilon}(\xi = 5\epsilon) = \iiint_{\xi=\infty} \eta_\epsilon(\mathbf{x})\mathrm{d}V - \iiint_{\xi=5\epsilon} \eta_\epsilon(\mathbf{x})\mathrm{d}V < 10^{-10}\,. \tag{2.65}$$

This difference being sufficiently small, ξ is set to five times the mollification kernel width in the rest of this thesis. For this value of ξ the volume ratios between the coarse level and the finer level are $V_{cyl}/V_{box} = 4.10^{-3}$ and $V_{sphere}/V_{box} = 8.10^{-4}$. If the mesh is homogenous in cell size near the turbine, this ratio of volume will be equivalent to the ratio of cells on which the mollification process needs to be performed. The coarse level will deal with 1250 times more cells during the mollification process. As the mollification process consists of a loop over every nearby cell and for every actuator point, fewer calculations are required. Therefore, this high difference in volume considered can be translated into a non-negligible computational time reduction of the mollification process.

Tab. 2.1 gives an idea of the computational cost reduction by activating the different selection levels. The reduced computation time (RCT) are presented in the table to assess the computational performance, defined as:

$$\mathrm{RCT} = \frac{WCT \cdot N_{CPU}}{N_{\Delta t} \cdot N_n}\,, \tag{2.66}$$

where WCT is the wall clock time, N_{CPU} is the number of cores, $N_{\Delta t}$ is the number of completed time steps, and N_n is the number of vertices in the mesh. The computational cost significantly increases with the number of actuator elements per blade, N_{ALM} when using only the coarse selection level as expected from the volume ratios. The activation of the second and third selection levels strongly decreases the computational cost dependency with the number of actuator

Cases / Selection Levels	Case 1: T1, $N_{ALM} = 27$ $N_{proc} = 4$, Mesh: $N_{element} = 10^6$			Case 2: NREL5MW, $N_{ALM} = 64$ $N_{proc} = 20$, Mesh: $N_{element} = 10^6$		
	Time [s] / [%]	RCT [μs]	Diff RCT	Time [s] / [%]	RCT [μs]	Diff RCT
1st	0.59 / 2.3	0.46	0%	376.4 / 73.4	73.6	0%
1st and 2nd	0.43 / 1.7	0.34	-26.1%	1.9 / 1.34	0.38	-99.4%
1st, 2nd and 3th	0.16 / 0.63	0.12	-74.0%	1.1 / 0.8	0.21	-99.7%

Table 2.1: Computational cost of the mollification process when activating the different cells selection for two wind turbine cases. The percent, [%] is the ratio between the overall computational time and the time elapsed in the mollification process.

elements. From the percentage of the time passed in the ALM and the overall computational time, this three-level selection algorithm leads to a negligible ALM cost compared to the solving of the flow equations.

- **Note on Parallel computing**

The ALM use in YALES2 is not yet optimized for several turbines; this aspect will be furtherly improved after this thesis. At the moment, each turbine represented by the ALM is known by each processor participating in the computation. This has several impacts: the duplication of information and the serial calculation of the actuator line methodology. As a consequence, adding more turbines leads to an increase in computational cost. This cost increase remains around two percent with two turbines in the computational domain. Still, this highly increases for windfarm cases, up to 80% of the global cost when thirty turbines are present. The idea would be to allocate the turbine data only on the processors containing control volumes in the turbine global bounding box range, presented in the mollification section. This would allow dealing with the different actuator lines turbine in parallel, thereby reducing the cost of windfarm cases. This is not problematic in this thesis since, at most, only two turbines are investigated.

2.3.4.2 Substep for ALM

The second optimization is the modification of the limiting time step when using the actuator line method. The notion of CFL number is well known in CFD, as it characterizes the necessity to link the time step, the cell size, and the local velocity to conserve the stability of the numerical scheme during the transport of the information on the Eulerian grid. A similar number can be introduced to quantify the actuator element displacement according to the local cell size during the time step.

$$CFL_{Rotor} = \max_{j=1,N_{blade}}(\max_{i=1,N}(CFL_{j,i})) \text{ with } CFL_{j,i} = \frac{\|\mathbf{u}_{j,i}\|\Delta t}{h_i}, \tag{2.67}$$

where h_i is the cell size near the actuator line element, Δt the flow limiting time-step, j is the blade indice and i is the blade elements indices. If $CFL_{Rotor} > 1$ it means that at least one actuator element displacement will be greater than the local cell size. The limiting element is often the blade tip element since its displacement is higher, yet this depends on the unstructured mesh. A $CFL_{Rotor} >> 1$ introduces discontinuities in the projected forces of the trailing time-steps and therewith introduces purely numerical fluctuations in the velocity field. In the case of flow surrounding wind turbine, the limiting time step is due to the convective time-step, which

is determined according to the CFL number:

$$\Delta t = CFL \times \min_{nodes} \frac{h}{\|\mathbf{u}_{flow}\|} , \tag{2.68}$$

where h and $\mathbf{u}_{flow}$ are the local node[1] cell size and flow velocity. Δt represents the minimum time-step computed over all the Eulerian grid nodes to satisfy the chosen CFL number. For such an application, $CFL = 0.9$ is a good trade-off between numerical stability and computational cost reduction. From this evaluation of Δt and by considering the limiting actuator element at the blade tip, CFL_{Rotor} can be expressed as follows:

$$CFL_{Rotor} = \frac{\|\mathbf{u}_{blade,tip}\|}{h_{tip}} \times CFL \times \min_{nodes} \frac{h}{\|\mathbf{u}_{flow}\|} . \tag{2.69}$$

In the case of a constant cell size, or a similar cell size at the tip and at the highest velocity localisation, the CFL_{Rotor} becomes independent from the mesh resolution:

$$CFL_{Rotor} \sim \lambda \times CFL \times \min_{nodes} \frac{U_\infty}{\|\mathbf{u}_{flow}\|} . \tag{2.70}$$

This formulation introduces the tip speed ratio $\lambda = \frac{\|\mathbf{u}_{blade,tip}\|}{U_\infty}$ as a key parameter of CFL_{Rotor}. This formulation is based on various assumptions yet shows that the actuator element displacement is limiting compared to the convective time-step for high tip speed ratios. To prevent numerical fluctuations, two solutions are possible, either by reducing the simulation time-step, which strongly increases the computational cost, or preserving the time-step and through a time-mollification mollify the forces with a substeping process. The second solution was developed during this thesis.

The substep in the mollification process is defined as follows in YALES2. First, the number of substeps to prevent discontinuities in the convoluted force is evaluated as :

$$N_{substep} = \text{ceil}(CFL_{Rotor}) . \tag{2.71}$$

Then, after the force computations, i.e. the second step of the actuator line method (see **Section 2.3.3**) a loop over the number of substep is introduced. **Fig. 2.13** represents a schematic overview of the substeping method.

3⋆ Blade intermediate advancement: At first the blade is advanced according to a reduced time-step defined as $\tau = \Delta t / N_{substep}$. The position of the blade is now intermediary between the final position and the initial position depending on the number of elapsed substeps, i.e. $s \rightarrow 1, N_{substep}$. This intermediate position is $\mathbf{x}_i^{n+\frac{s}{N_{substep}}}$ referred to as $\mathbf{x}_i^{\star,s}$. During this step, the forces initially computed in the element reference frame are reprojected in the global reference frame according to the new element orientation.

4⋆ Convection of mollification kernel center: Then the force application positions are deduced by convecting the intermediate position of the blade, by the local flow velocity during the remaining time of the timestep:

$$\mathbf{x}_{i,mol}^{\star,s} = \mathbf{x}_i^{\star,s} + \Delta t (1 - \frac{s}{N_{substep}}) \times \mathbf{u}_{gas,i} , \tag{2.72}$$

[1] Actually in YALES2, the CFL conditions are determined based on the pairs, the interface between two nodes. The velocity at the pair is compared to the pair element length and it is the minimum value computed at the pairs of the node that is considered. Yet, it is presented here at the nodes to facilitate the understanding.

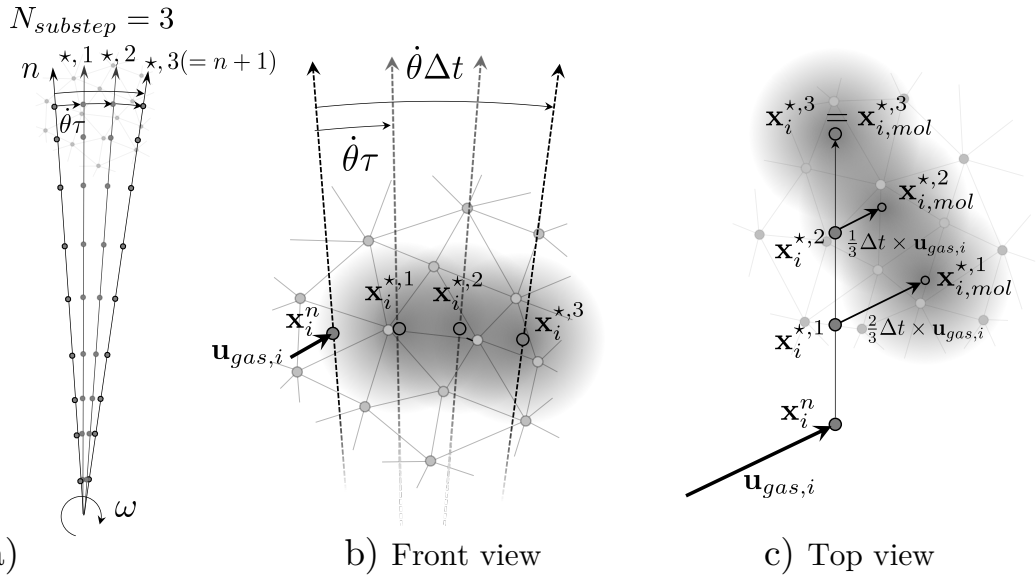

Figure 2.13: Scheme of the substep of the mollification for the ALM. Exemple when $N_{substep} = 3$: a) evaluation of the number of substep, b) front and c) top view of the blade displacement and the convection of the mollification kernel center according to the local gas velocity.

where s is the substep number and $\mathbf{x}_{i,mol}^{\star,s}$ is the convected mollification kernel center. This step allows preserving the direction of the flow perturbation once the mollified forces are applied in the momentum equations. For the last substep one can notice that $\mathbf{x}_{i,mol}^{\star,s} = \mathbf{x}_i^{\star,s}$ and therewith the force is mollified at the element position. It is important to mention that if $N_{substep}$ is too high, this can lead to a strong error in the generation of the helicoidal structure of the wake. This will be discussed at the end of this subsection.

5⋆ Force mollification : The last step is the mollification of the forces at the newly evaluated position. Therewith, **Eq. 2.59** is rewritten as

$$\mathbf{f}^{\star,s}(\mathbf{x}) = -\frac{1}{\rho}\left(\sum_{i=1}^{N} \frac{\mathbf{F}_i}{N_{substep}}\, \eta_\epsilon\left(\|\mathbf{x} - \mathbf{x}_{i,mol}^{\star,s}\|\right)\right) . \tag{2.73}$$

It is essential to notice that only $\frac{1}{N_{substep}}$ of the computed element force is applied during each substep.

At the end of the loop over the substeps the body force source term on the Eulerian grid is :

$$\mathbf{f}(\mathbf{x}) = -\frac{1}{\rho}\sum_{s=1}^{N_{substep}}\left(\sum_{i=1}^{N} \frac{\mathbf{F}_i}{N_{substep}}\, \eta_\epsilon\left(\|\mathbf{x} - \mathbf{x}_{i,mol}^{\star,s}\|\right)\right) , \tag{2.74}$$

This convoluted force, $\mathbf{f}$ is used in the prediction step of the incompressible solver (see **Eq. 2.45**).

The main goal of this methodology is to reduce the computational time without reducing the fidelity of the simulation. Therefore, the impact of the substeps process is evaluated through the simulation of the flow around an NREL5MW [167] wind turbine, which is presented hereafter. The considered computational domain is $8D \times 8D \times 10D$ with $D = 126\,\text{m}$ being the turbine diameter. The wind turbine rotor center is set at $4D$ from the inlet. A $4D$ distance between the rotor center and the side slip walls is considered sufficient to prevent confinement effects. The

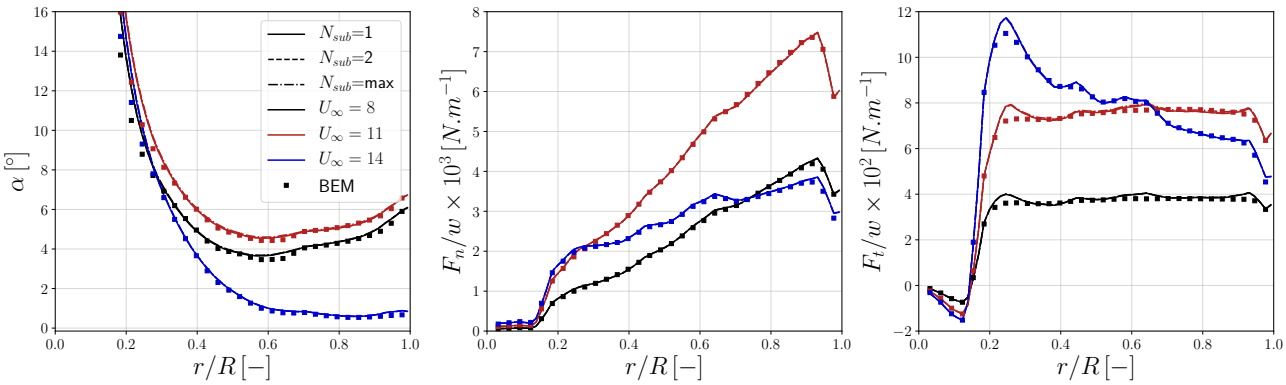

Figure 2.14: Time averaged angle of attack (left), normal (middle) and tangential forces (right) along the NREL 5MW blades at different wind speeds and different number of substeps predicted by ALM simulations compared to BEM results. The curves for the different number of substeps are overlapping and no discrepancies are observed.

cell size in the wake, a cylinder of three times the turbine diameter, is set as $D/h_{wake} = 50$. Around this cylinder, the cell size is slowly coarsening at a 1.2 rate. The overall tetrahedral mesh is composed of 156×10^6 elements. The mollification kernel size is set at $\epsilon/h_{wake} = 2$. Three operating tip speed ratios are simulated $\lambda = 7.6$, 7 and 5.7. These are achieved at constant inflows of $U_\infty = 8$, 11 and $14\,\mathrm{m.s^{-1}}$ and constant rotation speeds $\omega = 9.2$, 11.75 and 12.1 rpm. According to the NREL5MW reference controller, the blades are pitched of 8.7° only for $\lambda = 5.7$. No corrections are applied to the computed angle of attacks or loads.

After the transient part of the computation, statistics are accumulated over three flow-through times which corresponds to $100s$ for the lowest wind speed case, $8\mathrm{m.s^{-1}}$. **Fig. 2.14** shows the time-averaged angle of attack, normal and tangential forces over the blade span for the three different tip speed ratios and three substeps values. Additional BEM results are presented without any hub/tip corrections applied. The obtained loads allow assessing that the increasing number of substeps does not impact the fidelity of the loads in the simulations. The maximal relative discrepancy for AoA at $\lambda = 7.6$ between $N_{substep} = 1$ and 4 is reaching locally $1° \times 10^{-2}$ near the hub. For the rest of the simulations, the averaged value for the relative difference between the cases with substeps and the case without remains below $1° \times 10^{-3}$. This low impact on the loads shows the substeping method to be interesting to reduce the computational time. Moreover, the loads are shown to be in good accordance with the BEM results, further validating the methodology.

The generated helicoidal wake structure can be observed in **Fig. 2.15** through instantaneous contours of $Q_{criterion}$. For the different tip speed ratios, a three vortex helicoidal structure is observed in the wake. The tip speed ratio induces a different spacing between the helicoidal vortex. The variation of substep is shown through juxtaposed simulations demarked by black lines. The generated tip vortices for the different substep values are similarly convected and show similar thickness. Overall, the vortices overlap at the same given time, and this shows the flow physics to be unperturbed by the substep process values.

The integrated performances of the turbine for the different substeps values compared to the case without substeps are presented in **Fig. 2.16** for the power (left) and thrust (right). The variations are below 1% for the power and below 0.2% for the integrated thrust. As a consequence, these discrepancies are considered negligible. The comparison to BEM results shows higher variations, up to $2 - 3\%$ for the high tip-speed ratio.

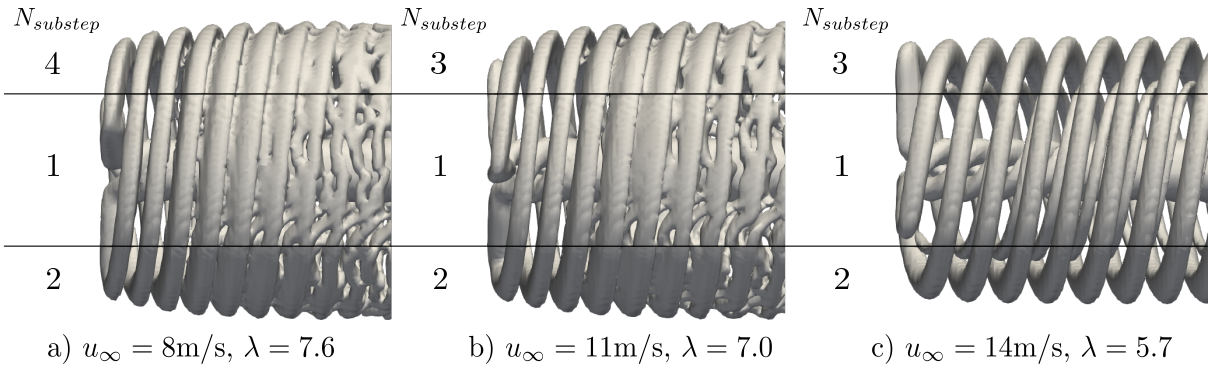

a) $u_\infty = 8$m/s, $\lambda = 7.6$ b) $u_\infty = 11$m/s, $\lambda = 7.0$ c) $u_\infty = 14$m/s, $\lambda = 5.7$

Figure 2.15: Instantaneous contour of $Q_{criterion} = 0.01s^{-2}$ representing the helicoidal wake structure generated with different substep values, black lines denotes the limits between simulations. The tip speed ratio is decreasing from left to right.

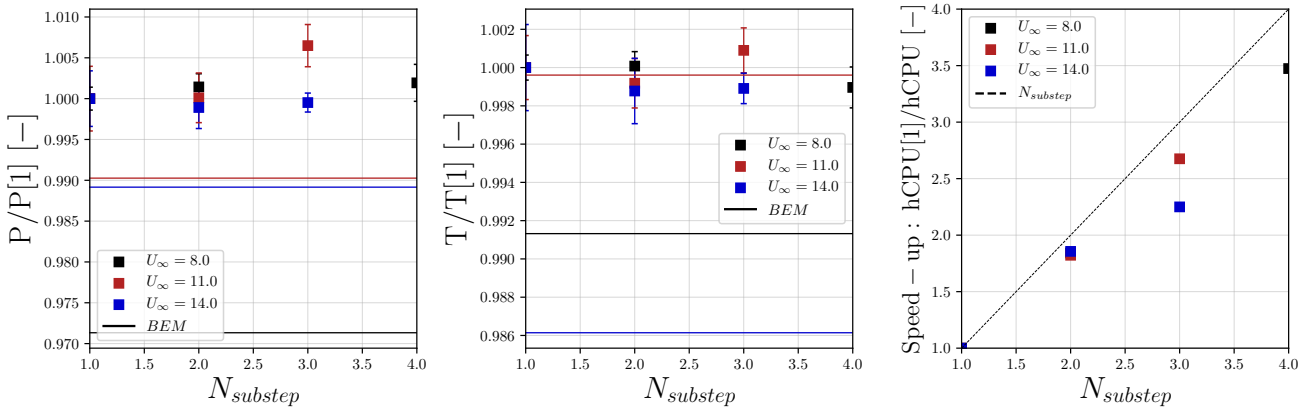

Figure 2.16: Evolution of the power (left) and thrust (middle) according to the number of substeps. Mean and standard deviation are presented non-dimensionnalized by the case without substeping, BEM results are presented with straight lines. (right) Evolution of the computational cost speed-up for the different number of substeps and differents wind speed. For each simulations 384 cores are used, the CPU cost is divided by the case without substeping.

The computational cost evolution according to the substep value is presented in **Fig. 2.16** (right). Each simulation is run with the Joliot-Curie supercomputer, funded by GENCI and held in CEA's Very Large Computing Centre (TGCC). The nodes are AMD Rome (Epyc) dual-processor with 128 cores, 64 per processor. Each node has 256 GB DDR4 memory and is interconnected using the Infiniband HDR100 technology. The simulations used three nodes, i.e., 384 cores. The global computational time reduction from the substeping reaches almost $1/N_{substep}$. This was expected since the number of fluid iterations is reduced by the number of substeps, the fluid iteration representing the most computation time. It is important to notice that when $U_\infty = 8\,\mathrm{m.s^{-1}}$, the highest TSR is achieved, and the maximal substeping value can reach the value of 4. Whereas for the two other cases, the maximal achievable substep value is 3. Up to four substeps, this methodology has yielded a negligible impact on the flow physics and the turbine loads while tremendously reducing the computational cost. In this thesis, the substeps are in the range of 1 to 4, depending on the turbine operating conditions.

2.4 Conclusions

This chapter presented the physics and the principal methodologies used in this thesis. First, the context of turbulent flows and the solving of the Navier Stokes equations is presented. Secondly, a quick presentation of the YALES2 CFD library is given, going from the main tools used during this thesis towards the incompressible constant density solver. The last part present and discuss the wide range of modeling strategies for horizontal axis wind turbines in turbulent flows. The Actuator Line Method is explained from the literature, and the implemented version during this thesis is described. Optimization strategies to increase computational efficiency are presented. The algorithm used to select the cells considered during force mollification is presented and validated. This showed to reduce significantly the dependency between the number of points for each actuator line and the computational cost. The second strategy is the substeping of the actuator line to achieve a blade CFL number higher than one while preserving the flow physics and reducing the computation wall clock time. This is validated under different inflow with the NREL5MW wind turbine. A quick comparison between the simulation of wind turbines on a structured and unstructured mesh is finally discussed with a closer look at the mollification kernel width influence.

This framework is then used in the following chapters, where the results are compared to wind tunnel results, and then extrapolation to offshore academic and industrial wind turbines is presented.

Chapter 3

Application to small wind tunnel turbines

This chapter applies the numerical framework combining ALM and LES to wind turbines in a complex wind tunnel configuration. The wind tunnel combines different inflows with a turbulence grid, and an original strategy is presented for the turbulence grid modeling using a dynamic version of the ALM. By changing the yaw misalignment, various wind turbine wake interactions are investigated. The wake deflection of a single wind turbine is investigated under three inflows and three yaw angles. Then, the wake interaction with a second downstream wind turbine is presented.

Contents

3.1 Introduction 52
3.1.1 Objectives 52
3.1.2 Case description 52
3.1.3 Numerical parameters 55
3.2 Turbulence grid modeling: A dynamic actuator line method 57
3.2.1 A new actuator line method-based turbulence generation approach . . . 57
3.2.2 Validation on NTNU turbulence generation passive heterogeneous grid . 65
3.2.3 Results with heterogeneous and homogeneous passive grid 72
3.3 Single Turbine configuration: wake deflection 73
3.3.1 Turbine performance and loads 73
3.3.2 Wake flow topology 78
3.3.3 Wake destabilisation and generated turbulence 86
3.4 Two Turbines configuration: wake interaction 88
3.4.1 T1 wake impact on T2 loads 90
3.4.2 Flow topology 91
3.5 Conclusion 94

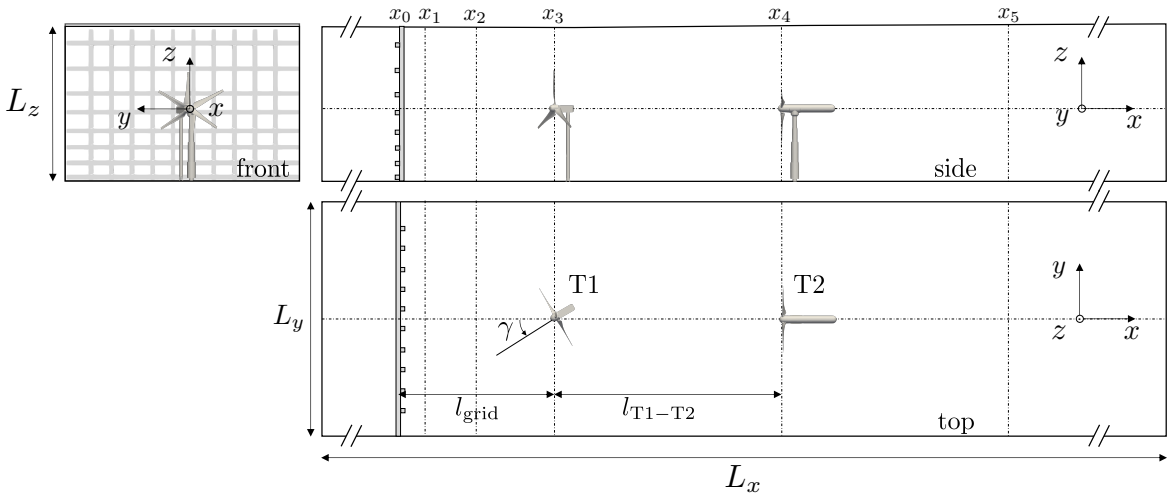

Figure 3.1: Visualization of the front, side and top view of the computation domain of NTNU wind tunnel with a turbulence grid and two wind turbines.

3.1 Introduction

3.1.1 Objectives

Before investigating a large offshore wind turbine, the ALM for yawed wind turbine needs to be validated in the YALES2 flow solver. Such methodology is widely used with LES since it releases the constraint from the small limiting scales of the flow around the blade geometry by modeling the loads through tabulated aerodynamic coefficients. Nevertheless, such a method suffers from various modeling errors, especially in the computation of the turbine loads. Many corrections [125, 127] of the loads have been tested under optimal conditions, but the case of yawed turbines remains an open topic.
This chapter aims at investigating the impact of yaw angle on one and two aligned wind turbines configurations. The numerical simulation results are compared to the experimental results from J. Bartl et al. [44] and F. Mühle. et al. [49] operated in the wind tunnel of the Norwegian University of Science and Technology [168] (NTNU). The major aspect of this configuration is the various operating conditions (inflows with turbulence grids, yaw angles), the geometries complexity (tower and nacelle), and the large number of measurements available. Three major aspects are therefore investigated:

- the impact of turbulence grids on the wind tunnel flow,
- the yaw angle ($+30°$, $0°$ and $-30°$) impact on the wake of a single turbine,
- the wake interaction with a downstream aligned wind turbine.

3.1.2 Case description

The wind tunnel dimensions are $L_x \times L_y \times L_z = 14 \times 2.71 \times 1.801\,\text{m}^3$, see **Fig. 3.1**. The tunnel has a flexible roof, adjusted in the experiment for a zero pressure gradient at the operating freestream velocity. The inlet turbulence can be adjusted by adding a turbulence grid. It is presented in the following subsection.

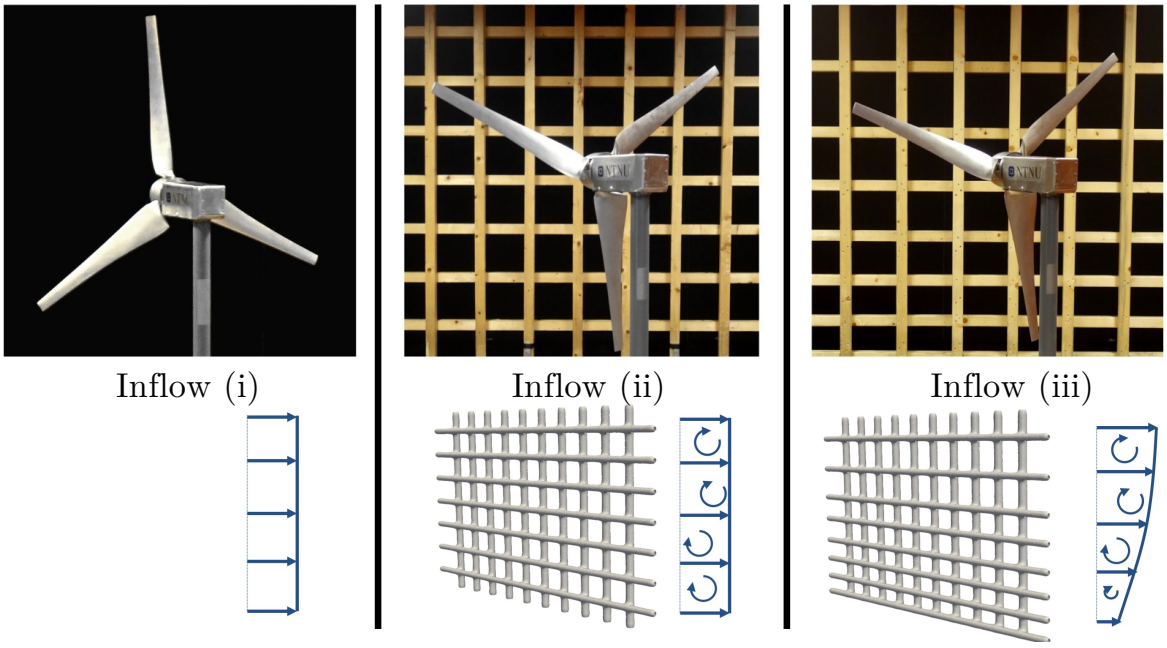

Figure 3.2: Top: Pictures of the experimental turbulence grids from J. Bartl et al. [44], Bottom: Global grid geometry considered in the computations and sketch of the corresponding velocity profile.

3.1.2.1 Wind tunnel inflow

Three inflow conditions are presented in this chapter: i) uniform laminar, ii) uniform turbulent, and iii) non-uniform sheared turbulent. The freestream velocity at the entrance of the tunnel is uniform, $u_x = 10\,\mathrm{m/s}$. The turbulent inflows (ii) and (iii) are generated using static turbulence grids at $l_{\mathrm{grid}} = 1.788\,\mathrm{m}$ upstream this turbine (see **Fig. 3.1**). The experimental grids are depicted in **Fig. 3.2**, and the specific inflow characteristics are presented in the following.

Inflow (i) exposes the turbine to the free-stream velocity and a low turbulence level ($\mathrm{TI_i} = 0.23\%$) from the wind tunnel, which is far below actual atmospheric boundary layer conditions. The second inflow (ii) is generated using a homogeneously spaced grid of horizontal and vertical square rods. The aim is to expose the turbine to a uniform velocity $u_x = 10\,\mathrm{m/s}$ and a high turbulence intensity $\mathrm{TI_{ii}} = 10\%$. This level of turbulence is comparable to those of a neutral atmospheric boundary layer, although the inevitable decay of the grid-generated turbulence remains.

The last inflow (iii) is also generated using a turbulence grid but with the horizontal rods clustered closer to the tunnel floor. This grid setup results in exposing the turbine to a non-uniform sheared inflow with a high turbulence level $\mathrm{TI_{iii}} = 10\%$. The velocity profile and turbulence level present similar conditions as an onshore site for a neutral atmospheric boundary layer.

In **Fig. 3.1**, the downstream grey vertical lines (x_3, x_4 and x_5) refer to experimental measurements without wind turbines. The experimental flow measurements from J. Bartl et al. [44] were conducted using a two-component Dantec FiberFlow laser Doppler anemometer system used in differential Doppler mode. More details on the experimental procedure are given in the paper of J. Bartl et al. [44]. The velocity measurement uncertainties reach up to 5% for the last inflow (iii). Since no other data was available, the experimental uncertainties are not considered.

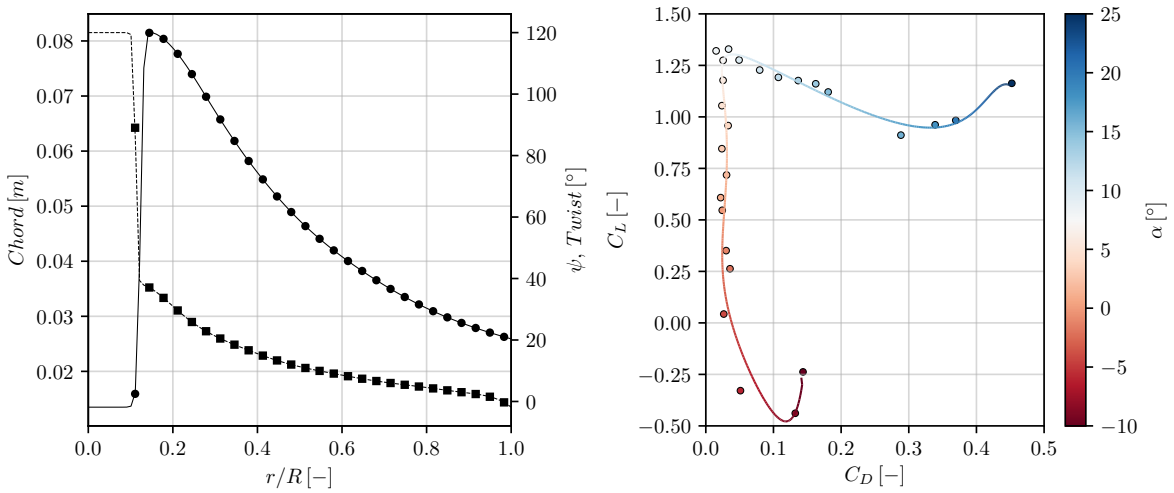

Figure 3.3: (a) Radial distribution of the twist angle (■) and chord (●). Solid lines show analytical curve fitting model from experimental data [44, 169], markers show the actuator point value. (b) Comparison of C_L/C_D datasets colored by the angle of attack for the NRELS826 airfoil. Solid lines show analytical curve fitting model from experimental data and ∘ the experimental datasets taken from [44]

The replication of inflows (ii) and (iii) in a numerical setup is challenging. It can lead to a high computational cost when fitting the mesh to the grid geometry or poor fidelity in the generated turbulent structures when using synthetic turbulence. This is why a strategy based on the actuator line method is developed in **Section 3.2**. This method aims at replicating with high fidelity and a low computational cost the turbulent structures generated in the vicinity of the grids.

3.1.2.2 Single turbine configuration

The single wind turbine (T1, on **Fig. 3.1**) configuration aims at investigating the effect of yaw misalignment and inflow type on the wind turbine deviated wake. The wind turbine has three operating conditions associated with three different yaw angles ($\gamma = +30°$, $0°$ and $-30°$). These three operating conditions are investigated under the three inflow conditions presented previously. The three-bladed rotor has a diameter $D = D_{T1} = 0.894\,\mathrm{m}$. The blades use the NREL S826 airfoil with variable chord and twist as described in the work of J. Bartl et al. [44]. **Fig. 3.3**(a) presents the chord and twist distribution along the turbine blade. The twist reaches zero at the blade's tip to conserve an optimal angle of attack along the blade span. **Fig. 3.3**(b) shows the evolution of lift and drag coefficients according to the angle of attack α for the NREL S826 airfoil. The rotation speed is imposed to obtain the designed tip speed ratio $\lambda_{\mathrm{opt}} = 6$, giving a Reynolds number of approximately $Re_{\mathrm{tip}} \approx 10^5$ at the blade tip. The tower and nacelle are designed to have a negligible effect on the wake. It is important to note that experimentally the turbines are spinning in the counterclockwise (CCW) direction, and the yaw angle is defined in the clockwise (CW) direction from the top. Because the majority of the worldwide wind turbines are spinning in the CW direction [170], in YALES2, the same convention is adopted. To replicate the experimental setup of J. Bartl et al. [44] the simulations yaw angle is defined in the CCW direction, see **Fig. 3.1**. This yaw angle definition allows comparing the simulations and the experimental measurements by using a symmetry plane in the $y = 0$ plane. In the

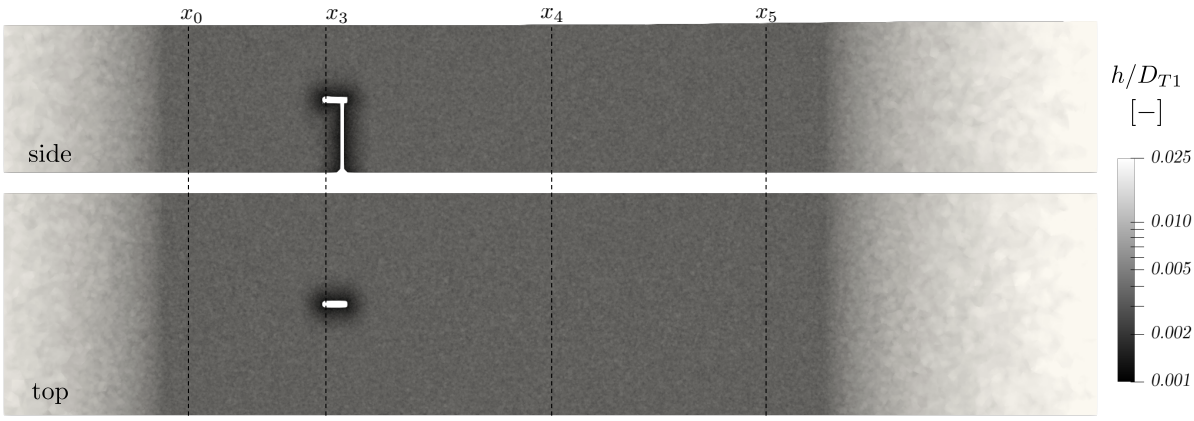

Figure 3.4: Slices of the mesh cell size for the single turbine configuration with a yaw angle $\gamma = 0°$ and for all inflows. For the other cases the cell sizes are similar, only the tower and nacelle orientation changes. For the two wind turbines configuration, T2 is added downstream in the same way as T1.

following, this symmetry is used to compare results. This single turbine configuration under the three inflows and for the three yaw angles is investigated in **Section 3.3**.

3.1.2.3 Two turbines configuration

The two turbines configuration aims at investigating the interaction of the wake of a yawed wind turbine with a downstream wind turbine under the realistic conditions of inflow (iii). A second turbine (T2, on **Fig. 3.1**) is added $3D$ downstream the turbine T1, i.e. $l_{\mathrm{T1-T2}} = 3D$. T2 has the same rotor geometry as T1 ($D = D_{T1} = D_{T2}$), although the nacelle and tower shapes are different. The nacelle is circular and significantly longer, see **Fig. 3.1**. In this configuration, T1 is operating with a yaw angle $\gamma = +30°$ and T2 is aligned with the wind. The tip speed ratio for T1 is the same as in the single turbine configuration, while for T2, it is slightly below the designed tip speed ratio, $\lambda_{\mathrm{T2}} = 5$. As in the single turbine configuration, the same workaround defines the yaw angle (CCW) and the blade spinning (CW) direction. Consequently, a symmetry at $y = 0$ plane is used to compare the experimental measurement and the simulation. The interaction between the yawed turbine T1 and the aligned turbine T2 is investigated under inflow (iii) in **Section 3.4**.

3.1.3 Numerical parameters

For these investigations, the global simulation parameters are the following. The numerical domain is constructed to match the wind tunnel dimensions and to be able to emulate the turbulence grids effect, setting the inlet distance to the turbine T1 at $l_{\mathrm{in}} = 4D$, see **Fig. 3.1**. The fluid density is $\rho = 1.225\,\mathrm{kg.m^{-3}}$ and the kinematic viscosity is $\nu = 1.517 \times 10^{-5}\,\mathrm{m^2.s^{-1}}$. The inlet velocity is constant, $u_{ref} = u_x = 10\,\mathrm{m/s}$ for all cases. For inflows (ii) and (iii) the turbulence grid is emulated using a Dynamic Actuator Line Method developped in **Section 3.2**.

An example of the type of mesh used in this chapter is presented in **Fig. 3.4**. For the sake of brevity, only the mesh of the single turbine configuration with a yaw angle of $\gamma = 0°$ is presented here. Yet, seven meshes are used: three for the empty wind tunnel (see **Section 3.2**), three for the single turbine configuration (one for each yaw angle since the tower and nacelle direction need to be adjusted), and one for the two turbines configuration. For the overall domain, the tetrahedral mesh skewness is below 0.7, and the maximum cell size gradient is set

Mesh	Inflow	Yaw angle γ	$N_{elements}$	N_{nodes}	N_{cores}	Δt [μs]	hCPU [kh]
1	(ii) DALM	no turbine	157×10^6	40×10^6	1120	357	22
	(iii) DALM					371	21
2	(iii) Body Fitted	no turbine	284×10^6	73×10^6	1960	49	213
3	(iii) HIT	no turbine	139×10^6	36×10^6	1120	369	17
4	(i)	T1: $+30°$	171×10^6	44×10^6	1092	169	25
	(ii) DALM					155	38
	(iii) DALM					158	37
5	(i)	T1: $0°$	170×10^6	44×10^6	1092	164	28
	(ii) DALM					146	45
	(iii) DALM					153	42
6	(i)	T1: $-30°$	171×10^6	44×10^6	1092	168	25
	(ii) DALM					145	46
	(iii) DALM					144	46
7	(iii) DALM	T1: $+30°$ T2: $0°$	191×10^6	49×10^6	1400	139	42

Table 3.1: Computational mesh size and cost associated with the different configurations. The time step and CPU cost are given for 15 flow-through times, τ. Meshes 1 to 3 are used in **Section 3.2**, 4 to 6 in **Section 3.3** and 7 in **Section 3.4**.

to 0.1 for a proper grid stencil allowing to conserve the spatial scheme order [171]. Between the positions x_0 to x_5+1D, the cell size is set to $h_{tunnel}/D_{T1} = 0.013$. In this region, the wall model developped by Duprat et al. [172] is applied on the wind tunnel walls. The non-dimensionalized wall distance $\langle y^+ \rangle$ does not exceed 200, which remains in the domain of validity of this model. For the single and two turbines configuration, the wind turbines tower and nacelle are taken into account by the mesh, and the cell size is imposed to $h_{T1,T2}/D_{T1} = 0.0011$. The same wall model for the wind tunnel wall is used, and $\langle y^+ \rangle$ does not exceed 100. The turbine blades are modeled using the Actuator Line Method (ALM, see Chapter 2), and the cell size in the rotor region requests 32 elements per blade. The Gaussian kernel smearing width is set to $\epsilon/h = 2.0$. With this set of parameters, the mesh sizes are in the range of hundreds of million elements. **Tab. 3.1** gathers the number of element and the computational time for the different mesh. A mesh refinement study for the two turbines case, Mesh 7, is provided in **Appendix ??** For all cases, the flow-through time τ is taken according to the distance between the turbulence grid, x_0 and x_5, i.e. $8D$ behind the grid which results in $\tau = 8D/u_{\text{ref}} = 0.715\,\text{s}$. The physical duration of the simulations with meshes 4 to 7 is 5τ for the flow establishment and 10τ for statistics accumulation. This is slightly higher for cases 1 to 3, reaching 7τ for the flow establishment and 15τ for statistics accumulation. The reported computational cost for all cases is given for 15τ. These simulations are run on the supercomputer Occigen, held at CINES. The nodes are Intel Broadwell bi-socket with 28 cores, 14 per socket. The used nodes per simulations ranged between 39 and 70, the exact number of cores for each simulations is presented by N_{cores} in **Tab. 3.1**.

Case	$Re(\times 10^4)$	$\langle C_L \rangle$	$\langle {C'_L}^2 \rangle^{1/2}$	$\langle C_D \rangle$	$\langle {C'_D}^2 \rangle^{1/2}$	St
F. Lesage et al. [173]	3.3	-	1.33	2.04	-	0.130
C.W. Knisely [174]	$2.2 - 6.2$	0.0	1.0	2.017	-	0.130
B.J. Vickery [175]	$4 - 16.0$	-	1.32	-	0.17	0.120
LES, reference case	3.1	0.01	1.42	2.07	0.13	0.132

Table 3.2: Aerodynamic coefficients around a square rod obtained from experimental data and from present simulation. The vortex shedding frequency, St, is based on the lift fluctuations.

3.2 Turbulence grid modeling: A dynamic actuator line method

3.2.1 A new actuator line method-based turbulence generation approach

The replication of the turbulence grid effect on the unperturbed wind tunnel inflow is mandatory to study the grid impact on the downstream wind turbine(s). The full resolution of the geometrical details of the wind tunnel turbulence grid constitutes the highest level of fidelity to reproduce the same turbulent inflow as that produced in a wind tunnel. Yet, such simulation leads to prohibitive computational costs due to the high resolution needed to resolve or model the boundary layers and the wakes released by the turbulence generators. To alleviate this cost, an original method called the dynamic actuator line method (DALM), derived from the standard ALM, is presented in this section. This method and the traditional actuator line method will be compared by inspecting the turbulent flow around a square rod similar to those found in wind tunnel applications.

3.2.1.1 Reference case results

The square rod flow test case considered here to validate the approach is well documented in the literature. Indeed, aerodynamic experimental data [173, 174, 175] for the flow over a square rod at a fairly high Reynolds number ($Re = \mathcal{O}(10^4)$) have been gathered and are summarized in **Tab. 3.2**, which provides time-averaged lift, $\langle C_L \rangle$ and drag,$\langle C_D \rangle$ coefficients as well as their RMS values $\langle {C'_L}^2 \rangle^{1/2}$, $\langle {C'_D}^2 \rangle^{1/2}$. The Strouhal number St is defined as $St = f\,l/u_{ref}$, where f is the frequency of the vortex shedding in the wake, u_{ref} is the reference velocity and l a reference length scale, chosen here as the side length of the rod. For the LES considered here, the flow regime is such that $Re = \frac{u_{ref}\,l}{\nu} = 3.0 \times 10^4$ where the reference velocity u_{ref} is the inlet velocity. The computational domain and the rod geometry are displayed in **Fig. 3.5**. According to the work of Fukumoto et al. [176] the choice of $3l$ in the spanwise direction is sufficient to estimate the aerodynamic forces fluctuations correctly. A periodicity along the rod span axis is set on the side boundaries. Slip wall conditions are used for the upper and lower boundaries, and they are far enough to have a negligible effect on the flow. The same wall model as for the wind turbine [172] is applied on the rod faces. This wall model allows to take into account the presence of a streamwise pressure gradient and applies both in the viscous sublayer and the inertial region. The reference mesh for the body-fitted (BF) case, M_{BF}, contains cells of various sizes, as reported in **Tab. 3.3**: $l/h_{rod} = 160$ around the rod, h_{wake} is the size in the wake region and h_{far} is the size elsewhere. The given dimensionless time-step, $\Delta t.u_{ref}/l$, shows the limitation of time discretization due to the Courant number at this operating conditions. The flow-through time is defined as $\tau = l/u_{ref}$. The spin-up time is $230\,\tau$, and $230\,\tau$ are also required to gather statistics and perform frequency analysis.

A visualization of the vorticity field in a plane perpendicular to the rod axis is provided

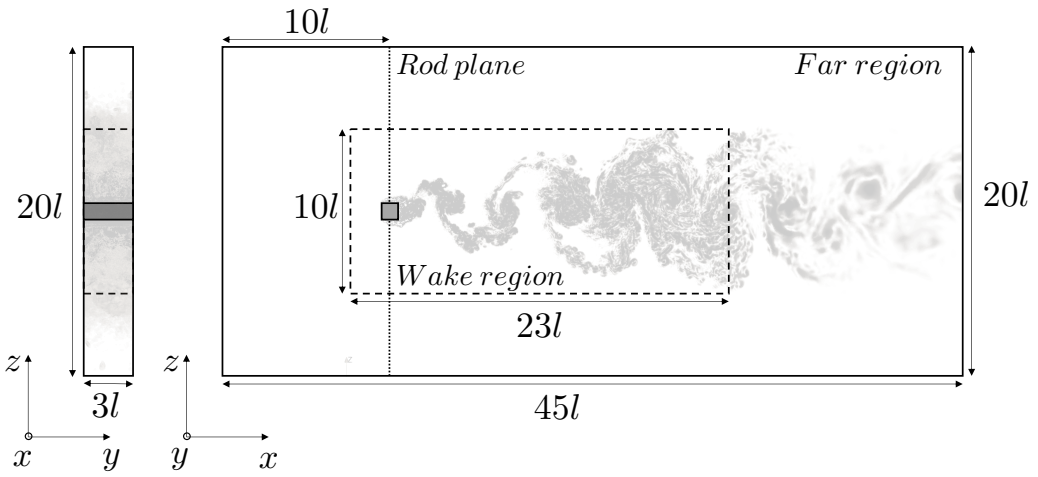

Figure 3.5: Description of the rod geometry and computation domain. l is the side length of the square rod.

Mesh	# elements ($\times 10^6$)	# nodes ($\times 10^6$)	h_{rod}/l	h_{wake}/l	h_{far}/l	$\Delta t.u_{ref}/l$ ($\times 10^{-3}$)
M_{BF}	344.13	88.2	0.0063	0.0159	0.175	1.06
M_{ALM}	3.41	0.87	N/A	0.0635	0.7	4.68

Table 3.3: Mesh characteristics for the rod simulations.

in **Fig. 3.6** (a). The wake of the bluff body presents a coherent vortex shedding where a '2S' mode [177] is observable in the wake. The distribution of time-averaged pressure coefficient, $\langle C_p \rangle$ and its fluctuations on the rod surface are represented in **Fig. 3.7**. From the surface integration of the $\langle C_p \rangle$ curve, $\oint_S \langle C_p \rangle \mathbf{n} \mathrm{d}S$, the drag force is mainly due to the back face of the rod $(2-3)$, with a contribution amounting to 67.4%. The front face induces 32.2% of the drag, and the 0.4% remaining are due to the friction contribution. The induced lift fluctuations on the top and bottom faces oscillate from 131% to -31%. The friction contribution is negligible compared to the pressure, which was expected for a bluff body at this Reynolds number as it presents massive boundary layer separation. The computation gives a time-averaged dimensionless wall distance $\langle y^+ \rangle$ around ten which is above the limit of the linear viscous sub-layer. The use of the wall model of Duprat et al. [172] is well suited for this near-wall resolution.

As the aim of the proposed technique is to generate realistic turbulent structures downstream of a turbulence grid, the proper modeling of the shear stress at the rod walls is of less importance. Integrating the instantaneous pressure and friction coefficient allow obtaining the resulting lift and drag coefficient of the rod. Their time evolution are presented in **Fig. 3.8**, with their corresponding spectrum. **Tab. 3.2** presents the mean, the root-mean-square, and the Strouhal number that are computed from these signals. These values are within the range of the available experimental data.

3.2.1.2 Assessment of the standard ALM method

The ability of the ALM to reproduce rod wakes at a low computational cost is assessed here. It seems natural to model the flow around an airfoil using an ALM. It is less evident that this method is suitable for bluff-body flows that feature massive boundary layer separation with

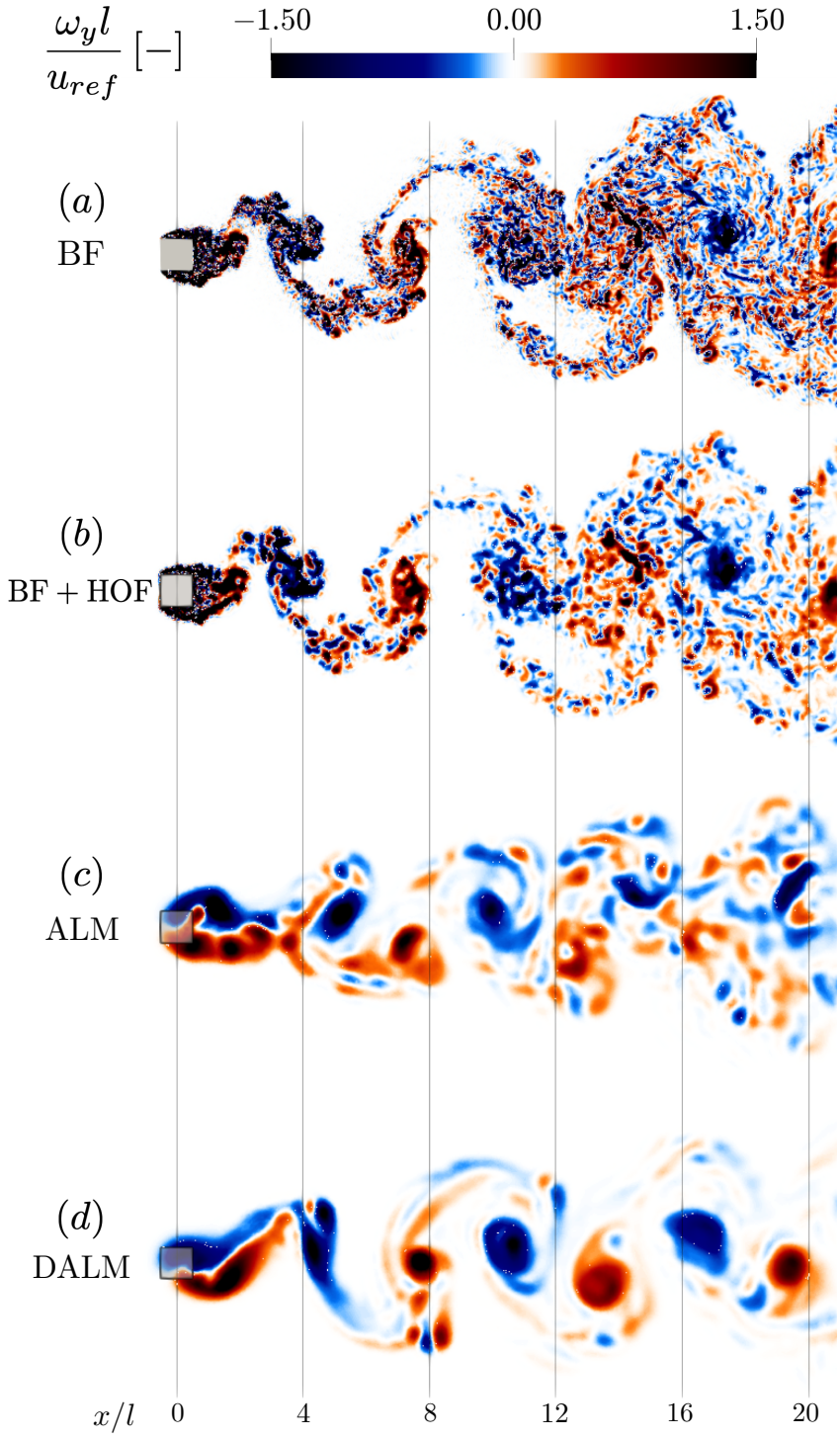

Figure 3.6: Slice of the instantaneous vorticity magnitude fields in the wake of a square rod for BF (a), filtered BF (b), ALM (c) and DALM (d) cases.

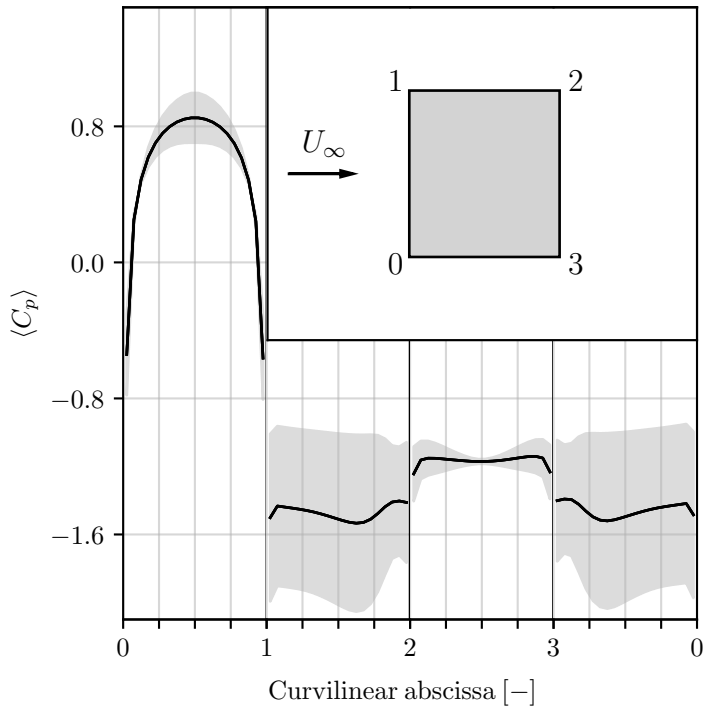

Figure 3.7: Time and spanwise average of $\langle C_p \rangle$ (—) and its fluctuations ( ) distribution on the rod surface. Front is between vertices 0 and 1. Top is between vertices 1 and 2. Rear is between vertices 2 and 3. Bottom is between vertices 3 and 0.

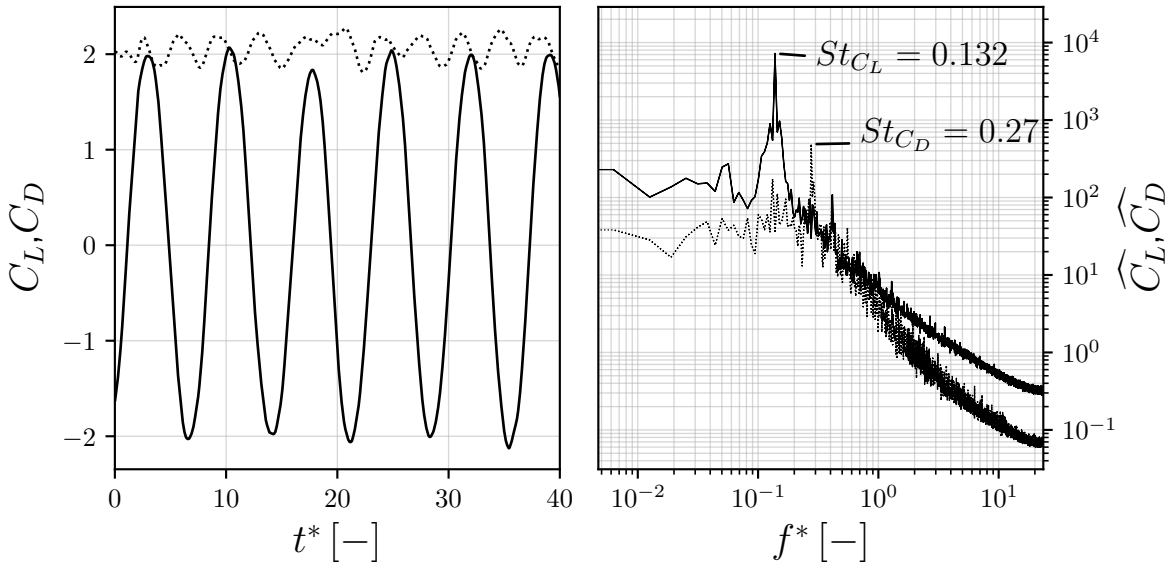

Figure 3.8: (a) Evolution of Lift, C_L (—), and Drag, C_D (·····), coefficients over dimensionless time, $t^* = t/\tau$, for the wake of a 3D square rod at $Re = 3 \times 10^4$. (b) Spectrum of both signals are presented as $\widehat{C_L}$ (—), and $\widehat{C_D}$ (·····).

vortex shedding.

The assessment of the method is performed using a continuous mesh (i.e., that does not include a solid body representing the rod) referred here as M_{ALM}. The characteristics of this mesh are summarized in **Tab. 3.3**. The rod is discretized along its span with 15 actuator elements in order to obtain $w/l = \epsilon/l = 0.2$. The influence of the rod on the flow is taken into account by the ALM using as input the mean aerodynamic coefficients, $\langle C_L \rangle$, and $\langle C_D \rangle$, from the reference case, summarized in **Tab. 3.2**.

The flow topology provided by the ALM is displayed in **Fig. 3.6** (c). The ALM method generates coherent vortical structures that are shed in the wake. For $x/l > 12$, the wake has lost its coherence, while in the BF case, coherent structures can be identified in the far wake. The small-scale content of the ALM turbulent wake is also lower: this was expected as the mesh of the reference case (BF) is four times more refined than the ALM case.

To make a fair comparison between both methods, the instantaneous results of the reference case (BF) are filtered using a high order filter (HOF) (10^{th}-order) [178, 101] such that its filter size is equal to the ALM mesh size, see **Fig. 3.6** (b). Even though the small scale content of the filtered BF vorticity field is still higher compared to the ALM solution, the filtering allows identifying the topology of the large scale vortical filaments.

Flow statistics are provided in **Fig. 3.9**. The velocity profiles are extracted at five positions downstream of the rod. Even if the flow topology provided by the ALM seems correct on a qualitative basis, the mean and fluctuating velocity profiles feature discrepancies compared to the reference case. Indeed, velocity fluctuations are significantly under-estimated in the center of the wake and exhibit a flatter profile than the reference case.

3.2.1.3 Description of the Dynamic Actuator Line Method (DALM)

As the standard ALM method features modest performance to reproduce turbulence fluctuations, a variant of this method is proposed here. The first assessment of this new method is performed on the single square rod test case presented above. It is shown here that it is required to take lift fluctuations into account to provide accurate modeling of the bluff body wake fluctuations.

The lift coefficient variations are superimposed to the lift coefficient of the ALM formulation $\langle C_L \rangle$ as pictured in **Fig. 3.10**. The time variation of the coefficients is thus written as:

$$C_L(t) = \langle C_L \rangle + \langle {C'_L}^2 \rangle^{1/2} \sqrt{2} \sin\left(2\,\pi f\, t + \tilde{\varphi}\right) , \tag{3.1}$$

$$C_D(t) = \langle C_D \rangle , \tag{3.2}$$

where f is the frequency of the vortex shedding and $\tilde{\varphi}$, the random phase of the fluctuations that has to be modeled. The aim of this random phase is to de-synchronize the vortex shedding when more than one rod is taken into account. The drag fluctuations are not taken into account here since they are small. As a consequence, they will not affect the largest structures of the wake (this point is further discussed in **Section 3.2.1.4**).

Even though this new Actuator Line Method requires setting the lift's RMS and the Strouhal number, it remains easy to implement. These physical properties can be retrieved for a wide variety of static or translating bluff bodies from the literature [179, 180, 181]. In the next section, this new formulation will be applied and compared in the case of a square rod wake. An

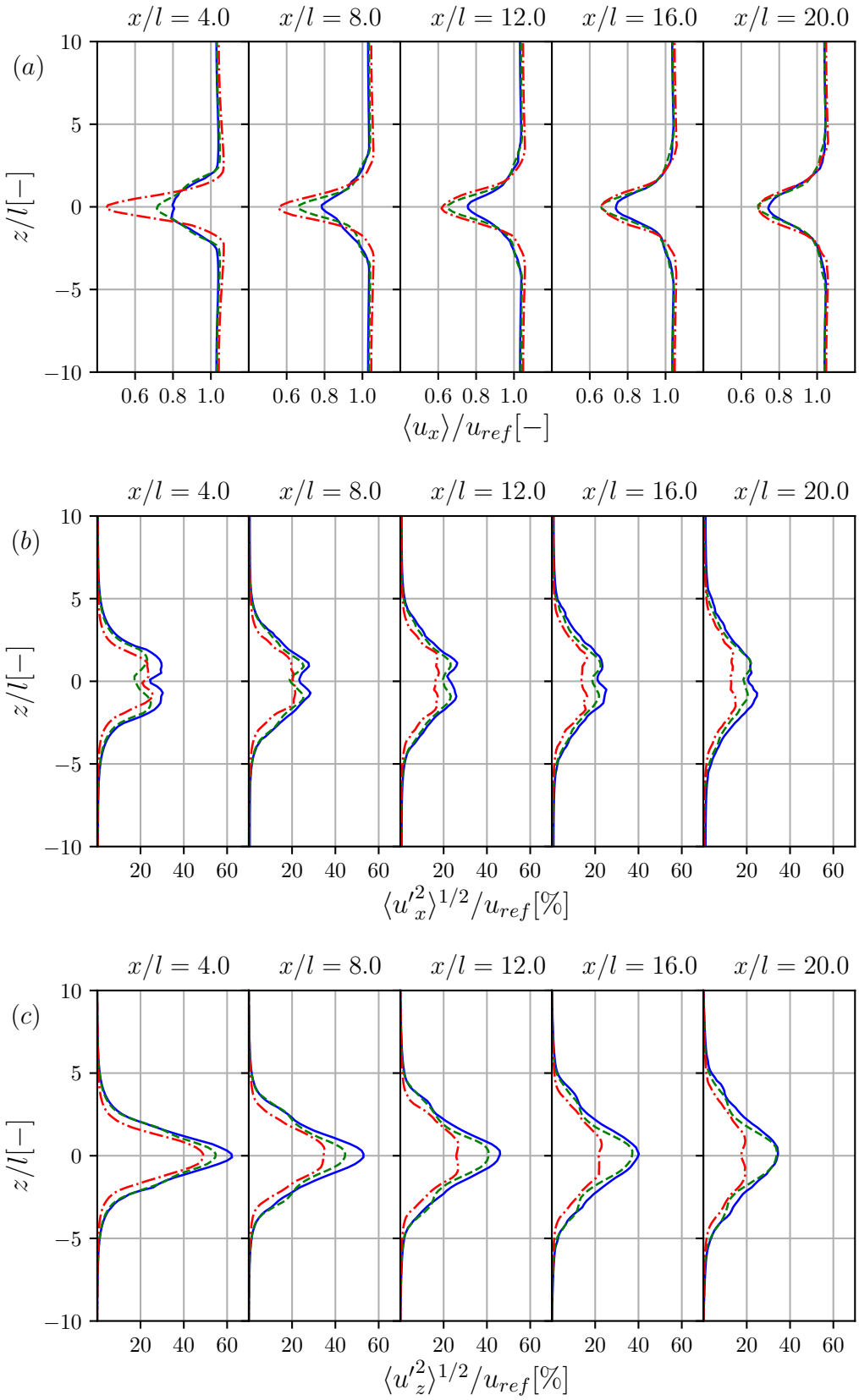

Figure 3.9: Mean streamwise velocity (a), RMS of streamwise velocity component (b) and RMS of vertical velocity component (c) behind the rod at x/l = 4,8,12,16 and 20 for BF (——), ALM (-·-·-) and DALM (- - -).

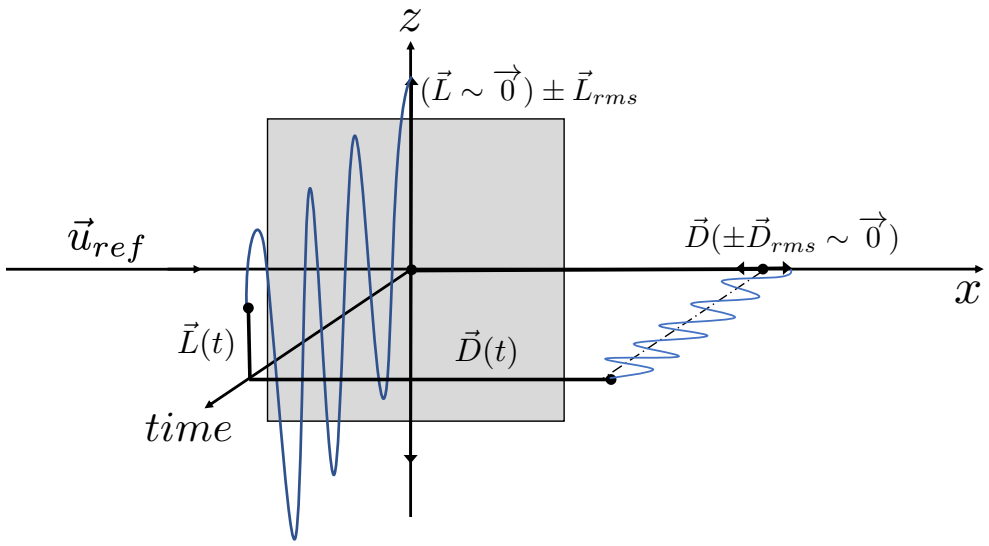

Figure 3.10: Oscillating lift and drag forces evolution over time for one section of a rod.

application to grid turbulence generation will be provided in **Section 3.2.2**.

3.2.1.4 Validation of the DALM

The validation of the DALM formulation is performed on the flow around a square rod. The results are compared with those of the reference body fitted computation and classical ALM. The mesh M_{ALM} and the spanwise discretization of the rod are the same as in the ALM case. The DALM result presents a vortex shedding frequency that is similar to the reference case (see **Fig. 3.6**). As the boundary layers are not captured with the DALM, small-scale vortices are not present in the wake. Nevertheless, the large scale coherent structures generated at the rod location are very similar to those obtained with the BF case, and they are also transported similarly.

Flow statistics are compared using the mean streamwise velocity in the wake (**Fig. 3.9**(a)) and the RMS values of vertical and streamwise velocity components (**Fig. 3.9**(b)-**Fig. 3.9**(c)) for profiles at five positions downstream of the rod. Considering the mean wake deficit, all the profiles are almost coincident for $x/l > 20$. The velocity fluctuations profiles (vertical and streamwise) obtained using the DALM have the same shape as the BF case, two local maxima for the streamwise component and one single maximum for the vertical fluctuations.

A more detailed analysis of the velocity fluctuations is provided through a frequency analysis, depicted in **Fig. 3.11**. The velocity signals are gathered over $230\tau \approx 1.08$s with a fixed timestep $dt = 0.1$ ms at $x/l = 4$, 8, 12, 16 and 20 for the three cases. The normalized 1D transverse energy spectra E_{zz} is provided in **Fig. 3.11**. The vertical dotted lines are located on the eigenfrequency of the reference case: $f_0^* = 0.137$, and its second harmonic $f_2^* = 0.273$. The same eigenfrequency can be retrieved for the DALM case showing a good behavior of the wake fluctuations. This is not the case for the standard ALM case with a higher eigenfrequency $f^* = 0.169$. Furthermore, the relative amplitudes at the eigenfrequencies are very similar for both the reference and DALM cases, while velocity fluctuations provided by ALM decay rapidly in the wake. Another critical

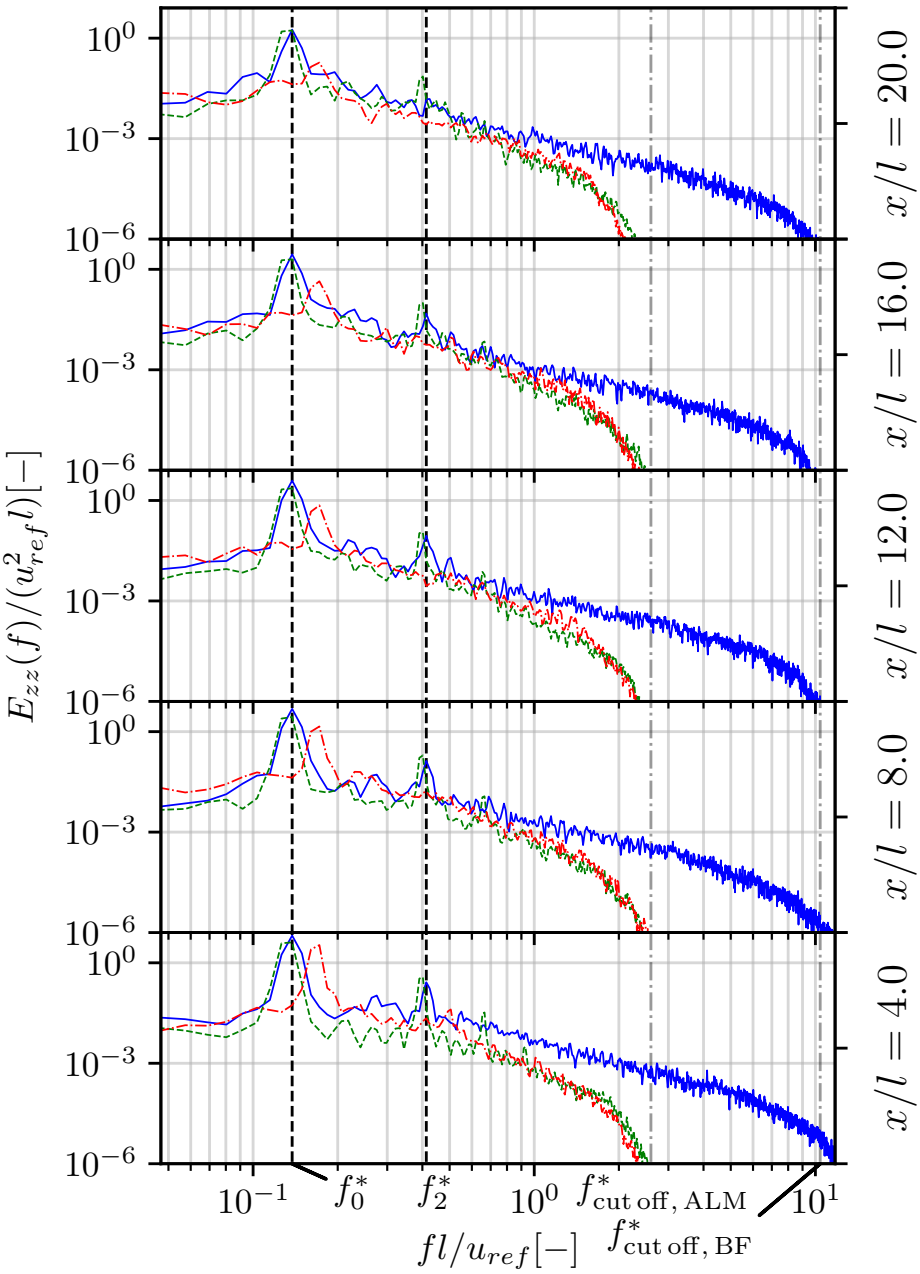

Figure 3.11: 1D Energy spectra of the vertical velocity behind the rod at at various axial location, with $f^* = fl/u_{ref}$, for BF (——), ALM (-·-·) and DALM (- - -).

point is the difference in the cut-off frequency between the reference case and the actuator line cases, a direct result of the mesh resolution.

The cut-off frequency of the BF mesh is such that $f^*_{\text{cut off,BF}} \approx 8$. The two other cases have a four times smaller frequency cutoff: $f^*_{\text{cut off,ALM}} \approx 2$. In this study, it doesn't impact the frequency range of interest.

It has been shown in this section that DALM was able to improve the description of the flow behind a single square rod compared to the classical ALM. The following section aims at applying this new method to the simulation of a turbulence generation grid.

3.2.2 Validation on NTNU turbulence generation passive heterogeneous grid

The DALM proposed here is applied to the heterogenous turbulence generation system of the NTNU wind tunnel, inflow (iii). Several modeling strategies are compared to experimental measurements: I) DALM, II) resolved flow around the rods (Body Fitted, BF), and III) Homogeneous Isotropic Turbulence (HIT) injection.

3.2.2.1 Case description

The turbulence grid is located at x_0 (see **Fig. 3.1**) and is composed of $l \times l = 47 \times 47\,\mathrm{mm}^2$ square cylinder rods [182]. The grid presents a constant horizontal spacing between the vertical rods of $5.1l$. The horizontal rods are arranged with an increasing vertical spacing from the floor to the roof [182]. The purpose of this arrangement is to generate a vertically sheared flow profile after the grid. The horizontal rods are upstream of the vertical rods, and both are bound to each other at each grid nodes, i.e., horizontal and vertical rods sections center are shifted by l in the streamwise direction. The resulting grid blockage ratio, σ, is 34.5% in this wind tunnel and the effective grid mesh size [183] defined as $M_{\text{eff}} = \frac{4T^2}{P}\sqrt{1-\sigma}$ is $M_{\text{eff}} = 8.5l$, where P is the perimeter of the grid and $T^2 = L_y \times L_z$. Experiments have shown that upstream of the grid, the streamwise velocity profile is flat with $u_x = u_{ref} = 10\,\mathrm{m.s}^{-1}$ while downstream, this profile can be accurately described by a power law:

$$\frac{u_x(z)}{u_{ref}} = \left(\frac{z}{L_z}\right)^{\alpha}, \tag{3.3}$$

where z is the height in the wind tunnel, and the power coefficient $\alpha = 0.11$ is selected to fit experimental data [182]. Experiments provide velocity and turbulent intensity profiles at three positions downstream the grid $x_3/l = 38$, $x_4/l = 95$ and $x_5/l = 152$, presented as dash dotted lines in **Fig. 3.1**. Although not present in the experimental data-set, the positions $x_1/l = 5$ and $x_2/l = 20$ are also investigated numerically to study the grid wake destabilization.

For all cases, the flow-through time is taken according to the distance between x_0 and x_5 and equal to $\tau = (x_5 - x_0)/u_{ref} = 0.715\,\mathrm{s}$. The physical duration of the three simulations is 7τ for the flow establishment and 15τ for statistics accumulation.

3.2.2.2 Computational setup

This work aims at assessing the DALM and at comparing it to other strategies: a resolved flow around the rods, set as a reference, and a Homogeneous Isotropic Turbulence (HIT) injected with the experimental velocity profile. Each of these methods requires different mesh resolutions: the mesh around the rods needs to be fine enough to capture the boundary layer for the BF case. This significantly increases the number of elements in the grid with a total of around 284×10^6 tetrahedra. The two other methods do not require such a fine mesh and contain approximately 157×10^6 elements for the DALM case and 139×10^6 elements for the HIT case. Theses meshes are illustrated in **Fig. 3.12**. Although the three cases are very similar in most aspects, the peculiarities of each approach are presented in the following sections.

- **DALM case**

In this case, a flat velocity profile upstream of the grid is set at the inlet of the computational domain with $u_x = 10\,\mathrm{m.s}^{-1}$. The grid resolution near the position of the rods is the same as in the wake region, $h/l \approx 0.08$ as shown in **Fig. 3.12**. The rods are discretized with DALM

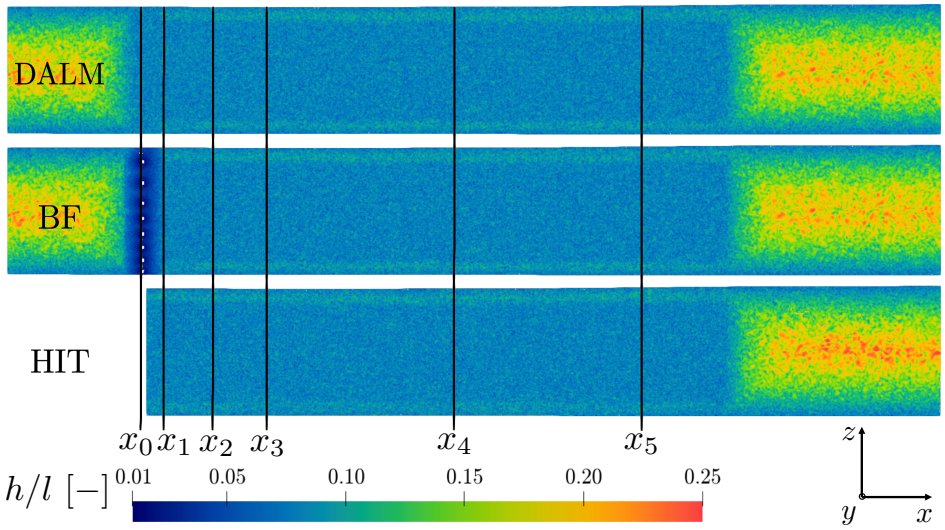

Figure 3.12: Side view of the unstructured grid size, h/l, used to capture grid turbulence generation. From top to bottom: DALM, BF and HIT mesh. The mesh size h is defined here as the cubic root of the cell volume. It can be seen that $h/l \approx 0.08$ in the wake region for the three cases.

Rod	$\langle C_L \rangle$	$\langle {C'_L}^2 \rangle^{1/2}$	$\langle C_D \rangle$	St
Vertical, 1-10	0.0	1.21	2.16	0.128
Horizontal, 1	-0.154	1.34	2.22	0.128
Horizontal, 2	0.00	1.39	2.23	0.128
Horizontal, 3	0.00	1.34	2.21	0.128
Horizontal, 4	0.00	1.29	2.19	0.128
Horizontal, 5	0.00	1.24	2.17	0.128
Horizontal, 6	0.00	1.20	2.14	0.128
Horizontal, 7	0.00	1.16	2.11	0.128
Horizontal, 8	0.00	1.16	2.11	0.128

Table 3.4: Aerodynamic coefficients of the grid rods depending on their environment [184, 185].

in order to obtain $w/l = \epsilon/l = 0.2$. Therefore, according to the turbulence grid geometric properties, horizontal and vertical rods are composed of 288 and 190 actuator elements. To apply the DALM presented above, the aerodynamic coefficients of the square rods are needed. Moreover, those rods are not isolated compared to the single rod case, and those coefficients need to consider the rods interactions between each other and the wind tunnel walls. Literature provides experimental data for two parallel rods interacting at different distances [184] or a single rod interacting with a wall [185]. Taking those effects into account is mandatory to recover the correct mean velocity shear. Here, the interactions between crossing vertical and horizontal rods are neglected. Moreover, no specific treatment has been applied to the mollification process at these locations: vertical and horizontal rod mollification kernels overlap. This assumption relies mainly on the observation that these crossings marginally contribute to the blockage ratio. The spacing of the vertical bars remains constant, and the aerodynamic coefficients based on the rod/rod spacing are used. For the horizontal bars, the rod/rod spacing and wall/rod spacing are used to evaluate the aerodynamic coefficients [184, 185]. The resulting coefficients are summarized in **Tab. 3.4**. It can be observed that the drag coefficient and the lift fluctuations

decrease as the spacing between rods gets larger. Experimental studies [184, 185] have shown that the Strouhal number is not impacted by such high spacing. For the first horizontal rod, the negative mean lift is due to the wall proximity, which is lower than $0.4l$. Another assumption lies in the rod to rod wake synchronization through the phase offset $\tilde{\varphi}$ of the DALM process. This parameter has been investigated by Chatterjee and Biswas [186] for a laminar flow passing through a homogeneous grid. Due to the flow complexity and the grid geometry, each rod's phase is set randomly at the computation initialization. This prevents the creation of large-scale coherent structures that would be convected in the wind tunnel.

- **BF case**

This case uses a "brute force" approach in which the grid influence is resolved similarly to **Section 3.2.1**. As in the DALM case, the inlet velocity profile is set as a flat velocity profile upstream of the grid. The mesh takes into account the rod geometry with a cell size around the grid rods of $h_{rod}/l \approx 0.01$. This leads to $\langle y^+ \rangle < 50$. Consequently, the first mesh point is not in the viscous sub-layer, and a wall model must be used: Duprat et al. [172] wall model is chosen here.

- **HIT case**

In this case, a precursor is used to simulate the flow past the grid without considering the rods. Therefore, the inlet boundary of the domain is located at $x = 2l$ (**Fig. 3.12**). The inlet velocity flow profile is set according to experimental data with a fitted power law (see **Eq. 3.3**). A Passot-Pouquet [187] spectrum is used to generate the homogeneous isotropic turbulence. To represent the grid-generated turbulence using HIT injection, it is required to estimate the turbulence intensity and the integral length scale at the inlet. The integral length scale is chosen to account for the constant grid spacing, $l_t = 5.1l$. The estimation of the streamwise turbulence intensity, defined as $TI = \langle {u'_x}^2 \rangle^{1/2}/u_{ref}$, requires experimental results and therefore its value downstream of the grid. The Frenkiel-Roach correlation established for a square rod grid with homogeneous spacing [188] is used for this purpose:

$$TI = c\left(\frac{x}{l}\right)^{-n}, \tag{3.4}$$

where c is a constant depending on the grid geometry ($c = 1.13$ when the grid spacing is homogeneous [188]), n a constant evaluated at $5/7$ experimentally, x the distance to the grid and l the rod width.

The turbulence intensity was measured experimentally at three positions downstream of the grid. With this data, the evaluated TI from **Eq. 3.4** is 65%. As expected after a first simulation, this value is high and overestimates the experimental turbulence intensity profiles.

To obtain better results with the HIT injection method, a "trial and error" strategy was used: five different TI values were tested to match experimental results. The final chosen TI value is 35%. In what follows, the flow fields presented for homogeneous isotropic turbulence injection were obtained with $TI = 0.35$.

3.2.2.3 Flow visualization

Fig. 3.13 shows the mid vertical plane colored by the instantaneous norm of vorticity. This allows observing how the vorticity decays along the wind tunnel. The rod's wakes destabilization just downstream x_1 position can be observed for DALM and BF cases. In addition to that, two regions appear downstream of the grid, the mixing region, and the decay region. In the mixing

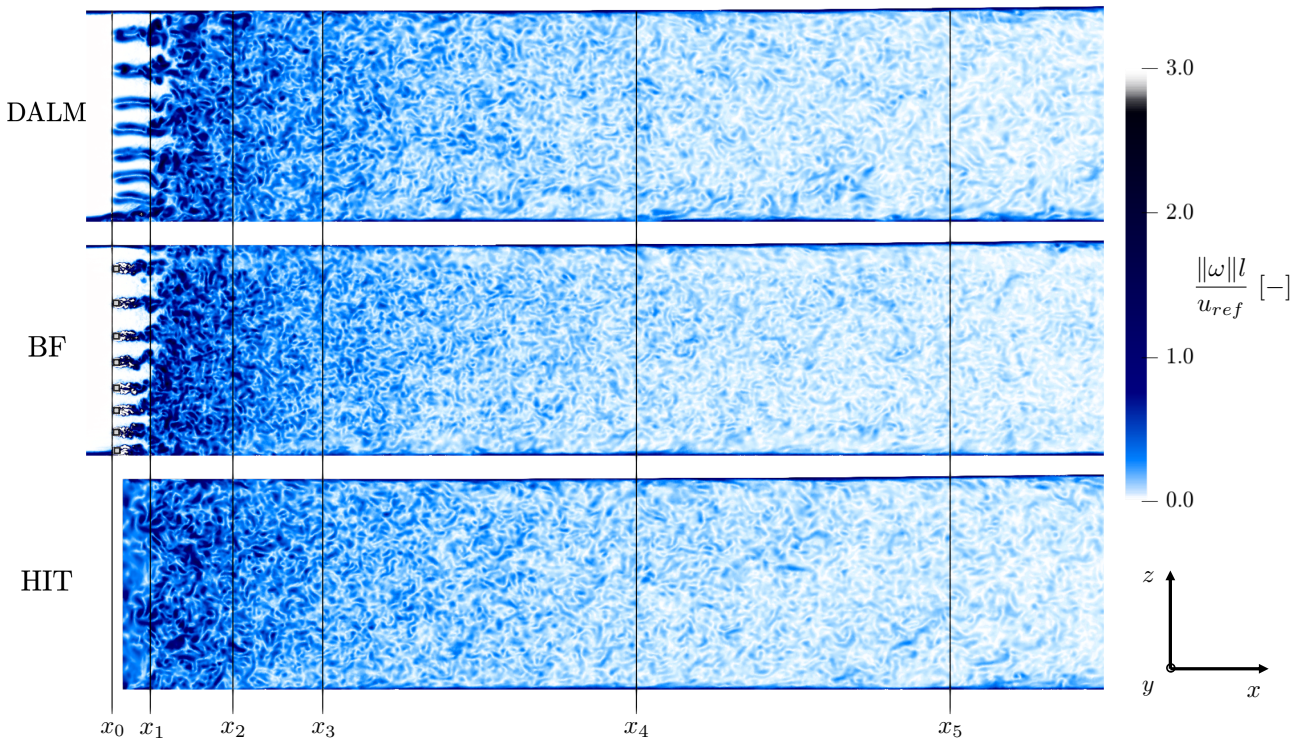

Figure 3.13: Magnitude of the vorticity field in the vertical plane of the wind tunnel for all cases. From top to bottom: DALM, BF, and HIT.

area, the wake of the grid is not destabilized, involving coherent flow structures. Indeed, the wakes interact with each other to generate a fully turbulent flow between x_1 and x_2, depending on the vertical grid spacing. Further downstream, turbulence becomes homogeneous in the decay region, and its intensity decays along the wind tunnel. This phenomenon is not observed for the HIT case since the injected homogeneous isotropic turbulence is already fully developed, and the actual grid geometry is not represented.

3.2.2.4 Wake destabilization

It has been shown that the proper capture of the wake destabilization highly depends on the mesh resolution [189, 190]. The importance of this phenomenon on the flow statistics is investigated in this subsection.

- **Mixing and decay regions**

Fig. 3.14 shows the streamwise turbulence intensity as a function of the downstream position at two different lateral positions, one behind a vertical rod of the grid and the other between two rods. For the reference BF and DALM cases, the two TI curves cross at $x \approx 10l$ and show a significant decay after this position, in agreement with the Frenkiel-Roach equation. Nevertheless, discrepancies can be observed on the maximum values of the TI between these cases. The two curves are similar for the HIT injection case since this method cannot reproduce the mixing region. The behavior of all instances is similar beyond x_2 and matches the experimental turbulence intensity value in x_3.

The quantification of the turbulence anisotropy, see **Section 2.1.2**, is investigated inside the mixing and decay regions. **Fig. 3.15** presents the barycentric map of the DALM, BF, and HIT cases. The invariants are computed along the two lines presented in **Fig. 3.14**, i.e., in the wake

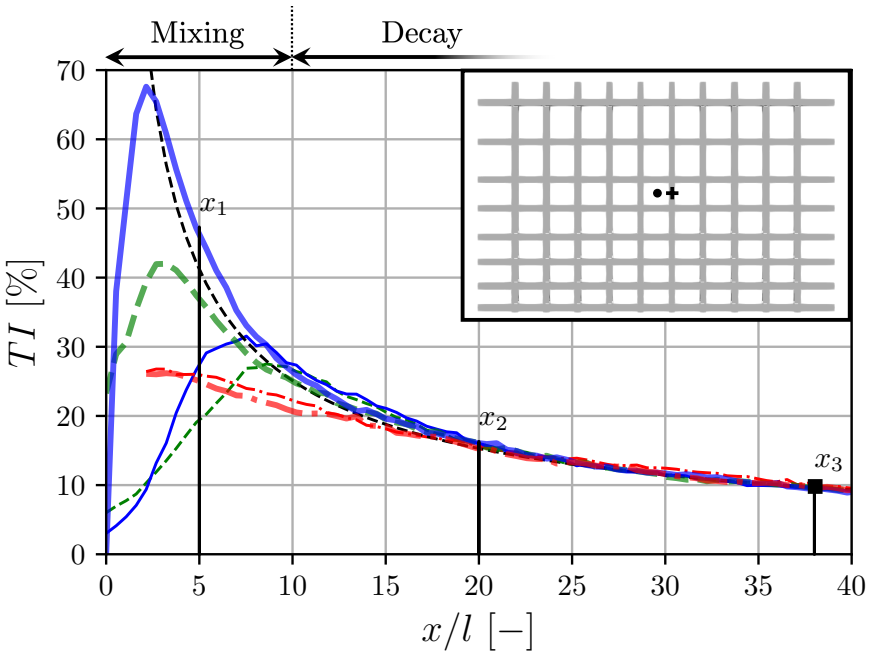

Figure 3.14: Streamwise evolution of streamwise turbulence intensity, TI, at two different lateral locations on the turbulence grid for the three cases. One at the center of the grid mesh, $y/l = 0$ (thin line), and the other behind a rod of the grid, $y/l = 2.55$ (thick line). DALM (- - -), BF (——), HIT (-·-·-) , experiment at x_3 (■) and **Eq. 3.4** (- - -) .

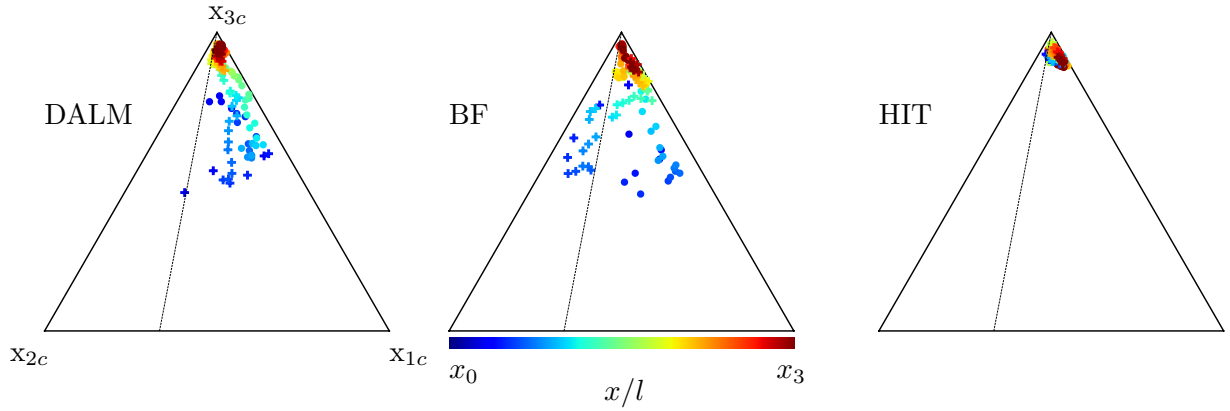

Figure 3.15: Barycentric maps showing the streamwise evolution of the anisotropy invariants behind the grid, color depends on the position between x_0 and x_3. Two positions on the grid are presented, one at the center of the grid mesh, $y/l = 0$ (•), and the other behind a rod of the grid, $y/l = 2.55$ (✚), see **Fig. 3.14**. The three different cases, DALM, BF and HIT are presented. The limiting states of componentality are labeled along with the plane-strain limit (·····).

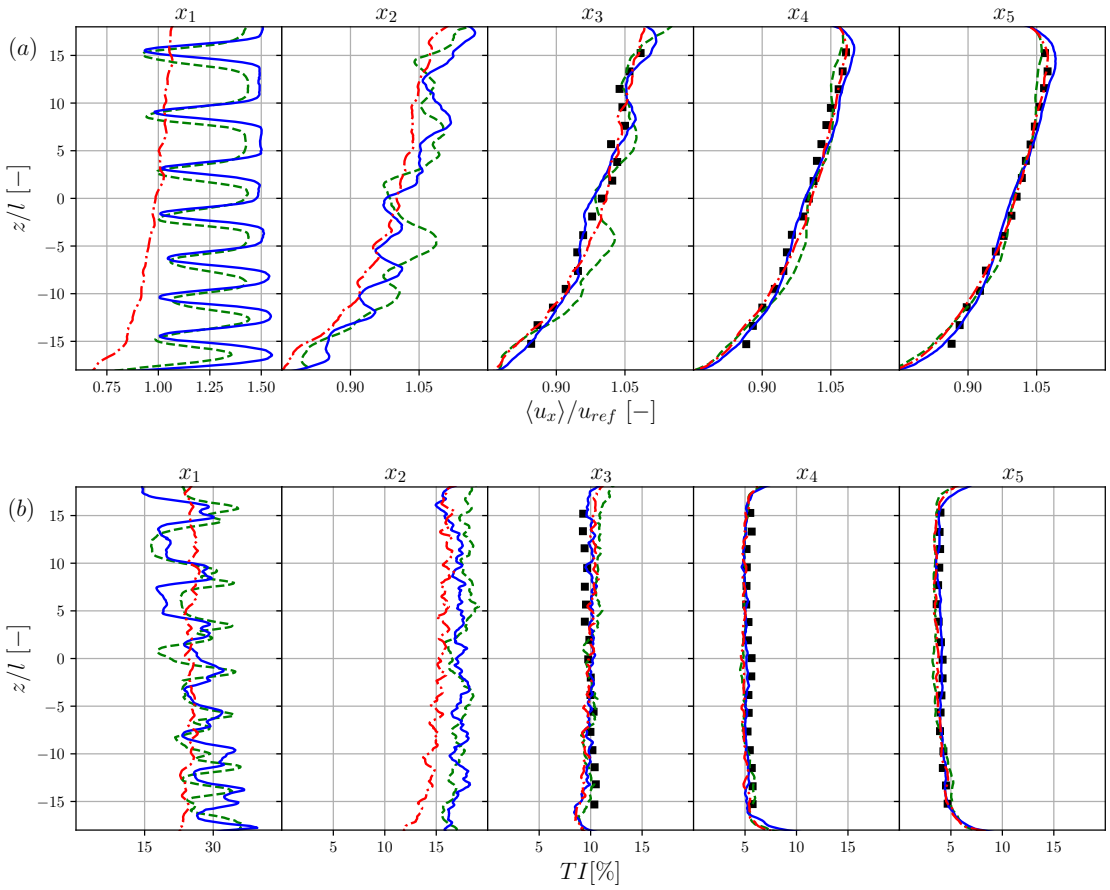

Figure 3.16: Vertical profiles of mean streamwise velocity (a) and turbulence intensity (b) at x_1, x_2, x_3, x_4 and x_5: experiment (■), DALM (- - -), BF (——) and HIT (-·-·-).

of a rod and at the center of a grid cell. A significant observation from the barycentric map is that all methods present an isotropic state of turbulence in the decay region. The turbulence state of the HIT case is always isotropic since the injected velocity fluctuations represent a developed isotropic state.

Discrepancies in the mixing region can be observed between BF and DALM cases. Indeed in the wake of the grid rod, the actuator grid doesn't reproduce the effective state of turbulence. This shows one limit of the method to emulate the wake of a turbulence grid. A better estimation of the mixing region turbulence state could be provided by improving the phasing strategy for the vortex shedding in DALM. From these observations, the destabilization of the grid wake remains a crucial phenomenon to generate homogeneous and isotropic turbulence in the flow.

- **Time-averaged velocity and turbulence intensity profiles**

The flow statistics are compared considering the profiles of mean streamwise velocity, **Fig. 3.16** (a), and streamwise turbulence intensity, **Fig. 3.16** (b), at five positions downstream of the grid. A comparison with the experimental profiles is provided for positions in the decay region, at x_3, x_4, and x_5.

In the mixing region, at x_1, the BF and DALM cases can represent the rod wakes through a velocity deficit at the position of the rods, while the sheared profile cannot be observed. They present thus a similar profile shape with an underestimated amplitude for the DALM case. The HIT case presents a sheared profile, which is expected since the experimental profile is used as

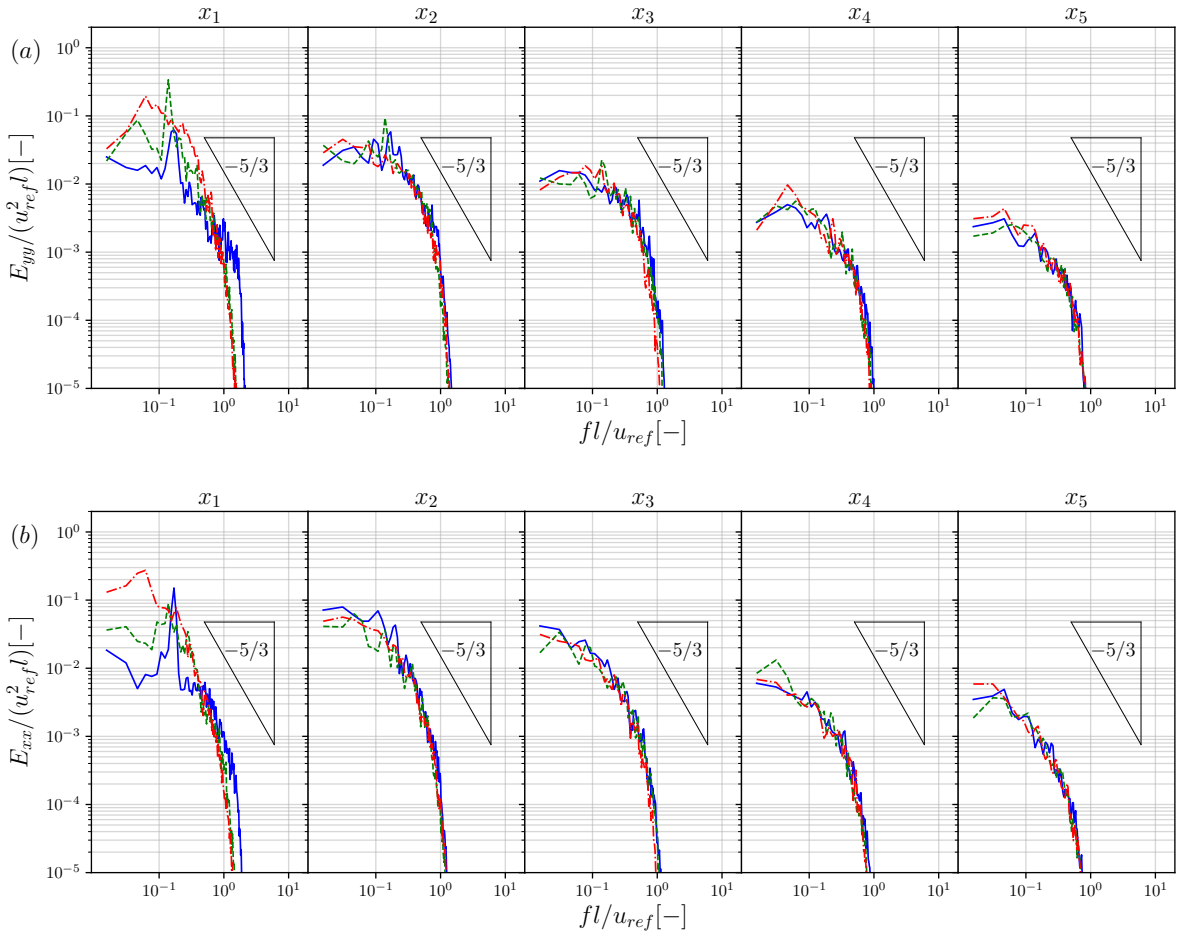

Figure 3.17: 1D power spectra of the transverse velocity fluctuations (a), E_{yy}, and the streamwise velocity fluctuations (b), E_{xx} behind the rod at stations x_1, x_2, x_3, x_4 and x_5 for DALM (- - -), BF (——) and HIT (-·-·-).

an input parameter. Right after the destabilization, all cases present a sheared velocity profiles shape. Still, the reference and DALM cases present fluctuations due to the velocity deficit behind the grid rods with a slight over-prediction of the DALM. The destabilization of the grid wake is essential here, as mentioned in **Section 3.2.2.4**. The time-averaged streamwise velocity profiles of all the presented cases are in good accordance with the experimental results in the decay region. The BF and DALM cases both show a fair prediction of the downstream velocity field.

The streamwise turbulence intensity profiles (**Fig. 3.16** (b)) are also investigated. In the mixing region, between x_0 and x_2, the reference case and DALM present high levels of fluctuations, up to 35% at x_1. The profiles become nearly flat right after the destabilization of the wake and almost homogeneous in the middle of the wind tunnel. The experimental data are only available after x_3, but at this position, the profiles of all the cases are already identical.

- **Energy spectra**

The mixing and decay regions can be further investigated in terms of transverse, E_{yy} **Fig. 3.17** (a), and longitudinal, E_{xx} **Fig. 3.17** (b), frequency 1D power spectra of the velocity fluctuations on the centerline taken at various positions in the flow: x_1, x_2, x_3, x_4 and x_5. The temporal signals are gathered during a period of 3τ with a fixed time-step, $\Delta t\, l/u_{ref} = 9.4{\times}10^{-7}$.

In the mixing region, at position x_1, one can observe a frequency peak for both the DALM

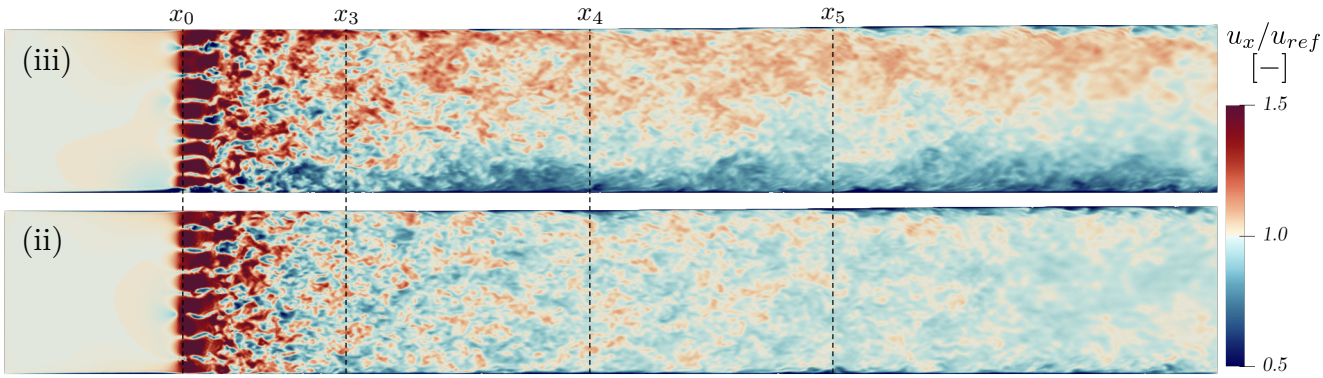

Figure 3.18: Vertical slice in the middle of the wind tunnel colored by streamwise velocity, from top to bottom: inflow (iii) heterogeneous grid and inflow (ii) homogeneous grid.

and the reference case such that $fl/u_{ref} = 0.1-0.2$. This is consistent with the Strouhal number of a single square rod. The spectra obtained with HIT injection have a higher energy level for the large scales since the injected turbulence is already developed with this precursor method.

As for the decay region, for both figures, a downward shift to the large scales, or small frequencies, is observed when advancing in the decay region. The decrease of the area under the spectrum illustrates the decay of the turbulent kinetic energy as expected. For DALM and BF cases, the previously observed eigenfrequency disappears after the destabilization of the grid wake.

For sufficiently large Reynolds numbers, the spectra $E_{xx/yy}$ should exhibit a $f^{-5/3}$ spectral behavior in the inertial subrange according to Kolmogorov's theory. This trend is observed in the decay region, for $x > x_3$, showing sufficiently high Reynolds number and turbulence isotropy, as observed in **Fig. 3.15**.

3.2.2.5 Computational cost & performances

The computational times needed to reach 15 flow-through times are reported for each case, Mesh 1 to 3, in **Tab. 3.1**. The computational cost of the BF case is almost ten times higher compared to HIT and DALM cases. This is due to the much smaller cells around the discretized grid geometry, requiring a smaller Δt to keep a constant CFL number. The cost of DALM and HIT present the same order of magnitude, yet, HIT injection remains at a lower cost. However, the CPU time for HIT doesn't consider the cost related to the "trial and error" procedure required to find the correct inlet turbulence intensity. This cost can highly depend on the application case. Here, five additional simulations were necessary to tune the turbulence parameters correctly. Moreover, this trial and error procedure is only relevant if the Turbulence Intensity is known accurately: it thus requires either experimental data or empirical correlations.

3.2.3 Results with heterogeneous and homogeneous passive grid

As previously mentioned, three inflows are presented in this chapter. The turbulent inflows (ii) and (iii) are experimentally generated using static turbulence grids upstream the turbine at $l_{\text{grid}} = 2D$. Based on the previous validation of the DALM on the heterogenous grid, inflow (iii), the same strategy is applied to the homogeneous grid of NTNU wind tunnel, inflow (ii). **Fig. 3.18** shows the mid vertical plane colored by the instantaneous streamwise velocity. This allows observing how the velocity fluctuations evolve along the wind tunnel. The rod's wakes

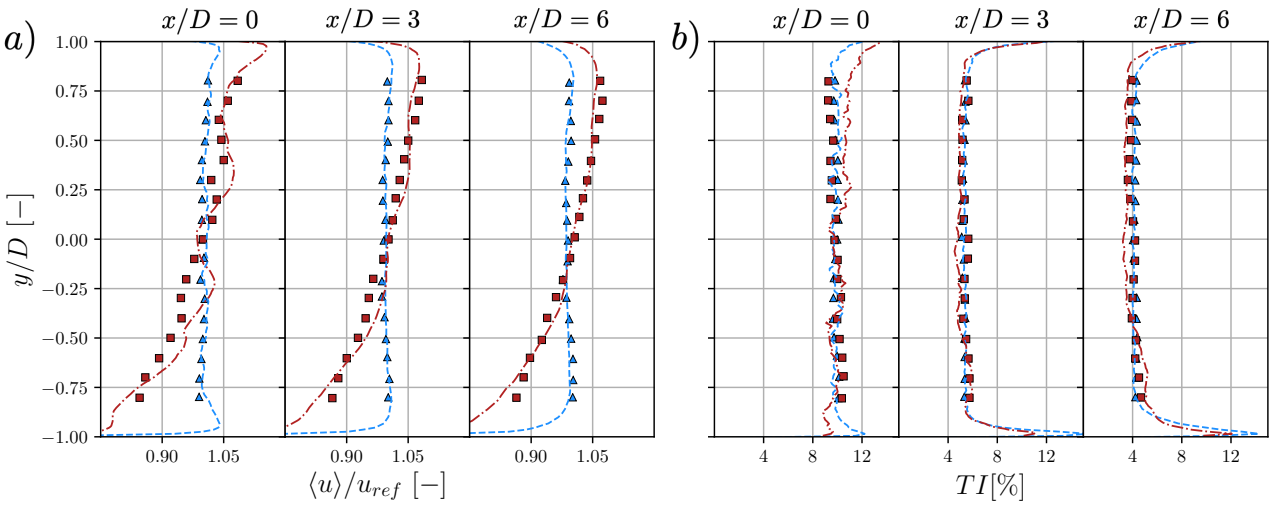

Figure 3.19: Vertical profiles of the time-averaged a) streamwise velocity and b) the streamwise turbulent intensity in the wind tunnel without the turbine. The results of the inflows generated with the turbulence grids are presented: (ii) Experimental (▲), LES (- - -); (iii) Experimental (■), LES (-·-·-)

destabilization just downstream the grids positions can be observed for both inflows. The mixing and decay regions presented in the previous subsection are observed for both inflows and tend to be similar. In the mixing region, the wake of the grid is not destabilized, involving coherent flow structures. Further downstream, turbulence becomes homogeneous in the decay region, and its intensity seems to decay along the wind tunnel. The primary observable difference between the inflows (ii) and (iii) is the shear induced by the vertical rod spacing of the grid.

Fig. 3.19 presents the vertical profiles of the streamwise velocity and the turbulence intensity in the empty wind tunnel compared to experimental data [44] for inflows (ii) and (iii). These results show a perfect prediction of both streamwise velocity and turbulence intensity profiles. This highlights the ability of the DALM to generate turbulence at a lower degree of empiricism than with precursor methods by using only the geometry of the grid. Now that the turbulence grids effects are replicated, the following sections will study the impact on the wind turbine(s) performances and wake.

3.3 Single Turbine configuration: wake deflection

In this section, the wind turbine T1 is placed into the wind tunnel, and nine configurations are investigated. The wind turbine wake is studied for three different yaw angles (+30°, 0° and −30°) and under the effect of three different inflows: (i) uniform laminar, (ii) uniform turbulent and (iii) non-uniform sheared turbulent. The reader can find the numerical setup information in the previous **Section 3.1.3**. Firstly, this section presents the performances and the aerodynamic loads on T1. Secondly, the flow topology and the mean wake flow are investigated through the wake shape and the wake center deflection. And thirdly, the turbulence generated in the vicinity of T1 is reviewed.

	$\gamma = -30°$				$\gamma = 0°$				$\gamma = +30°$			
inflow	$\langle \mathbf{C_P} \rangle$	E_{C_P}	$\langle C_T \rangle$	E_{C_T}	$\langle C_P \rangle$	E_{C_P}	$\langle C_T \rangle$	E_{C_T}	$\langle C_P \rangle$	E_{C_P}	$\langle C_T \rangle$	E_{C_T}
(i)	**0.382**	+16%	**0.64**	-9%	**0.553**	+18%	**0.91**	+2%	**0.387**	+20%	**0.65**	-8%
(ii)	**0.369**	+11%	**0.64**	-9%	**0.541**	+15%	**0.9**	+3%	**0.350**	+8%	**0.65**	-7%
(iii)	**0.371**	+13%	**0.62**	-6%	**0.544**	+18%	**0.89**	+8%	**0.368**	+14%	**0.63**	-6%

Table 3.5: Time averaged power and thrust coefficients of the turbine (C_P and C_T) at the optimal operating point ($\lambda = 6$) for the three yaw angles and the three inflow conditions. The power E_{C_P} and thrust E_{C_T} errors are computed with respect to the experimental data from J. Bartl et al. [44].

3.3.1 Turbine performance and loads

The wind turbine loads are investigated and the impact of yaw misalignment and inflow are discussed. **Tab. 3.5** presents the averaged power and thrust coefficients under inflow (i), (ii) and (iii) for the different yaw angles, computed as

$$\langle C_P \rangle = \frac{8\langle P \rangle}{\pi \rho u_{\text{ref}}^3 D^2}, \quad \langle C_T \rangle = \frac{8\langle T \rangle}{\pi \rho u_{\text{ref}}^2 D^2}, \tag{3.5}$$

where P is the power, ρ the fluid density and T the thrust force, estimated as the streamwise component of the force induced by the flow on T1. The table rrors are defined as follow:

$$E_{C_P} = \frac{\langle C_P \rangle - C_{P,\text{exp}}}{C_{P,\text{exp}}}, \quad E_{C_T} = \frac{\langle C_T \rangle - C_{T,\text{exp}}}{C_{T,\text{exp}}}, \tag{3.6}$$

The simulated power and thrust show similar behavior for all three inflow conditions. The investigated yaw angles $\gamma = \pm 30°$ power production is reduced from $30-32\%$. An approximation of this reduction can be obtained with sufficient accuracy by multiplying the maximum power of the non-yawed turbine by $\cos^3(30°)$. A fair estimate of the $\langle C_T \rangle$ of the yawed rotor can be obtained assuming a reduction by $\cos^2(30°)$ on the thrust of the non-yawed rotor. This observation made in various investigations from the literature [40, 191] is well represented here.

The comparison to the experimental data from J. Bartl et al. [44] gives an insight into the difficulties encountered when using standard ALM with no forces corrections (see **Section 2**). The power production differs significantly regarding the experimental data. Indeed, even if the profiles in the wake are in good accordance with the experiment, the retrieved power remains overestimated, up to 20% ($\gamma = +30°$, inflow (i)). These discrepancies can be discussed with **Fig. 3.20** depicting the mean radial and azimuthal contribution to the power production for all cases. The azimuthal component of each blade section is averaged over time and for each azimuth and radius. To obtain the power contribution, it is multiplied by the element radius and rotation speed. Independent of the inflow, the power production's contribution strictly increases with the radius for the aligned cases. From the literature [151, 152, 125, 153], the tip-loss corrections applied to the actuator line occur at around 90% of the blade span reducing the loads exponentially until the tip of the blade. Consequently, the overestimation of the power coefficient compared to the experimental setup could be reduced by using tip-loss corrections. Yet, tip corrections are not evaluated in this work and are irrelevant for wind turbines under yaw misalignment. Indeed, by looking at the power contribution for $\gamma = \pm 30°$, azimuthal discrepancies appear, this behavior is similar to previous observations on yaw misalignment configurations [35, 36].

The thrust coefficient for the non-yawed turbine case is slightly overestimated for all the inflows, while for the misaligned cases, it is underestimated. For the yawed cases, two effects are

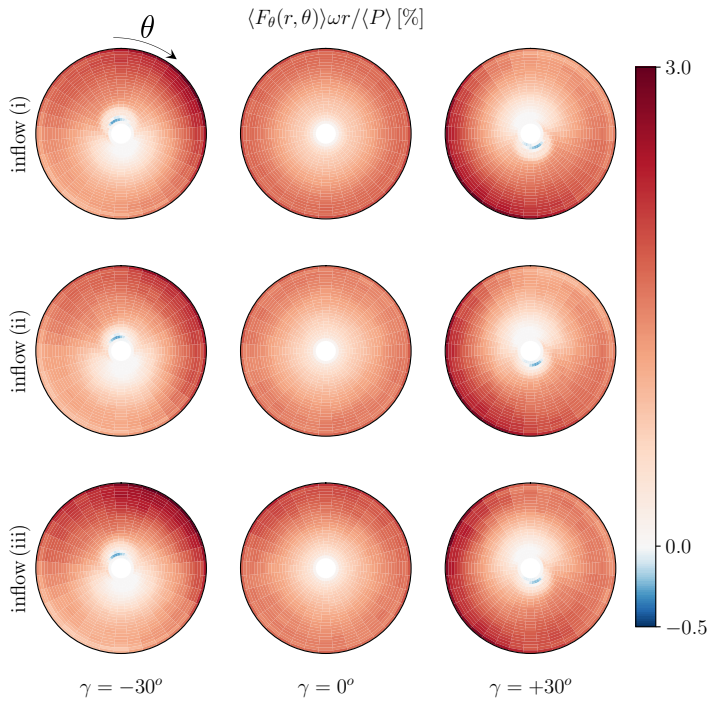

Figure 3.20: Radius and azimuth averaged temporal mean contribution to the power output of T1 in percent, $\langle F_\theta(r,\theta)\rangle\omega r/\langle P_{T1}\rangle$ [%] for $\gamma = 30°$, $0°$ and $-30°$ under inflow (i), (ii) and (iii).

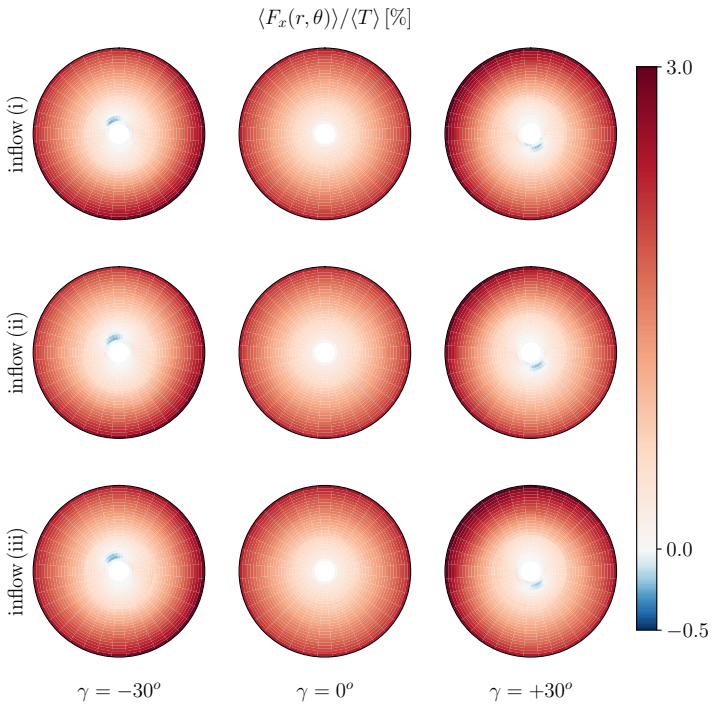

Figure 3.21: Radius and azimuth averaged temporal mean streamwise force component divided by the time averaged Thrust force of T1 in percent, $\langle F_x(r,\theta)\rangle/\langle T\rangle$ [%] for $\gamma = 30°$, $0°$ and $-30°$ under inflow (i), (ii) and (iii).

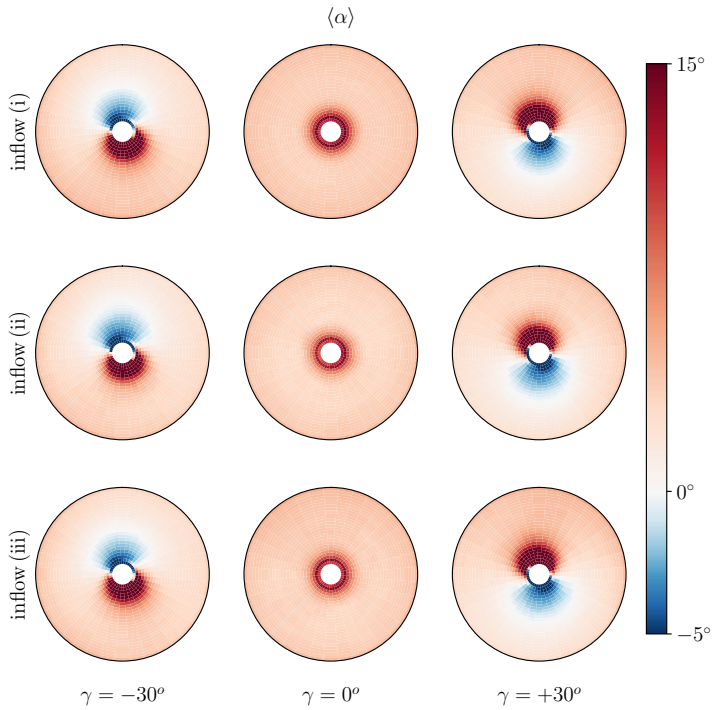

Figure 3.22: Radius and azimuth averaged temporal mean of angle of attack, α for $\gamma = 30°$, $0°$ and $-30°$ under inflows (i), (ii) and (iii).

counterbalancing each other. This can be observed from **Fig. 3.21** depicting the mean radial and azimuthal contribution to the turbine thrust for all cases. First, the lack of tip corrections tends to increase the turbine's thrust by overestimating the contribution near the tip. In opposition, the thrust force near the hub is changing of sign at the azimuth angles $-20°$ ($\gamma = -30°$) and $-160°$ ($\gamma = +30°$). This observation implies a large variation of the angle of attack during the rotation and will be further discussed in the following subsection.

3.3.1.1 Impact of yaw angle

The variation of the integrated coefficients, C_P and C_T, shows the impact of yaw misalignment on the turbine performance behavior. To get a proper insight of the yawed wind turbine aerodynamics, **Fig. 3.22** presents the time-averaged radial and azimuthal distribution of the angle of attack, $\langle\alpha\rangle$. When the thrust and torque contribution gets negative near the turbine hub, the angle of attack is also negative. The phenomena inducing this behaviour on α is represented in **Fig. 3.23** depicting the velocity triangles and the resulting α when the blade is at $\theta = 0°$ and $180°$ for $\gamma = 30°$. The yaw angle induces a supplementary angle between the gas and the blade local velocity near the hub. When $\theta = 0°$ this increases α whereas for $\theta = 180°$ the angle of attack is reduced and can even become potentially negative. Similar azimuthal repartition of the angle of attack is observed in the literature either on wind tunnel expirement [192] ($D = 4.5$m) or field measurements [193] ($D = 77$m). The variation of the angle of attack for yawed wind turbine will therefore generate a sheared distirbution of the loads at a given azimuth position contributing to the blade fatigue [194]. The other aspect is the near hub variations of α due to azimuth for $\gamma = -30°$ and $+30°$. Indeed values fluctuate from $-5°$ up to $30°$ showing the potential appearance of a dynamic stall in these areas. Their respective positions are shifted from $180°$ between the two different yaw angles. During dynamic stall, the drag coefficient gets

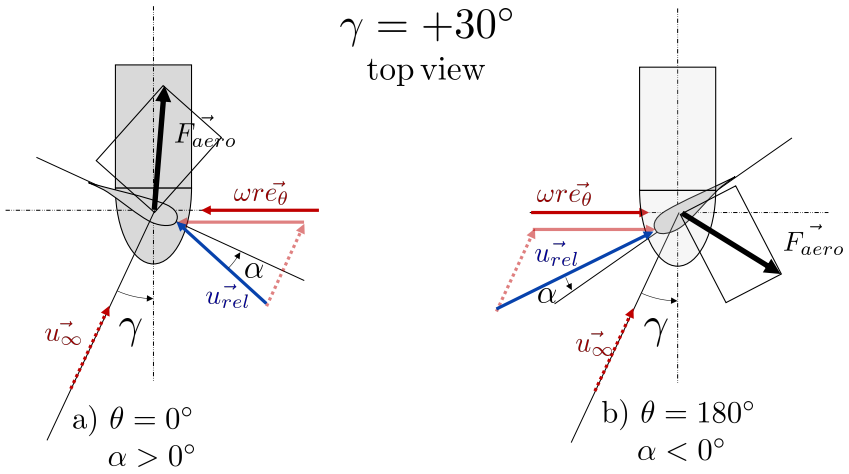

Figure 3.23: Layout of the impact of yaw angle on the velocity triangle and resulting angle of attack in the near hub region, $r/D \sim 0.1$. a) the blade is at $\theta = 0°$, upper vertical position and b) the blade is at $\theta = 180°$, lower vertical position.

higher while the lift is dropping [154]. This potential appearance of dynamic stall due to the high variation of α over time, either positive or negative, explain the underestimation of the global thrust for yawed cases. When looking at the power contribution, **Fig. 3.20**, the yaw misalignment induces a higher production (for $r > 0.3D_{T1}/2$) when the blade are upstream the rotor, i.e. when the azimuth is between 180° and −30° for $\gamma = +30°$ (0° and 120° for $\gamma = -30°$). In the same way a higher thrust force, **Fig. 3.21** is observed when the blade is between −120° and 0° for $\gamma = +30°$ (60° and 180° for $\gamma = -30°$). From these higher streamwise forces, a higher streamwise velocity deficit at these positions is expected near the turbine since more flow momentum will be exchanged to the turbine. At last, the misaligned turbines have a positive or negative lateral force for a positive or negative yaw misalignement angle, respectivly. This can be observed in **Fig. 3.24** presenting the radial and azimuthal averaged temporal mean of the lateral force component. These results will also be linked to the wake deviation in **Section 3.3.2.4**.

3.3.1.2 Impact of turbulence and shear

The turbulence intensity within the flow increases the fluctuations while the shear induces slight discrepancies on the mean load's repartition. The power contribution, **Fig. 3.20**, at the tip of the blade differs up to 0.5% for inflow (iii) when there is no misalignment. The time-averaged fluctuations of the azimuth and radial average angle of attack are depicted in **Fig. 3.25**. Fluctuations of the angle of attack are present only for inflows (ii) and (iii). The highest fluctuations are mainly present in the near hub region for the three yaw angle configurations, reaching oscillations up to 6°. For $\gamma = -30°$ and $+30°$ the fluctuations arise where their mean value is maximal, triggering even more the potential dynamic stall effect. For the yawed wind turbine cases, the maximum fluctuations occur in the maximum mean angle of attack region and not when α is negative. For both turbulent inflows, the temporal fluctuations of azimuthal and radial averaged thrust force remain below 0.5% of the integrated thrust.

3.3.2 Wake flow topology

To obtain a first insight of the the flow behaviour, the nine configurations can be observed through a slice of the instantaneous velocity field in **Fig. 3.26**, a) at the rotor level and b)

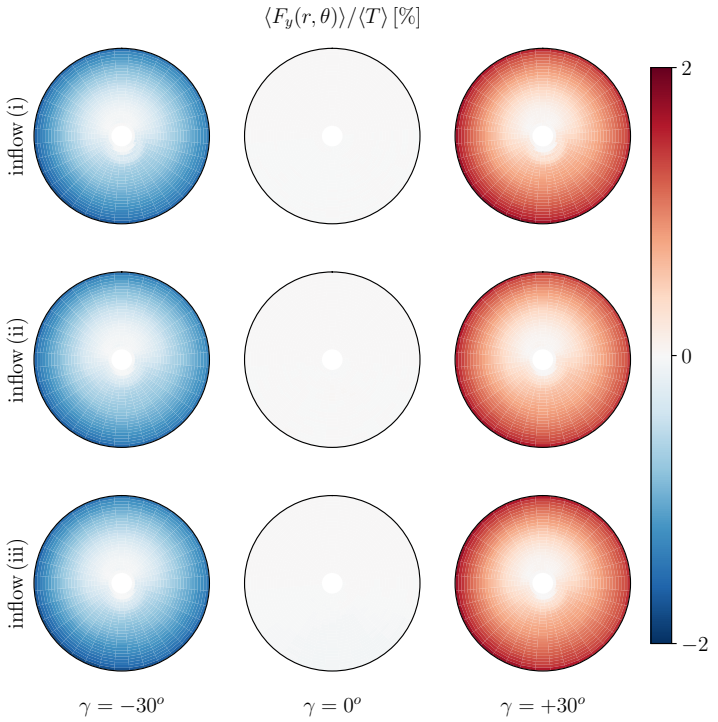

Figure 3.24: Radius and azimuth averaged temporal mean lateral force component divided by the time averaged Thrust force of T1 in percent, $\langle F_y(r,\theta)\rangle/\langle T\rangle\,[\%]$ for $\gamma = 30°$, $0°$ and $-30°$ under inflow (i), (ii) and (iii).

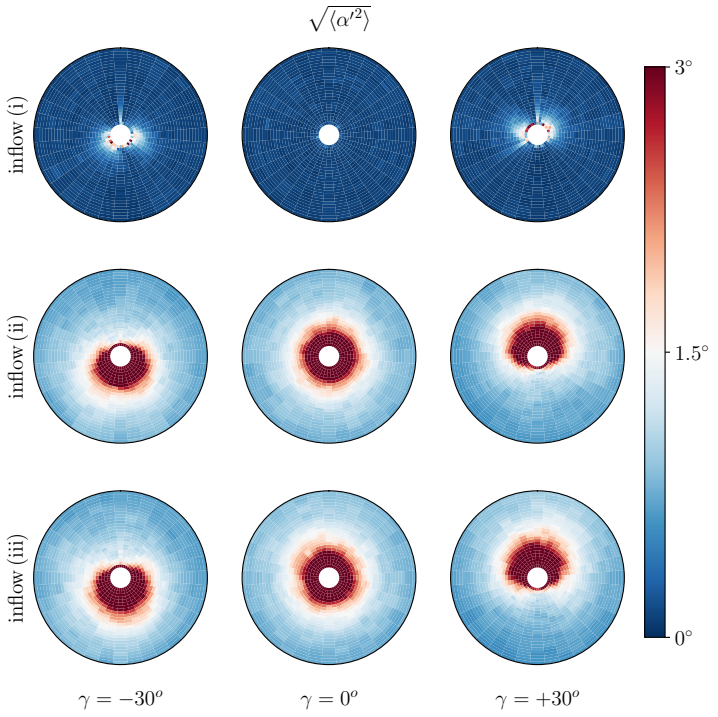

Figure 3.25: Radius and azimuth root mean square of angle of attack, α for $\gamma = 30°$, $0°$ and $-30°$ under inflow (i), (ii) and (iii).

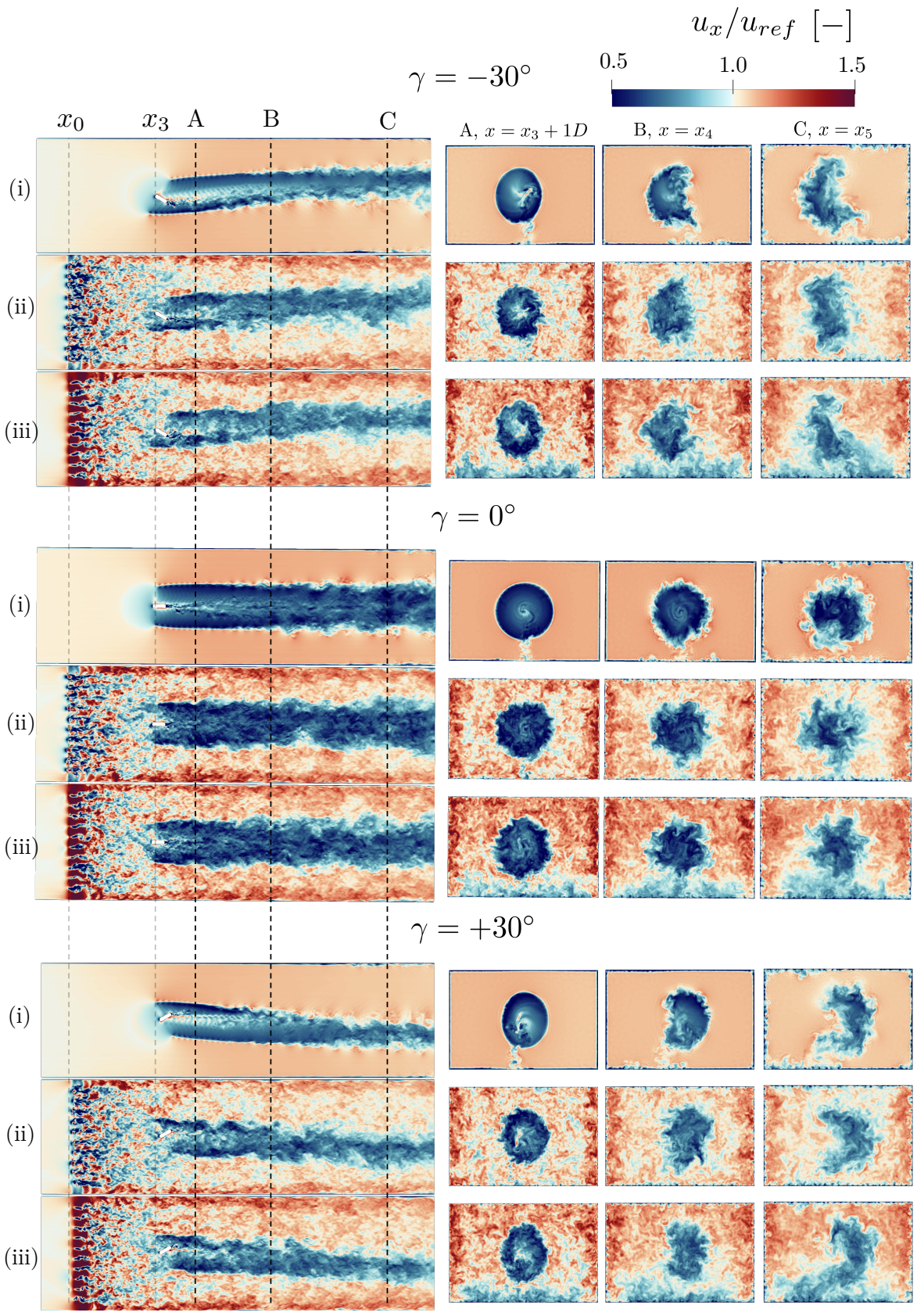

(a) Top view (b) Front views

Figure 3.26: Slices of instantaneous streamwise velocity fields for $\gamma = -30°, 0°, +30°$ under inflows (i), (ii) and (iii). (a) is a top view of the horizontal slice at rotor hight, dashed black lines show the position of the slices A, B and C. (b) is a front view of slices at different streamwise position in the wind tunnel: A ($x = x_3 + 1D$), B ($x = x_4$) and C ($x = x_5$).

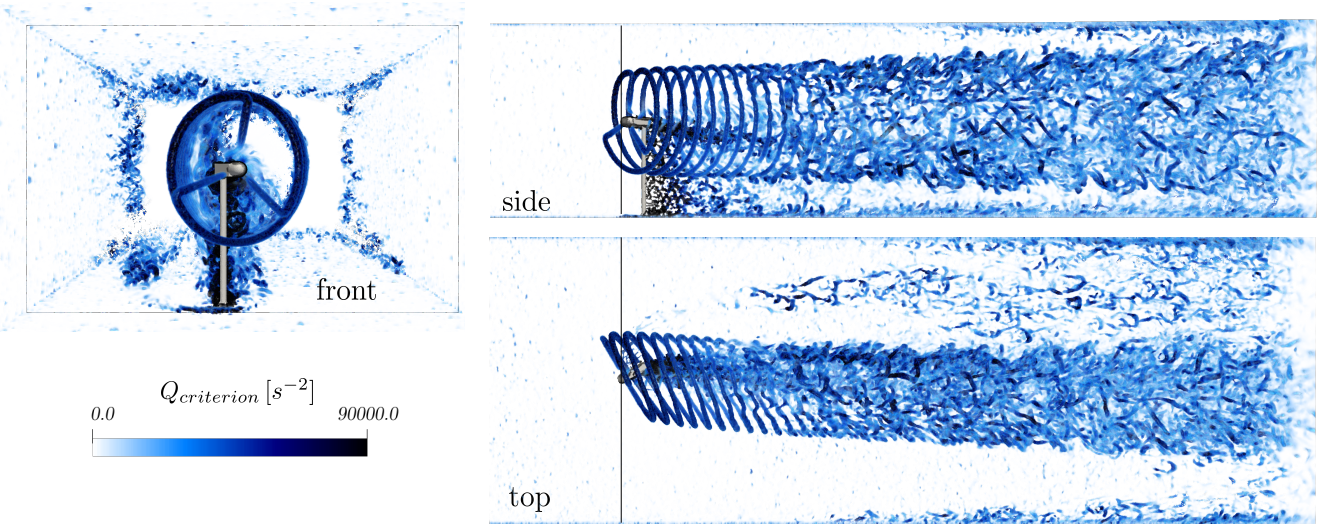

Figure 3.27: Front, top and side views of the instantaneous 3D visualization of the wake generated by the turbine blades, tower and nacelle at $\gamma = +30°$ under inflow (i) using a volumic rendering of the $Q_{\text{criterion}}$ colored by intensity. The tower and nacelle surfaces are in dark grey.

slices at different streamwise position. In **Fig. 3.26** b) the slices are located at A:$x = x_3 + 1D$, B:$x = x_4$ and C:$x = x_5$.

The wake of the grid rods can be observed at a short distance from the grid and interacts with each other to generate a high level of free-stream turbulence. In **Fig. 3.26** a) the near grid difference between the turbulent inflows depicting lower velocities for (ii) and higher for (iii) is due to the proximity to the plane of a rod for inflow (ii) and not for inflow (iii), yet similar flow structures are generated. Due to the large rod spacing with sidewalls of the wind tunnel, high velocities are observed on the left and right sides of the tunnel. In the same way, the sheared velocity profile can be observed for inflow (iii) on the slice at the different downstream positions with low velocities at the bottom and high velocities at the top.

For the yawed turbine cases, $\gamma = -30°$ and $+30°$, the wake of T1 has deviated from the center of the wind tunnel, and an asymmetrical behavior can be observed further downstream. For the cases under the first inflow, the evolution of the vortices generated at the tip of the blades gives information on the destabilization of the turbine wake. In the case without yaw misalignment, the tip vortices are convected until they interact with each other and with the wake of the tower, thus delaying the destabilization to $x = 1.75D$. As for the yawed cases, the deviated vortices generated at the blade tip interact with the tower and the ones developed in the wake of the nacelle. This is highlighted in **Fig. 3.27** by a volumic rendering of $Q_{\text{criterion}}$ of the wake showing the vortices development under the first inflow (i) for a yaw misalignment of $\gamma = -30°$. In **Fig. 3.27** a) and b), one can notice the asymmetry of the bottom turbulent boundary layer in the wind tunnel along z-axis. Similar observations from **Fig. 3.26** b) are made for $\gamma = +30°$ through a velocity deficit at the bottom of the wind tunnel on the other side of the tower. For the case with $\gamma = 0°$, this asymmetry is not observed, and a horse-shoe vortex is developed on the tunnel floor around the tower.

3.3.2.1 Mean wake flow

After the previous qualitative overview of the flow instantaneous topology, the time averaged velocity fields are analysed with **Fig. 3.28** depicting slices of time averaged streamwise velocity

field $\langle u_x \rangle$. The presented flow slices are at the same location as in **Fig. 3.26**. The velocity deficit in the wake is observed to reduce significantly when the turbine is misaligned with the streamwise direction. This behavior was expected: the rotor thrust is reduced in yawed cases (**Tab. 3.5**), meaning that a smaller amount of the flow momentum is lost in the streamwise direction. The yawed wind turbine wake has deviated from the wind tunnel center as aforementioned from the instantaneous velocity fields. The deviation direction is in the opposite direction of the integrated lateral force component presented in **Fig. 3.24**. The misaligned turbines are therefore inducing a cross-stream momentum on the flow by counterbalancing the lateral force. This cross-stream momentum explains why the velocity deficit has deviated sideways. An asymmetry is observed by comparing the positive and negative yaw misalignment cases through slices at different streamwise positions. This asymmetry increases with the distance to the rotor, and a kidney-shaped cross-section, signature of a yawed wind turbine wake [43] is observed on slice C, especially for the laminar inflow (i). In the same way, the position of the maximum velocity deficit is not symmetric between opposite yaw angles. These observations are analyzed in the following subsections. It is essential to mention the streaks of velocity between the free stream flow and the wake for inflow (i) on slice B for $\gamma = -30°, 0°, +30°$. These gradients are not due to a lack of time accumulation since the same accumulation time is used for the nine configurations. Compared to the statistic time accumulation, these streaks correspond to a static azimuthal destabilization of the tip vortices with low-frequency fluctuations. This behavior does not appear when high turbulence levels are present in the free stream since turbulent structures trigger the tip vortices' instability at various positions in time. As for the turbine performances, a comparison to experimental measurements from J. Bartl et al. [44] is provided. **Fig. 3.29** presents the horizontal profiles of time-averaged streamwise velocity at hub level and for two downstream positions, x_4 and x_5. The experimental data were not available at position x_4 for inflows (i) and (ii). Thus no experimental results are presented for these cases. The velocity deficit is well predicted with respect to experimental data, as it can be seen for the non-yawed wind turbine. For the yawed cases, the wake velocity deficit seems to recover faster than in the experimental configuration. Indeed, the velocity deficit tendency remains close to the experiment but is slightly underestimated. This under-prediction of the velocity deficit is also related to the under-prediction of T1 thrust compared to experiments discussed in the previous section.

3.3.2.2 Effect of inflow turbulence

The impact of the background turbulence intensity on the wake is observed in **Fig. 3.28** a). The recovery of the velocity deficit starts earlier when comparing inflows (ii) or (iii) with (i). The turbulent mixing has completely smoothened the velocity streaks observed for inflow (i). This is even more highlighted by comparing the velocity profiles in **Fig. 3.29** where steeper velocity gradients between the inner wake and the wind tunnel free stream are observed under inflow (i). A curled kidney-shaped velocity deficit is observed at x_5 for turbulent cases; however, the curl is not as pronounced as for inflow (i).

3.3.2.3 Effect of inflow shear

The sheared velocity profile impact can be observed on the front views of **Fig. 3.28**. Regardless of the sheared inflow, the wake shapes for all three yaw angles are very similar to those of inflow (ii), with the same turbulence intensity level. The shear impact is observed in the outer wake region by low velocity on the bottom of the wind tunnel. From observation on the instantaneous fields, an asymmetry on the bottom turbulent boundary layer is highlighted for inflow (i). The

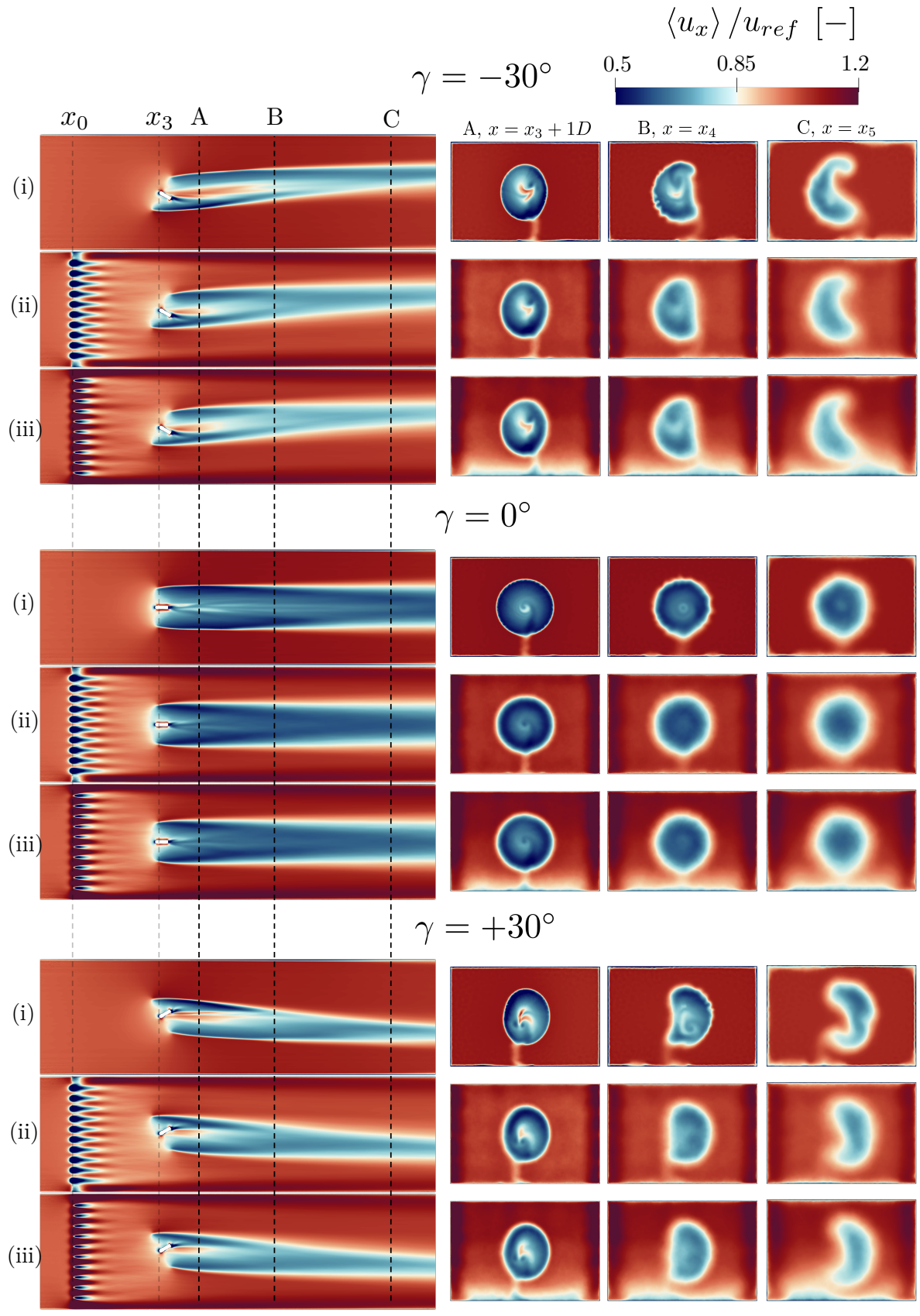

(a) Top view (b) Front views

Figure 3.28: Slices of time averaged streamwise velocity fields for $\gamma = -30°, 0°, +30°$ under inflows: (i), (ii) and (iii). (a) is a top view of the horizontal slice at rotor hight, dashed black lines show the position of the slices A, B and C. (b) is a front view of slices at different streamwise position in the wind tunnel: A ($x = x_3 + 1D$), B ($x = x_4$) and C ($x = x_5$).

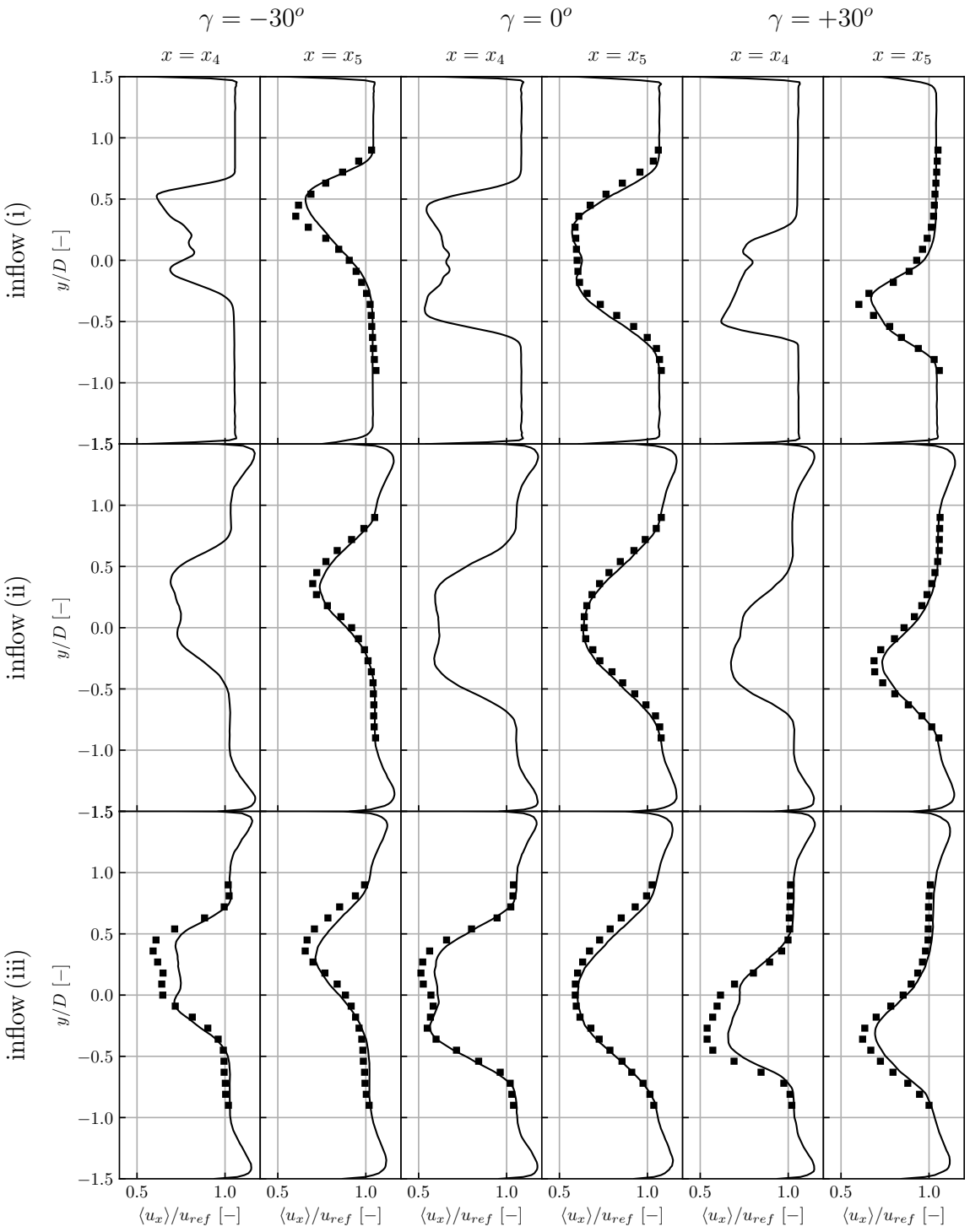

Figure 3.29: Horizontal profiles of the time-averaged streamwise velocity at $x = x_4$ and $x = x_5$ behind the T1 under all inflows: (i) top, (ii) middle and (iii) bottom for the three yaw angles configuration: (left) $\gamma = -30°$, (middle) $\gamma = 0°$ and (right) $\gamma = +30°$. Experimental (■) and LES (—) results are presented.

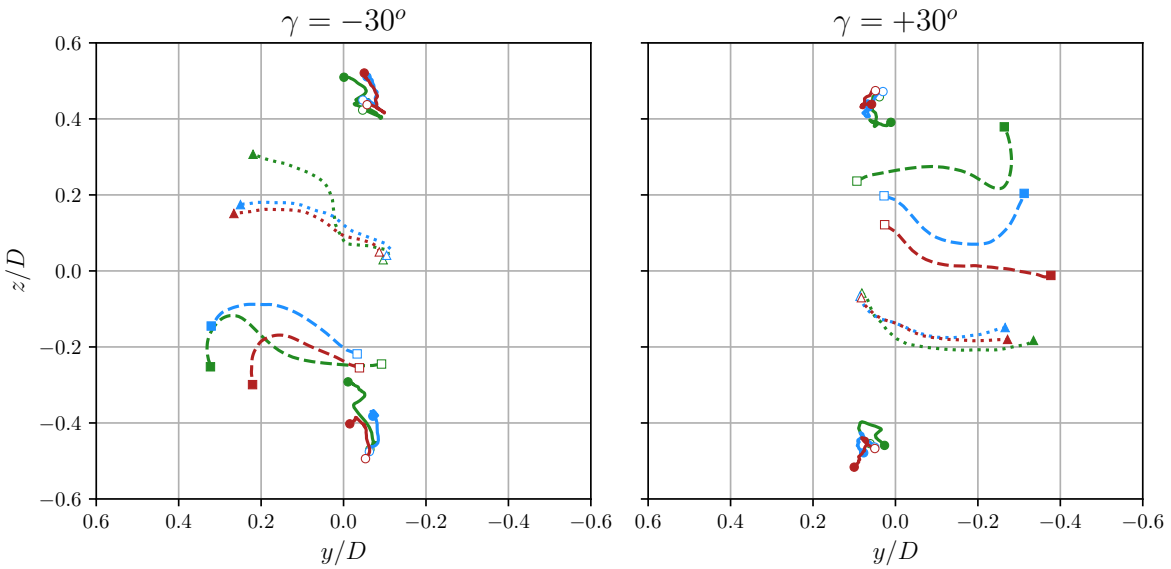

Figure 3.30: Streamwise evolution of the wake center (□- - -■), primary CVP position, positive and negative (○——●) and the secondary CVP center position, generated by the nacelle (△·····▲) in the wind tunnel from $x = x_1$ to $x = x_5$. $\gamma = -30°$ (left) and $\gamma = -30°$ (right) for inflows (i) (——), (ii) (——) and (iii) (——).

time-averaged velocity fields for inflow (i) shows a bottom velocity deficit increasing with the distance to the rotor; either on both side ($\gamma = 0°$), right side ($\gamma = -30°$), or left side ($\gamma = +30°$). This phenomenon is even more pronounced in the shear inflow, especially at the streamwise distance x_5. The modification of the sheared profile behind a yawed wind turbine is, in this configuration, the results of a counter-rotating vortex generated in the wake and of the closed wind tunnel environment.

3.3.2.4 Yawed wind turbine curled wake

The downstream wake slices of time average streamwise velocity from **Fig. 3.28** depict a kidney-shaped velocity deficit for yawed cases. The curled kidney shape of the wake can be explained by the formation of a counter-rotating vortex pair (CVP), which was previously discussed in the litterature [43, 195, 44]. Bastankhah and Porté-Agel [43] also presented a comprehensive explanation employing the differential form of the continuity equation and simpler two-dimensional potential flow. This provided useful insights into how the CVP interacts with the wake rotation and the ground, yet unable to predict the wake center position accurately. **Fig. 3.31** shows slices of the transverse vectors of the velocity fields for inflow (ii) and $\gamma = +30°$ at different streamwise positions. The CVP centers are obtained using a gradient descent algorithm based on the positive and negative time-averaged streamwise vorticity $\langle\omega_x\rangle$. The positive vortex of the CVP is in red while the negative vortex is in blue, the wake center is in black. A secondary CVP is observed in the vicinity of the nacelle, represented with smaller circles at position A. This secondary CVP interacts with the lower vortex of the primary CVP between positions A and B. Only the negative vortex remains after position B and slowly disappears by losing intensity. In **Fig. 3.31**, 80% of the maximum velocity deficit is highlighted by the green contour. At position A, the maximal velocity deficit is generated where the thrust forces (**Fig. 3.21**) are the greatest, i.e., for a blade azimuth between −120° and 0°. Then, due to the impact of the CVP,

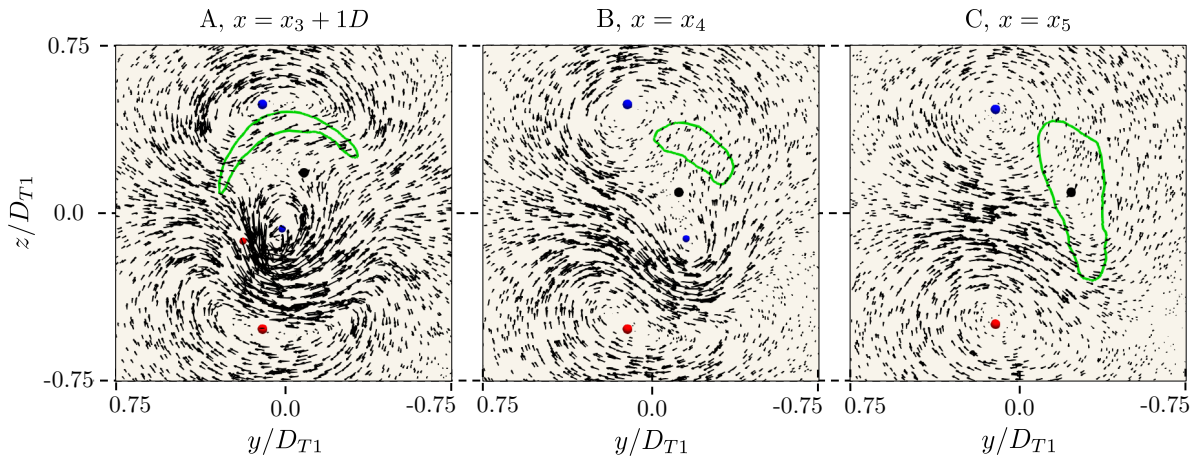

Figure 3.31: Cross velocity fields represented with black vectors at three downstream positions for inflow (ii) and $\gamma = +30°$. The wake center based on the available power approach is represented by (●). The counter rotating vortex pair is represented by (●), positive and (●), negative vortex. The secondary counter rotating vortex pair, generated by the nacelle, is represented by (●), positive and (●), negative vortex only for position A and B. The green contour represent 80% of the maximum streamwise velocity deficit on the slice.

it is deflected and slowly redirected through the bottom. This is reproduced on slices between $x/D_{T1} = 0.5$ and $x/D_{T1} = 8.0$, allowing to obtain the evolution of the CVP position in the wake of T1 for all inflows and the two yaw angles displayed in **Fig. 3.30**. Position $x/D_{T1} = 0.5$ corresponds to the empty symbols and $x/D_{T1} = 8.0$ to the filled ones. The primary CVP is displayed with circles. The CVP is mainly static in the wind tunnel, which differs from the insights based on the two-dimensional potential flow theory cited earlier. Yet these observations were made on a 15 cm diameter turbine in a similar wind tunnel with a lower blockage ratio than in this work. The yaw angle influence on the CVP is only a shift in the positive or negative direction, making it symmetric. The secondary CVP position, represented by triangles, is computed between $x/D_{T1} = 0.5$ and $x/D_{T1} = 4.5$ since it slowly disappears after interacting with the primary CVP. The secondary CVP is deviated by the cross-stream flow generated by the primary CVP, similarly to the wake center depicted with the square symbols. Moreover, when the yaw angle is positive, the secondary CVP goes to the bottom; to the top for negative yaw misalignment. The experimental study showed the asymmetry of the velocity deficit position by computing the maximum velocity deficit at different vertical positions. The same behavior is observed in the simulations, as shown by the wake center deviations presented hereafter.

3.3.2.5 Yawed wind turbine wake deflection

The horizontal wake center deflection is depicted in **Fig. 3.32** for $\gamma = -30°$ and $+30°$ and the three inflow conditions. The wake deflection quantification was made using an available power approach to replicate the experimental results [196] and remove any method-dependant error. The computed wake center deflection is slightly lower than in the experiment for $\gamma = -30°$ while in fairly good agreement for $\gamma = +30°$. The TI-dependent wake deflection model of Bastankhah and Porté-Agel [43] is also presented for the two values of turbulent intensity. The model replicates the behavior of the LES properly until $x = x_5$. This model does not consider the confinement of the wind tunnel, and the wake has no constraint, drifting away from the turbine indefinitely. In contrast, the LES considers the confinement due to the wind tunnel walls, and

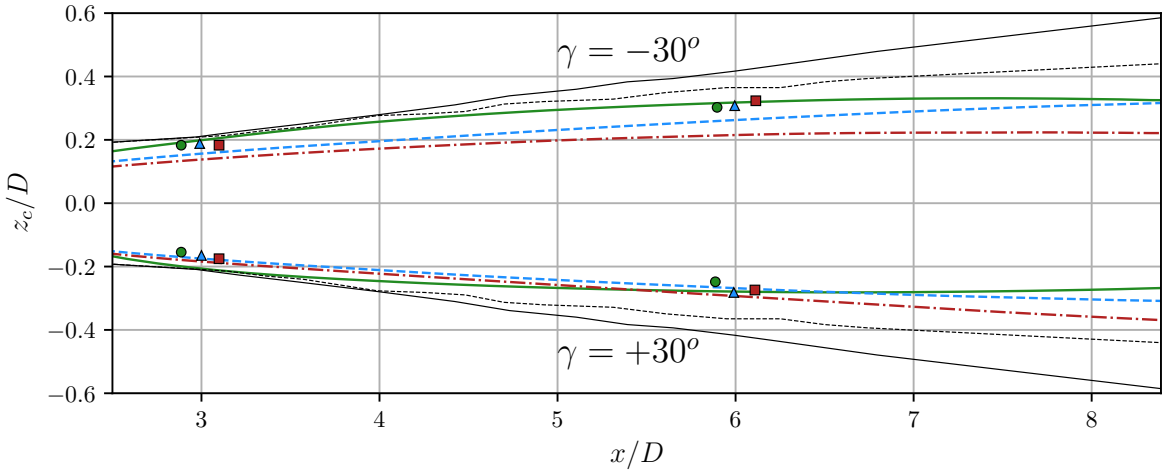

Figure 3.32: Calculated wake deflection z_c/D for $\gamma = -30°$ (top) and $+30°$ (bottom) under three different inflow conditions compared to experiment (at $3D$ and $6D$ only): (i) Experimental (●), LES (——); (ii) Experimental (▲), LES (- - -); (iii) Experimental (■), LES (-·-·-). A comparison to the wake deflection model of Bastankhah and Porté-Agel [43] for TI_i (——) and TI_{ii} (- - -) is provided.

the wake center is redirected towards the center of the channel after $x = x_5$. The vertical and horizontal wake center deflection is depicted in **Fig. 3.30** by square markers for all inflows and the two yaw angles. This shows, even more, the impact of confinement on the wake deviation. For $\gamma = -30°$, all the wakes are redirected to the bottom of the wind tunnel independently of the inflows. For $\gamma = +30°$, the wakes under inflows (i) and (ii) are redirected to the top of the wind tunnel, while for inflow (iii), the wake continues to drift in the cross-stream direction. This observation is similar to the one of Bastankhah and Porté-Agel [43], where the yaw angle can either push the wake towards the ground or upward (inducing a more considerable wake deflection). In the case of inflow (iii), the shear velocity profile slightly impacts the computation of the wake center according to the available power approach, explaining why the cases under inflow (iii) have their wake center redirected faster to the wind tunnel bottom.

3.3.2.6 Tower wake deflection

The wake of the tower can be observed in **Fig. 3.28** b), inducing a slight velocity deficit. For misaligned cases, the tower wake is deflected in the opposite direction than the turbine wake. This is due to the counter-rotating vortex presented earlier. The tower wake is between the wind tunnel bottom and the bottom vortex, therefore impacted by a cross-flow velocity component going in the opposite direction of the wake deflection. This cross-flow balances the counter-rotating vortex pair above and deflects the tower wake further to the side.

3.3.3 Wake destabilisation and generated turbulence

The wake destabilisation and generated turbulence is analysed in this subsection with **Fig. 3.33** depicting slices of time averaged turbulent kinetic energy (TKE) $\langle k \rangle = 1/2 \left\langle \widetilde{u}_i'^2 \right\rangle$. The presented flow slices are at the same location as in **Fig. 3.26**.

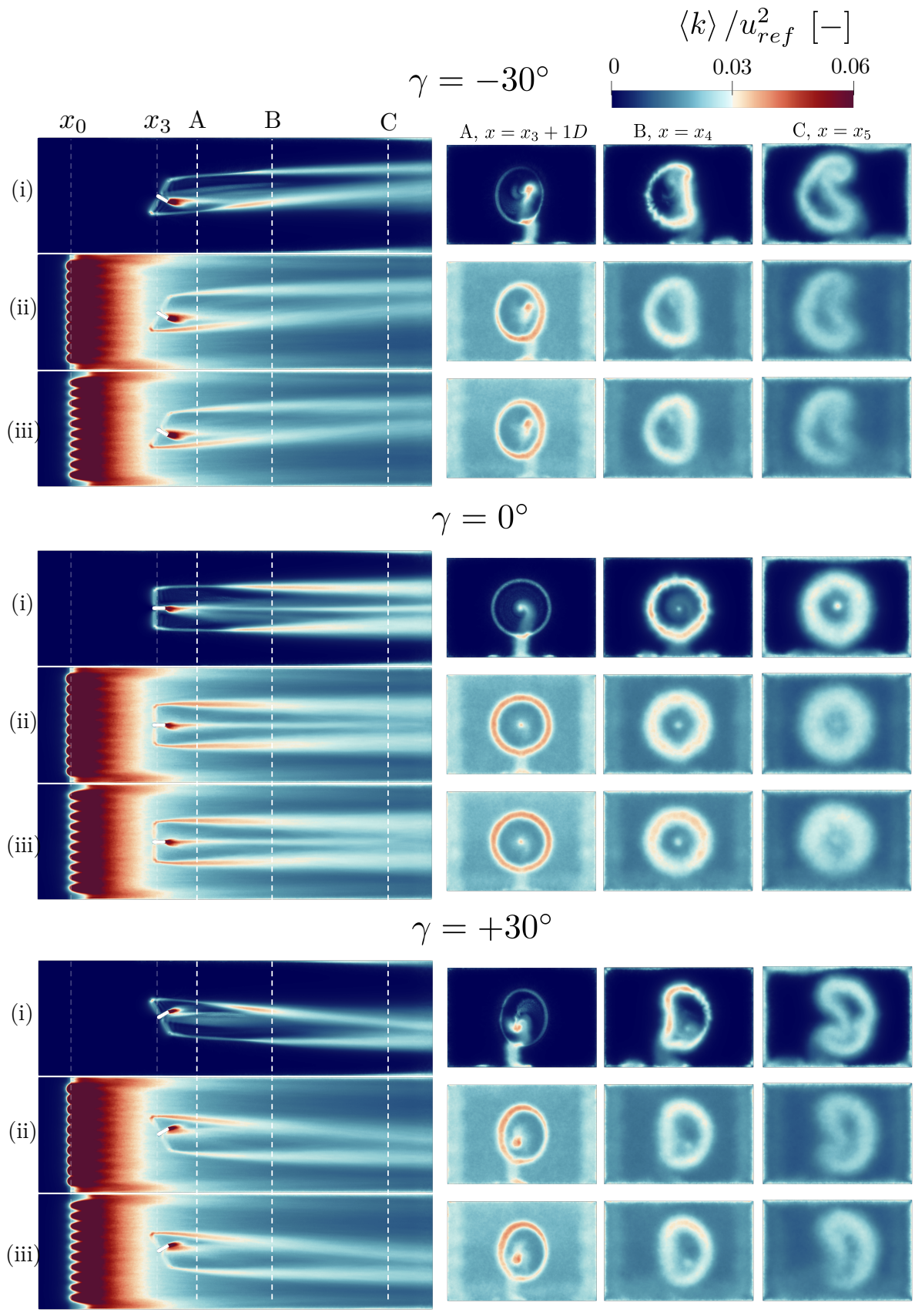

(a) Top view (b) Front views

Figure 3.33: Slices of time averaged TKE fields for $\gamma = -30°, 0°, +30°$ under inflows: (i), (ii) and (iii). (a) is a top view of the horizontal slice at rotor hight, dashed black lines show the position of the slices A, B and C. (b) is a front view of slices at different streamwise positions in the wind tunnel: A ($x = x_3 + 1D$), B ($x = x_4$) and C ($x = x_5$).

3.3.3.1 Effect of yawing on the rotor generated turbulence

For inflow (i) at position x_3 and $\gamma = 0°$, a ring of velocity fluctuation is formed behind the tips of the rotor blades with a higher level of turbulence when the flow is past the blade tip and the tower. The fluctuations generated by the tower and nacelle in the rotor area are slightly rotated in opposition to the rotor rotation. The fluctuations caused by the lower part of the tower (i.e., not in the rotor swept area) are only convected by the free stream. For $\gamma = -30°$ and $+30°$, the ring of peak turbulence is laterally deflected and deformed accordingly. A higher level of fluctuations appears behind the nacelle due to the misalignment. Still, for inflow (i), between slices A and B, the tip vortices are interacting and pairing (**Fig. 3.27**) with each other generating higher levels of turbulent kinetic energy. With increasing downstream distance, the sharp peaks of TKE decrease in magnitude and blur out to their surroundings. At the same time, the velocity deficit starts to recover. For the misaligned cases, the destabilization of the tip vortices arises faster on the inner deflected side, and a higher turbulent kinetic energy peak is observed, especially in **Fig. 3.33** a). Previous experimental studies [197, 198] showed that the production of rotor-generated turbulent kinetic energy is finished at x_4 for measurements on the same rotor and under similar inflow conditions. Here it is slightly decayed downstream for the aligned case for inflow (i). The kidney shape observed on the streamwise velocity deficit is as well observed here for yawed cases. Structures on the TKE, similar to the streaks of velocity, are observed between the free stream flow and the wake for inflow (i) on slice B for $\gamma = -30°, 0°, +30°$. The same explanation as in **Section 3.3.2** is given. The fluctuations generated by the nacelle are observed further downstream in the non-yawed case. For the yawed cases, they appear to be deflected in the the same way as the secondary CVP, i.e. for $\gamma = +30°$ to the right and bottom.

The streamwise turbulent kinetic energy is compared to the experimental results of J. Bartl et al. [44]. The **Fig. 3.34** depicts the horizontal profiles of time-averaged TKE at hub level and for two downstream positions, x_4 and x_5. The experimental data were not available at position x_4 for inflows (i) and (ii). Thus no experimental results are presented for these cases. The decay of turbulence in the turbine wake is shown to be slightly overestimated for yawed cases. The TKE of the non-yawed cases presents similar results between LES and experiment. Yet, at x_4, simulations present a higher turbulence level in the wake of the nacelle than in the experiment and a lower level at $z/D = -0.25$. No TKE steep profile is present at the nacelle position for the yawed turbines. As observed in **Section 3.3.2**, this seems to be due to the interactions of the tower wake with the tip vortices, mixing and diffusing the TKE. It is important to notice that the level of TKE outside of the wake center is well reproduced.

3.3.3.2 Impact of background turbulence and shear

From **Fig. 3.33**, the higher TKE levels in the flow lead to a faster destabilization of the tip vortices and, in consequence, peaks of TKE closer to the rotor position. The free-stream TKE increases the flow's mixing, which quickly smoothens the TKE peaks in the tip region. The TKE levels between inflows (ii) and (iii) are very similar, like in the experimental measurements. A slightly higher TKE is observed in the upper rotor tip vortices for inflow (iii).

3.4 Two Turbines configuration: wake interaction

In this section, a second wind turbine, T2, is placed in the wake of T1 to replicate the experimental configuration of F. Mühle et al. [49]. One configuration is presented here, T1 has a

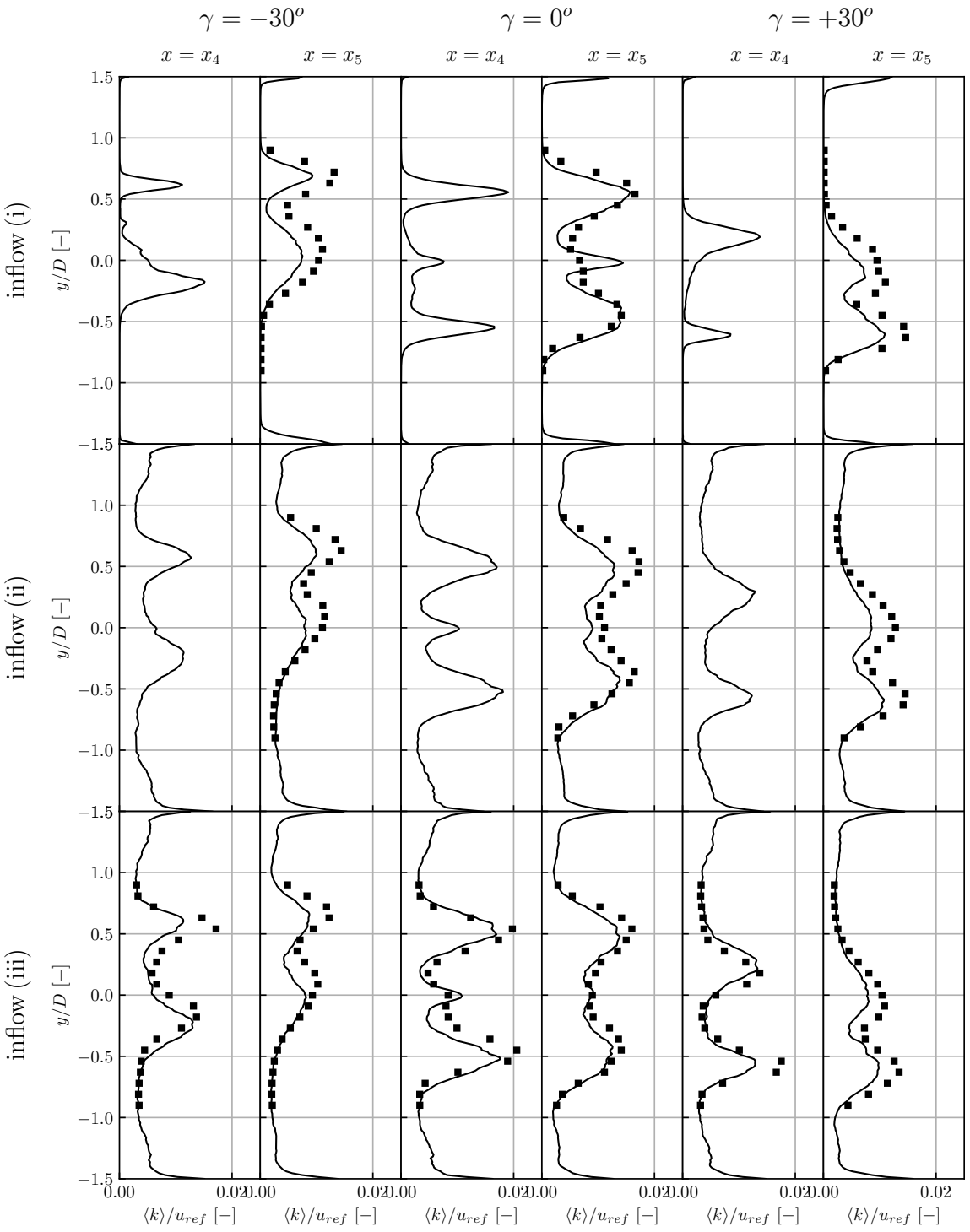

Figure 3.34: Horizontal profiles of the time-averaged turbulent kinetic energy at $x = x_4$ and $x = x_5$ behind the T1 under all inflows: (i) top, (ii) middle and (iii) bottom for the three yaw angles configuration: (left) $\gamma = -30°$, (middle) $\gamma = 0°$ and (right) $\gamma = +30°$. Experimental (■) and LES (—) results are presented.

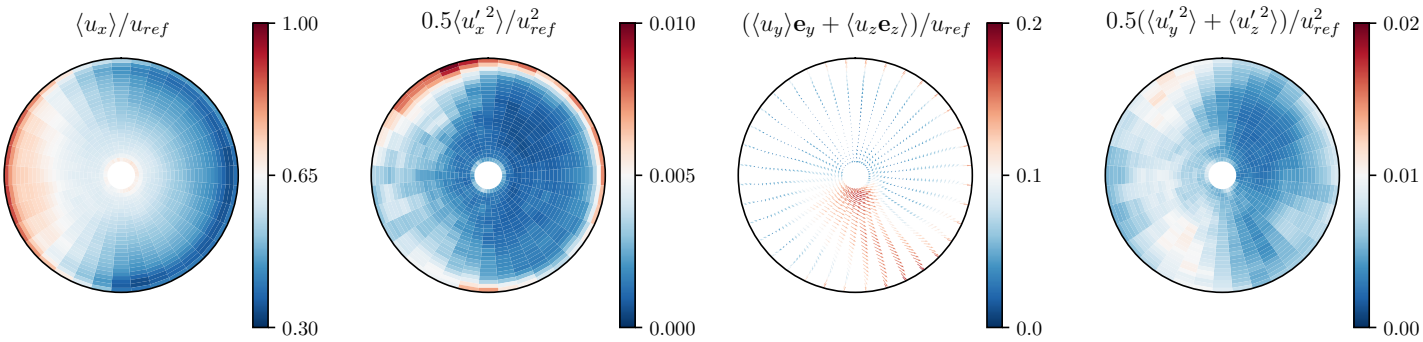

Figure 3.35: Radius and azimuth averaged temporal mean of velocity component seen by the blades of T2. From left to right: mean streamwise velocity, streamwise turbulent kinetic energy, transverse velocity components (vectors) and transverse turbulent kinetic energy.

yaw misalignment of 30° while T2 is aligned with the inflow direction. The two turbines are confronted to a sheared velocity profile with high free-stream turbulence, inflow (iii). The reader can find the numerical setup information in the previous **Section 3.1.3**. Firstly, this section presents the performances and the aerodynamic loads on T2. Secondly, the flow topology and the mean wake flow are investigated. Since the loads and wake characteristics of T1 are the same as in **Section 3.3**, they won't be discussed in this section.

3.4.1 T1 wake impact on T2 loads

The simulated power and thrust coefficient of T2 are $\langle C_P \rangle = 0.21$ and $\langle C_T \rangle = 0.57$. In comparison to T1 in the single turbine investigation with the same inflow, the output shows a reduction of -61% for $\langle C_P \rangle$ and -35% for $\langle C_T \rangle$. This shows the importance of investigating wake interactions; the power output is divided by more than two, even though the wake of T1 is deviated due to yaw. This power reduction is expected to be even greater if T1 is aligned. Compared to the experiments, the discrepancies are of $+10\%$ for $\langle C_P \rangle$ and -9% for $\langle C_T \rangle$ showing a good accordance compared to the loads of T1, yet remaining overestimated for the power output and underestimated for the thrust force. Time-averaged velocity seen by the rotor blades is represented in **Fig. 3.35**. The flow seen by T2 is perturbed due to the presence of T1. The impact of T1 is observed through the streamwise velocity deficit on the right part of the rotor. The cross-flow generated by the counter-rotating vortex pair discussed in **Section 3.3** is observed on the lower right portion of T2 rotor. Higher velocity fluctuations are observed on the opposite side (left) of T2 rotor. This corresponds to the peak of TKE generated by the tip vortices of T1 deflected to the side. The radius and azimuth averaged temporal mean and root-mean-square of the angle of attack are presented in **Fig. 3.36**. The left side of T2 rotor being less impacted by the velocity deficit of T1 depicts a higher angle of attack. Fluctuations arise at the limit of T1 wake. This is directly impacting the local contribution to the turbine power output displayed in **Fig. 3.37**. This asymmetry in the contribution to the power output is observed on the streamwise force, and a higher generated velocity deficit is expected in this area. The lateral force is not as much impacted, similar to the one of T1 without misalignment and inflow (iii) of the previous **Section 3.3**.

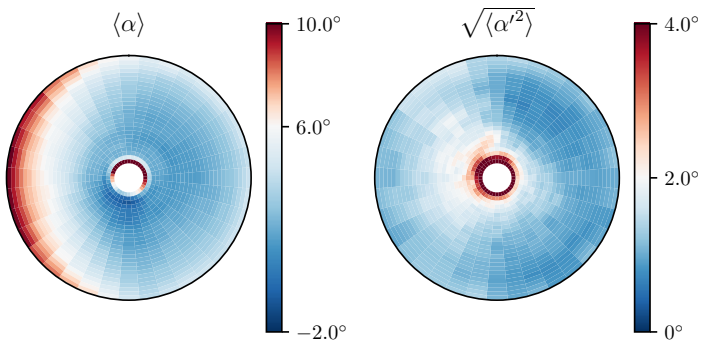

Figure 3.36: Radius and azimuth averaged temporal mean (left) and temporal RMS (right) of angle of attack, α for the second turbine T2 under a non-uniform sheared inflow with a high turbulence level, inflow (iii).

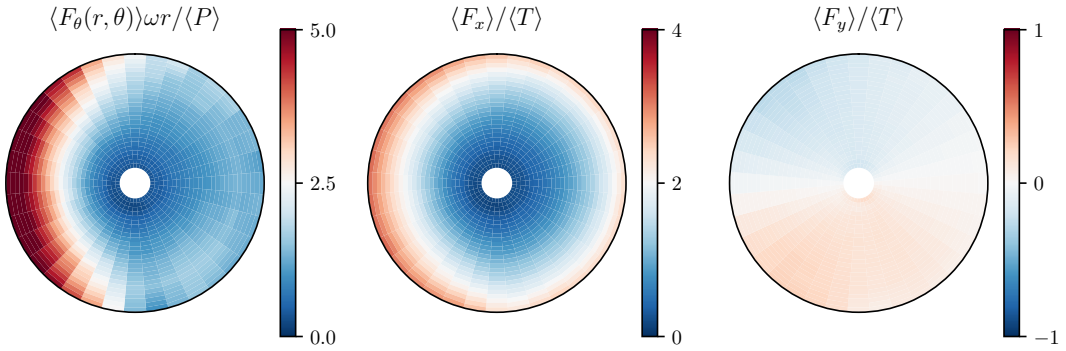

Figure 3.37: Radius and azimuth averaged temporal mean: contribution to the power output in percent (left), streamwise force (middle), and lateral force (right) for the second turbine T2 under a non-uniform sheared inflow with a high turbulence level, inflow (iii).

3.4.2 Flow topology

The impact of inflow (iii) and T1 wake over T2 can be observed through the horizontal and vertical slices of the instantaneous velocity field in **Fig. 3.38**. As mentioned in the single turbine investigation, the wake of the grid rods can be observed at a short distance from the grid and interact with each other to generate a high level of free-stream turbulence. The rod spacing generates higher velocities on the left and right sides of the tunnel. For T1, the wake of the nacelle produces a peak of velocity on the downwind side of the nacelle. The second wind turbine rotor area is in the majority impacted by the velocity deficit generated by T1, slightly off-centered to the left of T2 as observed in **Fig. 3.35**. Due to T1 wake deflection to the left, the wake generated by T2 seems to have a higher velocity deficit in this direction. The tower and nacelle of T2 are causing small-scale velocity fluctuations, especially at the foundation position in the bottom part of the sheared velocity profile. The instantaneous velocity field allows observing the coarsening of the mesh near the outlet where the flow diagnostics are not relevant.

The flow statistics are presented through vertical and horizontal slices of mean streamwise velocity, **Fig. 3.39**, and streamwise resolved turbulent kinetic energy (TKE), **Fig. 3.40**. As a reminder, the TKE is expressed as $\langle k\rangle = 1/2\,\langle\widetilde{u}_i'^2\rangle$. The flow analysis past the grid and around T1 is similar to the case $\gamma = 30°$ with inflow (iii) in **Section 3.3**. Nevertheless, at the vicinity of the second turbine, a higher blocage effect is observed in the wind tunnel. The velocity deficit past T2 is asymmetric and is higher for the azimuth impacted by T1 wake. This

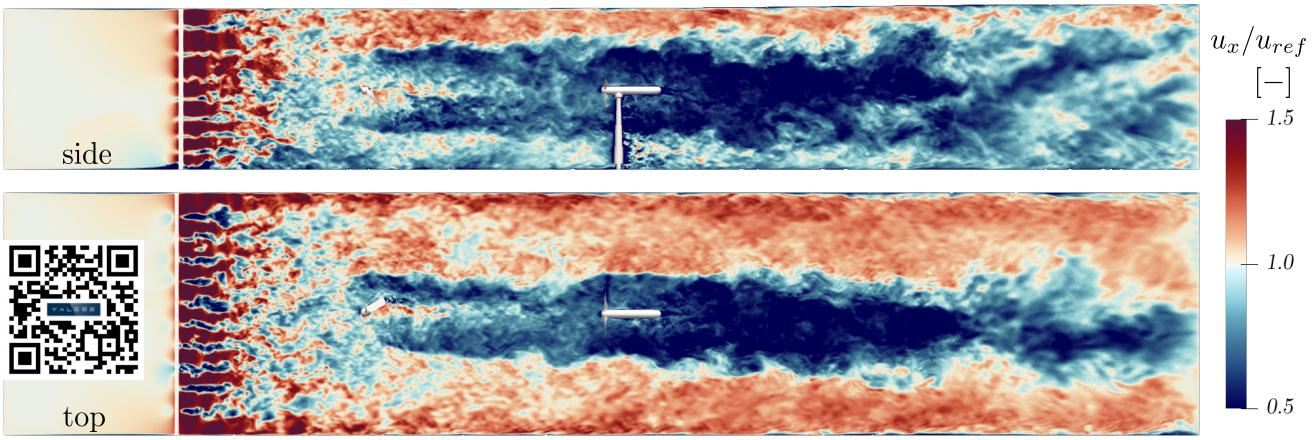

Figure 3.38: Vertical (side) and Horizontal (top) slices of the instantaneous velocity around T1 and T2 under inflow (iii). The tower and nacelle meshed surfaces appear in grey, the turbulence grid and the wind turbine blades are displayed for a better understanding. The QR-code is a link to the video showing the 3D evolution of the instantaneous velocity through $Q_{criterion}$ contour in the wind tunnel.

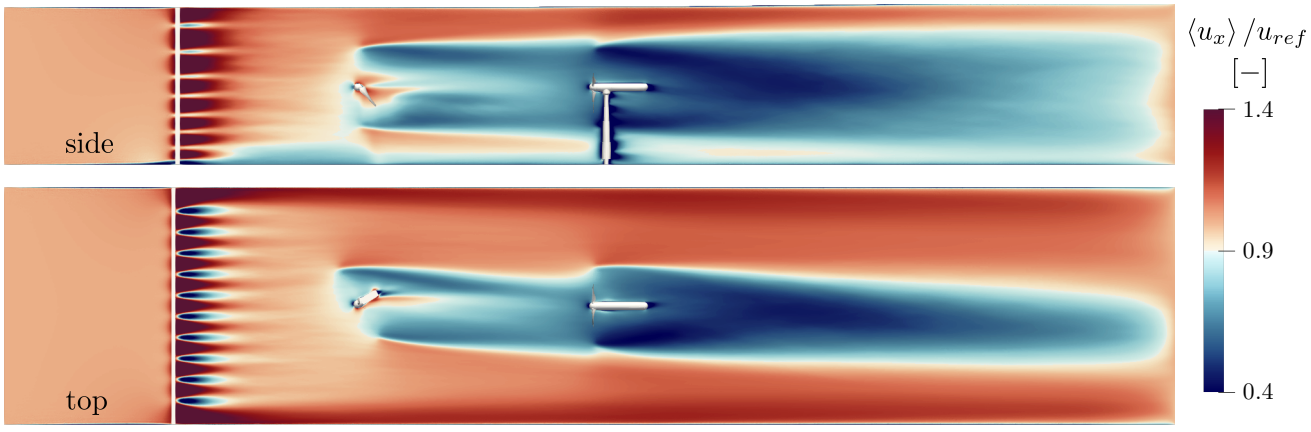

Figure 3.39: Vertical (side) and Horizontal (top) slices of the time averaged velocity around T1 and T2 under inflow (iii). The tower and nacelle meshed surfaces appear in grey, the turbulence grid and the wind turbine blades are displayed for a better understanding.

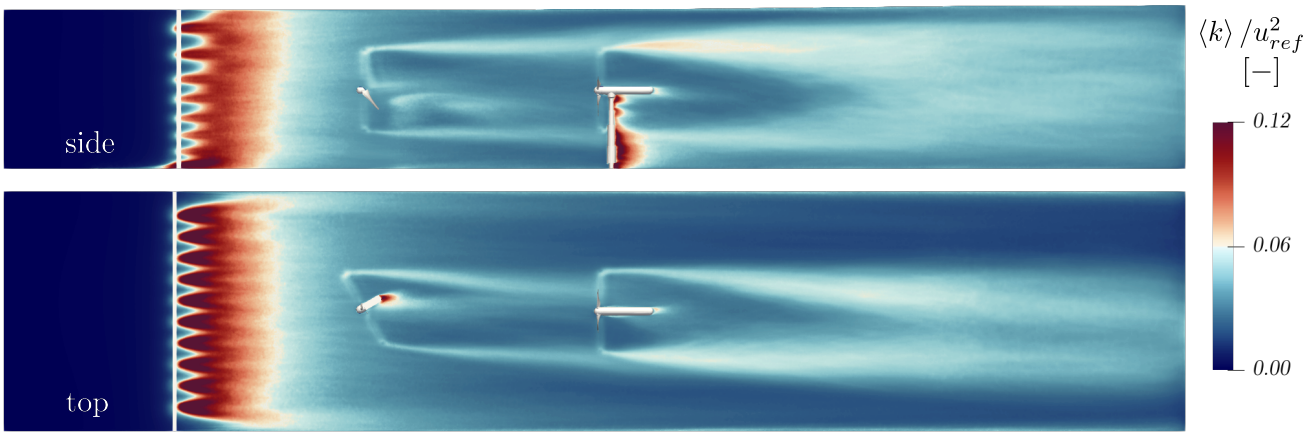

Figure 3.40: Vertical (side) and Horizontal (top) slices of the time averaged turbulent kinetic energy around T1 and T2 under inflow (iii). The tower and nacelle meshed surfaces appear in grey, the turbulence grid and the wind turbine blades are displayed for a better understanding.

is, at first sight, contradictory with the conclusion drawn from T2 streamwise force repartition depicted in **Fig. 3.37**. The streamwise force is higher where T1 wake is not impacting T2 rotor. Yet, the velocity deficit is higher due to the overlapping of T1 wake and T2 streamwise force, removing streamwise momentum from the flow once again. The wake of the tower induces a variable height velocity deficit due to the sectional discontinuities of T2 tower geometry. The velocity deficit behind T2 is slightly deflected due to the impact of the cross-stream velocity emanating from the still present CVP generated by T1. Peaks of TKE are generated at T2 blade tip position. On the horizontal slice, the blade tip impacted by the T1 wake sees his peaks of TKE quickly smoothen downstream as a higher local level of TKE is present upstream T2. The turbulent mixing is higher due to the presence of T1 wake. Fluctuations due to the nacelle are mixed in the wake and are not observable two diameters downstream. The time-averaged streamwise velocity, vertical velocity, and turbulent kinetic energy are compared to the experimental and some of the numerical results of F. Mühle et al. [49] in **Fig. 3.41**. The coarser mesh results presented for YALES2 are computed with a cell size twice larger than the actual mesh. For this resolution, fluctuations appear in the free stream for the mean velocity profiles, streamwise and vertical. Furthermore, the TKE peaks are underestimated compared to experimental measurements. For the YALES2 simulation, the streamwise velocity deficit and TKE is reasonably well reproduced compared to the experiments. All simulation cases underestimate the velocity in the free-stream flow $y/D > 0.5$, showing an overestimated evolution of the sheared velocity profile. The framework on the fine mesh adequately resolves both TKE peaks in terms of magnitude and lateral position.

3.5 Conclusion

This chapter aimed to evaluate the actuator line method in an LES framework for a yawed wind turbine with respect to an extensive experimental dataset. Three significant aspects are investigated: the impact of turbulence grids on the wind tunnel flow, the effect of yaw angle and inflow on the wake of a single turbine, and the interaction of such wake with a downstream aligned wind turbine.

The first section presented a modeling substitute to emulate a turbulent flow representative of the experimental wind tunnel grid. At first, the development and initial validation of the

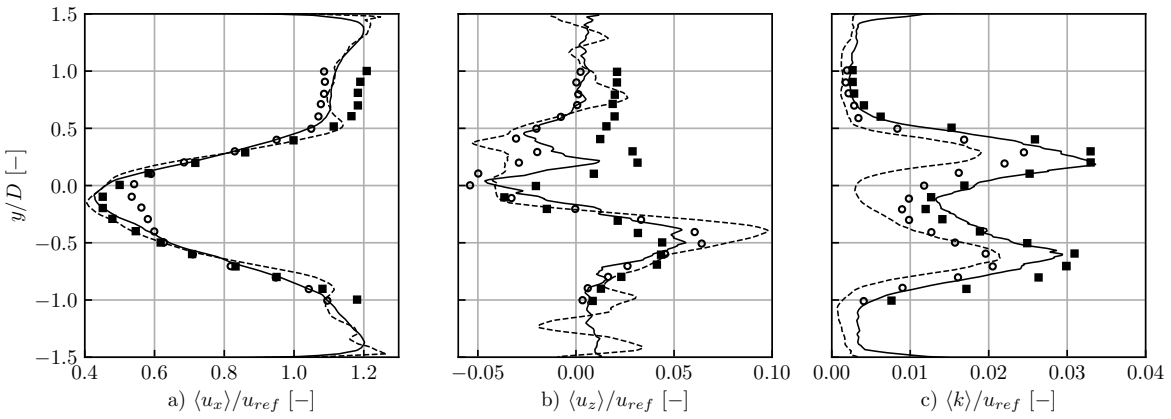

Figure 3.41: Horizontal profiles of the time-averaged (left) streamwise velocity, (middle) vertical velocity and (right) turbulent kinetic energy at $3D$ behind T2 under inflow (iii). YALES2 simulation (——) and on a coarser mesh (- - -) compared to experimental measurements [49] (■) and numerical result with NEK5000 code [49] (○) .

Dynamic Actuator Line Method (DALM) are presented on a single grid rod showing an adequate replication of the velocity fluctuations in the rod wake. Then the DALM is applied to the wind tunnel non-uniform grid and compared to other methods. The DALM results are close to the "brute force", resolving the flow around the grid rods, yet with a ten-time lower CPU cost. The DALM based on geometrical properties and tabulated aerodynamics coefficients requires less trial and error search than classical precursor methods that inject homogeneous isotropic turbulence. The application to the second wind tunnel grid, with a uniform rod spacing, is provided and showed a reasonably good agreement to vertical velocity profiles and turbulent kinetic energy measured experimentally.

The second section introduced the first turbine, T1, in the simulation setup. The influence on the turbine properties of the two previously emulated turbulent inflows and a laminar inflow is investigated, as well as the impact of yaw misalignment. For these cases, the turbine loads show coherent variations when the turbine misalignment changes. Yet, the power coefficient differs significantly from the experimental measurements, up to +20%, while the thrust is in better accordance with a deviation of up to 9%. Discussion on the radial and azimuthal time averaging of the angle of attack and contribution to thrust and torque highlighted several effects. The probability of dynamic stall near the hub of yawed turbines is high and even more triggered by the high level of turbulence present in the free stream. The lateral force induced by yawed wind turbine explains why the resulting wind turbine wake is deflected. Then, the main flow topology highlights various geometrical and three-dimensional effects: the free-stream turbulence, the sheared velocity profile, the tower wake deflection, the rotor wake deflection, the curled-wake shape, and the wake destabilization process. The horizontal velocity and turbulent kinetic energy profiles reproduce the main features of the experimental data, yet are slightly underestimated for the yawed cases. For the latter, the nacelle's wake triggers the wake's destabilization, while for yaw angle $\gamma = 0°$ the nacelle-generated TKE is still appearing three diameters behind the turbine. The wake center is identified and compared to the experiments by using the minimum available power approach. The magnitude of the deflection is slightly overestimated compared to experiments. Comparison to the wake deflection model shows a realignment of the wake due to the confinement induced by the wind tunnel walls.

The last section studied a second turbine, T2, located behind T1, exposed to a sheared

velocity profile with high turbulence intensity. The impact of the first turbine is investigated on the loads of T2. This first comparison showed how a velocity deficit and velocity fluctuations deteriorate the wind turbine loads of T2. These observations on the loads were related to the flow structures observed in the vicinity of T2, explaining the asymmetry of velocity deficit. The comparison to the flow measurements is in good agreement, especially for the TKE profiles.

This first application of the actuator line method in YALES2 and comparison to the experimental data from J. Bartl et al. and F. Mühle et al. showed the level of complexity required to replicate the flow around yawed wind turbines. The wind tunnel environment involves complex geometrical effects: grids and blockage effect. The wind turbine aerodynamics are impacted by yaw misalignment, upstream flow field, tower and nacelle. The overall methodology has shown good agreement on the flow properties yet, pointing out the necessity of specific corrections to predict the loads with the actuator line method. The large variety of physical effects around yawed wind turbines has shown the complexity of comparing the influence of different environments or operating conditions on the turbine wake. This introduces the next chapter, where a robust post-processing methodology is developed to investigate the wake of (yawed) offshore wind turbines.

Chapter 4

Recovery and turbulent mixing within the yawed wind turbine wake

The framework validated in the previous chapter is applied in this chapter to real-scale offshore wind turbines. This chapter aims to quantitatively discuss the wake recovery and the turbulent mixing within a yawed wind turbine wake. For this matter, a methodology based on the transport of level-set functions by the instantaneous and mean flow is conducted. The time-averaged flow transporting the second function has the property of a streamtube surrounding the turbine. First, the impact of yaw angle and external turbulence intensity over the streamtube and turbulent mixing layer topology is discussed. Second, mean kinetic energy and mean momentum budgets are integrated over the streamtubes depicting four wake regions with similar flow dynamics and correlated to local flow structures.

Contents

4.1 Introduction 98
4.2 A level set framework for the wind turbine wake analysis 98
4.2.1 Wake envelope definition 98
4.2.2 Accurate conservative level set functions: a numerical tool to define the wake 101
4.2.3 Parallel with the 1D momentum theory 104
4.3 Application to the DTU10MW: cases overview 106
4.4 Evolution of the wake topology 109
4.4.1 Streamtube 109
4.4.2 Turbulent mixing layer expansion for yawed wind turbines 112
4.5 Budgets applied on streamtubes 119
4.5.1 The wake recovery explained from Mean Kinetic Energy budget 120
4.5.2 The wake deflection explained from Mean Momentum budget 126
4.5.3 Comparison to the 1D momentum theory 128
4.6 Conclusions 130

4.1 Introduction

The previous chapter presented an overview of the quantity of data and the richness of physical effects present in the wake of a yawed wind turbine. In addition to that, high-fidelity unsteady flow simulations based on the actuator line method (ALM) [126] are becoming a state-of-the-art tool to better predict and understand wind turbine wakes. Such simulations require a high spatial resolution, leading to meshes counting tens of millions up to several billion cells. With the tremendous amount of generated data, the analysis is therefore complex. Nonetheless, these simulations should help understand the wake behavior and improve reduced engineering models [199, 200] based on 1D momentum theory [123]. The idea is to develop a sufficiently robust workflow to extract the relevant piece of information and quantify the global phenomena arising between the wake and its surroundings. Two methodologies are introduced. The first wake analysis aims at investigating the expansion of the wake turbulent mixing layer width. For this purpose, using Level Set functions transported by the instantaneous flow dynamics, the fluid particles crossing the rotor area are flagged and followed along time. The tracking of the particles through the rotor allows to highlight the turbulent mixing between the wake and the background flow, external turbulence included. The time-averaging of such function gives the spatial probability of presence of fluid particles that went through the rotor during the simulation. From this, the wake turbulent mixing layer width is defined according to these probabilities. The second wake analysis is based on the construction of a streamtube [201] surrounding the turbine obtained via level set functions [202] transported by the time-averaged flow. From this, global quantities can be integrated over streamtube sections. Variations of velocity, pressure, and turbulent kinetic energy allow to draw connections between the mean flow behavior explained through 1D momentum theory and the highly resolved flow dynamics. This analysis seeks to complete the already observed flow deflection downstream yawed wind turbine [43]. Then, the mean kinetic energy (MKE) and mean momentum (MM) budgets are performed. The MKE budget terms are associated with the wake destabilization process depending on the inflow turbulence. The deflection of the wake is finally investigated through the MM transport terms projected onto the horizontal axis.

These post-processings are applied to eight cases. The cases investigated are with or without yaw misalignment and different inflow turbulence conditions. Furthermore, the considered wind turbine is an academic wind turbine representative of new offshore designs with a diameter of 178.3 meters. This chapter is divided into four parts. The first part presents the level set framework used to generate streamtubes and the spatial probability of the wake presence. The second part presents the numerical setup and global information such as the turbine performances. In the third part, the wake topology is investigated based on the two previous analysis. The streamtube geometrical properties are presented and then the turbulent mixing layer width is defined similarly to a self-similar turbulent jet. In the final part, the budgets are integrated over the streamtubes and the evolution of integrated quantities is compared to the 1D momentum theory.

4.2 A level set framework for the wind turbine wake analysis

4.2.1 Wake envelope definition

The first step in understanding the wake recovery is to be able to define or retrieve a proper estimation of the wake envelope. Given the tremendous amount of data resulting from LES

simulations over wind turbines, one should be able to retrieve the wake bounding. Many ways can be used to define the wake spatially: the averaged velocity contours, the instantaneous available power density with mask convolution [203], a disk of the turbine diameter at different downwind locations [204]. Yet, the wake is subject to various effects that can either deflect, reshape or meander the induced velocity deficit. From this and the observations made in Chapter 3, developing a robust method to define the wake envelope, that helps to understand how the velocity deficit recovers, is not straightforward.

In this work, the focus is made on the fluid particles passing through the rotor area. For this matter, the indicator function ψ is introduced to flag the particles that have crossed the rotor area, ψ takes the value of one if particles went through the rotor and zero if they are outside. Such methodology is similar to the seeding of inert gas in experiments to follow the path of fluid particles. This tracking function is therefore responding to a classical advection equation based on the instantaneous local fluid velocity as follows:

$$\frac{\partial \psi}{\partial t} + \nabla \cdot \mathbf{u}\psi = 0, \text{ with: } \nabla \cdot \mathbf{u} = 0\,. \tag{4.1}$$

An example is presented in **Fig. 4.1** (top), the particles passing through the rotor are in the volume surrounded by the depicted surface. The surface curvature is strongly impacted by the turbulent structures inherent to the upstream flow and the ones generated by the rotor blades. As the particles pursue downstream the rotor area, they mix with the surrounding particles and are slowly dispersed in the downstream region. This is depicted by smaller and smaller volumes of flagged particles. The time-averaging of ψ gives the probability, $\langle\psi\rangle$ of the presence of particles that went through the rotor over the investigated time. From this **Eq. 4.1** can be expressed as

$$\nabla \cdot \langle \mathbf{u}\psi \rangle = 0\,. \tag{4.2}$$

The decomposition of instantaneous variables between their averaged and fluctuating parts is expressed as $\mathbf{u} = \langle\mathbf{u}\rangle + \mathbf{u}'$ for the velocity and $\psi = \langle\psi\rangle + \psi'$ for the tracking scalar. Applying this decomposition to the previous equation gives

$$\langle \mathbf{u} \rangle \cdot \nabla \langle \psi \rangle = -\nabla \cdot \left\langle \mathbf{u}'\psi' \right\rangle\,. \tag{4.3}$$

The right term corresponds to the fluctuations of the wake envelope, while the left term corresponds to the static footprint of the wake. An example is presented in **Fig. 4.1** (middle), showing two slices of the wake. The dark area represents the regions where fluid particles that went through the rotor are most likely to be found $\langle\psi\rangle \sim 1$. Then as the fluid particles pursue downstream, the probability is reduced, and the region becomes lighter $\langle\psi\rangle \sim 0$.

A second approach would be to consider only the time-averaged solution of the flow field. The wake bound can therefore be defined from the fluid particles that went through the rotor based on the time-averaged flow. For this matter, a second tracking function, Ψ is introduced with the same definition in the rotor area as ψ, i.e., $\Psi = 1$ in the rotor disk and $\Psi = 0$ elsewhere. In the same way as for ψ, the function Ψ is the solution of a classical advection equation based on the time-averaged velocity field as

$$\frac{\partial \Psi}{\partial \tau} + \nabla \cdot \langle \mathbf{u} \rangle \Psi = 0\,, \tag{4.4}$$

where τ is a pseudo-time advancement used to propagate the function since the flow is time-averaged. When the first term becomes negligible after a large pseudo-time, **Eq. 4.4** is equivalent to the definition of a streamtube surrounding the turbine:

$$\langle \mathbf{u} \rangle \cdot \nabla \Psi = 0\,. \tag{4.5}$$

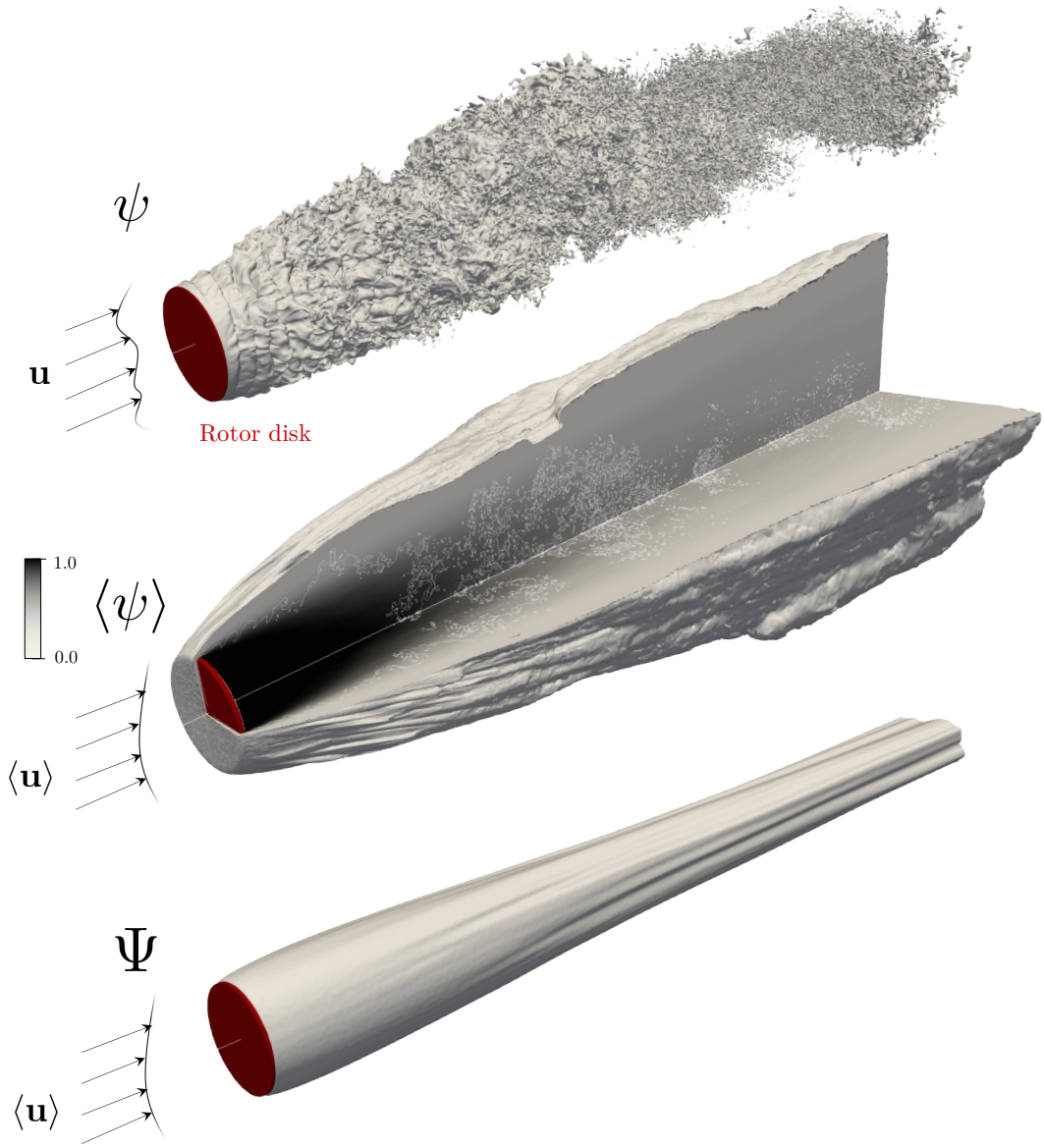

Figure 4.1: Representation of the wake envelope based on the two tracking methods: instantaneous fluid particles going through the rotor, ψ (top), Probability of presence of fluid particles that went through the rotor $\langle\psi\rangle$ (middle) and path of fluid particles following the time-averaged velocity, Ψ (bottom).

By definition, a streamtube is a closed control volume where fluid enters by the inlet section and gets out at the downstream section only. It is important to notice that in **Eq. 4.3**, if there are no time-fluctuations in the flow, the right term is equal to zero so the equation is equivalent to **Eq. 4.5** since $\langle\mathbf{u}\rangle \cdot \nabla \langle\psi\rangle = 0$. The two scalars Ψ and $\langle\psi\rangle$ are therewith mostly equivalent due to their similar initialization but Ψ is not directly subjected to turbulent mixing. These scalars fields are represented in **Fig. 4.1** for a clearer understanding. The area where $\langle\psi\rangle$ is high corresponds mostly to areas within the streamtube, Ψ. This is discussed in **Section 4.4**.

The use of streamtube to evaluate the wake envelope is already present in the literature since it provides a robust method to assess and compare how the wake behaves. In 2012, Lebron et al. [201] constructed a streamtube using PIV measurement of the flow around a 12 cm diameter turbine. This provided interesting insights on the wake recovery but with the

hypothesis of constant pressure at the inlet and outlet of the streamtube. Then, Meyers and Meneveau [205] introduced the notion of mass, momentum, and energy tubes. They discussed the topology of these tubes based on wind farm simulations with the turbine emulated with the actuator disk method. Streamtubes have also been used in the study of Ghate et al. [206] to observe how the anisotropic Reynolds stress tensor invariants (see Chapter 2.1.2) evolved on the streamtube interface. The effect of the turbine thrust on the streamtube topology and budgets is investigated by West and Lele [207] where they discussed the theoretical Betz limit. Ge et al. [208] used streamtube to integrate the velocity in the wake and observe how the wake recovers for a turbine upstream an urban district model. Following this, another study by Ge et al. [204] investigated the impact of a cube-shaped building wake impact on the streamtube topology of a downstream turbine. From all the studies mentioned above, the use of streamtubes has shown to be robust over several configurations involving complex 3D terrain and especially efficient in a simulation framework. Yet, these studies investigated large arrays of turbines or the flow largest scales only. Moreover, they used the actuator disk to comply with the expensive computational cost. Furthermore, the construction of streamtubes is based on the Lagrangian advection of particles along streamlines and the a posteriori reconstruction of surfaces. This reconstruction can be complex in particular cases when the section is not cylindrical, i.e., the wake of yaw misaligned turbines. For this matter, another methodology is used in this chapter and is presented hereafter.

4.2.2 Accurate conservative level set functions: a numerical tool to define the wake

It is important to use efficient and accurate numerical methods to generate the fields representing the different tracking functions in a numerical framework. The goal is to track volumes of fluid particles emanating from a region of the domain, here the blade sweeping area. Therefore, the scalar used to transport the information requires to prevent numerical diffusion. For this matter, the different post-processing proposed in this chapter relies on Accurate Conservative Level Set functions (ACLS) [202].

Such functions are commonly used for two-phase flow simulations where the primary difficulty is to track a liquid-gas interface while remaining strictly conservative and with low diffusion errors. Furthermore, the use of an unstructured grid for the fluid domain discretization in a massively parallel computation requires a particularly efficient algorithm [103]. Such methodology is already implemented in the YALES2 library for two-phase flow solvers. Here is how such functions are defined in this framework. The liquid-gas interface is represented using a hyperbolic tangent profile:

$$\psi(\mathbf{x},t) = \frac{1}{2}\left(\tanh\left(\frac{\phi(\mathbf{x},t)}{2\varepsilon}\right)+1\right), \tag{4.6}$$

where the parameter ε sets the thickness of the profile, and $\phi(\mathbf{x},t) = \pm|\mathbf{x}(t)-\mathbf{x}_\Gamma(t)|$ is the signed-distance function where $\mathbf{x}_\Gamma(t)$ is the liquid-gas interface. Using ψ, the interface is located at the iso-level $1/2$. For the application made in this chapter, the considered "liquid-gas" interface is actually a "particles that went through the rotor and particles that did not" interface. In this set-up, the flow velocity field $\mathbf{u}$ is divergence-free and the scalar ψ is advected by the fluid using **Eq. 4.1**. Then, ψ is reshaped using the reinitialization equation [202] as

$$\frac{\partial\psi}{\partial\tau} + \nabla\cdot(\underbrace{\psi(1-\psi)\mathbf{n}}_{\text{Resharpening}}) = \nabla\cdot(\underbrace{\varepsilon(\boldsymbol{\nabla}\psi\cdot\mathbf{n})\mathbf{n}}_{\text{Diffusion}}), \text{ with: } \mathbf{n} = \frac{\boldsymbol{\nabla}\phi}{|\boldsymbol{\nabla}\phi|}, \tag{4.7}$$

where τ is a pseudo-time, and $\mathbf{n}$ is the interface normal defined from the gradient of the signed-distance ϕ. Two terms are highlighted, the compression term that aims at resharpening the profile and the diffusion that ensure the profile remains of characteristic thickness ε.

The signed-distance function ϕ is reconstructed at nodes in the narrow band around the interface using a Geometric-Projection Marker Method (GPMM), to estimate the smallest distance to the interface. This function is furthermore used to compute the mean curvature κ by using Goldman's formula [209] based on the Hessian matrix of ϕ. This curvature is used to calculate the surface tension term in the pressure jump at the interface location when applied to two-phase flow configurations. This step is unnecessary for the presented post-processing as the ACLS remains passive to the fluid.

Yet, such methods are not strictly conservative for several reasons. One of the reasons for losing volume on irregular meshes is the variation of the mesh resolution from fine to coarse, which leads to the smoothing of ψ, and may imply a loss of the $\psi = 1/2$ iso-surface. In this case, the interface is not detected anymore and flagged fluid particles are removed from the volume. Finally, the reinitialization process on non-homogeneous meshes may also induce errors in the transport speed: the profile thickness parameter ε is mesh dependant, here it is typically set to Δx. Spatial variations of this parameter induce changes in the profile thickness, which may cause errors in the transport velocity of the $\psi = 1/2$ iso-surface. In the YALES2 library, when such functions are used in two-phase flow configurations, the methodology is coupled with dynamic mesh adaptation. This allows bypassing the aforementioned reasons by providing constant cell size in the interface region.

In this post-processing, the ACLS function does not impact the fluid and remains passive. Yet, the regions where this function is advected request a constant cell size to remain a low diffusion tracker. For this matter, the meshes used in this section are generated using a methodology based on ACLS functions and presented in **Appendix B.** Such methodology provides meshes with homogeneous cell sizes in the region of interest by using iterations over coarse precursor simulations. The ACLS is used to emulate both: ψ, the instantaneous fluid particles passing through the rotor; and Ψ, the streamtube.

4.2.2.1 Instantaneous fluid particles

For evaluating ψ, the ACLS function is advected according to the instantaneous fluid motions. This means that for each fluid iteration the **Eq. 4.6** for the advection and the **Eq. 4.7** for the reinitialization are resolved. The level set function initialization is based on the mean regularized forces of the wind turbine on the Eulerian grid. It ensures that all the fluid particles affected by the turbine forces are tracked. This gives the volume depicted in **Fig. 4.2**, the white circle represents a slice at the exact rotor position, which is slightly larger than the actual turbine diameter due to the mollification kernel size. This way of defining the source term allows to easily handle different geometrical properties and operating conditions, i.e., variations of cone, tilt, and yaw angles. The scalar ψ is then time-averaged to obtain the probability of presence $\langle\psi\rangle$.

4.2.2.2 Streamtubes

For the streamtubes, the ACLS function Ψ is not synchronized with the fluid since it requires the time-averaged velocity. Therefore, Ψ is computed at the end of the fluid simulation. The level set function initialization on the Eulerian grid is the same as for ψ. Then, two ACLS functions are advected, one in the upstream direction Ψ_- and one in the downstream direction Ψ_+.

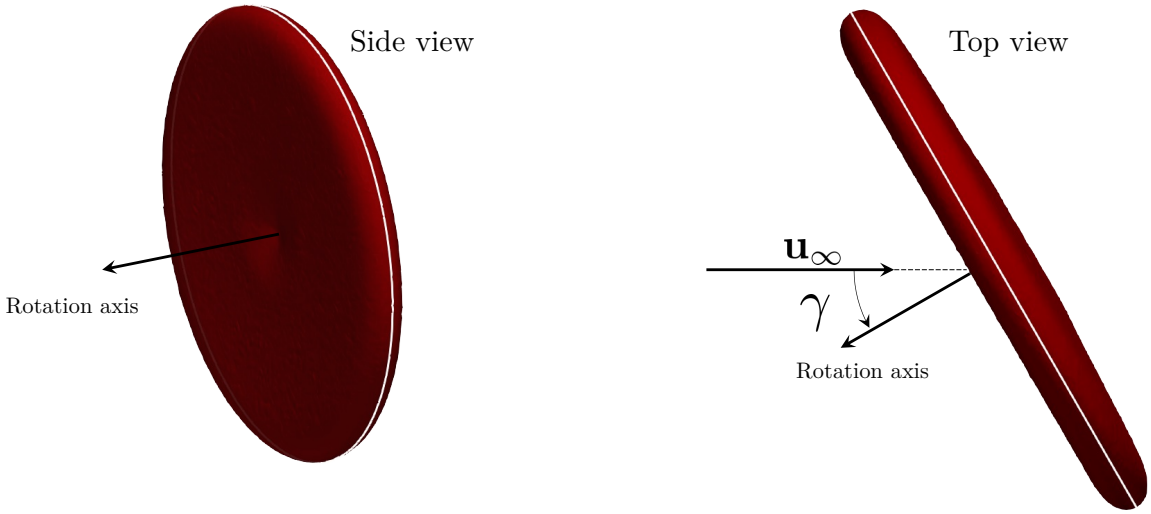

Figure 4.2: Side and top view of the source volume (red) for the ACLS functions used to determine ψ and Ψ. The white curve represent a slice of this volume according to the rotation axis.

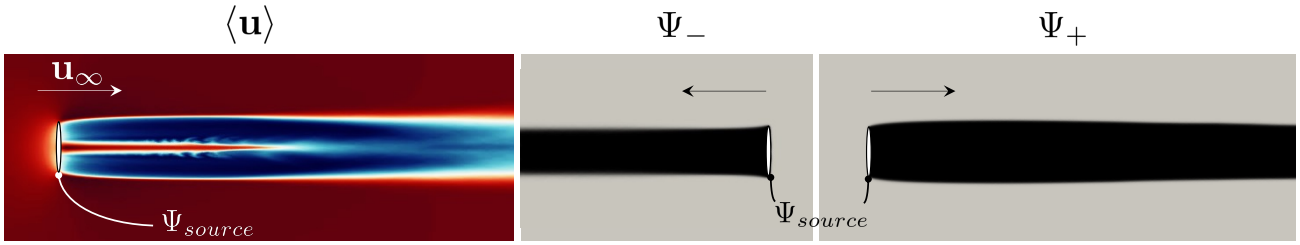

Figure 4.3: Horizontal slice of the time averaged velocity (left), the upstream (middle) and downstream (right) part of the streamtube. The overall streamtube, is evaluated as $\Psi = \Psi_- \cup \Psi_+$.

$$\begin{aligned} \frac{\partial \Psi_-}{\partial \tau_{st}} - \nabla \cdot \langle \mathbf{u} \rangle \, \Psi_- = 0 \,, \\ \frac{\partial \Psi_+}{\partial \tau_{st}} + \nabla \cdot \langle \mathbf{u} \rangle \, \Psi_+ = 0 \,, \end{aligned} \tag{4.8}$$

where τ_{st} is the pseudo-time to advance the ACLS function until convergence of the streamtube. This pseudo-time differs from the one used in the reinitialization equation, **Eq. 4.7**. An example is given in **Fig. 4.3** displaying a horizontal slice of the flow and the fields of the two scalars. The fields are considered converged when the overall domain integral reaches a convergence factor $\frac{\partial \Psi_-}{\partial \tau_{st}} < \epsilon$ and $\frac{\partial \Psi_+}{\partial \tau_{st}} < \epsilon$. Thanks to the free divergence of velocity, this ensures the correct streamtube property $\langle \mathbf{u} \rangle \cdot \nabla \Psi_{+/-} \approx 0$ if the convergence factor ϵ is sufficiently small. Then, Ψ, defining the global streamtube, is evaluated as $\Psi = \Psi_- \cup \Psi_+$.

The streamtube integrals are then obtained by triangulating the streamtubes faces as depicted on **Fig. 4.4**(a). Each pair containing the 1/2 iso-surface of Ψ is cut into two pairs and a new node face is generated to match the exact interface location. The number of elements generated from this fluctuates depending on the number of elements faces cut by the interface. Streamwise volume slices of the streamtube, are then used to study the evolution of the wake quantities, see **Fig. 4.4**(b). The exterior streamtube section surface is noted S_{st}, the upstream

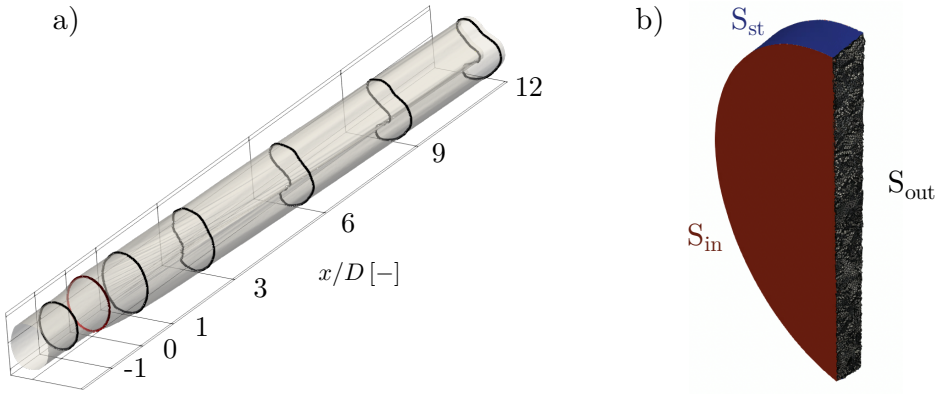

Figure 4.4: (a) Streamtube surface based on the level set position around a wind turbine with a yaw angle $\gamma = 30°$ under a turbulent inflow $TI = 14\%$, various streamwise slices are represented by bold lines (b) Half of a streamtube slice, picturing the considered surfaces and volume for data integration.

face is S_{in}, the downstream face is S_{out}, and the volume within the streamtube slice is V_{st}. Integrals averaging, are denoted for the surfaces as:

$$\langle \bullet \rangle_S = \frac{1}{S} \iint_S \bullet \, \mathrm{d}S \,, \tag{4.9}$$

where $\bullet$ is a scalar, vector or tensor and S is refering to one of the following surfaces S_{st}, S_{in} or S_{out}. The volume averaging is denoted as:

$$\langle \bullet \rangle_{V_{st}} = \frac{1}{V_{st}} \iiint_{V_{st}} \bullet \, \mathrm{d}V_{st} \,. \tag{4.10}$$

For all cases $\epsilon D/u_{\mathrm{ref}} = 1.783 \times 10^{-4}$ and the dot product $\langle \widetilde{u}_i \rangle \, n_i / \| \langle \widetilde{u} \rangle \|_{S,st}$ remains below 0.6%. Therewith, the streamtube surface normal is considered orthogonal to the the local mean filtered velocity. The streamtubes are computed from $2D$ upstream to $12D$ downstream the turbine and discretized into 150 cross-sections of approximately 20 mesh cells thickness.

4.2.3 Parallel with the 1D momentum theory

Considering a streamtube surrounding the wind turbine is the basis of the momentum theory. Momentum theories are based on applying the conservation laws of fluid mechanics under some simplifying assumptions. By deriving the Navier-Stokes equations, various theories can be obtained with different assumptions and inconsistencies. As streamtubes around wind turbines are investigated in this chapter, a comparison to the results of such ideal models is given. Exhaustive explanations of the various theories can be found in the books from Sørensen [123] or Hansen [210]. As a first approach, the analogy is provided only with the standard axial momentum theory without wake rotation [211, 212, 151], referred to as the 1D momentum theory. The basis and the different hypotheses on which it relies are presented in the following.
The first assumptions are that the flow is steady, incompressible, and axisymmetric; that the fluid is homogeneous and inviscid; and that the rotor loads are axisymmetric and concentrated onto an actuator disk, with an infinite number of blades. The rotor loads result in a uniform pressure drop in the flow over the rotor area. The velocity is constant and purely axial, which means there is no rotational velocity in the wake. No molecular or turbulent mixing occurs

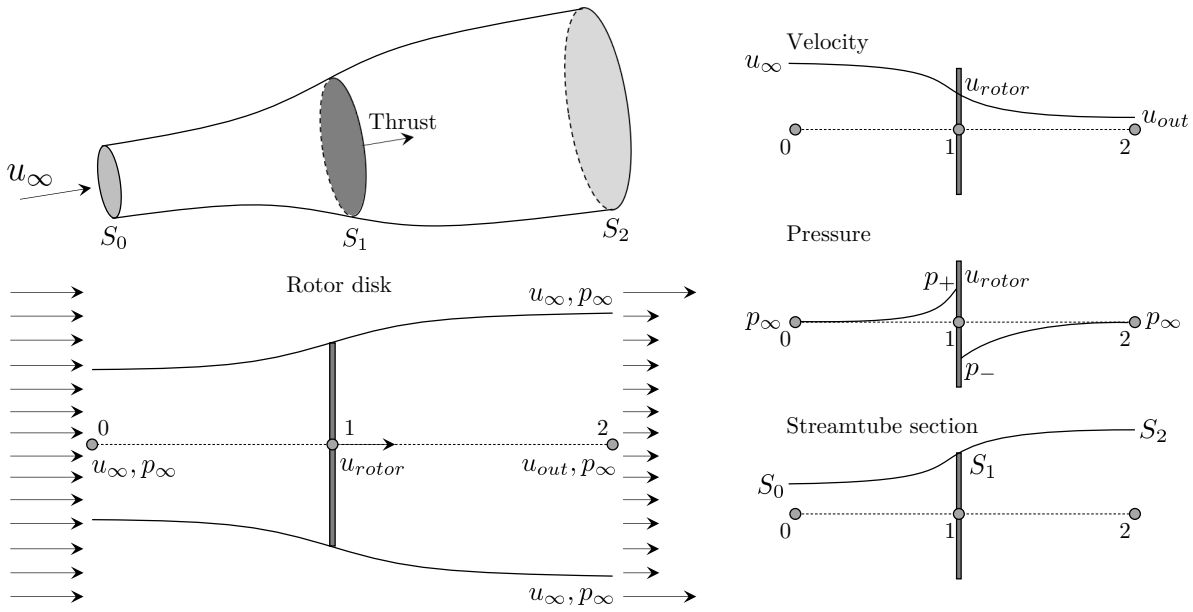

Figure 4.5: (left) 3D and 2D representation of the streamtube with the different pressure and velocity through the rotor disk for the 1D momentum theory. The thrust is the force exerced by the fluid on the rotor disk. (right) Evolution of velocity, pressure and streamtube section according to the 1D momentum theory. Inspired from [210].

between the free-stream and the wake flow. The static pressure far upstream and downstream is equal to the undisturbed ambient pressure.

A representation of the considered regions is presented in **Fig. 4.5**. The far upstream region is annotated as (0), the rotor disk is (1) with the upstream part denoted (1_+) and the downstream part (1_-). The far downstream region is annotated as (2). Each of these regions has a surface depicted as the cross-section of the streamtube, S_0, S_1, and S_2. The conservation laws of fluid mechanics are then applied to this streamtube surrounding the rotor disk. The assumptions of steady-state homogeneous, inviscid, incompressible fluid allow the application of the Bernoulli equation for the region upstream, ($0 \rightarrow 1_+$) and downstream the rotor disk, ($1_- \rightarrow 2$) in **Fig. 4.5**(left). Combining these two equations the pressure jump accross can be expressed as

$$\Delta p = p_+ - p_- = \frac{1}{2}\rho\left(u_\infty^2 - u_{out}^2\right) , \tag{4.11}$$

where Δp is the pressure jump, p_+/p_- is the pressure in $(1_+)/(1_-)$, u_∞ is the far upstream velocity, and u_{out} is generated velocity deficit downstream. This equation can be obtained only if the pressure in the far-wake (2) is back to the undisturbed ambient pressure p_∞. In **Fig. 4.5**(right), the velocity variations are related to the pressure variations. Due to the streamtube definition the conservation of mass implies that the mass flow rate is constant in every of its cross-sections, giving:

$$\rho S_0 u_\infty = \rho S_1 u_{rotor} = \rho S_2 u_{out} . \tag{4.12}$$

The thrust force represented in **Fig. 4.5** is the effect of the fluid on the rotor disk. It can be related to the pressure jump since the velocity and the pressure is assumed to be constant on the overall disk surface, S_1.

$$T = \Delta p S_1 = \frac{1}{2}\rho S_1\left(u_\infty^2 - u_{out}^2\right) , \tag{4.13}$$

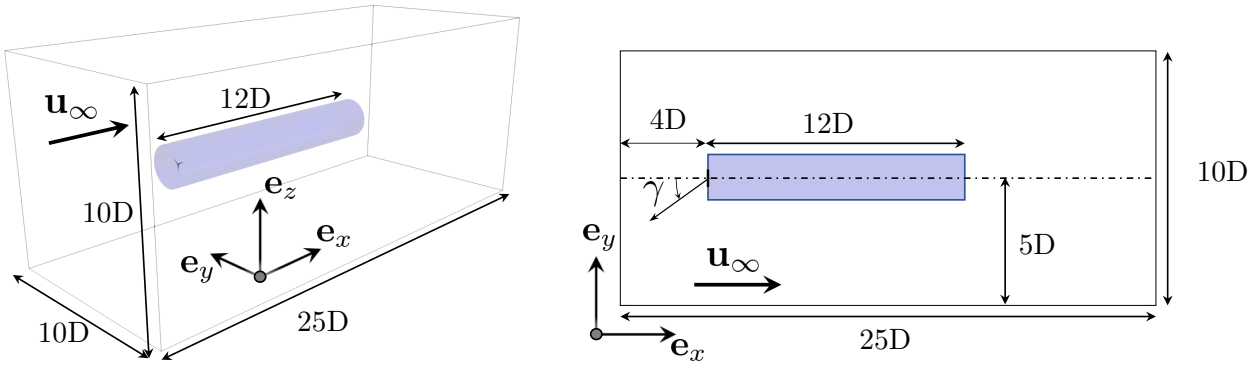

Figure 4.6: Computational domain for the one wind turbine configuration, (left) 3D view and (right) slice view of the domain. The turbine is in black centered in the domain and the blue region is representing the position in which the post-processings are applied.

where T is the thrust force. The application of the conservation of axial momentum over the streamtube, along the streamwise axis, combined with **Eq. 4.12** allows to express the thrust force differently from the previous equation:

$$T = \rho S_1 u_{rotor} \left(u_\infty - u_{out}\right) . \tag{4.14}$$

It is important to mention that the influence of the pressure force on the side of the streamtube is being neglected to obtain the previous equation. Finally, combining the previous two thrust equations gives the velocity at the rotor position, u_{rotor}:

$$u_{rotor} = \frac{u_\infty + u_{out}}{2} . \tag{4.15}$$

The 1D momentum theory uses this evaluation of u_{rotor} to define the axial induction factor, noted a, as

$$a = \frac{u_\infty - u_{rotor}}{u_\infty} . \tag{4.16}$$

It is used to provide simple equations for the dimensionless power and thrust coefficients:

$$\begin{aligned} C_P &= 4a(1-a)^2 , \\ C_T &= 4a(1-a) . \end{aligned} \tag{4.17}$$

The majority of the 1D momentum theory assumptions do not fit the ones used for the LES. Yet, this chapter aims at evaluating if the 1D momentum theory can properly assess the turbines performances from the integrated LES flow quantities based on the few parameters given. The comparison is presented in **Section 4.5.3**.

4.3 Application to the DTU10MW: cases overview

In this work, the modeled wind turbine is the academic turbine named DTU10MW [213]. This turbine follows the technological evolution of offshore wind turbines, reaching hundreds of meters in diameter today. In the following, all quantities are scaled by the wind turbine diameter $D = 178.3\,\mathrm{m}$ and the free-stream velocity $u_{\mathrm{ref}} = 10\,\mathrm{m/s}$. The blades use multiple airfoils along the span with variable chord and twist [213]. The deformation of the blades is not taken into account in this study, which implies a strong hypothesis on the loads computation. Indeed, for

Refinement level	D/h_{wake} [−]	D/h_{ext} [−]	$N_{elements}$ $\times 10^6$	N_{nodes} $\times 10^6$	N_{cores}
1	81	20	196.8 - 212.8	55.7 - 60.2	1 024
2	162	40	1 536 - 1 702	448.9 - 484.9	8 448

Table 4.1: Evolution of the number of element in the mesh and the cell size in the wind turbine wake area for the two level of refinement investigated in this chapter. The number of elements, $N_{elements}$ and the number of nodes, N_{nodes} are given as a range since each cases as a unique mesh, due to the mesh generation methodology based on the flow characteristics.

Case	γ	TI_{-2D} [%]	$\langle C_P \rangle \pm {C_P}'$	$\langle C_T \rangle \pm {C_T}'$
$TI_{0\%}\gamma_{0°}$	0°	0	0.466 ± 0.003	0.772 ± 0.002
$TI_{0\%}\gamma_{30°}$	+30°	0	0.366 ± 0.006	0.606 ± 0.003
$TI_{3.5\%}\gamma_{0°}$	0°	3.5	0.483 ± 0.022	0.786 ± 0.015
$TI_{3.5\%}\gamma_{30°}$	+30°	3.5	0.382 ± 0.016	0.61 ± 0.011
$TI_{7\%}\gamma_{0°}$	0°	7	0.485 ± 0.053	0.785 ± 0.035
$TI_{7\%}\gamma_{30°}$	+30°	7	0.386 ± 0.043	0.619 ± 0.027
$TI_{14\%}\gamma_{0°}$	0°	14	0.491 ± 0.103	0.782 ± 0.07
$TI_{14\%}\gamma_{30°}$	+30°	14	0.388 ± 0.080	0.62 ± 0.06

Table 4.2: Cases and mesh properties. Reference values for a laminar inflow are $\langle C_P \rangle = 0.476$ and $\langle C_T \rangle = 0.814$ [213].

such diameters, the flapwise blade deformation at the tip can reach up to tens of meters [214]. With this hypothesis, the non-prebended blades are used with the designed cone angle of 2.5°. The rotation speed is imposed to obtain the design tip speed ratio $\lambda_{\text{opt}} = 7.5$, giving a Reynolds number of approximately $Re_{\text{tip}} \approx 6 \times 10^6$ at the blade tip. No control is applied, and the pitch angle is kept to zero as the operating point lies in the first control region. The rotor blades are modeled as actuator lines which compute the blade forces at each time step based on the inflow velocity, the angle of attack α and the chord-based Reynolds number lift C_L and drag C_D coefficients obtained from the airfoil properties [213]. Each blade is discretized using 75 sections, i.e., 75 points per actuator line.

The computational domain dimensions are $L_x \times L_y \times L_z = 25D \times 10D \times 10D$. The turbine is centered at $5D$ from the inlet. Such dimensions allow the study of the far wake properly and prevent the confinement effect due to the boundary proximity. Eight cases are investigated in this work, two yaw angles ($\gamma = 0°, +30°$) and four inflows with different turbulence intensity ($TI_x =$ 0, 3.5, 7 and 14%). The inlet velocity, $u_\infty = 10$m/s is superposed with synthetic turbulence, generated using Mann's algorithm [215]. Three synthetic turbulence boxes are generated and the turbulence intensity for each is then evaluated two diameters upstream of the turbine during the simulation, the four TI measured are $TI_x = 0$, 3.5, 7 and 14%.

To apply the previous post-processing special attention was paid to having a homogeneous cell size in the wake and upstream of the turbine, whether the turbine is yawed or under turbulence by using pre-computation and streamtube volumes to refine the mesh in the proper area. This part is further discussed in **Appendix B.** The cell sizes in the different regions of the domain for two levels of refinement are given in **Tab. 4.1**. These two mesh resolutions are used to assess the reliability of the wake destabilization process. If no ambient turbulence is present, a higher resolution is required to capture the vortex pairing and destabilization that trigger the wake recovery. The results of the following sections are discussed as follows. For each observation, the cases are compared to each other on the first level of refinement for $TI_x > 0$

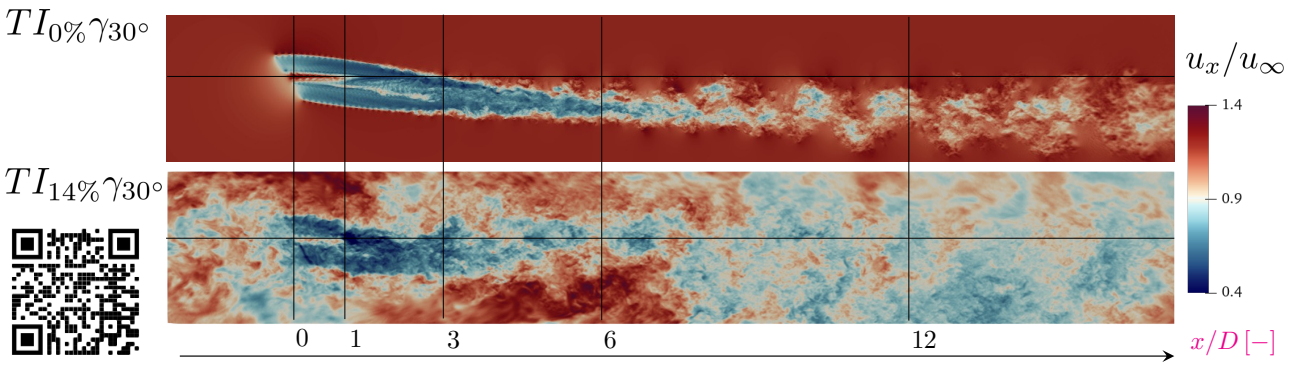

Figure 4.7: Horizontal slices at $z/D = 0$ of instantaneous streamwise velocity for cases $TI_{0\%}\gamma_{30°}$ and $TI_{14\%}\gamma_{30°}$. The full domain is not represented, $x/D \in [-2.5; 18.0]$ and $y/D \in [-2.0; 1.0]$. The QR-code is a link to the video showing the 3D evolution of the instantaneous velocity through $Q_{criterion}$ contour in the domain.

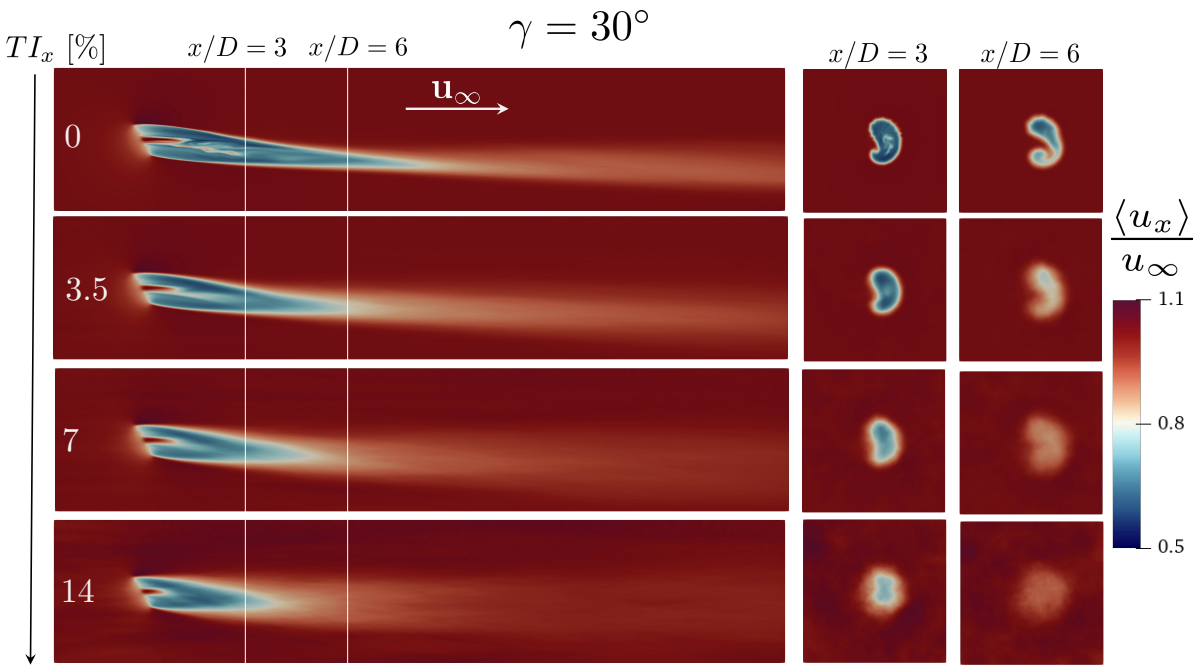

Figure 4.8: (left) Horizontal slices at $z/D = 0$ and (right) transverse slices at $x/D = 3$ and 6 of time-averaged streamwise velocity for $TI_x = 0$, 3.5, 7, 14% and $\gamma = 30°$. The full domain is not represented, $x/D \in [-2.5; 18.0]$, $y/D \in [-2.0; 2.0]$, $z/D \in [-2.0; 2.0]$.

and the second level for $TI_x = 0$; then a comparison between the first and the second level is conducted for $TI_x = 0$ and 14% with both yaw angles. This formulation is used for a clearer understanding of the physical and then numerical phenomenon occurring in the wake.

The simulations were run on the Joliot-Curie supercomputer, funded by GENCI and held in CEA's Very Large Computing Centre (TGCC), under the PRACE allocation "WIMPY". The nodes are AMD Rome (Epyc) dual-processor with 128 cores, 64 per processor. The used nodes per simulation ranged between 8 and 66; the exact number of cores for each simulation is presented by N_{cores} in **Tab. 4.1**.

To give an overview of the cases the turbine performances and velocity fields are presented before the further investigation of the wake topology. The normalized turbine performances of

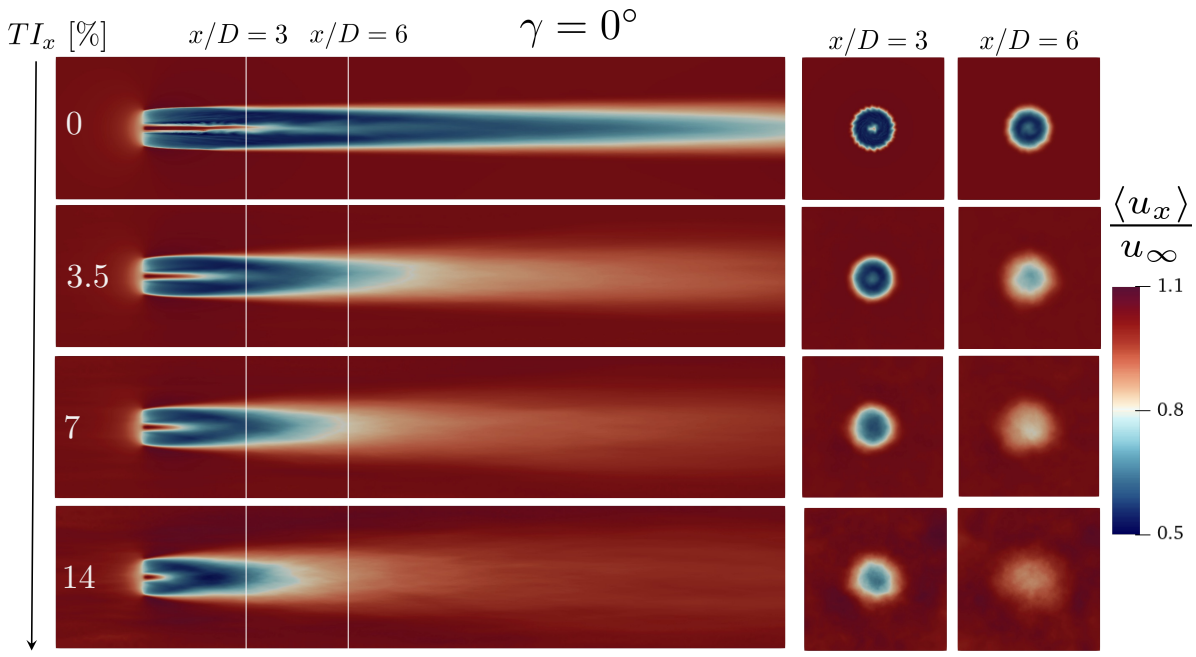

Figure 4.9: (left) Horizontal slices at $z/D = 0$ and (right) transverse slices at $x/D = 3$ and 6 of time-averaged streamwise velocity for $TI_x = 0$, 3.5, 7, 14% and $\gamma = 0°$. The full domain is not represented, $x/D \in [-2.5; 18.0]$, $y/D \in [-2.0; 2.0]$, $z/D \in [-2.0; 2.0]$.

each case is presented in **Tab. 4.2**. The temporal statistics, denoted with $\langle \bullet \rangle$, and their fluctuations, $\sqrt{\langle \bullet'^2 \rangle}$ are averaged over 100 D/u_∞. The power and thrust coefficients increase with the turbulence intensity and are lower for the misaligned cases. **Fig. 4.7** presents a horizontal slice of the instantaneous streamwise velocity fields for cases $TI_{0\%}\gamma_{30°}$ and $TI_{14\%}\gamma_{30°}$ on the second level of refinement. The instantaneous velocity fields present a wide range of turbulent scales, from tip vortices being convected ($TI_{0\%}\gamma_{30°}$) to wake meandering ($TI_{14\%}\gamma_{30°}$). Horizontal and transverse slices of the time-averaged velocity fields for the different turbulence intensity are presented for $\gamma = 30°$ in **Fig. 4.8** and for $\gamma = 0°$ in **Fig. 4.9**. From the horizontal slices, it is observed that the wake velocity deficit recovers closer to the rotor when turbulence intensity increases. This tendency is noticed for both aligned and misaligned rotors. The transverse slices depict the iconical kidney shape wake for the $\gamma = 30°$ cases, especially for the three lower turbulent intensities. The turbulence does not seem to impact the wake deflection induced by the yaw angle.

4.4 Evolution of the wake topology

With the methodology introduced in **Section 4.2**, the evolution of the wake envelope is investigated in the following section from the streamtube topology and the expansion of the wake turbulent mixing layer.

4.4.1 Streamtube

The streamtubes based on the iso-level value $\Psi = 1/2$ of the different cases are depicted in **Fig. 4.10**. Slices of the streamtube are depicted at different streamwise positions showing the curvature of the interface. First, the streamtube remains mostly circular for $\gamma = 0°$. The streamtube appears to have a small inlet section that increases across the rotor disk, highlighted

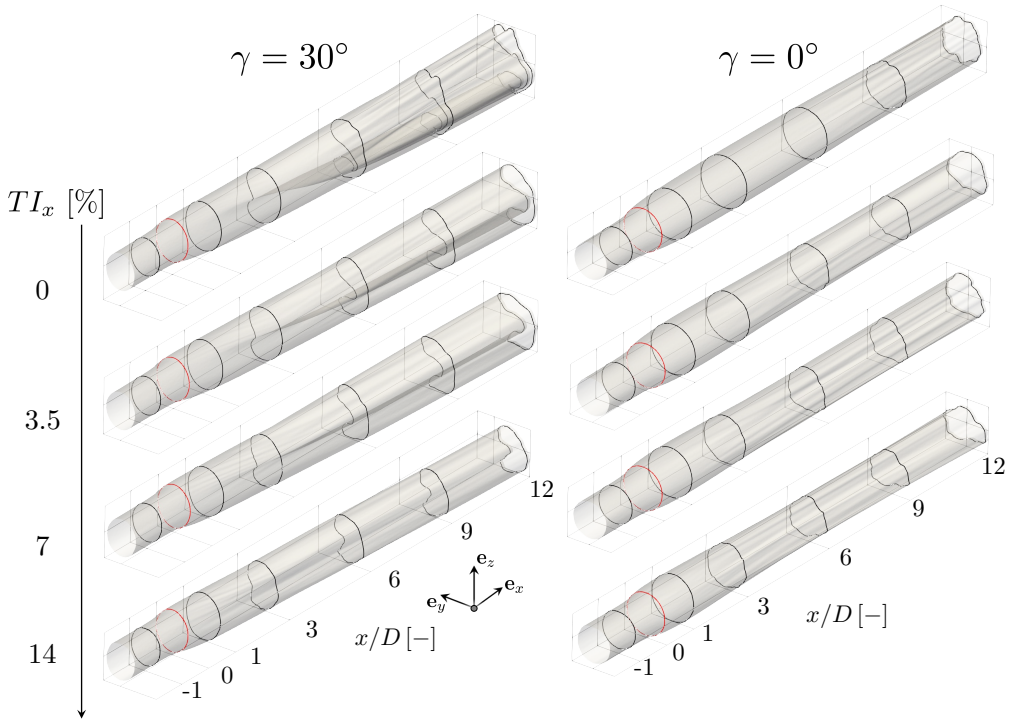

Figure 4.10: Iso-contour of $\Psi = 1/2$ depicting the streamtube interface from $x/D = -2$ up to $x/D = 12$ for $TI_x = 0$, 3.5, 7, 14% and $\gamma = 30°$, 0°. Various streamwise slices are represented by bold black lines and red at the turbine position.

by a red contour in the figure. After some distance from the rotor, the section is reduced again. The turbulent intensity present in the free stream flow triggers this phenomenon, i.e., if the TI increases the streamtube section is reduced again closer to the rotor disk. Second, the streamtube for $\gamma = 30°$ fold up upon itself, and the sections appear to be kidney-shaped. Different downstream sections of the streamtube are depicted for $\gamma = 30°$ in **Fig. 4.11**. The upstream turbulence triggers the meandering of the wake, mixing the fluid particles crossing the rotor and the rest, which results in a thicker and less expanded shape for the streamtube.

Fig. 4.12 depicts the streamtube cross-section area, the center of mass, and the transverse mean velocity evolution along the axial axis. This quantifies the previous observation made from the visualizations of the streamtube. The cross-section increases up to a maximal value before decreasing again, see **Fig. 4.12a)**. This maximum is closer to the rotor when the background turbulence increases. As the streamtube volume is mass-conserving, the change of cross-section area implies a modification of the axial velocity. When the streamtube approaches the turbine, the section expands until the maximum velocity deficit is reached. Afterward, the section shrinks when the wake starts to recover. This last part differs from the 1D momentum theory, where only upstream and downstream cross-section/velocity states are considered [123]; the velocity deficit recovery is not included in this theory. Nevertheless, the maximum section position would correspond to the region (2) defined in **Section 4.2.3**.

The wake center deflection represents one of the main features of a yawed wind turbine, and the streamtube center is presented in **Fig. 4.12b)**. The case without turbulence is less deflected after $5D$ downstream the turbine. The analysis of Bastankhah and Porté-Agel [43] based on experimental results is contradictory at first glance, presenting that a decrease in the incoming turbulence intensity is found to increase wake deflection for a yawed turbine. Yet the computed

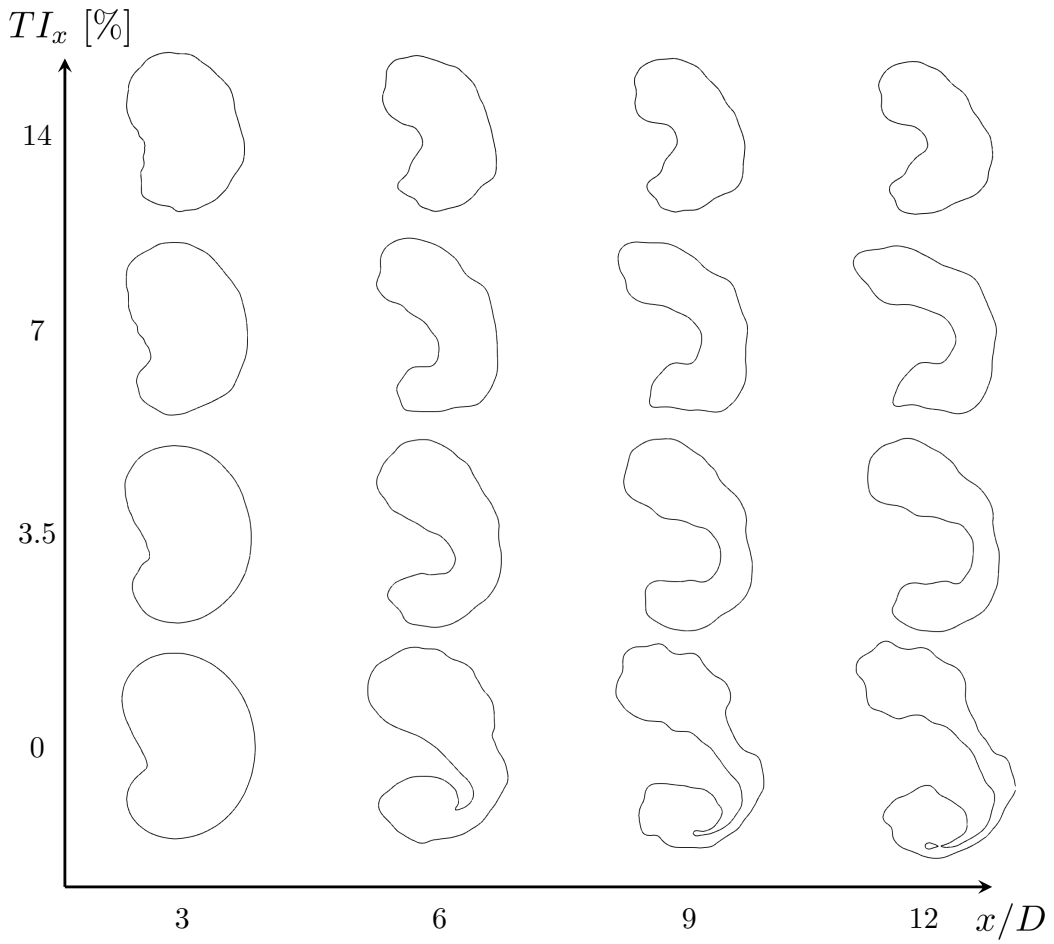

Figure 4.11: Streamwise slices of the streamtube interface, $\Psi = 1/2$, at different downstream position, $x/D = 3$, 6, 9, 12 for $TI_x = 0$, 3.5, 7, 14% and $\gamma = 30°$.

deflection here is based on the mean streamtube center while it is based on the maximum velocity deficit position in [43]. It is qualitatively visible in **Fig. 4.12b)** that the maximum velocity deficit is less deflected for the turbulent cases. Furthermore, all the streamtubes for the turbulent cases, $TI > 0\%$, have the same center deflection. This is consistent with the observation of the streamtube slices, where only the shape is modified. As the TI increases, most of the volume moves from the shape extremities, the left side of the wake located under and above the horizontal axis, towards the mid-plane. As a consequence, the center of mass remains the same.

The horizontal velocity depicted in **Fig. 4.12c)** is directly linked to the streamtube center deflection. At the turbine position, the local mean velocity goes from positive to negative values, which implies a redirection of the flow and will be further discussed in **Section 4.5.2**.

- **Impact of the mesh resolution**

The cell size impact on the results is discussed from **Fig. 4.13**, where simulations with the two levels of refinement are presented, (1) and (2) see **Tab. 4.1**. Cases with $\gamma = 0°$ and 30° are shown with $TI_x = 0\%$ and 14%. First, the cases with turbulence present the same behavior independently from the cell size or yaw angle in terms of streamtube section, mass center, or velocity in the transverse direction. Second, the case without turbulence reaches a higher section on mesh (1) for both yaw angles. The mass conservation within the streamtube implies that

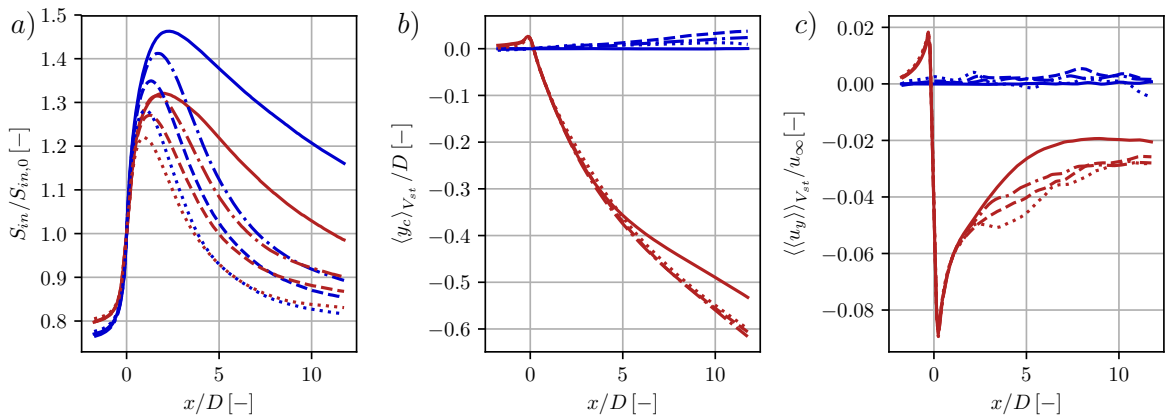

Figure 4.12: Streamwise evolution of (a) the streamtube sectional area, S_{in} normalized by the section at the rotor position, (b) the streamtube center in the transverse plane direction (c) the horizontal mean velocity. Cases are depicted as $\gamma = 0°$ (—), $\gamma = 30°$ (—) for the yaw angle and for the inflow turbulence intensity as $TI_x = 0\%$ (—), 3.5% (-·-·), 7% (- - -) and 14% (·····).

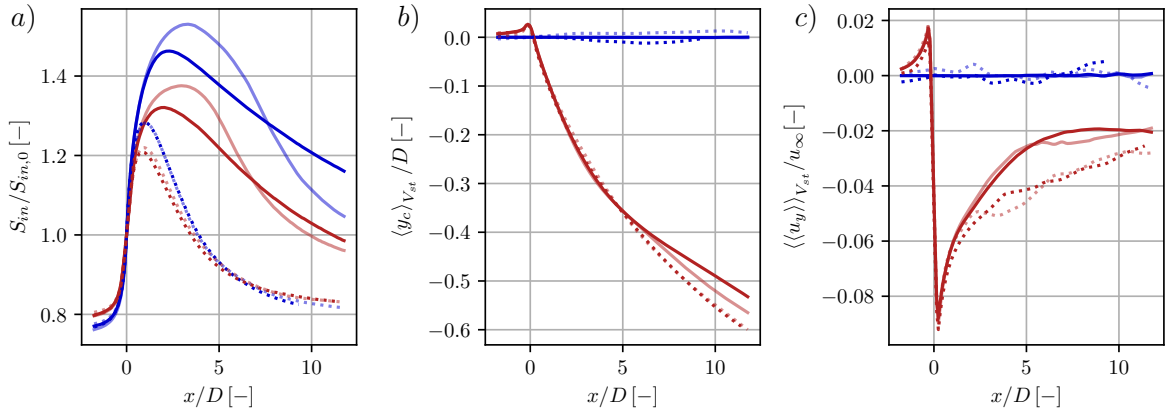

Figure 4.13: Mesh refinement impact on the streamwise evolution of (a) the streamtube sectional area, S_{in} normalized by the section at the rotor position, (b) the streamtube center in the transverse plane direction (c) the horizontal mean velocity. Cases are depicted as $\gamma = 0°$ (—), $\gamma = 30°$ (—) for the yaw angle, as $TI_x = 0\%$ (—), 14% (·····) for the turbulent intensity and using oppacity for the refinement level as (1) (—) and (2) (—).

the maximal velocity deficit is higher for the coarse mesh. Furthermore, the maximal section position is delayed downstream of the rotor. Nevertheless, the discrepancies for $TI_x = 0\%$ over the center of mass and transverse velocity are minor between the two levels. This shows that the external turbulence helps removing the dependence on the refinement level for the streamtube topology. Nevertheless, the streamtube section expansion is delayed downstream and is higher when no turbulence is added.

4.4.2 Turbulent mixing layer expansion for yawed wind turbines

The interest in investigating the turbulent mixing layer comes from the similarity between the turbulence behavior found in different types of flows [216]. The physics involved in the interfacial layers between regions of different turbulent intensities appears to be similar in many engineering and flows of natural interest. It is even more apparent for unbounded shear flows, where the

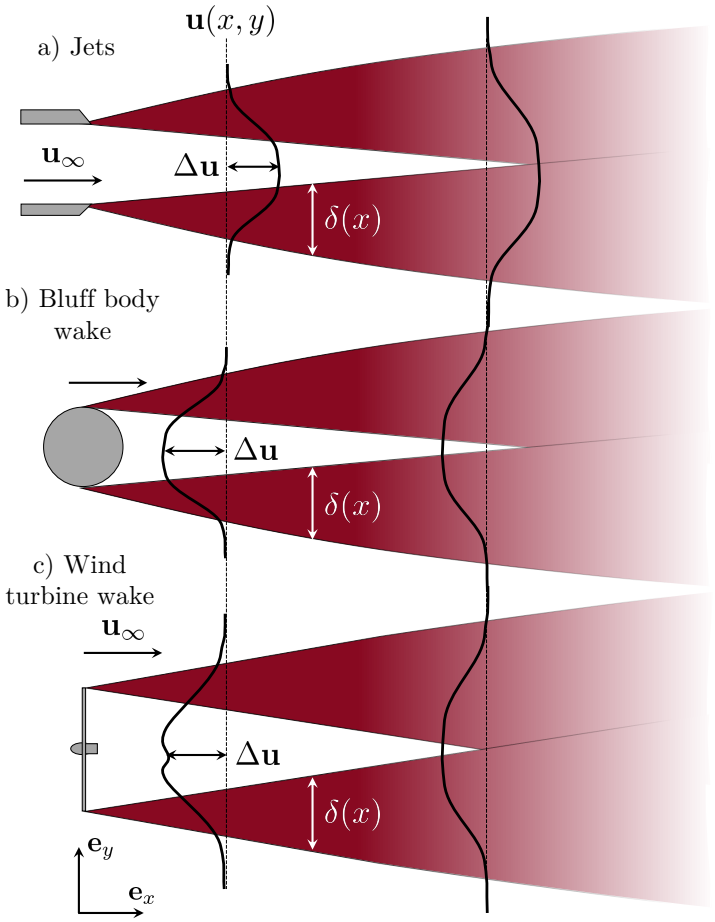

Figure 4.14: Exemple of unbounded shear flows and definition of the turbulent mixing layer width $\delta(x)$ based on the local velocity difference $\Delta\mathbf{u}$.

boundaries are not close enough to affect the turbulent structures significantly, examples are depicted in **Fig. 4.14**. The definition of the turbulent mixing layer width, $\delta(x)$ in a wake or a jet, is one of the first steps for deriving models. In wake or jets, the turbulent mixing layer expands as the fluid particles pursue downstream the object. After a sufficient distance, the two turbulent mixing widths merge at the center of the wake or jet.

The notion of turbulent/non-turbulent interface is well developed in the literature to define this turbulent mixing layer [217]. The applications on jets [218, 219, 220], bluff body wakes [221, 222, 223, 224, 225, 226], boundary layers [227, 228, 225] and even wind turbines wakes [229] are numerous and show the legitimacy of such post-processings. This is mainly used in experiments where PIV [218, 229, 225] sheets allow the retrieval of the flow quantities but as well in numerical studies [227]. Still, an axisymmetric hypothesis for the flow is common to reduce the required data.

This section investigates how the yaw misalignment and external turbulence impact the turbulent mixing layer width. The wake of a yaw misaligned wind turbine is not compatible with the axisymmetric hypothesis, as the wake is deflected. Furthermore, the external turbulence contradicts the notion of a "turbulent/non-turbulent interface" as turbulence is present on both sides of the interface, delimiting the wake from the external flow. As the standard definition of such an interface is to use a threshold on the vorticity magnitude, it is not applicable with such

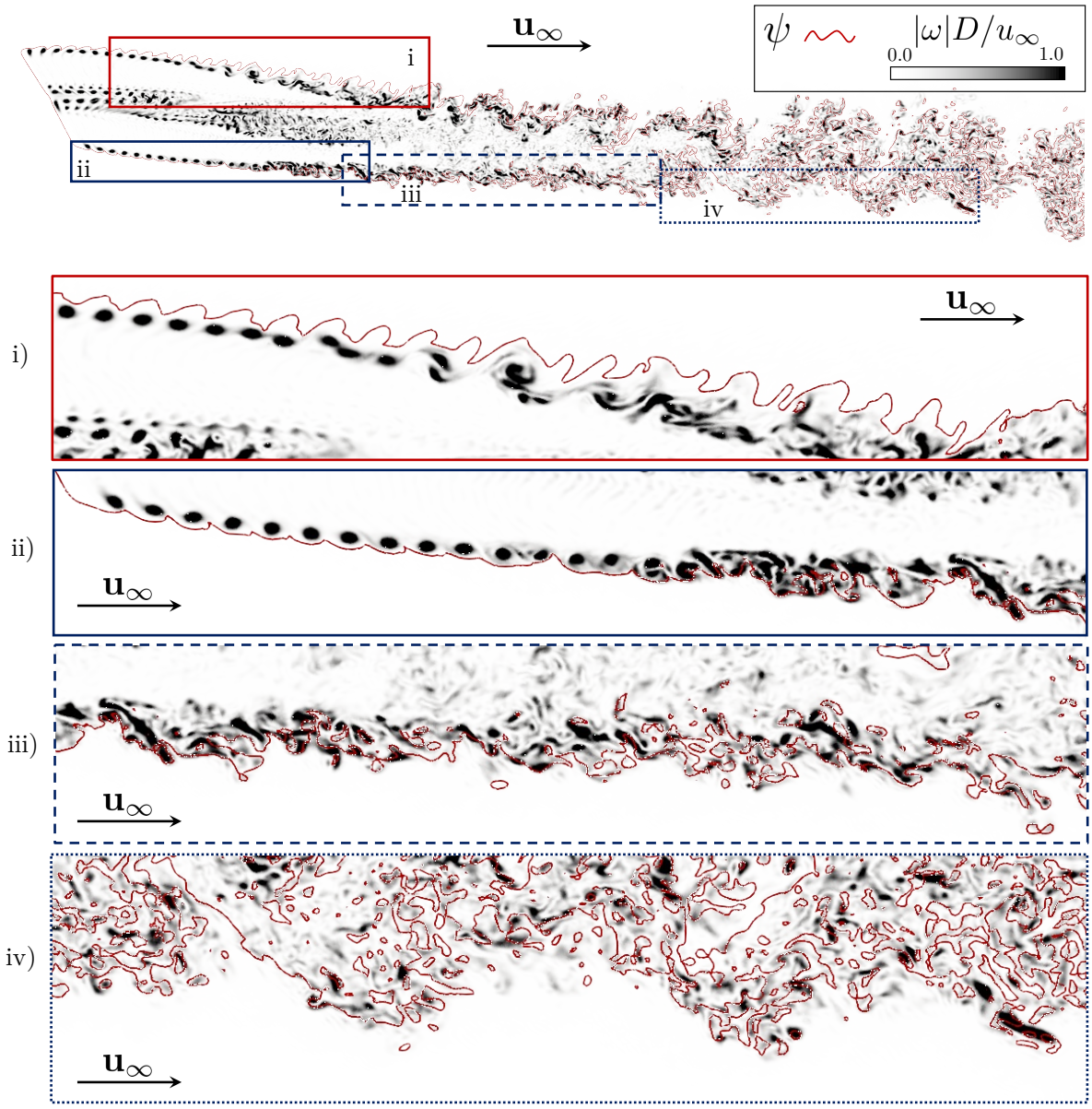

Figure 4.15: Visualization of the interface between fluid particles crossing the yawed rotor disk and a laminar external flow: case $TI_{0\%}\gamma_{30°}$. Horizontal slice of normalized vorticity magnitude with the iso-contour of $\psi = 1/2$. A global overview is given at the top and four zooms are presented as i, ii, iii, iv to observe the close interaction between the vorticity field and the tracking function ψ.

background flow. Here, the level set function ψ flagging the instantaneous particles emanating from the rotor is used to define the interface.

The interface is depicted in **Fig. 4.15** over a horizontal slice of vorticity magnitude in the wake of a yawed turbine without turbulence in the free stream ($TI_{0\%}\gamma_{30°}$). In this figure, different regions of the wake are highlighted. First, close to the rotor, regions (i) and (ii) show that the interface is englobing the vortices generated at the tip of the blades on the wake side. Furthermore, all the regions with high vorticity magnitude are on the wake side. The tip-vortices interact with the interface, generating engulfment. The engulfment appears with larger structures in the region (i). Engulfment is a common observation in "turbulent/non-turbulent"

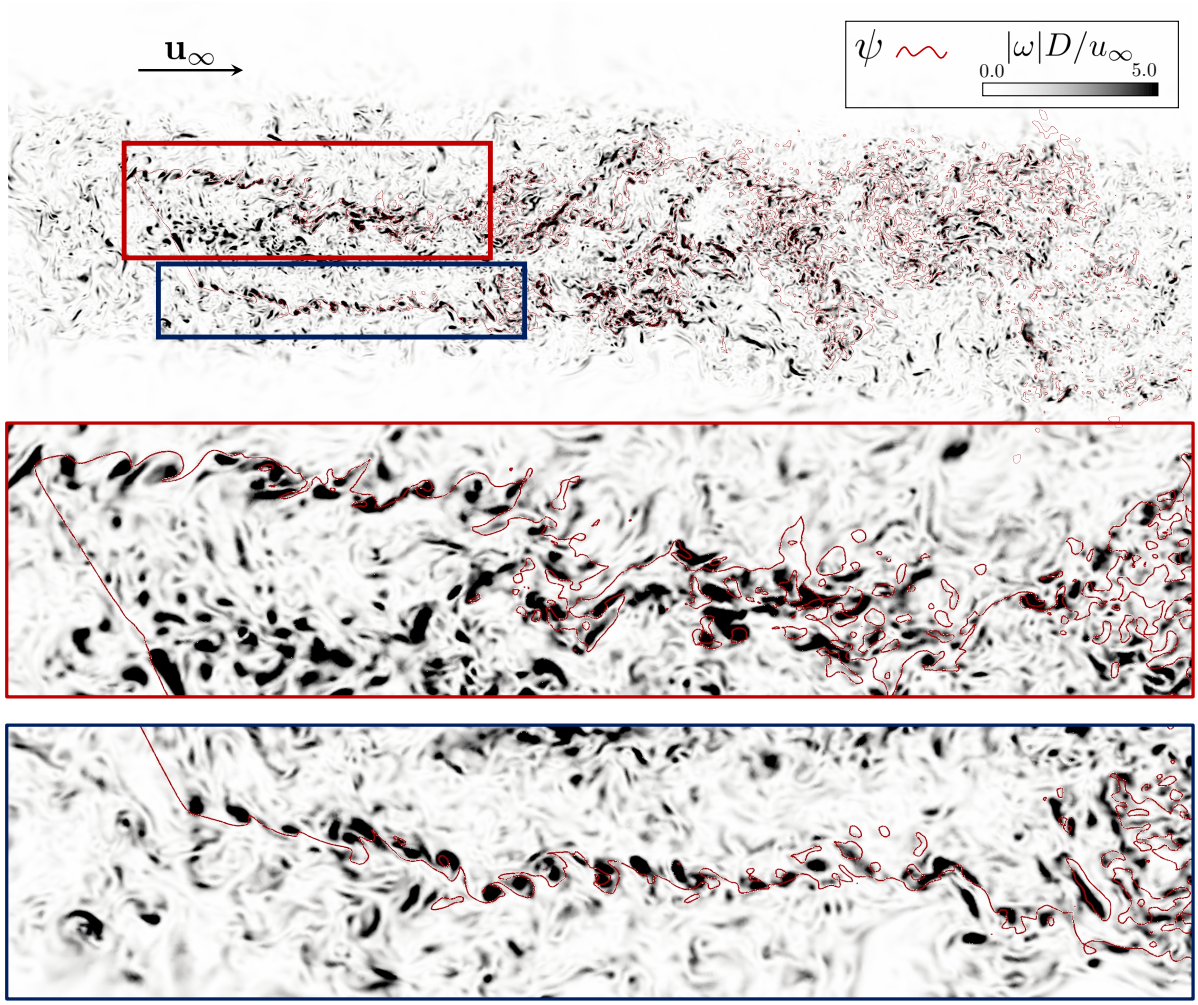

Figure 4.16: Visualization of the interface between fluid particles crossing the yawed rotor disk and a turbulent external flow for case $TI_{14\%}\gamma_{30°}$. Horizontal slice of normalized vorticity magnitude with the iso-contour of $\psi = 1/2$. A global overview is given at the top and two zooms are presented to observe the close interaction between the vorticity field and the tracking function ψ.

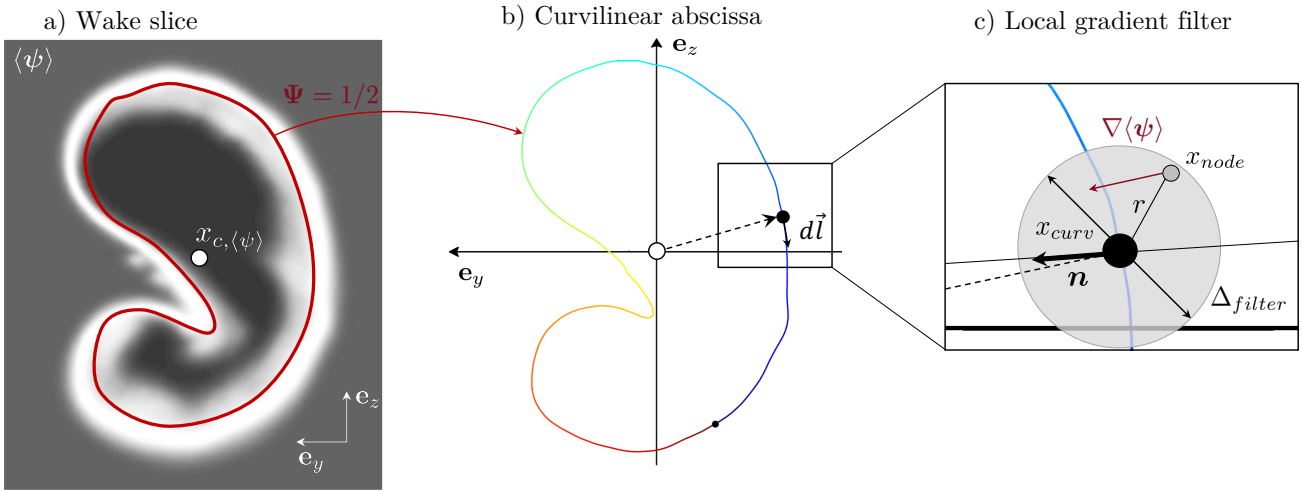

Figure 4.17: First steps to determine the turbulent mixing layer width: a) Discretization of the wake with slices at different downstream position; b) use the iso-level $\Psi = 1/2$ to construct a discretized curvilinear abscissa supposedly located within the turbulent mixing layer; c) use the filtered local gradient of ψ to evaluate the normal to the interface. The turbulent mixing layer is then evaluated along this direction.

studies [217]. Then the tip-vortices start to pair, i.e., the vortex close to the rotor leaps over the following tip-vortex, increasing the fluctuations of the interface and the engulfment. This is less visible in (ii) as the external flow impacts this side of the wake, and the tip vortices get destabilized from their interaction with the inner turbulence of the wake. In region (iii), more and more flagged fluid particles are separated from the core of the wake, highlighting the mixing with the external fluid particles. Finally, the wake is thoroughly destabilized in the region (iv), and the large scales motion is driving the interface displacement. In this region, small areas where vorticity appears are not within the wake interface; this is expected as the fluid particles of the wake exchange momentum with external flow locally, generating vorticity. Nevertheless, at this point the turbulent mixing layers of each side of the wake are indistinguishable and the evaluation will be conducted only in the upstream regions where the mixing layers did not merge.

As the methodology is not based on the vorticity magnitude, the same interface can be observed when turbulence is present in the free stream ($TI_{14\%}\gamma_{30°}$), see **Fig. 4.16**. Only two regions close to the rotor are shown as the large-scale motions related to meandering drive the interface displacement closer to the rotor. Engulfment appears just after the tip vortices are generated. As a consequence, external fluid particles are trapped in the wake core. Like for the laminar external flow, the breakup of the wake envelope occurs, and flagged fluid particles are separated from the core of the wake.

The mixing layer width is defined according to the time averaging of the interface position, $\langle\psi\rangle$. The methodology is built as follows. First, the wake is discretized into slices at different x/D downstream positions **Fig. 4.17a)**. Using the streamtube interface defined and discussed previously, a curvilinear abscissa of length L is defined and discretized into 200 points spaced by **dl**, see **Fig. 4.17b)**. Each point is associated with a length l defining the position on the curvilinear abscissa. The turbulent mixing layer width, δ_l, is then evaluated at each of these positions. This allows more flexibility than cylindrical coordinates as the envelope of the wake of the yawed turbine can bend back on itself, so several portions of the interface can be observed

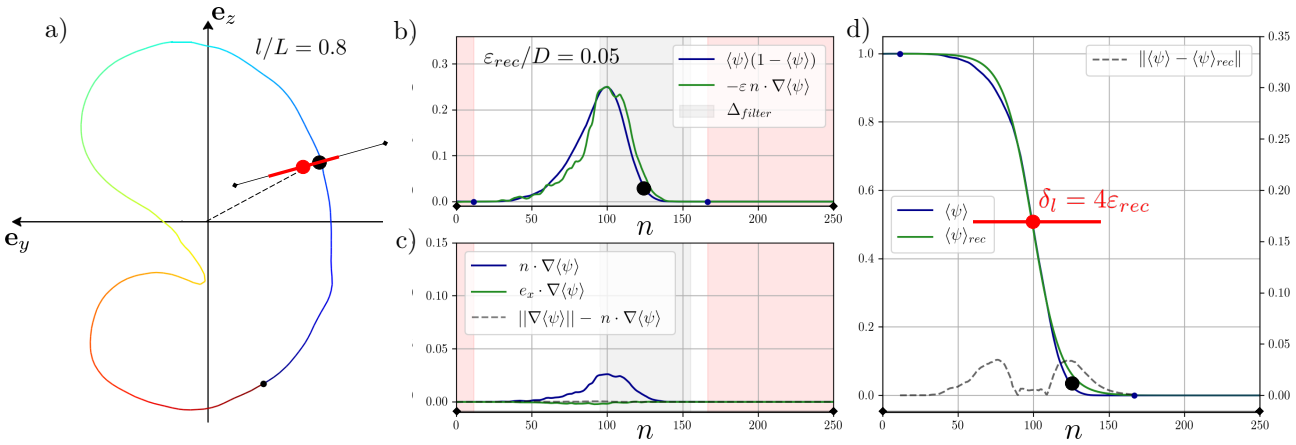

Figure 4.18: Evaluation of the turbulent mixing layer width from a line in the wake. a) Position of the line on the curvilinear abscissa. b) evaluation of the reconstructed hyperbolic tangent profile width, ε_{rec}. c) Check if the line direction is properly set by comparing to $\nabla\langle\psi\rangle$ along the line. d) Superposition of the newly reconstructed profile, $\langle\psi\rangle_{rec}$ to the actual profile of $\langle\psi\rangle$. The root-mean-square values are represented by the area around the curves.

from a single azimuth. As the axisymmetric hypothesis is not valid, and the mixing layer width cannot be evaluated from lines starting from the wake center, the filtered local gradient of $\langle\psi\rangle$ is used to predict in which direction the mixing layer expands, see **Fig. 4.17c)**. In this figure, the grey circle denotes the filter size, using a Heaviside filter for the distance between the mesh nodes and the point of the curvilinear abscissa. The filter is applied on $\nabla\langle\psi\rangle$ resulting in the normal $\boldsymbol{n}$. Only the transverse components of this normal are used and the streamwise direction is removed to evaluate the width only on the slice. This vector is used to construct a line on which the turbulent mixing layer width is evaluated.

Once the lines for every point of the curvilinear abscissa at the downstream position x/D are defined, the turbulent mixing layer is characterized according to a reconstructed hyperbolic tangent profile $\langle\psi\rangle_{rec}$. For this, the reinitialization equation, **Eq. 4.7** is used, the transient term is dropped as the reconstructed hyperbolic tangent profile is static. The goal is to evaluate ε_{rec}, to match the turbulent mixing layer width, δ_l. This is done by integrating the reinitialization equation along the line as follows

$$\varepsilon_{rec} = \frac{\int_{line} \langle\psi\rangle\,(1-\langle\psi\rangle)\,\mathrm{d}n}{\int_{line} \boldsymbol{n}\cdot\nabla\langle\psi\rangle\,\mathrm{d}n}\,, \tag{4.18}$$

where $\mathrm{d}n$ denotes an infinitesimal fraction of the line. The integral over the line is used since $\langle\psi\rangle$ is not an hyperbolic tangent profile and the goal is to approximate the profile to obtain the equivalent width, ε_{rec}.

As an example, the methodology is applied in **Fig. 4.18** for $TI_{0\%}\gamma_{30°}$, at the streamwise position $x/D = 4$ and for the point at $l/L = 0.8$ on the curvilinear abscissa. The position on the wake slice is shown in **Fig. 4.18a)**, with the orientation of the line as a black line and the computed width in red.

The evolution over the line of $\langle\psi\rangle\,(1-\langle\psi\rangle)$ is compared to $\varepsilon_{rec}\boldsymbol{n}\cdot\nabla\langle\psi\rangle$ in **Fig. 4.18b)**. The large black circle represents the position of $\Psi = 1/2$. For this position $\varepsilon_{rec}/D = 0.049$ and the turbulent mixing width, $\delta_l/D = 4\times\varepsilon_{rec}/D = 0.196$.

To validate the line direction, based on the filtered gradient, the comparison between the

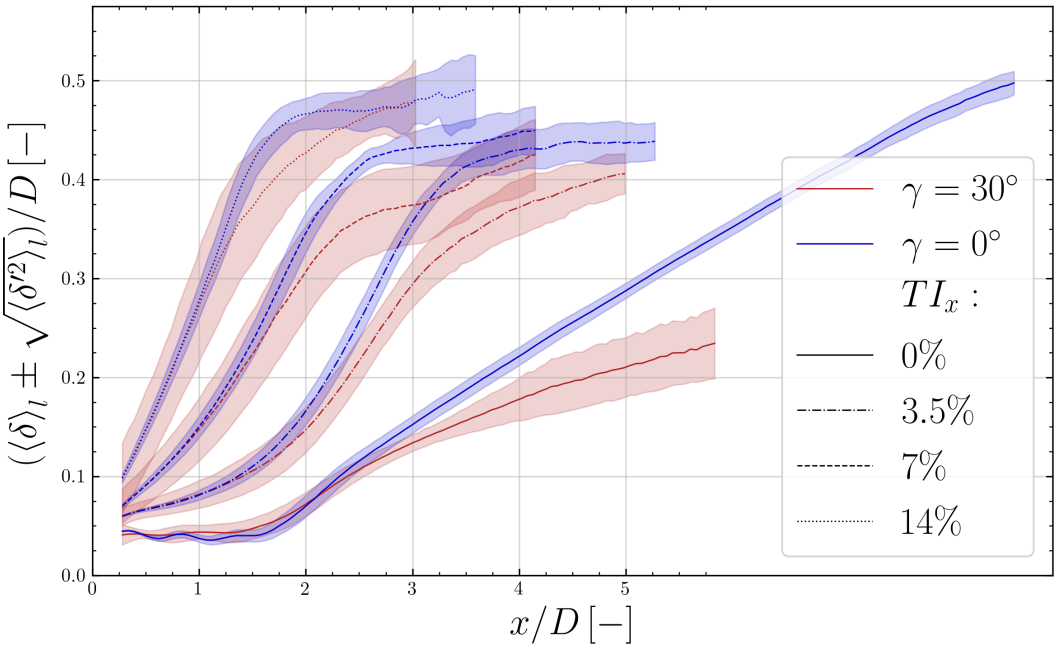

Figure 4.19: Evolution of the turbulent mixing layer width, averaged and root-mean-square values over the curvilinear abscissa of each streamwise position. Cases are depicted as $\gamma = 0°$ (——), $\gamma = 30°$ (——) for the yaw angle and for the inflow turbulence intensity as $TI_x = 0\%$ (——), 3.5% (-·-·), 7% (- - -) and 14% (·····).

gradient projection over the normal $\boldsymbol{n}$ and the streamwise direction, $\mathbf{e}_x$ is shown in **Fig. 4.18c)**. The error $||\nabla\langle\psi\rangle||-\boldsymbol{n}\cdot\nabla\langle\psi\rangle$ remains below 10^{-4} and assesses that the direction is well estimated.

Finally, the reconstructed hyperbolic tangent profile can be superposed to the actual $\langle\psi\rangle$ profile, see **Fig. 4.18d)**. The reconstructed profile position on the line is selected to minimize the discrepancies with the actual profile. This methodology is applied to all the cases and the results are compared at the end of this section.

The evolution of the turbulent mixing layer width for both yaw angles and the different inflows is presented in **Fig. 4.19**. The turbulent mixing layer width is presented using the averaged and root-mean-square of δ_l over the curvilinear abscissa for each downstream position. The width expands at a higher rate with the increasing turbulence intensity. After some distance to the rotor, the width remains constant, at this distance the wake is fully destabilized and the mixing layers merge at the center of the wake core. The previous methodology does not take this into account. The root-mean-square of the yaw misaligned cases shows higher discrepancies of the width for a given streamwise position. The maximum value is located where the wake is bending on itself while the minimum is on the opposite side, not depicted here. The cases without turbulence are expanding at a lower rate showing the strong impact of the free-stream turbulence. Furthermore, during the convection of the tip-vortices, the turbulent mixing layer width remains constant, see **Fig. 4.15** regions i) and ii). After their destabilization, the turbulent mixing layer expands linearly.

- **Impact of the mesh resolution**

The cell size impact on the results is discussed from **Fig. 4.20**, where simulations with the two levels of refinement are presented, (1) and (2) see **Tab. 4.1**. Cases with $\gamma = 0°$ and 30° are shown with $TI_x = 0\%$ and 14%. First, the cases with turbulence present the same behavior

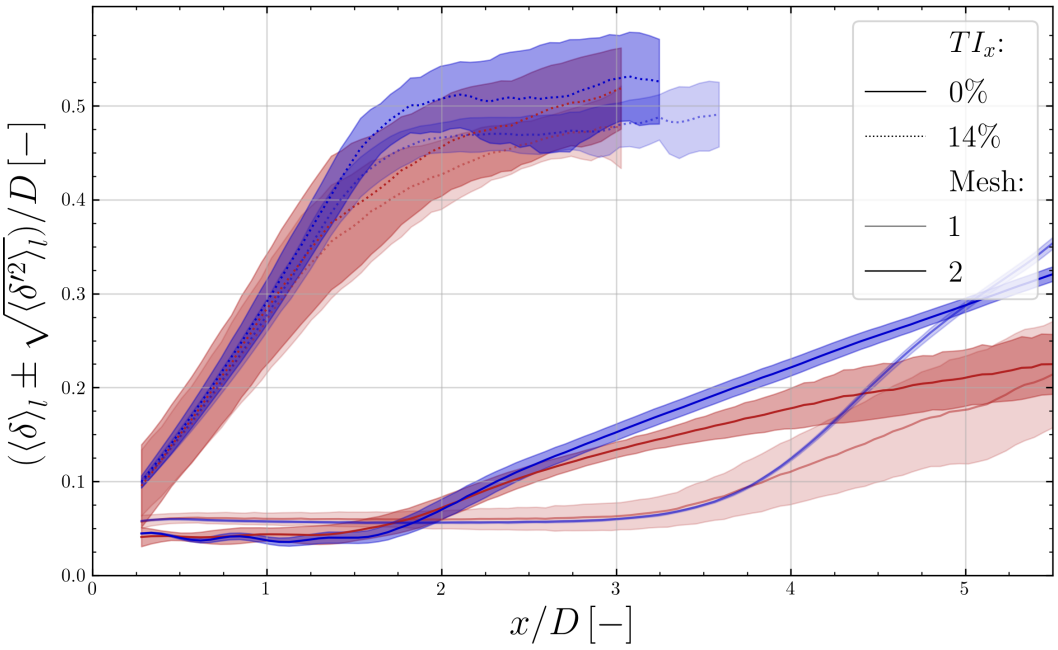

Figure 4.20: Evolution of the turbulent mixing layer width, averaged and root-mean-square values over the curvilinear abscissa of each streamwise position. Comparison between the mesh refinement level is given, (1) light curves, (2) dark curves. Cases are depicted as $\gamma = 0°$ (—), $\gamma = 30°$ (—) for the yaw angle and for the inflow turbulence intensity as $TI_x = 0\%$ (—) and 14% (·····).

independently from the cell size or yaw angle in terms of turbulent mixing layer width (averaged and root-mean-square). Second, the case without turbulence has a longer distance before the width expansion on mesh (1) for both yaw angles. Furthermore, after this position, the width expands at a higher rate. Here, this shows that the external turbulence helps to remove the dependence on the refinement level for the turbulence mixing layer width. Nevertheless, the width expansion is delayed downstream and is higher when no turbulence is added.

4.5 Budgets applied on streamtubes

To quantify on the evolution of the wake, the following sections discuss the wake recovery and the wake center deflection according to the Mean Kinetic Energy (MKE) and Mean Momentum (MM) budgets applied to the streamtube volume. A comparison of the integrated quantities to the 1D momentum theory is finally presented

4.5.1 The wake recovery explained from Mean Kinetic Energy budget

To quantify the wake destabilisation process and wake recovery, mean kinetic energy (MKE) budgets are performed. The MKE transport equation are derived from the filtered Navier Stokes equations using the Boussinesq hypothesis, **Eq. 2.36**. First, the filtered velocity, pressure and external body force terms are decomposed as a time-averaged value and a resolved fluctuation:

$$\bar{u}_i = \langle\bar{u}_i\rangle + \bar{u}'_i, \bar{p} = \langle\bar{p}\rangle + \bar{p}', \bar{f}_i = \langle\bar{f}_i\rangle + \bar{f}'_i\,, \tag{4.19}$$

where $\langle\bullet\rangle$ denotes time averaged data and $\bullet'$ the time fluctuations. The filter operator $\bar{\bullet}$ is dropped to facilitate the notation, giving the following equation for momentum-conservation:

$$\frac{\partial u_i'}{\partial t}+\frac{\partial}{\partial x_j}\left(\left(\langle u_i\rangle+u_i'\right)\left(\langle u_j\rangle+u_j'\right)\right)=-\frac{1}{\rho}\frac{\partial\left(\langle p\rangle+p'\right)}{\partial x_i}+(\nu+\nu_t)\frac{\partial^2\left(\langle u_i\rangle+u_i'\right)}{\partial x_j\partial x_j}+\langle f_j\rangle+f_j'\,. \quad (4.20)$$

The equation is time-averaged to remove a part of the fluctuating terms:

$$\frac{\partial}{\partial x_j}\left(\langle u_i\rangle\langle u_j\rangle\right)=-\frac{1}{\rho}\frac{\partial\langle p\rangle}{\partial x_i}+(\nu+\nu_t)\frac{\partial^2\langle u_i\rangle}{\partial x_j\partial x_j}-\frac{\partial}{\partial x_j}\left\langle u_i'u_j'\right\rangle+\langle f_i\rangle\,, \quad (4.21)$$

with $\left\langle u_i'u_j'\right\rangle$ denoting the Reynolds stress tensor. The resulting equation is the mean momentum equation. This equation is multiplied by $\rho\langle u_i\rangle$ to obtain the mean kinetic energy equation:

$$\begin{aligned}\rho\langle u_i\rangle\frac{\partial}{\partial x_j}\left(\langle u_i\rangle\langle u_j\rangle\right)=&-\langle u_i\rangle\frac{\partial\langle p\rangle}{\partial x_i}+(\nu+\nu_t)\rho\langle u_i\rangle\frac{\partial^2\langle u_i\rangle}{\partial x_j\partial x_j}\\&-\rho\langle u_i\rangle\frac{\partial}{\partial x_j}\left\langle u_i'u_j'\right\rangle+\rho\langle u_i\rangle\langle f_i\rangle\,.\end{aligned} \quad (4.22)$$

Re-assembling the transport equation of mean kinetic energy by taking into account:

- the incompressibility of the flow: $\dfrac{\partial\langle u_i\rangle}{\partial x_i}=0$,
- the strain rate tensor $S_{ij}=\frac{1}{2}\left(\frac{\partial u_i}{\partial x_j}+\frac{\partial u_j}{\partial x_i}\right)$,
- the viscosity and the sub-grid scale turbulent viscosity terms:

$$(\nu+\nu_t)\rho\langle u_i\rangle\frac{\partial^2\langle u_i\rangle}{\partial x_j\partial x_j}=2(\nu+\nu_t)\rho\frac{\partial}{\partial x_j}\left(\langle u_i\rangle\langle S_{ij}\rangle\right)-2(\nu+\nu_t)\rho\langle S_{ij}\rangle\frac{\partial\langle u_i\rangle}{\partial x_j} \quad (4.23)$$

- that the following tensors are symmetric: $\dfrac{\partial\langle u_i\rangle}{\partial x_j}$, $\langle S_{ij}\rangle$ and $\left\langle u_i'u_j'\right\rangle$,

gives:

$$\begin{aligned}\frac{\partial}{\partial x_j}\left(\frac{1}{2}\rho\langle u_i\rangle\langle u_i\rangle\langle u_j\rangle\right)=&\frac{\partial}{\partial x_j}\left(-\langle u_j\rangle\langle p\rangle+\langle u_i\rangle 2(\nu+\nu_t)\rho\langle S_{ij}\rangle-\langle u_i\rangle\rho\left\langle u_i'u_j'\right\rangle\right)\\&-\langle S_{ij}\rangle\left(2(\nu+\nu_t)\rho\langle S_{ij}\rangle-\rho\left\langle u_i'u_j'\right\rangle\right)+\rho\langle u_i\rangle\langle f_i\rangle\end{aligned} \quad (4.24)$$

Then, terms are integrated over slices of the streamtube, giving:

$$\begin{aligned}\oiint_S\Bigg(\underbrace{\frac{1}{2}\rho\langle u_i\rangle\langle u_i\rangle\langle u_j\rangle}_{i}+\underbrace{\langle u_j\rangle\langle p\rangle}_{ii}+\underbrace{\langle u_i\rangle\rho\left\langle u_i'u_j'\right\rangle}_{iii}+A_{j,S}\Bigg)n_j\,\mathrm{d}S\\-\iiint_{V_{st}}\Bigg(\underbrace{\rho\langle S_{ij}\rangle\left\langle u_i'u_j'\right\rangle}_{iv}+\underbrace{\rho\langle u_i\rangle\langle f_i\rangle}_{v}+A_V\Bigg)\mathrm{d}V=0\,,\end{aligned} \quad (4.25)$$

Viscous and subgrid-scale terms, on the surface and in the volume, are gathered as A_S and A_V, respectively, and are further ignored in the analysis since they are negligible at such high Reynolds numbers, but are correctly taken into account in the budget residual. Numbered terms respectively denote: *i*) the change in flux of MKE by advection, *ii*) the pressure work, *iii*) the

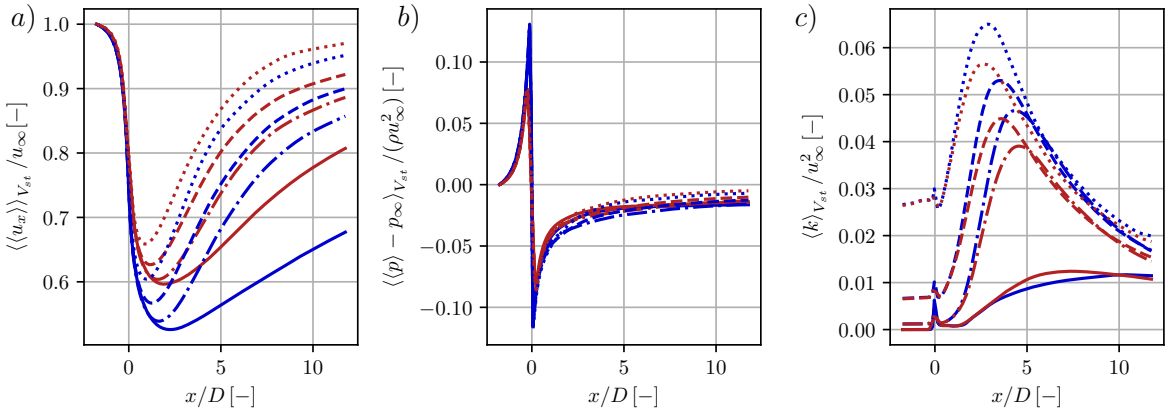

Figure 4.21: Streamwise evolution of (a) mean streamwise filtered velocity (b) hydrodynamic pressure and (c) turbulent kinetic energy integrated over the streamtube volume for all cases. Cases are depicted as $\gamma = 0°$ (——), $\gamma = 30°$ (——) for the yaw angle and for the inflow turbulence intensity as $TI_x = 0\%$ (——), 3.5% (-·-·), 7% (- - -) and 14% (·····).

work of the Reynolds stress tensor on the streamtube surfaces, *iv*) the production of TKE within the streamtube volume and *v*) the work of the turbine.

In order to understand the yawed wake behavior from the MKE budgets, quantities of interest are averaged over control volume cross-sections, using the streamtubes control volume. **Fig. 4.21** shows the evolution of streamwise velocity, pressure and mean TKE for each case. TKE is defined as $k = 1/2\left\langle u_i'^2\right\rangle$. The pressure drop is located at the turbine position when the flow decelerates as a consequence of the turbine momentum extraction from the flow. For yawed cases, inducing a lower thrust coefficient, the velocity deficit and the pressure difference are lower. For cases with turbulence injection, half of the deficit is restored after 4.5 to $7D$ downstream the turbine. Without turbulence, the deficit takes at least twice this length to recover, demonstrating the major role of turbulence on the velocity deficit recovery. The TKE evolution also gives information on the wake recovery dynamics. For $TI = 0\%$ cases, a plateau can be observed up to $1.5D$ behind the rotor followed by an increase of TKE. This variation of TKE is precisely located at the maximum velocity deficit position. The evolution of the streamwise velocity compared to the streamtube section evolution presented from the wake topology is in good accordance with the mass conservation statement, i.e., when the velocity decrease/increase the section increase/decrease.

The MKE integrated budget is shown, for the turbulence levels $TI_x = 0\%$, 3.5%, 7%, 14% with the turbine operating at $\gamma = 0°$ in **Fig. 4.22** and at $\gamma = 30°$ in **Fig. 4.23**. One of the major contributions to the MKE budget is the turbine work, generating the first energy drop. It is counterbalanced by the pressure and advection of MKE, therewith being the first source of MKE. Afterward, the wake can be decomposed in different regions, denoted with colors as I, II, III and IV. The first, appearing only for $TI_x = 0\%$, is the vortex advection region. In this region, the tip vortices remain helical until $1.5D$ ($\gamma = 30°$) and $1.75D$ ($\gamma = 0°$) downstream. The first vortices instabilities appear in the streamwise direction. The second region starts with the production of TKE, removing energy from the mean (as observed in **Fig. 4.21c)**). The Reynolds stress work balances this production by supplying energy to the streamtube. The tip vortices pair up with each other in this region or interact with background turbulence generating a TKE production peak. The third region is delimited by the MKE advection becoming negative in the wake until it begins to increase again. Here, the wake velocity deficit starts to recover due

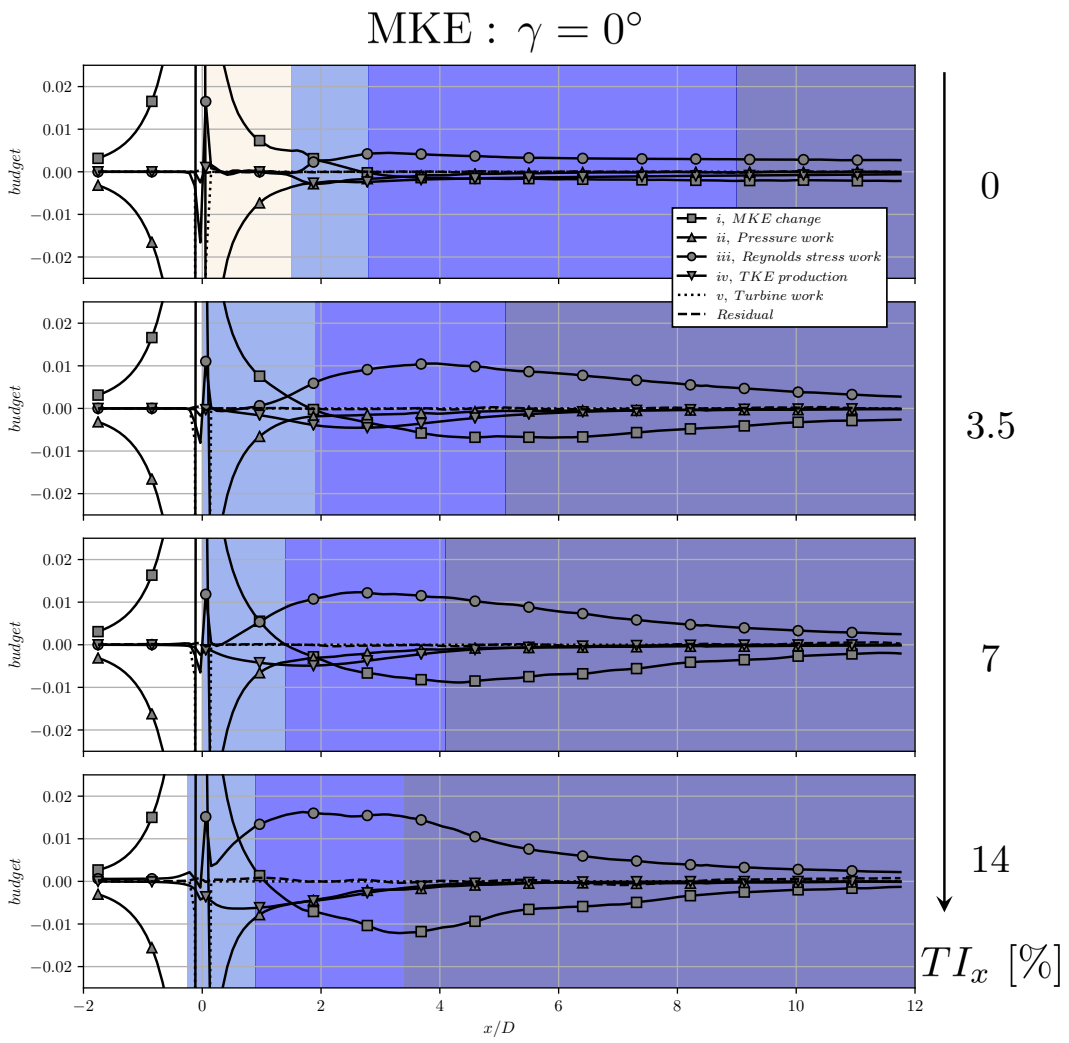

Figure 4.22: Mean kinetic energy equation terms integrated over the streamtube cross-section for $\gamma = 0°$ and, from top to bottom, $TI_x = 0\%$ (——), 3.5% (-·-·), 7% (- - -) and 14% (·····). Each term is normalized by the total turbine power such as the integral of term v is equal to -1. The residual corresponds to the sum of all terms of **Eq. 4.25**.

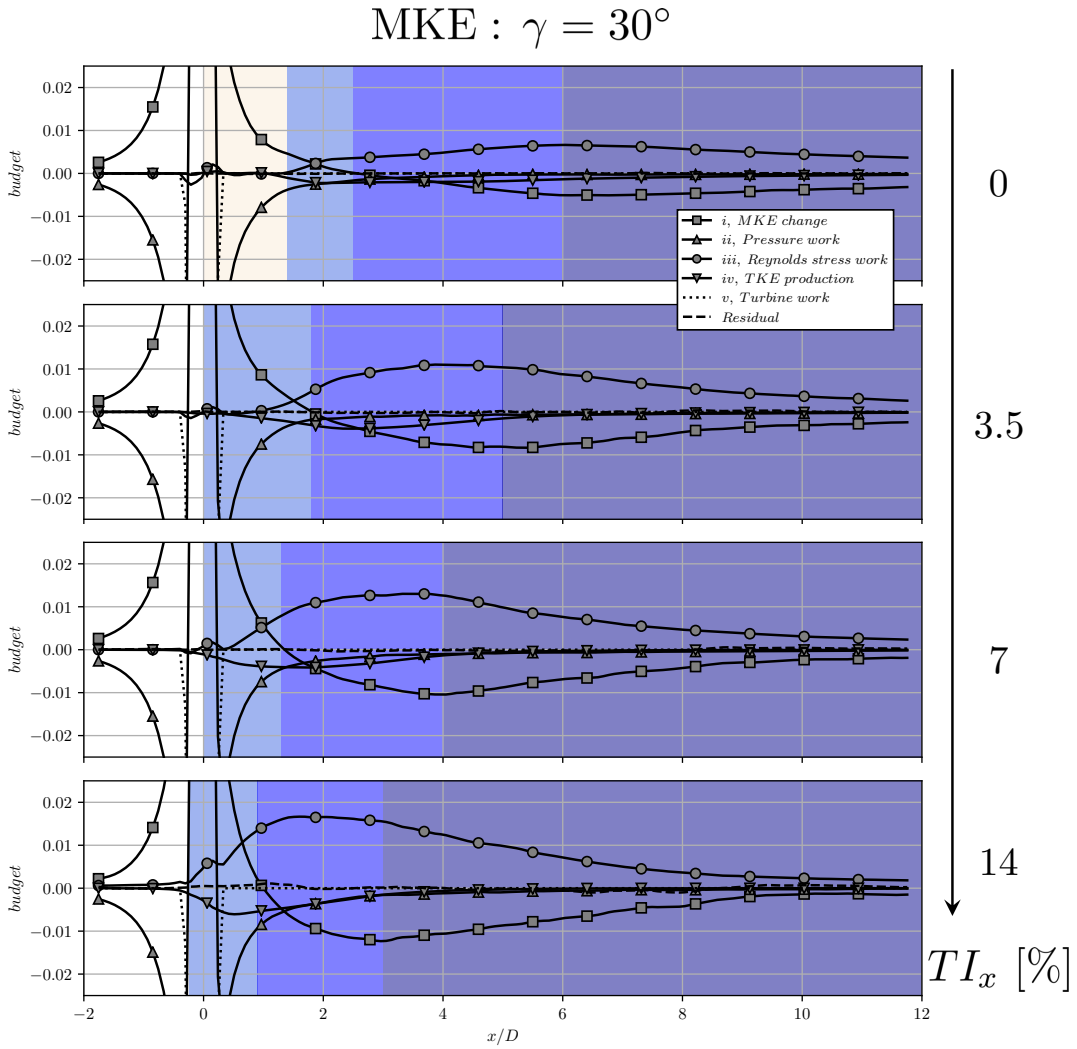

Figure 4.23: Mean kinetic energy equation terms integrated over the streamtube cross-section for $\gamma = 30°$ and, from top to bottom, $TI_x = 0\%$ (—), 3.5% (-·-·), 7% (- - -) and 14% (·····). Each term is normalized by the total turbine power such as the integral of term v is equal to -1. The residual corresponds to the sum of all terms of **Eq. 4.25**.

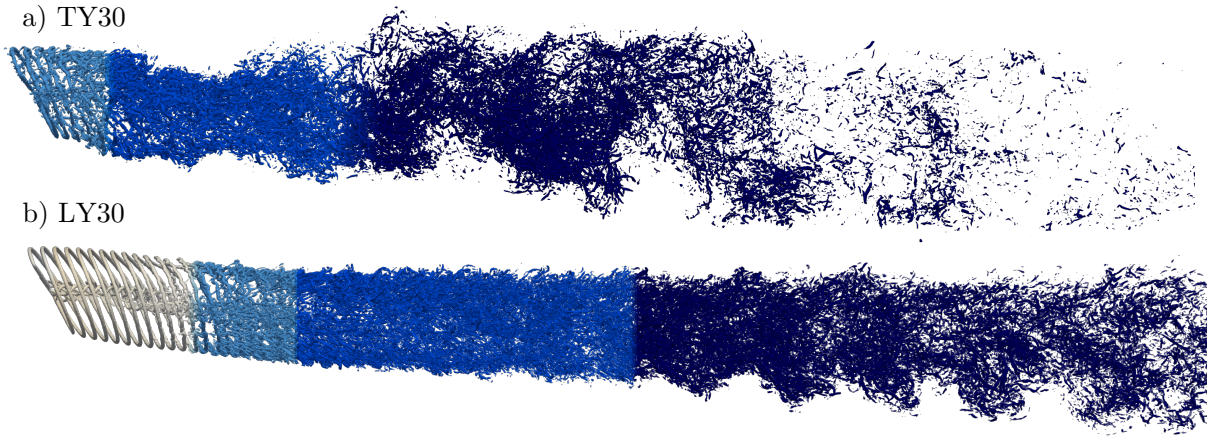

Figure 4.24: 3D visualisation of the instantaneous Q-criterion colored by the regions determined from the MKE budgets for cases $TI_{14\%}\gamma_{30°}$ and $TI_{0\%}\gamma_{30°}$.

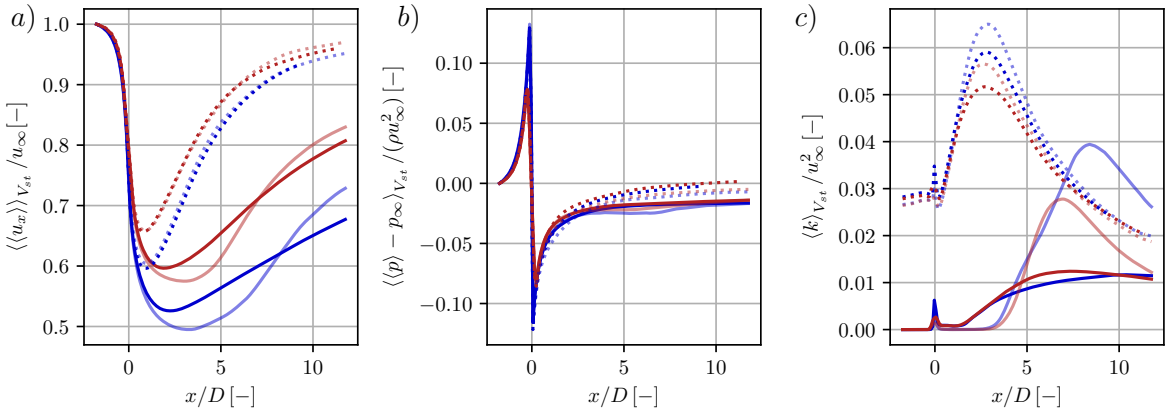

Figure 4.25: Mesh refinement impact on the streamwise evolution of (a) mean streamwise filtered velocity (b) hydrodynamic pressure and (c) turbulent kinetic energy integrated over the streamtube volume. Cases are depicted as $\gamma = 0°$ (—), $\gamma = 30°$ (—) for the yaw angle, as $TI_x = 0\%$ (—), 14% (·····) for the turbulent intensity and the refinement level as (1) (—) and (2) (—).

to the large Reynolds stress contribution. From **Fig. 4.21c)** the end of this region presents the maximum of turbulent kinetic energy. The last identified region contains the wake turbulence decaying. Turbulence production becomes negligible and the Reynolds stress work decreases significantly. The velocity deficit continues to recover but at a lower rate than the previous region. **Fig. 4.24** figures the 3D iso-contour of Q-criterion for both cases, colored by the different regions presenting the vortex dynamics.

The comparison of $\gamma = 0°$ and 30° for $TI_x = 0\%$ shows that region III ends further downstream for $TI_{0\%}\gamma_{0°}$ $(9D)$ compared to $TI_{0\%}\gamma_{30°}$ $(6D)$. This last point implies a slower wake recovery for the yaw misaligned case under uniform inflow, which is not observed with the turbulent cases. Yet comparing the different TI cases, the background turbulence plays a large role in the wake dynamics as mentioned in the literature [230, 207].

- **Impact of the mesh resolution**

The cell size impact on the results is discussed according to **Fig. 4.25**, for the integrated quantities where simulations over the two levels of refinement are presented, (1) and (2) see **Tab. 4.1**. Cases with $\gamma = 0°$ and 30° are shown with $TI_x = 0\%$ and 14%. First, the cases with turbulence present the same behavior independently from the cell size or yaw angle in terms of streamwise velocity deficit, and pressure jump. The maximum of turbulent kinetic energy is slightly higher for (1) but the tendencies are similar. Second, the case without turbulence reaches a higher velocity deficit on mesh (1) for both yaw angles. This is in accordance with the previous observations made from the streamtube section. The TKE starts to increase further downstream for the coarse mesh and the maximal value is two to three times higher. Furthermore, the position of the maximum TKE is delayed downstream of the rotor. The pressure jump is not impacted by the mesh. The impact of the mesh is furtherly discussed using the MKE integrated budget with the turbine operating at $\gamma = 30°$ for the turbulence levels $TI_x = 0\%$ in **Fig. 4.27** and 14% in **Fig. 4.26**. For $TI_x = 0\%$, the end of region I is achieved 1D downstream for mesh 1 when compared to mesh 2. With the coarse mesh, the second region is shorter since the TKE production increase when the MKE advection becomes negative. Region IV, the far-wake, starts at the same location for both refinement levels. For $TI_x = 14\%$, the budget terms are evolving

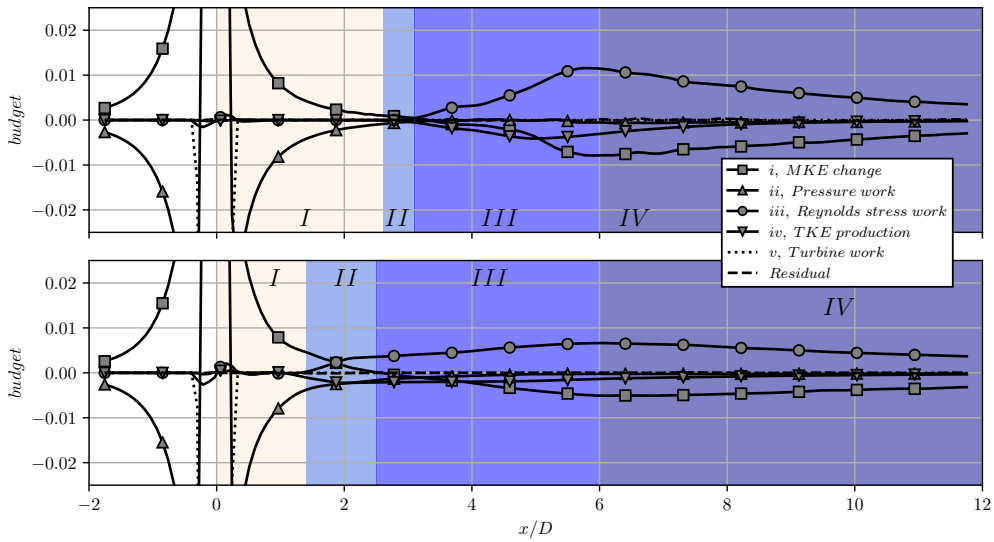

Figure 4.26: Mean kinetic energy equation terms integrated over the streamtube cross-section for case $TI_{0\%}\gamma_{30°}$ on mesh 1 (top) and 2 (bottom). Each term is normalized by the total turbine power such as the integral of term v is equal to -1. The residual corresponds to the sum of all terms of **Eq. 4.25**.

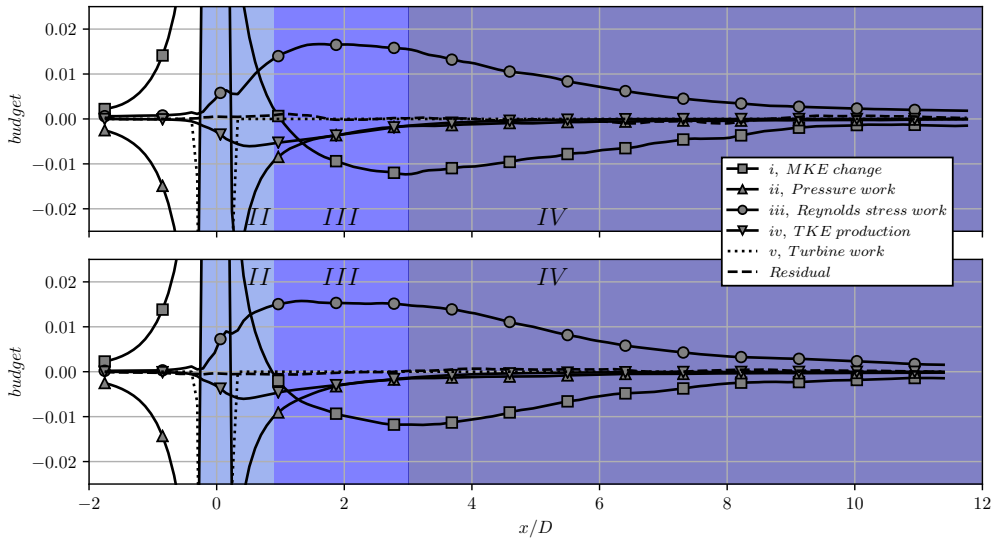

Figure 4.27: Mean kinetic energy equation terms integrated over the streamtube cross-section for case $TI_{14\%}\gamma_{30°}$ on mesh 1 (top) and 2 (bottom).. Each term is normalized by the total turbine power such as the integral of term v is equal to -1. The residual corresponds to the sum of all terms of **Eq. 4.25**.

with the same behavior and the regions are located at the same positions.

Consequently, this again underlines that the external turbulence helps to reduce the dependence of the wake evolution to the refinement level. When no turbulence is added, the wake recovery is delayed downstream, the velocity deficit is higher and the production of TKE is overestimated.

4.5.2 The wake deflection explained from Mean Momentum budget

Mean momentum transport equations are used to understand the wake deflection of the turbine under yaw misalignment. For this matter, the mean momentum-conservation equation obtain in the previous section, see **Eq. 4.21**, is integrated over slices of the streamtube. The projection of the terms onto the streamwise and horizontal axis gives, respectively:

$$\oiint_S \Big(\underbrace{\langle \widetilde{u}_x \rangle \langle \widetilde{u}_j \rangle n_j}_{i} + \underbrace{\frac{1}{\rho} \left\langle \widetilde{P} \right\rangle n_x}_{ii} + \underbrace{\langle \widetilde{u}'_x \widetilde{u}'_j \rangle n_j}_{iii} + A_x \Big) \mathrm{d}S - \iiint_{V_{st}} \underbrace{\left\langle \widetilde{f}_x \right\rangle}_{iv} \mathrm{d}V = 0 \,, \tag{4.26}$$

$$\oiint_S \Big(\underbrace{\langle \widetilde{u}_y \rangle \langle \widetilde{u}_j \rangle n_j}_{i} + \underbrace{\frac{1}{\rho} \left\langle \widetilde{P} \right\rangle n_y}_{ii} + \underbrace{\langle \widetilde{u}'_y \widetilde{u}'_j \rangle n_j}_{iii} + A_y \Big) \mathrm{d}S - \iiint_{V_{st}} \underbrace{\left\langle \widetilde{f}_y \right\rangle}_{iv} \mathrm{d}V = 0 \,. \tag{4.27}$$

Similarly to **Eq. 4.25**, viscous and sub-grid scale terms are gathered in $A_{x/y}$ and are negligible, yet included in the budget residual. Numbered terms respectively denote: i) change in momentum, ii) pressure force, iii) forces due to Reynolds stress and iv) the turbine forces on the flow. The wake deflection is investigated using only the budget projected on the horizontal axis, **Eq. 4.27**. For the cases with a zero yaw angle, the wake is mostly axisymmetric and the terms are null over the transverse axis, therefore, only the case with $\gamma = 30°$ are presented.

The terms projected on the horizontal axis for all the turbulence intensities are depicted in**Fig. 4.28**. When $\gamma \neq 0°$, a portion of the forces are imposed in the horizontal direction and induces a drop in the horizontal momentum. As in the streamwise direction, this sink of momentum is counterbalanced by the pressure forces and the change in momentum. Note that when the change in momentum is negative (on the opposite, positive), horizontal velocity increases (decreases). The absolute value informs on the velocity change rate.

In the $TI_x = 0\%$ case, since the change of momentum upstream of the turbine is negative, the flow field is slightly reoriented in the horizontal direction (around 1.0° from **Fig. 4.12c)**). In region I, the momentum changes abruptly to positive values to counter the turbine forces and the horizontal flow direction changes to $-8°$. Then the horizontal velocity starts recovering quickly. These comments on the horizontal velocity can be correlated to the streamtube center deflection (see **Fig. 4.12b-c)**). In the second region, pressure forces drop due to Reynolds stress forces triggering the vortices pairing. A balance between the pressure term and the Reynolds stress was suggested in the experimental work of Bastankhah and Porté-Agel [43] but could not be measured. The momentum flux becomes constant, but remains almost negative and the horizontal velocity recovers linearly. In region III, MM terms are mainly constant. In the last region, all MM terms slightly tend to 0: the wake deflection direction is kept downstream.

For the cases with freestream turbulence, the observations on the change of mean momentum are the same but as the turbulence level increase, the pressure force on the streamtube is reduced and is replaced by the Reynolds stress force.

4.5.3 Comparison to the 1D momentum theory

Following the previous observations on the evolutions of the wake integrated quantities, this section aims at comparing these results to the 1D momentum theory. From the variations of velocity and pressure within the streamtube and by identifying the far upstream region (0), rotor disk (1), and downstream region (2), one can assess if the equations presented in **Section 4.2.3** are reliable. Here the different regions are defined as shown in **Fig. 4.29**, where region (2) is the limit between the wake region II and III as the velocity deficit starts to recover. At this

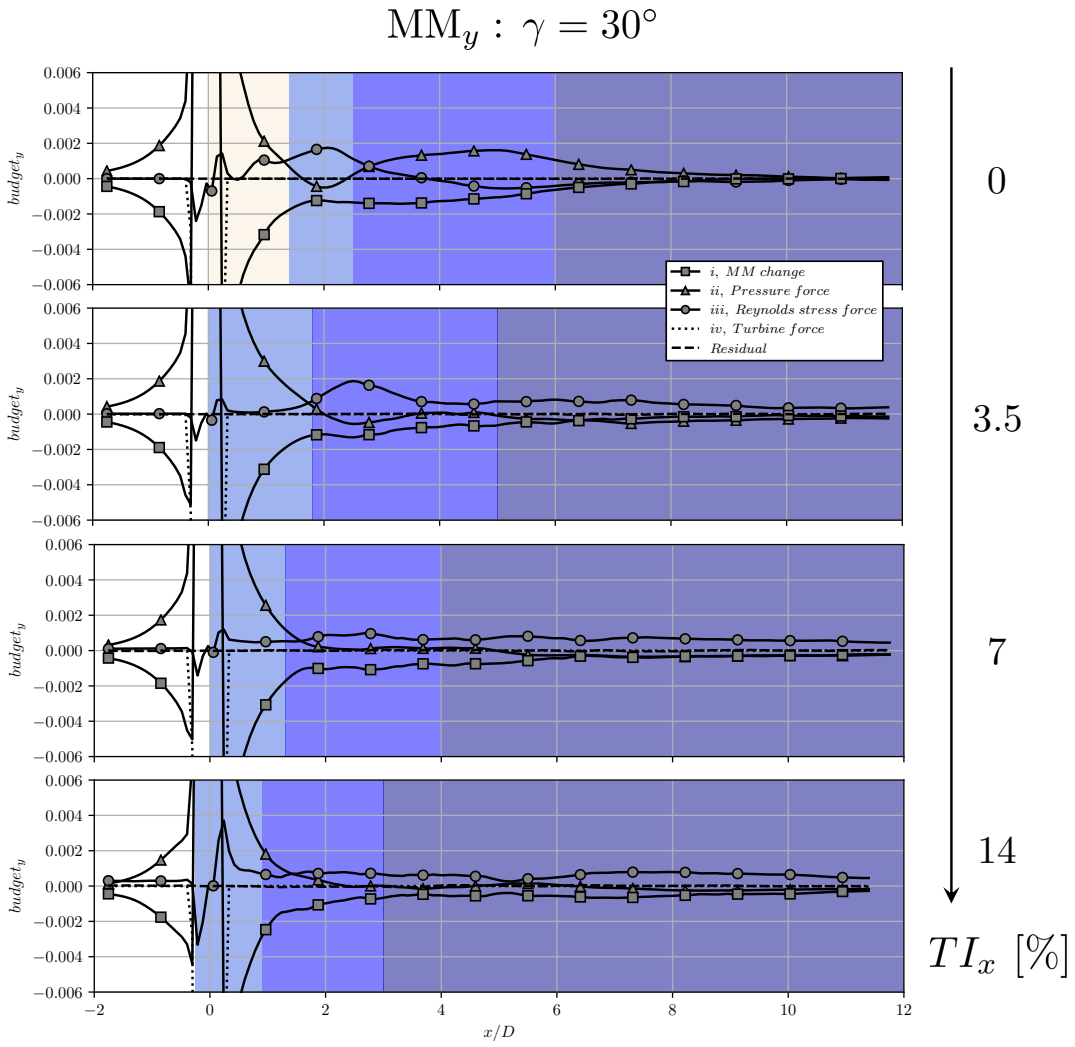

Figure 4.28: Mean momentum equation terms projected over the horizontal axis and integrated over the streamtube cross-section for $\gamma = 30°$ and, from top to bottom, $TI_x = 0\%$ (—), 3.5% (-·-), 7% (- - -) and 14% (·····). Each term is normalized by the total turbine forces such as the integral of term *iv* is equal to -1. The residual corresponds to the sum of all terms of the equations. The regions discussed in the previous section are colored.

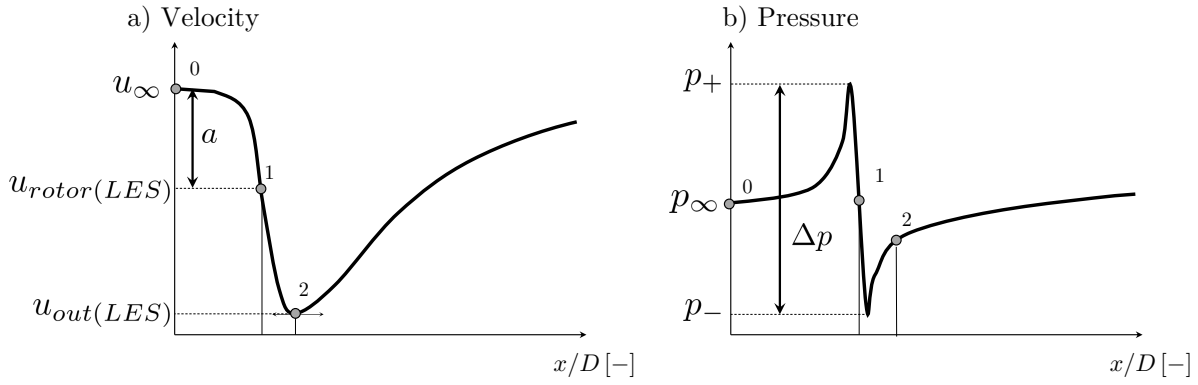

Figure 4.29: Sketch of the (a) streamwise velocity and (b) pressure evolution along the streamtube, based on the simulations results. Regions (0), (1) and (2) are represented according to the 1D momentum theory.

Cases	$u_{rotor(LES)}$ $[m.s^{-1}]$	$u_{out(LES)}$ $[m.s^{-1}]$	$u_{out(1D)}$ $[m.s^{-1}]$	Δ[%]	a [–]	$C_{T(LES)}$ [–]	$C_{T(a)}$ [–]	Δ[%]	$C_{T(\Delta P)}$ [–]	Δ[%]
$TI_{0\%}\gamma_{0°}$	7.55	5.21	5.19	-0.45	0.238	0.772	0.726	-5.96	0.537	-30.50
$TI_{0\%}\gamma_{30°}$	7.94	5.92	5.95	+0.50	0.200	0.606	0.641	+5.74	0.347	-42.67
$TI_{3.5\%}\gamma_{0°}$	7.54	5.34	5.17	-3.09	0.239	0.786	0.727	-7.46	0.533	-32.23
$TI_{3.5\%}\gamma_{30°}$	7.91	6.00	5.89	-1.83	0.204	0.610	0.649	+6.33	0.351	-42.53
$TI_{7\%}\gamma_{0°}$	7.57	5.62	5.23	-6.87	0.236	0.785	0.721	-8.12	0.535	-31.90
$TI_{7\%}\gamma_{30°}$	7.92	6.22	5.91	-5.04	0.202	0.619	0.646	+4.36	0.352	-43.13
$TI_{14\%}\gamma_{0°}$	7.59	5.93	5.24	-11.68	0.237	0.782	0.723	-7.58	0.546	-30.23
$TI_{14\%}\gamma_{30°}$	7.91	6.51	5.91	-9.20	0.202	0.620	0.644	+3.94	0.361	-41.84

Table 4.3: Comparison between the integrated quantities along the streamtubes for all cases and the 1D momentum theory.

position, the maximum velocity deficit is achieved due to the sign (positive to negative) change of the MKE flux. The results and comparison are gathered in **Tab. 4.3** and are explained below.

At first, the quantities $u_{rotor(LES)}$ and $u_{\infty(LES)}$ are determined for each cases, here $u_{\infty(LES)} = u_\infty = 10\,\mathrm{m.s^{-1}}$ since it is evaluated at the sufficiently far upstream entrance of the streamtube. By remodeling **Eq. 4.15**, the velocity at the downstream position can be obtained from the 1D momentum theory:

$$u_{out(1D)} = 2 \times u_{rotor(LES)} - u_{\infty(LES)} \text{ and: } \Delta u_{out(1D)} = \frac{u_{out(1D)} - u_{out(LES)}}{u_{out(LES)}}\,, \tag{4.28}$$

where $u_{out(LES)}$ is the maximal velocity deficit along the streamtube as shown in **Fig. 4.29**. The discrepancies ranged between -11.7% and $+0.5\%$, giving a good overall accordance. For cases with background turbulence, the discrepancies are increasing with the TI, which is expected as the 1D momentum assumes no turbulent mixing in the upstream and downstream regions. Therefore, the expected downstream velocity is higher in LES than for the ideal case obtained from the 1D momentum theory. For the yaw misaligned scenarios, the discrepancies are lower than for the aligned turbine, around 1%. This is interesting as the streamtubes of the yawed turbines are subjected to lateral velocities, in contradiction to the purely axial hypothesis on which relies the 1D momentum theory. The axial induction factor, a is determined from **Eq. 4.16** using $u_{rotor(LES)}$ and $u_{\infty(LES)}$. It is used to determined the thrust coefficient according to the

1D momentum theory, $C_{T(a)}$ according to **Eq. 4.17**. The difference with the actual thrust computed from the wind turbine loads, $C_{T(LES)}$ is expressed as

$$\Delta C_{T(a)} = \frac{C_{T(a)} - C_{T(LES)}}{C_{T(LES)}} \,. \tag{4.29}$$

Another thrust coefficient is computed based on the pressure jump measured from the pressure variation in the streamtube. $C_{T(\Delta p)}$ is obtained from **Eq. 4.13** using the rotor disk surface and Δp, see **Fig. 4.29**. The difference between $C_{T(\Delta p)}$ and $C_{T(LES)}$ is expressed as

$$\Delta C_{T(\Delta p)} = \frac{C_{T(\Delta p)} - C_{T(LES)}}{C_{T(LES)}} \,. \tag{4.30}$$

First of all, the discrepancies observed for $C_{T(a)}$ are between -8% and 5% and show an underprediction of the 1D momentum theory for the yaw misaligned cases and an overprediction when $\gamma = 0°$. Second, $C_{T(\Delta p)}$ has larger discrepancies than $C_{T(a)}$, they range between -30 and -40%. This inconsistency between $\Delta C_{T(a)}$ and $\Delta C_{T(\Delta p)}$ can be related to the way the pressure jump is evaluated from the LES. The streamtube is discretized in slices of finite thickness and these slices are used to integrate the flow quantities.

The volume integral of the pressure over the slice tends to reduce the sharpness of the jump. If the jump is underestimated, the thrust coefficient relying on it will also be underestimated. Yet, even if the streamtube were discretized with finer and finer slices, it would not be possible to reach the requested pressure jump. This is due to the forces mollification on the Eulerian grid, which counters the indefinitely thin rotor disk hypothesis of the 1D momentum theory. It is interesting to note for the misaligned case that the discrepancies are 10% higher, this is the consequence of the transverse pressure force impacting the streamtube, see **Section 4.5.2**. This contradicts the 1D momentum hypothesis, neglecting the side pressure forces on the control volume. In the literature, this term is removed by considering that the streamtube is surrounded by the atmospheric pressure [210] which is not the case in the LES. Finally, the pressure at region (2) does not reach the background pressure, with region (2) defined at the maximum velocity deficit position. Therefore the hypothesis of $p_{out} = p_\infty$ is questionable. Nevertheless, such theory is based on few parameters compared to LES, and the results are acceptable. Further comparison to the general momentum theory with fewer hypotheses than the 1D momentum theory could assess its validity in complex scenarios.

4.6 Conclusions

In this chapter, the wake envelope of a yawed wind turbine is investigated. For this, post-processings based on accurate conservative level set functions are introduced to define the wake. The methodology relies on the tracking of fluid particles crossing the rotor disk, either averaged over time or instantaneous. The tracking functions allow the construction of streamtubes surrounding the wind turbine and the probability of the presence of fluids particles emanating from the rotor. The advantage of this method strategy is triple. First, it allows reducing the amount of information from high-fidelity simulation counting billions of elements. Second, the obtained results are comparable to classical 1D momentum theory for steady, inviscid, and irrotational flows, which are the basis of wake models for the design of modern wind turbines. Finally, such methods are shown to be robust and applicable independently of the turbine operating condition or the inflow turbulence level. These post-processings are then applied to eight cases. The cases investigated are with or without yaw misalignment and different inflow turbulence conditions.

First, the wake envelope is discussed according to the streamtube topology and the turbulent mixing layer expansion. The streamtube section increase from the upstream section until past the turbine where at some point the section starts to reduce. The background turbulence triggers this phenomenon as with increasing turbulence intensity this appears closer and closer to the rotor. Similar observations are made for yaw misaligned turbines, yet the section shape is not circular but kidney-shaped. Furthermore, the streamtubes are deflected independently of the turbulence level. The turbulent mixing layer expansion is discussed using the probability of presence of fluid particles emanating from the rotor. The mixing layer width is evaluated using a reconstructed hyperbolic tangent profile over the probability field. While the width is constant azimuthally for $\gamma = 0°$, this allowed observing the azimuthal variation for yaw misaligned turbines. The turbulent mixing layer width is expanding as the wake pursues downstream the turbine and the expansion rate is correlated to the external turbulence intensity. From this, self-similarity analysis based on the mixing layer width and the averaged velocity and Reynolds stress tensor components will be conducted in future works.

Second, mean momentum and kinetic energy budgets were performed on wind turbine wake streamtubes constructed from high-fidelity LES. Variations of yaw angle or turbulence inflow have shown a similar behavior of the streamtube averaged quantities compared to theory. Indeed, the streamtube expands as it approaches the turbine and a velocity deficit appears. Moreover, the mean kinetic energy budget analysis showed that the wake recovers in different regions downstream of the turbine: I, II, III, and IV. These regions are related to the local vortex structures in the vicinity of the turbine. The first region is where the helicoidal vortices are convected. The second region starts when the vortices start pairing resulting in the production of turbulent kinetic energy. The maximal velocity deficit defines the entrance in the third region. In this region the production of turbulent kinetic energy is maximal. In the last region, considered as the far wake, the wake velocity deficit continues to recover and the turbulence is decaying. The external turbulence level plays a large role in the downstream position of these regions, they appear closer to the rotor as the external turbulence intensity increase. The wake deflection induced by yaw misalignment on a wind turbine is explained through pressure forces and momentum fluxes in the mean horizontal momentum budget. Yet the deflection is not impacted by the increasing external turbulence. The evolution of the streamtube averaged quantities is then compared to the 1D momentum theory. The predicted rotor downstream velocity is shown to be in good accordance with the LES results and the recomputed thurst coefficient based on the axial induction factor have the same tendency. Nevertheless, the thrust coefficient based on the pressure jump within the streamtube is underpredicted compared to LES. Several 1D momentum theory hypotheses are pined out and could explain these discrepancies. Further work should focus on the comparison with the general momentum theory (taking into account the wake rotation) to assess their validity in complex scenarios. This analysis should also help to derive inputs for reduced engineering wake models.

The mesh refinement is investigated throughout this chapter. It showed that if there is background turbulence in the free stream flow, the wake destabilization process is less dependent on the grid resolution. When there is no external turbulence, which is not representative of a real offshore wind condition, the destabilization is delayed downstream with coarser mesh resolution. The destabilization is mainly due to the helicoidal vortices pairing and interacting with each other, with coarse mesh these physical phenomena are not captured in the simulation and impact the larger scales of the flow. Background turbulence triggers the destabilization of the vortices making these scenarios less sensitive to the mesh resolution.

The developed post-processing helped to compare cases with different operating conditions

and to obtain a quantitative alleviation of the wake destabilization process. They are used in the next chapter where an aero-servo-elastic framework is introduced and helped to compare the wake behavior in a close-to-real scenario involving two offshore industrial wind turbines.

Chapter 5

Aero-servo-elastic simulations of yawed wake interactions

This chapter investigates the yaw misalignment impact in a close-to-real scenario. For this matter, the previously used framework of Large Eddy Simulation and Actuator Line Method is coupled to an aero-servo-elastic solver named BHawC. Industrial wind turbines are modeled for this case, with their actual geometry, deformation, and control. At first BHawC solver and the coupling with YALES2 are presented. A scenario of a two turbine row is then investigated. The first scenario of two aligned wind turbines is discussed and compared to representative low order models. To follow up, yaw misalignment is introduced on the first turbine. The wake, loads, and deformations of the turbines are analyzed. The globality of the results is discussed, showing the positive yaw strategy to be relevant for this particular configuration.

Contents

5.1 Introduction . . . 134
5.2 Coupling to a structural solver . . . 135
5.2.1 A Aero-servo-elastic solver: BHawC . . . 135
5.2.2 Coupling between YALES2 and BHawC . . . 136
5.3 Case and Numerical parameters . . . 143
5.3.1 Industrial wind turbine: SWT-6.0-154 . . . 143
5.3.2 Two turbine configuration . . . 143
5.3.3 Numerical setup . . . 144
5.4 Two aligned wind turbines: Reference case . . . 150
5.4.1 Singular events occurring in the flow and wind turbines performances . 150
5.4.2 Flow topology . . . 155
5.4.3 Structural deformations . . . 157
5.4.4 Discussion . . . 162
5.5 Influence of yaw misalignement . . . 162
5.5.1 Flow topology . . . 163
5.5.2 Streamtubes . . . 164
5.5.3 Mean kinetic energy budgets . . . 169
5.5.4 Turbines response and performances . . . 172
5.5.5 Loads repercussions on structural deformations and fatigue . . . 173
5.6 Conclusions . . . 180

5.1 Introduction

The finality of this thesis is to investigate the impact of yaw angle in a close-to-real offshore wind turbine scenario. The previous chapter showed that the actual offshore wind turbine diameters reach hundreds of meters. Until now, the numerical framework was based on the hypothesis of a rigid wind turbine structure. Yet, in the real world, wind turbines blades are deformable. The flapwise deformations, i.e., deformations in the wind direction, can reach tens of meters at the tip. Not to mention those wind turbines are designed such that the induced torsion of the blade needs to be taken into account for the proper estimation of the aerodynamic loads. Furthermore, industrial wind turbines use controllers to adapt the operating point to the inflow conditions. For example, controllers adjust the rotation speed or the blade pitch, reducing or increasing the loads on the structure. These controllers differ from one turbine to another yet are mandatory for increasing the turbine lifetime and having optimal power production.

For this matter, a particular focus will be paid to the impact of yaw misalignment on the structural deformations and controller response. And in a second time, the effect of the deviated wake on the deformations of a downstream turbine will be investigated. A multi-physical approach is necessary to succeed in these investigations, the so-called Aero-Elasticity topic. Several works from the literature review the state of the art in wind turbine aero-elasticity [231, 232]. The central aspect is the strong coupling between the aerodynamic loads and the time-dependent behavior of the wind turbine structure. In the same way as the aerodynamics modeling of horizontal axis wind turbine, there are several ways to model the structural dynamics of a wind turbine:

- the brute force where the discretization of the entire structure is done using the Finite Element Method (FEM) [233, 234, 235],
- the multi-body formulation, where different rigid parts are connected through springs and hinges [236],
- the finite beam element model to describe the blade and tower deflections, which is the case for most wind turbine structural models [237, 129, 238].

Different couplings between structural solver and aerodynamic models are investigated through the literature, and the notion of elastic/deformable actuator line is already present [239, 240, 241]. In this matter, the ALM implemented in the Large Eddy Simulation framework is coupled with an aero-servo-elastic code. This coupling allows to estimate the structural deformations occurring on the turbine blades and relate these to the flow characteristics. The overall structure is modeled using finite beam elements, and the impact of the tower, shaft, and bearings deformations are taken into account. Furthermore, the aero-servo-elastic code includes the same controller as the investigated industrial wind turbine.

This chapter is divided into four parts. The first part presents the servo-elastic solver and the coupling strategy. The second part shows the two industrial wind turbine cases and the numerical setup. The third part investigates the reference scenario of two aligned wind turbines to pave the way for the yaw misalignment study. In this part, comparisons to representative blade element momentum computations are made, and the influence of the fluid mesh resolution is shown. The final part investigates the impact of the first turbine yaw misalignment. The flow topology is discussed by the mean of streamtubes and mean kinetic energy budget. This is followed by comparing the performances, deformations, and fatigue of the wind turbines.

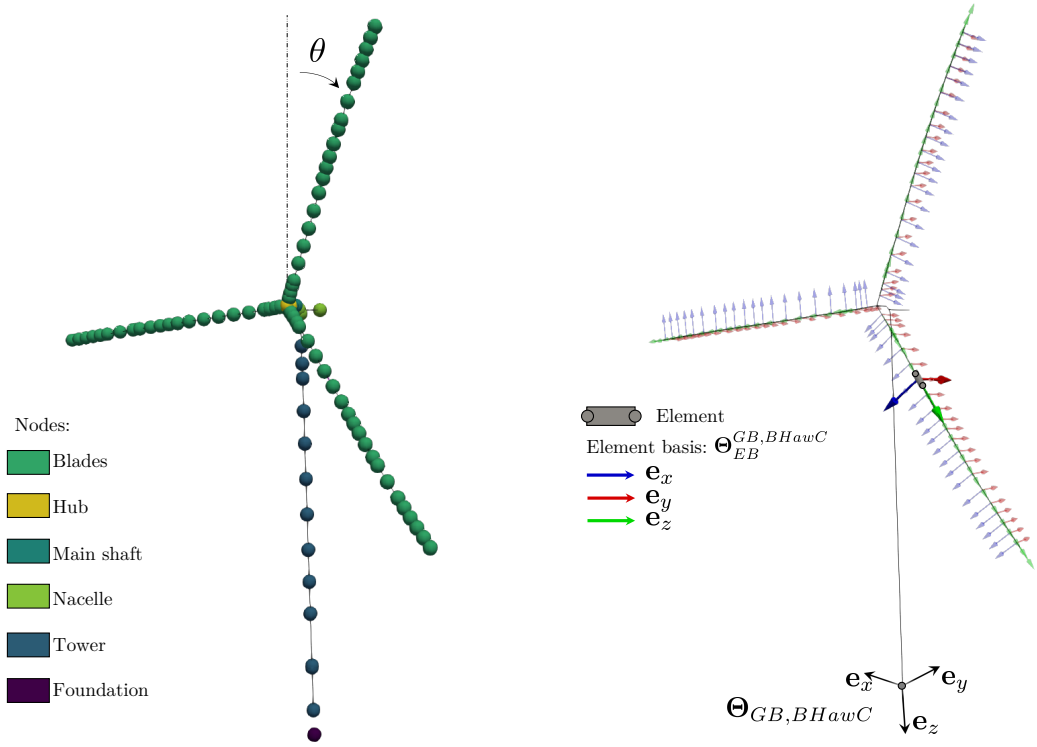

Figure 5.1: Nodes and elements definition in BHawC.

5.2 Coupling to a structural solver

5.2.1 A Aero-servo-elastic solver: BHawC

The nonlinear aeroelastic code BHawC has been developed in-house at Siemens Gamesa Renewable Energy (SGRE). It is used for the design and certification of wind turbines, and it is continuously being validated against measured data. The primary purpose of BHawC is to simulate the dynamic response and calculate the loads on three-bladed wind turbines. The model consists of substructures for foundation, tower, nacelle, drivetrain, shaft, hub, and blades, as shown in **Fig. 5.1**. The structure is modeled primarily with finite beam elements, and the aerodynamics is modeled using blade element momentum theory (BEM) [123]. The coupling presented in the next section aims to replace blade element momentum theory. Moreover, BHawC is coupled to a controller identical to the one of an actual turbine.

5.2.1.1 BHawC structural solver

The finite beam element model in BHawC uses a co-rotational formulation where each element has its coordinate system that rotates with the element. BHawC uses linear two-node Timoshenko beam elements [242] with 12 degrees of freedom: three positions and three rotations in each node. Special elements are introduced where bearings are present, and the drivetrain consists of purely torsional elements [243]. The substructures are connected through a predefined, direct kinematic coupling. All elements structural degrees of freedom are given relative to a global coordinate system, fixed at the turbine base (tower foundation) $\mathbf{\Theta}_{GB,BH}$, where GB denotes the Global Basis and BH is for BHawC. The configuration of the turbine is given by the nodal positions $\mathbf{x}_s$ and orientations $\mathbf{\Theta}_{GB,BH}^{NB}$, and their velocities $\dot{\mathbf{x}}_s$ and accelerations $\ddot{\mathbf{x}}_s$. An overview of the nodes of the different substructures is presented in **Fig. 5.1**, the nodal orientation is obtained from the element orientation expressed as $\mathbf{\Theta}_{GB,BH}^{EB}$. The structural solver

of BHawC aims to satisfy the equilibrium equation in global coordinates as

$$\mathbf{f}_{\text{damp}}\left(\mathbf{\Theta}^{NB}_{GB,BH},\dot{\mathbf{x}}_s\right)+\mathbf{f}_{\text{int}}\left(\mathbf{x}_s,\mathbf{\Theta}^{NB}_{GB,BH}\right)+\mathbf{f}_{\text{iner}}\left(\mathbf{x}_s,\mathbf{\Theta}^{NB}_{GB,BH},\dot{\mathbf{x}}_s,\ddot{\mathbf{x}}_s\right)= \mathbf{f}_{\text{ext}}\left(\mathbf{x}_s,\mathbf{\Theta}^{NB}_{GB,BH},\dot{\mathbf{x}}_s,\ddot{\mathbf{x}}_s\right), \tag{5.1}$$

where $\mathbf{f}_{\text{damp}}$ is the structural viscous damping force vector, $\mathbf{f}_{\text{int}}$ is the internal force related to elastic deformation, $\mathbf{f}_{\text{iner}}$ is the inertial force and $\mathbf{f}_{\text{ext}}$ is the external force majoritairly represented by the aerodynamic and gravity effects. The damping, internal and inertial forces are evaluated at each nodal position according to the given orientation and transformed into the global coordinates. To find the equilibrium implied by **Eq. 5.1** increments of the positions and orientations $\delta\mathbf{x}_s$, velocities $\delta\dot{\mathbf{x}}_s$ and accelerations $\delta\ddot{\mathbf{x}}_s$ are found from a variation of the equilibrium equation and gives the tangent relation

$$\mathcal{M}(\mathbf{\Theta}^{NB}_{GB,BH})\delta\ddot{\mathbf{x}}_s+\mathcal{C}(\mathbf{\Theta}^{NB}_{GB,BH},\dot{\mathbf{x}}_s)\delta\dot{\mathbf{x}}_s+\mathcal{K}(\mathbf{x},\mathbf{\Theta}^{NB}_{GB,BH},\dot{\mathbf{x}}_s,\ddot{\mathbf{x}}_s)\delta\mathbf{x}_s=\mathcal{R} \tag{5.2}$$

where $\mathcal{M}$, $\mathcal{C}$, and $\mathcal{K}$ are the matrices for mass, damping/gyroscopic forces and stiffness respectively. The residual vector is equivalent to $\mathcal{R}=\mathbf{f}_{\text{ext}}-\mathbf{f}_{\text{damp}}-\mathbf{f}_{\text{int}}-\mathbf{f}_{\text{iner}}$. The stiffness matrix consists of constitutive, geometric, and inertial stiffness. Where the geometric stiffness is related to internal and external forces. The system is updated using a Newton-Raphson iterative process [244] and combined with a suitable solution procedure [245] to predict $\delta\dot{\mathbf{x}}_s$ and $\delta\ddot{\mathbf{x}}_s$ and recuce the problem to the determination of $\delta\mathbf{x}_s$. At each step the matrices and residual are updated to reflect the new state of the system. In practice, BHawC standalone does not revaluate the aerodynamics external forces at each iterative step. In a massively parralel framework this is not afordable, yet it will be discussed in the coupling section. When $\mathcal{R}\sim 0$ the system is considered at equilibrium. Increments to the rotations in $\delta\mathbf{x}_s$, which are assumed infinitesimal, are for each node represented as a rotation pseudo-vector, whose direction determines the axis of rotation and whose length determines the magnitude of rotation. The nodal positions $\mathbf{x}_s$, velocities $\dot{\mathbf{x}}_s$ and accelerations $\ddot{\mathbf{x}}_s$ are updated by regular addition of the positional part of $\delta\mathbf{x}_s$, $\delta\dot{\mathbf{x}}_s$ and $\delta\ddot{\mathbf{x}}_s$, respectively, as determined by the solution procedure. For further details on BHawC structural solver, see the Ph.D. thesis of Skjoldan [246].

5.2.1.2 BHawC aerodynamic solver

In BHawC, the aerodynamic forces are initially computed from the BEM approach, determining the tangentially and axially induced velocities at aerodynamic calculation points. These aerodynamic calculation points are positioned independently of the structural nodes on the blades. The number of points changes depending on the turbine blades geometry. To take into account tip loss effect, thrust correction at high induction values, and tower shadow effect, various corrections are implemented. Yet, it does not enable to study of the wake interactions between rows of turbines, and this is why the coupling with the ALM in an LES framework is relevant. Moreover, several various 3D effects (tower shadow effect, terrain, induction of a skewed wake) corrected in the BEM are, by definition, already taken into account by ALM and LES. The following section presents the coupling strategy designed and implemented during this PhD thesis.

5.2.2 Coupling between YALES2 and BHawC

This coupling aim at taking into account the deformation of the blades in an extended LES framework and investigating the impact on the generated wake. Accordingly, loose two-way coupling between the aerodynamic solver YALES2 and the servo-elastic solver BHawC has been designed for this purpose. It is presented hereafter.

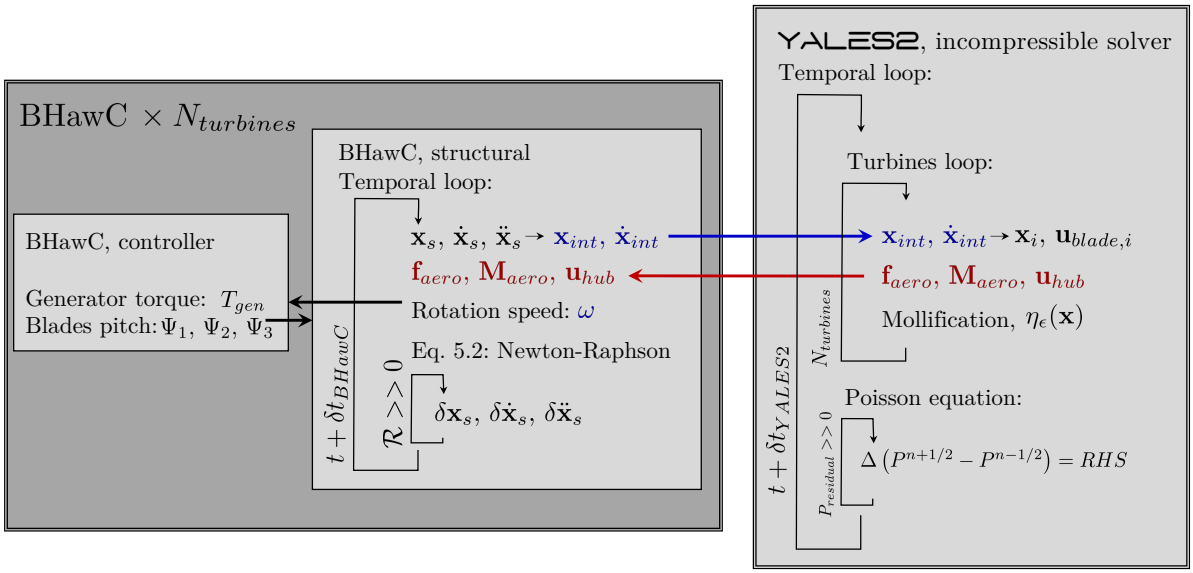

Figure 5.2: Coupling strategy between YALES2 and BHawC.

5.2.2.1 Coupling strategy

The goal is to replace the aerodynamic resolution based on BEM from BHawC with the forces computed through the ALM in YALES2. In addition to that, the blade shape and displacement will no longer be computed in YALES2 but given by BHawC to take into account the deformations and control. **Fig. 5.2** presents the coupling strategy. This strategy is referred to as the Conventional Serial Staggered (CSS) procedure discuss in [247]. The coupling is achieved using MPI to handle the communications between processors, depicted by red and blues arrows in **Fig. 5.2**. It is important to mention that YALES2 can deal with several turbines while BHawC is not. This is why separated instances of BHawC are launched for each turbine, while all YALES2 processors are aware of all the wind turbines. The current implementation of the coupling handles an arbitrary number of turbines and is conceived to be efficient for massively parallel simulations, which are required by high-fidelity simulations. By using the communicator splitting, the simulation processors allow the following communications: YALES2-YALES2, first turbine BHawC-YALES2, ..., nth turbine BHawC-YALES2. As a consequence, a coupled simulation with $N_{turbines}$ the number of turbines has $N_{turbines} + 1$ communicators. The number of processors requested for this is $N_{turbines}$ plus the number requested for the flow simulation depending on the fluid mesh. This process is displayed in **Fig. 5.3**. The data sent from BHawC to YALES2 is broadcasted to all YALES2 processors. In the other way, BHawC receives only the Forces known by one YALES2 processor, one for each turbine. It is essential to remind that the cost of the structural solver is negligible compared to the resolution of the flow. The following section presents the initialization and connectivity between the actuator element and the structural mesh and how the data is exchanged during the temporal loop.

5.2.2.2 Implementation

- **Initialisation**

Once the MPI communicators are registered for each turbine, the coupling needs to build the connectivity between the actuator element positions and the structural nodes, see **Fig. 5.4**. The number of structural nodes (■) and aerodynamic nodes (●) is not the same, and usually,

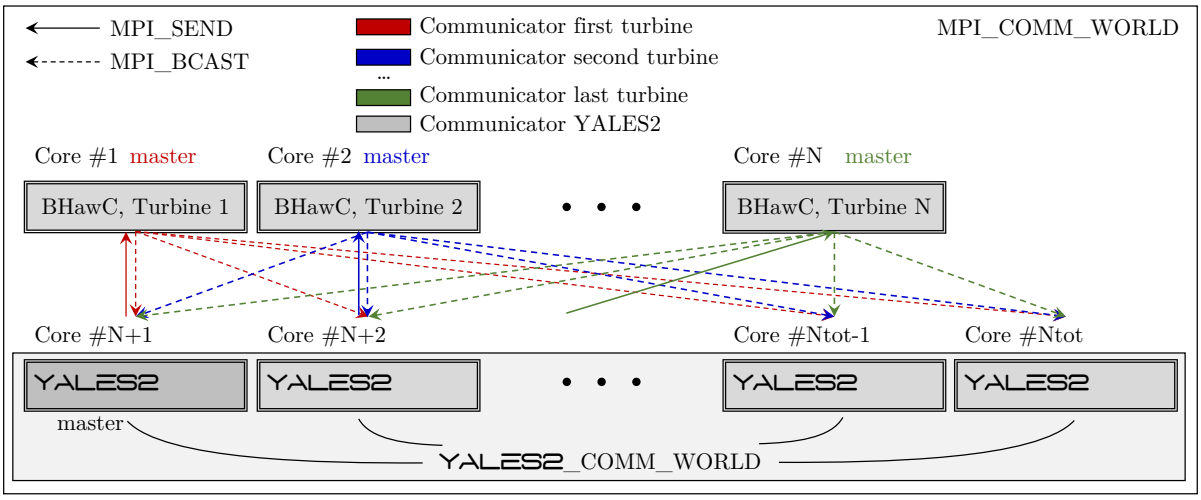

Figure 5.3: Communications during the coupling of YALES2 and BHawC for N turbines and $Ntot$ processors.

aerodynamic nodes outnumber the structural nodes. The BHawC model of the D6-154 blade used in the following applications is discretized into 19 linear elements, while the blades in YALES2 are discretized with 75 elements. The aerodynamic loads need to be transferred to the structural nodes. With this aim, BHawC builds an intermediate mesh based on the number of aerodynamic elements sent by YALES2. The intermediates nodes ($\star$) are placed on the structural elements and at the same radial position as the aerodynamic elements on the blade. Then, based on the structural properties of the beam the distributed aerodynamic loads on the structural elements are transferred to the structural nodes [248]. Moreover, the beam elements are straight, and an elastic axis defines the actual shape and curvature of the structure. When solving **Eq. 5.2**, BHawC needs to obtain the aerodynamic induced moments on this axis. The projection of the intermediate nodes on the elastic axis is presented as ($\circledcirc$). It is essential to mention that the distance between the structural element and the elastic axis is constant in the structural element reference frame along time. Therefore, several vectors and matrices[1] need to be computed to build the connectivity between those meshes, see **Fig. 5.4**.

The first quantity to initialize is the transformation matrix $\mathcal{M}_{st\to aero}$ between the structural and the aerodynamic element orientation. In BHawC, the structural orientation does not consider the aerodynamic twist and has a structural twist based on the blade materials. BHawC reads the structural orientation of the intermediate mesh in the blade basis from input files and sends to YALES2 $\mathbf{\Theta}_{B_j,BH}^{E_{ij},int,BH} = (\mathbf{e}_{c,st}, \mathbf{e}_{t,st}, \mathbf{e}_{s,st})$. In the meantime, YALES2 reads the aerodynamic orientation of the airfoils $\mathbf{\Theta}_{B_j,Y2}^{E_{ij},Y2} = (\mathbf{e}_c, \mathbf{e}_t, \mathbf{e}_s)$, taking into account the aerodynamic twist. From this the transfer matrix from the structural intermediate nodes to the aerodynamic element can be computed as

$$\mathcal{M}_{st\to AL} = \mathbf{\Theta}_{B_j,BH}^{E_{ij},int,BH} \Big|_{t=0}^{-1} \mathbf{\Theta}_{B_j,Y2}^{E_{ij},Y2} \Big|_{t=0} . \tag{5.3}$$

[1]Here is the notation used for transfer matrix, basis, and vectors. Transfer matrix from basis A to basis B is expressed as $\mathbf{\Theta}_A^B$. The inversion of the transfer matrix $\mathbf{\Theta}_A^B$ gives the transfer matrix from B to A as $\left(\mathbf{\Theta}_A^B\right)^{-1} = \mathbf{\Theta}_B^A$. A vector $\mathbf{x}_B$ in basis B can be expressed in basis A as $\mathbf{x}_A = \mathbf{\Theta}_A^B \mathbf{x}_B$.Transfer matrix can be combined such that $\mathbf{\Theta}_A^B \mathbf{\Theta}_B^C = \mathbf{\Theta}_A^C$. In addition to that: E_{ij} denotes the basis of the ith Element on the jth blade, B_j the basis of the jth Blade, R the rotor basis, and G the Global basis. This is supplemented by the reference domain, $Y2$ if it is YALES2 or BH if it is BHawC. As an example: $\mathbf{\Theta}_{G,Y2}^{E_{ij},int,BH}$ is the transfer matrix from YALES2 Global basis to the basis of the i intermediate Element of the j blade defined in BHawC.

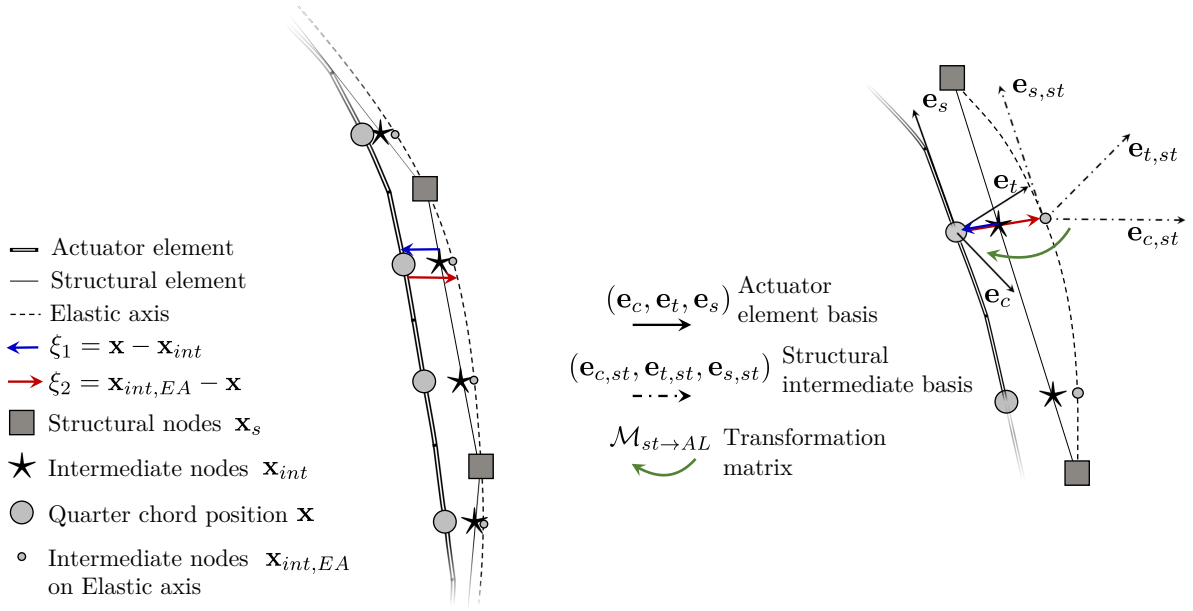

Figure 5.4: Connectivity between BHawC structural mesh and YALES2 actuator line elements.

This matrix allows recomputing the deformed aerodynamic twist when the structural orientation changes (see the temporal loop implementation for more).

The second quantity is the vector $\boldsymbol{\xi}_1$, which is the distance in the aerodynamic element basis between the intermediate nodes $\mathbf{x}_{int}$ and the actuator element $\mathbf{x}$ known by YALES2. In the same way as for $\mathcal{M}_{st\to AL}$, BHawC sends $\mathbf{x}_{int}$ in the blade basis read from input files, and YALES2 computes $\boldsymbol{\xi}_1$ with $\mathbf{x}$ in the blade basis as well:

$$\boldsymbol{\xi}_1 = \boldsymbol{\Theta}_{G,Y2}^{E_{ij},Y2} \Big|^{-1} \left[\boldsymbol{\Theta}_{G,Y2}^{B_j,Y2} \left(\mathbf{x} - \mathbf{x}_{int} \right)_{B_j,Y2} \right] . \tag{5.4}$$

This translation vector allows recomputing the quarter of chord position from the deformed blade structure.

The last data is the vector $\boldsymbol{\xi}_2$, which is the distance from the intermediate nodes projected on the elastic axis to $\mathbf{x}$ in the aerodynamic element basis:

$$\boldsymbol{\xi}_2 = \boldsymbol{\Theta}_{G,Y2}^{E_{ij},Y2} \Big|^{-1} \left[\boldsymbol{\Theta}_{G,Y2}^{B_j,Y2} \left(\mathbf{x}_{int,EA} - \mathbf{x} \right)_{B_j,Y2} \right] . \tag{5.5}$$

This translation allows YALES2 to send the aerodynamic moments on the elastic axis, which BHawC requests. This connectivity step is performed once, during the coupling initialization. It is based on the hypothesis that $\boldsymbol{\xi}_1$, $\boldsymbol{\xi}_2$, and $\mathcal{M}_{st\to AL}$ are constant in the aerodynamic element basis along time.

After the connectivity, the transfer matrix between YALES2 and BHawC has to be set since they do not share the same global basis. BHawC is tailored for single turbine analysis, and thereby the domain is the same and centered on the turbine, independently of the configuration. In YALES2, several turbines can be defined at different positions and orientations. Thereby, the transfer matrix for one turbine is defined as:

$$\boldsymbol{\Theta}_{G,Y2}^{G,BH} = \boldsymbol{\Theta}_{G,Y2}^{R,Y2} \begin{bmatrix} 0 & 0 & -1 \\ 1 & 0 & 0 \\ 0 & -1 & 0 \end{bmatrix} . \tag{5.6}$$

As well, the translation from BHawC foundation towards YALES2 foundation is set as:

$$\mathbf{x}_{tr,BH\to Y2} = \mathbf{x}_{found,Y2} - \boldsymbol{\Theta}_{G,Y2}^{G,BH} \mathbf{x}_{found,BH} , \tag{5.7}$$

where $\mathbf{x}_{found,BH}$ is the foundation position in BHawC global coordinates and $\mathbf{x}_{found,Y2}$ is the foundation position in YALES2 global coordinates. Since each BHawC instance deals only with one turbine $\mathbf{x}_{found,BH}$ is always set at the origin of BHawC global coordinates and thereby equal to zero which gives:

$$\mathbf{x}_{tr,BH\to Y2} = \mathbf{x}_{found,Y2}\,. \tag{5.8}$$

- **Temporal loop**

The temporal loop is decomposed similarly to the standard actuator line method implemented in YALES2, see Chapter 2. The differences in each step are presented below. The actual time iteration is n.

1 **Local velocity evaluations:** In a similar way as in the standard methodology, the gas velocity is evaluated from the Eulerian grid at the actual blade position, i.e., at the position of the mollification kernel center of the last time iteration $n-1$. Then the blade velocity, $\mathbf{u}_{blade,ij,G,Y2}$ is set according to the velocity sent by the structural solver at the previous step; see step three. At the beginning of the simulation, the blade velocity is null.

2 **Force computations:** The forces are computed as in the standard methodology and registered in the aerodynamic element basis.

3 **Blade displacement:** It is during this step that most of the coupling takes place. YALES2 needs to advance the blades to mollify the forces, while BHawC requests the external forces applied at this new position. Thereby, the message exchange is the following:

- **BHawC → YALES2:** The structural solver sends the blade basis $\mathbf{\Theta}^{B_j,BH}_{G,BH}$, the blade root position $\mathbf{x}_{br,j,G,BH}$, the positions of the intermediate nodes in the blade basis $\mathbf{x}_{int,ij,B_j,BH}$, the orientation of the intermediate node in the blade basis $\mathbf{\Theta}^{E_{ij},int,BH}_{B_j,BH}$, the intermediate node translational velocity $\mathbf{u}_{int,ij,G,BH}$ and angular velocity $\boldsymbol{\omega}_{int,ij,G,BH}$ at the new position. Then, from the initialized connectivity the following operations arise: The blade root in BHawC global basis is transfered in YALES2 global basis as follow:

$$\mathbf{x}_{br,j,G,Y2} = \mathbf{\Theta}^{G,BH}_{G,Y2}\,\mathbf{x}_{br,j,G,BH} + \mathbf{x}_{tr,BH\to Y2}\,. \tag{5.9}$$

The blade basis orientation in BHawC global basis is transfered in YALES2 global basis as follow:

$$\mathbf{\Theta}^{B_j,BH}_{G,Y2} = \mathbf{\Theta}^{G,BH}_{G,Y2}\,\mathbf{\Theta}^{B_j,BH}_{G,BH}\,. \tag{5.10}$$

The aerodynamic element i of blade j orientation in YALES2 global basis is expressed according to the orientation of the intermediate node in the blade basis.

$$\mathbf{\Theta}^{E_{ij},Y2}_{G,Y2} = \mathbf{\Theta}^{B_j,BH}_{G,Y2}\,\mathbf{\Theta}^{E_{ij},int,BH}_{B_j,BH}\,\mathcal{M}_{st\to AL}\,. \tag{5.11}$$

Once the aerodynamic element orientation is computed, the position of the aerodynamic elements is recomputed from the position of the intermediate nodes:

$$\mathbf{x}_{ij,G,Y2} = \mathbf{\Theta}^{B_j,BH}_{G,Y2}\,\mathbf{x}_{int,ij,B_j,BH} + \underbrace{\mathbf{\Theta}^{E_{ij},Y2}_{G,Y2}\boldsymbol{\xi}_1}_{(\star)} + \mathbf{x}_{br,j,G,Y2}\,, \tag{5.12}$$

where, the $(\star)$ term in the following equation corresponds to the distance between the intermediate node and the aerodynamic element on YALES2 global basis. The last

quantity is the aerodynamic element velocity. BHawC sends two types of velocities at the positions of the intermediate nodes: the translational velocity and the angular velocity. Since the translational velocity is given at the intermediate node, a correction ($\star\star$) based on the distance between the aerodynamic element and the intermediate node is computed using the angular velocity. Thereby, the velocity at the aerodynamic element in YALES2 global basis is given as:

$$\mathbf{u}_{blade,ij,G,Y2} = \mathbf{\Theta}_{G,Y2}^{G,BH}\mathbf{u}_{int,ij,G,BH} + \underbrace{\mathbf{\Theta}_{G,Y2}^{G,BH}\boldsymbol{\omega}_{int,ij,G,BH} \times \mathbf{\Theta}_{G,Y2}^{E_{ij},Y2}\boldsymbol{\xi}_1}_{(\star\star)} . \tag{5.13}$$

- **YALES2 → BHawC:** Once all the positions, vectors, and basis are updated, YALES2 projects the element basis forces computed earlier in YALES2 global basis:

$$\mathbf{F}_{ij,G,Y2} = \mathbf{\Theta}_{G,Y2}^{E_{ij},Y2}\mathbf{F}_{ij,E_{ij},Y2} . \tag{5.14}$$

This is the force in the global basis that will be mollified on the Eurlerian grid. The local moment, at the quarter of chord position in the element basis of YALES2, is projected in the global basis and the lever arm to the elastic axis is added ($\star\star\star$). From this, the moment on the elastic axis in the global basis of YALES2 is computed as follow:

$$\mathbf{M}_{ij,G,Y2}(\mathbf{x}_{int-EA,ij,G,Y2}) = \mathbf{\Theta}_{G,Y2}^{E_{ij},Y2}\left(\mathbf{M}_{ij,E_{ij},Y2}(\mathbf{x}_{ij,G,Y2}) + \underbrace{\boldsymbol{\xi}_2 \times \mathbf{F}_{ij,E_{ij},Y2}}_{(\star\star\star)}\right) . \tag{5.15}$$

These two quantities are then projected from YALES2 global basis to BHawC global basis and sent to the structural solver:

$$\begin{aligned} \mathbf{F}_{ij,G,BH} &= \mathbf{\Theta}_{G,BH}^{G,Y2}\mathbf{F}_{ij,G,Y2} , \\ \mathbf{M}_{ij,G,BH}(\mathbf{x}_{int-EA,ij,G,BH}) &= \mathbf{\Theta}_{G,BH}^{G,Y2}\mathbf{M}_{ij,G,Y2}(\mathbf{x}_{int-EA,ij,G,Y2}) . \end{aligned} \tag{5.16}$$

However, preliminary simulations showed the angles of attack along the blades to fluctuate too much, leading to time-step size correlated frequencies in the computed aerodynamic loads. As a consequence, premature failures of the structural solver have been observed. To fix this issue, a simple relaxation mechanism is implemented and applied to the forces and moments computed at all actuator points. This solved the premature failures of the structural solver, especially during the initial transient of the simulation. The relaxation is formulated as follows:

$$g(t) = (1-\gamma)\, f(t) + \gamma\, g(t - \Delta t_{Y2}) . \tag{5.17}$$

where Δt_{Y2} is the time step used in YALES2, and $\gamma \in [0, 1]$ is the relaxation coefficient. The function $f(t)$ represents an aerodynamic force or moment, computed above. The function $g(t)$ stands for the corresponding force or moment that is actually mollified and sent to BHawC. The previously stated relaxation equation is equivalent to a first-order low pass filter where the cutoff frequency $f_c(\Delta t_{Y2}, \gamma)$ is given by:

$$f_c(\Delta t_{Y2}, \gamma) = \frac{1}{2\pi}\left[\frac{1-\gamma}{\Delta t_{Y2}\,\gamma}\right] \tag{5.18}$$

Figure 5.5: Picture of several SWT-6.0-154 gathered in an offshore wind farm, taken from Siemens Gamesa Renewable Energy website.

The relaxation coefficient is set to $\gamma = 0.5$, and the time step Δt_{Y2} is set to 0.02 s, equal to the time step Δt_{BH} commonly used in BHawC for a wind turbine dynamic response analysis. It should be mentioned that those values comply with the flow CFL condition for the later-on considered wind speed. It also complies with the particle CFL condition (see Chapter 2). Such values lead to a cutoff frequency $f_c \approx 8$ Hz. Such cutoff frequency remains higher than the relevant natural frequencies of the turbine. The isolated blades natural frequencies for a representative offshore academic wind turbine (DTU10MW) are between 0.6 and 6.6 Hz [213]. Such range includes the 4th flap mode, the 3rd edge mode, and the 1st torsion mode. For the whole turbine system, the natural frequencies are below 2 Hz [213, 249]. For the SWT-6.0-154 wind turbine, the range is similar and the 8 Hz cutoff frequency should not be impacting up to the 4th flap and edge modes of the blades.

4 Force mollification: The forces are then mollified at the quarter chord position, $\mathbf{x}_{ij,G,Y2}$.

A substepping strategy similar to the one presented in Chapter 2 can be used in the coupling. The slight difference is that the substep number is a multiple of the time step ratio between BHawC and YALES2. As aforementioned, the time step of BHawC is constant during the simulation and set to 0.02 s. This is roughly six or seven times lower than the one of YALES2, depending on the tip speed ratio and the blade deformation. With the maximum number of substep, the structural solver often diverges since forces in the element basis are updated only once every $N_{substep}$. Preliminary studies show that a maximum substepping value of two does not impact the flow physics or play a significant role in the blade deformations. Yet, no substep is used in the following since the substepping requires further validations.

Validation of the coupling under laminar inflow compared to BEM results was conducted but not presented here. The validation over field measurements is about to be published. The following section applies this coupling to a two wind turbines array, the first being misaligned with the wind. A comparison to a representative BEM is conducted for the reference case.

Case	Structure	γ_{T_1} [°]	γ_{T_2} [°]	Δt_{Y2} [s]	Δt_{BH} [s]	t_{max} [s]
(REF)	Deformable	0	0	0.02	0.02	550+1100
$(+\gamma)$	Deformable	+20	0	0.02	0.02	550+1100
$(-\gamma)$	Deformable	-20	0	0.02	0.02	550+1100

Table 5.1: Operating conditions for the different configurations of $T1$ and $T2$ investigated. Convergence and statistics accumulation time is expressed as t_{max}

5.3 Case and Numerical parameters

5.3.1 Industrial wind turbine: SWT-6.0-154

The three-bladed turbine SWT-6.0-154, illustrated in **Fig. 5.5**, has a 6MW nominal power output for a diameter D of 154 m, giving a swept area of 18 600 square meters. This wind turbine is widely present worldwide in various wind farms: Westermost Rough, England; Gode Wind I/II, Germany; Formosa 1, Taiwan; and plenty others. This turbine is designed for a wind class type I,S with a nominal power achievable with wind speed above 13 m.s^{-1}. This is a direct drive turbine, i.e. without a gearbox, and the power regulation is enabled through a variable rotation speed and pitch control. With the coupling, the target rotation speed and pitch angles are set according to the same controller as the actual turbine. The hub height depends on the site, yet in this study is set at $h_{hub} = 105.52$ m above the mean sea level. The blades length are 75 meters long, $L_{Blade} = 75$m. Due to confidentiality reasons, the blade geometry, tower sections, nacelle shape, and controller regions are not given. Yet, other pieces of information can be found on SGRE website. The following results are normalized according to the turbine reference operating conditions.

5.3.2 Two turbine configuration

The flow interaction with two wind turbines is investigated in this chapter. The computational domain dimensions are $L_x \times L_y \times L_z = 20D \times 10D \times 7D$ m^3 with x the streamwise direction, see **Fig. 5.6**. The first wind turbine, $T1$ is located at the origin of the computational domain: $(x, y, z)_{T1} = (0D, 0D, h_{hub})$. The distance between $T1$ and the inlet of the domain is $5D$. The yaw angle definition is counterclockwise looking from above the turbine. Various operating conditions are considered for this turbine from yaw angle variations ($\gamma_{T1} = -20°, 0°, +20°$) or blade rigidity. The second wind turbine, $T2$ is downstream $T1$ at a distance of five diameters giving $(x, y, z)_{T2} = (5D, 0D, h_{hub})$. This second turbine remains aligned with the wind for all cases ($\gamma_{T2} = 0°$). The domain outlet is located $10D$ behind $T2$. The streamwise reference velocity of 13 m.s^{-1} is slightly above the rated wind speed of the turbines. Therefore, $T1$ is expected to be at nominal power, while $T2$ should be impacted by the first turbine wake. A total of four configurations are investigated, which are listed in **Tab. 5.1**. The reference case denoted (REF) corresponds to $\gamma_{T1} = 0°$ and deformable blades for $T1$ and $T2$. Case $(+\gamma)$ corresponds to the positive yaw angle case: $\gamma_{T1} = +20°$ and deformable blades for $T1$ and $T2$. And finally, case $(-\gamma)$ corresponds to the negative yaw angle with $\gamma_{T1} = -20°$ and deformable blades for $T1$ and $T2$. At first, the reference case is investigated in terms of mesh refinement and comparison to BEM results. Then, the comparison to (REF) of cases $(+\gamma)$ and $(-\gamma)$ permits to draw conclusions on yawing strategies in this particular configuration.

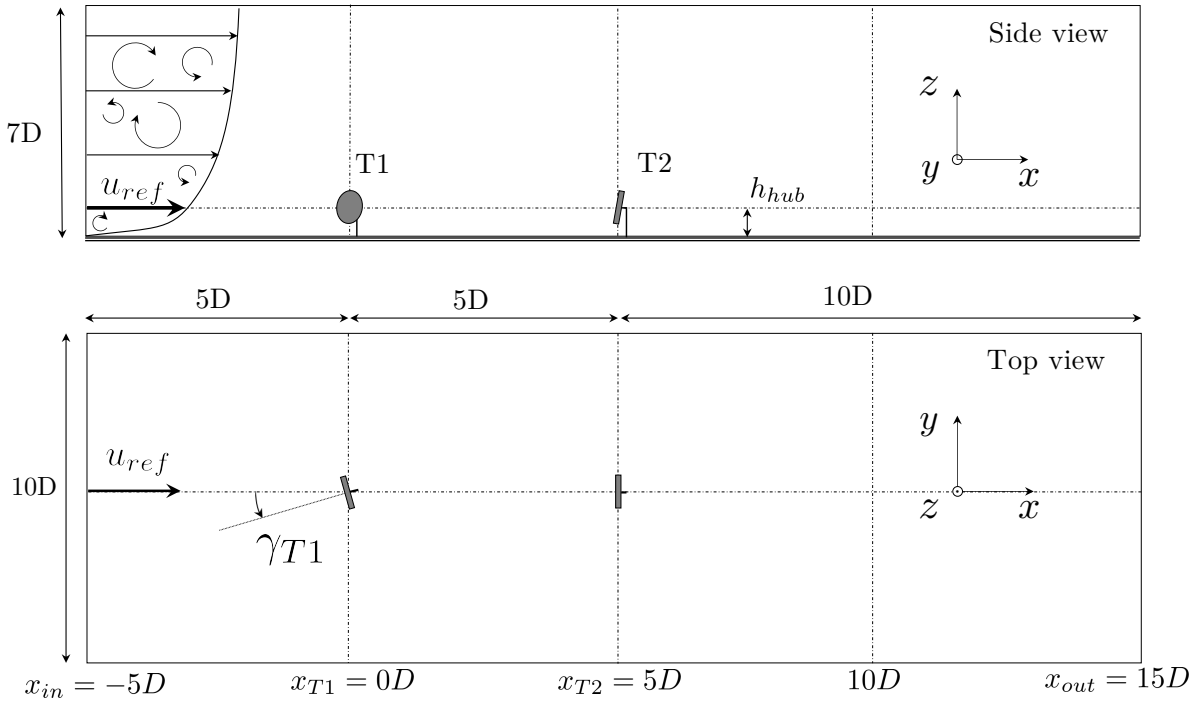

Figure 5.6: Computational domain for the two turbines configuration, (top) side view and (bottom) top view of the domain.

5.3.3 Numerical setup

The numerical parameters used in the coupling between YALES2 and BHawC are the following.

5.3.3.1 Servo-Structural solver

The structural solver mesh is composed of 19 linear elements per blade. The tower, nacelle, shaft, and hub are composed of 15 and 8 nodes with particular elements characterizing the different bearings and actuators to model the turbine motion adequately. The displacement of the tower and nacelle are small. From the simulations the top tower maximum displacement is below 30 cm with fluctuations around 10 cm. The yaw and tilt bearings are set as almost rigid by increasing their stiffness, the resulting variations of yaw are below 0.001°. Damping is used during the initialization of the flow in the domain. The damping is used to dampen the initial fluctuations related to the transient state. In BHawC, the damping matrix $\mathcal{C}$ from **Eq. 5.2** is based on the classical Rayleigh damping definition, and can be expressed as:

$$\mathcal{C} = \alpha_{damp}\mathcal{M} + \beta_{damp}\mathcal{K}\,, \tag{5.19}$$

where α_{damp} and β_{damp} are the damping coefficients of mass and stiffness defined for each component of the wind turbine model. During this structural damping of 200 s the stiffness coefficient β_{damp} is multiplied by ten for all elements and is linearly decreasing to the real values. This allows preventing the structural solver from diverging when stiff flow variations arrive at the turbine position, see **Section 5.4.1**. The gravity is enabled on the structure and the acceleration set at $g = 9.82\,\mathrm{m.s^{-2}}$, representative of the Sweden lattitude.

Case	D/h_{wake} [−]	D/h_{floor} [−]	D/h_{ext} [−]	$N_{elements}$ $\times 10^6$	N_{nodes} $\times 10^6$
$REF0$				30	9
$+\gamma 0$	38	20	2	29	8
$-\gamma 0$				29	8
$REF1$				240	62
$+\gamma 1$	77	40	4	233	60
$-\gamma 1$				232	60
$(-\gamma 2)$	154	80	8	1 857	478

Table 5.2: Cell size in the different regions of the mesh for all cases and the resulting meshes sizes based on these metrics.

Turbulence box	unit	x	y	z
Resolution	[−]	1024	256	256
Length	[m]	46D	10D	10D
$\langle u_i \rangle$	[m.s^{-1}]	13.0	0	0
$\langle TI_i \rangle = \langle u_i'^2 \rangle^{1/2} / \langle u_x \rangle$	[%]	6.22	4.67	3.33
$\langle L_{u_i u_i} \rangle$	[m]	250.0	97.3	58.0

Table 5.3: Integrated quantities over the all synthetic turbulence box generated with Mann's algorithm.

5.3.3.2 Flow solver

The numerical domain is constructed according to the dimensions mentioned above. Different cell sizes are used in the fluid regions: the close wake, the floor, and the upstream turbulence. Moreover, each configuration is performed over two levels of mesh refinement, $(-\gamma 0)$ denotes the coarse mesh, and $(-\gamma 1)$ denotes the fine mesh. For case $(-\gamma 1)$, a supplementary level of refinement $(-\gamma 2)$ was launched until the convergence of the flow and will be used only for qualitative observations. The different cell sizes are gathered in **Tab. 5.2**. According to the requested cell sizes, the meshes are generated using the procedure presented in **Appendix B.** Finally, the obtained meshes number of elements and nodes for cases (REF), $(+\gamma)$, and $(-\gamma)$ are gathered in **Tab. 5.2**.

The subgrid-scale model used for the simulation is the Dynamic Smagorinsky model presented in Chapter 2. The CFL number is below 1.0 for all simulations with a fixed timestep of 0.02 s. Yet, higher timesteps are not achievable due to the coupling to BHawC. The fluid density is $\rho = 1.225\,\text{kg.m}^{-3}$ and the kinematic viscosity is $\nu = 1.517 \times 10^{-5}\,\text{m}^2\text{.s}^{-1}$. The boundary conditions are the same for all configurations, and the parameters are presented hereafter.

- **Boundary conditions**

The idea of the application is to observe how the wake and structure behave in a close to reality configuration. In this matter, the turbines are placed in a sheared turbulent flow. The turbulent fluctuations impacting the turbines are generated using the anisotropic synthetic turbulence emulated with Mann's algorithm [215]. The ground roughness length for the generation of the tubulence box is set to $z_0 = 5 \times 10^{-4}\,\text{m}$ [250], the mean wind speed is $u_{ref} = 13\,\text{m.s}^{-1}$ and the height above the ground is $z = 105.52\,\text{m}$, corresponding to the hub height of the rotor. The box size is $46D \times 10D \times 10D$ with a resolution in the lateral and vertical direction of $\Delta = 6\,\text{m}$.

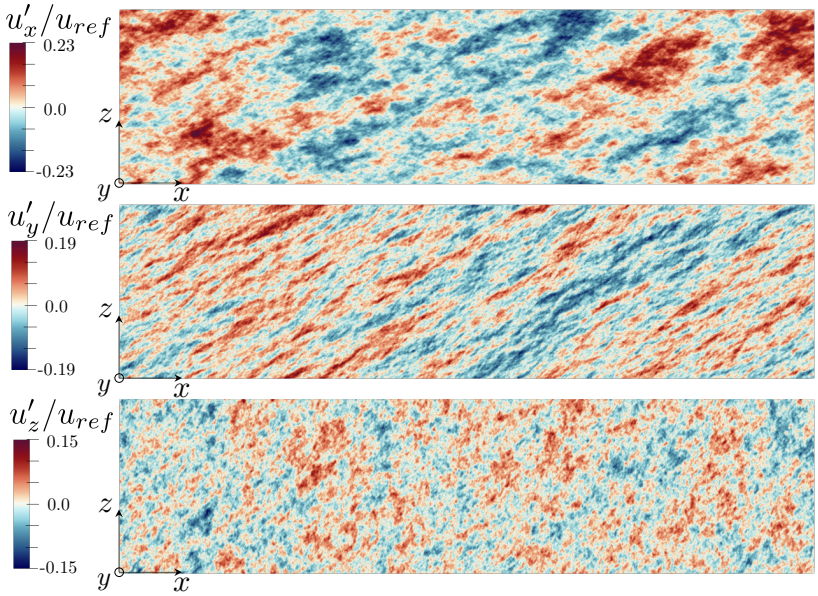

Figure 5.7: Vertical slice of the synthetic turbulence box colored by velocity fluctuations in the three direction (top) streamwise, (middle) transverse and (bottom) vertical.

The turbulence box given by the Mann algorithm has a resolution of 256 points in the lateral and vertical direction and 1024 in the streamwise direction. The statistics of the resulting velocity fluctuations do not vary with the height of the box, and on the whole vertical length, are typical of those observed in a neutral atmospheric flow. The generated turbulence box is displayed in **Fig. 5.7** as slices colored by the velocity fluctuations in the three different directions. The turbulent properties of the injected turbulence box are gathered in **Tab. 5.3**. The turbulence box flow-through time is estimated using the streamwise length L_x and the reference velocity u_{ref} and gives $\tau_{Mann} = L_x/u_{ref} = 545\,\mathrm{s}$.

The fluctuations are then added to a mean shear velocity profile as follow:

$$\mathbf{u}(x,y,z) = u_{ref}\left(\frac{z}{h_{hub}}\right)^{\alpha}\mathbf{e}_x + \mathbf{u}'(x,y,z)\,, \tag{5.20}$$

where h_{hub} is the hub height above the sea level and the power-law coefficient $\alpha = 0.13$, which is a typical value for neutral atmospheric flow in offshore conditions as shown by Stull [251]. Combining synthetic fluctuations with shear velocity profile does not give the best level of fidelity for the free-stream turbulence, since the turbulence and velocity profile might evolve along the streamwise direction. In a specific configuration without turbines, **Fig. 5.8** depicts the vertical profiles of average streamwise velocity and fluctuations at different locations in the streamwise direction. The time-averaged velocity and fluctuations are well transported, especially in the rotor regions. A slight evolution of the profiles is observed in the computational domain, yet the results are sufficient for this study. In the rotor region, the streamwise fluctuations are ranged between five and six percent turbulent intensity while the target power law is emulated correctly. This methodology for the emulation of ABL flow should not be used for larger domains, i.e., in the case of wind farms simulations. Other methodologies, such as recycling or precursor methods are recommended [252, 253, 254] for such cases since the injected turbulence, and velocity profiles are fully developed already.

The other boundary conditions are the following. The ground boundary of the domain is using a wall model to take into account the same roughness, $z_0 = 5\times10^{-4}\,\mathrm{m}$ as for the generation

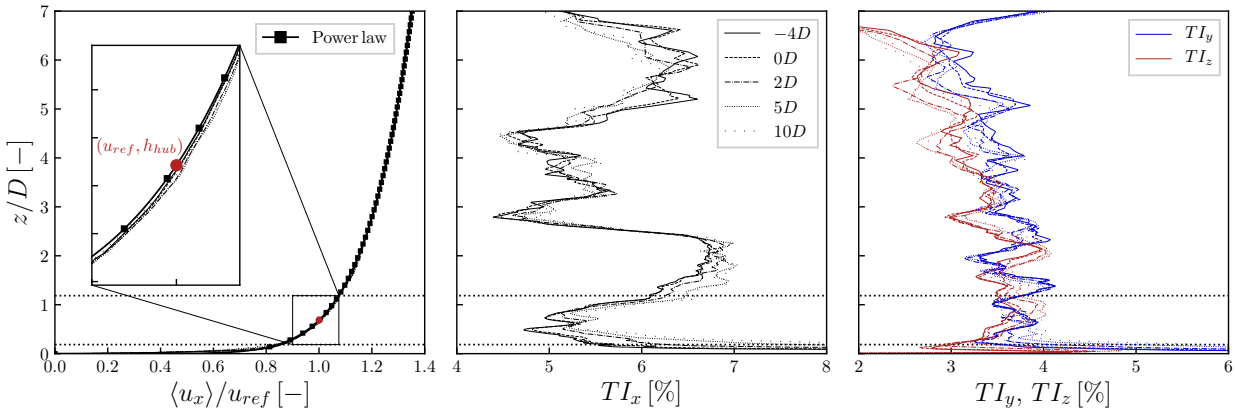

Figure 5.8: Vertical profiles of (left) averaged streamwise velocity, (middle) streamwise turbulent intensity and (right) lateral (——) and vertical (——) turbulent intensities. Five positions in the streamwise direction are shown: $-4D$ (——), $0D$ (- - -), $2D$ (-·-·), $5D$ (·····) and $10D$ (· · ·). The rotor region is represented by the two horizontal lines (·····). The target power law (■) is represented over the averaged streamwise velocity.

of the turbulence box. The wall model used is the one introduced by Thomas and Williams [255] that states that the wall shear stress, τ_w, should satisfy the following equation:

$$\tau_w = \rho u_\tau^2, \quad \text{with:} \quad u_\tau = \kappa u_\parallel(z_1) \log\left(\frac{z_1 - z_0}{z_0}\right)^{-1} \tag{5.21}$$

where u_τ is the wall friction velocity, $\kappa = 0.415$ is the von Karman's constant, z_1 is the height of the closest node to the boundary and $u_\parallel(z_1)$ is the velocity tangential to the ground at the closest node to the boundary. The outlet consists of an "outflow" configuration preventing the fluid from entering back into the domain appearing when large eddies are close to the boundary. This type of outlet applies flat velocity profiles on outlets, based on mass conversation, and to avoid backflow issues. This outlet impacts the flow in the domain up to two diameters upstream of the outlet. In this mater, the flow diagnostics are conducted only up to $10D$ behind $T1$, see **Fig. 5.6**. At this position, no impact of the outlet is observed on the flow, and the vertical pressure gradient is mostly constant. Moreover, the domain lateral and vertical dimensions are sufficient to properly resolve the blockage effect induced by the turbines in the investigated configurations.

- **Wind turbine modeling**

The blades are discretized with 75 actuator elements and the mollification kernel width is set to $\epsilon/h = 2$ and with $h = h_{wake}$. The tabulated polars are based on the actual blade airfoils geometry. The tower and nacelle were emulated using actuator lines, a method already used in the litterature [256, 145]. This modeling of the static geometries is analogous to the DALM methodology presented in Chapter 3, yet the Reynolds range is much higher. For instance, at the mid-tower position, the Reynold number reaches 10^6. For such Reynolds number, the flow surrounding a cylindrical body is highly turbulent, and the vortex shedding frequency tends to be too high to be resolved in this scenario. In consequence, no lift fluctuations are used to compute the forces on the tower. The tower is discretized into $N_{tower} = 50$ elements and the nacelle into $N_{nacelle} = 10$. At the difference from the methodology used by Churchfield et al. [145], here the velocity used to compute the aerodynamic force exercising on the tower and

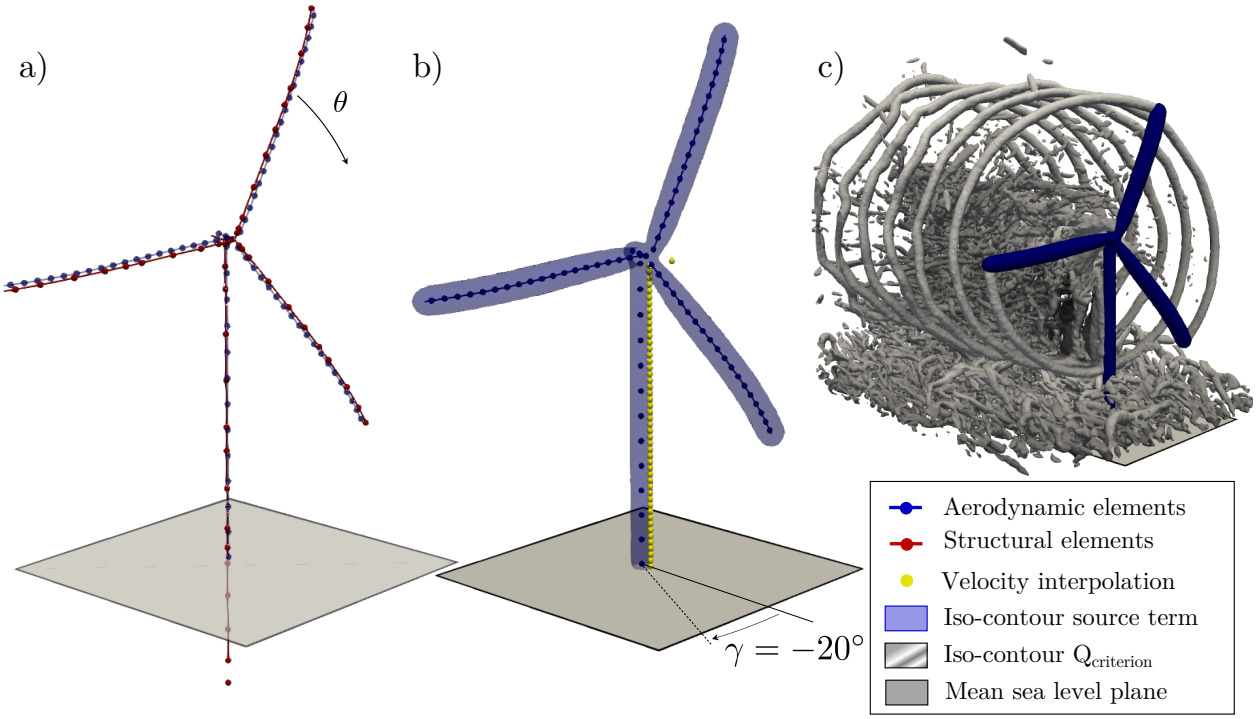

Figure 5.9: 3D visualization of (a) Aerodynamic and structural element for the rotor, nacelle, and tower; (b) aerodynamic elements and iso contour of the source term applied in the Navier Stokes equations. The relative velocity used to compute the tower and nacelle forces is taken from the yellow sphere locations. (c) iso contour of the source term and iso-contour of Q-criterion depicting the generated vortices in the vicinity of the wind turbine.

nacelle is taken slightly upstream the geometry. The idea is to remove the impact of the local induction generated by the source term representing the static geometries. This is depicted in **Fig. 5.9** by yellow spheres. For the tower, the velocity used in the force computation is located at half the local tower diameter upstream of the actuator element:

$$\mathbf{x}_{u,tower,i} = \mathbf{x}_{tower,i} - \frac{1}{2} d_i \frac{\mathbf{u}_{ref}}{u_{ref}} \,, \tag{5.22}$$

where d_i is the local tower diameter of the element i, $\mathbf{x}_{tower,i}$ the tower actuator element position and $\mathbf{x}_{u,tower,i}$ the position at which the velocity is interpolated from the eulerian grid. The computation of the forces for the nacelle is slightly different, especially for the yawed cases. A unique force is computed based on basic geometric assumptions and this force is then divided between the element and mollified with 3D isotropic gaussian kernels. Since a unique force is computed only the velocity at D_{hub} upstream the rotor center is used. The force is then derived in two parts as follow

$$\mathbf{F}_{nacelle} = \mathbf{F}_{side} + \mathbf{F}_{front} \,, \tag{5.23}$$

where $\mathbf{F}_{front}$ is the force arising from the front surface of the nacelle and $\mathbf{F}_{side}$ is the force from the side of the nacelle which is non-negligible for yawed cases.

$$\begin{aligned} \mathbf{F}_{side} &= \frac{1}{2}\rho(\mathbf{u}_{nacelle} \cdot \mathbf{n}_{side})^2 S_{side} C_{D,side} \mathbf{n}_{side} \,, \\ \mathbf{F}_{front} &= \frac{1}{2}\rho(\mathbf{u}_{nacelle} \cdot \mathbf{n}_{front})^2 S_{front} C_{D,front} \mathbf{n}_{front} \,. \end{aligned} \tag{5.24}$$

The tower and nacelle forces are currently not sent to the structural solver. In this matter, the tower and nacelle external forces are disabled in the structural solver. After the force evaluation,

they are mollified on the eulerian grid using the same mollification kernel size as the blades, i.e., $\epsilon/h = 2$. The maximal ratio of the mollification kernel size, ϵ, and the local tower diameter, d_i, is around 1.

5.3.3.3 Computational performances

The computational performances of the different simulations are given in **Tab. 5.4**. The simulations are run with the Joliot-Curie supercomputer, funded by GENCI and held in CEA's Very Large Computing Centre (TGCC). The nodes are AMD Rome (Epyc) dual-processor with 128 cores, 64 per processor. Each node has 256 GB DDR4 memory and is interconnected using the Infiniband HDR100 technology. The used nodes per simulations ranged between 2 and 75, the exact number of cores for each simulations is presented as N_{cores} in **Tab. 5.4**. Two cores are allocated to two BHawC instances for these simulations, while the rest are allocated to YALES2. Due to the high CPU cost, the case $(-\gamma 2)$ over a 1.8Billion elements has not reached the statistics accumulation, and only qualitative observations are provided for this case. The following results are shown for the intermediate level of mesh refinement, and the cases (REF), $(+\gamma)$, and $(-\gamma)$ will refer to $(REF1)$, $(+\gamma 1)$ and $(-\gamma 1)$ unless explicitly mentioned.

To discuss the computational performances, it is important to remember that a simulation with cells twice smaller than a coarse simulation should have its computational cost 16 times higher. This increase is due to the more significant number of cells since they are smaller for the same domain dimensions. The cost is multiplied by a factor of two for each spatial dimension and, consequently, by two over the time resolution due to the CFL constraints. Furthermore, if the number of cells per core is conserved to obtain the same loading per processor, the wall clock time should increase by a factor of two if a proper scaling is obtained. This factor two is due to the reduced time step and the increased number of iterations required to achieve the simulation.

It slightly differs in this case, the wall clock time for convergence and statistics, 27.5 minutes of physical time, for $(REF/+\gamma/-\gamma)$ is around 30 hours, while for $(REF0/+\gamma 0/-\gamma 0)$, it is around 27 hours. The wall clock times are close, independently of the mesh refinement, and subsequently, no factor two is observed. The same number of cells per core is used since $8 \times N_{cores}(REF0) = N_{cores}(REF)$. The similar wall clock time is due to the imposed time step inherited from the coupling with the aero-servo-elastic code. The overall computational cost ratio between the two refinement levels is roughly equal to eight as expected and the remaining small difference is due to the scalability of the simulations. It is important to mention that the actuator line method and the coupling to the structural solver represent only 4% of this overall cost.

It is essential to take into consideration that the ratio of simulated time versus computational time is in the range of $1.7 \times 10^{-2} - 1.5 \times 10^{-2}$ which for industrial applications investigating hundreds to thousands of scenarios is too low but could be within reach if further optimizations are made. Indeed, as mentioned in Chapter 2, all YALES2 processors are computing all the turbine loads, which is not computationally efficient at the moment. In a future implementation, only the processors with control volumes close to the turbine will process the forces in YALES2. The coupling will be easily updated for BHawC to exchange data with the concerned processors, reducing the number of processors receiving the information. Furthermore, a substepping of the structural solver as mentioned in the coupling methodology would drastically reduce the overall computation cost and wall clock time.

Case	N_{cores}	Mesh $N_{elem} \times 10^6$	Convergence [khCPU]	Statistics [khCPU]	Streamtube/Budgets [khCPU]
$REF0$	254+2	30	2.6	4.9	0.7
REF	2046+2	240	19	41	11
$+\gamma 0$	254+2	29	2.4	4.6	0.6
$+\gamma$	2046+2	233	17	40	10.4
$-\gamma 0$	254+2	29	2.3	4.6	0.6
$-\gamma$	2046+2	232	17.2	40.4	10.6
$-\gamma 2$	9598+2	1 857	650 [200s]	-	-

Table 5.4: Computational cost of the different cases presented in this chapter.

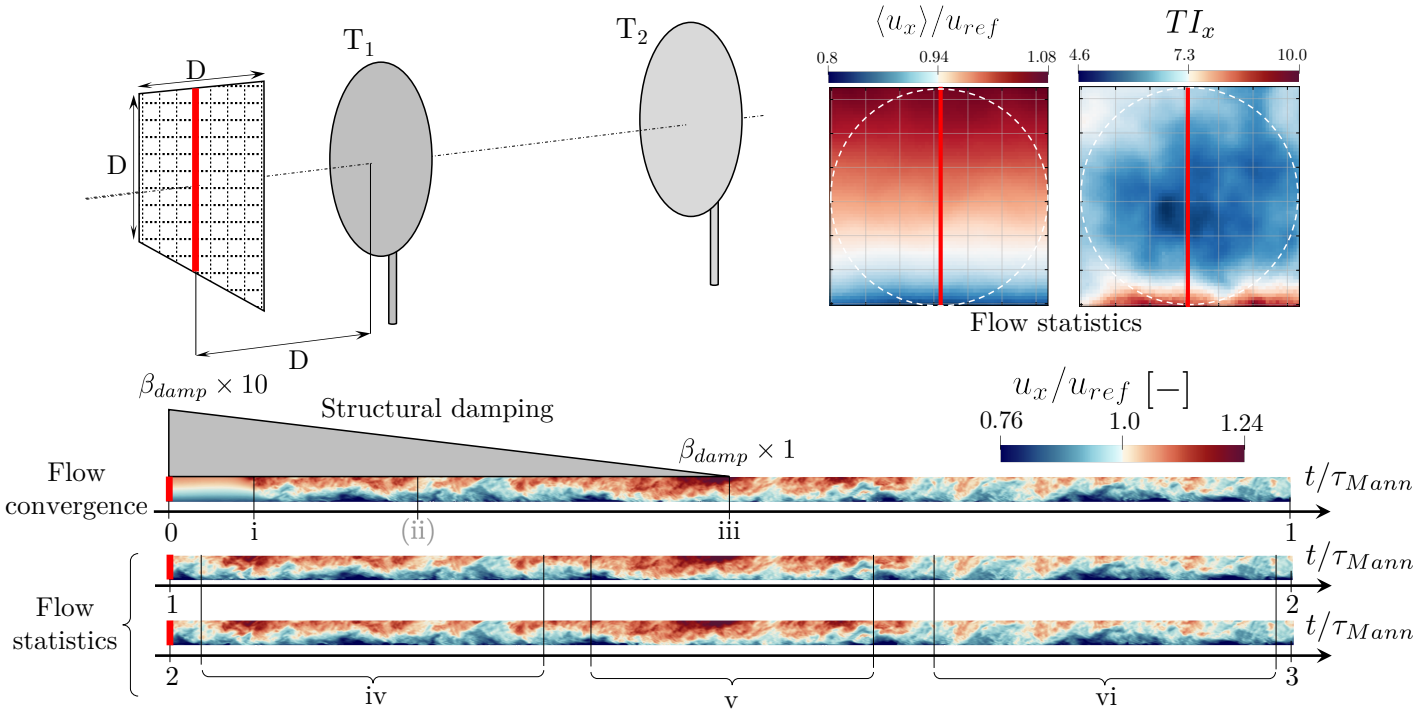

Figure 5.10: Timeline of instantaneous vertical velocity profile, highliting a serie of events (i,ii,iii,iv,v,vi) occuring during the simulation. The velocity samples are taken on a 64×64 grid one diameter upstream $T1$ at every time step in the reference case (REF).

5.4 Two aligned wind turbines: Reference case

In this section, the reference case (REF) is analyzed in the following way. At first, the wind turbines performance fluctuations are explained by observing singular events occurring in the flow. Then, the flow topology is presented through instantaneous data and statistics. To finish, the blades deformations are shown. The mesh resolution is evaluated in the overall process, and a comparison to BEM results on representatives cases is conducted.

5.4.1 Singular events occurring in the flow and wind turbines performances

It is important to have a global overview of the flow fields and events occurring at the turbines. This helps to understand how and why the turbines behave in such ways. With this aim, **Fig. 5.10** displays the chronological evolution of the flow one diameter upstream $T1$, for case

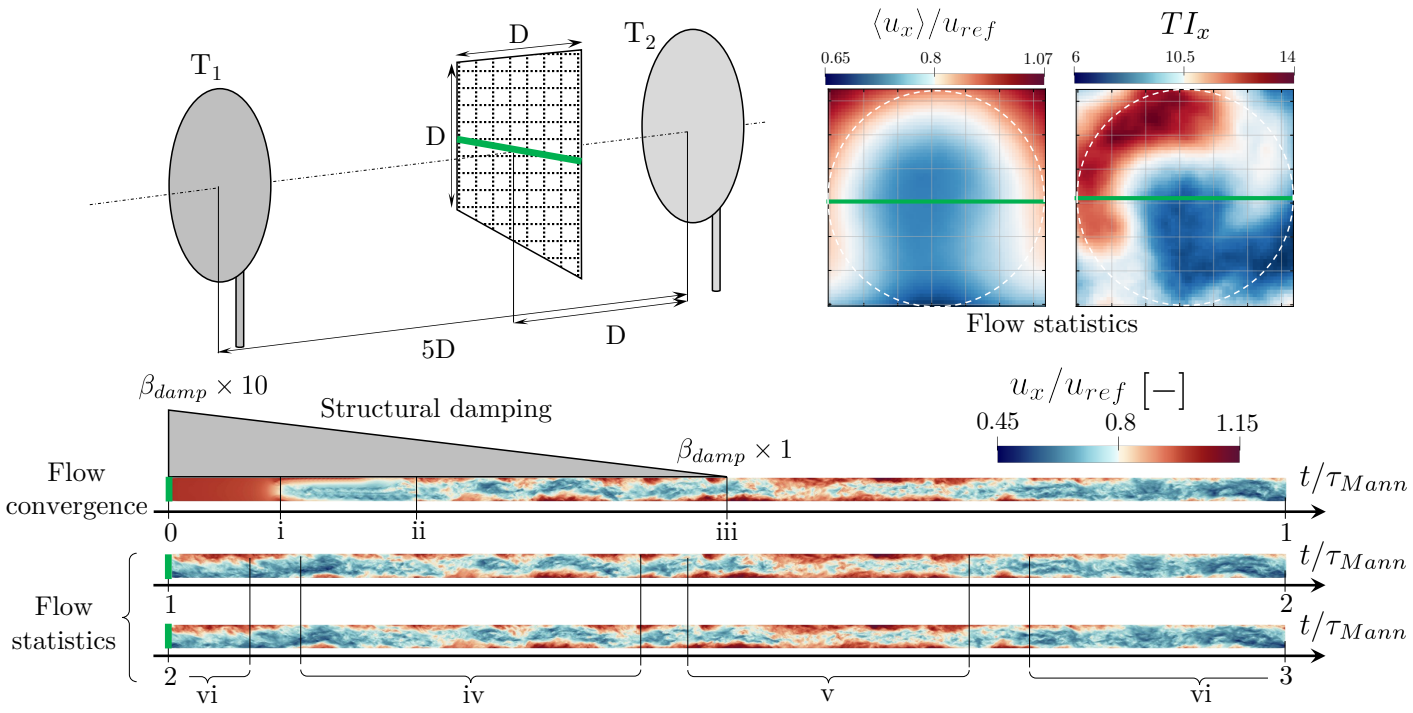

Figure 5.11: Timeline of instantaneous horizontal velocity profile, highliting a serie of events (i,ii,iii,iv,v,vi) occuring during the simulation. The velocity samples are taken on a 64×64 grid one diameter upstream $T2$ at every time step in the reference case (REF).

(REF). At first, a grid of 64×64 points is set upstream $T1$, and the grid dimension is D×D. Velocity samples at these locations are taken at each fluid iteration. At the bottom of the figure, the graphical timeline is presented by looking at the streamwise velocity component in the vertical direction, displayed as a bright red line. This timeline is divided into flow convergence, when the turbulence is setting up in the domain and when structural damping is applied on the turbine, and flow statistics, when statistics are accumulated to perform reliable and quantitative postprocessing. The first part duration is one flow-through time of the turbulence box, τ_{Mann}, the second part is over $2\tau_{Mann}$. Statistics over the second part are presented through mean streamwise velocity and streamwise turbulence intensity in the top right of the figure. Similarly, **Fig. 5.11** presents the flow one diameter upstream $T2$, for the same case. The only difference is that the flow is shown horizontally, displayed as a bright green line. In parallel, these velocity time series are used to inject turbulence in BHawC standalone, where the aerodynamic forces are computed using a BEM. This allows observing if the servo-elastic ALM response is similar to the servo-elastic BEM. The BEM results are shown as (BEM) in the following of this section.

The events occurring during the simulations are denoted with (i), (ii), (iii), (iv), (v), and (vi). During flow statistics (iv-v-vi), periodic events are observed. All these events are discussed hereafter according to the two previously introduced figures:

(i) This first event is during the flow convergence, in the case of $T1$ the injected turbulence 5D upstream is reaching the turbine. In the case of $T2$, the velocity deficit due to the wake of $T1$ starts to impact the turbine.

(ii) Secondly, the flow upstream $T2$ starts to witness the apparition of turbulent motion over $T1$ wake. The meandering of $T1$ wake begins to be observed due to the interaction with the synthetic turbulence injection.

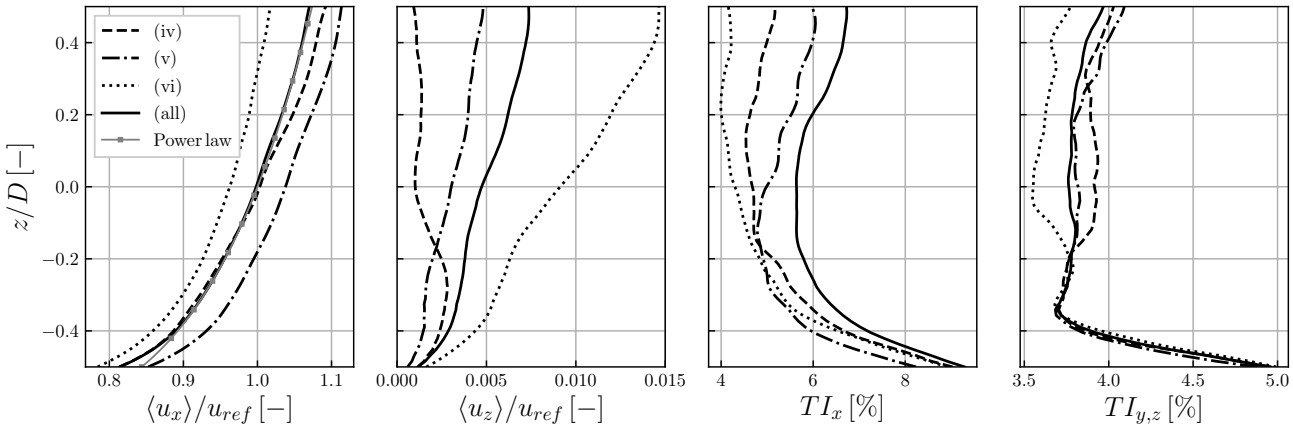

Figure 5.12: Vertical profiles of statistics on velocity components during the overall time (all) and the three periodic events; (iv),(v),(iv); encountered by $T1$ turbine in case (REF). From left to right, the events statistics are the streamwise velocity, the vertical velocity, the streamwise turbulent intensity and the transverse and vertical turbulent intensity.

(iii) The third and last event occurring during the flow convergence is the end of the ramping on the structural damping. After this event, both turbines behave close to the natural way.

(iv) Now that the flow reached convergence, the first periodic event is a stable boundary layer flow. The velocity deficit seen by $T2$ is subjected to meandering.

(v) For this event, higher velocities are observed for both rotors, which can be assimilated to gusts occurring within the simulation. They are due to larger scales structures within the synthetic turbulence box. Here, the wake velocity deficit of $T1$ seen by $T2$ is less marked due to higher velocities in the free stream.

(vi) This final periodic event represents an increase in the atmospheric boundary layer width resulting in lower wind speeds at the turbine locations.

Fig. 5.12 depicts vertical profiles of average streamwise and vertical velocity, as well as fluctuations in the streamwise and transverse directions during all the flow statistics compared to statistics conditioned to the periodic events (iv), (v), and (vi). The average streamwise velocity of the overall flow is the same as in **Fig. 5.8** and follows the power-law profile imposed at the inlet. A similar observation can be made for the event (iv), yet with a TI_x one percent lower. Event (v) has a higher averaged streamwise velocity profile, +3.8% at the hub, still with a power-law shape. In opposition, during the event (vi), the streamwise velocity is reduced by −3.5% at the hub. It is essential to notice the repeatability of the periodic events during the flow statistics. This shows that the flow is well established and fluctuates due to the synthetic turbulence injection. The following statistics are presented over the final $2\tau_{Mann}$ time series.

The time-averaged electrical power production, blade pitch, and rotation speeds are represented in **Fig. 5.13**. This figure compares the fine mesh reference case (REF), the coarse mesh reference case ($REF0$), and results obtained from BEM using the instantaneous flow fields of the reference case (BEM). The first turbine is at its nominal power with fluctuations reaching 1%, and this, for all cases. The operating condition is slightly above the rated wind speed, meaning the controller limits the power by pitching the blades. The second turbine has a reduced power

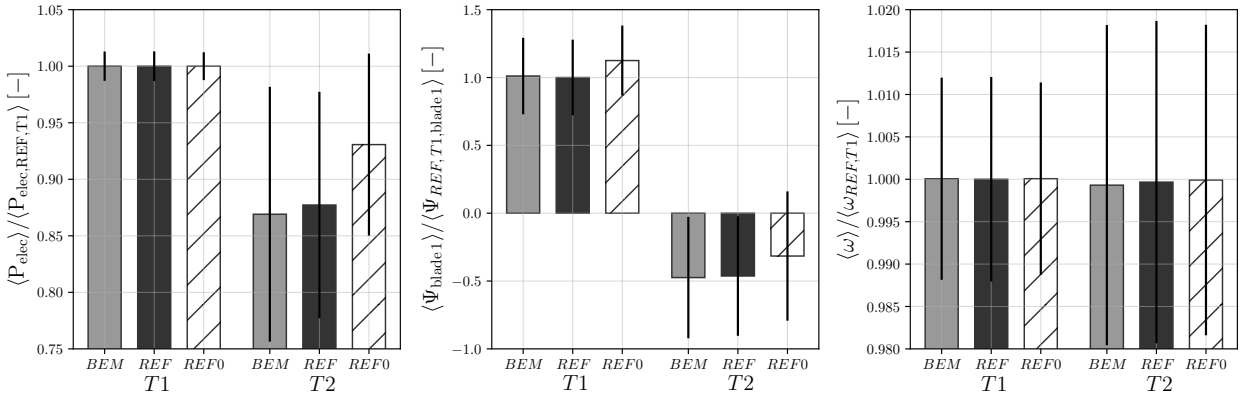

Figure 5.13: Time averaged electrical power production (left), blade 1 pitch angle (middle), rotation speed (right), all datas are normalized by turbine $T1$ in case (REF). Root mean square are shown with error bars. Cases: BEM ( ), REF ( ), and $REF0$ ( )

of -12.5% for the reference case. This is due to the wake of $T1$ impacting the turbine and inducing large fluctuations. The difference with (BEM) is low, $+0.8\%$, while higher with the coarse mesh reference, $+5.4\%$. This discrepancy with the coarse scenario is due to the resolution difference at the actuator line position $38/D$ against $77/D$, leading to overestimating the loads in the coarse scenario. This is characterized by the pitch angle as well. The first turbine being in the overrated region has its blades pitched all the time, while for the second turbine, lower pitch angles are recorded. A good accordance between the (BEM) and (REF) pitch angles is found while higher pitch angles are found for ($REF0$), due to the overestimated loads. The rotation speed is similar for all cases and both turbines, yet higher fluctuations are observed for $T2$. The thrust coefficient not shown here are similar for the three cases. $REF0$ is the case with the higher discrepancies to REF, reaching $+2\%$ for $T1$ and $+1\%$ for $T2$. The major observation from the thrust coefficient is that $T2$ has a thrust 30% higher than $T1$.

Time series of the turbines electrical power evolution are represented in **Fig. 5.14**. This gives supplementary information compared to the time-averaged results. At first sight, $T1$ electrical power is similar for all cases, with slight discrepancies appearing over time; the turbine constantly fluctuates around the nominal power. The fast Fourier transform presents several harmonics related to the mean rotating speed of the turbine. The curves of cases BEM and $REF0$ are offset for clearer observation of the peaks. Significant peaks are appearing at 1.35ω, 3ω, 6ω, 9ω, 21ω, 24ω, 36ω. The first peak, at 1.35ω, is related to the tower side-to-side bending mode, a similar peak is observed on the tower displacement; the tower top fluctuations are below 10 cm. The next peak, at 3ω, corresponds to the blade-passage frequency and the smaller amplitude peaks correspond to the harmonics of this frequency. This blade-passage frequency denotes the unbalanced aerodynamic forces between the three blades during the rotation due to the sheared inflow and the potential tower-shadow effect.

The BEM results present a variable phase shift of the power signal. This is the consequence of the injection of the turbulent LES flow. Since the turbulence is taken one diameter upstream of the turbine, there is a lag between the velocity measurement and the moment it impacts the turbine rotor. Moreover, this lag changes over time since the velocities are changing, i.e., transporting faster or slower the fluctuations to the rotor. Yet, it is impossible to use a velocity measured closer to the rotor in the LES and reduce this lag since the rotor induction would impact the flow field. This variable phase shift does not change the similarity with the REF,

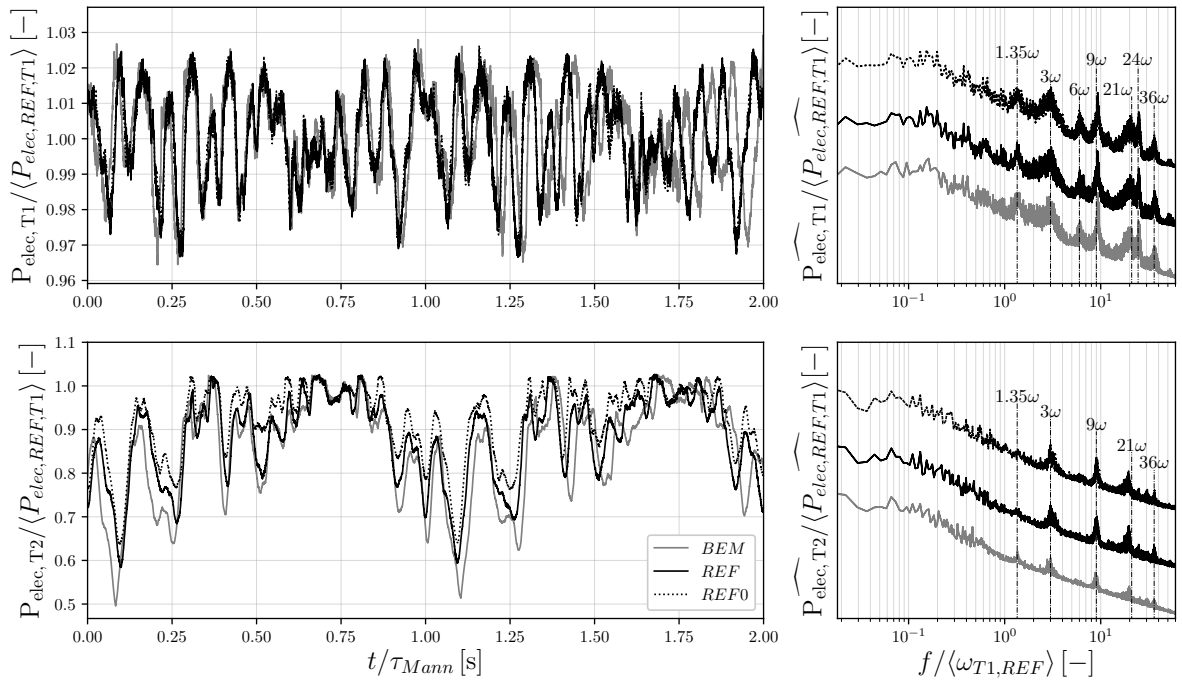

Figure 5.14: Time evolution (left) and power spectra (right) of the electrical power of each turbine, (top) $T1$ and (bottom) $T2$. Cases: BEM (—), REF (—), and $REF0$ (·····)

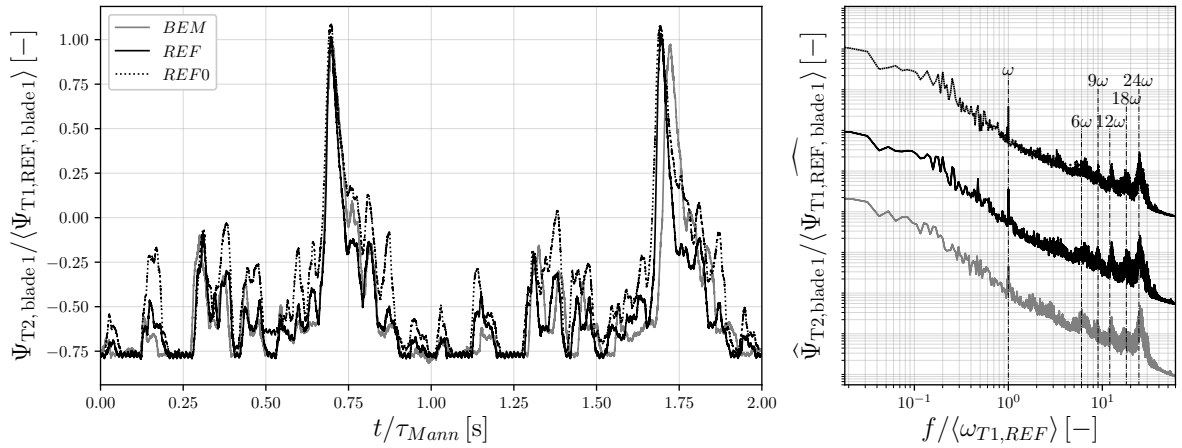

Figure 5.15: Time evolution (left) and power spectra (right) of the first blade pitch angle for $T2$. Cases: BEM (—), REF (—), and $REF0$ (·····)

especially with the similar frequency peaks highlighted above.

The evolution of power production of $T2$ shows more significant fluctuations correlated to the synthetic turbulence box period. The turbine operating conditions are at the limit between the control regions two and three, meaning that depending on the inflow, the rotor will reach nominal power and eventually pitch the blades or not. The same variable phase shift is observed between the BEM and REF. For this turbine, the peaks at 6ω and 24ω are not present anymore, and the other peaks are weaker. This results from the large fluctuations in the power production related to the synthetic turbulence box period. It is essential to mention that no particular peak associated with an eventual wake meandering is observed.

The blade pitch evolution over time for $T2$ presented in **Fig. 5.15** substantiates the behavior

of the second turbine. The first blade of $T2$ sees his pitch fluctuating between a no pitch case, related to the second control region, and a pitch similar to the one of $T1$, in the above-rated region or third control region. When there is no pitch, the power production is the lowest and shows a lack of available energy within the wind, i.e., lower velocities at the second turbine position. The power spectra show a peak at the rotation speed of $T2$, depicting the pitch variation according to the blade azimuthal position due to the wind shear. Then, other harmonics of the 3ω can be observed: 6ω, 9ω, 12ω, 18ω, 24ω. These harmonics, except 9ω, do not appear on the electrical power production spectra of $T2$ due to the large power variations.

5.4.2 Flow topology

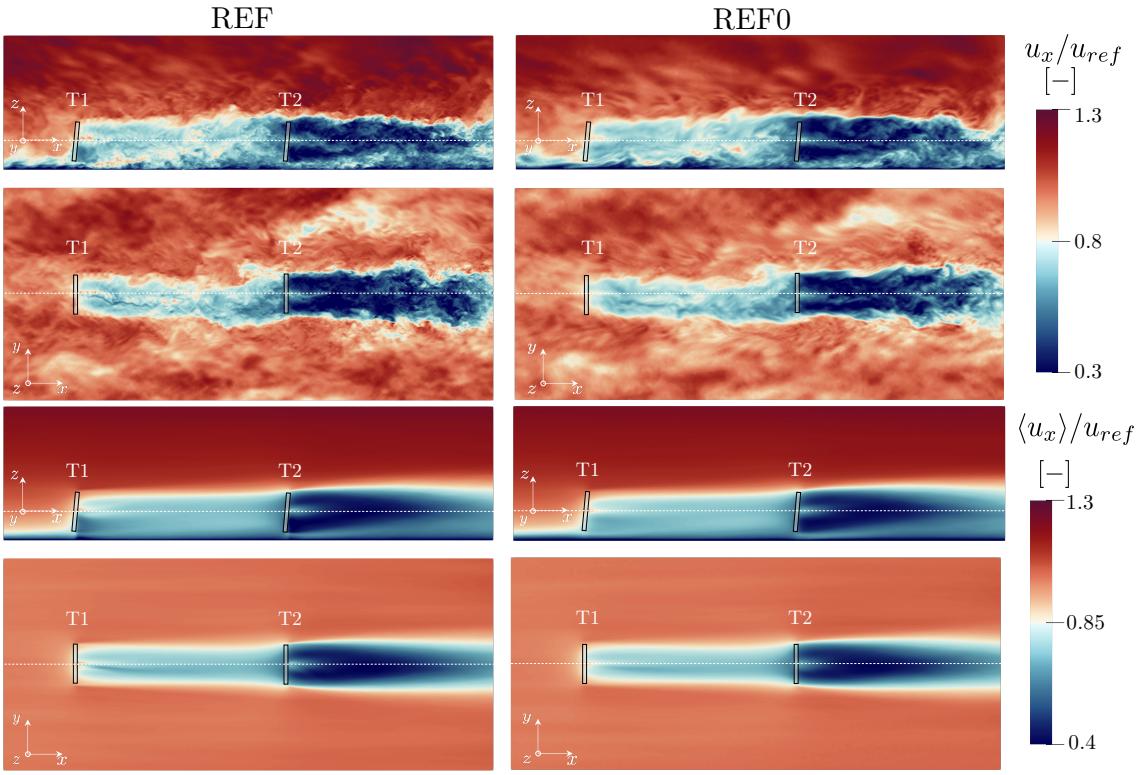

Figure 5.16: Vertical and Horizontal slices of the instantaneous (top) and time averaged (bottom) streamwise velocity around $T1$ and $T2$ for cases REF (left) and $REF0$ (right). Wind turbines are represented in grey and hub height is denoted by the white dotted lines.

The $T1$ wake interaction with $T2$ can be observed through the horizontal and vertical slices of the instantaneous and time-averaged streamwise velocity field in **Fig. 5.16** for REF and $REF0$. Several observations can be made from the instantaneous and time-averaged data. At first, the velocity deficit generated by $T1$ seems smaller than the one past $T2$. Two phenomena occur: the wakes of $T1$ and $T2$ are superposed past $T2$ and the thrust of $T2$ is 30% higher than $T1$, generating a higher velocity deficit. In addition to that, the velocity deficit caused by $T1$ does not recover before impacting $T2$. Secondly, the wakes are not deflected laterally in the time-averaged fields, and compared to the instantaneous fields, some wake meandering can be observed. A slight redirection in the vertical direction due to the wind turbine tilt is observed. The wake of the tower and nacelle appears, especially for REF with lower velocities between the rotor area and the sea level. Finally, on the instantaneous fields, REF and $REF0$ have

similar behavior of the large turbulent scales, yet $REF0$ mesh is too coarse to observe the tip vortices generated by the rotors. To confirm the low discrepancies between the two refinement

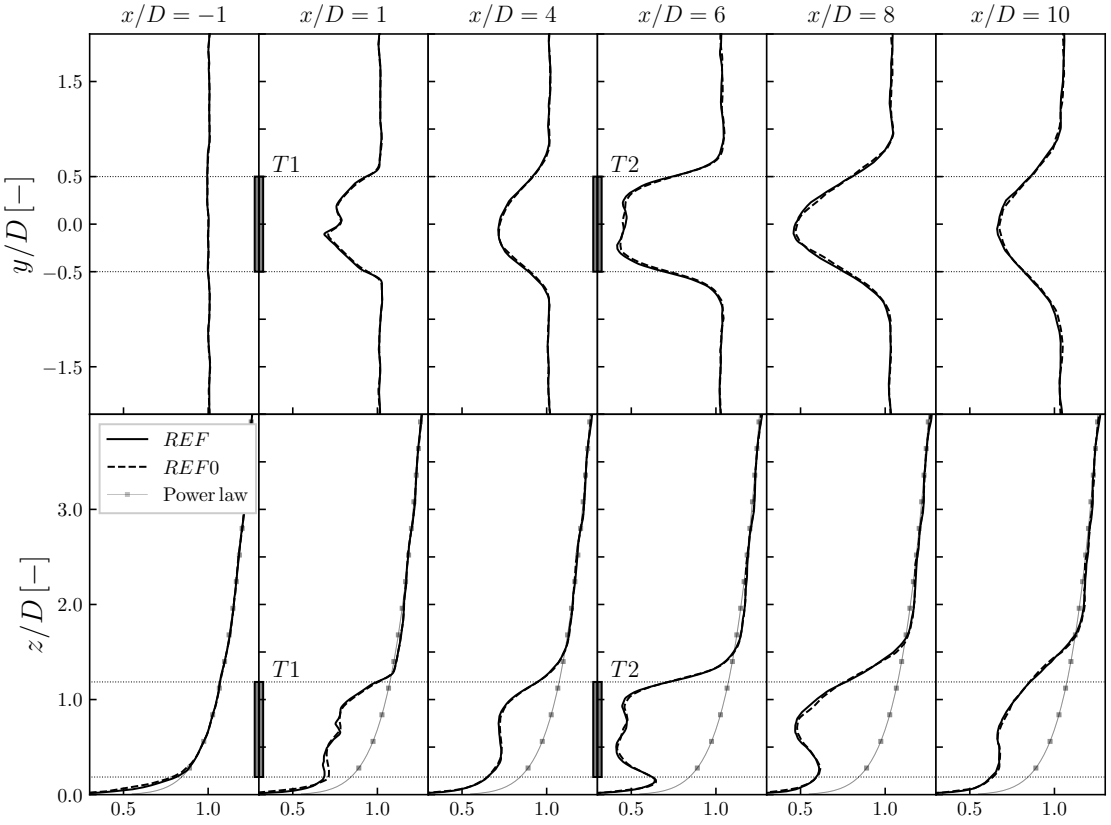

Figure 5.17: Horizontal, $z = h_{hub}$ (top) and vertical, $y/D = 0$ (bottom) time averaged streamwise velocity profiles at six streamwise positions: $x/D = -1$; 1; 4; 6; 8 and 10 for cases REF (——), $REF0$ (- - -) and the inlet power law profile (▪). Wind turbines are represented in grey and rotor region is denoted by the black dotted lines.

levels, the time-averaged velocity profiles are presented in **Fig. 5.17**. This figure represents the horizontal (top) and vertical (bottom) streamwise velocity profiles at different streamwise positions. On the vertical profiles, the inlet power-law profile is represented for more evident observation of the velocity deficit due to the wind turbines. The first observation is the close to perfect match between the flow field for the two mesh resolutions. Furthermore, on the vertical profiles, the wake, represented by the velocity reduction, is redirected through the top of the domain as qualitatively observed on the slices. By comparing positions $x/D = 1$ and 6, the velocity deficit behind $T2$ is more than twice the one behind $T1$.

The turbulent kinetic energy (TKE) can be observed through the horizontal and vertical slices in **Fig. 5.18** for REF and $REF0$. As a reminder, the TKE is expressed as $\langle k \rangle = 1/2 \langle \widetilde{u}_i'^2 \rangle$. The levels of TKE past $T1$ and $T2$ are different. In the flow between $T1$ and $T2$, low levels are observed, and a slight increase in the streamwise direction can be observed on the vertical slices. Past $T2$, high levels appear straight after the rotor tip position. The peaks generated at the tip of the blade are getting wider when going in the downstream direction. This results from the tip vortices pairing with each other and interacting with the wake of $T1$. An asymmetry is observed in the TKE on the horizontal slice; this might be due to the difference of deformations of the blade during the rotation, especially caused by gravitational effects. Similar levels of TKE

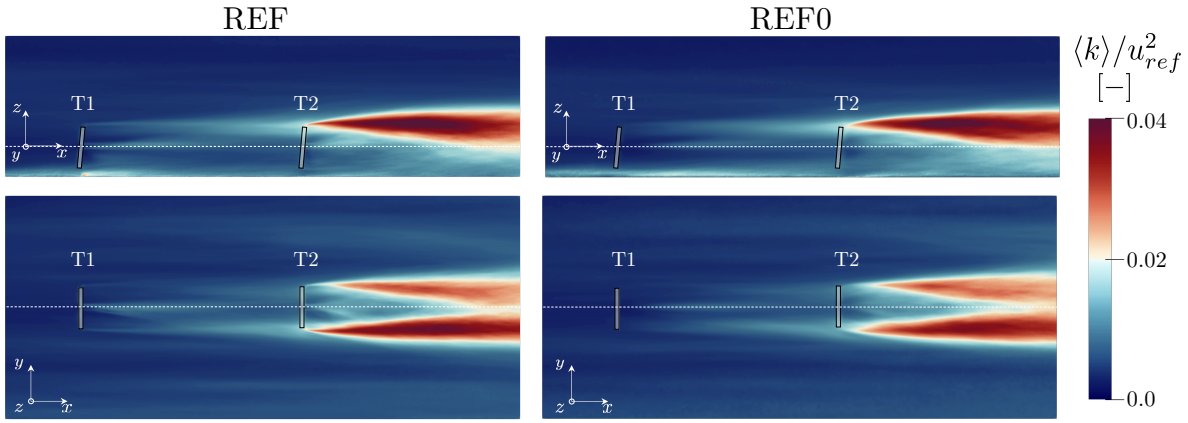

Figure 5.18: Vertical and Horizontal slices of the turbulent kinetic energy around $T1$and $T2$ for cases REF (left) and $REF0$ (right). Wind turbines are represented in grey and hub height is denoted by the white dotted lines.

are represented for the two resolutions, and as for the time-averaged streamwise velocity, TKE vertical and horizontal profiles are shown in **Fig. 5.19**. On the horizontal profiles, the peaks are located at the extremities of the rotor area. These peaks are coincident for both REF and $REF0$ with only slight variations in intensity. This consolidates the close match between the two cases.

5.4.3 Structural deformations

The structural deformations are investigated through azimuthal and radial time-averaged quantities. Statistics are given for ε_{edge}, ε_{flap} and θ_{span}. They represent, respectively, the deformation in the edgewise direction ($\mathbf{e}_\theta$), the deformation in the flapwise direction ($\mathbf{e}_x$), and the torsion around the blade spanwise axis. The dimensionless blade deformations quantities are presented with the following formalism.

All deformations are given in comparison to REF case. For a given turbine, the different deformations, $\varepsilon_{flap/edge}$ or the blade torsion θ_{span} in the rotor basis are given through a ratio with the maximal value of the reference case at the blade tip:

$$\phi^\star_{T,\,Case}(r,\theta) = \frac{\phi_{T,\,Case}(r,\theta)}{\max \langle \phi_{T1,\,REF,\,tip} \rangle (\theta)}\,, \tag{5.25}$$

where $\phi_{T,\,Case}(r,\theta)$ represent the mean or the root-mean square of the deformation/torsion during the simulation for turbine T at given radius r and azimuth θ, $\phi^\star$ denotes the dimenssionless value of ϕ. $\langle \phi_{T1,\,REF,\,tip} \rangle (\theta)$ is the time averaged azimuthal deformation/torsion at the tip for $T1$. As an example, **Fig. 5.20** shows the mean flapwise deformations of $T1$ and $T2$ for case (REF) as

$$\langle \varepsilon_{flap} \rangle^\star_{T1/T2,\,REF}(r,\theta) = \frac{\langle \varepsilon_{flap} \rangle_{T1/T2,\,REF}(r,\theta)}{\max \langle \varepsilon_{flap} \rangle_{T1,\,REF,\,tip}(\theta)}\,. \tag{5.26}$$

The blade flapwise deformations increase with the radial position, which is expected and correlated to forces increasing near the blade tip. For the first wind turbine, the maximal deformation is located at the tip when the blade is close to a 0° azimuth, i.e., when the blade is pointing to the top. This is due to the wind shear involving higher wind velocities when the blade is at this azimuthal position. The second wind turbine has a higher maximal deformation reaching 1.39 times the one of $T1$. This is due to the blades being less pitched and generating

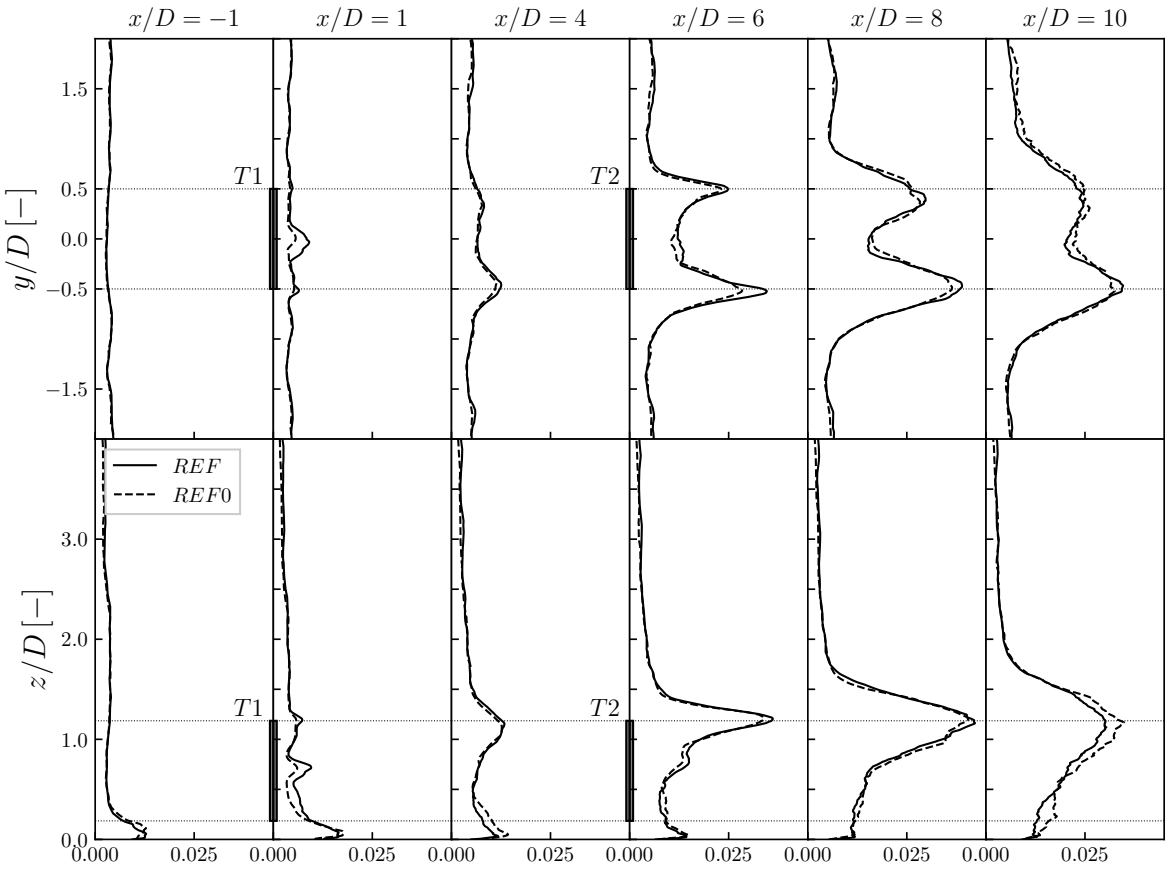

Figure 5.19: Horizontal, $z = h_{hub}$ (top) and vertical, $y/D = 0$ (bottom) turbulent kinetic energy profiles at six streamwise positions: $x/D = -1$; 1; 4; 6; 8 and 10 for cases REF (——) and $REF0$ (- - -). Wind turbines are represented in grey and rotor region is denoted by the black dotted lines.

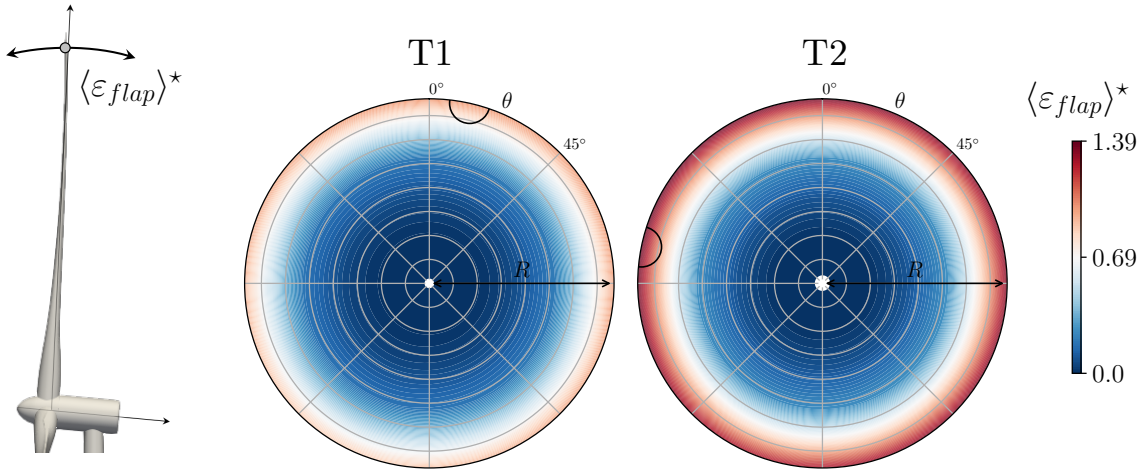

Figure 5.20: Azimuthal and radial mean flapwise deformations for $T1$ (right) and $T2$ (left) for Reference case (REF), it is depicted according to $T1$ maximal flapwise deflection, see **Eq. 5.25**. The localisation of the maximal deformation is shown for each turbine with a black circle.

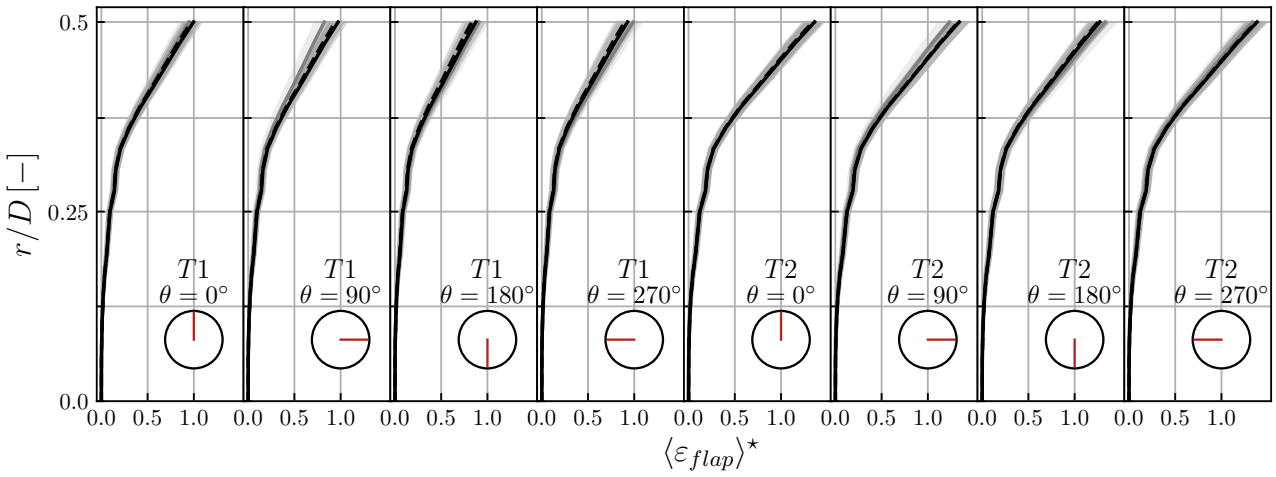

Figure 5.21: Radial profiles of mean flapwise deformations at $\theta = 0°$, 90°, 180° and 270° for $T1$ (right) and $T2$ (left), depicted according to $T1$ maximal flapwise deflection, see **Eq. 5.25**. The root-mean-square of the deformations are shown with an area around the curves. Cases: BEM (—), REF (—), and $REF0$ (- - -).

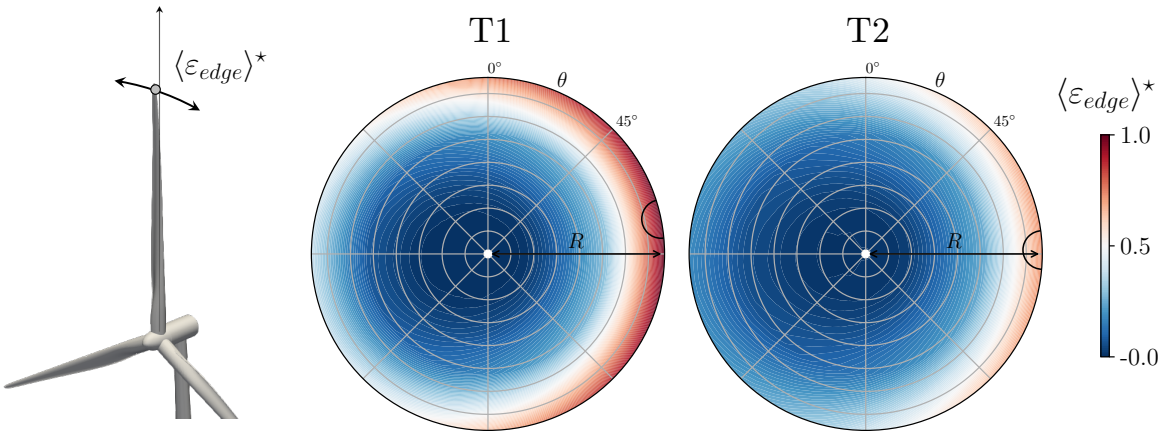

Figure 5.22: Azimuthal and radial mean edgewise deformations for $T1$ (right) and $T2$ (left) for Reference case (REF), it is depicted according to $T1$ maximal edgewise deflection, see **Eq. 5.25**. The localisation of the maximal deformation is shown for each turbine with a black circle.

a higher resistance to the wind field. The maximal deformation is located at $\theta = 270°$ for this second turbine.

The comparison to BEM and $REF0$ is presented in **Fig. 5.21**. This figure shows the average deformations of the three cases for $\theta = 0°$, 90°, 180° and 270° with the according root-mean-square values. The deformations are similar for $REF0$ yet underpredicted by 1% independently from the azimuth. The BEM has flapwise deformations that differ from ±10% compared to REF; the maximal deformation is not located at the same position, yet its amplitude varies only by 0.4%. These discrepancies seem to arise from the temporal shift between the turbulence box injected in the BEM inducing a different response of the turbine. Furthermore, due to the lag, turbulence structures do not arrive simultaneously on the rotor area, and the blades are not at the same azimuthal position as the blade. The BEM turbulence injection emanating from the LES fields should be rethought to tackle this dilemma since its limits are shown.

The edgewise deformations are presented in **Fig. 5.22**. The blade edgewise deformations

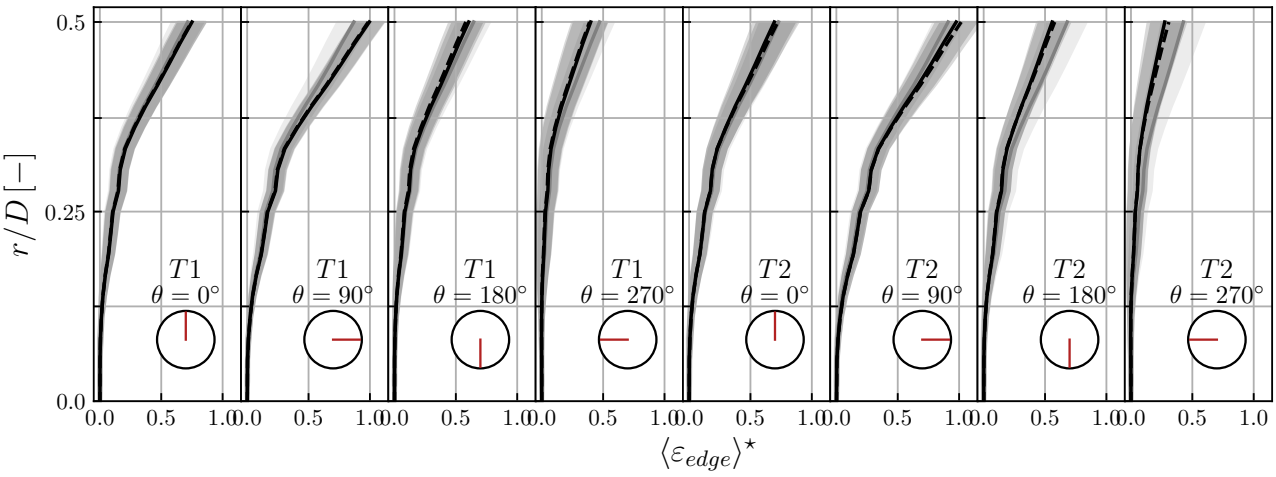

Figure 5.23: Radial profiles of mean edgewise deformations at $\theta = 0°$, $90°$, $180°$ and $270°$ for $T1$ (right) and $T2$ (left), depicted according to $T1$ maximal edgewise deflection, see **Eq. 5.25**. The root-mean-square of the deformations are shown with an area around the curves. Cases: BEM (—), REF (**—**), and $REF0$ (**- - -**).

are in the majority due to gravitational effects. When the blade is at $\theta = 90°$, and therefore going down, the blade achieves its maximal deformation in the bottom direction due to its weight. In opposition, when the blade is going up at $\theta = 270°$, the weight is opposing the blade displacement, and the deformation is reduced compared to the previous scenario. This is similar for both turbines, yet for $T2$, the maximal amplitude is reduced by 4%.

The cases BEM and $REF0$ are compared to REF in **Fig. 5.23**. This figure shows the average deformations for $\theta = 0°$, $90°$, $180°$ and $270°$ with according root-mean-square values. The fluctuations of the edgewise deformation are higher for the second turbine due to the higher pitch fluctuations. The deformations are similar for $REF0$, yet differ of -1% for $T1$ and $+1\%$ for $T2$. When compared to BEM results, higher discrepancies are appearing for $T2$. The deformations differ, from $+8\%$ to -10%. The edgewise deformations are highly impacted by the blade pitch and the variable phase shift on the instantaneous pitch of $T2$, observed in **Fig. 5.15**, could explain these over predictions.

The blade torsion around its axis is presented in **Fig. 5.24** for the two turbines in (REF). It is important to note that the blade torsion will directly impact the angle of attack of the local airfoil section. In this scenario, the local angle of attack is reduced when the torsion increases. Here, the maximal torsion is in the range of one to five degrees. The radial and azimuthal variations are similar to the edgewise deformations, and the maximal torsion is located at 90° as well. The difference from the edgewise deformations is that $T2$ has a higher torsion than $T1$.

In a similar way to the flapwise and edgewise deformation, the torsion of REF is compared to BEM and $REF0$ in **Fig. 5.25**. In the close-to-tip sections, the torsion is constant while increasing in the middle of the blade. The inflection resulting from this observation is even more marked for $T2$. This prevents reaching a too high torsion and, therefore, deteriorating the tip angle of attack. The results of the different cases are mostly the same here. The discrepancies of the BEM with REF are below $+10\%$.

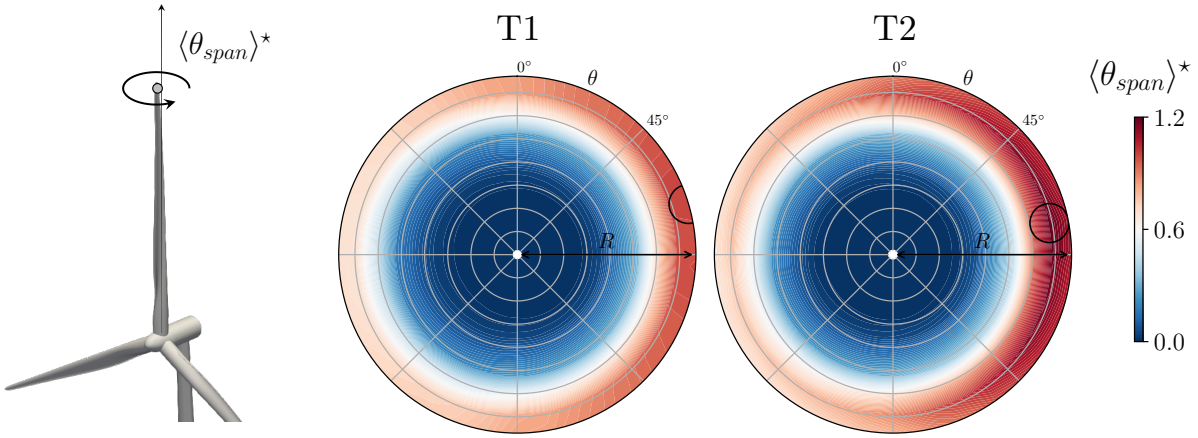

Figure 5.24: Azimuthal and radial mean blade torsion for $T1$ (right) and $T2$ (left) for Reference case (REF), it is depicted according to $T1$ maximal torsion, see **Eq. 5.25**. The localisation of the maximal torsion is shown for each cases with a black circle.

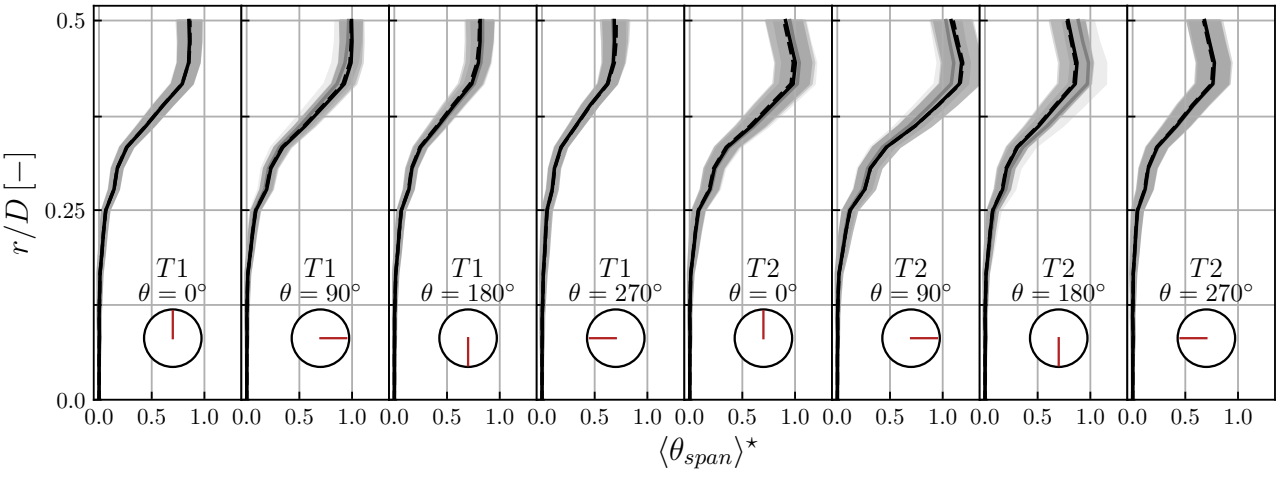

Figure 5.25: Radial profiles of mean torsion at $\theta = 0°$, $90°$, $180°$ and $270°$ for $T1$ (right) and $T2$ (left), depicted according to $T1$ maximal torsion, see **Eq. 5.25**. The root-mean-square of the deformations are shown with an area around the curves. Cases: BEM (—), REF (—), and $REF0$ (- - -).

5.4.4 Discussion

This first section of results investigates the various physical effects and the associated wind turbine response for this scenario of two aligned wind turbines. Furthermore, the influence of mesh refinement is analyzed, and the turbine performances and deformations are compared to representative BEM results.

The wind turbines are exposed to an inflow close to their rated wind speed and should be limited between control regions two and three. The injection of synthetic Mann turbulence overlayed to a power-law velocity profile generates several events with a repetitive pattern. These repetitive events are represented by low (-3%), reference, and high ($+3\%$) averaged velocities at hub height, impacting the turbine response and performances. These events impact the velocity deficit generated by the first turbine - the second turbine receiving this velocity deficit switches from one control region to another. On average, the pitch angle of the second turbine is lower than the first turbine, and the thrust coefficient is higher. This higher thrust generates a more significant velocity deficit behind $T2$, which overlays with the wake of $T1$. The wakes are mostly symmetric from the horizontal slices, while from the vertical slices, they seem redirected through the top of the domain. Peaks of TKE are appearing downstream the tip of $T2$ blades.

The discrepancies between REF and $REF0$, with a mesh of twice the cell size, appear on the turbine performances. The electrical power output of $T2$ is 5.4% higher for $REF0$, which is translated by a higher pitch caused by an overestimation of the loads. The resolution near the turbine is 77 cells per diameter for REF while it is 38 for $REF0$. The guidelines from the litterature [158] assess that at least 64 cells per diameter should be used for a proper loads evaluation, which is not the case for $REF0$. Nevertheless, the thrust from the rotor only differs by 1%, and the resulting flow topology is close to similar in the wakes.

The cell size reduction only near the turbines in $REF0$ would supposedly improve the turbine performances according to REF. Under this hypothesis, the computational cost of $REF0$ would increase but give reliable results at a lower price than REF. Since the coupling with the structural solver limits the simulation time-step, the wall clock time would not be impacted. Nevertheless, the number of processors could be significantly reduced and, with it, the computational cost.

Turbulence boxes located one diameter upstream of the turbine are built from the simulated flow. These turbulence boxes are then injected into the BEM module present in BHawC, providing comparative results from two different methodologies. The BEM results showed to be in good accordance with the REF case for the time-averaged turbine performances, yet a variable phase shift is observed on the turbine instantaneous response. The flapwise deformations, edgewise deformations, and blade torsion have the same order of magnitude yet slightly differing, especially for the edgewise deformations of the second wind turbine.

5.5 Influence of yaw misalignement

From the previous observations of the reference case, the following section investigates the repercussions of the first turbine yaw misalignment. Two yaw misalignment of $T1$ are investigated, $\gamma = -20°$ and $+20°$. Firstly, the flow topology is presented and followed by the constructions of streamtubes around $T1$ and $T2$ with the methodology developed in Chapter 4. From these streamtubes, mean kinetic energy budgets are computed, highlighting the wake recovery of the turbines. Secondly, the performances and loads of the turbines are then discussed, showing the power gain associated with the first turbine misalignment with the wind. Thirdly, the deforma-

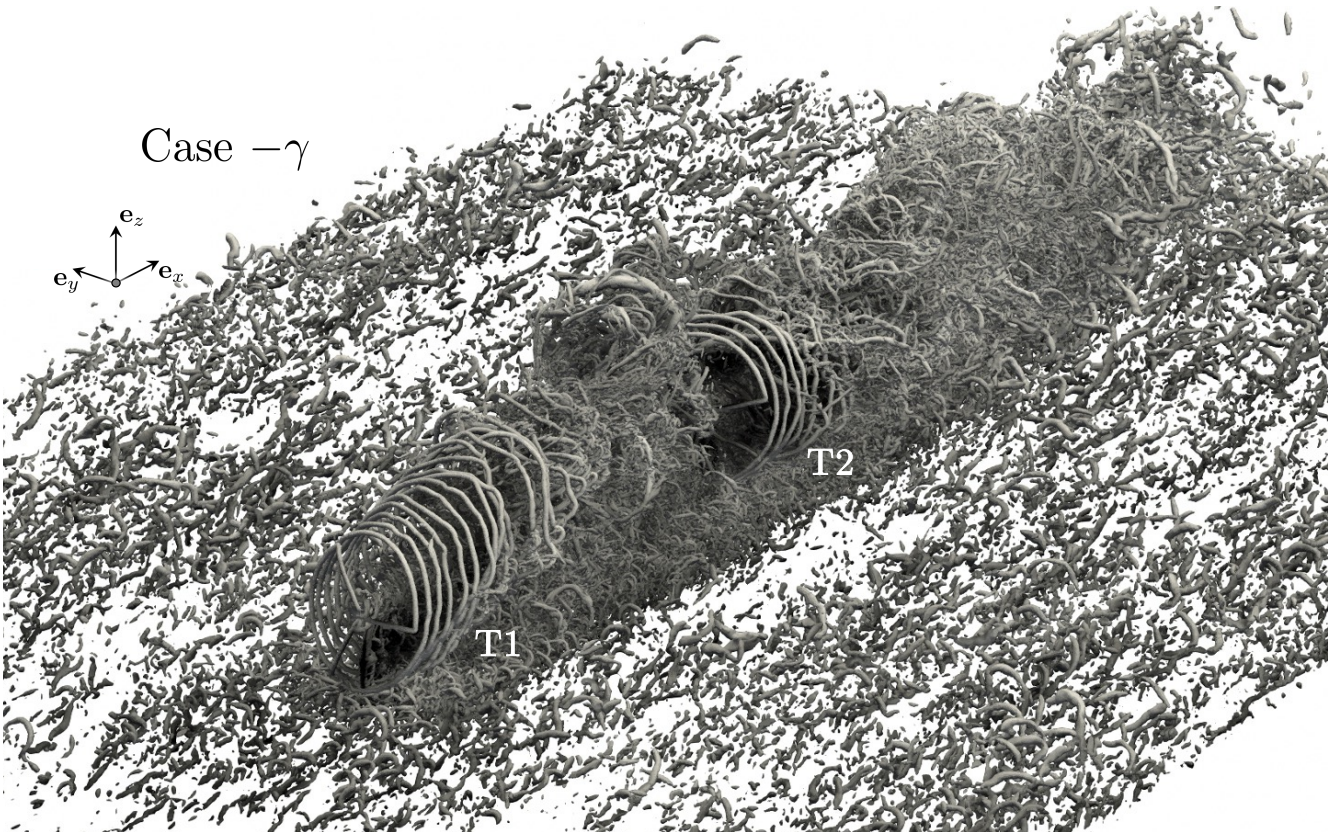

Figure 5.26: 3D visualization of the wake generated by the turbine blades, tower and nacelle at $\gamma = -20°$ on the fine mesh ($-\gamma 2$) using a iso-contour of the $Q_{\text{criterion}}$.

tions of the turbines and the equivalent fatigue are presented.

5.5.1 Flow topology

A qualitative overview of the vortices generated in the wake of the turbines is given in **Fig. 5.26** for the case $-\gamma$, on the finer refinement level ($-\gamma 2$). The helicoidal vortices generated by the blades is slowly destabilized due to the interaction with the sheared turbulent flow. After 2D behind $T1$, the turbulent structures appear to be smaller and smaller and the tip-vortices are hardly visible. Since the first turbine is misaligned with the wind the turbulent structures generated in the wake are deflected and impact only the left side of the second turbine.

The impact of $T1$ yaw misalignment on the flow topology is presented through the time-averaged streamwise velocity horizontal and vertical slices in **Fig. 5.27**. As in the previous observations of the reference case, the velocity deficit generated by $T1$ seems smaller than the one past $T2$. In the yaw misaligned cases, the wake velocity deficit is deflected in the transverse direction. The wake of this first turbine is still impacting a large part of the second turbine rotor. For the positive yaw misalignment case, the horizontal slice of the wake past $T2$ shows a distinct asymmetry in the velocity deficit. The wake of $T1$ tower is less apparent in the overall velocity deficit for this case. The time-averaged velocity profiles are presented in **Fig. 5.28**. This figure represents the horizontal (top) and vertical (bottom) streamwise velocity profiles at different streamwise positions. On the vertical profiles, the inlet power-law profile is represented for a more evident observation of the velocity deficit due to the wind turbines. The horizontal profiles depict a clear deviation of the velocity deficit even past the second turbine. From the horizontal profiles at $x/D = 6$, one can notice the asymmetry in this deficit for the case $+\gamma$.

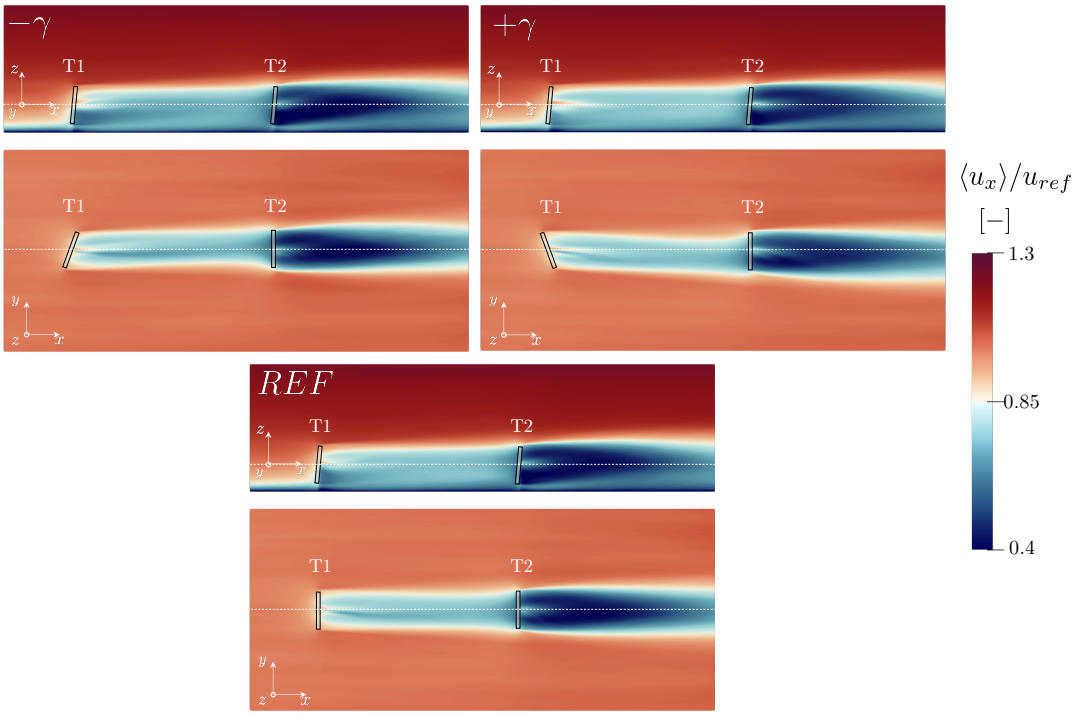

Figure 5.27: Vertical (top) and Horizontal (bottom) slices of the time averaged streamwise velocity around $T1$and $T2$ for cases $(-\gamma)$,$(+\gamma)$, and (REF). Wind turbines are represented in grey and hub height is denoted by the white dotted lines.

This results from an imbalance of the streamwise force generated by $T2$ between the left and right parts of the rotor. This does not appear for the negative yaw misalignment. The negative yaw misalignment profiles are similar to the align case. The vertical profiles highlight a lower velocity deficit downstream of the tower for the case $+\gamma$. This is explained in the following section when streamtubes are constructed.

The turbulent kinetic energy (TKE) can be observed through the horizontal and vertical slices in **Fig. 5.29** for $-\gamma$, $+\gamma$ and REF. The levels of TKE past $T1$ and $T2$ are different. In the flow between $T1$ and $T2$, low levels are observed, and a slight increase in the streamwise direction can be observed on the vertical slices. But past $T2$ high levels appear straight after the rotor tip position. The peaks generated at the tip of the blade are getting wider when going in the downstream direction. The yaw misalignment impacts the asymmetry observed in the TKE on the horizontal slice for the reference case. The negative case tends to symmetrical levels of TKE while the positive case increases even more, this asymmetry. This is well represented on the vertical and horizontal TKE profiles shown in **Fig. 5.30**. On the horizontal profiles, the peaks of $-\gamma$ and $+\gamma$ are slightly shifted from the extremities of the rotor area.

5.5.2 Streamtubes

The wake bounds are then investigated by constructing streamtubes emanating respectively from $T1$ and $T2$. The constructions of the streamtubes are made with the methodology presented in Chapter 4. According to the time-average velocity field, the principle is to transport the level set function. The level set function is represented by a hyperbolic tangent profile where the interface is located at the iso-level $1/2$. Once the level set function is converged, i.e., when $\frac{\partial \psi}{\partial \tau} < 1.2\times10^{-4}$, the streamtube interface is located on this iso-level. For each case, two streamtube sources are

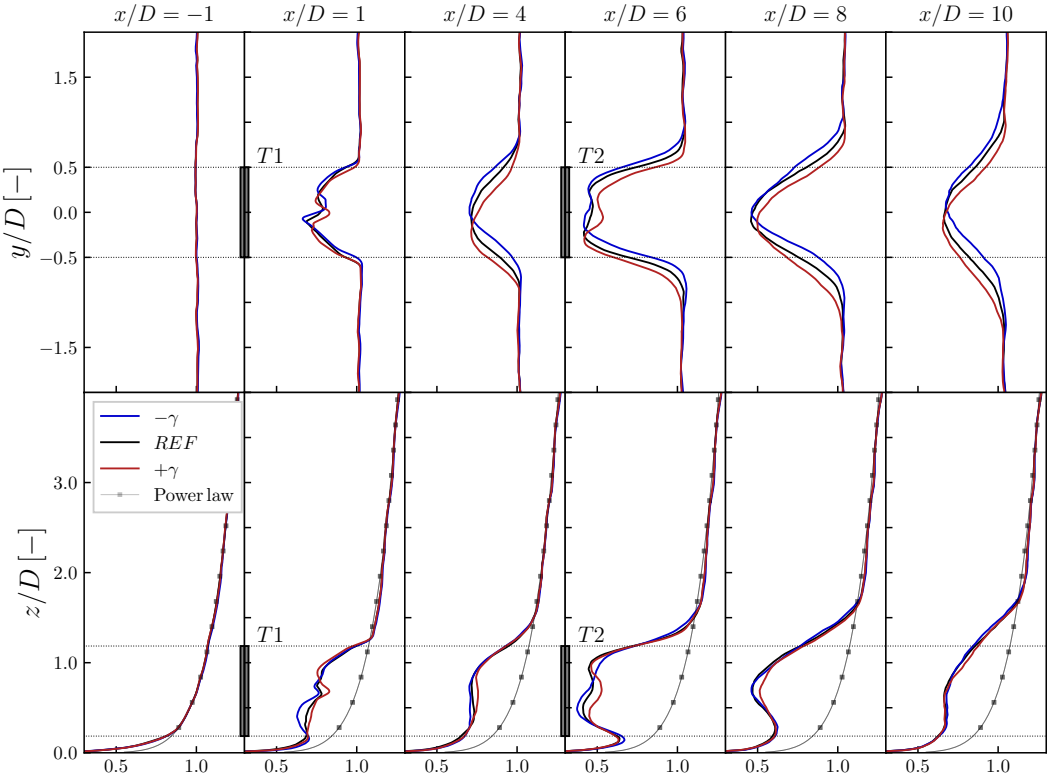

Figure 5.28: Horizontal, $z = h_{hub}$ (top) and vertical, $y/D = 0$ (bottom) time averaged streamwise velocity profiles at six streamwise positions: $x/D = -1$; 1; 4; 6; 8 and 10 for cases $-\gamma$ (—), REF (—), $+\gamma$ (—) and the inlet power law profile (■). Wind turbines are represented in grey and rotor region is denoted by the black dotted lines.

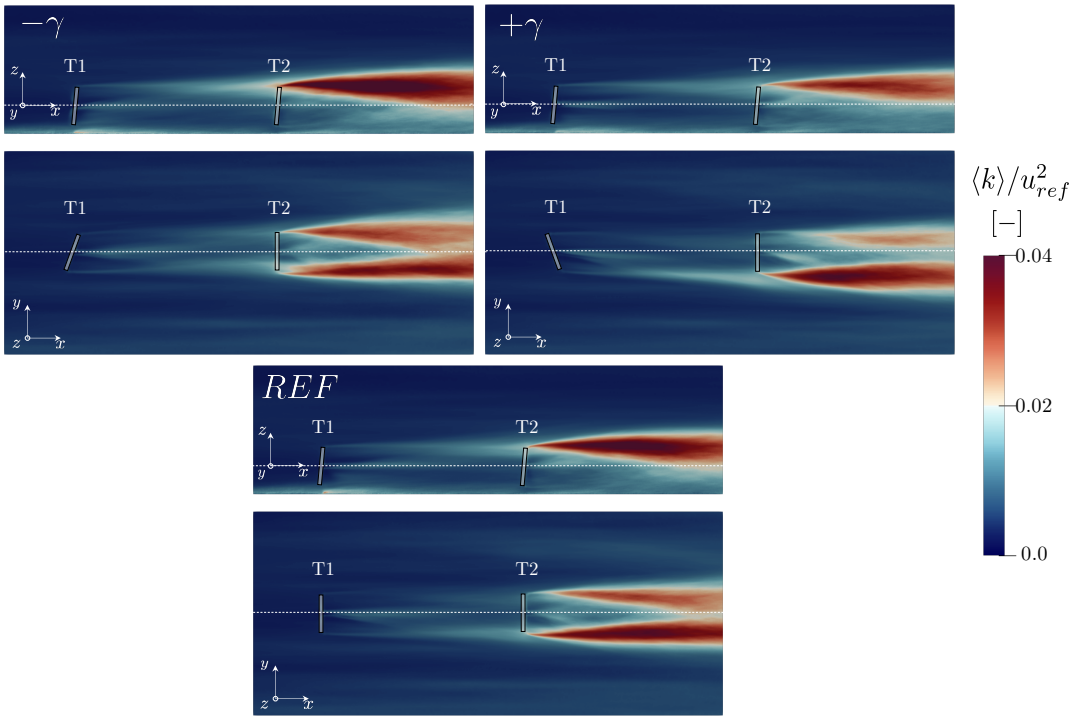

Figure 5.29: Vertical (top) and Horizontal (bottom) slices of turbulent kinetic energy around $T2$ and $T2$ for cases $(-\gamma)$,$(+\gamma)$, and (REF). Wind turbines are represented in grey and hub height is denoted by the white dotted lines.

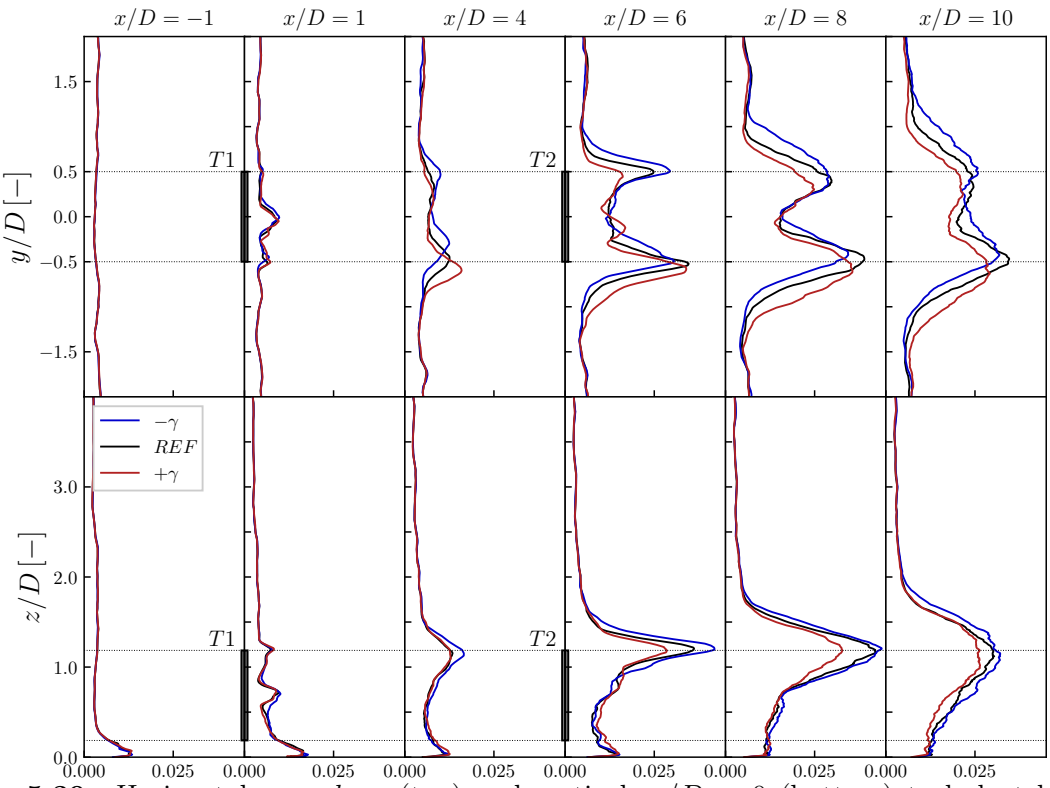

Figure 5.30: Horizontal, $z = h_{hub}$ (top) and vertical, $y/D = 0$ (bottom) turbulent kinetic energy profiles at six streamwise positions: $x/D = -1$; 1; 4; 6; 8 and 10 for cases $-\gamma$ (—), REF (—) and $+\gamma$ (—). Wind turbines are represented in grey and rotor region is denoted by the black dotted lines.

used and based on the rotor swept area of $T1$ or $T2$ as depicted in **Fig. 5.31**. It is essential to mention that the tower and nacelle volumes are present in the source terms. Both streamtubes are computed from $2D$ upstream to $10D$ downstream $T1$.

Slices of the streamtubes for cases $-\gamma$, REF and $+\gamma$ are presented in **Fig. 5.32**. The top of the figure is representing $\psi_{T1} = 0.5$ for $x/D = -1$; 1; 2 and 4 while the bottom is representing $\psi_{T2} = 0.5$ for $x/D = 4$; 6; 8 and 10. On the streamtube generated past $T1$, the streamtube is deflected for yaw misaligned cases, which is coherent with the observations on the velocity deficit. Nevertheless, the iconic curled wake is not distinguishable; the streamtube remains mostly circular. This is a consequence of two phenomena. Firstly, the meandering and turbulent mixing occurring due to the background turbulence are smoothing the curled shape. Secondly, and maybe the most important, $T1$ exercises a small transversal force on the flow despite the yaw misalignment. A low transversal force on the flow will generate a counter-rotating vortex pair (CVP, see Chapter 3) of lower intensity, and the wake shape will be less deformed. Nevertheless, the comma shape between the rotor area and the ground slowly deviates. This shape corresponds to the fluid particles passing near the tower, veering either left or right, depending on the yaw misalignment. This is the consequence of the low-intensity counter-rotating vortex pair (CVP) generated past the yawed rotor. The second streamtube, emanating from $T2$, remains mostly round downstream $T2$ and is redirected upwards. These streamtubes are then discretized into 150 cross-sections of approximately ten mesh cell thicknesses and used to integrate global flow quantities. As a reminder, the exterior streamtube section surface is noted S_{st}, the upstream face is S_{in}, the downstream face S_{out} and the volume V_{st}. Integrals averaging, either on volume or surface, are denoted with $\langle \bullet \rangle_S$, S being the corresponding surface

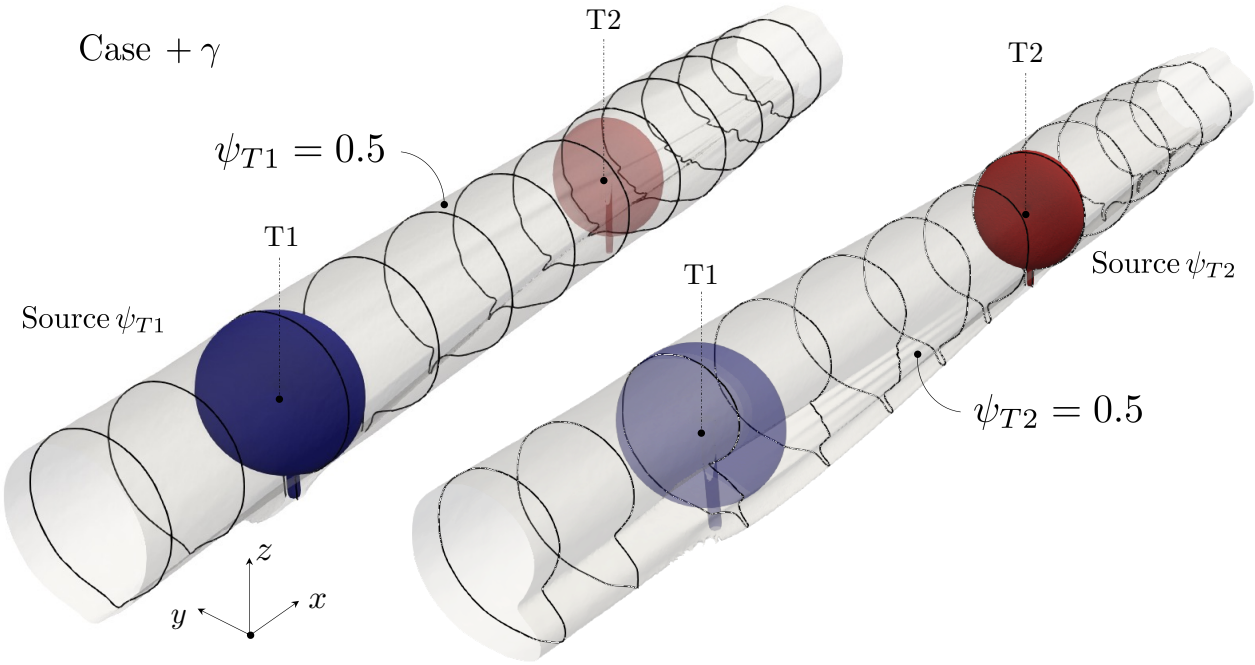

Figure 5.31: Streamtubes emanating from $T1$ (left) and $T2$ (right) in the case of a positive yaw misalignement ($\gamma = +20°$). The streamtube surface is depicted by $\psi = 0.5$ ( ) and transverse slices (—) are spaced by one diameter in the streamwise direction. The source term are depicted for the streamtube of $T1$ ( ) and $T2$ ( ). The source terms are based on the rotor swept area and the tower/nacelle positions.

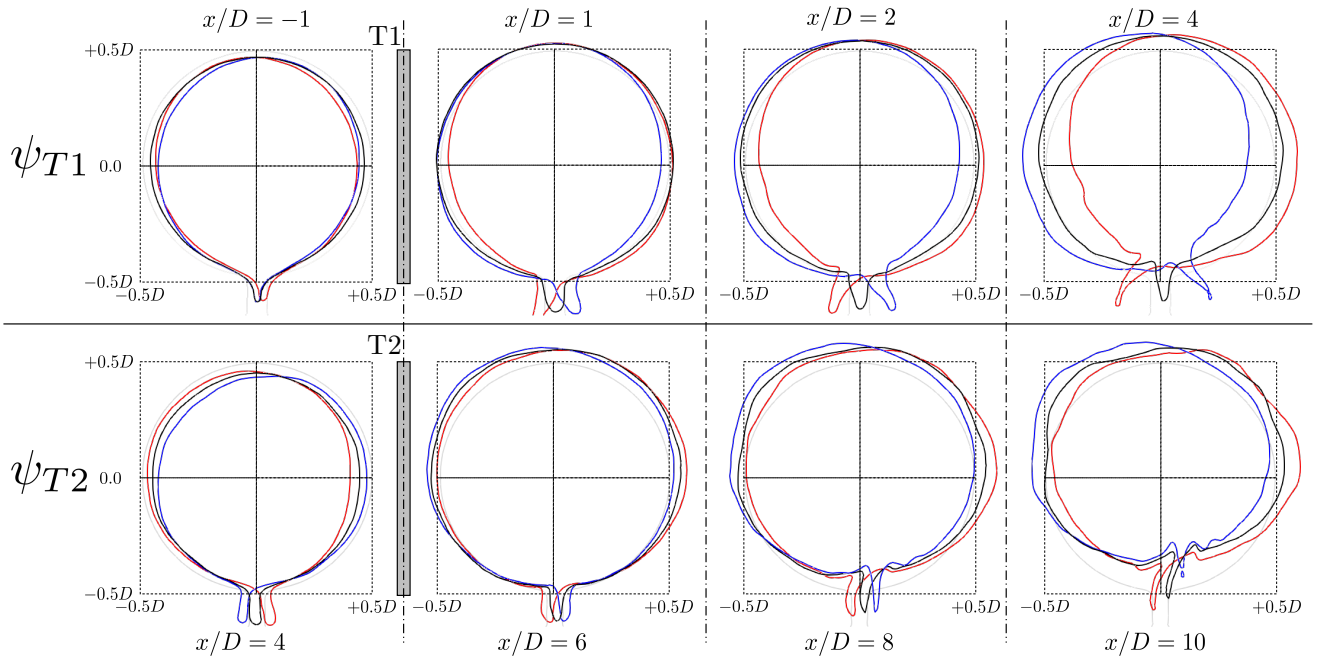

Figure 5.32: Slices of streamtubes emanating from $T1$ (top) and $T2$ (bottom) for cases $-\gamma$ (—), REF (—) and $+\gamma$ (—). The slices are at different upstream and downstream positions of the turbines depicted in grey.

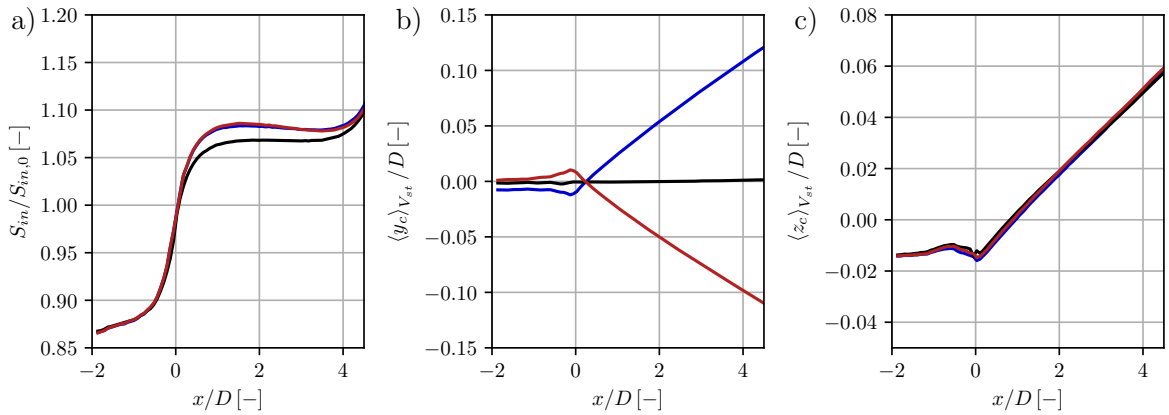

Figure 5.33: Streamwise evolution for $T1$ of (a) the streamtube sectional area, S_{in} normalized by the section at the rotor position, the streamtube center in (b) the transverse plane direction and (c) the vertical direction. Cases $-\gamma$ (—), REF (—) and $+\gamma$ (—). $T1$ is located in $x/D = 0$.

or volume. The streamtubes topology is presented through the streamwise evolution of the cross-section, the horizontal deflection, and the vertical deflection in **Fig. 5.33** for ψ_{T1} and **Fig. 5.34** for ψ_{T2}.

In **Fig. 5.33.a)**, the evolution of ψ_{T1} is shown from two diameters upstream $T1$ towards 4.5 diameter downstream. The streamtube cross-section, $S_{in}/S_{in,0}$, shows the expected increase between the upstream positions and the turbine. This is related to the wind turbine streamwise induction. Yet, downstream, the streamtube section remains mostly constant until four diameters when approaching the second turbine. From the observation in Chapter 4, the behavior is different. The section variations are higher close to the rotor, around one or two diameters. In their work, West J. R. and Lele S. K. [207] discussed the impact of variable thrust over the streamtubes sections. They showed that a higher thrust coefficient would lead to a higher cross-section variation of the streamtube and a faster reduction of the section past the turbine, i.e., quicker recovery of the velocity deficit. The yaw misaligned case has a more significant section variation, and a slight inflection past the turbine appears. From the observation in [207], $T1$ thrust for the misaligned cases is higher than the REF case. In **Fig. 5.33.b-c)**, the streamtube center position in the transverse and vertical plane shows the wake to deviate in yaw misaligned case and deflection through the top of the domain. This second aspect is due to the turbines tilt preventing the blades from colliding with the tower.

In **Fig. 5.34.a)**, the evolution of ψ_{T2} between two diameters behind $T1$ and five diameters behind $T2$ tells another story. The variation of the cross-section increases and reduces fast; the section starts to diminish at one diameter behind $T2$. From the REF scenario study, $T2$ has a thrust 30% higher than $T1$. These observations furtherly comfort the hypothesis of the lack of ψ_{T1} section reduction past $T1$. The deviation of the streamtube center is still observable in the transverse direction, see **Fig. 5.34.b)**. **Fig. 5.34.c)** shows that a positive yaw misalignment slightly reduces the streamtube elevation; while it is the opposite for $-\gamma$.

The integral of ψ_{T1} over ψ_{T2} gives an insight into how the streamtubes are overlapping. The more the streamtube are overlapping, the more the wake of $T1$ will impact the aerodynamics of $T2$. For the aligned REF case $\langle \psi_{T1} \rangle_{\psi_{T2},V_{st}} \sim 96\%$ while it is only 85% for the misaligned cases $-\gamma$ and $+\gamma$. This percentage represents the ratio of particles passing through $T2$ with a mean path crossing $T1$. This alleviates that $T1$ has a greater impact on $T2$ when yaw strategies are inactive.

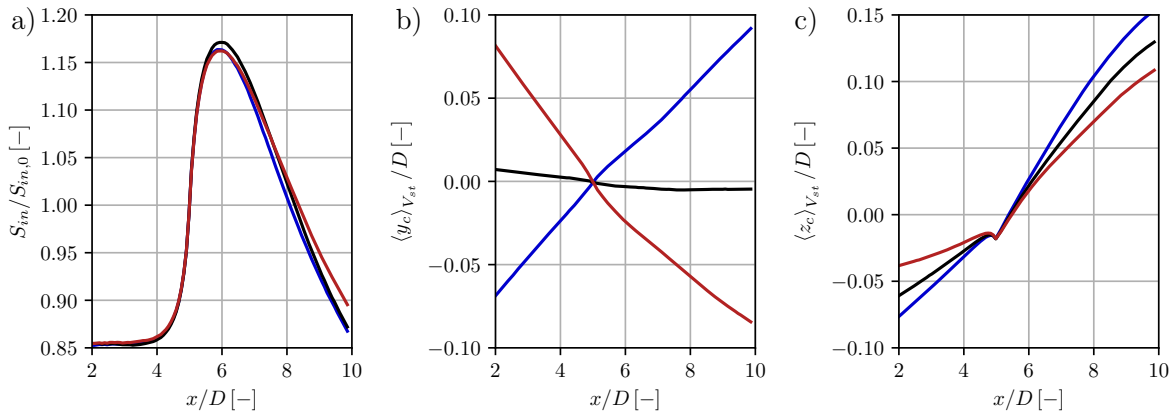

Figure 5.34: Streamwise evolution for $T2$ of (a) the streamtube sectional area, S_{in} normalized by the section at the rotor position, the streamtube center in (d) the transverse plane direction and (c) the vertical direction. Cases $-\gamma$ (—), REF (—) and $+\gamma$ (—). $T2$ is located in $x/D = 5$.

5.5.3 Mean kinetic energy budgets

To quantify the wake destabilization process and wake recovery, mean kinetic energy (MKE) budgets are performed, see Chapter 4 especially **Eq. 4.25**. This integrated budget over ψ_{T1} is shown on **Fig. 5.35**, comparing cases $-\gamma$, REF and $+\gamma$. The numbered terms on the figure respectively denote: i) the change in flux of MKE by advection, ii) the pressure work, iii) the work of the Reynolds stress tensor on the streamtube surfaces, iv) the production of TKE within the streamtube volume and v) the work of the turbine. As aforementioned in Chapter 4, the major contribution to the MKE budget is the turbine work, generating the first energy drop. It is counterbalanced by the pressure and advection of MKE, being the first source of MKE. The three cases give similar results with slight variations. The four regions (I, II, III, IV) highlighted in Chapter 4 are not appearing. Due to the upstream turbulence, the first region associated with the unperturbed helical tip vortices advection is not present. The upstream turbulence triggers the helical vortex instabilities, and there is a production of TKE. The light blue represents this second region starting from the rotor position. The third region, depicted in dark blue, is delimited by the MKE advection, becoming negative in the wake until it begins to increase again. The MKE advection barely reaches a negative value in these configurations. This is translated into a close-to-no velocity deficit recovery. This can be observed in **Fig. 5.36.a)** depicting the evolution of streamwise velocity. The second turbine induction is already perturbing the wake recovery of $T1$. This can be observed from the MKE advection increasing again and the pressure work reducing. By looking at the TKE in **Fig. 5.36.c)**, the evolution is still linear, meaning that the maximum is not reached and the "far wake" region, IV is not occurring. The evolution of the transverse velocity in **Fig. 5.36.b)** is mostly the same as the observation of Chapter 4.

The recovery of $T2$ behaves differently, and in a closer way to the cases presented in Chapter 4, as shown by the budget for this turbine in **Fig. 5.37**. The regions II, III, and IV are represented. The second region, supposedly starting when TKE is produced is influenced by the wake of $T1$ as the production of TKE is already present upstream of $T2$. This was not observed for $T1$ even if the turbine was submitted to a turbulent inflow. The third region starts when the MKE advection becomes negative in the wake. The last region appears in the range of four diameters behind $T2$ where the maximum level of TKE appears, see **Fig. 5.38.c)**. The limits of these regions are similar to the one computed for the case $TI_{7\%}\gamma_{30°}$ in Chapter 4.

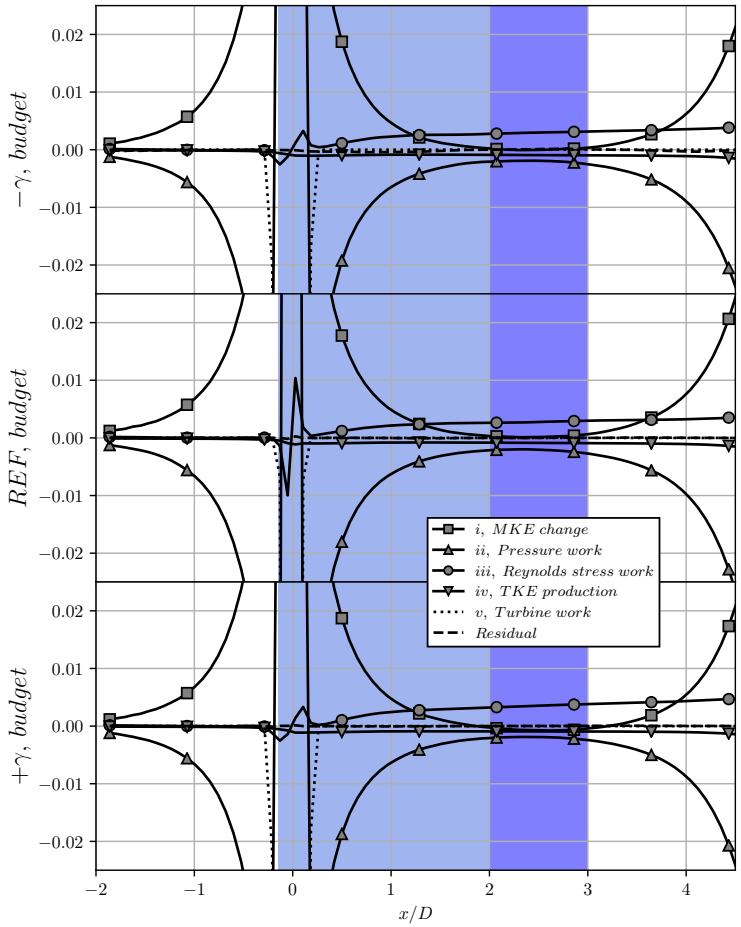

Figure 5.35: Mean kinetic energy equation terms integrated over the streamtube ψ_{T1} cross-section for cases (top) $-\gamma$, (midlle) *REF* and (bottom)$+\gamma$. Each term is normalized by the total turbine power such as the integral of term v is equal to -1. The residual corresponds to the sum of all terms of **Eq. 4.25**.

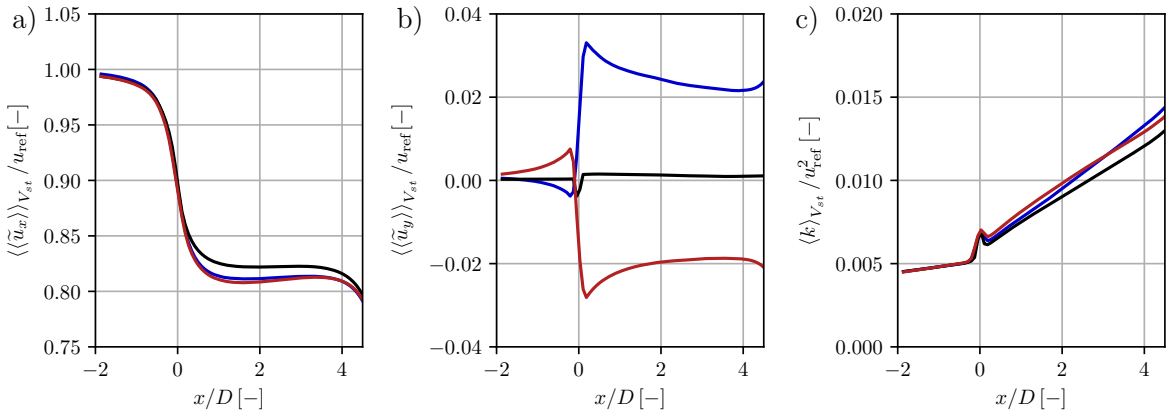

Figure 5.36: Streamwise evolution for ψ_{T1} of (a) mean streamwise velocity, (b) mean tranverse velocity and (c) turbulent kinetic energy integrated over the streamtube volume for cases $-\gamma$ (—), *REF* (—) and $+\gamma$ (—).

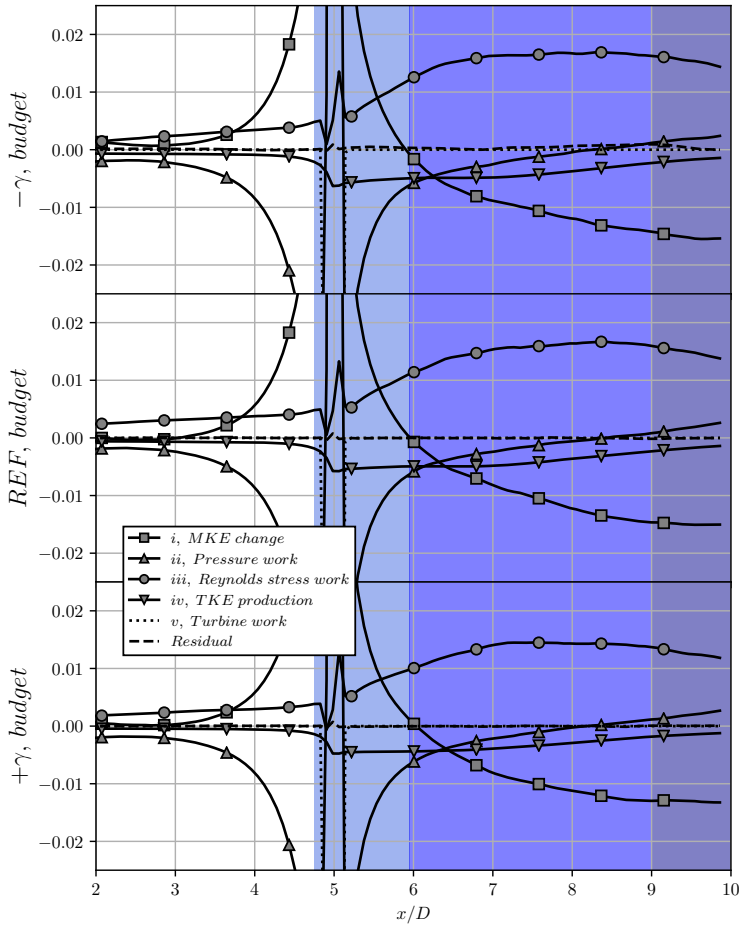

Figure 5.37: Mean kinetic energy equation terms integrated over the streamtube ψ_{T2} cross-section for cases (top) $-\gamma$, (midlle) *REF* and (bottom)$+\gamma$. Each term is normalized by the total turbine power such as the integral of term v is equal to -1. The residual corresponds to the sum of all terms of **Eq. 4.25**.

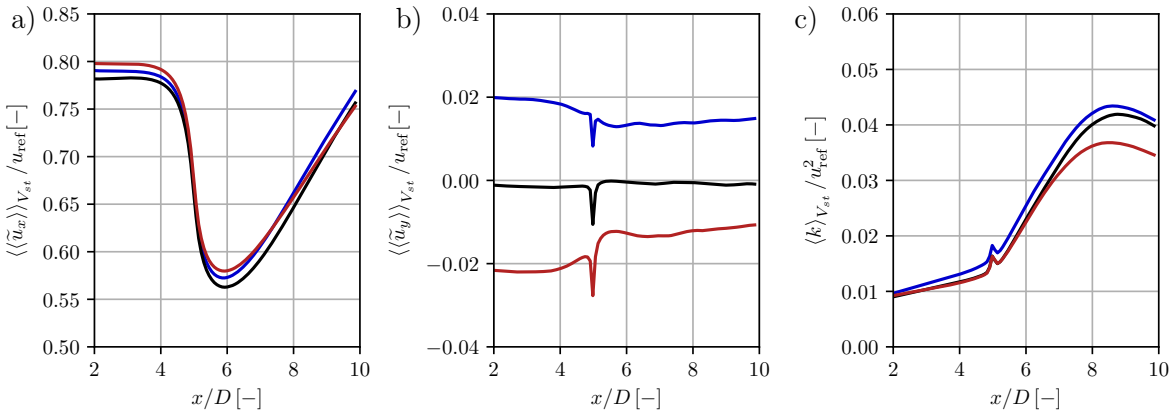

Figure 5.38: Streamwise evolution for ψ_{T2} of (a) mean streamwise velocity, (b) mean tranverse velocity and (c) turbulent kinetic energy integrated over the streamtube volume for cases $-\gamma$ (—), *REF* (—) and $+\gamma$ (—).

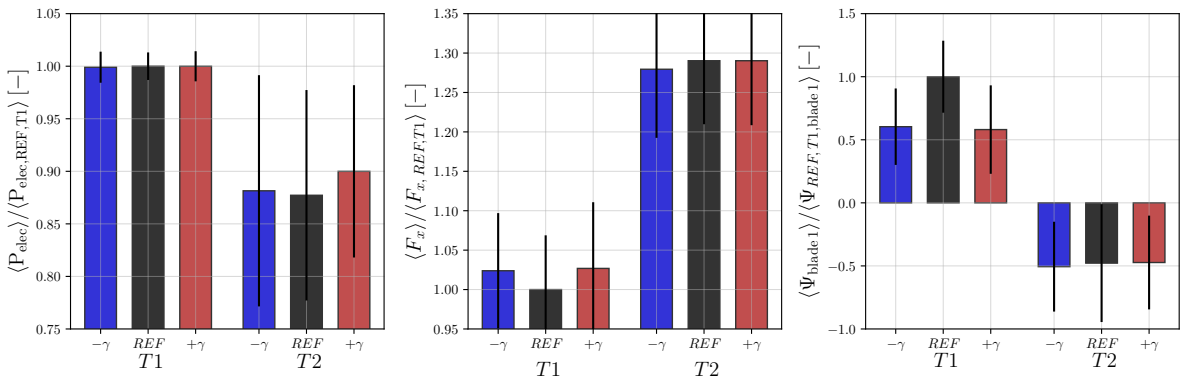

Figure 5.39: Time averaged electical power production (left) normalized by the electrical power production of $T1$ in case (REF), root-mean-square are shown with error bars. Time avergaed thrust force (middle) normalized by the thrust force of $T1$ in case (REF), fluctuations are displayed yet too small to be observed. Time averaged first blade pitch angle (middle) normalized by the pitch angle of $T1$ in case (REF). Cases: $-\gamma$ ( ), REF ( ) and $+\gamma$ ( ).

Now that the global wake diagnostics are presented, the following sections focus on the response of the wind turbines in terms of control and deformations.

5.5.4 Turbines response and performances

The time-averaged electrical power production, turbine thrust, and pitch angles are represented in **Fig. 5.39**. The first turbine is at its nominal power with fluctuations reaching 1% for the three cases. The negative or positive yaw angle does not impact the power production. The approximation from the literature [40, 191] which consists in multiplying the maximum power of the non-yawed turbine by $\langle P \rangle \cos^3(\gamma)$ is not applicable here. This is due to the wind speed being slightly above the rated point. This means the turbine controller is activating the pitch of the blades. For the turbines misaligned with the wind, this is translated by a pitch half the one of the REF case. In the same way, the thrust of the turbine is 2% higher for scenario $-\gamma$ and $+\gamma$. Yet, it opposes the reduction by $\langle F_x \rangle \cos^2(\gamma)$ on the thrust of the non-yawed rotor.

The second turbine, impacted by the wake of $T1$, sees a drop in its power production of roughly 12% depending on the scenario. The aligned case (REF) is the worse scenario where the power of $T2$ is reduced by -12.5% compared to the first turbine. The negative yaw angle misalignment scenario ($-\gamma$) gives -11.8%. The power fluctuations are similar to (REF). The positive yaw angle misalignment scenario ($+\gamma$) shows promising results. Indeed, the second turbine power production is only reduced by -10% making this scenario the most adequate in terms of power production. Even more, the power fluctuations for $+\gamma$ are 2% lower than for REF. The fact that $T2$ is producing more for $-\gamma$ and $+\gamma$ is explained by the wake of $T1$ being deflected to the side of $T2$. As shown in **Section 5.5.2**, the streamtube for $-\gamma$ and $+\gamma$ are overlapping at 85% against 96% for REF. This means that $T2$ is less impacted by fluid particles that went through the rotor of $T1$ for $-\gamma$ and $+\gamma$.

For REF and $+\gamma$, the averaged thrust is roughly 28% higher for the second turbine than $T1$ in REF while it is 27% higher for the case $-\gamma$. The pitch angles for this second turbine are similar for all cases compared to the first turbine pitch. The fluctuations of pitch angle are identical.

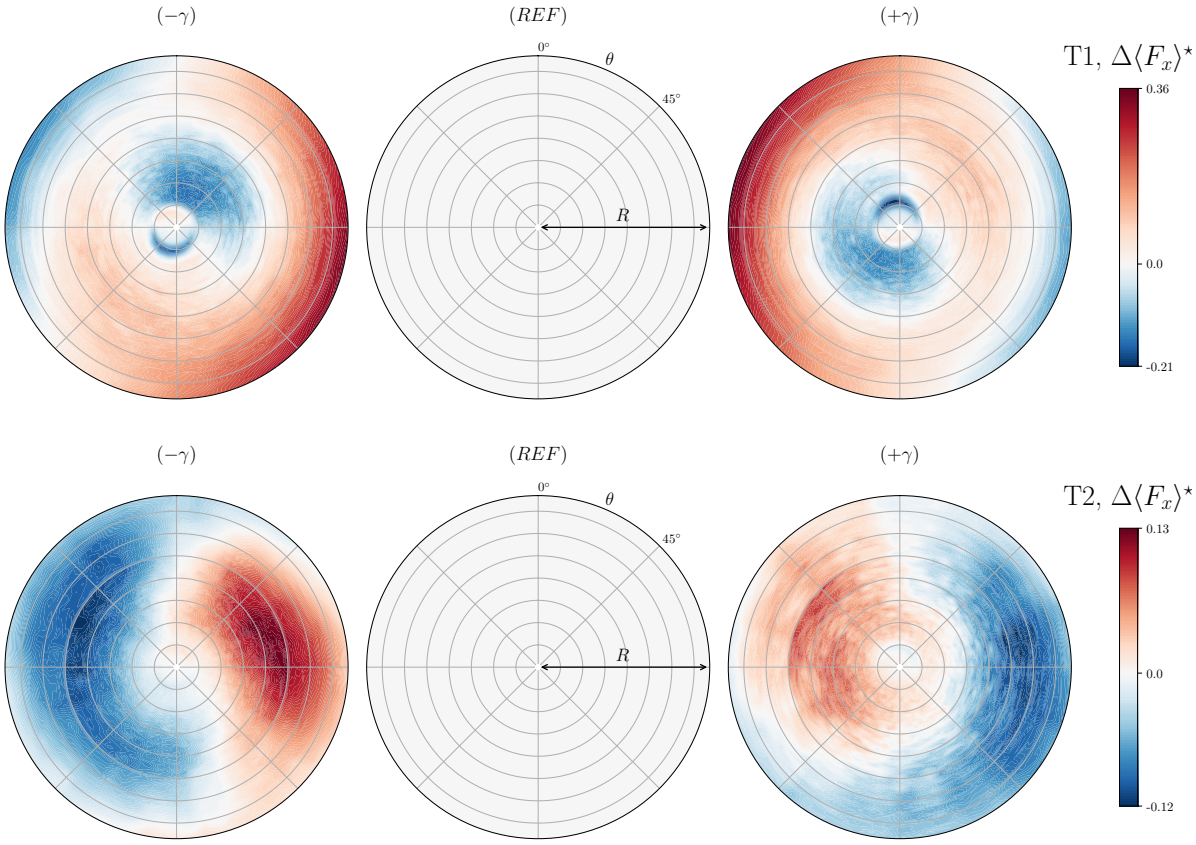

Figure 5.40: Azimuthal and radial mean streamwise force (equivalent to the contibution to thrust) for $T1$ (top) and $T2$ (bottom). The results display the discrepancies for each case in comparison to the reference case (C).

The observation of the time series of the electrical power production has the same tendency as in **Fig. 5.14** and therefore are not presented. The first turbine response is similar for all cases, with slight discrepancies appearing over time; the turbine constantly fluctuates around the nominal power. The evolution of power production of $T2$ shows significant fluctuations correlated to the synthetic turbulence box period. The frequencies appearing in the power spectra of REF (see **Fig. 5.14**) are the same for $-\gamma$ and $+\gamma$ and no supplementary peaks are observed.

5.5.5 Loads repercussions on structural deformations and fatigue

This section focuses on the wind turbines response to the fluid motions. At first, the blade loads are evaluated, and the close linkage between them and the blade deformation is shown. Finally, the flapwise and edgewise blade root moment damage equivalent loads are computed.

The comparison of the loads is provided through the azimuthal and radial discrepancies with REF of the time-averaged streamwise (**Fig. 5.40**) and tangential (**Fig. 5.42**) forces. The discrepancies are shown as:

$$\Delta\langle F_{x/\theta,T,\,Case}\rangle^{\star}(r,\theta) = \frac{\langle F_{x/\theta,T,\,Case}\rangle(r,\theta) - \langle F_{x/\theta,T,\,REF}\rangle(r,\theta)}{\langle F_{x/\theta,T,\,REF}\rangle}\,. \tag{5.27}$$

The evolution of the streamwise force, **Fig. 5.40**, representative of the contribution to thrust, shows one pattern for the yaw misaligned rotors. When the blade is at its horizontal position

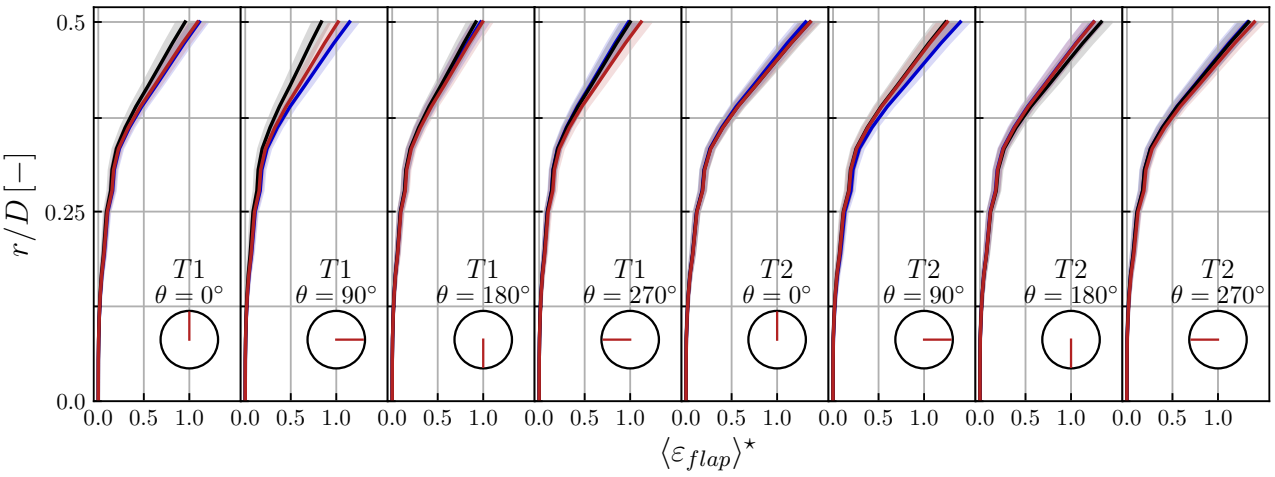

Figure 5.41: Radial profiles of mean flapwise deformations at $\theta = 0°$, 90°, 180° and 270° for $T1$ (right) and $T2$ (left), depicted according to $T1$ maximal flapwise deflection, see **Eq. 5.25**. The root-mean-square of the deformations are shown with an area around the curves. Cases: $-\gamma$ ( ), REF ( ) and $+\gamma$ ( ).

and facing upstream, i.e., $\theta = 90°$ for $-\gamma$ and $\theta = 270°$ for $+\gamma$, the streamwise force is higher for the top half of the blade than in the REF case. The forces are also slightly increased for the vertical positions, up or down. And for the second horizontal position, the blade is submitted to a reduced force in the top half of the blade. By comparing these observations to the flapwise deformation presented in **Fig. 5.41** a higher deformation is observed when the blade is at its horizontal position and facing upstream, i.e., when the streamwise force is higher. At these azimuths the deformations are +16% for $\gamma = -20°$ and +13% for $\gamma = +20°$. For the second turbine impacted by the wake of the first, the streamwise forces are reduced on one half of the rotor and increased on the other one. This is due to the deflection of the velocity deficit observed in **Fig. 5.28** one diameter upstream $T2$ compared to the reference case. There is a reduction of the local velocity on one side of the rotor and augmentation on the other side. The flapwise deformations follow the same pattern with higher/lower deformations when the streamwise force is higher/lower. As observed in **Section 5.4.3**, the flapwise deformation is ∼20% higher for the second turbine. For both yaw misalignments, the deformation is reduced when the blade points down, reducing the distance between the blade tip and the tower and preventing collisions.

The evolution of the tangential force, **Fig. 5.42**, representative of the contribution to the turbine torque, shows a pattern similar to the streamwise force. When the blade is at its horizontal position and facing upstream, i.e., $\theta = 90°$ for $-\gamma$ and $\theta = 270°$ for $+\gamma$, the contribution to the torque is higher for the top half of the blade than in the REF case. The forces are also slightly increased for the vertical positions, up or down depending on the yaw angle sign. By comparing these observations to the edgewise deformation presented in **Fig. 5.43** a higher deformation is observed when the blade is at its horizontal position and facing upstream, i.e., when the tangential force is higher. At these azimuths the deformations are +15% for $\gamma = -20°$ and +3% for $\gamma = +20°$. The difference in edgewise deformation between the two opposing yaw angles is due to the superposition of the gravitational forces on the blade. For $+\gamma$, the aerodynamic forces are reduced compared to REF when the weight is colinear to the tangential force. This is the opposite for $-\gamma$, which results in a higher deformation in the edgewise direction. The blade torsion is impacted in the same manner. For the second turbine, the conclusions

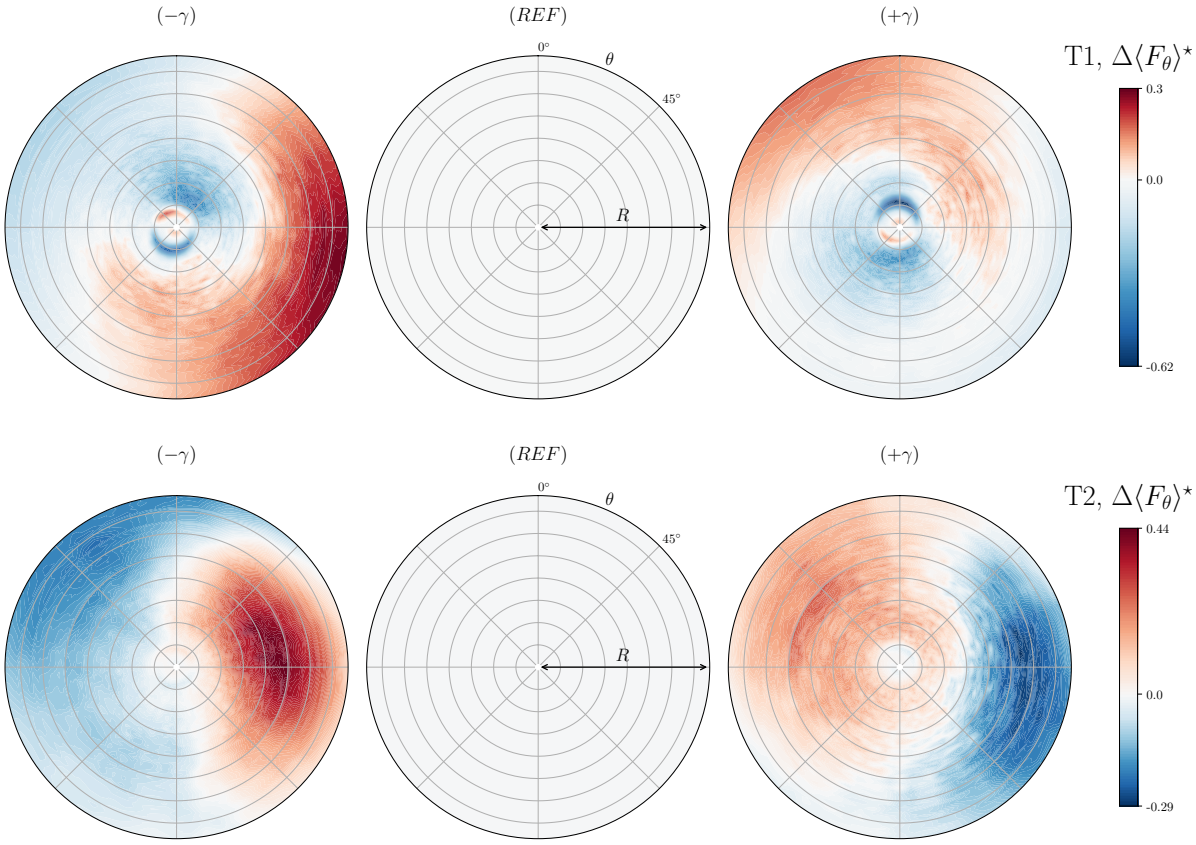

Figure 5.42: Azimuthal and radial mean tangential force (equivalent to the contibution to torque) for $T1$ (top) and $T2$ (bottom). The results display the discrepancies for each case in comparison to the reference case (C).

are similar but not due to the same effect. The torque contribution of the second turbine is reduced on the side impacted by the first turbine wake and increased on the other side. $T2$ is less impacted by the velocity deficit when $T1$ is misaligned. The edgewise deformations variations are similar to the one of $T1$. On the side impacted by the wake, the tangential force is lower and the equilibrium with the weight of the blade is impacted resulting in larger $(-\gamma)$ or smaller $(+\gamma)$ edgewise deformations on this side. The positive yaw angle scenario reduces the maximal edgewise deformations of the turbine. The torsion of the blade presented in **Fig. 5.44** is resulting from a combination of both forces presented above.

The Damage Equivalent Loads (DEL) [257] is a constant load value that, when applied over a defined number of cycles, leads to the same damage as a time-varying load. From this, it is possible to compare different load signals and analyze the factors that influence the fatigue reduction on the wind turbine structure. The damage D perceived by a component submitted to a varying moment $M(t)$ over a finite time period T is given by Palmgren-Miner′s rule

$$D = \sum_{i=0}^{n} \frac{n_{c,i}}{N_{F,i}}\,, \tag{5.28}$$

where n is the number of range stress classes, $n_{c,i}$ is the number of cycles for each range stress class according to the rainflow algorithm, and $N_{F,i}$ is the number of cycles to failure for each range stress class. The DEL is the sinusoidal load $M_{a,eq}$ at frequency f_{eq} and thus showing $n_{c,eq} = f_{eq}T$ cycles over the period T whose damage $D = \frac{n_{c,eq}}{N_{F,eq}}$ would be equivalent to that of

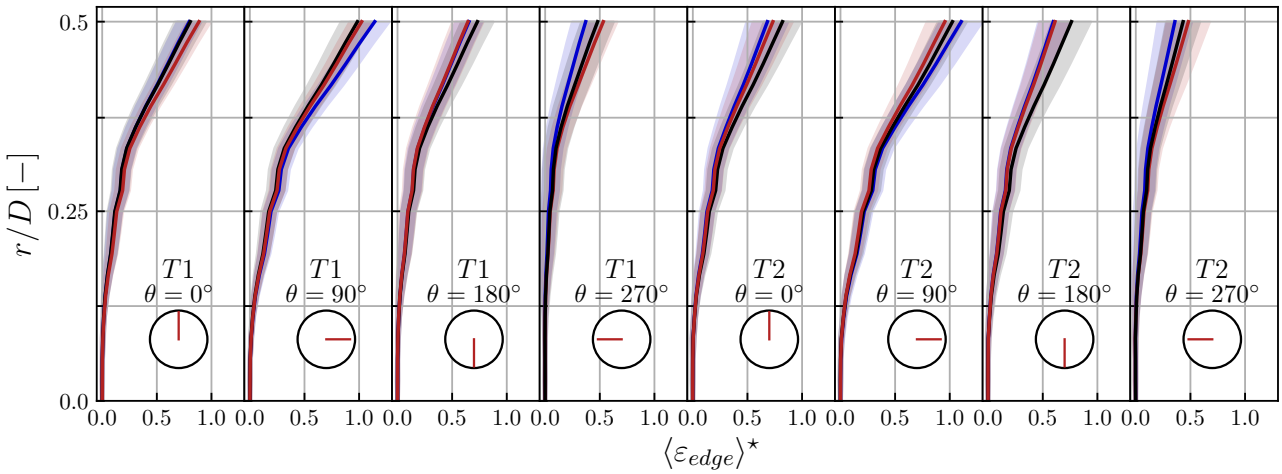

Figure 5.43: Radial profiles of mean edgewise deformations at $\theta = 0°$, $90°$, $180°$ and $270°$ for $T1$ (right) and $T2$ (left), depicted according to $T1$ maximal edgewise deflection, see **Eq. 5.25**. The root-mean-square of the deformations are shown with an area around the curves. Cases: $-\gamma$ ( ), REF ( ) and $+\gamma$ ( ).

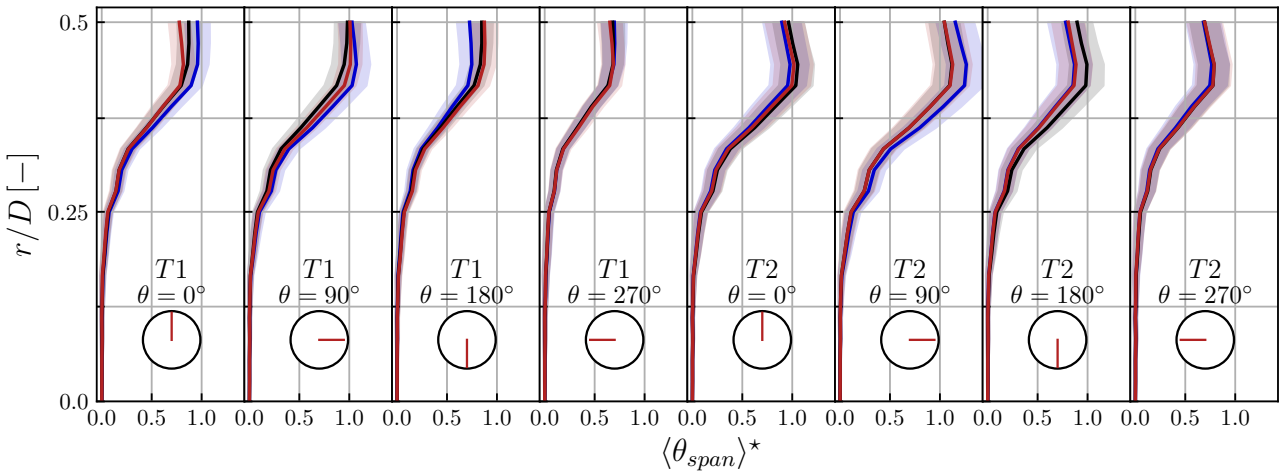

Figure 5.44: Radial profiles of mean torsion at $\theta = 0°$, $90°$, $180°$ and $270°$ for $T1$ (right) and $T2$ (left), depicted according to $T1$ maximal torsion, see **Eq. 5.25**. The root-mean-square of the deformations are shown with an area around the curves. Cases: $-\gamma$ ( ), REF ( ) and $+\gamma$ ( ).

Case	$\Delta DEL^{\star}_{M_x}$		$\Delta DEL^{\star}_{M_y}$	
	$T1$	$T2$	$T1$	$T2$
$+\gamma$	-1.5%	-2.5%	$+6\%$	$+41\%$
REF	$-$	$+3\%$	$-$	$+45\%$
$-\gamma$	$+3\%$	$+9\%$	$+10\%$	$+43\%$

Table 5.5: Evolution of the damage equivalent loads for the edgewise and flapwise blade root moments given according to $T1$ in the reference case REF.

the signal of interest. This approach is based on S-N curves (Stress vs number of cycle), also known as the Wohler′s curves, for the particular material. From this, and by assuming that the moment is proportional to the stress, the number of cycles to failure and equivalent cycles are expressed as $N_{F,i} = kM_{a,i}^{-m}$ and $N_{F,eq} = kM_{a,eq}^{-m}$, with k and m being material properties. Finally, the DEL can be expressed as

$$DEL_M = M_{a,eq} = \left(\sum_{i=0}^{n} \frac{n_{c,i} M_{a,i}^{m}}{n_{c,eq}} \right)^{1/m} \tag{5.29}$$

The m exponent depends on the material. Its value for fiberglass is 10 [258] and will be used in this study.

To consistently compare the cycle counts, a period of $T = 1100\,\mathrm{s}$ is considered, corresponding to two Mann box lengths or roughly 6800 revolutions. Two different input signals have been chosen, the flapwise (M_y) and edgewise (M_x) blade root moment, respectively. The first one is called the "bending moment", while the second is referred to as the blade torque. It is essential to mention that the rainflow algorithm considers only the fluctuations while the mean value is unused; the selected ranges for cycles are bins from 0 to 10 MN.m of 0.2 MN.m size. The dimensionless difference $\Delta DEL^{\star}_{M_i}$ are presented according to the $DEL_{M_i,T1,REF}$, i.e., the damage equivalent loads of the first turbine in the case without yaw misalignment:

$$\Delta DEL^{\star}_{M_i,T,Case} = \frac{DEL_{M_i,T,Case} - DEL_{M_i,T1,REF}}{DEL_{M_i,T1,REF}} \tag{5.30}$$

Sample of signal, power spectra, and histogram of cycles are shown for the flapwise and edgewise moments of $T1$ in **Fig. 5.45** (left) and (right) respectively. The peaks beginning from the lower frequencies of blade-root flapwise bending moment, shown in **Fig. 5.45**, correspond to the harmonics of the rotor rotational frequency (ω, 2ω, 3ω). The amplitudes of these harmonics decrease with increasing frequency. The turbulent flow field exerts forces onto the blade with an extensive range of frequencies such that the harmonics of the rotational speed are captured in these spectra. The highest peak corresponding to ω indicates that the most significant load cycle amplitudes are due to asymmetric blade loading. This asymmetry is due to the vertical wind shear or the passage of turbulent structures through one side of the rotor disk. For the blade-root edgewise moment, peaks are appearing at ω, 2ω, 5ω, 12ω and 25ω. Similarly to the flapwise bending moment, several harmonics of the rotation speed appear. Note that the blade passing frequency 3ω is not appearing. The same figure including the sample of signal, power spectra, and histogram of cycles for the flapwise and edgewise moments is presented for $T2$ in **Fig. 5.46**. The significant discrepancies with the previous observations are the peak amplitude, but the behavior remains the same.

The $\Delta DEL^{\star}_{M_x}$, and $\Delta DEL^{\star}_{M_y}$ are gathered in **Tab. 5.5**. At first, the reference scenario has a higher DEL for the second turbine, up to +45% with the flapwise moment and only +3% for

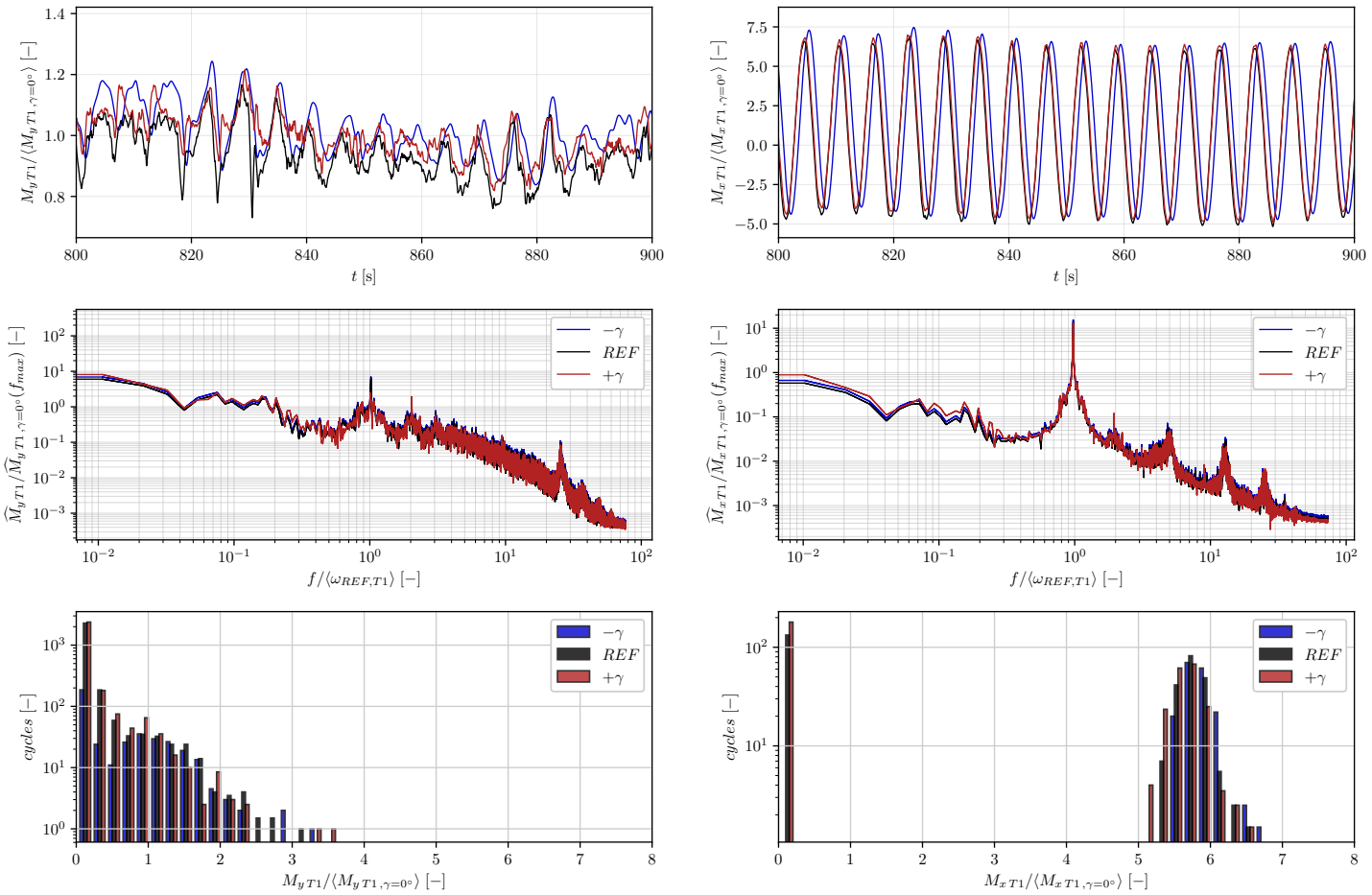

Figure 5.45: Estimation of the DEL for the first turbine $T1$: (top) Sample of the temporal evolution of the flapwise (left) and edgewise (right) blade root moment. (middle) Power spectra of these blade-root moments. (bottom) Histogram of the number of cycle per amplitude used to compute the DEL. Cases: $-\gamma$ ( ), REF ( ) and $+\gamma$ ( ).

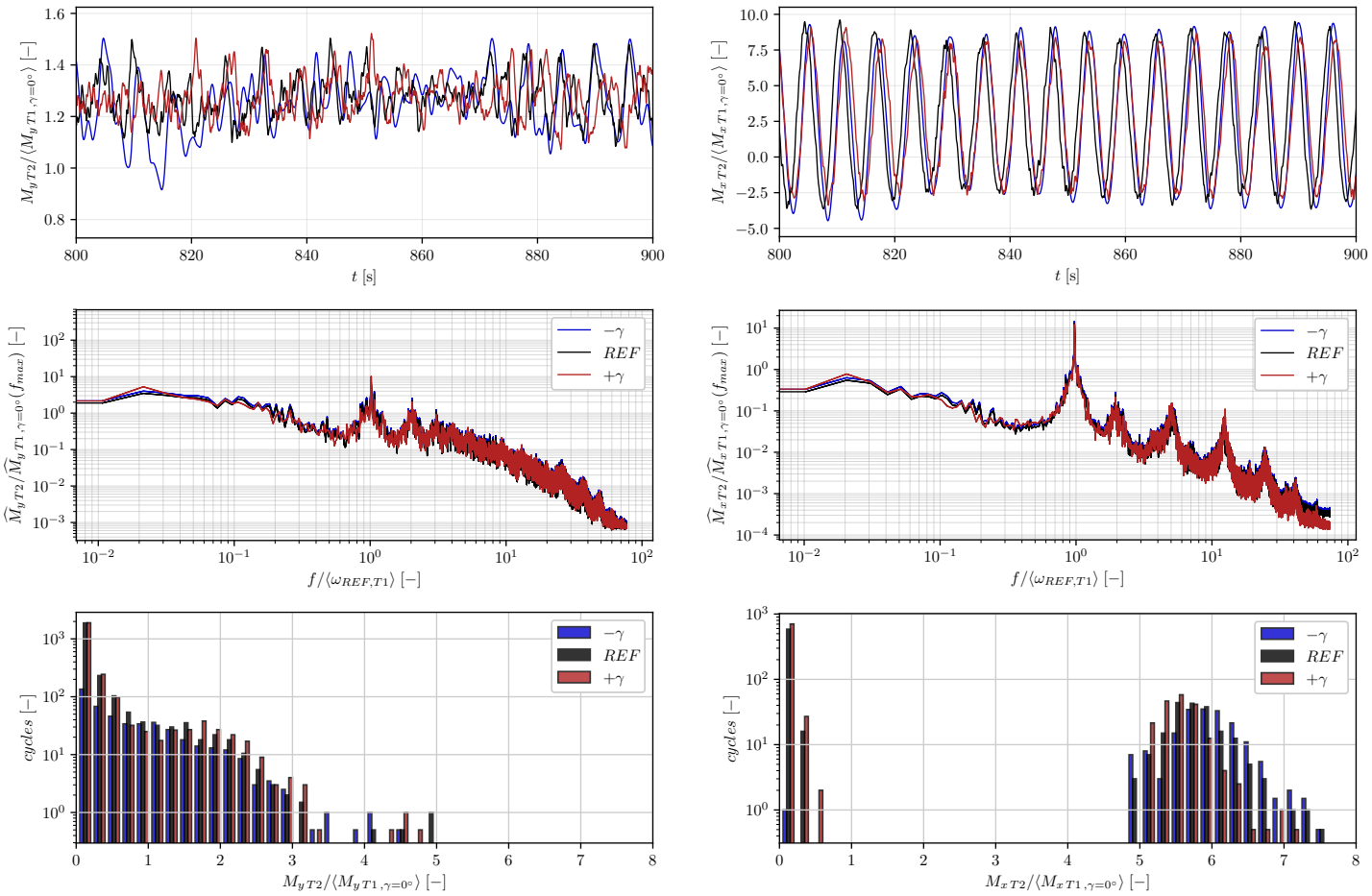

Figure 5.46: Estimation of the DEL for the first turbine $T2$: (top) Sample of the temporal evolution of the flapwise (left) and edgewise (right) blade root moment. (middle) Power spectra of these blade-root moments. (bottom) Histogram of the number of cycle per amplitude used to compute the DEL. Cases: $-\gamma$ ( ), REF ( ) and $+\gamma$ ( ).

the edgewise moment. For the positive yaw misalignment, the edgewise DEL is reduced for both turbines -1.5% for $T1$ and -5% for $T2$. For the $-\gamma$ case, the edgewise DEL of the turbines is increased by $+3\%$ and $+6\%$, respectively. For both yaw misalignments, the flapwise DEL is increased for the first turbine and reduced for the second. The edgewise blade root moment is strongly reduced for both turbines in the case of a positive yaw angle, while it is increased for a negative yaw angle.

5.6 Conclusions

This chapter proposes a coupling between an aero-servo-elastic solver and the ALM in YALES2. The aim is to take into account the structural deformation of the blades during the LES. Furthermore, the coupling has the controller of the actual wind turbine implemented. This allows the investigation of close-to-real scenarios with a representative turbine response. This coupling introduces a supplementary layer of physics to understand and increase the richness of the results. The investigated scenario is the interaction between two inline wind turbines represented by actuator lines for the blades, as well as for the tower and nacelle. The structure of both turbine blades is deformable.

The first results highlight the various physical effects and the associated wind turbine response for this scenario without yaw misalignment. Furthermore, the influence of mesh refinement is investigated, and the turbine performances and deformations are compared to representative BEM results. The wind turbines are exposed to an inflow close to their rated wind speed and operate under the control regions two and three. The injection of synthetic Mann turbulence overlayed to a power-law velocity profile generates several events with a repetitive pattern. These repetitive events are represented by low (-3%), reference, and high ($+3\%$) velocities at hub height, impacting the turbine response and performances. These events impact the velocity deficit generated by the first turbine. The second turbine receiving this velocity deficit will switch from one control region to another. On average, the pitch angle of the second turbine is lower than the first turbine, and the thrust coefficient is higher. This higher thrust generates a more significant velocity deficit behind $T2$, which overlays with the wake of $T1$. The wakes are mostly symmetric from the horizontal slice, while they are redirected through the top of the domain as seen from the vertical slice. Peaks of TKE are appearing downstream the tip of $T2$ blades. The discrepancies between REF and $REF0$, with a mesh of twice the cell size, are in the majority appearing on the turbine performances. The electrical power output of $T2$ is 5.4% higher for $REF0$, which is translated by a higher pitch caused by an overestimation of the loads. The resolution near the turbine is 77 cells per diameter for REF while it is 38 for $REF0$. The guideline from the litterature [158] assesses that at least 64 cells per diameter should be used for a proper loads evaluation, which is not the case for $REF0$. Nevertheless, the thrust from the rotor only differs by 1%, and the resulting flow topology is close to similar in the wakes. The cell size reduction only near the turbines in $REF0$ would supposedly improve the turbine performances according to REF. Under this hypothesis, the computational cost of $REF0$ would slightly increase but give reliable results at a lower cost than REF. The wall clock time would not be impacted since the coupling with the structural solver limits the simulation time-step. Nevertheless, the number of processors could be significantly reduced and, with it, the computational cost. Turbulence boxes located one diameter upstream of the turbine are built from the simulated flow. These turbulence boxes are then injected into the BEM present in BHawC, providing comparative results from two different methodologies. The BEM results showed to be in good accordance with the REF case for the time-averaged turbine performances,

yet a variable phase shift is observed on the turbine instantaneous response. The flapwise deformations, edgewise deformations, and blade torsion have the same order of magnitude yet slightly differing, especially for the edgewise deformations of the second wind turbine.

After this first investigation, the first turbine yaw misalignment repercussions are investigated. Two yaw misalignment of $T1$ are simulated, $\gamma = -20°, +20°$. Firstly, the flow topology showed the wakes of the yawed turbines to be redirected, impacting a smaller portion of the second turbine rotor. The streamtube construction showed how the yaw misalignment of $T1$ impacts the wake bounds. The streamtube source gathers the rotor area and the tower of the turbine. The streamtube behind the tower of $T1$ deviates in opposition to the wake as observed in Chapter 3 when yaw misalignment is applied. Furthermore, the thrust of the first turbine is low due to the turbine operating above rated wind speed. A reduced thrust for a yawed turbine means a lower deviation due to the lower forces in the transverse direction. The mean kinetic energy budget over the streamtubes explains the difference in wake recovery between the two turbines, which is directly related to the thrust of the turbines. The first turbine, misaligned or not, has a thrust 30% lower than the second turbine. Nevertheless, the power production of the turbines draws interesting conclusions. The first turbine is at its nominal power with fluctuations reaching 1% for all cases. The negative or positive yaw angle does not impact the power production. But, when a positive yaw angle is applied on the first turbine, the electrical power production of $T2$ is increased by +2.5%. If the yaw is negative, the output only reaches +0.7%. The deformations of $T1$ show a flapwise deformation $\sim$ 15% higher than the reference case when the blade is at the vertical position and upstream the rotor hub, i.e. when $\gamma = -20°$ for $\theta = 270°$ deformations are +16% and when $\gamma = +20°$ for $\theta = 90°$ deformations are +13%. The edgewise deformations increase at the same locations, +15% for $-\gamma$ and +3% for $+\gamma$. The difference of deformation between the two opposing yaw angles is due to the superposition of the gravitational forces on the blade. For $+\gamma$, the aerodynamic forces are reduced compared to REF when the weight is colinear to the tangential force. This is the opposite for $-\gamma$, which results in a higher deformation in the edgewise direction. The blade torsion is impacted in the same manner. For the second turbine, the conclusions are different. The wake is redirected for yawed cases, and $T2$ is less impacted by the velocity deficit. The deformations are in the majority lower when yaw misalignment is applied on the upstream turbine. The edgewise deformations are reduced by 10%. To follow up, the induce fatigue is presented through damage equivalent loads (DEL) based on the flapwise and edgewise blade root moments. The reference scenario has a higher DEL for the second turbine, up to +45% with the flapwise moment. For the positive yaw angle, the edgewise DEL is reduced for both turbines −1.5% for $T1$ and −5% for $T2$. For the $-\gamma$ case, the edgewise DEL of the turbines is increased by +3% and +6%, respectively. For both yaw misalignment, the flapwise DEL increases for the first turbine and is reduced for the second.

In conclusion, the first turbine positive yaw angle misalignment shows the most promising results. The coupling with the aero-servo-elastic solver allows drawing concrete solutions over a scenario of wake interactions. The multi-physical aspect of the coupled simulations is encouraging. It enables the investigations of fully turbulent wakes interactions of yawed wind turbines and to observe the repercussions on the structural properties. The perspective of this work would be to investigate more complex scenarios with different inflow and in wind farm configurations with a significant amount of turbines. Strategies based on yaw misalignment should now focus on below-rated wind speed scenarios. As highlighted in Chapter 4 and the literature, the wake redirection is related to the transverse force applied by the turbine on the flow. Higher wind speed impacting the turbines will result in a lower transverse force due to the turbine controller

pitching the blade. Therefore, scenarios with higher wind speed will have a lower impact on the wake redirection and the fatigue reduction of a downstream turbine.

Chapter 6

Conclusions and perspectives

Contents

6.1 Conclusions 183

6.1.1 Implementation, optimizations, and validations of the Actuator Line Method in YALES2 184

6.1.2 Quantify the yawed wind turbine wake recovery and the turbulent mixing layer expansion 185

6.1.3 Multiphysical approach by coupling ALM-LES to a servo-elastic solver . 186

6.2 Perspectives 188

6.2.1 Optimizations and improvements of the framework 188

6.2.2 Wake investigations and models 188

6.2.3 Extend the solved physics and further investigation of strategies relying on yaw misalignement 189

6.1 Conclusions

The main objective of this thesis project is to replicate numerically the behavior of the flow surrounding wind turbines under yaw misalignment. Three main milestones can be highlighted. First, reach the state-of-the-art in terms of wake modeling in an extensive high-performance computing and Computational Fluid Dynamics (CFD) framework. This gathers the implementation and optimization of the Actuator Line Method (ALM) within a Large-Eddy Simulation (LES) framework. This methodology is then compared to experimental wind tunnel results. The second milestone is the development of quantitative post-processing based on the transport of level set functions. Two types of transport are evaluated, one from the time-averaged streamflow and the second from the instantaneous flow field. The first tracking level set function displayed the properties of a streamtube surrounding the turbine. The integrated quantities over such streamtube are compared to the so-called 1D momentum theory and used to close mean kinetic energy and momentum budgets. The transport from the instantaneous flow field gives an insight into how the wake turbulent mixing layer expands in the wake of a wind turbine. The final milestone is the multiphysical approach based on coupling this framework to a servo-elastic solver. This aimed at combining the fidelity of CFD and the structural deformations occurring on actual wind turbines to quantify the relevance of yaw misalignment strategies. The main conclusions over these three milestones are presented in the following sections.

6.1.1 Implementation, optimizations, and validations of the Actuator Line Method in YALES2

The choice to use the ALM in the LES framework comes from the ratio between fidelity and computational time. The ALM aim at modeling the forces occurring at each blade section by using the local fluid quantities. This prevents resolving the flow at the blade boundary layer and the use of really small cells near the blade, limiting the timestep of the computation. Yet, this methodology relies on tabulated aerodynamic coefficients for each airfoil section, the corrections to properly emulate the loads, and the notion of mollification to apply the forces on the Eulerian grid. From that, several implementations are possible. When looking at the literature, numerous works describe the method and introduce various ameliorations. In this thesis, using a massively parallel CFD code on unstructured mesh led to different optimization strategies to increase computational efficiency. The first is the selection of the cells on which to mollify the evaluated forces. The mollification can be resumed as a way to spread a force at a given location on the surrounding volume depending on the distance to the point. Depending on its parameters, the volume can gather numerous cells close to the blade. This is why an algorithm selects the cells to be considered during force mollification. The validation significantly reduced the dependency between the number of points for each actuator line and the computational cost. The second strategy is the substeping of the actuator line. This allows achieving a blade CFL number higher than one while preserving the flow physics and reducing the computation wall clock time. The validation under different inflows with the NREL5MW wind turbine showed good accordance for the loads and flow structures while gaining a three-times speed-up on the wall clock time.

These implementations and optimizations are validated for a yawed wind turbine with respect to an extensive experimental dataset. Three significant aspects are investigated: the impact of turbulence grids on the wind tunnel flow, the effect of yaw angle and inflow on the wake of a single turbine, and the interaction of such wake with a downstream aligned wind turbine. The first aspect is investigated and led to the development of a modeling substitute to emulate a turbulent flow representative of the experimental wind tunnel grid. The Dynamic Actuator Line Method (DALM) is presented on a single grid rod showing an adequate replication of the velocity fluctuations in the rod wake. Then the DALM is applied to the wind tunnel non-uniform grid and compared to other methods. The DALM results are close to the body-fitted configuration, resolving the flow around the grid rods, yet with a ten-time lower CPU cost. The DALM based on geometrical properties and tabulated aerodynamics coefficients requires less trial and error search than classical precursor methods that inject homogeneous isotropic turbulence. The application to the second wind tunnel grid, with a uniform rod spacing, is provided and showed a reasonably good agreement to vertical velocity profiles and turbulent kinetic energy measured experimentally. The influence of yaw misalignment and inflow is then investigated in the wind tunnel for a single turbine, T1. For these cases, the turbine loads show coherent variations when the turbine misalignment changes. Yet, the power coefficient differs significantly from the experimental measurements, up to +20%, while the thrust is in better accordance with a deviation of up to 9%. Discussion on the radial and azimuthal time averaging of the angle of attack and contribution to thrust and torque highlighted several effects. The probability of dynamic stall near the hub of yawed turbines is high and even more triggered by the high level of turbulence present in the free stream. The lateral force induced by yawed wind turbine explains why the resulting wind turbine wake is deflected. Then, the main flow topology highlights various geometrical and three-dimensional effects: the free-stream turbulence, the

sheared velocity profile, the tower wake deflection, the rotor wake deflection, the curled-wake shape, and the wake destabilization process. The horizontal velocity and turbulent kinetic energy profiles reproduce the main features of the experimental data, yet are slightly underestimated for the yawed cases. For the latter, the nacelle wake triggers the wake destabilization, while for yaw angle $\gamma = 0°$ the nacelle-generated TKE is observed up to three diameters behind the turbine. Based on the minimum available power, the wake center is identified and compared to the one from the experiments. The magnitude of the deflection is slightly overestimated compared to experiments. Comparison to the wake deflection model shows a realignment of the wake due to the confinement induced by the wind tunnel walls. The wake interaction is investigated by adding a second turbine in the vicinity of T1 exposed to a sheared velocity profile with high turbulence intensity. The impact of the first turbine on the loads of T2 is investigated. This first comparison showed how a velocity deficit and velocity fluctuations deteriorate the wind turbine loads of T2. These observations on the loads were related to the flow structures observed in the vicinity of T2, explaining the asymmetry of velocity deficit. The comparison to the flow measurements is in good agreement, especially for the TKE profiles.

This first application of the actuator line method in YALES2 and comparison to the experimental data from J. Bartl et al. and F. Mühle et al. showed the level of complexity required to replicate the flow around yawed wind turbines. The wind tunnel environment involves complex geometrical effects: grids and blockage effects. The wind turbine aerodynamics are impacted by yaw misalignment, upstream flow field, tower and nacelle. The overall methodology showed good agreement on the flow properties yet, pointing out the necessity of specific corrections to predict loads of yawed rotors with the actuator line method. The large variety of physical effects around yawed wind turbines showed the complexity of comparing the influence of different environments or operating conditions on the turbine wake.

6.1.2 Quantify the yawed wind turbine wake recovery and the turbulent mixing layer expansion

The wake envelope evolution of a yawed wind turbine is evaluated from Large-Eddy Simulations. Post-processings based on accurate conservative level set functions are introduced to define the wake. The methodology relies on tracking fluid particles crossing the rotor disk, either averaged over time or instantaneous. The tracking functions allow the construction of streamtubes surrounding the wind turbine and the probability of the presence of fluids particles emanating from the rotor. The advantage of this method strategy is triple. First, it reduces the amount of information from high-fidelity simulation, even when the simulations count billions of fluid elements. Second, the obtained results are comparable to classical 1D momentum theory for steady, inviscid, and irrotational flows, which are the basis of wake models for the design of modern wind turbines. Finally, such methods are robust and applicable independently of the turbine operating condition or the inflow turbulence level. The cases investigated are with or without yaw misalignment and different inflow turbulence conditions.

According to the streamtube topology and the turbulent mixing layer expansion, the wake envelope is discussed. The streamtube section increases from the upstream section until past the turbine, where the section starts to reduce at some point. The background turbulence triggers this phenomenon; the section reduction appears closer and closer to the rotor when turbulence intensity increases. Similar observations are made for yaw misaligned turbines, yet the section is not circular but kidney-shaped. Furthermore, the streamtubes are deflected independently of the turbulence level. The turbulent mixing layer expansion is discussed using the probability

of presence of fluid particles emanating from the rotor. The mixing layer width is evaluated using a reconstructed hyperbolic tangent profile over the probability field. While the width is constant azimuthally for $\gamma = 0°$, this allowed observing the azimuthal variation for yaw misaligned turbines. The turbulent mixing layer width expands as the wake pursues downstream the turbine and the expansion rate correlates to the external turbulence intensity.

Second, mean momentum and kinetic energy budgets were performed on wind turbine wake streamtubes constructed from high-fidelity LES. Variations of yaw angle or turbulence inflow have shown a similar behavior of the streamtube averaged quantities compared to theory. Indeed, the streamtube expands as it approaches the turbine and a velocity deficit appears. Moreover, the mean kinetic energy budget analysis showed that the wake recovers in different regions downstream of the turbine: I, II, III, and IV. These regions are related to the local vortex structures in the vicinity of the turbine. The first region is where the helicoidal vortices are convected. The second region starts when the vortices start pairing resulting in the production of turbulent kinetic energy. The maximal velocity deficit defines the entrance in the third region. In this region, the production of turbulent kinetic energy is maximal. In the last region, considered as the far wake, the wake velocity deficit continues to recover and the turbulence is decaying. The external turbulence level plays a large role in the downstream position of these regions, they appear closer to the rotor as the external turbulence intensity increase. The wake deflection induced by yaw misalignment on a wind turbine is explained through pressure forces and momentum fluxes in the mean horizontal momentum budget. Yet the deflection is not impacted by the increasing external turbulence. The evolution of the streamtube averaged quantities is then compared to the 1D momentum theory. The predicted rotor downstream velocity is shown to be in good accordance with the LES results. The recomputed thurst coefficient based on the axial induction factor has the same tendency. Nevertheless, the thrust coefficient based on the pressure jump within the streamtube is underpredicted compared to LES. Several 1D momentum theory hypotheses are pined out and could explain these discrepancies.

The comparison of different levels of mesh refinement showed that if there is background turbulence in the free stream flow, the wake destabilization process is not dependent on the grid resolution. While, when there is no external turbulence, which is not representative of an actual offshore wind condition, the destabilization is delayed downstream with a coarser mesh resolution.

6.1.3 Multiphysical approach by coupling ALM-LES to a servo-elastic solver

A multiphysical approach is presented during this thesis where the coupling between an aero-servo-elastic solver and the ALM in YALES2 is proposed. The aim is to take into account the structural deformation of the blades during the LES. Furthermore, the external code, BHawC, coupled with YALES2 has the controller of the actual wind turbine implemented. This allows the investigation of close-to-real scenarios with a representative turbine response. This coupling introduces a supplementary layer of physics to understand and increase the richness of the results. The investigated scenario is the interaction between two inline wind turbines represented by actuator lines for the blades as well as the tower and nacelle. The structure of both turbines is deformable. At the difference from other methodologies focusing on a single turbine, these simulations enable the proper generation of the wake and the impact on the second turbine, which is not included in engineering models.

The results without yaw misalignment highlight the various physical effects and the associated wind turbine response. Furthermore, the influence of mesh refinement is investigated, and

the turbine performances and deformations are compared to representative BEM results. The wind turbines are exposed to an inflow close to their rated wind speed and are limited between control regions two and three. The injection of synthetic Mann turbulence overlayed to a power-law velocity profile generates several events with a repetitive pattern. These repetitive events impact the turbine response and performance. On average, the pitch angle of the second turbine is lower than the first turbine, and the thrust coefficient is higher. This higher thrust generates a more significant velocity deficit behind $T2$, which overlays with the wake of $T1$. The wakes are mostly symmetric from the horizontal slices, while they seem redirected through the top of the domain from the vertical slices. Peaks of TKE appear downstream the tip of $T2$ blades. The mesh refinement impacts the loads but not the flow characteristics. This is directly related to the resolution near the turbine. From these observations, a cell size reduction near the turbines for the coarse scenario would result in similar loads as the reference case. Yet, the wall clock time would not be impacted since the coupling with the structural solver limits the simulation time-step. Nevertheless, the number of processors could be significantly reduced and, with it, the computational cost. Turbulence boxes located one diameter upstream of the turbine are built from the simulated flow. These turbulence boxes are then injected into BHawC standalone (BEM), providing comparative results from two different methodologies with the same inflow. The BEM results showed to be in good accordance with the REF case for the time-averaged turbine performances, yet a variable phase shift is observed on the turbine instantaneous response. The flapwise deformations, edgewise deformations, and blade torsion have the same order of magnitude yet slightly differing, especially for the edgewise deformations of the second wind turbine.

The first turbine is then misaligned with the wind and its influence is investigated. Two yaw misalignment of $T1$ are simulated: $\gamma = -20°$ and $+20°$. First, the flow topology showed the wakes of the yawed turbines to be redirected, impacting a smaller portion of the second turbine rotor. The streamtube construction showed how the yaw misalignment of $T1$ impacts the wake bounds. The streamtube source gathers the rotor area and the tower of the turbine. The streamtube behind the tower of $T1$ deviates in opposition to the wake when yaw misalignment is applied. Furthermore, the thrust of the first turbine is low due to the turbine operating above rated wind speed. A reduced thrust for a yawed turbine means a lower deviation due to the lower forces in the transverse direction. The mean kinetic energy budget over the streamtubes explains the difference in wake recovery between the two turbines, which is directly related to the thrust of the turbines. The first turbine, misaligned or not, has a thrust 30% lower than the second turbine. Nevertheless, the power production of the turbines draws interesting conclusions. The first turbine is at its nominal power with fluctuations reaching 1% for all cases. The negative or positive yaw angle does not impact the power production. But, when a positive yaw angle is applied to the first turbine, the electrical power production of $T2$ is increased by +2.5%. If the yaw is negative, the output only reaches +0.7%. The deformations of $T1$ show a flapwise deformation ∼15% higher than the reference case when the blade is at the vertical position and upstream the rotor hub, i.e., when $\theta = 270°$ for $\gamma = -20°$ and when $\theta = 90°$ for $\gamma = +20°$. The edgewise deformations increase at the same locations, +15% for $-\gamma$ and +3% for $+\gamma$. The difference in deformations between the two opposing yaw angles is due to the superposition of the gravitational forces on the blade. For $+\gamma$, the aerodynamic forces are reduced compared to REF when the weight is colinear to the tangential force. This is the opposite for $-\gamma$, which results in a higher deformation in the edgewise direction. The blade torsion is impacted in the same manner. For the second turbine, the conclusions are different. The wake is redirected for yawed cases, and $T2$ is less impacted by the velocity deficit. The deformations are mainly

lower when yaw misalignment is applied to the upstream turbine. The edgewise deformations are reduced by 10%. The induced fatigue is presented through damage equivalent loads (DEL) based on the flapwise and edgewise blade root moments. The reference scenario has a higher DEL for the second turbine, up to +45% with the flapwise moment. For the positive yaw angle, the edgewise DEL is reduced for both turbines -1.5% for $T1$ and -5% for T2. For the $-\gamma$ case, the edgewise DEL of the turbines is increased by +3% and +6%, respectively. For both yaw misalignments, the flapwise DEL increases for the first turbine and is reduced for the second.

The first turbine positive yaw angle misalignment shows the most promising results. The coupling with the aero-servo-elastic solver allows for drawing applicable solutions over a scenario of wake interactions. The multi-physical aspect of the coupled simulations is encouraging. It enables the investigations of fully turbulent wake interactions of yawed wind turbines and to observe the impact on the structural properties.

6.2 Perspectives

6.2.1 Optimizations and improvements of the framework

One of the significant perspectives relies on the further reduction of the computational cost and the accuracy of wind turbine wake simulation. This is a necessity to apply this framework to more complex scenarios. At first, the ALM use in YALES2 is not yet optimized for several turbines; this aspect will be furtherly improved after this thesis. Each turbine represented by the ALM is known by each processor participating in the computation. This has several impacts: the duplication of information and the serial calculation of the actuator line methodology. Consequently, adding more turbines leads to an increase in computational cost. This cost increase remains around two percent with two turbines in the computational domain. Still, this over cost highly increases for windfarm cases, up to 80% of the global cost when thirty turbines are present. The idea would be to allocate the turbine data only on the processors containing control volumes in the turbine global bounding box range, presented in the mollification section. This would allow dealing with the different actuator lines turbine in parallel, thereby reducing the cost of windfarm cases.

Furthermore, the framework of LES with ALM could be improved in the loads evaluation as new corrections are developed in the literature. Several corrections, primarily based on the lifting line theory, are observed to prevent the use of classical tip loss corrections. In the same way, dynamic stall models are necessary to better evaluate the loads in the blade root region.

The notion of static and dynamic mesh adaptation could further reduce computational costs. The use of static mesh adaptation in this thesis showed great potential as a user-independent methodology and for estimating the region of interest. Yet, it did not assess the eventual cost reduction achieved. The amelioration of the local cell size determination based on the flow characteristics remains a crucial aspect either on computational cost or the user dependency.

As mentioned in the previous chapter, the simulated time versus computational time is in the range of $1.7 \times 10^{-2} - 1.5 \times 10^{-2}$ which, for industrial partners, should be closer to a ratio of 1. Therefore, reducing computational time and improvements in the methodology would pave the way toward the industrial use of aero-servo-elastic LES in particular scenarios.

6.2.2 Wake investigations and models

The wake destabilization process is presented with four different regions in this thesis. The turbulent mixing layer width expands as the wake pursues downstream the turbine and the

expansion rate correlates to the external turbulence intensity. Further investigations on the wake would give key parameters for wake models. For example, evaluating the self-similarity in the wake turbulent mixing layer based on the mixing layer width, the averaged velocity, and Reynolds stress tensor components could help improve wake models. Comparing the wake emanating from LES with the general momentum theory could provide sufficient information to assess the validity of the theoretical hypotheses but requires the construction of concentric annular streamtubes in complex scenarios. Engineering wake models rely on validation in various operating and inflow conditions. The streamtube integrated quantities provide meaningful information for improving and validating such models.

6.2.3 Extend the solved physics and further investigation of strategies relying on yaw misalignement

The presented framework allows access to an extensive range of information, either on the wake analysis or on the structural properties of the turbine. Yet, this could be further extended to consider other phenomena occurring within offshore wind farms.

First, the wind conditions could be improved. The use of precursor simulations or a recycling buffer zone would prevent any evolution of the wind shear in a larger domain, i.e., wind turbine rows and wind farm layout. Furthermore, the notion of a neutral, stable, or unstable atmospheric boundary layer is not new in the literature and plays a significant role in the daily fluctuations of the wind. It requests to consider temperature fluctuations and stratification resulting in density variation and buoyancy effect in the flow. Such effects drive the fluid motion within the wind farm and impact the wakes.

Second, the waves could be considered as it is one of the other external forces impacting the turbine. In this thesis, their impact is neglected as the investigated wind turbines, especially in the last chapter, use monopiles foundation. From the perspective of floating wind turbines, the wave impact on the structure is not negligible anymore as it introduces new degrees of freedom due to the floating platform, such as surge, roll, sway, and many others.

From the wind farm perspective, there are plenty of other scenarios to investigate with a significant amount of turbines. The evaluation of global yaw strategies at the wind farm scale and using an aero-servo-elastic framework could provide reliable information on whether such strategies are efficient or not. Strategies based on yaw misalignment should now focus on below-rated wind speed scenarios. As highlighted in chapter 4 and the literature, the wake redirection is related to the transverse force applied by the turbine on the flow. Higher wind speed impacting the turbines will lower transverse force due to the turbine controller pitching the blade. Therefore, scenarios with higher wind speed will have a lower impact on the wake redirection and the fatigue reduction of a downstream turbine.

Appendices

A. Wind turbine reference frames and transformations

This Appendix describes the different reference frames and the global transformations[1] involved in the modeling of horizontal axis wind turbines. Their definition is the one implemented in YALES2 during this thesis.

A.1 Rotor reference frame

First of all, the rotor reference frame represents the direction in which the wind turbine is pointing. This reference frame considers the yaw angle γ and the tilt angle χ. The rotation speed, ω, is not taken into account by this reference frame. Yet, the rotation according to $\mathbf{e}_\omega$ is applied directly on the blade basis presented in the next subsection. The angles definitions and the axis orientation are represented in **Fig. A.1** according to a global coordinate system.

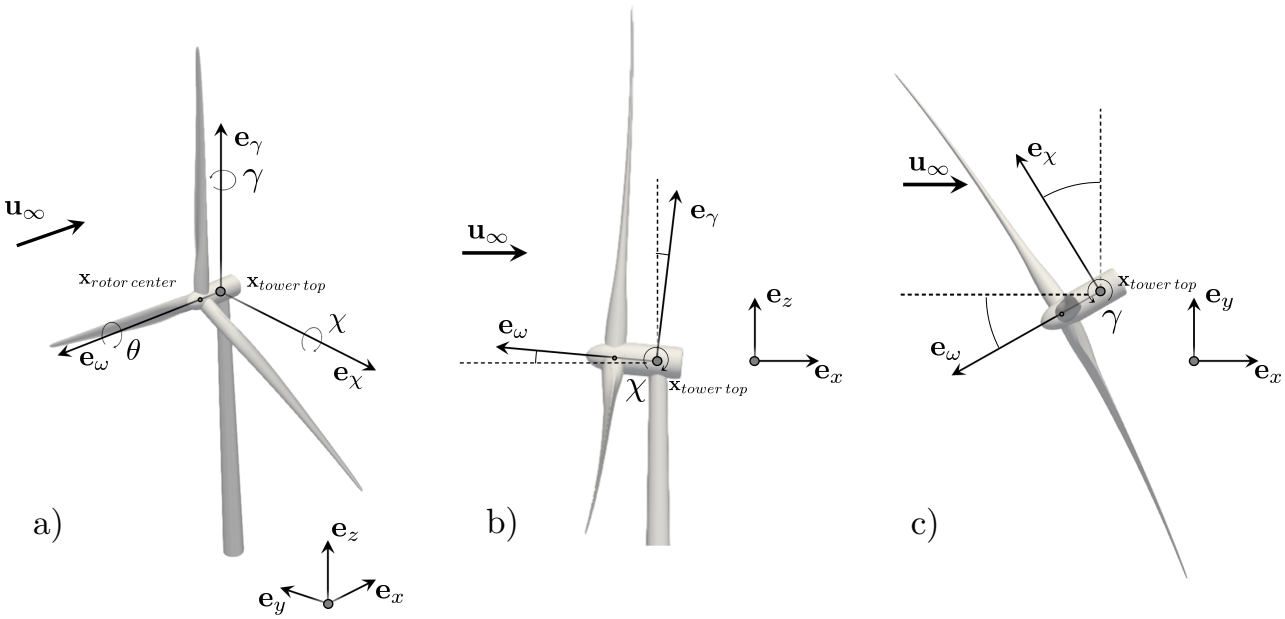

Figure A.1: Rotor reference frame definition in YALES2 library. a) 3D view b) lateral view c) top view.

[1]Here is the notation used for transfer matrices, basis, and vectors. Transfer matrix from basis A to basis B is expressed as $\mathbf{\Theta}_A^B$. The inversion of the transfer matrix $\mathbf{\Theta}_A^B$ gives the transfer matrix from B to A as $\left(\mathbf{\Theta}_A^B\right)^{-1} = \mathbf{\Theta}_B^A$. A vector $\mathbf{x}_B$ in basis B can be expressed in basis A as $\mathbf{x}_A = \mathbf{\Theta}_A^B\,\mathbf{x}_B$. Transfer matrix can be combined such that $\mathbf{\Theta}_A^B\mathbf{\Theta}_B^C = \mathbf{\Theta}_A^C$. In addition to that: E_{ij} denotes the basis of the ith element on the jth blade, B_j the basis of the jth blade, R the rotor basis, and G the global basis. As an example: $\mathbf{\Theta}_G^{E_{ij}}$ is the transfer matrix from YALES2 global basis to the basis of the element i of the blade j.

The basis $(\mathbf{e}_\gamma, \mathbf{e}_\chi, \mathbf{e}_\omega)$ is denoted as the reference frame of the rotor basis, $\mathbf{\Theta}_G^R$. This basis is defined according to the computational domain global reference frame $(\mathbf{e}_x, \mathbf{e}_y, \mathbf{e}_z)$, denoted $\mathbf{\Theta}_G$. The eventual rotations of yaw and tilt are defined according to the tower top position, $\mathbf{x}_{tower\,top}$. The transformation matrix and quaternions associated are the following for the yaw:

$$\mathcal{M}_\gamma = \begin{bmatrix} 1 & 0 & 0 \\ 0 & \cos(d\gamma) & -\sin(d\gamma) \\ 0 & \sin(d\gamma) & \cos(d\gamma) \end{bmatrix}, \quad \mathbf{q}_\gamma \left[\cos\left(\frac{d\gamma}{2}\right), \sin\left(\frac{d\gamma}{2}\right) \mathbf{e}_\gamma \right], \tag{A.1}$$

and for the tilt:

$$\mathcal{M}_\chi = \begin{bmatrix} \cos(d\chi) & 0 & \sin(d\chi) \\ 0 & 1 & 0 \\ -\sin(d\chi) & 0 & \cos(d\chi) \end{bmatrix}, \quad \mathbf{q}_\chi \left[\cos\left(\frac{d\chi}{2}\right), \sin\left(\frac{d\chi}{2}\right) \mathbf{e}_\chi \right], \tag{A.2}$$

where $d\gamma$ and $d\chi$ are the advancement angles during the time step and are computed in the following manner:

$$\begin{aligned} d\gamma =& \Delta t\, \dot{\gamma} + \frac{1}{2}\Delta t^2\, \ddot{\gamma}\,, \\ d\chi =& \Delta t\, \dot{\chi} + \frac{1}{2}\Delta t^2\, \ddot{\chi}\,, \end{aligned} \tag{A.3}$$

with $\dot{\gamma}/\dot{\chi}$ and $\ddot{\gamma}/\ddot{\chi}$ the yaw/tilt angular velocity and acceleration. These quantities are either user defined functions or given by a coupled controller. Usually and in reality the tilt angle is held constant. The tilt and yaw transformation matrix are then applied in the following order:

$$\mathbf{\Theta}_G^R(d\gamma, d\chi) = \mathbf{\Theta}_G^R \mathcal{M}_\gamma \mathcal{M}_\chi\,. \tag{A.4}$$

As aforementioned, the rotor basis does not take into account the azimuth angle of the blades, yet the rotation of the turbine is defined by the following matrix and quaternion:

$$\mathcal{M}_\theta = \begin{bmatrix} \cos(d\theta) & -\sin(d\theta) & 0 \\ \sin(d\theta) & \cos(d\theta) & 0 \\ 0 & 0 & 1 \end{bmatrix}, \quad \mathbf{q}_\theta \left[\cos\left(\frac{d\theta}{2}\right), \sin\left(\frac{d\theta}{2}\right) \mathbf{e}_\theta \right], \tag{A.5}$$

with $d\theta$ the advancement angle of each blades during the time-step defined as:

$$d\theta = \Delta t\, \dot{\theta} + \frac{1}{2}\Delta t^2\, \ddot{\theta}\,. \tag{A.6}$$

When the turbine is set to a constant rotation speed, $\dot{\theta}$ is equal to the rotor rotation speed ω otherwise the angular acceleration $\ddot{\theta}$ and velocity $\dot{\theta}$ are given by the wind turbine controller.

A.2 Blade basis

The second reference frame is the blade basis. This reference frame considers the cone angle β, the pitch angle Ψ and the azimuth angle of the blade θ. The angles definitions and the axis orientation are represented in **Fig. A.2** according to a global coordinate system and the rotor reference frame. The basis $(\mathbf{e}_{x,B_j}, \mathbf{e}_{y,B_j}, \mathbf{e}_{z,B_j})$ is denoted as the blade basis, $\mathbf{\Theta}_G^{B_j}$. It is defined according to the computational domain global reference frame. There is one reference frame for each blade j of the turbine. At the initialization and for a three-bladed turbine, the azimuth angles for the three blades are $\theta_1 = 0°$, $\theta_2 = 120°$ and $\theta_3 = 240°$. This with θ defined as the

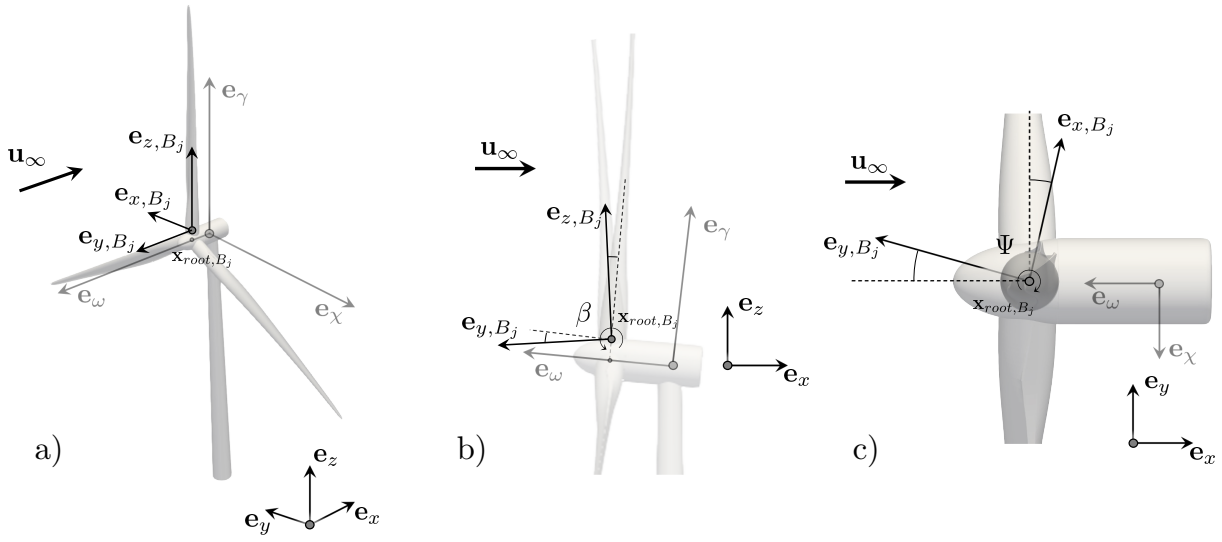

Figure A.2: Blade reference frame definition in YALES2 library. a) 3D view b) lateral view c) top view.

angle between $\mathbf{e}_\gamma$ and the projection of $\mathbf{e}_{z,B_j}$ on the plane $(\mathbf{e}_\gamma, \mathbf{e}_\chi)$. The blade basis is initialized as follows:

$$\mathbf{\Theta}_G^{B_j} = \mathbf{\Theta}_G^R \begin{bmatrix} \sin(\theta_j) & 0 & \cos(\theta_j) \\ -\cos(\theta_j) & 0 & \sin(\theta_j) \\ 0 & 1 & 0 \end{bmatrix} \mathcal{M}_\beta \mathcal{M}_\Psi \,. \tag{A.7}$$

With the initial pitch angle and eventual coning defined as follow:

$$\mathcal{M}_\Psi = \begin{bmatrix} \cos(\Psi) & -\sin(\Psi) & 0 \\ \sin(\Psi) & \cos(\Psi) & 0 \\ 0 & 0 & 1 \end{bmatrix}, \quad \mathcal{M}_\beta = \begin{bmatrix} 1 & 0 & 0 \\ 0 & \cos(\beta) & -\sin(\beta) \\ 0 & \sin(\beta) & \cos(\beta) \end{bmatrix}. \tag{A.8}$$

Then, two transformations can be applied to the blade basis during the simulation, one depending on the pitch variation and the other on the blade rotation. The pitch transformation matrix is defined according to the blade root position, $\mathbf{x}_{root,\,B_j}$, either an individual or global pitch is defined by $\mathcal{M}_\Psi$ introduced previously but with the angle, Ψ replaced by the pitch increment for the blade $d\Psi_j$:

$$d\Psi_j = \Delta t\, \dot{\Psi}_j + \frac{1}{2}\Delta t^2\, \ddot{\Psi}_j \,. \tag{A.9}$$

The blade rotation transformation is applied according to the rotor basis $\mathbf{\Theta}_G^R$ and is defined in **Eq. A.5**. The application of this transformation and the pitch transformation gives:

$$\mathbf{\Theta}_G^{B_j}(d\theta, d\Psi_j) = \mathbf{\Theta}_G^R \mathcal{M}_\theta \mathbf{\Theta}_G^{R\mathbf{T}} \mathbf{\Theta}_G^{B_j} \mathcal{M}_{\Psi_j}, \tag{A.10}$$

And with all previously introduced transformations, i.e., adding yaw and tilt angles:

$$\mathbf{\Theta}_G^{B_j}(d\gamma, d\chi, d\theta, d\Psi_i) = \mathbf{\Theta}_G^R \mathcal{M}_\gamma \mathcal{M}_\chi \mathcal{M}_\theta \mathbf{\Theta}_G^{R\mathbf{T}} \mathbf{\Theta}_G^{B_j} \mathcal{M}_{\Psi_j}, \tag{A.11}$$

Other transformations on the rotor basis could be easily implemented, on the foundation for example, if one wants to take into account the rotation/translation due to roll, pitch, yaw/surge, sway or heave appearing in a floating wind turbine context.

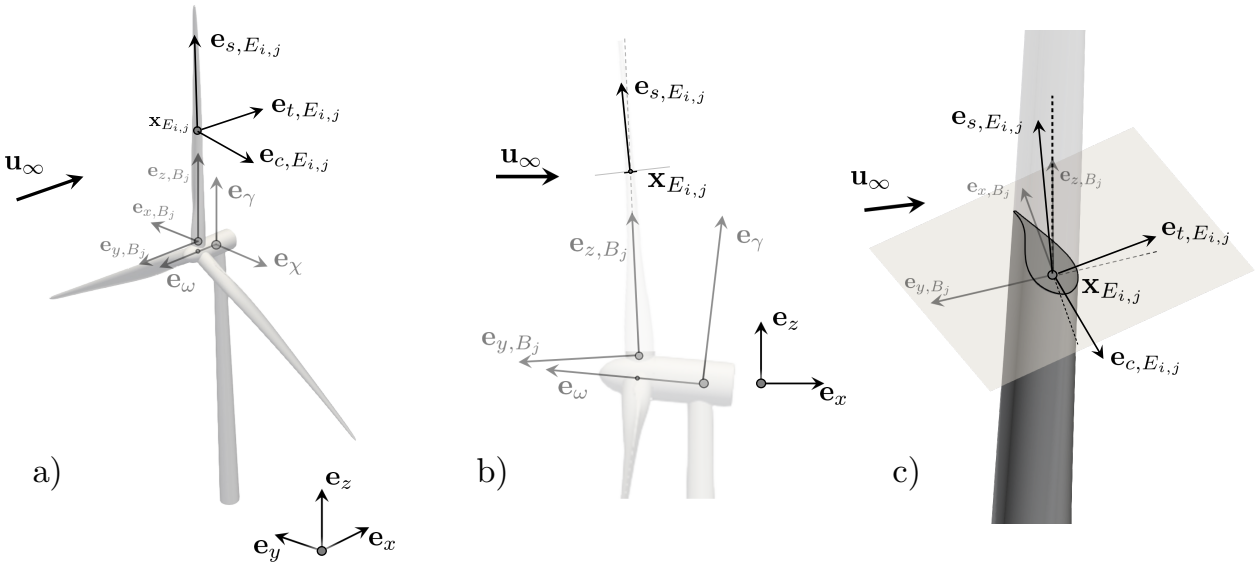

Figure A.3: Element reference frame definition in YALES2 library. a) 3D view b) lateral view c) top view.

A.3 Element basis

The last reference frame defines the airfoil section/element basis. This basis is held constant in the blade reference frame unless blade deformations are taken into account by coupling the ALM with an external structural solver. This reference frame considers the twist angle ψ and the eventually imposed curvature of the blade. The angles definitions and the axis orientation are represented in **Fig. A.3** according to a global coordinate system and the rotor reference frame. The basis $(\mathbf{e}_{c,E_{ij}}, \mathbf{e}_{t,E_{ij}}, \mathbf{e}_{s,E_{ij}})$ is denoted as the blade basis, $\mathbf{\Theta}_G^{E_{ij}}$. It is defined according to the computational domain global reference frame. There is one reference frame for each element i of each blade j of the turbine. The element basis is initialized as follows:

$$\mathbf{\Theta}_G^{E_{ij}} = \mathbf{\Theta}_G^{B_j} \begin{bmatrix} -1 & 0 & 0 \\ 0 & -1 & 0 \\ 0 & 0 & 1 \end{bmatrix} \mathcal{M}_{\psi_i} \mathcal{M}_{\mathrm{curv_i}} \,, \tag{A.12}$$

where $\mathcal{M}_{\psi_i}$ and $\mathcal{M}_{\mathrm{curv_i}}$ define the local twist and curvature at a given blade length, l_i. The used curvature has to be the one at the operating condition, with the strong hypothesis to be constant along time. If one wants to use a pre-deformed blade, proper attention has to be given to how the curvature is generated. This curvature can be given by rapid computation using an elastic-BEM or by coupling the ALM to an external structural solver as presented in Chapter 5. Depending on the previously introduced transformations, the element reference frame is given by:

$$\mathbf{\Theta}_G^{E_{ij}}(d\gamma, d\chi, d\theta, d\Psi_j) = \mathbf{\Theta}_G^R \mathcal{M}_\gamma \mathcal{M}_\chi \mathcal{M}_\theta \mathbf{\Theta}_G^{R\mathbf{T}} \mathbf{\Theta}_G^{B_j} \mathcal{M}_{\Psi_j} \mathbf{\Theta}_G^{B_j\mathbf{T}} \mathbf{\Theta}_G^{E_{ij}} \,. \tag{A.13}$$

The element reference frame allows to easily obtain the airfoil relative normal and tangential velocities easily by computing the following scalar products:

$$\begin{aligned} V_t &= -(\mathbf{u}_{gas,ij} \cdot \mathbf{e}_{c,E_{ij}} - \mathbf{u}_{blade,ij} \cdot \mathbf{e}_{c,E_{ij}}) \,, \\ V_n &= \mathbf{u}_{gas,ij} \cdot \mathbf{e}_{t,E_{ij}} - \mathbf{u}_{blade,ij} \cdot \mathbf{e}_{t,E_{ij}} \,. \end{aligned} \tag{A.14}$$

B. High fidelity mesh generation

The generation of the computational domain mesh is one of the first problematic and strongly influences the final output of the simulation. For this matter, this appendix presents how high fidelity mesh has been generated during this thesis. The philosophy here is to create a mesh refined in the areas of interest and where it is requested. Various methodologies and criteria already exist in the literature. Here several routines of the YALES2 library are used: the mesh adaptation module calling instances of MMG [259] and passive marker based on level set functions, see Chapter 4.

B.1 What is important on a mesh for wind turbines applications ?

Several factors are important for wind turbine wake investigations. The first is the complexity level of the physics involved and the second is the importance given to the different phenomena. For instance, if one wants to study the flow past a single turbine in an urban environment, proper care should be given to resolving the turbulent structures generated in the vicinity of buildings. Depending on the wind turbine location, these large structures would directly impact the performance and the wake. A cell size sufficient to transport the turbulent structures between the building and the turbine should be set between the two objects. In the case of two turbines wake interaction, the wake of the upstream wind turbine should be sufficiently resolved to transport the high vortical flow to the second turbine rotor position. In this scenario, proper care has to be given to the background turbulence, for instance, if there is a sheared wind field or even more if temperature fluctuations and buoyancy effect need to be taken into account. Having a constant cell size in the overall domain would be the easiest, yet it is a nogo in terms of computational costs. Furthermore, domains are often vast, in the range of tenths to hundred of turbine diameters long. What is essential here is to find the important regions of the domain that will impact the flow physics and, moreover, the flow physics of interest. The following methodology aims at finding the location of the areas of interest and the local cell size to be imposed in these regions. Several works in the literature [166, 81, 260, 104, 261] estimate the required local size based on the fluxes or other local physical indicators; it is not the case here.

B.2 Methodology and applications

The generation of mesh in this methodology is based on three steps, (i) coarse precursor simulation, (ii) metric definition based on average phase marker (Level-Set function), and (iii) Target mesh or iterate to (i) until convergence. The methodology is applied to cases of Chapter 4, representing a single turbine being misaligned with the wind direction; and in Chapter 5, where a two turbine configuration is considered. **Fig. B.4** shows the various steps involved in the methodology for different cases, cases of Chapter 4 are used for this example.

(i) Precursor: The first step is to conduct a simulation on a coarse mesh. At first, the cell size is constant on the overall mesh, reaching $D/h_{coarse} = 15$. This resolution is insufficient to resolve the flow near the turbine represented by the ALM. A resolution of at least $[32 - 64]$ cells per diameter is required to provide a good estimation of the loads and turbine performance. Yet this is sufficient to generate an estimation of the wake. The initial mesh should be sufficiently refined if background turbulence is involved, especially if a turbulence box is injected. The cell size should be set according to the turbulence box cell size to respect the Nyquist-Shannon theorem [262]. During the simulation, the

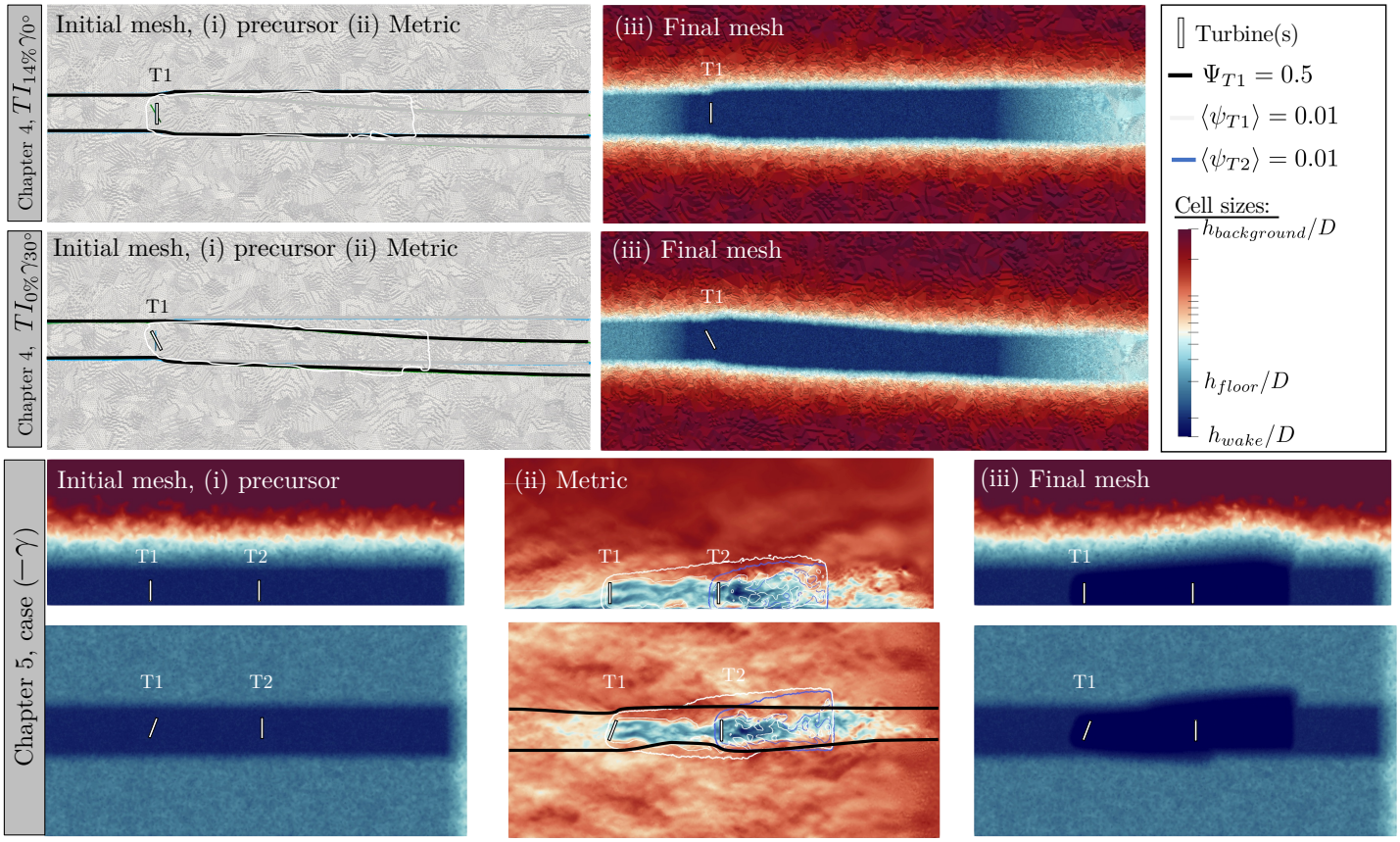

Figure B.4: Overview of the mesh generation methodology. Several application from chapters 4 and 5 are shown displaying the capability to obtain a refinement based on the wake position.

instantaneous under-resolved wake is tracked using a marker represented by a Level-Set function, see Chapter 4 for the exact definitions. This function source term is initialized at the turbine position with a disk of 1.5 to twice the turbine diameter. Statistics are conducted on this tracking function, $\langle\psi\rangle$. At the end of the simulation, a twice the turbine diameter streamtube surrounding the turbine is computed, Ψ. Two scalar fields are then available: $\langle\psi\rangle$ depicting the mean downstream fluctuations of the wake and Ψ the regions upstream AND downstream of the mean flow path through the turbine.

(ii) Mesh adaptation: From the previous two scalar fields based on the precursor simulation, the new metric is set to a constant $D/h_{wake} = 40$ if $\Psi > 0.5$ (black lines in **Fig. B.4**) and $\langle\psi\rangle > 0.01$ (white and blue lines in **Fig. B.4**). NB: $\Psi = 0.5$ is the streamtube interface while $\langle\psi\rangle$ is the probability of fluid particles that went through the $2D$ disk to be present locally. This metric is then sent to the remeshing library MMG3d [259]. Once the mesh has converged between the requested new metric and a required skewness below 0.8, the simulation is relaunched on the new mesh. The two scalars, $\langle\psi\rangle$ and Ψ, are reevaluated; if no changes are observed on their volume integral, the mesh is considered converged. Otherwise, the mesh is readapted according to the new metric until convergence. Usually, two iterative steps are sufficient, but this depends on the configuration complexity.

(iii) Target mesh and simulation: The final mesh is obtained by recursively dividing each mesh vertex by two. One 3D element of the mesh (tetrahedra) is divided into eight elements until the local cell size is the one requested by the user. This is regarded as one Main Grid

Chapter	Case	Initial mesh		After Methdology		MGR1		MGR2	
	⋆(see **Fig. B.4**)	N_{elem}	D/h_{wake}	N_{elem}	D/h_{wake}	N_{elem}	D/h_{wake}	N_{elem}	D/h_{wake}
4	$TI_{14\%}\gamma_{0°}$ ⋆	20	15	26.6	40	212.8	81	1 702	162
	$TI_{0\%}\gamma_{30°}$ ⋆	20	15	24.6	40	196.8	81	1 536	162
5	$-\gamma^{\star}$	9	20	29	38	232	77	1 857	154
	REF	9	20	30	38	240	77	N/A	N/A

Table B.1: Evolution of the number of element in the mesh and the cell size in the wind turbine wake area from a coarse mesh to the final level of reffinement of the mesh. Various cases from this thesis are taken, the first column indiquate from which chapter the case is taken. N_{elem} are given in millions of elemnts ($\times 10^6$)

Refinement (MGR). It allows to quickly obtain large refined meshes with the small cells located in the areas of interest. The cell size evolution is given in **Tab. B.1** for some of the applications presented in this thesis.

With an inlet flow aiming to represent a sheared velocity profile, in Chapter 5, another step is required adding a cell size gradient from floor to top to resolve the shear stress on the floor correctly. The initial mesh should not be homogeneous but properly resolve the free stream turbulence from the start. For these cases, the cell size at the bottom gives roughly $D/h_{floor} = 20$ and at the top $D/h_{top} = 2$, see **Fig. B.4** (bottom).

Even though this methodology remains "basic" in the context of static adaptative mesh refinement, it allows generating sophisticated meshes based on the global fluid motions. The use of streamtubes to highlight upstream and downstream areas of interest is a major aspect that could be used more often in other scenarios. Furthermore, this allows reaching a supplementary level of user independence by using an automatic method that can adapt to any configurations, i.e., wind farm layout and operating conditions.

C. Summary of research on HAWT rotors in yaw

A comprehensive summary of various experiments on HAWT rotors under both controlled and open field conditions is given in **Tab. C.2**.

Contibutor	Year	Type	Rotor Diameter	Blade	Variables	Information
Clayton and Filby, University College London [41]	1982	HWA in the wake (for averages velocities and turbulence measurements) and power output	0,5m	3-bladed, no chord given, twisted, NACA4415, tapered blades	Tip speed ratio, yaw angle, pitch angle	$1.4 \leq \lambda \leq 9.8$ $0^\circ \leq \gamma \leq 40^\circ$ $-15^\circ \leq \theta \leq 15^\circ$
Vestas Tjaereborg 2MW wind turbine	1983	Load measurement	61,1m	3-bladed, tapered	N/A	Field experiments
NREL UAE Phase I-IV Experiments	1987	Blade pressure And load Measurements	10m	3-bladed, downwind, Constant chord, Twisted	N/A	Field experiments
Vermeer, TU-Delft	1987	HWA	2,24m	2-bladed, constant chord, twisted,NACA0012	Yaw angle	$Re = 2. - 4.10^5$
Butterfield et al, NREL [35]	1991	pressure and power measurements	10m, Field experiments	3-bladed, constant chord, untwisted, SERI s809 airfoil	yaw angle	$0^\circ \leq \gamma \leq 30^\circ$
Bruining, TU-Delft	1994	Blade pressure Measurements	10m	2-bladed, untapered, untwisted	Tip speed ratio, yaw angle	$4 \leq \lambda \leq 10$ $Re = 0.5 - 1.10^6$
Grant Heriot-Watt University	2000	Smoke visualisation and power output	0,9m in open jet tunnel	2 and 3-bladed, tapered	Yaw angle	$6 \leq \lambda \leq 7$ $Re = 0.5 - 1.10^5$
Grant Heriot-Watt University [263]	2000	PIV	0,9m in open jet tunnel	3-bladed, tapered, untwisted but pitched, NACA4613, NACA3712 and NACA4611	Yaw angle	$2 \leq \lambda \leq 5$ $-30^\circ \leq \gamma \leq 30^\circ$
NREL UAE Phase VI Experiments	2000	Blade pressure Measurements	10m in a 4.4x36.6m wind tunnel	2-bladed, tapered, Twisted, S809	Tip speed ratio, yaw angle	$1.5 \leq \lambda \leq 7.6$ $0^\circ \leq \gamma \leq 60^\circ$
Medici, KTH Mechanics	2005	HWA and load measurement	0,18m in a 1,2x0,8m wind tunnel	2-bladed, tapered, untwisted, Gottingen417A	Freestream, tip speed ratio, turbulence and yaw angle	$0^\circ \leq \gamma \leq 60^\circ$ $Re = 1.2 - 3.4.10^4$
Maeda, Mie University	2005	Blade pressure measurements and tuft vizualisation	10m, field experiments	3-bladed, tapered, twisted, DU and NACA airfoils	Wind speed and yaw angle	$-45^\circ \leq \gamma \leq 45^\circ$ $Re = 3.5 - 5.5.10^5$
Sant and Haans, TU-Delft	2005-2006	HWA and smoke visualisation	1,2m in 2,24m open jet tunnel	2-bladed, constant chord, twisted, NACA0012	Yaw angle, pitch, tip speed ratio	$-45^\circ \leq \gamma \leq 45^\circ$ $Re = 1.7.10^5$
Maeda, Mie University	2007	Blade pressure measurements	2,4m in 3,6m open jet tunnel	3-bladed, tapered, twisted, DU91-W2-250 DU93-W-210 and NACA63-215	Yaw angle, tip speed ratio	$1.6 \leq \lambda \leq 6.6$ $0^\circ \leq \gamma \leq 45^\circ$ $Re = 2.1.10^5$
MEXICO Experiment [264]	2007	Blade pressure measurements and PIV	4,5m in a 9,5x9,5m open jet wind tunnel	3-bladed, tapered, twisted	Yaw angle, tip speed ratio, pitch, Parked rotor	$0^\circ \leq \gamma \leq 45^\circ$ and $\gamma = \pm 45^\circ$ $Re = 6.5.10^5$
Micallef, TU-Delft	2011-2012	SPIV measurements	2m in a octogonal open jet tunnel of 3m equivalent diameter	2-bladed, tapered, twisted, DU96-W180	Yaw angle, Tip speed ratio	$\gamma = 0^\circ$ and 45° $\lambda = 5$ and 7 $Re = 3.6.10^5$
Krogstad and Adaramola, NTNU [265]	2012	Power and load measurements, wake measurement using pitot-static probe and LDA	0,9m in a 1.9x2.7m wind tunnel	3-bladed, tapered, twisted, s826	Freestream, yaw angle, tip speed ratio	$0^\circ \leq \gamma \leq 50^\circ$ $Re = 0.2 - 5.0.10^5$
Bastankhah and Porté Agel, EPFL [43]	2015	power and wake (PIV) measurements, model derivation	0,15m in a 2x2,57x28 m wind tunnel	3-bladed, 5% thick plate with 5% circular arc camber	yaw angle, tip speed ratio	$3 \leq \lambda \leq 6$ $0^\circ \leq \gamma \leq 30^\circ$
Bartl et al., NTNU [44]	2018	power and wake scans (LDA) measurements	0,9m in a 2,71x1,81x11,15m wind tunnel	3- bladed, twisted, NREL S826 airfoil	inflow (laminar, turbulent, sheared profile) yaw angle	$2 \leq \lambda \leq 5$ $TI = 0$ and 10%
Bartl, Mulhe and Saetran, NTNU [46]	2018	power and Loads measurements (HBM torque transducer)	0,9m in a 2,71x1,81x11,15m wind tunnel	two 3-bladed turbine interaction, twisted, NREL S826 airfoil	yaw angle, turbine lateral placement	$-40^\circ \leq \gamma \leq 40^\circ$ $-0,5D \leq z \leq +0,5D$

Blind test 5, NTNU [49]	2018	power and wake scans (LDA) measurements	0,9m in a 2,71x1,81x11,15m wind tunnel	two 3-bladed turbine interaction, twisted, NREL S826 airfoil	yaw angle	$\gamma = -30°; 0°; -30°$

Table C.2: Overview of experimental campaigns for HAWTs in axial and yawed flow

List of Figures

1.1 Trend in total electricity consumption and final energy consumption for other energies in France, taken from RTE's report [4]. 2

1.2 Annual offshore wind installations by country (left axis) and cumulative capacity (right axis) (GW) [5]. 3

1.3 Scheme of a horizontal axis wind turbine operating with a yaw angle γ under inflow $\mathbf{u}_\infty$ at a constant rotation speed ω. 4

1.4 Chronological evolution of the largest wind turbine compared to various worlwide structures [19]. 6

1.5 Time series of yaw angle during testing of (left) the Carter 25 turbine (wind direction sensor behind nacelle) [28] and (right) the Tellus turbine [29]. . 8

1.6 (left) Azimuth averaged Angle of Attack and lift coefficient at 30% span for 30^o yaw case [35]. (right) Predicted and measured normal force coefficient (C_n) at $0.47R$ for a test section speed of $15m.s^{-1}$ and a yaw angle of 60^o [36]. 9

1.7 Power coefficient normalised by the maximum power coefficient (zero yaw) against yaw angle. Experimental data of Grant et al. (2 bladed and 3 bladed rotor) [40] are compared to experimental data of Clayton and Filby (3-bladed rotor) [41] and Anderson BEM analysis (2-bladed rotor) [42]. . 9

1.8 Contours of the normalised mean streamwise velocity u/u_h in the horizontal plane at hub height downwind of a turbine for different yaw angles ($\gamma = 0°, 10°, 20°$ and $30°$) at the optimal tip speed ratio of the turbine. White dots and represent the wake-centre trajectory in the horizontal plane obtained from the wind tunnel measurements [43]. Black and white lines show models results [45]. 10

1.9 Contours of the normalized streamwise velocity deficit in the transverse planes at different downwind locations and different yaw angles for a turbine operating at the optimal tip speed ratio. Black circles indicate the frontal area of the wind turbine and white dots represent the wake-center position at each downwind location. The vector field represents the in-plane velocity components. [43] 11

2.1 A schematic diagram of the energy cascade at very high Reynolds number. From Pope [66]. 20

2.2 Arbitrary representation of $E(\kappa)$ (—) and the one-dimensional energy spectrum, $E_{11}(\kappa_1)$ (- - -) in isotropic turbulence. The maximal production of turbulent kinetic energy, $E(\kappa_0)\mathrm{d}\kappa$ is represented by (▬). Inspired from [66]. 22

2.3 a) Lumley map representing the limits of invariant η and ξ with a spheroid visualization of the different turbulent states [73]. b) Barycentric map of the anisotropy tensor using $C_{off} = 0.65$ and $C_{exp} = 5$ [74]. 23

2.4 Representative overview of the different CFD approaches: Spectra representing the Energy evolution as function of the wavenumber (proportional to the inverse of the length scales) (left), temporal evolution of a local variable (middle) and slice of the velocity field representing the turbulent structures in an atmospheric flow (right). 25

2.5 Control volume based on a mesh node in YALES2: $\mathbf{x}_p$ representing the mesh node and $\overline{\mathbf{x}}_p$ the barycenter of the control volume. The control volume is in grey ( ) and one of the interface between the control volume and a neighbour is represented (—). From [100] 30

2.6 Representation of the Double-Domain Decomposition (DDD) (left). The highlighted elements are participating in the communications inside and outside each processor and those in the black subdomain are participating in the communications between processors. Scheme of the communications and structures used during the simulations (right). From [100] 32

2.7 Schematic diagram of the evolution of the computational costs and fidelity of the different wind turbines modeling methods. a) Global methodologies b) CFD coupled methodologies. 35

2.8 Exemple of the cell size requested arround the rotor according to the Actuator Disk Method, Actuator Line Method or a "Resolved" geometry. For the Disk and Line methodlogies an iso-contour of the source term emulating the turbines forces in the momentum equation is represented. For the resolved geometry, a closer look on a profile section is shown. 36

2.9 Scheme representing the different steps of the Actuator Line Method. a) Blade geometry discretisation as a line of N elements. b) Evaluation of the aerodynamic forces, $\mathbf{F}_{aero,i}$ for each element i. c) Mollification of the previously computed forces $\mathbf{F}_{aero,i}$ on the eulerian grid with a gaussian kernel of standard deviation $\epsilon/\sqrt{2}$. 37

2.10 Representation of the element velocity evaluation for a given time-step, Δt. a) The actuator line is advanced from time n to $n+1$, an intermediate time $\star$ is introduced with $\tau = \Delta t/a$. b) The element velocity is computed from the positions at n and $\star$, if $a = 1$ the intermediate time is equivalent to $n+1$. c) Impact of a on $\mathbf{u}^{n,\star}_{blade,i}$ for one DOF, $\omega r_i \mathbf{e}_\theta$ is the exact velocity: (left axis) error on amplitude, $\delta_{\omega r_i} = \frac{\omega r_i - \|\mathbf{u}^{n,\star}_{blade,i}\|}{\omega r_i}$ (—) and (right axis) misalignment with the tangential unit vector, $\delta_\alpha = \cos^{-1}\left(\frac{\mathbf{e}_\theta \cdot \mathbf{u}^{n,\star}_{blade,i}}{\|\mathbf{u}^{n,\star}_{blade,i}\|}\right)$ in degree (- - -). 40

2.11 Principle of the three level algorithm allowing to select the nodes close to the actuator element. a) Coarse level: Bounding box comparison rotor-ELGRP. b) Medium level: Nodes proximity to the blade (Cylinder). c) Fine level: Nodes proximity to the blade element (Sphere). 43

2.12 Evolution of the volume fraction for the medium and fine levels according to the cylinder and sphere bounding length, ξ (left axis). Evolution of the volume integral of the mollification kernel $\eta_\epsilon(\mathbf{x})$ according to the considered ξ values (right axis). 44

2.13 Scheme of the substep of the mollification for the ALM. Exemple when $N_{substep} = 3$: a) evaluation of the number of substep, b) front and c) top view of the blade displacement and the convection of the mollification kernel center according to the local gas velocity. 46

2.14 Time averaged angle of attack (left), normal (middle) and tangential forces (right) along the NREL 5MW blades at different wind speeds and different number of substeps predicted by ALM simulations compared to BEM results. The curves for the different number of substeps are overlapping and no discrepancies are observed. 48
2.15 Instantaneous contour of $Q_{criterion} = 0.01s^{-2}$ representing the helicoidal wake structure generated with different substep values, black lines denotes the limits between simulations. The tip speed ratio is decreasing from left to right. 48
2.16 Evolution of the power (left) and thrust (middle) according to the number of substeps. Mean and standard deviation are presented non-dimensionnalized by the case without substeping, BEM results are presented with straight lines. (right) Evolution of the computational cost speed-up for the different number of substeps and differents wind speed. For each simulations 384 cores are used, the CPU cost is divided by the case without substeping. 49

3.1 Visualization of the front, side and top view of the computation domain of NTNU wind tunnel with a turbulence grid and two wind turbines. . . 52
3.2 Top: Pictures of the experimental turbulence grids from J. Bartl et al. [44], Bottom: Global grid geometry considered in the computations and sketch of the corresponding velocity profile. 53
3.3 (a) Radial distribution of the twist angle (■) and chord (●). Solid lines show analytical curve fitting model from experimental data [44, 169], markers show the actuator point value. (b) Comparison of C_L/C_D datasets colored by the angle of attack for the NRELS826 airfoil. Solid lines show analytical curve fitting model from experimental data and ○ the experimental datasets taken from [44] 54
3.4 Slices of the mesh cell size for the single turbine configuration with a yaw angle $\gamma = 0°$ and for all inflows. For the other cases the cell sizes are similar, only the tower and nacelle orientation changes. For the two wind turbines configuration, T2 is added downstream in the same way as T1. . 55
3.5 Description of the rod geometry and computation domain. l is the side length of the square rod. 58
3.6 Slice of the instantaneous vorticity magnitude fields in the wake of a square rod for BF (a), filtered BF (b), ALM (c) and DALM (d) cases. 59
3.7 Time and spanwise average of $\langle C_p \rangle$ (—) and its fluctuations (▬) distribution on the rod surface. Front is between vertices 0 and 1. Top is between vertices 1 and 2. Rear is between vertices 2 and 3. Bottom is between vertices 3 and 0. 60
3.8 (a) Evolution of Lift, C_L (—), and Drag, C_D (·····), coefficients over dimensionless time, $t^* = t/\tau$, for the wake of a 3D square rod at $Re = 3 \times 10^4$. (b) Spectrum of both signals are presented as $\widehat{C_L}$ (—), and $\widehat{C_D}$ (·····). . . 60
3.9 Mean streamwise velocity (a), RMS of streamwise velocity component (b) and RMS of vertical velocity component (c) behind the rod at x/l = 4,8,12,16 and 20 for BF (—), ALM (-·-) and DALM (- - -). 62
3.10 Oscillating lift and drag forces evolution over time for one section of a rod. 63
3.11 1D Energy spectra of the vertical velocity behind the rod at at various axial location, with $f^* = fl/u_{ref}$, for BF (—), ALM (-·-) and DALM (- - -). 64
3.12 Side view of the unstructured grid size, h/l, used to capture grid turbulence generation. From top to bottom: DALM, BF and HIT mesh. The mesh size h is defined here as the cubic root of the cell volume. It can be seen that $h/l \approx 0.08$ in the wake region for the three cases. 66

3.13 Magnitude of the vorticity field in the vertical plane of the wind tunnel for all cases. From top to bottom: DALM, BF, and HIT. 68
3.14 Streamwise evolution of streamwise turbulence intensity, TI, at two different lateral locations on the turbulence grid for the three cases. One at the center of the grid mesh, $y/l = 0$ (thin line), and the other behind a rod of the grid, $y/l = 2.55$ (thick line). DALM (- - -), BF (——), HIT (-·-·-) , experiment at x_3 (■) and **Eq. 3.4** (- - -) 69
3.15 Barycentric maps showing the streamwise evolution of the anisotropy invariants behind the grid, color depends on the position between x_0 and x_3. Two positions on the grid are presented, one at the center of the grid mesh, $y/l = 0$ (●), and the other behind a rod of the grid, $y/l = 2.55$ (✚), see **Fig. 3.14**. The three different cases, DALM, BF and HIT are presented. The limiting states of componentality are labeled along with the plane-strain limit (·····). 69
3.16 Vertical profiles of mean streamwise velocity (a) and turbulence intensity (b) at x_1, x_2, x_3, x_4 and x_5: experiment (■), DALM (- - -), BF (——) and HIT (-·-·-). 70
3.17 1D power spectra of the transverse velocity fluctuations (a), E_{yy}, and the streamwise velocity fluctuations (b), E_{xx} behind the rod at stations x_1, x_2, x_3, x_4 and x_5 for DALM (- - -), BF (——) and HIT (-·-·-). 71
3.18 Vertical slice in the middle of the wind tunnel colored by streamwise velocity, from top to bottom: inflow (iii) heterogeneous grid and inflow (ii) homogeneous grid. 72
3.19 Vertical profiles of the time-averaged a) streamwise velocity and b) the streamwise turbulent intensity in the wind tunnel without the turbine. The results of the inflows generated with the turbulence grids are presented: (ii) Experimental (▲), LES (- - -); (iii) Experimental (■), LES (-·-·-) 73
3.20 Radius and azimuth averaged temporal mean contribution to the power output of T1 in percent, $\langle F_\theta(r,\theta)\rangle \omega r / \langle P_{T1}\rangle$ [%] for $\gamma = 30°$, $0°$ and $-30°$ under inflow (i), (ii) and (iii). 74
3.21 Radius and azimuth averaged temporal mean streamwise force component divided by the time averaged Thrust force of T1 in percent, $\langle F_x(r,\theta)\rangle / \langle T\rangle$ [%] for $\gamma = 30°$, $0°$ and $-30°$ under inflow (i), (ii) and (iii). 75
3.22 Radius and azimuth averaged temporal mean of angle of attack, α for $\gamma = 30°$, $0°$ and $-30°$ under inflows (i), (ii) and (iii). 76
3.23 Layout of the impact of yaw angle on the velocity triangle and resulting angle of attack in the near hub region, $r/D \sim 0.1$. a) the blade is at $\theta = 0°$, upper vertical position and b) the blade is at $\theta = 180°$, lower vertical position. 77
3.24 Radius and azimuth averaged temporal mean lateral force component divided by the time averaged Thrust force of T1 in percent, $\langle F_y(r,\theta)\rangle / \langle T\rangle$ [%] for $\gamma = 30°$, $0°$ and $-30°$ under inflow (i), (ii) and (iii). 77
3.25 Radius and azimuth root mean square of angle of attack, α for $\gamma = 30°$, $0°$ and $-30°$ under inflow (i), (ii) and (iii). 78
3.26 Slices of instantaneous streamwise velocity fields for $\gamma = -30°, 0°, +30°$ under inflows (i), (ii) and (iii). (a) is a top view of the horizontal slice at rotor hight, dashed black lines show the position of the slices A, B and C. (b) is a front view of slices at different streamwise position in the wind tunnel: A ($x = x_3 + 1D$), B ($x = x_4$) and C ($x = x_5$). 79
3.27 Front, top and side views of the instantaneous 3D visualization of the wake generated by the turbine blades, tower and nacelle at $\gamma = +30°$ under inflow (i) using a volumic rendering of the $Q_{\text{criterion}}$ colored by intensity. The tower and nacelle surfaces are in dark grey. 80

3.28 Slices of time averaged streamwise velocity fields for $\gamma = -30°, 0°, +30°$ under inflows: (i), (ii) and (iii). (a) is a top view of the horizontal slice at rotor hight, dashed black lines show the position of the slices A, B and C. (b) is a front view of slices at different streamwise position in the wind tunnel: A ($x = x_3 + 1D$), B ($x = x_4$) and C ($x = x_5$). 82

3.29 Horizontal profiles of the time-averaged streamwise velocity at $x = x_4$ and $x = x_5$ behind the T1 under all inflows: (i) top, (ii) middle and (iii) bottom for the three yaw angles configuration: (left) $\gamma = -30°$, (middle) $\gamma = 0°$ and (right) $\gamma = +30°$. Experimental (■) and LES (—) results are presented. 83

3.30 Streamwise evolution of the wake center (□- - -■), primary CVP position, positive and negative (○—●) and the secondary CVP center position, generated by the nacelle (△·····▲) in the wind tunnel from $x = x_1$ to $x = x_5$. $\gamma = -30°$ (left) and $\gamma = -30°$ (right) for inflows (i) (—), (ii) (—) and (iii) (—). 84

3.31 Cross velocity fields represented with black vectors at three downstream positions for inflow (ii) and $\gamma = +30°$. The wake center based on the available power approach is represented by (●). The counter rotating vortex pair is represented by (●), positive and (●), negative vortex. The secondary counter rotating vortex pair, generated by the nacelle, is represented by (●), positive and (●), negative vortex only for position A and B. The green contour represent 80% of the maximum streamwise velocity deficit on the slice. 84

3.32 Calculated wake deflection z_c/D for $\gamma = -30°$ (top) and $+30°$ (bottom) under three different inflow conditions compared to experiment (at $3D$ and $6D$ only): (i) Experimental (●), LES (—); (ii) Experimental (▲), LES (- - -); (iii) Experimental (■), LES (-·-·-). A comparison to the wake deflection model of Bastankhah and Porté-Agel [43] for TI_i (—) and TI_{ii} (- - -) is provided. 86

3.33 Slices of time averaged TKE fields for $\gamma = -30°, 0°, +30°$ under inflows: (i), (ii) and (iii). (a) is a top view of the horizontal slice at rotor hight, dashed black lines show the position of the slices A, B and C. (b) is a front view of slices at different streamwise positions in the wind tunnel: A ($x = x_3 + 1D$), B ($x = x_4$) and C ($x = x_5$). 87

3.34 Horizontal profiles of the time-averaged turbulent kinetic energy at $x = x_4$ and $x = x_5$ behind the T1 under all inflows: (i) top, (ii) middle and (iii) bottom for the three yaw angles configuration: (left) $\gamma = -30°$, (middle) $\gamma = 0°$ and (right) $\gamma = +30°$. Experimental (■) and LES (—) results are presented. 89

3.35 Radius and azimuth averaged temporal mean of velocity component seen by the blades of T2. From left to right: mean streamwise velocity, streamwise turbulent kinetic energy, transverse velocity components (vectors) and transverse turbulent kinetic energy. 90

3.36 Radius and azimuth averaged temporal mean (left) and temporal RMS (right) of angle of attack, α for the second turbine T2 under a non-uniform sheared inflow with a high turbulence level, inflow (iii). 90

3.37 Radius and azimuth averaged temporal mean: contribution to the power output in percent (left), streamwise force (middle), and lateral force (right) for the second turbine T2 under a non-uniform sheared inflow with a high turbulence level, inflow (iii). 91

3.38 Vertical (side) and Horizontal (top) slices of the instantaneous velocity around T1 and T2 under inflow (iii). The tower and nacelle meshed surfaces appear in grey, the turbulence grid and the wind turbine blades are displayed for a better understanding. The QR-code is a link to the video showing the 3D evolution of the instantaneous velocity through $Q_{criterion}$ contour in the wind tunnel. 92
3.39 Vertical (side) and Horizontal (top) slices of the time averaged velocity around T1 and T2 under inflow (iii). The tower and nacelle meshed surfaces appear in grey, the turbulence grid and the wind turbine blades are displayed for a better understanding. 92
3.40 Vertical (side) and Horizontal (top) slices of the time averaged turbulent kinetic energy around T1 and T2 under inflow (iii). The tower and nacelle meshed surfaces appear in grey, the turbulence grid and the wind turbine blades are displayed for a better understanding. 93
3.41 Horizontal profiles of the time-averaged (left) streamwise velocity, (middle) vertical velocity and (right) turbulent kinetic energy at $3D$ behind T2 under inflow (iii). YALES2 simulation (—) and on a coarser mesh (- - -) compared to experimental measurements [49] (■) and numerical result with NEK5000 code [49] (○) 93

4.1 Representation of the wake envelope based on the two tracking methods: instantaneous fluid particles going through the rotor, ψ (top), Probability of presence of fluid particles that went through the rotor $\langle\psi\rangle$ (middle) and path of fluid particles following the time-averaged velocity, Ψ (bottom). 100
4.2 Side and top view of the source volume (red) for the ACLS functions used to determine ψ and Ψ. The white curve represent a slice of this volume according to the rotation axis. 103
4.3 Horizontal slice of the time averaged velocity (left), the upstream (middle) and downstream (right) part of the streamtube. The overall streamtube, is evaluated as $\Psi = \Psi_- \cup \Psi_+$ 103
4.4 (a) Streamtube surface based on the level set position around a wind turbine with a yaw angle $\gamma = 30°$ under a turbulent inflow $TI = 14\%$, various streamwise slices are represented by bold lines (b) Half of a streamtube slice, picturing the considered surfaces and volume for data integration. . 104
4.5 (left) 3D and 2D representation of the streamtube with the different pressure and velocity through the rotor disk for the 1D momentum theory. The thrust is the force exerced by the fluid on the rotor disk. (right) Evolution of velocity, pressure and streamtube section according to the 1D momentum theory. Inspired from [210]. 105
4.6 Computational domain for the one wind turbine configuration, (left) 3D view and (right) slice view of the domain. The turbine is in black centered in the domain and the blue region is representing the position in which the post-processings are applied. 106
4.7 Horizontal slices at $z/D = 0$ of instantaneous streamwise velocity for cases $TI_{0\%}\gamma_{30°}$ and $TI_{14\%}\gamma_{30°}$. The full domain is not represented, $x/D \in [-2.5; 18.0]$ and $y/D \in [-2.0; 1.0]$. The QR-code is a link to the video showing the 3D evolution of the instantaneous velocity through $Q_{criterion}$ contour in the domain. 108
4.8 (left) Horizontal slices at $z/D = 0$ and (right) transverse slices at $x/D = 3$ and 6 of time-averaged streamwise velocity for $TI_x = 0$, 3.5, 7, 14% and $\gamma = 30°$. The full domain is not represented, $x/D \in [-2.5; 18.0]$, $y/D \in [-2.0; 2.0]$, $z/D \in [-2.0; 2.0]$. 108

4.9 (left) Horizontal slices at $z/D = 0$ and (right) transverse slices at $x/D = 3$ and 6 of time-averaged streamwise velocity for $TI_x = 0$, 3.5, 7, 14% and $\gamma = 0°$. The full domain is not represented, $x/D \in [-2.5; 18.0]$, $y/D \in [-2.0; 2.0]$, $z/D \in [-2.0; 2.0]$. 109
4.10 Iso-contour of $\Psi = 1/2$ depicting the streamtube interface from $x/D = -2$ up to $x/D = 12$ for $TI_x = 0$, 3.5, 7, 14% and $\gamma = 30°$, 0°. Various streamwise slices are represented by bold black lines and red at the turbine position. 110
4.11 Streamwise slices of the streamtube interface, $\Psi = 1/2$, at different downstream position, $x/D = 3$, 6, 9, 12 for $TI_x = 0$, 3.5, 7, 14% and $\gamma = 30°$. . 111
4.12 Streamwise evolution of (a) the streamtube sectional area, S_{in} normalized by the section at the rotor position, (b) the streamtube center in the transverse plane direction (c) the horizontal mean velocity. Cases are depicted as $\gamma = 0°$ (—), $\gamma = 30°$ (—) for the yaw angle and for the inflow turbulence intensity as $TI_x = 0\%$ (—), 3.5% (-·-), 7% (- - -) and 14% (·····). 112
4.13 Mesh refinement impact on the streamwise evolution of (a) the streamtube sectional area, S_{in} normalized by the section at the rotor position, (b) the streamtube center in the transverse plane direction (c) the horizontal mean velocity. Cases are depicted as $\gamma = 0°$ (—), $\gamma = 30°$ (—) for the yaw angle, as $TI_x = 0\%$ (—), 14% (·····) for the turbulent intensity and using oppacity for the refinement level as (1) (—) and (2) (—). 112
4.14 Exemple of unbounded shear flows and definition of the turbulent mixing layer width $\delta(x)$ based on the local velocity difference $\Delta\mathbf{u}$. 113
4.15 Visualization of the interface between fluid particles crossing the yawed rotor disk and a laminar external flow: case $TI_{0\%}\gamma_{30°}$. Horizontal slice of normalized vorticity magnitude with the iso-contour of $\psi = 1/2$. A global overview is given at the top and four zooms are presented as i, ii, iii, iv to observe the close interaction between the vorticity field and the tracking function ψ. 114
4.16 Visualization of the interface between fluid particles crossing the yawed rotor disk and a turbulent external flow for case $TI_{14\%}\gamma_{30°}$. Horizontal slice of normalized vorticity magnitude with the iso-contour of $\psi = 1/2$. A global overview is given at the top and two zooms are presented to observe the close interaction between the vorticity field and the tracking function ψ. 115
4.17 First steps to determine the turbulent mixing layer width: a) Discretization of the wake with slices at different downstream position; b) use the iso-level $\Psi = 1/2$ to construct a discretized curvilinear abscissa supposedly located within the turbulent mixing layer; c) use the filtered local gradient of ψ to evaluate the normal to the interface. The turbulent mixing layer is then evaluated along this direction. 116
4.18 Evaluation of the turbulent mixing layer width from a line in the wake. a) Position of the line on the curvilinear abscissa. b) evaluation of the reconstructed hyperbolic tangent profile width, ε_{rec}. c) Check if the line direction is properly set by comparing to $\nabla\langle\psi\rangle$ along the line. d) Superposition of the newly reconstructed profile, $\langle\psi\rangle_{rec}$ to the actual profile of $\langle\psi\rangle$. The root-mean-square values are represented by the area around the curves. 117
4.19 Evolution of the turbulent mixing layer width, averaged and root-mean-square values over the curvilinear abscissa of each streamwise position. Cases are depicted as $\gamma = 0°$ (—), $\gamma = 30°$ (—) for the yaw angle and for the inflow turbulence intensity as $TI_x = 0\%$ (—), 3.5% (-·-), 7% (- - -) and 14% (·····). 118

4.20 Evolution of the turbulent mixing layer width, averaged and root-mean-square values over the curvilinear abscissa of each streamwise position. Comparison between the mesh refinement level is given, (1) light curves, (2) dark curves. Cases are depicted as $\gamma = 0°$ (—), $\gamma = 30°$ (—) for the yaw angle and for the inflow turbulence intensity as $TI_x = 0\%$ (—) and 14% (·····). 119
4.21 Streamwise evolution of (a) mean streamwise filtered velocity (b) hydrodynamic pressure and (c) turbulent kinetic energy integrated over the streamtube volume for all cases. Cases are depicted as $\gamma = 0°$ (—), $\gamma = 30°$ (—) for the yaw angle and for the inflow turbulence intensity as $TI_x = 0\%$ (—), 3.5% (-·-), 7% (- - -) and 14% (·····). 121
4.22 Mean kinetic energy equation terms integrated over the streamtube cross-section for $\gamma = 0°$ and, from top to bottom, $TI_x = 0\%$ (—), 3.5% (-·-), 7% (- - -) and 14% (·····). Each term is normalized by the total turbine power such as the integral of term v is equal to -1. The residual corresponds to the sum of all terms of **Eq. 4.25**. 122
4.23 Mean kinetic energy equation terms integrated over the streamtube cross-section for $\gamma = 30°$ and, from top to bottom, $TI_x = 0\%$ (—), 3.5% (-·-), 7% (- - -) and 14% (·····). Each term is normalized by the total turbine power such as the integral of term v is equal to -1. The residual corresponds to the sum of all terms of **Eq. 4.25**. 123
4.24 3D visualisation of the instantaneous Q-criterion colored by the regions determined from the MKE budgets for cases $TI_{14\%}\gamma_{30°}$ and $TI_{0\%}\gamma_{30°}$. . . 124
4.25 Mesh refinement impact on the streamwise evolution of (a) mean streamwise filtered velocity (b) hydrodynamic pressure and (c) turbulent kinetic energy integrated over the streamtube volume. Cases are depicted as $\gamma = 0°$ (—), $\gamma = 30°$ (—) for the yaw angle, as $TI_x = 0\%$ (—), 14% (·····) for the turbulent intensity and the refinement level as (1) (—) and (2) (—). 125
4.26 Mean kinetic energy equation terms integrated over the streamtube cross-section for case $TI_{0\%}\gamma_{30°}$ on mesh 1 (top) and 2 (bottom). Each term is normalized by the total turbine power such as the integral of term v is equal to -1. The residual corresponds to the sum of all terms of **Eq. 4.25**. 125
4.27 Mean kinetic energy equation terms integrated over the streamtube cross-section for case $TI_{14\%}\gamma_{30°}$ on mesh 1 (top) and 2 (bottom).. Each term is normalized by the total turbine power such as the integral of term v is equal to -1. The residual corresponds to the sum of all terms of **Eq. 4.25**. 126
4.28 Mean momentum equation terms projected over the horizontal axis and integrated over the streamtube cross-section for $\gamma = 30°$ and, from top to bottom, $TI_x = 0\%$ (—), 3.5% (-·-), 7% (- - -) and 14% (·····). Each term is normalized by the total turbine forces such as the integral of term iv is equal to -1. The residual corresponds to the sum of all terms of the equations. The regions discussed in the previous section are colored. . . . 127
4.29 Sketch of the (a) streamwise velocity and (b) pressure evolution along the streamtube, based on the simulations results. Regions (0), (1) and (2) are represented according to the 1D momentum theory. 128

5.1 Nodes and elements definition in BHawC. 135
5.2 Coupling strategy between YALES2 and BHawC. 137
5.3 Communications during the coupling of YALES2 and BHawC for N turbines and $Ntot$ processors. 138
5.4 Connectivity between BHawC structural mesh and YALES2 actuator line elements. 139

5.5 Picture of several SWT-6.0-154 gathered in an offshore wind farm, taken from Siemens Gamesa Renewable Energy website. 142
5.6 Computational domain for the two turbines configuration, (top) side view and (bottom) top view of the domain. 144
5.7 Vertical slice of the synthetic turbulence box colored by velocity fluctuations in the three direction (top) streamwise, (middle) transverse and (bottom) vertical. 146
5.8 Vertical profiles of (left) averaged streamwise velocity, (middle) streamwise turbulent intensity and (right) lateral (—) and vertical (—) turbulent intensities. Five positions in the streamwise direction are shown: $-4D$ (—), $0D$ (- - -), $2D$ (-·-), $5D$ (·····) and $10D$ (· · ·). The rotor region is represented by the two horizontal lines (·····). The target power law (■) is represented over the averaged streamwise velocity. 147
5.9 3D visualization of (a) Aerodynamic and structural element for the rotor, nacelle, and tower; (b) aerodynamic elements and iso contour of the source term applied in the Navier Stokes equations. The relative velocity used to compute the tower and nacelle forces is taken from the yellow sphere locations. (c) iso contour of the source term and iso-contour of Q-criterion depicting the generated vortices in the vicinity of the wind turbine. . . . 148
5.10 Timeline of instantaneous vertical velocity profile, highliting a serie of events (i,ii,iii,iv,v,vi) occuring during the simulation. The velocity samples are taken on a 64×64 grid one diameter upstream $T1$ at every time step in the reference case (REF). 150
5.11 Timeline of instantaneous horizontal velocity profile, highliting a serie of events (i,ii,iii,iv,v,vi) occuring during the simulation. The velocity samples are taken on a 64×64 grid one diameter upstream $T2$ at every time step in the reference case (REF). 151
5.12 Vertical profiles of statistics on velocity components during the overall time (all) and the three periodic events; (iv),(v),(iv); encountered by $T1$ turbine in case (REF). From left to right, the events statistics are the streamwise velocity, the vertical velocity, the streamwise turbulent intensity and the transverse and vertical turbulent intensity. 152
5.13 Time averaged electrical power production (left), blade 1 pitch angle (middle), rotation speed (right), all datas are normalized by turbine $T1$ in case (REF). Root mean square are shown with error bars. Cases: BEM ( ), REF ( ), and $REF0$ ( ) 153
5.14 Time evolution (left) and power spectra (right) of the electrical power of each turbine, (top) $T1$ and (bottom) $T2$. Cases: BEM (—), REF (—), and $REF0$ (·····) 154
5.15 Time evolution (left) and power spectra (right) of the first blade pitch angle for $T2$. Cases: BEM (—), REF (—), and $REF0$ (·····) 154
5.16 Vertical and Horizontal slices of the instantaneous (top) and time averaged (bottom) streamwise velocity around $T1$ and $T2$ for cases REF (left) and $REF0$ (right). Wind turbines are represented in grey and hub height is denoted by the white dotted lines. 155
5.17 Horizontal, $z = h_{hub}$ (top) and vertical, $y/D = 0$ (bottom) time averaged streamwise velocity profiles at six streamwise positions: $x/D = -1$; 1; 4; 6; 8 and 10 for cases REF (—), $REF0$ (- - -) and the inlet power law profile (■). Wind turbines are represented in grey and rotor region is denoted by the black dotted lines. 156
5.18 Vertical and Horizontal slices of the turbulent kinetic energy around $T1$and $T2$ for cases REF (left) and $REF0$ (right). Wind turbines are represented in grey and hub height is denoted by the white dotted lines. 157

5.19 Horizontal, $z = h_{hub}$ (top) and vertical, $y/D = 0$ (bottom) turbulent kinetic energy profiles at six streamwise positions: $x/D = -1$; 1; 4; 6; 8 and 10 for cases REF (—) and $REF0$ (- - -). Wind turbines are represented in grey and rotor region is denoted by the black dotted lines. 158

5.20 Azimuthal and radial mean flapwise deformations for $T1$ (right) and $T2$ (left) for Reference case (REF), it is depicted according to $T1$ maximal flapwise deflection, see **Eq. 5.25**. The localisation of the maximal deformation is shown for each turbine with a black circle. 158

5.21 Radial profiles of mean flapwise deformations at $\theta = 0°$, 90°, 180° and 270° for $T1$ (right) and $T2$ (left), depicted according to $T1$ maximal flapwise deflection, see **Eq. 5.25**. The root-mean-square of the deformations are shown with an area around the curves. Cases: BEM (—), REF (—), and $REF0$ (- - -). 159

5.22 Azimuthal and radial mean edgewise deformations for $T1$ (right) and $T2$ (left) for Reference case (REF), it is depicted according to $T1$ maximal edgewise deflection, see **Eq. 5.25**. The localisation of the maximal deformation is shown for each turbine with a black circle. 159

5.23 Radial profiles of mean edgewise deformations at $\theta = 0°$, 90°, 180° and 270° for $T1$ (right) and $T2$ (left), depicted according to $T1$ maximal edgewise deflection, see **Eq. 5.25**. The root-mean-square of the deformations are shown with an area around the curves. Cases: BEM (—), REF (—), and $REF0$ (- - -). 160

5.24 Azimuthal and radial mean blade torsion for $T1$ (right) and $T2$ (left) for Reference case (REF), it is depicted according to $T1$ maximal torsion, see **Eq. 5.25**. The localisation of the maximal torsion is shown for each cases with a black circle. 161

5.25 Radial profiles of mean torsion at $\theta = 0°$, 90°, 180° and 270° for $T1$ (right) and $T2$ (left), depicted according to $T1$ maximal torsion, see **Eq. 5.25**. The root-mean-square of the deformations are shown with an area around the curves. Cases: BEM (—), REF (—), and $REF0$ (- - -). 161

5.26 3D visualization of the wake generated by the turbine blades, tower and nacelle at $\gamma = -20°$ on the fine mesh ($-\gamma 2$) using a iso-contour of the $Q_{\text{criterion}}$. 163

5.27 Vertical (top) and Horizontal (bottom) slices of the time averaged streamwise velocity around $T1$and $T2$ for cases ($-\gamma$),($+\gamma$), and (REF). Wind turbines are represented in grey and hub height is denoted by the white dotted lines. 164

5.28 Horizontal, $z = h_{hub}$ (top) and vertical, $y/D = 0$ (bottom) time averaged streamwise velocity profiles at six streamwise positions: $x/D = -1$; 1; 4; 6; 8 and 10 for cases $-\gamma$ (—), REF (—), $+\gamma$ (—) and the inlet power law profile (■). Wind turbines are represented in grey and rotor region is denoted by the black dotted lines. 165

5.29 Vertical (top) and Horizontal (bottom) slices of turbulent kinetic energy around $T2$ and $T2$ for cases ($-\gamma$),($+\gamma$), and (REF). Wind turbines are represented in grey and hub height is denoted by the white dotted lines. . 165

5.30 Horizontal, $z = h_{hub}$ (top) and vertical, $y/D = 0$ (bottom) turbulent kinetic energy profiles at six streamwise positions: $x/D = -1$; 1; 4; 6; 8 and 10 for cases $-\gamma$ (—), REF (—) and $+\gamma$ (—). Wind turbines are represented in grey and rotor region is denoted by the black dotted lines. 166

5.31 Streamtubes emanating from $T1$ (left) and $T2$ (right) in the case of a positive yaw misalignement ($\gamma = +20°$). The streamtube surface is depicted by $\psi = 0.5$ ( ) and transverse slices (—) are spaced by one diameter in the streamwise direction. The source term are depicted for the streamtube of $T1$ ( ) and $T2$ ( ). The source terms are based on the rotor swept area and the tower/nacelle positions. 167

5.32 Slices of streamtubes emanating from $T1$ (top) and $T2$ (bottom) for cases $-\gamma$ (—), REF (—) and $+\gamma$ (—). The slices are at different upstream and downstream positions of the turbines depicted in grey. 167

5.33 Streamwise evolution for $T1$ of (a) the streamtube sectional area, S_{in} normalized by the section at the rotor position, the streamtube center in (b) the transverse plane direction and (c) the vertical direction. Cases $-\gamma$ (—), REF (—) and $+\gamma$ (—). $T1$ is located in $x/D = 0$. 168

5.34 Streamwise evolution for $T2$ of (a) the streamtube sectional area, S_{in} normalized by the section at the rotor position, the streamtube center in (d) the transverse plane direction and (c) the vertical direction. Cases $-\gamma$ (—), REF (—) and $+\gamma$ (—). $T2$ is located in $x/D = 5$. 169

5.35 Mean kinetic energy equation terms integrated over the streamtube ψ_{T1} cross-section for cases (top) $-\gamma$, (midlle) REF and (bottom)$+\gamma$. Each term is normalized by the total turbine power such as the integral of term v is equal to -1. The residual corresponds to the sum of all terms of **Eq. 4.25**. 170

5.36 Streamwise evolution for ψ_{T1} of (a) mean streamwise velocity, (b) mean tranverse velocity and (c) turbulent kinetic energy integrated over the streamtube volume for cases $-\gamma$ (—), REF (—) and $+\gamma$ (—). 170

5.37 Mean kinetic energy equation terms integrated over the streamtube ψ_{T2} cross-section for cases (top) $-\gamma$, (midlle) REF and (bottom)$+\gamma$. Each term is normalized by the total turbine power such as the integral of term v is equal to -1. The residual corresponds to the sum of all terms of **Eq. 4.25**. 171

5.38 Streamwise evolution for ψ_{T2} of (a) mean streamwise velocity, (b) mean tranverse velocity and (c) turbulent kinetic energy integrated over the streamtube volume for cases $-\gamma$ (—), REF (—) and $+\gamma$ (—). 171

5.39 Time averaged electical power production (left) normalized by the electrical power production of $T1$ in case (REF), root-mean-square are shown with error bars. Time avergaed thrust force (middle) normalized by the thrust force of $T1$ in case (REF), fluctuations are displayed yet too small to be observed. Time averaged first blade pitch angle (middle) normalized by the pitch angle of $T1$ in case (REF). Cases: $-\gamma$ ( ), REF ( ) and $+\gamma$ ( ). 172

5.40 Azimuthal and radial mean streamwise force (equivalent to the contibution to thrust) for $T1$ (top) and $T2$ (bottom). The results display the discrepancies for each case in comparison to the reference case (C). . . . 173

5.41 Radial profiles of mean flapwise deformations at $\theta = 0°$, $90°$, $180°$ and $270°$ for $T1$ (right) and $T2$ (left), depicted according to $T1$ maximal flapwise deflection, see **Eq. 5.25**. The root-mean-square of the deformations are shown with an area around the curves. Cases: $-\gamma$ ( ), REF ( ) and $+\gamma$ ( ). 174

5.42 Azimuthal and radial mean tangential force (equivalent to the contibution to torque) for $T1$ (top) and $T2$ (bottom). The results display the discrepancies for each case in comparison to the reference case (C). . . . 175

5.43 Radial profiles of mean edgewise deformations at $\theta = 0°$, $90°$, $180°$ and $270°$ for $T1$ (right) and $T2$ (left), depicted according to $T1$ maximal edgewise deflection, see **Eq. 5.25**. The root-mean-square of the deformations are shown with an area around the curves. Cases: $-\gamma$ ( ), REF ( ) and $+\gamma$ ( ). 176
5.44 Radial profiles of mean torsion at $\theta = 0°$, $90°$, $180°$ and $270°$ for $T1$ (right) and $T2$ (left), depicted according to $T1$ maximal torsion, see **Eq. 5.25**. The root-mean-square of the deformations are shown with an area around the curves. Cases: $-\gamma$ ( ), REF ( ) and $+\gamma$ ( ). 176
5.45 Estimation of the DEL for the first turbine $T1$: (top) Sample of the temporal evolution of the flapwise (left) and edgewise (right) blade root moment. (middle) Power spectra of these blade-root moments. (bottom) Histogram of the number of cycle per amplitude used to compute the DEL. Cases: $-\gamma$ ( ), REF ( ) and $+\gamma$ ( ). 178
5.46 Estimation of the DEL for the first turbine $T2$: (top) Sample of the temporal evolution of the flapwise (left) and edgewise (right) blade root moment. (middle) Power spectra of these blade-root moments. (bottom) Histogram of the number of cycle per amplitude used to compute the DEL. Cases: $-\gamma$ ( ), REF ( ) and $+\gamma$ ( ). 179

A.1 Rotor reference frame definition in YALES2 library. a) 3D view b) lateral view c) top view. 191
A.2 Blade reference frame definition in YALES2 library. a) 3D view b) lateral view c) top view. 193
A.3 Element reference frame definition in YALES2 library. a) 3D view b) lateral view c) top view. 194
B.4 Overview of the mesh generation methodology. Several application from chapters 4 and 5 are shown displaying the capability to obtain a refinement based on the wake position. 196

List of Tables

2.1 Computational cost of the mollification process when activating the different cells selection for two wind turbine cases. The percent, [%] is the ratio between the overall computational time and the time elapsed in the mollification process. 44

3.1 Computational mesh size and cost associated with the different configurations. The time step and CPU cost are given for 15 flow-through times, τ. Meshes 1 to 3 are used in **Section 3.2**, 4 to 6 in **Section 3.3** and 7 in **Section 3.4**. 56

3.2 Aerodynamic coefficients around a square rod obtained from experimental data and from present simulation. The vortex shedding frequency, St, is based on the lift fluctuations. 57

3.3 Mesh characteristics for the rod simulations. 58

3.4 Aerodynamic coefficients of the grid rods depending on their environment [184, 185]. 66

3.5 Time averaged power and thrust coefficients of the turbine (C_P and C_T) at the optimal operating point ($\lambda = 6$) for the three yaw angles and the three inflow conditions. The power E_{C_P} and thrust E_{C_T} errors are computed with respect to the experimental data from J. Bartl et al. [44]. 74

4.1 Evolution of the number of element in the mesh and the cell size in the wind turbine wake area for the two level of refinement investigated in this chapter. The number of elements, $N_{elements}$ and the number of nodes, N_{nodes} are given as a range since each cases as a unique mesh, due to the mesh generation methodology based on the flow characteristics. 107

4.2 Cases and mesh properties. Reference values for a laminar inflow are $\langle C_P \rangle = 0.476$ and $\langle C_T \rangle = 0.814$ [213]. 107

4.3 Comparison between the integrated quantities along the streamtubes for all cases and the 1D momentum theory. 129

5.1 Operating conditions for the different configurations of $T1$ and $T2$ investigated. Convergence and statistics accumulation time is expressed as t_{max} 143

5.2 Cell size in the different regions of the mesh for all cases and the resulting meshes sizes based on these metrics. 145

5.3 Integrated quantities over the all synthetic turbulence box generated with Mann's algorithm. 145

5.4 Computational cost of the different cases presented in this chapter. . . . 150

5.5 Evolution of the damage equivalent loads for the edgewise and flapwise blade root moments given according to $T1$ in the reference case REF. . . 177

B.1 Evolution of the number of element in the mesh and the cell size in the wind turbine wake area from a coarse mesh to the final level of reffinement of the mesh. Various cases from this thesis are taken, the first column indiquate from which chapter the case is taken. N_{elem} are given in millions of elemnts ($\times 10^6$) 197
C.2 Overview of experimental campaigns for HAWTs in axial and yawed flow 199

Bibliography

[1] International energy agency (iea) data base. https://www.iea.org/data-and-statistics. Accessed: 2022-01-30.

[2] Paris agreements. Technical report, United Nations, 2015.

[3] Ar6 synthesis report: Climate change 2022. Technical report, Intergovernmental Panel on Climate Change - IPCC, 2022.

[4] Energy pathways to 2050, key results. Technical report, France transmission system operator (Réseau de Transport d'Électricité - RTE), 2021.

[5] Offshore wind in europe: Key trends and statistics. Technical report, Wind Europe, 2020.

[6] A. Betz. Schraubenpropeller mit Geringstem Energieverlust. *Dissertation, Gottingen Nachrichten, Gottingen*, 1919.

[7] D. Micallef, C.S Ferreira, T. Sant, and G. van Bussel. An Analytical Model of Wake Deflection Due to Shear Flow. *The 3rd EWEA Conference Torque 2010: The Science of making Torque from Wind, Heraklion, Crete, Greece*, 2010.

[8] D. Dolan and P. Lehn. Simulation model of wind turbine 3p torque oscillations due to wind shear and tower shadow. *Energy Conversion, IEEE Transaction on*, 21:717– 724, 10 2006.

[9] A. Rosen and Y. Sheinman. The average output power of a wind turbine in a turbulent wind. *Journal of Wind Engineering and Industrial Aerodynamics*, 51:287–302, 05 1994.

[10] R. Wagner, I. Antoniou, S. Pedersen, M. Courtney, and H. Jørgensen. The influence of the wind speed profile on wind turbine performance measurements. *Wind Energy*, 12:348 – 362, 05 2009.

[11] D. Micallef and T. Sant. A Review of Wind Turbine Yaw Aerodynamics. *Wind Turbines - Design, Control and Applications*, 2016.

[12] S. J. Johnson and D. E. Berg. Active Load Control Techniques for Wind Turbines. *Contract*, pages 1–132, 2008.

[13] M. Hoogwijk, B. de Vries, and W. Turkenburg. Assessment of the global and regional geographical, technical and economic potential of onshore wind energy. *Energy Economics*, 26(5):889–919, 2004.

[14] J. Bosch, I. Staffell, and A. D. Hawkes. Temporally-explicit and spatially-resolved global onshore wind energy potentials. *Energy*, 131:207–217, 2017.

[15] RJ Swart, C Coppens, H Gordijn, M Piek, P Ruyssenaars, JJ Schrander, P de Smet, M Hoogwijk, M Papalexandrou, E de Visser, et al. Europe's onshore and offshore wind energy potential: An assessment of environmental and economic constraints. Technical report, European Environment Agency, 2009.

[16] W. J. Zhu, N. Heilskov, W. Z. Shen, and J. N. Sørensen. Modeling of Aerodynamically Generated Noise From Wind Turbines. *Journal of Solar Energy Engineering*, 127(4):517–528, 2005.

[17] S.P. Gaultier, G. Marx, and D. Roux. Eoliennes et biodiversite : synthese des connaissances sur les impacts et les moyens de les attenuer. Technical report, Office national de la chasse et de la faune sauvage/LPO, 2019.

[18] S. M. Grodsky, M. J. Behr, A. Gendler, D. Drake, B. D. Dieterle, R. J. Rudd, and N. L. Walrath. Investigating the causes of death for wind turbine-associated bat fatalities. *Journal of Mammalogy*, 92(5):917–925, 2011.

[19] M. Liebreich. Technical report, Bloomberg New Energy Finance, 2017.

[20] J. Bosch, I. Staffell, and A. D. Hawkes. Temporally explicit and spatially resolved global offshore wind energy potentials. *Energy*, 163:766–781, 2018.

[21] T. Stehly and P. Duffy. Cost of wind energy review. Technical report, National Renewable Energy Laboratory (NREL), 2020.

[22] S. Degraer, D. A. Carey, J. W.P. Coolen, Z. L. Hutchison, F. Kerckhof, B. Rumes, and J. Vanaverbeke. Offshore wind farm artificial reefs affect ecosystem structure and functioning: A synthesis. *Oceanography*, 2020.

[23] O. Huppop, J. Dierschke, K. M. Exo, E. Fredrich, and R. Hill. Bird migration studies and potential collision risk with offshore wind turbines. *Ibis*, 148(s1):90–109, 2006.

[24] F. Karipoğlu, S. Öztürk, and M. S. Genç. Determining suitable regions for potential offshore wind farms in bandırma bay using multi-criteria-decision-making method. *Mühendislik Bilimleri ve Araştırmaları Dergisi*, 3(1):123–132, 2021.

[25] Projets français d'usines eoliennes en mer: une bombe à retardement écologique. Technical report, Sea Sheperd France, 2021.

[26] Wind technologies market report. Technical report, Lawrence Berkely National Lab (LBNL), 2020.

[27] R. ABD Jamil, A. Chaigneau, J-C Gilloteaux, P. Lelong, and A. Babarit. Comparison of the capacity factor of stationary wind turbines and weather-routed energy ships in the far-offshore. *Journal of Physics: Conference Series*, 1356(1):012001, oct 2019.

[28] D. Eggleston and K. Starcher. A comparative study of the aerodynamics of several wind turbines using flow visualization. *Journal of Solar Energy Engineering-transactions of The Asme*, 112:301–309, 11 1990.

[29] H. Madsen, N. Sørensen, and S. Schreck. Yaw aerodynamics analyzed with three codes in comparison with experiment. *AIAA Paper 2003, 41st AIAA Aerospace Sciences Meeting and Exhibit, Reno, Nevada*, 2003.

[30] Bu. Akay, D. Micallef, C. Ferreira, and G. van Bussel. Effects of geometry and tip speed ratio on the hawt blade's root flow. *Journal of Physics: Conference series - The Science of Making Torque from Wind 2012*, 555:1, 12 2014.

[31] D. Micallef, C. Ferreira, T. Sant, and G. Van Bussel. Experimental and numerical investigation of tip vortex generation and evolution on horizontal axis wind turbines. *Wind Energy*, 19, 09 2015.

[32] M. Hand, D. Simms, L. Fingersh, D. Jager, J. Cotrell, S. Schreck, and S. Larwood. Unsteady aerodynamics experiment phase vi: Wind tunnel test configurations and available data campaigns. *Technical Report NREL, National Renewable Energy Laboratory, Colorado*, 01 2001.

[33] J. Leishman. Challenges in modeling the unsteady aerodynamics of wind turbines. *Wind Energy*, 5:85 – 132, 04 2002.

[34] R. Barthelmie, S. Frandsen, O. Rathmann, K. Hansen, E. Politis, J. Prospathopoulos, J. Schepers, K. Rados, D. Cabezon, W. Schlez, A. Neubert, and M. Heath. Flow and wakes in large wind farms. *Final report for UpWind WP8, DTU*, 2011.

[35] C.P. Butterfield, A. C. Hansen, D. Simms, and G G.Scott. Dynamic Stall Wind Turbine Blades. *Windpower '91 Conference and Exposition, Palm Springs, California*, December 1991.

[36] S. Scott. The nrel full-scale wind tunnel experiment introduction to the special issue. *Wind Energy*, 5(2-3):77–84, 2002.

[37] D. Micallef. *3D flows near a HAWT rotor: A dissection of blade and wake contributions*. PhD thesis, Delft University of Technology, 12 2012.

[38] V. Campo, D. Ragni, D. Micallef, B. Akay, F. Diez, and C. Ferreira. 3d load estimation on a horizontal axis wind turbine using spiv. *Wind Energy*, 17, 11 2014.

[39] V. Campo, D. Ragni, D. Micallef, F. Diez, and C. Ferreira. Estimation of loads on a horizontal axis wind turbine operating in yawed flow conditions. *Wind Energy*, 18, 08 2015.

[40] I. Grant, P. Parkin, and X. Wang. Optical vortex tracking studies of a horizontal axis wind turbine in yaw using laser-sheet, flow visualisation. *Experiments in Fluids*, 23:513–519, 12 1997.

[41] B.R. Clayton and P. Filby. Measurements effects of oblique flows and change in blade pitch angle on performance and wake development of model wind turbines. *Proceedings of the BWEA Wind Energy Conference (British Wind Energy Association)*, pages 214–224, 01 1982.

[42] M. Anderson. Horizontal wind turbine in yaw. *Proc. 1st BWEA Wind Energy Conference, Cranfield University of Technology*, 1979.

[43] M. Bastankhah and F. Porté-Agel. Experimental and theoretical study of wind turbine wakes in yawed conditions. *Journal of Fluid Mechanics*, 806:506–541, 2016.

[44] J. Bartl, F. Mühle, J. Schottler, L. Sætran, J. Peinke, M. Adaramola, and M. Hölling. Wind tunnel experiments on wind turbine wakes in yaw : effects of inflow turbulence and shear. *Wind Energy Science*, pages 329–343, 2018.

[45] A. Jiménez, A. Crespo, and E. Migoya. Application of a les technique to characterize the wake deflection of a wind turbine in yaw. *Wind Energy*, 13(6):559–572, 2010.

[46] J. Bartl, F. Mühle, and L. Sætran. Wind tunnel study on power output and yaw moments for two yaw-controlled model wind turbines. *Wind Energy Science*, pages 489–502, 2018.

[47] P. Fleming, J. Annoni, L. A. Mart, K. Gruchalla, A. Scholbrock, M. Churchfield, and J. Roadman. Investigation into the shape of a wake of a yawed full-scale turbine. *Journal of Physics: Conf. Series*, 1037, 2018.

[48] S. P. Breton, J. Sumner, J. N. Sørensen, K. S. Hansen, S. Sarmast, and S. Ivanell. A survey of modelling methods for high-fidelity wind farm simulations using large eddy simulation. *Philosophical Transactions of the Royal Society A: Mathematical, Physical and Engineering Sciences*, 375, 2017.

[49] F. Mühle, J. Schottler, J. Bartl, R. Futrzynski, S. Evans, L. Bernini, P. Schito, M. Draper, A. Guggeri, E. Kleusberg, D. S. Henningson, M. Hölling, J. Peinke, M. S. Adaramola, and L. Sætran. Blind test comparison on the wake behind a yawed wind turbine. *Wind Energy Science*, 3(2):883–903, 2018.

[50] L. A. Martínez-Tossas, M. J. Churchfield, A. E. Yilmaz, H. Sarlak, P. L. Johnson, J. N. Sørensen, J. Meyers, and C. Meneveau. Comparison of four large-eddy simulation research codes and effects of model coefficient and inflow turbulence in actuator-line-based wind turbine modeling. *Journal of Renewable and Sustainable Energy*, 10(3), 2018.

[51] W. Munters and J. Meyers. Optimal dynamic induction and yaw control of wind farms: Effects of turbine spacing and layout. *Journal of Physics: Conference Series*, 1037(3), 2018.

[52] D. Astolfi, F. Castellani, and F. Natili. Wind turbine yaw control optimization and its impact on performance. *Machines*, 7(2), 2019.

[53] D. R. Houck. Review of wake management techniques for wind turbines. *Wind Energy*, 25(2):195–220, 2021.

[54] M.S. Adaramola and P.-Å. Krogstad. Experimental investigation of wake effects on wind turbine performance. *Renewable Energy*, 36(8):2078–2086, 2011.

[55] J. Park, S. Kwon, and K. H. Law. Wind farm power maximization based on a cooperative static game approach. In Henry Sodano, editor, *Active and Passive Smart Structures and Integrated Systems 2013*, volume 8688, pages 204 – 218. International Society for Optics and Photonics, SPIE, 2013.

[56] P. M. O. Gebraad, F. W. Teeuwisse, J. W. van Wingerden, P. A. Fleming, S. D. Ruben, J. R. Marden, and L. Y. Pao. Wind plant power optimization through yaw control using a parametric model for wake effects,Äîa cfd simulation study. *Wind Energy*, 19(1):95–114, 2016.

[57] M. Lin and F. Porté-Agel. Power maximization and fatigue-load mitigation in a wind-turbine array by active yaw control: an LES study. *Journal of Physics: Conference Series*, 1618(4):042036, sep 2020.

[58] P. Fleming, M. Churchfield, A. Scholbrock, A. Clifton, S. Schreck, K. Johnson, A. Wright, P. Gebraad, J. Annoni, B. Naughton, J. Berg, T. Herges, J. White, T. Mikkelsen, M. Sjöholm, and N. Angelou. Detailed field test of yaw-based wake steering. *Journal of Physics: Conference Series*, 753:052003, sep 2016.

[59] P. Fleming, J. King, K. Dykes, E. Simley, J. Roadman, A. Scholbrock, P. Murphy, J. K. Lundquist, P. Moriarty, K. Fleming, J. van Dam, C. Bay, R. Mudafort, H. Lopez, J. Skopek, M. Scott, B. Ryan, C. Guernsey, and D. Brake. Initial results from a field campaign of wake steering applied at a commercial wind farm – part 1. *Wind Energy Science*, 4(2):273–285, 2019.

[60] P. M. O. Gebraad, F.W. Teeuwisse, J.W. van Wingerden, P. A. Fleming, S. D. Ruben, J. R. Marden, and L. Y. Pao. A data-driven model for wind plant power optimization by yaw control. In *2014 American Control Conference*, pages 3128–3134, 2014.

[61] P. A. Fleming, A. Ning, P. M. O. Gebraad, and K. Dykes. Wind plant system engineering through optimization of layout and yaw control. *Wind Energy*, 19(2):329–344, 2015.

[62] P. M. O. Gebraad, J. J. Thomas, A. Ning, P. Fleming, and K. Dykes. Maximization of the annual energy production of wind power plants by optimization of layout and yaw-based wake control. *Wind Energy*, 20(1):97–107, 2017.

[63] Z. Dar, K. Kar, O. Sahni, and J. H. Chow. Windfarm power optimization using yaw angle control. *IEEE Transactions on Sustainable Energy*, 8(1):104–116, 2016.

[64] B. Dou, T. Qu, L. Lei, and P. Zeng. Optimization of wind turbine yaw angles in a wind farm using a three-dimensional yawed wake model. *Energy*, 209:118415, 2020.

[65] A. P. J. Stanley, C. Bay, R. Mudafort, and P. Fleming. Fast yaw optimization for wind plant wake steering using boolean yaw angles. *Wind Energy Science*, 7(2):741–757, 2022.

[66] S. B. Pope. *Turbulent flows*. Cambridge university press, 2000.

[67] R. Byron Bird, Warren E. Stewart, and Edwin N. Lightfoot. *Transport phenomena*. John Wiley & Sons, 1924.

[68] J. O. Hirschfelder, C. F. Curtiss, and R. B. Bird. *Molecular theory of gases and liquids*. Wiley, 1964.

[69] O. Reynolds. An experimental investigation of the circumstances which determine whether the motion of water shall be direct or sinuous, and of the law of resistance in parallel channels. *Proceedings of the Royal Society of London*, 35(224-226):84–99, 1883.

[70] L. F. Richardson and W. N. Shaw. The supply of energy from and to atmospheric eddies. *Proceedings of the Royal Society of London. Series A, Containing Papers of a Mathematical and Physical Character*, 97(686):354–373, 1920.

[71] A. N. Kolmogorov. The local structure of turbulence in incompressible viscous fluid for very large reynolds numbers. *Proceedings of the Royal Society of London. Series A: Mathematical and Physical Sciences*, 434(1890):9–13, 1991.

[72] N. Ali, N. Hamilton, M. Cortina, G.and Calaf, and R. B. Cal. Anisotropy stress invariants of thermally stratified wind turbine array boundary layers using large eddy simulations. *Journal of Renewable and Sustainable Energy*, 10(1):013301, 2018.

[73] J. L. Lumley and G. R. Newman. The return to isotropy of homogeneous turbulence. *Journal of Fluid Mechanics*, 82(1):161–178, 1977.

[74] B. M. Emory and G Iaccarino. Visualizing turbulence anisotropy in the spatial domain with componentality contours. *Center for Turbulence Research Annual Research Briefs*, pages 123–137, 2014.

[75] S. Banerjee, R. Krahl, F. Durst, and C. Zenger. Presentation of anisotropy properties of turbulence, invariants versus eigenvalue approaches. *Journal of Turbulence*, 8(December 2014):1–27, 2007.

[76] P. R. Spalart. Direct simulation of a turbulent boundary layer up to rθ= 1410. *Journal of fluid mechanics*, 187:61–98, 1988.

[77] S.J. Kline and S.K. Robinson. Turbulent boundary layer structure: Progress, status, and challenges. In *Structure of Turbulence and Drag Reduction*, pages 3–22. Springer, 1990.

[78] J. Jeong and F. Hussain. On the identification of a vortex. *Journal of Fluid Mechanics*, 285:69–94, 1995.

[79] J. C. R. Hunt, A. A. Wray, and P. Moin. Eddies, streams, and convergence zones in turbulent flows. In *Studying Turbulence Using Numerical Simulation Databases, 2*, pages 193–208, 1988.

[80] P. Sagaut. *Introduction à la simulation des grandes échelles pour les écoulements de fluide incompressible, Mathématique & Applications.* Springer Berlin Heidelberg, 1998.

[81] P. Benard, G. Balarac, V. Moureau, C. Dobrzynski, G. Lartigue, and Y. D'Angelo. Mesh adaptation for large-eddy simulations in complex geometries. *International Journal for Numerical Methods in Fluids*, 81(12):719–740, 2016.

[82] S. Ghosal and P. Moin. The basic equations for the large eddy simulation of turbulent flows in complex geometry. *Journal of Computational Physics*, 118(1):24–37, 1995.

[83] S. Ghosal. Mathematical and physical constraints on large-eddy simulation of turbulence. *AIAA Journal*, 37(4):425–433, 1999.

[84] O. V. Vasilyev, T. S. Lund, and P. Moin. A general class of commutative filters for les in complex geometries. *Journal of Computational Physics*, 146:82–104, 1998.

[85] A. L. Marsden, O. V. Vasilyev, and P. Moin. Construction of commutative filters for les on unstructured meshes. *Journal of Computational Physics*, 175(2):584–603, 2002.

[86] V. Moureau. *Simulation aux grandes échelles de l'aérodynamique interne des moteurs à piston.* PhD thesis, Ecole centrale de Paris, 2004.

[87] M. Germano. A proposal for a redefinition of the turbulent stresses in the filtered navier-stokes equations. *The Physics of Fluids*, 29(7):2323–2324, 1986.

[88] A. Leonard. Energy cascade in large-eddy simulations of turbulent fluid flows. In F.N. Frenkiel and R.E. Munn, editors, *Turbulent Diffusion in Environmental Pollution*, volume 18 of *Advances in Geophysics*, pages 237–248. Elsevier, 1975.

[89] J. A. Domaradzki and W. Liu. Approximation of subgrid-scale energy transfer based on the dynamics of resolved scales of turbulence. *Physics of Fluids*, 7(8):2025–2035, 1995.

[90] F. Nicoud, H. B. Toda, O. Cabrit, S. Bose, and J. Lee. Using singular values to build a subgrid-scale model for large eddy simulations. *Physics of Fluids*, 23(8):085–106, 2011.

[91] M. Germano, U. Piomelli, P. Moin, and W. H. Cabot. A dynamic subgrid-scale eddy viscosity model. *Physics of Fluids*, 3:1760–1765, 1990.

[92] D. K. Lilly. A proposed modification of the germano subgrid-scale closure method. *Physics of Fluids A: Fluid Dynamics*, 4(3):633–635, 1992.

[93] M. J. Boussinesq. *Théorie de l'écoulement tourbillonnant et tumultueux des liquides dans les lits rectilignes a grande section.* Gauthier-Villars et Fils, imprimeurs-libraires, 1897.

[94] J. Smagorinsky. General circulation experiments with the primitive equations: I. the basic experiment. 91(3):99 – 164, 1963.

[95] D. Carati, S. Ghosal, and P. Moin. On the representation of backscatter in dynamic localization models. *Physics of Fluids*, 7(3):606–616, 1995.

[96] F. Nicoud and F. Ducros. Subgrid-scale stress modelling based on the square of the velocity gradient tensor. *Flow, Turbulence and Combustion*, 62(3):183–200, 1999.

[97] A. W. Vreman. An eddy-viscosity subgrid-scale model for turbulent shear flow: Algebraic theory and applications. *Physics of Fluids*, 16(10):3670–3681, 2004.

[98] H. Sarlak, C. Meneveau, and J.N. Sørensen. Role of subgrid-scale modeling in large eddy simulation of wind turbine wake interactions. *Renewable Energy*, 77:386–399, 2015.

[99] M. Rieth, F. Proch, O.T. Stein, M.W.A. Pettit, and A.M. Kempf. Comparison of the sigma and smagorinsky les models for grid generated turbulence and a channel flow. *Computers & Fluids*, 99:172–181, 2014.

[100] V. Moureau, P. Domingo, and L. Vervisch. Design of a massively parallel cfd code for complex geometries. *Comptes Rendus Mécanique*, 339(2-3):141–148, 2011.

[101] N. Legrand, G. Lartigue, and V. Moureau. A multi-grid framework for the extraction of large-scale vortices in large-eddy simulation. *J. Comput. Phys.*, 349:528–560, 11 2017.

[102] F. Houtin-Mongrolle, L. Bricteux, P. Bénard, G. Lartigue, V. Moureau, and J. Reveillon. Actuator line method applied to grid turbulence generation for large-eddy simulations. *Journal of Turbulence*, 0:2–3, 2020.

[103] R. Janodet, C. Guillamón, V. Moureau, R. Mercier, G. Lartigue, P. Bénard, T. Ménard, and A. Berlemont. A massively parallel accurate conservative level set algorithm for simulating turbulent atomization on adaptive unstructured grids. *Journal of Computational Physics*, page 111075, 2022.

[104] P. Benard, G. Lartigue, V. Moureau, and R. Mercier. Large-eddy simulation of the lean-premixed preccinsta burner with wall heat loss. *Proceedings of the Combustion Institute*, 37:5233–5243, 2019.

[105] P. Domingo-Alvarez, P. Bénard, V. Moureau, G. Lartigue, and F. Grisch. Impact of spray droplet distribution on the performances of a kerosene lean/premixed injector. *Flow, Turbulence and Combustion*, 104(2):421–450, 2020.

[106] F. Houtin-Mongrolle, P. Benard, G. Lartigue, and V. Moureau. A level-set framework for the wind turbine wake analysis: from high-fidelity unsteady simulations to 1d momentum theory. *Journal of Physics: Conference Series*, 1934(1):012011, may 2021.

[107] G. Karypis and V. Kumar. Metis – unstructured graph partitioning and sparse matrix ordering system, version 2.0. Technical report, 1995.

[108] C. Chevalier and F. Pellegrini. PT-Scotch: A tool for efficient parallel graph ordering. *Parallel Computing*, 34(6-8):318–331, 2008.

[109] E.F. Kaasschieter. Preconditioned conjugate gradients for solving singular systems. *Journal of Computational and Applied Mathematics*, 24(1):265–275, 1988.

[110] R. A. Nicolaides. Deflation of conjugate gradients with applications to boundary value problems. *SIAM Journal on Numerical Analysis*, 24(2):355–365, 1987.

[111] M. Kraushaar. *Application of the compressible and low-Mach number approaches to Large-Eddy Simulation of turbulent flows in aero-engines.* PhD thesis, Institut National Polytechnique de Toulouse- INPT, 2011.

[112] S. Vantieghem. *Numerical simulations of quasi-static magneto hydrodynamics using an unstructured finite-volume solver: development and applications.* PhD thesis, Université Libre de Bruxelles, 2011.

[113] A. J. Chorin. Numerical solution of the navier-stokes equations. *Mathematics of Computation*, 22:745–762, 1968.

[114] J. Kim and P. Moin. Application of a fractional-step method to incompressible navier-stokes equations. *Journal of Computational Physics*, 59:308–323, 1984.

[115] J. B. Bell, P. Colella, and H. M. Glaz. A second-order projection method for the incompressible navier-stokes equations. *Journal of Computational Physics*, 85(2):257–283, 1989.

[116] M. Malandain, N. Maheu, and V. Moureau. Optimization of the deflated conjugate gradient algorithm for the solving of elliptic equations on massively parallel machines. *J. Comput. Phys.*, 238:32–47, 2013.

[117] M. Malandain. *Massively parallel simulation of low-Mach number turbulent flows.* PhD thesis, INSA de Rouen, 2013.

[118] H. A. Van der Vorst. Bi-cgstab: A fast and smoothly converging variant of bi-cg for the solution of nonsymmetric linear systems. *SIAM Journal on Scientific and Statistical Computing*, 13(2):631–644, 1992.

[119] J. N. Sørensen and A. Myken. Unsteady actuator disc model for horizontal axis wind turbines. *Journal of Wind Engineering and Industrial Aerodynamics*, 39(1):139–149, 1992.

[120] J. N. Sørensen and C. W. Kock. A model for unsteady rotor aerodynamics. *Journal of Wind Engineering and Industrial Aerodynamics*, 58(3):259–275, 1995.

[121] R. Mikkelsen, J. N. Sørensen, and W. Z. Shen. Modelling and analysis of the flow field around a coned rotor. *Wind Energy*, 4(3):121–135, 2001.

[122] M. Lin and F. Porté-Agel. Large-eddy simulation of yawed wind-turbine wakes: Comparisons with wind tunnel measurements and analytical wake models. *Energies*, 12(23), 2019.

[123] J. N. Sørensen. *The general momentum theory*, volume 4. Springer, 2016.

[124] M. Moens, M. Duponcheel, G. Winckelmans, and P. Chatelain. An actuator disk method with tip-loss correction based on local effective upstream velocities. *Wind Energy*, 21(9):766–782, 2018.

[125] W. Z. Shen, W. J. Zhu, and J. N. Sørensen. Study of tip loss corrections using CFD rotor computations. *Journal of Physics: Conference Series*, 555(1), 2014.

[126] J. N. Sørensen and W. Z. Shen. Numerical modeling of wind turbine wakes. *J Fluids Eng*, 124(2):393–399, 2002.

[127] A. R Meyer Forsting, G. R. Pirrung, and N. Ramos-García. The wake of an actuator line with a vortex-based tip/smearing correction in uniform and turbulent inflow. *Journal of Physics: Conference Series*, 1256, 2019.

[128] W. Z. Shen, W. J. Zhu, and H. Yang. Validation of the Actuator Line Model for Simulating Flows past Yawed Wind Turbine Rotors. *Journal of Power and Energy Engineering*, (July):7–13, 2015.

[129] C. Grinderslev, N. N. Sørensen, S. G. Horcas, N. Troldborg, and F. Zahle. Wind turbines in atmospheric flow: fluid–structure interaction simulations with hybrid turbulence modeling. *Wind Energy Science*, 6(3):627–643, 2021.

[130] M. De Oliveira, R. C. Puraca, and B. S. Carmo. Blade-resolved numerical simulations of the nrel offshore 5 mw baseline wind turbine in full scale: A study of proper solver configuration and discretization strategies. *SSRN Electronic Journal*, 2021.

[131] *A Novel Conservative Lagrangian Immersed Boundary Method For Wind Turbine Simulations*, 2001.

[132] P. Weihing. *Numerical Study of Transition, Flow Separation and Wake Phenomena of Wind Turbines with Enhanced Hybrid RANS/LES Methods*. PhD thesis, University of Stuttgart, 2021.

[133] M. Guilbot, S. Barre, G. Balarac, C. Bonamy, and N. Guillaud. A numerical study of vertical axis wind turbine performances in twin-rotor configurations. *J. Phys.: Conf. Ser.*, 1618:052012, 2020.

[134] A. C. Kirby, M. J. Brazell, Z. Yang, R. Roy, B. R. Ahrabi, M. K. Stoellinger, J. Sitaraman, and D. J. Mavriplis. Wind farm simulations using an overset hp-adaptive approach with blade-resolved turbine models. *The International Journal of High Performance Computing Applications*, 33(5):897–923, 2019.

[135] K. Takizawa, B. Henicke, D. Montes, T. E. Tezduyar, M. C. Hsu, and Y. Bazilevs. Numerical-performance studies for the stabilized space–time computation of wind-turbine rotor aerodynamics. *Computational Mechanics*, 48(6):647–657, 2011.

[136] M. Cormier, P. Weihing, and T. Lutz. Evaluation of the effects of actuator line force smearing on wind turbines near-wake development. *J. Phys.: Conf. Ser.*, 1934(1):012013, may 2021.

[137] M. C. Hsu, I. Akkerman, and Y. Bazilevs. Finite element simulation of wind turbine aerodynamics: validation study using nrel phase vi experiment. *Wind Energy*, 17(3):461–481, 2014.

[138] L. Ramírez, X. Nogueira, P. Ouro, F. Navarrina, S. Khelladi, and I. Colominas. A higher-order chimera method for finite volume schemes. *Archives of Computational Methods in Engineering*, 25(3):691–706, 2018.

[139] Y. Liu, Q. Xiao, A. Incecik, C. Peyrard, and D. Wan. Establishing a fully coupled cfd analysis tool for floating offshore wind turbines. *Renewable Energy*, 112:280–301, 2017.

[140] V. D. Nguyen, J. Jansson, A. Goude, and J. Hoffman. Direct finite element simulation of the turbulent flow past a vertical axis wind turbine. *Renewable energy*, 135:238–247, 2019.

[141] M. Guilbot. *Analyse et optimisation des performances de turbines à axe vertical et flux transverse par simulations numériques*. PhD thesis, Université Grenoble Alpes, 2021.

[142] N. Ramos-García, M. M. Hejlesen, J. N. Sørensen, and J. H. Walther. Hybrid vortex simulations of wind turbines using a three-dimensional viscous-inviscid panel method. *Wind Energy*, 20(11):1871–1889, 2017.

[143] K. Nilsson, W. Z. Shen, J. N. Sørensen, S. P. Breton, and S. Ivanell. Validation of the actuator line method using near wake measurements of the mexico rotor. *Wind Energy*, 18(3):499–514, 2015.

[144] N. Troldborg. *Actuator line modeling of wind turbine wakes*. PhD thesis, DTU-MEK Denmark, 2008.

[145] M. J. Churchfield, S. J. Schreck, L. A. Martinez, C. Meneveau, and P. R. Spalart. An advanced actuator line method for wind energy applications and beyond. *35th Wind Energy Symposium*, 2017.

[146] S. Xie. An actuator-line model with lagrangian-averaged velocity sampling and piecewise projection for wind turbine simulations. *Wind Energy*, 2021.

[147] H. Snel, R. Houwink, and J. Bosschers. Sectional prediction of lift coefficients on rotating wind turbine blades in stall. *NOVEM reports*, 1994.

[148] P. K. Chaviaropoulos and M. O.L. Hansen. Investigating three-dimensional and rotational effects on wind turbine blades by means of a quasi-3d navier-stokes solver. *Journal of Fluids Engineering, Transactions of the ASME*, 122:330–336, 2000.

[149] Lindenburg C. Modelling of rotational augmentation based on engineering considerations and measurements. *European Wind Energy Conference*, pages 22–25, 2004.

[150] Z. Du and M. S. Selig. A 3-d stall-delay model for horizontal axis wind turbine performance prediction. *1998 ASME Wind Energy Symposium*, pages 9–19, 1998.

[151] H. Glauert. Airplane Propellers. *Durand, W.F., Ed., Aerodynamic Theory*, IV:169–360, 1935.

[152] W. Z. Shen, R. Mikkelsen, J. N. Sørensen, and C. Bak. Tip loss corrections for wind turbine computations. *Wind Energy*, 8:457–475, 2005.

[153] T. Sant. *Improving BEM-based Aerodynamic Models in Wind Turbine Design Codes1*. PhD thesis, Delft University of Technology, 2007.

[154] Leishman J.G. and Beddoes T.S. A semi empirical model for dynamic stall. *J. Am. Helicopter Soc.*, 34(3):3–17, 1986.

[155] L. Beaudet. *Etude expérimentale et numérique du décrochage dynamique sur une éolienne à axe vertical de forte solidité*. PhD thesis, Université de Poitiers, 2014.

[156] N. Troldborg, J. N. Sørensen, and R. Mikkelsen. Numerical simulations of wake characteristics of a wind turbine in uniform inflow. *Wind Energy*, 13:86–99, 2010.

[157] L. A. Martínez-Tossas, M. J. Churchfield, and S. Leonardi. Large eddy simulations of the flow past wind turbines: actuator line and disk modeling. *Wind Energy*, 18(6):1047–1060, 2015.

[158] P. K. Jha, M. J. Churchfield, P. J. Moriarty, and S. Schmitz. Guidelines for volume force distributions within actuator line modeling of wind turbines on large-eddy simulation-type grids. *Journal of Solar Energy Engineering*, 136(3), 2014.

[159] L. A. Martínez-Tossas, M. J. Churchfield, and C. Meneveau. A highly resolved large-eddy simulation of a wind turbine using an actuator line model with optimal body force projection. *Journal of Physics: Conference Series*, 753, 2016.

[160] L. A. Martínez-Tossas, M. J. Churchfield, and C. Meneveau. Optimal smoothing length scale for actuator line models of wind turbine blades based on gaussian body force distribution. *Wind Energ.*, 2017.

[161] D. G. Caprace, P. Chatelain, and G. Winckelmans. Lifting line with various mollifications: theory and application to an elliptical wing. *AIAA Journal*, 57(1):17–28, 2019.

[162] L. A. Martínez-Tossas and C. Meneveau. Filtered lifting line theory and application to the actuator line model. *Journal of Fluid Mechanics*, 863:269–292, 2019.

[163] A. R. Meyer Forsting, G. R. Pirrung, and N. Ramos-García. A vortex-based tip/smearing correction for the actuator line. *Wind Energy Science*, 4(2):369–383, 2019.

[164] K. O. Dağ and J. N. Sørensen. A new tip correction for actuator line computations. *Wind Energy*, 23(2):148–160, 2020.

[165] O.K.G. Tietjens, L. Prandtl, and J.P. Den Hartog. *Applied Hydro- and Aeromechanics: Based on Lectures of L. Prandtl*. Number vol. 2. Dover Publications, 1957.

[166] S. Zeoli, G. Balarac, P. Bénard, G. Georis, F. Houtin-Mongrolle, and L. Bricteux. Large eddy simulation of wind turbine wakes using adaptative mesh refinement. *Journal of Physics: Conference Series*, 1618(6):062056, sep 2020.

[167] J.M. Jonkman, S. Butterfield, W. Musial, and G. Scott. Definition of a 5-mw reference wind turbine for offshore system development. *NREL reports*, pages 1–75, 2009.

[168] L. Satran, F. Mühle, J. Bartl, J. Schottler, and M. S. Adaramola. Invitation to the 2017 " Blind test 5 " workshop The wake behind a yawed wind turbine. 2017.

[169] P. Benard, A. Viré, V. Moureau, G. Lartigue, L. Beaudet, P. Deglaire, and L. Bricteux. Large-eddy simulation of wind turbines wakes including geometrical effects. *Computers & Fluids*, 173:133–139, 2018.

[170] A. Englberger, J. K. Lundquist, and A. Dörnbrack. Changing the rotational direction of a wind turbine under veering inflow: a parameter study. *Wind Energy Science*, 5(4):1623–1644, 2020.

[171] C. B. Sejekan and C. F. Ollivier-Gooch. Improving finite-volume diffusive fluxes through better reconstruction. *Computers & Fluids*, 139:216–232, 2016.

[172] C. Duprat, G. Balarac, O. Métais, P. M. Congedo, and O. Brugière. A wall-layer model for large-eddy simulations of turbulent flows with/out pressure gradient. *Physics of Fluids*, 23(1), 2011.

[173] F. Lesage and L.S. Gartshore. A method of reducing drag and fluctuating side force on bluff bodies. *Journal of Wind Engineering and Industrial Aerodynamics*, 25:229–245, 1987.

[174] C.W. Knisely. Strouhal numbers of rectangular cylinders at incidence: a review and new data . *Journal Fluids and Structures*, 4:371–393, 1990.

[175] B.J. Vickery. Fluctuating lift and drag on a long cylinder of square cross-section in a smooth and in a turbulent stream. *J. Fluid Mech.*, 25(3):481–494, 1966.

[176] H. Fukumoto, H. Aono, M. Tanaka, H. Matsuda, T. Osako, T. Nonomura, A. Oyama, and K. Fujii. Significance of computational spanwise domain length on LES for the flowfield with large vortex structure. *54th AIAA Aerospace Sciences Meeting*, pages 1–16, 2016.

[177] C. H.K. Williamson and A. Roshko. Vortex formation in the wake of an oscillating cylinder. *Journal of Fluids and Structures*, 2(4):355–381, 1988.

[178] L. Guedot, G. Lartigue, and V. Moureau. Design of high-order implicit filters on unstructured grids for the identification of large-scale features in large-eddy simulations. *Direct and Large-Eddy Simulation IX*, 20:81–87, 2015.

[179] G. W. Jones, J. J. Cincotta, and Walker R. W. Aerodynamic forces on a stationary and oscillating circular cylinder at high Reynolds numbers. *NASA technichal report*, 1969.

[180] L Fiabane, M Gohlke, and O Cadot. Characterization of flow contributions to drag and lift of a circular cylinder using a volume expression of the fluid force. *European Journal of Mechanics - B/Fluids*, 30(3):311–315, 2011.

[181] J. Zhao, K. Hourigan, and M. C. Thompson. Flow-induced vibration of D-section cylinders: An afterbody is not essential for vortex-induced vibration. *Journal of Fluid Mechanics*, 851:317–343, 2018.

[182] L. Sætran, F. Mühle, J. Bartl, J. Schottler, M. Hölling, and M. S. Adaramola. Invitation to the 2017 "blind test 5" workshop – the wake behind a yawed wind turbine. *http://doi.org/10.5281/zenodo.1218555*, 2018.

[183] D. Hurst and J. C. Vassilicos. Scalings and decay of fractal-generated turbulence. *Physics of Fluids*, 19(3):035–103, 2007.

[184] M. Alam, Y Zhou, and XW Wang. The wake of two side-by-side square cylinders. *Journal of Fluid Mechanics*, 669:432–471, 2011.

[185] R.J. Martinuzzi, S.C.C. Bailey, and G.A. Kopp. Influence of wall proximity on vortex shedding from a square cylinder. *Experiments in fluids*, 34(5):585–596, 2003.

[186] D. Chatterjee and G. Biswas. Dynamic behavior of flow around rows of square cylinders kept in staggered arrangement. *Journal of Wind Engineering and Industrial Aerodynamics*, 136:1–11, 2015.

[187] T. Passot and A. Pouquet. Numerical simulation of compressible homogeneous flows in the turbulent regime. *Journal of Fluid Mechanics*, 181:441–466, 1987.

[188] P. E. Roach. The generation of nearly isotropic turbulence by means of grids. *International Journal of Heat and Fluid Flow*, 8(2):82–92, 1987.

[189] U. Ciri, G. Petrolo, M. V. Salvetti, and S. Leonardi. Large-eddy simulations of two in-line turbines in a wind tunnel with different inflow conditions. *Energies*, 10:1–23, 2017.

[190] S. Laizet and J. C. Vassilicos. DNS of fractal-generated turbulence. *Flow, Turbulence and Combustion*, 87(4):673–705, 2011.

[191] T. Maeda, Y. Kamada, J. Suzuki, and H. Fujioka. Rotor Blade Sectional Performance Under Yawed Inflow Conditions. *Journal of Solar Energy Engineering*, 130(3), 2008.

[192] J. Schepers, H. A. Madsen, T. Lutz, K. Koen Boorsma, T. T. Cho, S. Sugoi Gomez-Iradi, P. Schaffarczyk, A. Jeromin, W. Z. Shen, K. Meister, B. Stoevesandt, S. J. Schreck, D. Micallef, R. Pereira, T. Sant, and N. N. Sørensen. Final report of iea task 29, mexnext (phase 1): Analysis of mexico wind tunnel measurements. 2012.

[193] R. Damiani, S. Dana, J. Annoni, P. Fleming, J. Roadman, J. van Dam, and K. Dykes. Assessment of wind turbine component loads under yaw-offset conditions. *Wind Energy Science*, 3(1):173–189, 2018.

[194] C. Butterfield, D. Simms, G. Scott, and A. Hansen. Dynamic stall on wind turbine blades. 1991.

[195] M. F. Howland, J. Bossuyt, L. A. Martínez-Tossas, J. Meyers, and C. Meneveau. Wake structure in actuator disk models of wind turbines in yaw under uniform inflow conditions. *Journal of Renewable and Sustainable Energy*, 8(4):043301, 2016.

[196] J. Schottler, J. Bartl, L. Mühle, F.and Sætran, J. Peinke, and M. Hölling. Wind tunnel experiments on wind turbine wakes in yaw : redefining the wake width. *Wind Energ. Sci.*, pages 257–273, 2018.

[197] J. Bartl and L. Sætran. Blind test comparison of the performance and wake flow between two in-line wind turbines exposed to different turbulent inflow conditions. *Wind Energy Science*, 2(1):55–76, 2017.

[198] P. E. Eriksen and P. Krogstad. Development of coherent motion in the wake of a model wind turbine. *Renewable Energy*, 108:449–460, 2017.

[199] H. Zong and F. Porté-Agel. A momentum-conserving wake superposition method for wind farm power prediction. *Journal of Fluid Mechanics*, 889:A8, 2020.

[200] F. Porté-Agel, M. Bastankhah, and S. Shamsoddin. Wind-Turbine and Wind-Farm Flows: A Review. *Boundary-Layer Meteorology*, 174(1):1–59, 2020.

[201] J. Lebron, L. Castillo, and C. Meneveau. Experimental study of the kinetic energy budget in a wind turbine streamtube. *Journal of Turbulence*, 13:1–22, 2012.

[202] O. Desjardins, V. Moureau, and H. Pitsch. An accurate conservative level set/ghost fluid method for simulating turbulent atomization. *J Comput Phys*, 227(18):8395–416, sep 2008.

[203] N. Coudou, M. Moens, Y. Marichal, J. Van Beeck, L. Bricteux, and P. Chatelain. Development of wake meandering detection algorithms and their application to large eddy simulations of an isolated wind turbine and a wind farm. *Journal of Physics: Conference Series*, 1037:072024, 6 2018.

[204] M. Ge, D. F. Gayme, and C. Meneveau. Large-eddy simulation of wind turbines immersed in the wake of a cube-shaped building. *Renewable Energy*, 163:1063–77, 2021.

[205] J. Meyers and C. Meneveau. Flow visualization using momentum and energy transport tubes and applications to turbulent flow in wind farms. *Journal of Fluid Mechanics*, 715:335–58, 2013.

[206] A. Ghate, N. Ghaisas, A. Towne, and S. Lele. Interaction of small scale homogenenous isotropic turbulence with an actuator disk. *Wind Energy Symposium, 2018*, 2018.

[207] J. R. West and S. K. Lele. Wind turbine performance in very large wind farms: Betz analysis revisited. *Energies*, 13(5):1–25, 2020.

[208] M. Ge, S. Zhang, H. Meng, and H. Ma. Study on interaction between the wind-turbine wake and the urban district model by large eddy simulation. *Renewable Energy*, 157:941–950, 2020.

[209] R. Goldman. Curvature formulas for implicit curves and surfaces. *Computer Aided Geometric Design*, 22(7):632–658, 2005.

[210] M. O.L. Hansen. *Aerodynamics of Wind Turbines, Third edition*, volume 3rd. 2015.

[211] W. J. M. Rankine. On the mechanical principles of the action of propellers. *Transactions of the Institution of Naval Architects*, 6, 1865.

[212] R. E. Froude. On the part played in propulsion by differences of fluid pressure. *Trans. Inst. Naval Architects*, 30:390, 1889.

[213] C. Bak, F. Zahle, R. Bitsche, T. Kim, A. Yde, L. C. Henriksen, A. Natarajan, and M. Hansen. DTU 10MW Reference Wind Turbine. Technical report, DTU Wind Energy, 2013.

[214] D. I. Manolas, G. R. Pirrung, A. Croce, M. Roura, V. A. Riziotis, H. A. Madsen, C. Pizarro, S. G. Voutsinas, and F. Rasmussen. Cross comparison of aeroelastic state-of-the-art design tools on a 10 mw scale wind turbine. *European Wind Energy Association Annual Conference and Exhibition 2015, EWEA 2015 - Scientific Proceedings*, (December), 2015.

[215] J. Mann. Wind field simulation. *Probabilistic Engineering Mechanics*, 13(4):269–82, 1998.

[216] F. K. Browand. The structure of the turbulent mixing layer. Technical report, 1986.

[217] C. B. Da Silva, J. C.R. Hunt, I. Eames, and J. Westerweel. Interfacial layers between regions of different turbulence intensity. *Annual Review of Fluid Mechanics*, 46:567–590, 2014.

[218] J. Westerweel, T. Hofmann, C. Fukushima, and J. C.R. Hunt. The turbulent/non-turbulent interface at the outer boundary of a self-similar turbulent jet. *Experiments in Fluids*, 33:873–878, 2002.

[219] J. Westerweel, A. Petracci, R. Delfos, and J. C.R. Hunt. Characteristics of the turbulent/non-turbulent interface of a non-isothermal jet. *Philosophical Transactions of the Royal Society A, Mathematical, Physical and Engineering Sciences*, 369:723–737, 2011.

[220] J. Westerweel, C. Fukushima, J. M. Pedersen, and J. C.R. Hunt. Momentum and scalar transport at the turbulent/non-turbulent interface of a jet. *Journal of Fluid Mechanics*, 631:199–230, 2009.

[221] T. R. Troutt. The turbulent mixing layer: Geometry of large vortices. *Journal of Fluid Mechanics*, 158:489–509, 1985.

[222] F. Stella, N. Mazellier, P. Joseph, and A. Kourta. Mass entrainment-based model for separating flows. *Physical Review Fluids*, 3, 2018.

[223] E. Varon, N. Mazellier, and A. Kourta. Transport mechanisms inside the turbulent wake of a bluff body. *MATEC Web of Conferences*, 286:07016, 2019.

[224] D. K. Bisset, J. C.R. Hunt, and M. M. Rogers. The turbulent/non-turbulent interface bounding a far wake. *Journal of Fluid Mechanics*, 451:383–410, 2002.

[225] N. Ikegaya, S. Morishige, Y. Matsukura, N. Onishi, and A. Hagishima. Experimental study on the interaction between turbulent boundary layer and wake behind various types of two-dimensional cylinders. *Journal of Wind Engineering and Industrial Aerodynamics*, 204:104250, 2020.

[226] V. B. Zametaev and I. I. Lipatov. Energy exchange in a compressible turbulent mixing layer. *Journal of Turbulence*, 22:48–77, 2021.

[227] M. M. Rogers and R. D. Moser. Direct simulation of a self-similar turbulent mixing layer. *Physics of Fluids*, 6:903–923, 1994.

[228] K. Chauhan, J. Philip, C. M. De Silva, N. Hutchins, and I. Marusic. The turbulent/non-turbulent interface and entrainment in a boundary layer. *Journal of Fluid Mechanics*, 742:119–151, 2014.

[229] L. E.M. Lignarolo, D. Ragni, F. Scarano, C. J. S. Ferreira, and G. J.W. Van Bussel. Tip-vortex instability and turbulent mixing in wind-turbine wakes. *Journal of Fluid Mechanics*, 781:467–493, 10 2015.

[230] Y. T. Wu and F. Porté-Agel. Atmospheric turbulence effects on wind-turbine wakes: An LES study. *Energies*, 5(12):5340–62, 2012.

[231] F. Rasmussen, M. H. Hansen, K. Thomsen, T. J. Larsen, F. Bertagnolio, J. Johansen, H. A. Madsen, C. Bak, and A. M. Hansen. Present status of aeroelasticity of wind turbines. *Wind Energy*, 6(3):213–228, 2003.

[232] M.O.L. Hansen, J.N. Sørensen, S. Voutsinas, N. Sørensen, and H.Aa. Madsen. State of the art in wind turbine aerodynamics and aeroelasticity. *Progress in Aerospace Sciences*, 42(4):285–330, 2006.

[233] C. L. Bottasso, F. Campagnolo, A. Croce, S. Dilli, F. Gualdoni, and M. B. Nielsen. Structural optimization of wind turbine rotor blades by multilevel sectional/multibody/3d-fem analysis. *Multibody System Dynamics*, 32(1):87–116, 2014.

[234] M. Alonso-Martinez, J. M Adam, F. P. Alvarez-Rabanal, and J. J. del Coz Díaz. Wind turbine tower collapse due to flange failure: Fem and doe analyses. *Engineering Failure Analysis*, 104:932–949, 2019.

[235] J. Seo, W. Schaffer, M. Head, M. Shokouhian, and E. Choi. Integrated fem and cfd simulation for offshore wind turbine structural response. *International Journal of Steel Structures*, 19(4):1112–1124, 2019.

[236] X. Zhao, P. Maißer, and J. Wu. A new multibody modelling methodology for wind turbine structures using a cardanic joint beam element. *Renewable Energy*, 32(3):532–546, 2007.

[237] S. Huang P. Zhang. Review of aeroelasticity for wind turbine: Current status, research focus and future perspectives. *Frontiers in Energy*, 5(4):419, 2011.

[238] T. Kim, A. M. Hansen, and K. Branner. Development of an anisotropic beam finite element for composite wind turbine blades in multibody system. *Renewable Energy*, 59:172–183, 2013.

[239] M. J. Churchfield, S. Lee, J. Michalakes, and P. J. Moriarty. A numerical study of the effects of atmospheric and wake turbulence on wind turbine dynamics. *Journal of Turbulence*, 13:N14, 2012.

[240] H. Meng, F. Lien, and L. Li. Elastic actuator line modelling for wake-induced fatigue analysis of horizontal axis wind turbine blade. *Renewable Energy*, 116:423–437, 2018.

[241] Z. Yu, Z. Hu, X. Zheng, Q. Ma, and H. Hao. Aeroelastic performance analysis of wind turbine in the wake with a new elastic actuator line model. *Water*, 12(5), 2020.

[242] J. T. Petersen. *Kinematically nonlinear finite element model of a horizontal axis wind turbine. Part 1: Mathematical model and results.* PhD thesis, Danmarks Tekniske Universitet, Risø Nationallaboratoriet for Bæredygtig Energi., 1992.

[243] R. Rubak and J. T. Petersen. Monopile as part of aeroelastic wind turbine simulation code. *Proceedings of Copenhagen Offshore Wind*, 20, 2005.

[244] G. Upton and I. Cook. *A Dictionary of Statistics.* Oxford University Press, 2008.

[245] J. Chung and G. M. Hulbert. A time integration algorithm for structural dynamics with improved numerical dissipation: The generalized-α method. *Journal of Applied Mechanics*, 60(2):371–375, 1993.

[246] P. F. Skjoldan. *Aeroelastic modal dynamics of wind turbines including anisotropic effects.* PhD thesis, Danmarks Tekniske Universitet, Risø Nationallaboratoriet for Bæredygtig Energi., 2011.

[247] C. Farhat and M. Lesoinne. Two efficient staggered algorithms for the serial and parallel solution of three-dimensional nonlinear transient aeroelastic problems. *Computer Methods in Applied Mechanics and Engineering*, 182(3):499–515, 2000.

[248] S. Krenk and P. J. Couturier. Equilibrium-based nonhomogeneous anisotropic beam element. *AIAA Journal*, 55(8):2773–2782, 2017.

[249] K. Wang, V. A. Riziotis, and S. G. Voutsinas. Aeroelastic stability of idling wind turbines. *Journal of Physics: Conference Series*, 753:042008, sep 2016.

[250] V. P. Stein and H. J. Kaltenbach. Validation of a large-eddy simulation approach for prediction of the ground roughness influence on wind turbine wakes. *Energies*, 15(7), 2022.

[251] R. B Stull. *An introduction to boundary layer meteorology*, volume 13. Springer Science & Business Media, 1988.

[252] T. S. Lund, X. Wu, and K. D. Squires. Generation of turbulent inflow data for spatially-developing boundary layer simulations. *Journal of Computational Physics*, 140:233–258, 1998.

[253] G. R. Tabor and M. H. Baba-ahmadi. Inlet conditions for large eddy simulation: A review. *Computers & Fluids*, 39:553–567, 2010.

[254] N. S. Dhamankar, G. A. Blaisdell, and A. S. Lyrintzis. Overview of turbulent inflow boundary conditions for large-eddy simulations. *AIAA Journal*, 56(4):1317–1334, 2018.

[255] T.G. Thomas and J.J.R. Williams. Generating a wind environment for large eddy simulation of bluff body flows. *Journal of Wind Engineering and Industrial Aerodynamics*, 82(1-3):189–208, August 1999.

[256] M. J. Churchfield, S. Lee, S. Schmitz, and Z. Wang. Modeling wind turbine tower and nacelle effects within an actuator line model. *AIAA 2015-0214: 33rd Wind Energy Symposium*, 2015.

[257] J.P. Blasques and A. Natarajan. Mean load effects on the fatigue life of offshore wind turbine monopile foundations. In *MARINE V: proceedings of the V International Conference on Computational Methods in Marine Engineering*, pages 818–829. CIMNE, 2013.

[258] L. Germanischer. Guideline for the certification of wind turbines. 2010.

[259] C. Dapogny, C. Dobrzynski, and P. Frey. Three-dimensional adaptive domain remeshing, implicit domain meshing, and applications to free and moving boundary problems. *Journal of Computational Physics*, 262:358–378, 2014.

[260] M. J Berger and P. Colella. Local adaptive mesh refinement for shock hydrodynamics. *Journal of computational Physics*, 82(1):64–84, 1989.

[261] D. Fuster, G. Agbaglah, C. Josserand, S. Popinet, and S. Zaleski. Numerical simulation of droplets, bubbles and waves: state of the art. *Fluid dynamics research*, 41(6):065001, 2009.

[262] C. E. Shannon. Communication in the presence of noise. *Proceedings of the IRE*, 37(1):10–21, 1949.

[263] I. Grant, X. Pan, P. Parkin, J. Powell, H. Reinecke, K. Shuang, F.N. Coton, and D. Lee. An experimental and numerical study of the vortex filaments in the wake of an operational, horizontal-axis, wind turbine. *Journal of Wind Engineering and Industrial Aerodynamics*, 85:177–189, 04 2000.

[264] S. Schreck, T. Sant, and D. Micallef. Rotational augmentation disparities in the uae phase vi and mexico experiments. *American Journal of Medical Genetics Part A*, 2010.

[265] P. Krogstad and M. Adaramola. Performance and near wake measurements of a model horizontal axis wind turbine. *Wind Energy*, 15:743–756, 07 2012.